Lecture Notes in Electrical Engineering 404

Yingmin Jia
Junping Du
Weicun Zhang
Hongbo Li
Editors

Proceedings of 2016 Chinese Intelligent Systems Conference

Volume I

Springer

Lecture Notes in Electrical Engineering

Volume 404

About this Series

"Lecture Notes in Electrical Engineering (LNEE)" is a book series which reports the latest research and developments in Electrical Engineering, namely:

- Communication, Networks, and Information Theory
- Computer Engineering
- Signal, Image, Speech and Information Processing
- Circuits and Systems
- Bioengineering

LNEE publishes authored monographs and contributed volumes which present cutting edge research information as well as new perspectives on classical fields, while maintaining Springer's high standards of academic excellence. Also considered for publication are lecture materials, proceedings, and other related materials of exceptionally high quality and interest. The subject matter should be original and timely, reporting the latest research and developments in all areas of electrical engineering.

The audience for the books in LNEE consists of advanced level students, researchers, and industry professionals working at the forefront of their fields. Much like Springer's other Lecture Notes series, LNEE will be distributed through Springer's print and electronic publishing channels.

More information about this series at http://www.springer.com/series/7818

Yingmin Jia · Junping Du · Weicun Zhang
Hongbo Li
Editors

Proceedings of 2016 Chinese Intelligent Systems Conference

Volume I

Springer

Editors
Yingmin Jia
Beihang University
Beijing
China

Junping Du
Beijing University of Posts
and Telecommunications
Beijing
China

Weicun Zhang
University of Science and Technology
Beijing
Beijing
China

Hongbo Li
Tsinghua University
Beijing
China

ISSN 1876-1100 ISSN 1876-1119 (electronic)
Lecture Notes in Electrical Engineering
ISBN 978-981-10-2337-8 ISBN 978-981-10-2338-5 (eBook)
DOI 10.1007/978-981-10-2338-5

Library of Congress Control Number: 2016948594

Printed on acid-free paper

This Springer imprint is published by Springer Nature
The registered company is Springer Nature Singapore Pte Ltd.
The registered company address is: 152 Beach Road, #22-06/08 Gateway East, Singapore 189721, Singapore

Contents

New Decoupling Conditions for Arbitrary Systems Based on Transcale Coupling to the Time-Derivative Order

Mingxing Li and Yingmin Jia

Abstract This paper proposes new coupling concepts: transcale coupling to the time-derivative order to give new decoupling conditions for a general system described by (A, B, C, D) quadruples. Based on these new coupling concepts, novel conditions for the diagonal/diagonal block decoupling and triangular/triangular block decoupling are obtained in the time domain.

Keywords Linear system · Transcale coupling · Time domain · Unifying conditions

1 Introduction

The decoupling problem is extensively investigated over several decades and arises in four class decoupling results which are diagonal/diagonal block and triangular/triangular block. The diagonal decoupling problem (DDP) was first initiated in [1], a necessary and sufficient solvability condition was presented by [2] in state domain, and a numerically verifiable necessary and sufficient solvability condition was given in [3] recently. The triangular decoupling problem (TDP) was first formulated by [4]. Numerically reliable methods were developed by Chu [5–7] in time domain recently. The diagonal block decoupling (DBDP) was presented firstly by Sato in [8] and the triangular block decoupling problem (TBDP) was presented in [9] by a transfer matrix approach and a stable coprime factorization method in [10].

Above mentioned and other decoupling methods such as [11–13] are all very valid and valuable for solving the decoupling problem, separately. However, the solvability decoupling conditions are quite different. It leads us to study the problem that whether there is a unifying condition or index to describe the four different decou-

M. Li (✉) · Y. Jia
The Seventh Research Division and the Center for Information and Control,
School of Automation Science and Electrical Engineering,
Beihang University (BUAA), Beijing 100191, China
e-mail: lmx196@126.com

Y. Jia et al. (eds.), *Proceedings of 2016 Chinese Intelligent Systems Conference*,
Lecture Notes in Electrical Engineering 404, DOI 10.1007/978-981-10-2338-5_1

pling results. This problem is answered partly in [14] by a frequency domain method. We will give a whole answer in time domain.

The paper is organized as follows: Sect. 2 provides some preliminary results. Section 3 establishes necessary and sufficient conditions of the four class decoupling results. Section 4 gives two examples to show the effectiveness of our results. Finally, Sect. 5 presents conclusions.

2 Problem Statement and Preliminary Results

Consider a proper LTI system described by

$$\begin{cases} \dot{x} = Ax + Bu \\ y = Cx + Du \end{cases} \tag{1}$$

where $x \in R^n, u \in R^m$ and $y \in R^p$ are the state, input, and output. For $v \in R^{m_v}$, permutation matrix P_{y_I}, and full rank G, substituting the state feedback law

$$u = Fx + Gv \tag{2}$$

into system (1) while let a new output $y_I = P_{y_I} y$, we obtain a closed-loop system which is

$$\begin{cases} \dot{x} = (A + BF)x + BGv \\ y_I = (C_I + D_I F)x + D_I G v \end{cases} \tag{3}$$

where $C_I = P_{y_I} C$ and $D_I = P_{y_I} D$. The transfer function of system (1) while its output is taken as y_I is $T(s) = C_I(sI - A)^{-1}B + D_I$. Relative to $(p_1, \ldots, p_k)$, we partition $T(s)$, C_I and D_I into

$$T(s) = \begin{bmatrix} T_1(s) \\ \vdots \\ T_k(s) \end{bmatrix}, C_I = \begin{bmatrix} C_1 \\ \vdots \\ C_k \end{bmatrix}, D_I = \begin{bmatrix} D_1 \\ \vdots \\ D_k \end{bmatrix}, y_I = \begin{bmatrix} y_{p,1} \\ \vdots \\ y_{p,k} \end{bmatrix}. \tag{4}$$

where $C_i \in R^{p_i \times n}, D_i \in R^{p_i \times m}, p_i \in Z^+$, and $\sum_{i=1}^{k} p_i = p$.

Definition 1 The static state feedback TBDP is solvable if there are F, G and permutation matrix P_{I_y} such that the transfer function of system (3) shown as

$$\hat{T}(s) \triangleq (C_I + D_I F)(sI - A - BF)^{-1}BG + D_I G \tag{5}$$

has the following triangular block form relative to partitions (4) while $G \in R^{m \times m_v}$ is full rank

$$\hat{T}(s) = \begin{bmatrix} \hat{T}_{11}(s) & 0 & \dots & 0 \\ \hat{T}_{21}(s) & \hat{T}_{22}(s) & \dots & 0 \\ \vdots & \vdots & \ddots & \vdots \\ \hat{T}_{k1}(s) & \hat{T}_{k2}(s) & \dots & \hat{T}_{kk}(s) \end{bmatrix} \tag{6}$$

where $\hat{T}_{ii}(s) \in R^{p_i \times m_i}$, $\hat{T}_{ii}(s) \neq 0, i = 1, \dots, k$. Furthermore, if $A + BF$ is stable, then the static state feedback TBDP with stability is solvable.

Remark 1 We just give the TBDP definition since the DDP, DBDP and TDP are special cases of the TBDP. Notice that, if $p_i = 1, \hat{T}_{i,j} = 0, i \neq j$ then the DDP is obtained, if there is $p_i > 1, \hat{T}_{i,j} = 0, i \neq j$ then the DBDP is obtained, and if $p_i = 1$ and there are $\hat{T}_{i,j} \neq 0, i \neq j$ then the TDP is obtained.

From [15], if $\text{rank}(D) = \bar{m}_0$ then there exist orthogonal matrix $T \in R^{m \times m}$, permutation matrix $P \in R^{p \times p}$, matrix L with non-zero rows, invertible D_t and $\bar{m}_1, \bar{m}_2 \in Z$, such that $\bar{m}_0 + \bar{m}_1 + \bar{m}_2 = p$ and

$$PDT = \begin{matrix} \\ \\ \\ \end{matrix} \begin{matrix} \bar{m}_0 & m - \bar{m}_0 \end{matrix} \begin{bmatrix} D_t & 0 \\ 0 & 0 \\ LD_t & 0 \end{bmatrix} \begin{matrix} \}\bar{m}_0 \\ \}\bar{m}_1 \\ \}\bar{m}_2 \end{matrix}. \tag{7}$$

Taking $y_p = Py$ and partitioning P, y_p, PC and $T^{-1}u$ into

$$P = \left[P_1^T, P_2^T, P_3^T\right]^T, y_p = \left[y_{p,1}^T, y_{p,2}^T, y_{p,3}^T\right]^T \tag{8}$$

$$PC = \left[C_{p,1}^T, C_{p,2}^T, C_{p,3}^T\right]^T, T^{-1}u = \left[u_{t,1}^T, u_{t,2}^T\right]^T \tag{9}$$

give

$$\begin{cases} y_{p,1} = C_{p,1}x + D_t u_{t,1} \\ y_{p,2} = C_{p,2}x \\ y_{p,3} = (C_{p,3} - LC_{p,1})x + Ly_{p,1}. \end{cases}$$

The coupling of $y_{p,1}, y_{p,2}$ and $y_{p,3}$ has three type, one is there are no coupling, another is $L \neq 0$ and $C_{p,3} - LC_{p,1} \neq 0$, the last one is $L \neq 0$ and $C_{p,3} - LC_{p,1} = 0$. Thus, we have following three new coupling conceptions

Definition 2 Complete transcale coupling to the time-derivative order (CTCTDO) If there are y_i, y_{i_0} which satisfy $y_i(s) = l_0(s)y_{i_0}(s)$ for a rational fraction matrix $l_0(s)$, then we call this type coupling complete transcale coupling to the time-derivative order.

Definition 3 Transcale coupling to the time-derivative order (TCTDO) If there are y_i, y_{i_0} which satisfy $y_i(s) = l_0(s)y_{i_0}(s) + g_i(s)u(s), y_{i_0}(s) = g_{i_0}(s)u(s)$ and Rank

$([g_{i_0}^T(s), g_i^T(s)]^T) > \text{Rank}(g_i(s))$ is physically realizable for rational fractions $l_0(s)$ and $g(s)$, then we call this type coupling transcale coupling to the time-derivative order.

Definition 4 Coupling without transcale to the time-derivative order (CWTTDO) If there are no y_{i_0} such that $y_i(s) = l_0(s)y_{i_0}(s) + g(s)u(s)$ where $l_0(s)$ and $g(s)$ are physically realizable rational fractions, then we call this type coupling without transcale to the time-derivative order (CWTTDO).

Without loss of generality, let G full column rank and $m_v \leq \min\{m, p\}$. In [9], the necessary and sufficient conditions for the TBDP of system (1) with partitions (4) while $m_v = m$ are obtained which are the following lemma:

Lemma 1 *The system (1) with transfer function $T(s)$, which is partitioned into Eq. (4) relative to $(p_1, \ldots, p_k)$, is triangularly block decouplable by a $m \times m$ proper admissible precompensator if and only if*

- $dim\left(\bigcap_{i=1}^{j-1} Ker(T_i(s))\right) > dim\left(\bigcap_{i=1}^{j} Ker(T_i(s))\right), j = 2, \ldots, k.$
- $dim(Ker(T_1(s))) < m.$

Remark 2 If $rank(T(s)C(s)) = rank(T(s))$ then physical realizable $C(s)$ is an admissible precompensator of $T(s)$.

3 Necessary and Sufficient Conditions of the Decoupling

The necessary and sufficient conditions of the four class decoupling results are given in this section. To achieve this goal, we define

$$D_1^* = \left[(d_{1,1}^*)^T, \ldots, (d_{1,p}^*)^T\right]^T \tag{10}$$

$$d_{1,1}^* = \begin{cases} d_1, \text{ if } d_1 \neq 0 \\ c_1 A^{\rho_1} B, \text{ if } d_1 = 0 \quad \text{and} \quad c_1 A^{\rho_1} B \neq 0 \\ 0, \text{ if } d_1 = 0 \text{ and } c_1 A^i B = 0, i = 1, \ldots, n \end{cases} \tag{11}$$

$$d_{1,i}^* = \begin{cases} d_i, \text{ if } rank \begin{bmatrix} D_{1,i-1}^* \\ d_i \end{bmatrix} > rank(D_{1,i-1}^*) \\ c_i A^{\rho_i} B, \text{ if } rank \begin{bmatrix} D_{1,i-1}^* \\ c_i A^{\rho_i} B \end{bmatrix} > rank(D_{1,i-1}^*) \\ \qquad and\ rank \begin{bmatrix} D_{1,i-1}^* \\ d_i \end{bmatrix} = rank(D_{1,i-1}^*) \\ c_i A^{n-1} B, \text{ if } rank \begin{bmatrix} D_{1,i-1}^* \\ c_i A^j B \end{bmatrix} = rank(D_{1,i-1}^*) \\ \qquad \text{here } j = 1, \ldots, n \end{cases} \tag{12}$$

$$D_{1,i}^{*} = \left[(d_{1,1}^{*})^{T}, \ldots, (d_{1,i}^{*})^{T}\right]^{T} \tag{13}$$

$$\rho_i = \begin{cases} -1, \text{ if } d_{1,i}^{*} = d_i \\ \min\{j | d_{1,i}^{*} = c_i A^j B, j = 0, \ldots, n-1\}. \end{cases} \tag{14}$$

With D_1^{*} of system (1), we have

Lemma 2 *rank*$(T(s)) = k_0$ *if and only if rank*$(D_1^{*}) = k_0$.

The sufficiency is easily proved. The necessity is deduced by Corollary 1 in the following content, thus it is omitted here. Lemma 2 indicates that there are two groups positive integers $(\bar{i}_1, \ldots, \bar{i}_{k_0})$, $(\rho_{\bar{i}_1}, \ldots, \rho_{\bar{i}_{k_0}})$ and $l = 2, \ldots, k_0$ such that

$$\bar{i}_j < \bar{i}_{j+1}, j = 1, \ldots, k_0 - 1 \tag{15}$$

$$\bar{D}_{k_0}^{*} = \left[(d_{1,\bar{i}_1}^{*})^{T}, \ldots, (d_{1,\bar{i}_{k_0}}^{*})^{T}\right]^{T} \tag{16}$$

$$\bar{i}_1 = \min\{i | \text{rank}(D_{1,i}^{*}) = 1\} \tag{17}$$

$$\bar{i}_l = \min\{i | \text{rank}(D_{1,i}^{*}) > \text{rank}(D_{1,i-1}^{*}), i > \bar{i}\ \}. \tag{18}$$

and $\text{rank}(\bar{D}_{k_0}^{*}) = k_0$. Moreover, for $i = 1, \ldots, p$ define

$$\sigma_i = \begin{cases} -1, \text{ if } d_i \neq 0 \\ \min\{j | d_i = 0, c_i A^j B \neq 0, j = 0, \ldots, n-1\} \end{cases} \tag{19}$$

then $\rho_i \geq \sigma_i$. Moreover, by combining (13) and (14) with Lemma 1, we get

Theorem 1 *For system (1) with partitions (4) relative to* $(p_1, \ldots, p_k)$*, the TBDP is solvable if and only if there exist* $y_{\bar{i}_j}, j = 1, \ldots, k_0$ *which is a vector component of* $y_{p,i}, i = 1, \ldots, k$.

Proof From (4), partitions of $T(s)$ can be rewritten as

$$T_i(s) = C_i(sI - A)^{-1}B + D_i, i = 1, \ldots, k \tag{20}$$

There are at least one $y_{\bar{i}_j}, j = 1, \ldots, k_0$ which is a vector component of $y_{p,i}$ for all $i = 1, \ldots, k$ implies

- $\dim\left(\bigcap_{i=1}^{j-1} \ker(T_i(s))\right) > \dim\left(\bigcap_{i=1}^{j} \ker(T_i(s))\right), j = 2, \ldots, k$
- $\dim(\ker(T_1(s))) < m$.

Thus, the sufficiency is derived by Lemma 1.

Assume there is $i_0 \in \{1, \ldots, k\}$ such that all components of y_{p,i_0} are not $y_{\bar{i}_j}$ for any $j = 1, \ldots, k_0$. Since

$$y_{p,i_0}^{(n)} = C_{i_0}A^n x + C_{i_0}A^{n-1}Bu + \cdots + C_{i_0}Bu^{(n-1)} + D_{i_0}u^{(n)}$$

and applying Lemma 2 into $T_{i_0}(s)$ gives

$$\begin{aligned} T_{i_0}(s) &= \sum_{j=0}^{n-1} \frac{r_{j+1}}{s^{j+1}} C_{i_0} A^j B + D_{i_0} \\ &= \sum_{j=0}^{n} \frac{r_j}{s^j} \sum_{l=1}^{k_{1,0}} t_{j,l} d^*_{1,\bar{i}_l} \end{aligned} \tag{21}$$

where $k_{1,0} \in \{1, \ldots, k_0\}, r_0 = 1$, we have

$$\bigcap_{j=1}^{k_{1,0}} (\ker(d^*_{\bar{i}_j})) \subset \ker(T_{i_0}(s))$$

Furthermore, from Lemma 2 and above results, we get

$$\bigcap_{j=1}^{i_0-1} \ker(T_j(s)) \subset \bigcap_{j=1}^{k_{1,0}} (\ker(d^*_{\bar{i}_j})) \subset \ker(T_{i_0}(s)) \tag{22}$$

$$\bigcap_{j=1}^{i_0} \ker(T_j(s)) \equiv \bigcap_{j=1}^{i_0-1} \ker(T_j(s)) \tag{23}$$

then for system (1) partitioned into (4), the TBDP is solvable while (23) is established. This result conflicts with Lemma 1. Thus, the necessity is obtained and Theorem 1 is proved.

Corollary 1 *For $i, i \notin \{\bar{i}_1, \ldots, \bar{i}_{k_0}\}$ and $i \in \{1, \ldots, p\}$, define*

$$j = \max\{l_1 | l_1 \in \{1, \ldots, k_0\}, \bar{i}_{l_1} < i\} \tag{24}$$

then there are $h_l(s), l = 1, \ldots, j$ such that

$$y_i = \sum_{l=1}^{j} h_l(s) y_{\bar{i}_l} \tag{25}$$

for system (1) with new output y_I and feedback law (2).

Proof For i with $i \notin \{i_1, \ldots, i_{k_0}\}, i \in \{1, \ldots, p\}$, j defined by (24) exists. Using the Laurent expansion gets

$$t_i(s) = \sum_{l=0}^{n} \frac{r_l}{s^l} \sum_{\bar{l}=1}^{j} t_{l,\bar{l}} d^*_{1,\bar{i}_{\bar{l}}}$$

where $r_0 = 1$, $t_i(s)$ is the ith row vector of $T(s)$. Thus for any $i \notin \{\bar{i}_1, \ldots, \bar{i}_{k_0}\}$, there exist rational $f_1(s), \ldots, f_j(s)$ such that

$$t_i(s) = \sum_{\bar{l}=1}^{j} f_{\bar{l}}(s) d^*_{1,\bar{i}_{\bar{l}}} \tag{26}$$

Furthermore, we define $\bar{T}_j(s)$ as

$$\bar{T}_j(s) = \left[t^T_{\bar{i}_1}(s), \ldots, t^T_{\bar{i}_j}(s) \right]. \tag{27}$$

It is easy to obtain that $\bar{T}_j(s)$ is full row rank and there is a rational matrix $\bar{T}_{j\perp}(s)$ such that $\bar{T}_{1,j}(s)$ invertible and

$$\bar{T}_{1,j}(s) = \left[\bar{T}^T_j(s), \bar{T}^T_{j\perp}(s) \right]^T, \ \bar{T}_j(s) T^T_{j\perp}(s) \equiv 0.$$

Defining $h(s) = t_i(s)(\bar{T}^T_{1,j}(s)\bar{T}_{1,j}(s))^{-1}\bar{T}^T_j(s)$ gets

$$\begin{aligned} t_i(s) &= t_i(s)\bar{T}^T_{1,j}(s)\bar{T}_{1,j}(s)(\bar{T}^T_{1,j}(s)\bar{T}_{1,j}(s))^{-1} \\ &= t_i(s)(\bar{T}^T_{1,j}(s)\bar{T}_{1,j}(s))^{-1}\bar{T}^T_j(s)\bar{T}_j(s) \\ &= h(s)\bar{T}_j(s) \end{aligned} \tag{28}$$

From Eq. (28), we get Eq. (25) for system (1) with feedback law (2).

Remark 3 From (28), $rank(T(s)) = rank(\bar{T}_{k_0}(s))$, thus the necessity of Lemma 2 is naturally concluded, Theorem 1 is established.

Corollary 2 *The DBDP of system (1) with partitions (4) is solvable if and only if there are only coupling without transcale to the time-derivative order between $y_{p,i}$ and $y_{p,j}$ for $i, j \in \{1, \ldots, k\}$ and $j \neq i$, and the DDP is solvable if and only if there are also have $k_0 = p = m$. TDP is solvable if there are no complete transcale coupling to the time-derivative order and $k_0 = p = m$.*

4 Numerical Example

Two more general examples are illustrated to show the effectiveness of our method. The first one is

$$A = \begin{bmatrix} -4.1476 & 1.4108 & 0.0633 \\ 0.2975 & -3.1244 & 0.0623 \\ -0.0429 & -0.1729 & -0.1325 \end{bmatrix}, \ B = \begin{bmatrix} 0.2491 & 0.0969 & -0.0112 \\ 0.2336 & 0.0335 & 0.0047 \\ 0.0624 & 0 & 0 \end{bmatrix}$$

$$C = \begin{bmatrix} 8.7379 & 0 & 0 \\ -3.3033 & 3.8052 & 0.0542 \\ 2.1940 & -2.5749 & -0.0295 \end{bmatrix}, \; D = \begin{bmatrix} 0 & 0 & 0 \\ 0.2383 & -0.2748 & 0.0224 \\ -0.1455 & 0.0580 & -0.2293 \end{bmatrix}$$

It is easy to obtain that $k_0 = 3$, $\rho_1 = \delta_1 = 0$ and $\rho_2 = \delta_2 = \rho_3 = \delta_3 = -1$, thus this system is diagonally decouplable. By our method, we get a diagonal decoupling controller as follows:

$$F = \begin{bmatrix} -14.7267 & -1.2687 & -0.2640 \\ -23.7392 & 12.1478 & -0.0292 \\ 12.9083 & -7.3517 & 0.0315 \end{bmatrix}, \; G = \begin{bmatrix} 2.1356 & -2.1400 & -0.4911 \\ 1.7782 & -5.4974 & -0.7719 \\ -0.9054 & -0.0326 & -4.2447 \end{bmatrix}$$

and the closed-loop system is stable and the transfer function is

$$T(s) = \begin{bmatrix} t_{11}(s) & 0 & 0 \\ 0 & t_{22}(s) & 0 \\ 0 & 0 & t_{33}(s) \end{bmatrix}.$$

Thus, the diagonal decoupling is achieved.

The second example is constructed to show our decoupling method further. Matrices A, B, C, D of (1) are taken as

$$A = \begin{bmatrix} -1.3757 & 0.3261 & 0.4995 & -0.5721 & 0 \\ 0.2702 & -1.1435 & -0.8610 & 0.4206 & 0 \\ 0.8118 & -1.2524 & 0.3698 & -0.1262 & 0 \\ -0.5691 & 0.3981 & -0.0216 & -4.8505 & 0 \\ 0 & 0 & 0 & 0 & 1.5567 \end{bmatrix}$$

$$B = \begin{bmatrix} 13.1252 & -6.5409 & 4.0484 & 4.0484 & 0 \\ -0.4581 & -14.8132 & -4.3977 & -4.3977 & 0 \\ 20.8573 & 18.3359 & -3.7853 & -3.7853 & 0 \\ 1.5788 & -3.4030 & -1.3937 & -1.3937 & 0 \\ 0 & 0 & 0 & 0 & 2.3867 \end{bmatrix}$$

$$C = \begin{bmatrix} -0.0637 & -0.0519 & -0.0093 & 0.0041 & 0 \\ 0.0959 & -0.1180 & -0.0126 & -0.0323 & 0 \\ 0.0537 & -0.0397 & -0.0101 & 0.3089 & 0 \\ 0 & 0 & 0 & 0 & 4.6789 \end{bmatrix}$$

$$D = \begin{bmatrix} 1 & -1 & 0 & 0 & 0 \\ -1 & 1 & 0 & 0 & 0 \\ 0 & 0 & 0 & 0 & 0 \\ 0 & 0 & 0 & 1 & 0 \end{bmatrix}$$

By directly computing, we get $\rho_1 = \rho_4 = -1$, $\rho_2 = 0$, $\rho_3 = 4$ and $rank(D^*_{1,k}) = 2$ where

$$D_{1,k}^{*}=\begin{bmatrix} d_1 \\ c_2B \\ c_3A^4B \\ d_4 \end{bmatrix}=\begin{bmatrix} 1 & -1 & 0\,0\,0 \\ 1 & 1 & 1\,1\,0 \\ 625 & -625 & 0\,0\,0 \\ 0 & 0 & 0\,1\,0 \end{bmatrix}$$

thus this system is transcale coupling. Furthermore, $k_0 = k = 3 < p$, thus this system is triangular block decouplable, $y_{p,1} = y_1,\ y_{p,2}^T = [y_2, y_3],\ y_{p,3} = y_4, \bar{i}_1 = 1, \bar{i}_2 = 2, \bar{i}_3 = 4$, and

$$C=\begin{bmatrix} C_1 \\ C_2 \\ C_3 \end{bmatrix}=\begin{bmatrix} c_1 \\ \begin{bmatrix} c_2 \\ c_3 \end{bmatrix} \\ c_4 \end{bmatrix},\ D=\begin{bmatrix} D_1 \\ D_2 \\ D_3 \end{bmatrix}=\begin{bmatrix} d_1 \\ \begin{bmatrix} d_2 \\ d_3 \end{bmatrix} \\ d_4 \end{bmatrix}$$

$$\bar{C}=\begin{bmatrix} c_1 \\ c_2 \\ c_4 \end{bmatrix},\ \bar{D}=\begin{bmatrix} d_1 \\ d_2 \\ d_4 \end{bmatrix},\ P_0=\begin{bmatrix} 1\,0\,0 \\ 0\,0\,1 \\ 0\,1\,0 \end{bmatrix},\ P_{y_I}=\begin{bmatrix} 1 & 0 & 0 \\ 0 & 0 & 1 \\ 0 & I_{2\times 2} & 0 \end{bmatrix}$$

then, we get

$$F=\begin{bmatrix} 0.0035 & 0.0753 & -0.0967 & 0.0190 & 0 \\ -0.0594 & 0.0308 & -0.1045 & -0.0023 & 0 \\ -0.1406 & 0.1580 & 0.1018 & 0.0481 & 0 \\ 0 & 0 & 0 & 0 & 0 \\ 0 & 0 & 0 & 0 & -3.1662 \end{bmatrix}$$

$$G=\begin{bmatrix} 2.7194 & -0.1090 & -3.4559 & 2 & 1 \\ 0 & 0 & -1 & 1 & 4 \\ 0.0081 & 0.0081 & 0.0993 & 0 & 0 \end{bmatrix}^T$$

The transfer function from v to $P_{I_y} y$ has the following form:

$$T(s)=\begin{bmatrix} T_{11}(s) & 0 & 0 \\ T_{21}(s) & T_{22}(s) & 0 \\ T_{31}(s) & 0 & T_{33}(s) \\ T_{41}(s) & 0 & T_{43}(s) \end{bmatrix}$$

Thus $P_{y_I} y$ and v is triangularly block decoupled and stable.

5 Conclusions

New coupling concepts, CTCTDO, TCTDO, and CWTTDO, are proposed to give new decoupling conditions for a general system described by (A, B, C, D) quadruples. Based on these new coupling concepts, the new conditions for the diagonal/diagonal

block decoupling and triangular/triangular block decoupling are obtained in the time domain. The numerical computable static feedback decoupling laws should be derived, robust decoupling and the combined problem with disturbance rejection should be pursued in more depth in the future.

Acknowledgments This work was supported by the National Basic Research Program of China (973 Program: 2012CB821200, 2012CB821201), the NSFC (61134005, 61327807, 61521091, 61520106010), and the Fundamental Research Funds for the Central Universities (YWF-16-GJSYS-31,YWF-16-GJSYS-32).

References

1. Morgan BS (1964) The synthesis of linear multivariable systems by state variable feedback. IEEE Trans Autom Control AC-9(4):404–411
2. Falb PL, Wolovich WA (1967) Decoupling in design and synthesis of multivariable control systems. IEEE Trans Autom Control AC-12(6):651–669
3. Chu D, Malabre M, Tan RCE (2009) State feedback decoupling problem with stability for (A, B, C, D) quadruples. SIAM J Matrix Anal Appl 30(4):1735–1760
4. Morse AS, Wonham WM (1970) Triangular decoupling of linear multivariable systems. IEEE Trans Auto Control 15(4):447–449
5. Chu D, Tan RCE (2002) Numerically reliable computation for the row by row decoupling problem with stability. SIAM J Matrix Anal Appl 23(4):1143–1170
6. Chu D, Tan RCE (2002) Solvability conditions and parameterization of all solutions for the triangular decoupling problem. SIAM J Matrix Anal Appl 23(4):1171–1182
7. Chu D, Hung YS (2006) A matrix pencil approach to the row by row decoupling problem for descriptor systems. SIAM J Matrix Anal Appl 28(3):682–702
8. Sato SM, Lopresti PV (1971) On the generalization of state feedback decoupling theory. IEEE Trans Autom Control 16(2):133–139
9. Commault C, Dion JM (1983) Transfer matrix approach to the triangular block decoupling problem. Automatica 19(5):533–542
10. Gómez GI, Goodwin GC (2000) An algebraic approach to decoupling in linear multivariable systems. Int J Control 73(7):582–599
11. Descusse J, Lizarzaburu R (1979) Triangular decoupling and pole placement in linear multivariate systems. Int J Control 30(1):139–152
12. Nguyen HT, Su SW (2009) Conditions for triangular decoupling control. Int J Control 82(9):1575–1581
13. Vafiadis D, Karcanias N (2003) Block decoupling and pole assignment of singular systems: a frequency domain approach. Int J Control 76(2):185–192
14. Williams TWC, Antsaklis PJ (1986) A unifying approach to the decoupling of linear multivariable systems. Int J Control 44(1):181–201
15. Li M, Jia Y, Du J, Zhang J (2014) Input-output decoupling by output feedback with disturbance attenuation of H_∞ control for any square system. Int J Control 87(10):1999–2011

Determination of the Vehicle Relocation Triggering Threshold in Electric Car-Sharing System

Guangyu Cao, Lei Wang, Yong Jin, Jie Yu, Wanjing Ma, Qi Liu, Aiping He and Tao Fu

Abstract The electric car-sharing system is an arising and promising urban transportation mode. Vehicle unbalance usually occurs in multi-station electric car-sharing systems. Threshold triggering method is the most practicable approach for vehicle relocation, while determination of thresholds is the key problem. This paper presents a method for the thresholds determination. First, a prototype of two-stage method is proposed to illustrate the function of upper and lower thresholds. Subsequently, an optimization-based model is derived to determine the thresholds under the objective of minimizing the out-of-service rate and number of moving vehicles. Order data of EVCard system in Shanghai, China was employed to test the method. The results indicate that the proposed calculative method lead to relative better service rate and less moving times.

Keywords Car sharing · Electric vehicle · Vehicle relocation · Threshold determination · EVCard

1 Introduction

Car-sharing system has been regarded as an emerging promising transportation mode, which contains a fleet of vehicles and several stations that allows members to access and return immediately and pay for their occupation hourly [1]. Technically, car-sharing system requires high quality of information accessibility and high efficiency of payment, while the popularity of mobile communication makes it possible for users to access information freely and instantly. Economically, con-

G. Cao · Y. Jin · J. Yu · A. He
Shanghai International Automobile City Group Co., Ltd., 904A, No.888, South Moyu Road, Anting Town, Jiading District, Shanghai 201805, China

L. Wang (✉) · W. Ma · Q. Liu · T. Fu
College of Transportation Engineering, Tongji University, 4800 Cao'an Road, Shanghai 201804, China
e-mail: wangleicuail@gmail.com

Y. Jia et al. (eds.), *Proceedings of 2016 Chinese Intelligent Systems Conference*, Lecture Notes in Electrical Engineering 404, DOI 10.1007/978-981-10-2338-5_2

temporary people are becoming more inclined to share cars instead of owning a car due to the low frequency of usage of a car and the low costs of electric vehicle (EV) [2]. Researches also suggest that car-sharing system has advantages on improving mobility, lowering emission, reducing traffic congestion, and saving parking space.

During the past decade, car-sharing mode has been widely practiced in Europe, North America, Japan, and Singapore [3–6]. Since the recent 5 years, as a result of a combination of the Internet revolution, the sharing economy boom, the awareness of resource and energy consumption, and the consciousness of carbon emission and pollution, car-sharing mode have obtained more and more attention as a new component in urban transportation structures. In China, the clear energy vehicle encouragement policy stimulates the electric vehicle sharing mode as a frontier to popularize the electric vehicle, which makes the electric car-sharing system as an arising market in urban transportation in China [7].

Multi-station car-sharing systems in large scale usually allow users to pickup and return vehicles at different stations, which will bring convenience to costumers and improve the service quality, however, accompanied with unbalance of vehicles location [8]. Hence, vehicle relocation is quite necessary to satisfy users' demand, keep the vehicle supply in balance, make full use of facilities, and maximize the profits. With the unprecedented expansion of car-sharing services, especially EV-sharing services in China, the vehicle relocation theory and techniques become even more urgent. Taking the EVCard—an EV-sharing system operated by Shanghai automobile city—as an example, the system was established and tested in 2013–2014, and started to operate in 2015. The system owned 56 stations and 120 vehicles in April 2015, and more than 200 stations and 500 vehicles by December 2015. System unbalance problem appeared more and more serious and the vehicle relocation method is pivotal to support the system for sustainable operation and development.

Another fact is that car relocation is not as easy as bicycle or container relocation. Conventionally, bicycles or containers can be conveyed in large scale. However, car-sharing stations are generally scattered in intensive urban area, which disallow large freight truck to deliver [9]. Car towing and staff driving are two typical measures, where towing refers to the pulling of one car by another, and staff driving refers to relocating a car by a pair of staffs with a working car, but both of them have restricted relocation capability.

These facts have made the car relocation problem attractive to many researchers. According to the basic thinking, the vehicle relocation methods can be divided into three categories: demand prediction-based method, dynamic optimization method, and threshold method [10–12].

- Demand prediction-based method. It refers to acquiring the demand patterns and deploying vehicles as predicted demand. In practice, the demand patterns are not quite obvious and stable, and the users' demands are somehow stochastic, which makes demand prediction not reliable enough [13].

- Dynamic optimization method. These methods have been subsequently introduced to acknowledge the stochastic changing of demand, which are complicated on dynamic stochastic solving [14].
- Threshold method. It is a triggering mechanism to decide whether vehicles should move in or move out in a station, and is clearly available for operator to practice [15].

In practice of EVCard, we have found that the threshold method appropriate and adoptable, because of the very random demand and its request on simplex method. For the threshold method, paper [15] presents a three-phase method which employs station thresholds as the triggering values and regards threshold as a necessary step of their procedure. Paper [16–18] also involve the threshold as a condition of car relocation. However, to the best of our knowledge, these researches generally set the thresholds as known, or decide the thresholds empirically, and there are seldom researches that gives detail on how to determine the threshold of each station.

In this paper, the authors propose a method to determine the vehicle relocation triggering threshold, which is the key parameters in the mechanism to decide when the station should move in or move out vehicles (in Sect. 2). Section 3 presents the threshold determination method: first the state transition model is constructed to describe the dynamic process of the pickup and return phenomenon of a station, then based on the state variables transition, a vehicle moving number minimization model is developed to find out the optimum value of the thresholds. In Sect. 4, the order data and the station data of EVCard in April 2015 were adopted as a calculation example to demonstrate the process of the method.

2 Basic Thinking on Threshold Method

In this part, a basic two-stage prototype of threshold method is proposed to address the car relocation problem. In this prototype, we focus on the determination of the threshold, which is the main idea of this paper.

2.1 Stages of Threshold Relocation Method

When should vehicles be moved into or out of a station? Typically, when there is no available car in the station (which means users cannot get a vehicle from the station or cannot access the service), vehicles should be located in; when there is no available parking space in the station (which means users cannot return a vehicle to the station or the service quality is bad), vehicles should be move out from the station.

So the number of vehicles in the station should be controlled by car relocation as much as possible to avoid the condition out of service. For a general station, the first

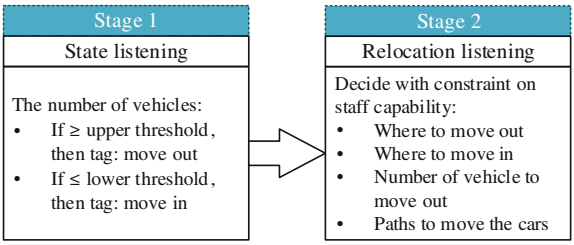

Fig. 1 The two-stage threshold based relocation method

stage is to monitor the number of vehicles in the station and decide the occasion to move in or move out; the second stage is to match proper pairs of stations where one is to move out cars and the other is to move in cars, i.e., where the overflowing cars should be relocate to. This two-stage method is shown in Fig. 1.

- **Stage 1**: state listening. The system listens to the change of the number of vehicles (the state variable) in each station. If the number of vehicles of a station accumulated above an upper threshold, tag the station as which need moving out cars (overflowing); if the number of vehicles of a station decreased below a lower threshold, tag the station as which need moving in cars (lacking).
- **Stage 2**: relocation listening. The system listens to the relocation tag of each station and decides the optimum solution of path to move vehicles from overflowing stations to lacking stations.

To this two-stage method, it should be noted that the two stages are relatively independent, i.e., the state listening decides when it should work and the relocation listening decide how it will work. In such case, relocating staff capability restricts the relocation processing in stage 2, but the stage 1 should tell whether each station should move cars in or out in advance, no matter whether the relocation would be successful. Another concern is that the upper and lower thresholds are pre-decided in order to make the monitoring mechanism work, so the method to determine the upper and lower thresholds of each station is necessary.

2.2 Thinking on Threshold Determination

Define the pickup and return counter as an accumulator which plus 1 if user returns one vehicle and minus 1 if user pickup one vehicle. If the initial number of the counter equals the number of vehicles in the station at the initial moment, the counter indicates the change of the number of vehicles in this station.

Figure 2 shows the pickup and return counter at two example stations in EVCard system. Figure 2a suggests that the returned cars are more than the pickup cars that would fill the station, which lead to the condition that user cannot return car to this station anymore if cars were not moved out. Figure 2b suggests that the pickup

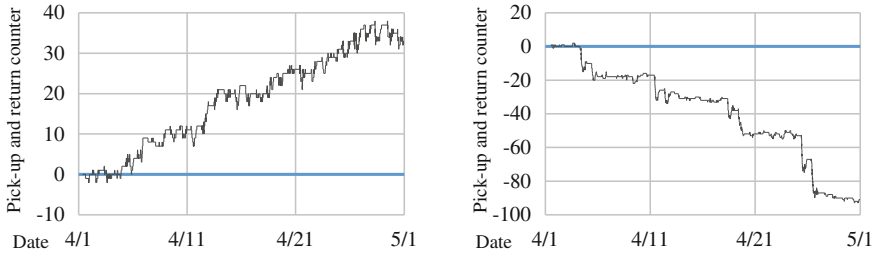

a. Station A: Tongji University Jiading Campus b. Station B: Jiatinghui Shopping Center

Fig. 2 The pickup and return counter at two example stations

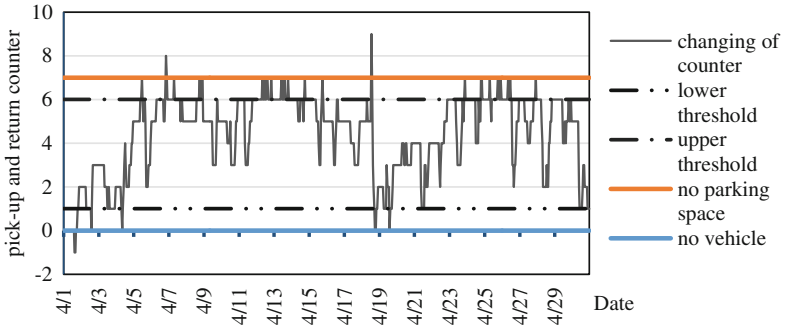

Fig. 3 Thresholds to control the pickup and return counter changing within a proper range

demands are more than the returned cars, which make the station unavailable for following demands if cars were not moved in.

The aim of setting the upper and lower thresholds is to maintain the pickup and return counter within a proper range that can satisfy the pickup and return requests (as shown in Fig. 3).

Considering that the threshold determination is the precondition before the car relocation, and the staff capability only restricts the stage 2 as well as the thresholds in stage 1 only offer the if-or-not signal for stage 2, in threshold determination, suppose that all the move in or out operations can be satisfied in each station.

For each station, there are two basic principles to decide the thresholds

- Service unavailable rate—lower. This implies that the system should satisfy the users' demands as much as possible.
- Number of moving cars—lower. This implies that the operator wants to lower its costs on relocating cars.

3 Threshold Determination Method

Generally, the pickup or return requests happen stochastically with time, so that the pickup and return counter (or the number of vehicles in the station) would dynamically and randomly change with time (as illustrated in Figs. 2 and 3). The upper and lower thresholds are unknown but fixed decision variables. The solving method for the thresholds would be quite particular to conventional optimization method.

To solve the variables of thresholds, the first step is to establish the state transition equations for describing the feature of the change with time in a station. Subsequently, the optimization objectives can be inferred from the state transition equations, as well as the constraints.

3.1 Vehicle Counter State Transition Equations

Set the pickup and return counter (or the number of vehicles in the station) as the state variable, to monitor the change of the state of the station, and the state transition equation of the variable can be given as formula (1) and its supplementary formulae (2)–(6), where symbols are defined in Table 1.

$$X_t = X_{t-1} + r_t - d_t + \delta_t. \tag{1}$$

Table 1 Definition of the symbols in the vehicle counter state transition equations

Symbol	Definition
t	The tth time segment, $t = 0, 1, \ldots, T$, and 0 is the initial time segment
T	The number of total time valid segments
X_t	The pickup and return counter in time t
r_t	The number of cars that are returned to the station and available in time t
d_t	The number of cars that are picked up at the station in time t
δ_t	The number of cars actually moved in or out in time t
$\delta_t^{'}$	The number of cars that need to be moved in or out in time t
s_t	The tag on whether there are cars moved in or out in time t
u_t	The tag on whether the pickup or return requests are satisfied in time t
t_{in}	Average moving time on moving cars into the station
t_{out}	Average responding time on moving cars out from the station
N	The maximum number of the parking space in the station
$S_{\max}$	Upper threshold to respond cars moving out
$S_{\min}$	Lower threshold to respond cars moving in

Define:

$$X_t^{'} = X_{t-1} + r_t - d_t; \tag{2}$$

$$\delta_t^{'} = \begin{cases} S_{\max} - X_t^{'}, & X_t^{'} \geq S_{\max} \\ 0, & S_{\min} < X_t^{'} < S_{\max} \\ S_{\min} - X_t^{'}, & X_t^{'} \leq S_{\min} \end{cases}; \tag{3}$$

$$\delta_t = \begin{cases} \delta_{t-t_{out}}^{'}, & X_t^{'} \geq S_{\max} \\ 0, & S_{\min} < X_t^{'} < S_{\max} \\ \delta_{t-t_{in}}^{'}, & X_t^{'} \leq S_{\min} \end{cases}; \tag{4}$$

$$s_t = \begin{cases} -1, & X_t^{'} \geq S_{\max} \\ 0, & S_{\min} < X_t^{'} < S_{\max} \\ 1, & X_t^{'} \leq S_{\min} \end{cases}; \tag{5}$$

$$u_t = \begin{cases} -1, & X_t \geq N \\ 0, & 0 < X_t < N \\ 1, & X_t \leq 0 \end{cases}. \tag{6}$$

Formula (1) implies that the number of vehicles in the station in time t equals the number of vehicles time $t - 1$ plus the number of cars that are returned to the station in time t minus the number of cars that are picked up at the station in time t then plus the number of vehicles that are actually moved into or out of the station. It should be noted that the number of cars that need to be moved in or out in time t is judged by the state variable with the thresholds (given by formula (3)), but because of the responding delay for moving cars, the actual moved number of cars at time t is given by formula (4). s_t and u_t are the detecting variables to summarize the number of moved cars and the service quality.

3.2 Thresholds Determination

Optimization techniques are employed in the thresholds determination. The final result of this model is to output the upper and lower thresholds of a station, so the decision variables are $S_{\max}$ and $S_{\min}$. In the state transition equations, $S_{\max}$ and $S_{\min}$ are not explicit in equation but as the condition of the piecewise functions, which brings peculiarity to this model. $S_{\max}$ and $S_{\min}$ are implicated in detecting variables s_t and u_t, which describe the performance of the model from two opposite direction.

Note that the principles to determine the thresholds include the moving costs and the service quality. If operator wanted to keep the relocation costs lower that may lead to more bad services, while if operator wanted to improve the service quality that may increase the relocation times. Giving the number of moved vehicle σ as

$$\sigma = \sum_{t=0}^{T} s_t \delta_t, \tag{7}$$

where $\sigma \in [0, +\infty)$ and σ is an integer. To make it compatible with the other objective, normalize σ as

$$\sigma' = \sigma / \max_{\forall S_{\max}, \forall S_{\min}} \sigma. \tag{8}$$

To describe the service quality, give the ratio of out-of-service time to the total time ρ as

$$\rho = \frac{1}{T} \sum_{t=0}^{T} |u_t|, \tag{9}$$

and $\rho \in [0, 1]$. To balance both sides of consideration, set weight ω_1 and ω_2. if $\omega_1 > \omega_2$, the model is more likely to take the costs in account, otherwise to consider service quality more.

$$\min y = \omega_1 \sigma' + \omega_2 \rho; \tag{10}$$

and for both weights there is

$$\omega_1 + \omega_2 = 1. \tag{11}$$

Constraints of this model are given as follows:
Subject to

(1) $S_{\max}$ and $S_{\min}$ are integers.
(2) Lower threshold should be lower than the upper threshold

$$S_{\min} < S_{\max}. \tag{12}$$

(3) Upper threshold should not be higher than the number of parking space

$$S_{\max} \leq N. \tag{13}$$

(4) Lower threshold should not be lower than 0

$$S_{\min} \geq 0. \tag{14}$$

(5) Give the initial condition of the pickup and return counter

$$X_0 = X. \tag{15}$$

where X is the initial number of vehicles in the station at the beginning of the study time segments. X can be 0 if initial number of vehicles is unknown.

To solve this model, the major obstacle lies on the hidden variables in state transition equations. The decision variables S_{max} and S_{min} are implicit in the piecewise conditions and not explicit in optimization objectives. This feature makes the objective function nonlinear and hard to formularize. Since the decision variables S_{max} and S_{min} are integers and finite, and other variables are determinable through S_{max} and S_{min}, enumeration would be feasible to determine the most proper solution.

4 Results and Discussions

To demonstrate the threshold determination method, two typical stations given in Fig. 2—station A: Tongji University Jiading Campus and station B: Jiatinghui Shopping Center—are taken as examples. The orders of EVCard in April, 2015, including information about the pickup time, return time, pickup station, and return station are involved as the input data. Upper thresholds and lower thresholds of both stations are as the outputs. In this demonstration, we set $\omega_1 = \omega_2 = 0.5$ to take the relocation costs and service quality as the same importance. The state transition of the pickup and return counter graphs and the calculation results are shown in Fig. 4.

An interesting discovery from the results should be drawn that the station with more returning vehicles could get lower upper threshold and the station with more

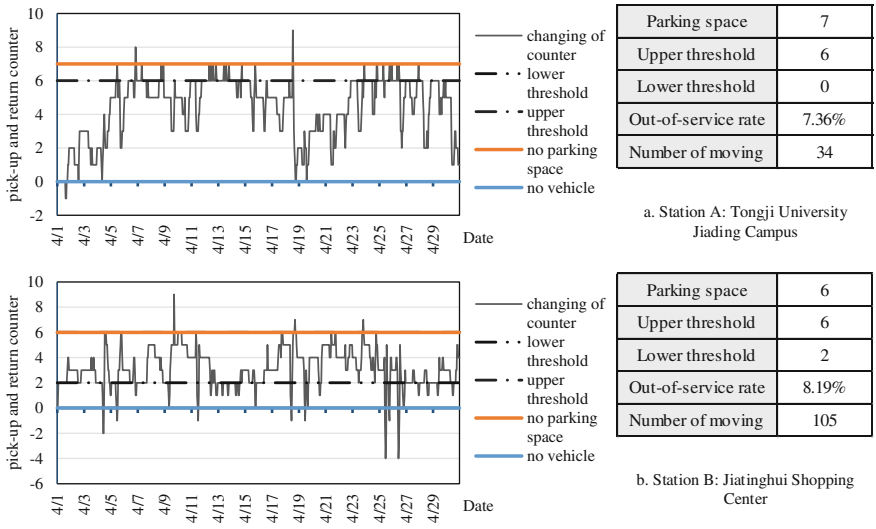

Fig. 4 The pickup and return counter graphs and the calculation results

Table 2 A comparison between the calculative method and the qualitative principle

	Station A		Station B	
	Calculative	Qualitative	Calculative	Qualitative
Parking space	7	7	6	6
Upper threshold	6	6	6	5
Lower threshold	0	1	2	1
Out-of-service rate (%)	7.36	10.56	8.19	12.78
Number of moving	34	36	105	104

pickup vehicles could get higher lower threshold. That is to say, when station has more return requests (as phenomenon of station A), the upper threshold should be lower to detect and respond to the returning overflowing vehicles, and the parking space should be enough for returning cars, but the lower threshold can be 0 because the returning cars will fulfill the pickup requests without additional cars moving in. Station B presents a phenomenon of more pickup requests than return, so that higher lower threshold will keep the station available on pickup cars, and returning cars may be more likely to be picked up, so less chance would the counter meet the maximum parking space and the overflowing cars be moved out.

To the most circumstances, we want this threshold determination solution to be more proper than other determination strategy. A qualitative determination principle is to ensure that there is at least one vehicle at the station and at least one parking space, so that the service on pickup requests and return requests can be both guaranteed. A comparison between the results by determination solution and the qualitative principle among both stations are drawn in Table 2. With better or similar number of moving, the calculative method achieves lower out-of-service rate or better service quality.

Considering that the pattern of the demand of the system and the feature of the requests of pickup and return at each station may not stable and can be influenced by some unknown or uncertain factors change, the thresholds should not be fixed. In practice, the thresholds need to be updated every time cycle, e.g., a week or a month, in order to make the vehicle relocation more reasonable and optimal.

5 Conclusions

Since the threshold determination is a critical problem in the threshold method for vehicle relocation method in electric car-sharing systems, and previous researches did not sufficiently focus on the determination of the thresholds, this paper presents an approach on determining the upper and lower thresholds. Upper threshold and lower threshold are respectively triggering conditions on vehicles moving in and out. First, a prototype of two-stage method was proposed to establish a mechanism, including state listening and relocation listening, in which the thresholds are pivotal

to drive both stages. Consequently, an optimization model was introduced to find out proper values of upper and lower thresholds. In this model, we established the state transition equations to describe the changing features of car number in a station, and involved both relocation costs and service quality into the optimization objective, in order to resolve the best values of the thresholds.

The pickup and return counter graphs are employed to demonstrate the results of the model, and the out-of-service rate and number of moving are evaluation indexes to present the relocation efficiency under the decision of the thresholds. The results showed that the method is capable to determine proper values of thresholds, and the calculative optimal method can be more reasonable than qualitative principles.

Although threshold method makes electric vehicle relocation problem in car-sharing system more practicable, there is still wide space to be discovered for researchers in electric vehicle fleet control and management especially vehicle relocation problems. Actually the threshold method involves deterministic parameters namely thresholds to cope with plentiful uncertainty in demand and system changing. In the future, with the introduction of stochastic method, fleet management, and car relocation in such systems, will become more intelligent, effective, and efficient.

Acknowledgments This work was supported by the Science and Technology Commission of Shanghai Municipality in project "Research and Application on the Key Technology of Connective Electric Vehicle Sharing System Fleet Management".

References

1. Katzev R (2003) Car sharing: a new approach to urban transportation problems. Anal Soc Issues Public Policy 3:65–86
2. Kley F, Lerch C, Dallinger D (2011) New business models for electric cars—a holistic approach. Energy Policy 39:3392–3403
3. Barth M, Shaheen S, Fukuda T, Fukuda A (2006) Carsharing and station cars in Asia: overview of Japan and Singapore. Transp Res Rec J Transp Res Board 106–115
4. Musso A, Corazza MV, Tozzi M (2012) Car sharing in Rome: a case study to support sustainable mobility. Proc Soc Behav Sci 48:3482–3491
5. Shaheen S, Cohen A, Roberts J (2006) Carsharing in North America: market growth, current developments, and future potential. Transp Res Rec J Transp Res Board 116–124
6. Shaheen S, Sperling D, Wagner C (2001) Carsharing in Europe and North American: past, present, and future. University of California Transportation Center
7. Zheng J, Mehndiratta S, Guo JY, Liu Z (2012) Strategic policies and demonstration program of electric vehicle in China. Transp Policy 19:17–25
8. Febbraro A, Sacco N, Saeednia M (2012) One-way carsharing: solving the relocation problem. Transp Res Rec J Transp Res Board 113–120
9. Bianchessi AG, Ongini C, Alli G, Panigati E, Savaresi S (2013) Vehicle-sharing: technological infrastructure, vehicles, and user-side devices-Technological review. In: 16th international IEEE conference on intelligent transportation systems-(ITSC), 2013. IEEE, pp 1599–1604
10. Boyacı B, Zografos KG, Geroliminis N (2015) An optimization framework for the development of efficient one-way car-sharing systems. Eur J Oper Res 240:718–733

11. Cepolina E, Farina A (2012) Urban car sharing: an overview of relocation strategies. WIT Trans Built Environ 128:419–431
12. Cepolina E, Farina A, Pratelli A (2014) Car-sharing relocation strategies: a state of the art. Public Mobility Syst 3:109
13. Fan W, Machemehl R, Lownes N (2008) Carsharing: dynamic decision-making problem for vehicle allocation. Transp Res Rec J Transp Res Board 97–104
14. Wang H, Cheu R, Lee D-H (2010) Dynamic relocating vehicle resources using a microscopic traffic simulation model for carsharing services. In: 2010 third international joint conference on Computational Science and Optimization (CSO). IEEE, pp 108–111
15. Kek AG, Cheu RL, Meng Q, Fung CH (2009) A decision support system for vehicle relocation operations in carsharing systems. Transp Res Part E Logistics Transp Rev 45:149–158
16. Alfian G, Rhee J, Yoon B (2014) A relocation simulation model for one-way carsharing service. In: 2014 IEEE international conference on Industrial Technology (ICIT). IEEE, pp 718–723
17. Barth M, Todd M (1999) Simulation model performance analysis of a multiple station shared vehicle system. Transp Res Part C Emerg Technol 7:237–259
18. Kek A, Cheu R, Chor M (2006) Relocation simulation model for multiple-station shared-use vehicle systems. Transp Res Rec J Transp Res Board 81–88

The Study of Voice Coil Motor Position Control System Based on Fuzzy Nonlinear PID

Xunfeng Yin, Songfeng Pan, Shuo Liu and Fengsong Yin

Abstract In view of the requirement of modern industry for voice coil motor (VCM) position control system's quickness and accuracy, on the basis of the classical PID control, this chapter which based on the working principle and mathematical model of VCM, combined with fuzzy control method and nonlinear PID control method, realized the rapid and precise control of position, and all these are based on the classic control to PID. Through designing the nonlinear PID controller in detail, and combining with the fuzzy control, it realized the parameter setting and position control system for quick response and high precision. The simulation and experimental results show that the fuzzy nonlinear PID controller can get following advantages: better position control system dynamic performance of VCM, faster response, and higher accuracy.

Keywords Voice coil motor (VCM) · Nonlinear PID · Fuzzy nonlinear PID · Position control

1 Introduction

The VCM belongs to the special linear motor. It has many characteristics, such as simple structure, small volume, low-noise, high specific thrust, strong acceleration (over 20 times than the force of gravity), fast response speed (millisecond class), high precision, convenient maintenance, high reliability, etc. [1]. The traditional VCM control used the classic PID, however, as the modern industry's requirement to the response speed and precision of VCM is higher and higher, the classic PID control cannot meet the industry requirement gradually [2, 3].

This paper proposed the control structure method that combined the fuzzy control and the nonlinear PID control on the basics of VCM's operation principle and mathematical model. Through designing the nonlinear PID controller in detail,

X. Yin (✉) · S. Pan · S. Liu · F. Yin
Institute of Automation, Qingdao University, Qingdao 266071, China
e-mail: yinxunfeng1109@163.com

Y. Jia et al. (eds.), *Proceedings of 2016 Chinese Intelligent Systems Conference*,
Lecture Notes in Electrical Engineering 404, DOI 10.1007/978-981-10-2338-5_3

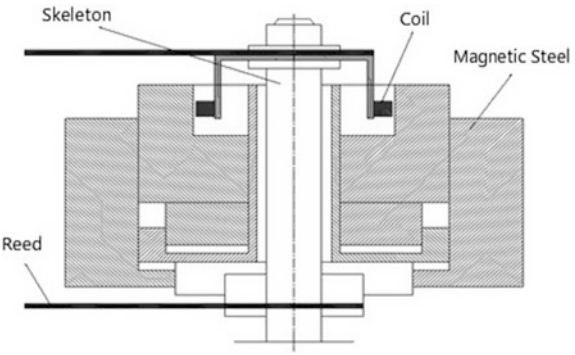

Fig. 1 The structure chart of VCM

and combining with the fuzzy control, it realized parameter setting and position control system for quick response and high precision.

2 The Structure Principle of Voice Coil Motor

The structure chart of VCM is showed as Fig. 1. The working principle of VCM is electric annular winding, which affected by Lorentz force in the permanent magnetic field and moved by rectilinear direction. So, the size and direction of Lorentz force is decided by the strength and direction of electric current in the annular winding [4, 5].

3 The Mathematical Model of Voice Coil Motor

According to the Kirchhoff's voltage law, we can get the electronic equilibrium equation [6].

$$u_a = R_a i_a + BLv + L_a \frac{\mathrm{d}i_a}{\mathrm{d}t} \tag{1}$$

In the equation, u_a is winding voltage, R_a is winding resistance, i_a is moving coil current, B is magnetic induction intensity, L is coil length, v is the linear velocity of active cell, $L_a \frac{\mathrm{d}i_a}{\mathrm{d}t}$ is voltage drop. In the state of move, the force which the active cell loops of VCM get has electromagnetic force f_e, inertial force ma and friction force cv. According to the relation among them, the equation is

$$f_e = ma + cv = m\frac{\mathrm{d}v}{\mathrm{d}t} + cv = m\frac{\mathrm{d}^2x}{\mathrm{d}t^2} + c\frac{\mathrm{d}x}{\mathrm{d}t} \tag{2}$$

In the equation, m is active cell partial quality, v is active cell movement linear speed, x is active cell movement displacement, c is dynamic friction coefficient. The equation group of VCM is composed of Eqs. (1) and (2), it is

$$\begin{cases} u_a = R_a i_a + BLv + L_a \frac{\mathrm{d}i_a}{\mathrm{d}t} \\ f_e = m\frac{\mathrm{d}^2 x}{\mathrm{d}t^2} + c\frac{\mathrm{d}x}{\mathrm{d}t} \\ f_e = BLi_a \end{cases} \tag{3}$$

Eliminate the intermediate variable f_e, v and i_a from the equation group of VCM, we can get the differential equation which put linear displacement $x(t)$ as generated quantity, put voltage u_a as input quantity.

$$BLu_a = mL\frac{\mathrm{d}^3 x}{\mathrm{d}t^3} + (mR_a + cL)\frac{\mathrm{d}^2 x}{\mathrm{d}t^2} + (B_2 L_2 + cR_a)\frac{\mathrm{d}x}{\mathrm{d}t} \tag{4}$$

4 The Structure of System Control

As this control system required the fast response speed of system control, so it used double loop control structure of position loop and current loop. As the motive friction coefficient c was so small that it was ignored, so Eq. (2) can be

$$\begin{cases} f_e = m\frac{\mathrm{d}^2 x}{\mathrm{d}t^2} \\ f_e = BLi_a \end{cases} \tag{5}$$

And it's state equation can be

$$\begin{cases} \dot{x}_1 = x_2 \\ \dot{x}_2 = \frac{BL}{m} i_a - \frac{F_L}{m} \end{cases} \tag{6}$$

In the equation, x_1 is the linear displacement of active cell of VCM, x_2 is the speed of active cell of VCM. The position loop control used nonlinear PID control and combined with fuzzy control, realized parameter setting and improved the anti-interference performance and accuracy of system.

5 The Design of Fuzzy Nonlinear PID Controller

The classic PID has many disadvantages in some aspects [7, 8]. The error it throws off is very big, and easy to get overshoot. The error integral feedback weakened the response speed of closed-loop system, strengthened the vibration frequency, and

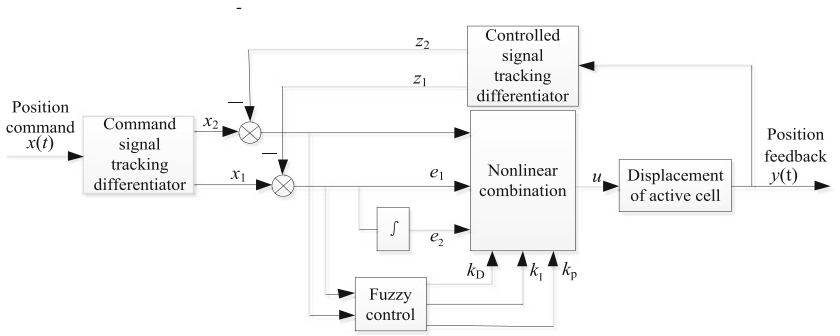

Fig. 2 The structure block diagram of fuzzy nonlinear PID controller

produced SAT controlled quantity. It cannot meet the requirement of system's quick response and small overshoot quantity at the same time.

Thus, the control system used nonlinear PID control, combined with the fuzzy control–fuzzy nonlinear PID control, in order to meet the requirement of control system [9]. The fuzzy nonlinear PID control consisted of four modules: The second order linear tracking differentiator, the second order nonlinear tracking differentiator, fuzzy control link and nonlinear control link. The structure block diagram of fuzzy nonlinear PID controller is as show as Fig. 2.

6 The Design of Tracking Differentiator

The function of nonlinear tracking differentiator where in position signal sending office is does differential dealing with the position order, arrange reasonably and solve the contradiction between quick response and overshoot efficiently, enlarge the feedback gain selection, easy for realize the parameter setting of controller [10].

$$\begin{cases} \dot{x}_1 = x_2 \\ \dot{x}_2 = -a_1|x_1|\text{sign}(x_1) - a_2|x_2|\text{sign}(x_2) \end{cases} \tag{7}$$

In the equation, x_1 is the setting linear displacement of VCM active cell, x_2 is the setting linear displacement differential of VCM active cell (that is the speed of VCM active cell), a_1 and a_2 are adjustable parameters that affect the tracking speed of the second order linear differential tracker, improve the dynamic performance and accuracy of system, choose the parameter by the biggest acceleration which generated by VCM.

The tracking differentiator of feedback signal used the second nonlinear tracing differentiator. It not only can track the controlled signal, but also it can put the controlled signal differential. And, it can make up the disadvantage of linear tracking differentiator enlarging the noise, improved the response speed of system.

For the nonlinear system

$$\begin{cases} \dot{z}_1 = z_2 \\ \dot{z}_2 = -a_1|z_1|^{\alpha}\sqrt{|z_1 - y|}\text{sign}(z_1 - y) - a_2|z_2|^{\alpha}\text{sign}(z_2) \end{cases} \tag{8}$$

When a_1, a_2, and α greater then 0, the system tend to stabilization gradually. In the equation, y is the actual linear displacement of VCM active cell, $z_1$is the feedback of y, z_2 is differential of z_1, a_1, and a_2 are adjustable parameters. The adjustable parameter decides the tracking speed of the second order nonlinear differential tracker, improves the response speed of system. We adjust the parameter according to the response speed of VCM position sensor.

7 The Design of Fuzzy Controller

This system used the method of combination of nonlinear PID control and fuzzy control, not only it has the characteristics of high accuracy and quick response of nonlinear PID control, but also it has the well-adapted and high-stabled characteristics of fuzzy control. As chart 2 showed us that in this control system, $e_1$is position error, e_2 is position error rate, nonlinear PID control system put e_1 and e_2, as input quantity, put Δk_P, Δk_I and Δk_D as output quantity, make real-time parameter setting to integral parameter k_I, scale parameter k_P and differential parameters k_D by fuzzy control algorithm.

$$\begin{cases} k_I = k_{I0} + \Delta k_I \\ k_P = k_{P0} + \Delta k_P \\ k_D = k_{D0} + \Delta k_D \end{cases} \tag{9}$$

In the equation, k_{I0} (equal to 5), k_{P0} (equal to 0.5) and k_{D0} (equal to 0) are the control parameter original value. The fuzzy real-time setting process of PID three parameters is to find out a fuzzy relationship between e_1, e_2, and when we get the different input value at the different time, use the accordingly fuzzy relationship between them to output three parameters accordingly, doing this we can accomplish one purpose: for different e_1 and $e_2$input value, we still can output the suitable and satisfied control parameters. According to the fuzzy relationship between e_1 and e_2, we designed the parameter table which was used for amend the k_p, k_I and k_D parameter fuzzy adjustment rule [11].

In the fuzzy control system, we used {Negative Big, Negative Middle, Negative Small, Zero, Positive Small, Positive Middle, Positive Big and marked {NB, NM, NS, ZO, PS, PM, PB} to describe the error e_1, error rate e_2 and output quantity (Δk_P, Δk_I, Δk_D) [3] of the nonlinear PID control system. Control rule of Δk_P, Δk_I, Δk_D are showed as Tables 1, 2 and 3.

Table 1 Control rule of Δk_P

e_1	e_2						
	NB	NM	NS	ZO	PS	PM	PB
NB	NB	NB	NM	NM	NS	ZO	ZO
NM	NB	NB	NM	NS	NS	ZO	ZO
NS	NB	NM	NS	NS	ZO	PS	PS
ZO	NM	NM	NS	ZO	PS	PM	PM
PS	NM	NS	ZO	PS	PS	PM	PB
PM	ZO	ZO	PS	PS	PM	PB	PB
PB	ZO	ZO	PS	PM	PM	PB	PB

Table 2 Control rule of Δk_I

e_1	e_2						
	NB	NM	NS	ZO	PS	PM	PB
NB	PB	PB	PM	PM	PS	ZO	ZO
NM	PB	PB	PM	PS	PS	ZO	NS
NS	PM	PM	PM	PS	ZO	NS	NS
ZO	PM	PM	PS	ZO	NS	NM	NM
PS	PS	PS	ZO	NS	NS	NM	NM
PM	PS	ZO	NS	NM	NM	NM	NB
PB	ZO	ZO	NM	NM	NM	NB	NB

Table 3 Control rule of Δk_D

e_1	e_2						
	NB	NM	NS	ZO	PS	PM	PB
NB	PS	NS	PB	PB	PB	NM	PS
NM	PS	NS	NB	NM	NM	NS	ZO
NS	ZO	NS	NM	NM	NS	NS	ZO
ZO	ZO	NS	NS	NS	NS	NS	ZO
PS	ZO	ZO	ZO	ZO	ZO	ZO	ZO
PM	PB	NS	PS	PS	PS	PS	PB
PB	PB	PM	PM	PM	PS	PS	PB

$$\begin{cases} \Delta k_P = \{e_1, e_2\} \times q_P \\ \Delta k_I = \{e_1, e_2\} \times q_I \\ \Delta k_D = \{e_1, e_2\} \times q_D \end{cases} \tag{10}$$

$\{e_1, e_2\}$ is the according to fuzzy reasoning, q_P, q_I and q_D are adjustment parameters. In order to ensure the small overshoot and good system response speed, k_P, k_I and k_D values which we get cannot be overlarge or oversmall; in order to make the stability of system good, the value of K_P and K_I should enlarge accordingly. In order to make the stability of system good, the value of K_P and K_I should enlarge accordingly. Besides, considering the system will vibrate around the stable value and the system's antijamming capability, the value of k_D should properly chose the

smaller value. By the simulation test, we got the most suitable parameter, k_P should be 7.5, k_I should be 0.9 and k_D should be 14.4.

8 The Design of Nonlinear Controlling Unit

The function of nonlinear controlling unit is through nonlinear combination by deviation's percentage, integral and differential, generate the control quantity and eliminate this deviation. Actually, nonlinear function fal() (when $0 < \alpha < 1$) is an experience knowledge for control engineering: "big error, small gain; small error, big gain" mathematic fitting.

$$\begin{cases} e_0 = \int_0^t e_1(\tau)\mathrm{d}\tau \\ e_1 = x_1 - z_1 \\ e_2 = x_2 - z_2 \\ u(t) = k_1\mathrm{fal}(e_0,\alpha,\delta) + k_p\mathrm{fal}(e_1,\alpha,\delta) + k_D\mathrm{fal}(e_2,\alpha,\delta) \end{cases} \tag{11}$$

In the equation,

$$\mathrm{fal}(e,\alpha,\delta) = \begin{cases} |e|^{\alpha}\mathrm{sign}(e) & |e| > \delta, \delta > 0 \\ \frac{e}{\delta^{1-\alpha}} & |e| \le \delta, \delta > 0 \end{cases} \tag{12}$$

k_I, k_P and k_D are integration element, percentage element and differential element's control parameter of nonlinear PID control accordingly. $\alpha = 0.5$, $\delta = 0.01$.

9 The Control System Simulation and Test Results

The motor used in this test is linear VCM, it's model is VCAR 0022-0448-00A, maximum input electric current is 5 A, winding resistance is 5 Ω, winding inductance is 2 mH, peak thrust is 22 N, maximum stroke is 44.8 mm, rotor weight is 52 g, stator diameter is 48 g, the enter length of loop is 75.7 mm. This system used Matlab simulation, simulated to fuzzy PID control and fuzzy nonlinear PID control accordingly, verified this method feasibility of system. Figure 3 showed the simulation result of the position control system.

The simulation result showed that fuzzy nonlinear PID control method made system response quickly, realized reserve setting quickly, shortened the time from start to stabilization stage, improved the stability of system at the same time, compared to the classic PID control and fuzzy PID control.

After the VCM stabled, set a new position command, the response curve of system as Fig. 4 showed, and the simulation result showed that the fuzzy nonlinear

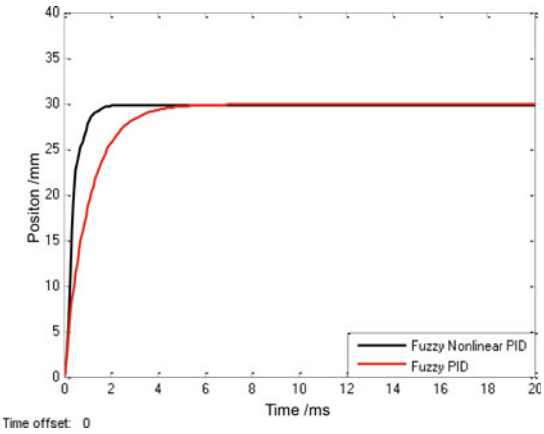

Fig. 3 System position step response curve

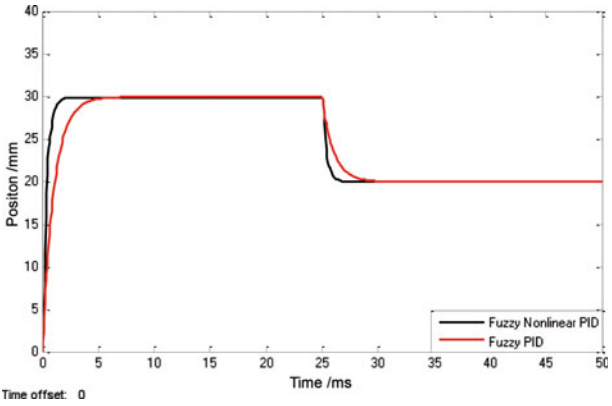

Fig. 4 The response curve of system when setting the new position

PID control method can make the system reach the settled position more quickly, stably, and accurately. It improved the disturbance rejection ability of system.

The position as shown in Fig. 5 for the system input sine signal tracking curve, for given positions of sine signal (a), (b) for the actual position signal, (c) for the position error of curve. Simulation results showed that the system response time is less than 1 ms, maximal position error less 0.02 mm, improve response time and accuracy of the system greatly.

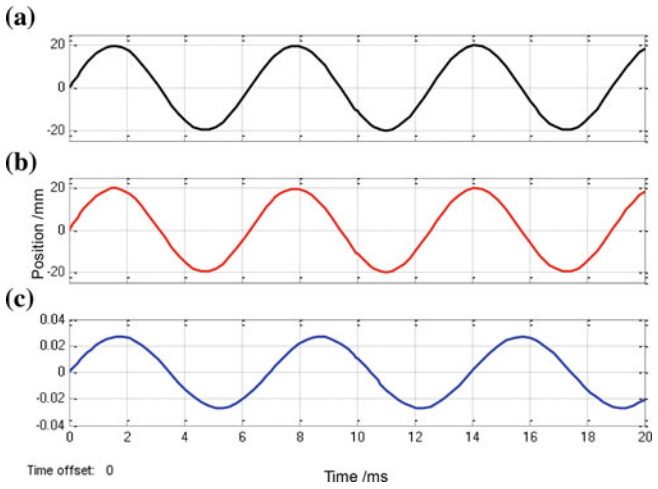

Fig. 5 System position sine signal tracking curve

10 Conclusion

On the basics of differential equation model and system mathematical model of VCM, this chapter used nonlinear PID control structure, combined with fuzzy control, realized the parameter setting, improved the system stability. The system simulation and performance result showed that in the same condition, this system can improve the response speed of position, strengthen the stability of control system, and meet the requirements of modern high precision industry.

References

1. Lianguo X, Zhou huixing H, Shulin H, Cao RM (2011) Research and application of voice coil motor. Micromotors, Xi'an, China
2. Wei H (2011) Research on dual—loop control system of coreless DC servo electrical-mechanical converter based on DSP. Mechatron Eng
3. Dawei Z, Xiaomei F (2006) The technical principle of voice—coil actuator. J North Univ
4. Yingyu Z, Shengquan Z, Dawei Z (2007) Design and simulation of the control system of precision position table driven by voice coil actuator. J Tianjin Univ
5. Cossu M, Bertinelli M, Riva C (2014) The impact of conditioned attenuation statistics on the performance of VCM techniques for Earth observation satellites in LEO orbit. IEEE Conf Publ 320–323
6. Xi Z, Delong Z (2014) The structure design and mathematical modeling analysis of linear voice coil motor. Scientific Innovation and Application, Heilongjiang, China
7. Yu W, Xi C, Xiaoyun Z (2013) A split-capacitor VCM-based capacitor-switching scheme for low-power SAR ADCs. IEEE Conf Publ 2014–2017

8. Hebei Z (2013) Design of stepper motor control system based on DSP. Acta Armamentarii, Beijing, China
9. Dayu W, Hong G, Liu Z (2011) A fuzzy nonlinear PID control of voice coil motor used in direct drive valve. Trans China Electrotech Soc
10. Jing H, Wei W (1994) Nonlinear tracking differentiator, System science and math. Beijing, China
11. Zhouzhang D (2006) Fuzzy logic control and reference. Beijing University Press, Beijing, China

Adaptive Finite-Time Bipartite Consensus for Nonlinear Coopetition Multi-agent Systems with Unknown External Disturbances

Lin Zhao, Yingmin Jia, Jinpeng Yu and Haisheng Yu

Abstract This paper studies the adaptive finite-time bipartite consensus problem for second-order nonlinear coopetition multi-agent systems subject to external disturbances. The novel continuous distributed adaptive protocols with update laws are proposed. By using the finite-time Lyapunov stable theory, the rigorous finite-time stable proofs and accurate expression of convergent regions of bipartite steady-state errors are given. An example is given to demonstrate the effectiveness of the presented method.

Keywords Coopetition multi-agent systems · Signed graphs · Bipartite consensus · Adaptive control · Finite-time convergence

1 Introduction

Recently, the consensus problem of multi-agent systems has drawn a lot of attention due to its potential applications in distributed computation, sensory networks, spacecraft formation, and so forth [1–3]. The consensus problems studied in [1–3] only focus on cooperative multi-agent systems over graphs with edge of nonnegative weights. But in some real networks such as social network [4], the interaction relationship between agents is not only cooperative but also competitive, which are usually called as coopetition networks. Compared with the consensus problem for cooperative multi-agent systems, one of the most important issues for coopetition multi-agent systems is the bipartite consensus problem, that is how to design distributed protocols such that all agents converge to a value, which is the same for all in modulus but not in sign [5]. For example, [5–7] studied the distributed bipartite

L. Zhao (✉) · J. Yu · H. Yu
School of Automation and Electrical Engineering,
Qingdao University, Qingdao 266071, China
e-mail: zhaolin1585@163.com

Y. Jia
The Seventh Research Division, Beihang University (BUAA), Beijing 100191, China

Y. Jia et al. (eds.), *Proceedings of 2016 Chinese Intelligent Systems Conference*,
Lecture Notes in Electrical Engineering 404, DOI 10.1007/978-981-10-2338-5_4

consensus protocols design for first-order, second-order, and higher order coopetition multi-agent systems, respectively, but the algorithms in there are all with asymptotic convergence rate.

It is worth noting that how to ensure the states of all agents achieve finite-time consensus is important for cooperative multi-agent systems [8–14]. Meng et al. [15, 16] studied the finite-time bipartite consensus problems for first-order coopetition multi-agent systems, respectively. However, many real physical systems are modeled as second-order multi-agent systems, especially for systems with nonlinear dynamics [3], such as distributed spacecrafts and coupled manipulators, so the distributed finite-time bipartite consensus problems for second-order nonlinear multi-agent systems over signed graphs should be further addressed. Moreover, in a real physical system network, the evolutions of multi-agent systems are unavoidably affected by external disturbances [14]. To the best of our knowledge, adaptive finite-time bipartite consensus for disturbed second-order nonlinear coopetition multi-agent systems have not been studied yet. Motivated by the above discussion, this paper is devoted to address the adaptive finite-time bipartite consensus problems for disturbed second-order nonlinear multi-agent systems over signed undirected graphs.

2 Problem Formulation

2.1 Algebraic Graph Theory and Some Lemmas

Signed graphs can be conveniently used to represent the coopetition networks. A weighted signed graph $\mathcal{G}$ is a triple $\mathcal{G} = (\mathcal{V}, \mathcal{E}, \mathcal{A})$, where $\mathcal{V} = \{1, \ldots, N\}$ is the node set, $\mathcal{E} \subseteq \mathcal{V} \times \mathcal{V}$ is the edge set, and $\mathcal{A} = [a_{ij}] \in \mathfrak{R}^{n\times n}$ is the adjacency matrix of the signed weights of $\mathcal{G}$, where $a_{ij} \neq 0 \Leftrightarrow (j, i) \in \mathcal{E}$. $\mathcal{G}$ are assumed to be no self-loops, i.e., $a_{ii} = 0, \forall i \in \mathcal{V}$. For undirected $\mathcal{G}$, $(j, i) \in \mathcal{E}$ implies $(i, j) \in \mathcal{E}$ and $\mathcal{A}$ is a symmetric matrix. The edge $(j, i) \in \mathcal{E}$ means that there exists information flow form j to i, and the index set of the neighbors of i is given by $\mathcal{N}_i = \{j : (j, i) \in \mathcal{E}\}$. If there is a finite sequence nodes $i_1, \ldots, i_m$ such that $(i_o, i_{o+1}) \in \mathcal{E}, \forall o = 1, \ldots, m-1$, we say $\mathcal{G}$ has a path. Moreover, if any two nodes are linked with a path, $\mathcal{G}$ is said to be strongly connected. For undirected $\mathcal{G}$, the strongly connected means connected. From [5], the signed graph $\mathcal{G}$ is structurally balanced which means that the nodes have a bipartition $\{\mathcal{V}_1, \mathcal{V}_2\}$, in which $\mathcal{V}_1 \cup \mathcal{V}_2 = \mathcal{V}$ and $\mathcal{V}_1 \cap \mathcal{V}_2 = \emptyset$, such that $a_{ij} \geq 0$ for $\forall i, j \in \mathcal{V}_l (l \in \{1, 2\})$ and $a_{ij} \leq 0$ for $\forall i \in \mathcal{V}_l, j \in \mathcal{V}_q, l \neq q (l, q \in \{1, 2\})$. For a given signed $\mathcal{A}$, the Laplacian $L = C - \mathcal{A}$, where C is the connectivity matrix, and the elements of L are $l_{ij} = \begin{cases} \sum_{j\in N_i} |a_{ij}|, j = i \\ -a_{ij}, j \neq i \end{cases}$ [5]. For a signed undirected graph $\mathcal{G}$, $\forall x = [x_1, \ldots, x_n]^T \in \mathfrak{R}^n$, the Laplacian potential is defined by $\boldsymbol{\Phi}(x) = x^T L x = \frac{1}{2} \sum_{i=1}^{n} \sum_{j\in N_i} |a_{ij}|(x_i - \text{sign}(a_{ij}) x_j)^2$.

Lemma 1 [16] *For a connected signed graph $\mathcal{G}$, if $\mathcal{G}$ is structurally balanced, then there exists a diagonal matrix $D = diag\{\sigma_1, \ldots, \sigma_n\}$ with $\sigma_i \in \{-1, 1\}$ for all $i \in \mathcal{V}$ such that $D\mathcal{A}D$ is nonnegative, and the following performances is given: 1. $\boldsymbol{\Phi}(x)$ is semipositive definite, and $\boldsymbol{\Phi}(x) = 0$ means $x = D\boldsymbol{I}_n c$ for some $c \in \mathfrak{R}$; 2. $\lambda_1(L) = 0, \lambda_2(L) > 0$, and $\boldsymbol{\Phi}(x) \geq \lambda_2(L)x^T x$ for all x that satisfies $\boldsymbol{I}_n^T Dx = 0$.*

Lemma 2 [8] *Suppose $V(x)$ is a C^1 smooth positive-definite function (defined on $U \subset \mathfrak{R}^n$) and $\dot{V}(x) + \lambda V^{\alpha}(x)$ is a negative semidefinite function on $U \subset \mathfrak{R}^n$ and $\alpha \in (0, 1)$, then there exists an area $U_0 \subset \mathfrak{R}^n$ such that any $V(x)$ which starts from $U_0 \subset \mathfrak{R}^n$ can reach $V(x) \equiv 0$ in finite time. Moreover, if T_{reach} is the time needed to reach $V(x) \equiv 0$, then $T_{reach} \leq \frac{V^{1-\alpha}(x_0)}{\lambda(1-\alpha)}$, where $V(x_0)$ is the initial value of $V(x)$.*

2.2 System Descriptions

Consider the coopetition network which contains n agents indexed by $1, 2, \ldots, N$, where the ith agent is described as

$$\begin{aligned} \dot{x}_i(t) &= v_i(t) \\ \dot{v}_i(t) &= f_i(v_i(t)) + u_i(t) + d_i(t), i \in \mathcal{V} \end{aligned} \tag{1}$$

where $x_i(t) \in \mathfrak{R}$, $v_i(t) \in \mathfrak{R}$ and $u_i(t) \in \mathfrak{R}$ are the position, velocity and control input, respectively. The intrinsic nonlinear dynamics $f_i : \mathfrak{R} \to \mathfrak{R}$ is continuously differentiable function and satisfied $f_i(0) = 0$. $d_i(t) \in \mathfrak{R}$ is the external disturbance. Regarding the ith agent as the node i, the topology relationship among the N agents are described by a weighted signed undirected graph $\mathcal{G} = \{\mathcal{V}, \mathcal{E}, \mathcal{A}\}$.

Assumption 1 For coopetition multi-agent system (1), $\mathcal{G}$ is structurally balanced and connected.

Assumption 2 There exists a known nonnegative constant γ_i such that $\|f_i(x) - f_i(y)\| \leq \gamma_i \|x - y\|$.

Assumption 3 $d_i(t)$ satisfies $|d_i(t)| \leq \eta_i$, where $\eta_i > 0$ is an unknown constant.

Definition 1 The finite-time bipartite consensus is achieved, if the following equalities are satisfied $\begin{cases} \lim\limits_{t \to T} x_i(t) - x_j(t) = 0, \forall i, j \in \mathcal{V}_1 \text{ or } \forall i, j \in \mathcal{V}_2 \\ \lim\limits_{t \to T} x_i(t) + x_j(t) = 0, \forall i \in \mathcal{V}_1 \text{ and } \forall j \in \mathcal{V}_2 \end{cases}$,

$\begin{cases} \lim\limits_{t \to T} v_i(t) - v_j(t) = 0, \forall i, j \in \mathcal{V}_1 \text{ or } \forall i, j \in \mathcal{V}_2 \\ \lim\limits_{t \to T} v_i(t) + v_j(t) = 0, \forall i \in \mathcal{V}_1 \text{ and } \forall j \in \mathcal{V}_2 \end{cases}$, where $T \in [0, \infty)$ is the settling time.

3 Main Results

Denote $\phi_i = \eta_i^2$, $\hat{\phi}_i$ as the estimation of ϕ_i, then the adaptive update law for estimating the upper bound of ϕ_i is designed as

$$\dot{\hat{\phi}}_i = -2o_i\rho_i\hat{\phi}_i + \frac{o_i}{((2-\alpha)k_i^{\frac{1}{\alpha}})^2\sigma_i^2}|v_i^{\frac{1}{\alpha}} + k_i^{\frac{1}{\alpha}}p_i|^{4-2\alpha}, i \in \mathcal{V}, \tag{2}$$

where $p_i = \sum_{j\in N_i}|a_{ij}|(x_i - \text{sign}(a_{ij})x_j)$, $\frac{1}{2} < \alpha = \frac{\alpha_1}{\alpha_2} < 1, \alpha_1, \alpha_2$ are positive odd integers, $k_i = \kappa + \kappa_1 + \kappa_2(1+n_i) + \kappa_3, \kappa > 0, \kappa_1 > 0, \kappa_2 > 0, \kappa_3 > 0, o_i > 0, \rho_i > 0, \sigma_i > 0$ are designed constants, and $n_i = \dim N_i$.

Based on the adaptive update law, the following distributed protocol is presented:

$$u_i = \hat{u}_i + u_{iadp}, i \in \mathcal{V}, \tag{3}$$

where $\hat{u}_i = -((2-\alpha)k_i^{\frac{1}{\alpha}})(\Theta + \Psi_i + \Upsilon_i + \kappa)(v_i^{\frac{1}{\alpha}} + k_i^{\frac{1}{\alpha}}p_i)^{2\alpha-1}$ and $u_{iadp} = -\frac{\hat{\chi}_i}{(2-\alpha)k_i^{\frac{1}{\alpha}}}(v_i^{\frac{1}{\alpha}} + k_i^{\frac{1}{\alpha}}p_i)^{2-\alpha}$, $\Theta = \frac{\alpha(2^{1-\alpha})^{\frac{1+\alpha}{\alpha}}(\frac{1}{\kappa_1(1+\alpha)})^{\frac{1}{\alpha}}}{1+\alpha}$, $\Psi_i = \frac{(1+\alpha)2^{2-2\alpha}\epsilon_i}{1+\alpha} + \frac{\alpha 2^{2-2\alpha}\sum_{j\in N_i}\varsigma_j}{1+\alpha} + \frac{2^{2-2\alpha}n_i\varsigma_i}{1+\alpha} + \frac{(\frac{\alpha}{\kappa_2(1+\alpha)})^{\alpha}(2^{1-\alpha}k_i\epsilon_i)^{1+\alpha}}{1+\alpha} + \frac{(\frac{\alpha}{\kappa_2(1+\alpha)})^{\alpha}\sum_{j\in N_i}(2^{1-\alpha}k_j\varsigma_i)^{1+\alpha}}{1+\alpha}$, $\Upsilon_i = \frac{\gamma_i}{(2-\alpha)k_i^{\frac{1}{\alpha}}}|v_i^{\frac{1}{\alpha}} + k_i^{\frac{1}{\alpha}}p_i|^{1-\alpha} + \frac{\left(\frac{\gamma_i}{(2-\alpha)k_i^{\frac{1}{\alpha}}}k_i|v_i^{\frac{1}{\alpha}} + k_i^{\frac{1}{\alpha}}p_i|^{1-\alpha}\right)^{1+\alpha}(\frac{\alpha}{\kappa_3(1+\alpha)})^{\alpha}}{1+\alpha}$, $\epsilon_i = \sum_{j\in N_i}|a_{ij}|, \varsigma_i = \max_{j\in N_j}\{|a_{ij}|\}, \hat{\chi}_i = \frac{\hat{\phi}_i}{2\sigma_i^2}$ and $\iota_i > 0$ is a constant.

Theorem 1 *Suppose that Assumptions 1 and 2 are satisfied, then the bipartite position and velocity errors of any two agents will converge to the region Ω in finite time under the adaptive finite-time consensus protocol (3), where*

$$\begin{aligned}
\Omega = &\Big\{|x_i - x_j| \le \frac{\sqrt{2(N-1)}}{\sqrt{\Gamma}}(\frac{\phi_0}{(1-\varrho)\bar{\theta}})^{\frac{1}{\alpha+1}},\\
&|v_i - v_j| \le 2(\frac{(2-\alpha)k_i^{\frac{1}{\alpha}}}{\alpha 2^{\frac{(\alpha-1)(2-\alpha)}{\alpha}-1}})^{\frac{\alpha}{2}}(\frac{\phi_0}{(1-\varrho)\bar{\theta}})^{\frac{\alpha}{\alpha+1}} + 2k_i(2\lambda_{\max}(L))^{\frac{\alpha}{2}}(\frac{\phi_0}{(1-\varrho)\bar{\theta}})^{\frac{\alpha}{\alpha+1}},\\
&\forall i,j \in \mathcal{V}_1 \text{ or } \forall i,j \in \mathcal{V}_2\Big\} \bigcup \Big\{|x_i + x_j| \le \frac{\sqrt{2(N-1)}}{\sqrt{\Gamma}}(\frac{\bar{\eta}_0}{(1-\varrho)\bar{\theta}})^{\frac{1}{\alpha+1}},\\
&|v_i + v_j| \le 2(\frac{(2-\alpha)k_i^{\frac{1}{\alpha}}}{\alpha 2^{\frac{(\alpha-1)(2-\alpha)}{\alpha}-1}})^{\frac{\alpha}{2}}(\frac{\phi_0}{(1-\varrho)\bar{\theta}})^{\frac{\alpha}{\alpha+1}} + 2k_i(2\lambda_{\max}(L))^{\frac{\alpha}{2}}(\frac{\phi_0}{(1-\varrho)\bar{\theta}})^{\frac{\alpha}{\alpha+1}},\\
&\forall i \in \mathcal{V}_1 \text{ and } \forall j \in \mathcal{V}_2\Big\}
\end{aligned} \tag{4}$$

$\varpi_i = \frac{o_i\rho_i(2\nu_i-1)}{2\nu_i}, \varpi_{\min} = \min\{\varpi_i^{\frac{\alpha+1}{2}}\}, \bar{\theta} = \min\{\vartheta_1, \varpi_{\min}\}, \vartheta_1 = \frac{\kappa}{\vartheta^{\frac{1+\alpha}{2}}}, \vartheta = \max\{\frac{1}{2\lambda_2}, \frac{2^{1-\alpha}}{(2-\alpha)k_i^{\frac{1}{\alpha}}}\}, \Gamma = \min|a_{ij}|, \phi_0 = \sum_{i=1}^n \frac{\sigma_i^2}{2} + \sum_{i=1}^n \rho_i\nu_i\eta_i^2, \nu_i > \frac{1}{2}, 0 < \varrho \le 1$ *are designed constants.*

Proof First, we consider the Lyapunov function $\bar{V} = V_0 + \sum_{i=1}^n V_i$, where $V_0 = \frac{1}{2}\Phi(x)$ and $V_i = \frac{1}{(2-\alpha)k_i^{\frac{1}{\alpha}}}\int_{v_i^*}^{v_i}(\theta^{\frac{1}{\alpha}} - v_i^{*,\frac{1}{\alpha}})^{2-\alpha}\mathrm{d}\theta$. It follows from [9] that $\int_{v_i^*}^{v_i}(\theta^{\frac{1}{\alpha}} - v_i^{*,\frac{1}{\alpha}})^{2-\alpha}\mathrm{d}\theta$ is differentiable, positive definite and proper. Taking the time derivative of V_0 yields $\dot{V}_0 = -\sum_{i=1}^n k_i p_i^{1+\alpha} + \sum_{i=1}^n p_i(v_i - v_i^*)$, where the virtual protocol v_i^* is chosen as $v_i^* = -k_i p_i^{\alpha}$.

Taking the time derivative of $\bar{V}$ yields

$$\begin{aligned}\dot{\bar{V}} = &-\sum_{i=1}^n k_i p_i^{1+\alpha} + \sum_{i=1}^n p_i(v_i - v_i^*) + \sum_{i=1}^n \frac{\partial V_i}{\partial v_i}f_i(v_i) + \sum_{i=1}^n \frac{\partial V_i}{\partial v_i}(u_i + d_i)\\ &+ \sum_{i=1}^n \frac{\partial V_i}{\partial p_i}\sum_{j\in N_i}|a_{ij}|(v_i - \mathrm{sign}(a_{ij})v_j),\end{aligned} \tag{5}$$

where $\frac{\partial V_i}{\partial v_i} = \frac{1}{(2-\alpha)k_i^{\frac{1}{\alpha}}}\xi_i^{2-\alpha}$, $\frac{\partial V_i}{\partial p_i} = -\frac{1}{k_i^{\frac{1}{\alpha}}}\frac{\partial v_i^{*,\frac{1}{\alpha}}}{\partial p_i}\int_{v_i^*}^{v_i}(\theta^{\frac{1}{\alpha}} - v_i^{*,\frac{1}{\alpha}})^{1-\alpha}\mathrm{d}\theta$ and $\frac{\partial v_i^{*,\frac{1}{\alpha}}}{\partial p_i} = -k_i^{\frac{1}{\alpha}}$. Based on Lemmas 3 and 4 in [13], we have

$$-\sum_{i=1}^n k_i p_i^{1+\alpha} + \sum_{i=1}^n p_i(v_i - v_i^*) \le -\sum_{i=1}^n k_i p_i^{1+\alpha} + \sum_{i=1}^n \kappa_1|p_i|^{1+\alpha} + \sum_{i=1}^n \Theta|\xi_i|^{1+\alpha}, \tag{6}$$

where $\xi_i = v_i^{\frac{1}{\alpha}} + k_i^{\frac{1}{\alpha}}p_i$.

From the definitions of ϵ_i and ς_i, we have $\left|\sum_{j\in N_i}|a_{ij}|(v_i - \mathrm{sign}(a_{ij})v_j)\right| \le \epsilon_i|v_i| + \varsigma_i\sum_{j\in N_j}|v_j|$, and based on Lemmas 3 and 4 in [13], we can further obtain $\epsilon_i|v_i - v_i^*||\xi_i|^{1-\alpha}|v_i| \le 2^{1-\alpha}\epsilon_i|\xi_i|^{\alpha}|\xi_i|^{1-\alpha}|v_i| \le 2^{2-2\alpha}\epsilon_i|\xi_i|^{1+\alpha} + \frac{(2^{1-\alpha}k_i\epsilon_i)^{1+\alpha}(\frac{\alpha}{\kappa_2(1+\alpha)})^{\alpha}}{1+\alpha}|\xi_i|^{1+\alpha} + \kappa_2|p_i|^{1+\alpha}$, and $\varsigma_i|v_i - v_i^*||\xi_i|^{1-\alpha}|v_j| \le \frac{2^{2-2\alpha}\varsigma_i}{1+\alpha}|\xi_i|^{1+\alpha} + \frac{2^{2-2\alpha}\varsigma_i\alpha}{1+\alpha}|\xi_j|^{1+\alpha} + \kappa_2|p_j|^{1+\alpha} + \frac{(2^{1-\alpha}k_j\varsigma_i)^{1+\alpha}(\frac{\alpha}{\kappa_2(1+\alpha)})^{\alpha}}{1+\alpha}|\xi_i|^{1+\alpha}$, then, we have

$$\sum_{i=1}^n\left|\frac{\partial V_i}{\partial p_i}\sum_{j\in N_i}|a_{ij}|(v_i - \mathrm{sign}(a_{ij})v_j)\right| \le \sum_{i=1}^n(\kappa_2 + n_i\kappa_2)|p_i|^{1+\alpha} + \sum_{i=1}^n \Psi_i|\xi_i|^{1+\alpha} \tag{7}$$

From Assumption 2 and $f_i(0) = 0$, we can obtain

$$\frac{\partial V_i}{\partial v_i} f_i(v_i) = \frac{1}{(2-\alpha)k_i^{\frac{1}{\alpha}}} \xi_i^{2-\alpha} f_i(v_i) \leq \frac{\gamma_i}{(2-\alpha)k_i^{\frac{1}{\alpha}}} \xi_i^{2-\alpha} |v_i| \tag{8}$$

and from the definition of ξ_i, we have $|v_i| \leq (|\xi_i| + |v_i^{*,\frac{1}{\alpha}}|)^\alpha = (|\xi_i| + k_i^{\frac{1}{\alpha}}|p_i|)^\alpha \leq |\xi_i|^\alpha + k_i|p_i|^\alpha$. From Lemmas 3 and 4 in [13], we can further obtain $\frac{\gamma_i}{(2-\alpha)k_i^{\frac{1}{\alpha}}} \xi_i^{2-\alpha}|v_i| \leq \frac{\gamma_i}{(2-\alpha)k_i^{\frac{1}{\alpha}}}|\xi_i|^{1-\alpha}|\xi_i|^{1+\alpha} + \kappa_3|p_i|^{1+\alpha} + \frac{\left(\frac{\gamma_i}{(2-\alpha)k_i^{\frac{1}{\alpha}}} k_i|\xi_i|^{1-\alpha}\right)^{1+\alpha} (\frac{\alpha}{\kappa_3(1+\alpha)})^\alpha}{1+\alpha}|\xi_i|^{1+\alpha}$. Substituting them into (8) yields

$$\sum_{i=1}^n \frac{\partial V_i}{\partial v_i} f_i(v_i) \leq \sum_{i=1}^n \kappa_3 |p_i|^{1+\alpha} + \sum_{i=1}^n \Upsilon_i |\xi_i|^{1+\alpha} \tag{9}$$

From $|p_i|^{1+\alpha} = p_i^{1+\alpha}$, $|\xi_i|^{1+\alpha} = \xi_i^{1+\alpha}$, we can obtain

$$\begin{aligned} \dot{\bar{V}} \leq & -\sum_{i=1}^n \left(k_i - \kappa_1 - \kappa_2(1+n_i) - \kappa_3\right) p_i^{1+\alpha} \\ & + \sum_{i=1}^n (\Theta + \Psi_i + \Upsilon_i)\xi_i^{1+\alpha} + \sum_{i=1}^n \frac{1}{(2-\alpha)k_i^{\frac{1}{\alpha}}} \xi_i^{2-\alpha}(u_i + d_i) \end{aligned} \tag{10}$$

Thus, if we choose the distributed protocol as (3), we can obtain

$$\dot{\bar{V}} \leq -\kappa \sum_{i=1}^n p_i^{1+\alpha} - \kappa \sum_{i=1}^n \xi_i^{1+\alpha} + \sum_{i=1}^n \frac{1}{(2-\alpha)k_i^{\frac{1}{\alpha}}} \xi_i^{2-\alpha}(u_{iadp} + d_i) \tag{11}$$

From Lemma 3 in [13], we have

$$V_i \leq \frac{1}{(2-\alpha)k_i^{\frac{1}{\alpha}}} |v_i - v_i^*||v_i^{\frac{1}{\alpha}} - v_i^{*,\frac{1}{\alpha}}|^{2-\alpha} = \frac{2^{1-\alpha}}{(2-\alpha)k_i^{\frac{1}{\alpha}}} \xi_i^2 \tag{12}$$

From $Lx = [p_1, \ldots, p_n]^T$, we can obtain $\sum_{i=1}^n p_i^2 = (Lx)^T Lx = x^T(L^2 \otimes I)x$. Since Assumption 2 is satisfied, we know that L is semipositive definite from Lemma 1, then L can be decomposed as $L = M^T M = M^2$, where M is also a semipositive definite matrix. Denote $MD\mathbf{1}_n = s = [s_1, \ldots, s_n]^T$, we have $s^T s = (MD\mathbf{1}_n)^T MD\mathbf{1}_n = \mathbf{1}_n^T DLD\mathbf{1}_n$. By Lemma 2, we can obtain $DLD\mathbf{1}_n = 0$, which means $s^T s = 0$ and $s^T = \mathbf{0}^T$, thus we have $\mathbf{1}^T D(Mx) = 0$. Then, we can obtain $\sum_{i=1}^n p_i^2 = (Mx)^T LMx \geq \lambda_2 x^T Lx = 2\lambda_2 V_0$, which means $\bar{V} = V_0 + \sum_{i=1}^n V_i \leq \vartheta(\sum_{i=1}^n p_i^2 + \sum_{i=1}^n \xi_i^2)$. From

Lemma 3 in [13], we have $\bar{V}^{\frac{1+\alpha}{2}} \leq \vartheta^{\frac{1+\alpha}{2}} \left(\sum_{i=1}^{n} p_i^{1+\alpha} + \sum_{i=1}^{n} \xi_i^{1+\alpha} \right)$, then it follows that $\dot{\bar{V}} \leq -\vartheta_1 \bar{V}^{\frac{1+\alpha}{2}} + \sum_{i=1}^{n} \frac{1}{(2-\alpha)k_i^{\frac{1}{\alpha}}} \xi_i^{2-\alpha}(u_{iadp} + d_i)$.

Next, we consider another Lyapunov function as

$$V = \bar{V} + \frac{1}{2} \sum_{i=1}^{n} o_i^{-1} \tilde{\phi}_i^2, \tag{13}$$

where $\tilde{\phi}_i = \phi_i - \hat{\phi}_i$. Thus, form (11), we can obtain

$$\begin{aligned} \dot{V} \leq & -\vartheta_1 \bar{V}^{\frac{1+\alpha}{2}} + \sum_{i=1}^{n} \frac{1}{((2-\alpha)k_i^{\frac{1}{\alpha}})^2} \xi_i^{4-2\alpha} \hat{\chi}_i + \sum_{i=1}^{n} \frac{1}{2((2-\alpha)k_i^{\frac{1}{\alpha}})^2 \sigma_i^2} |\xi_i|^{4-2\alpha} \eta_i^2 \\ & + \sum_{i=1}^{n} \frac{\sigma_i^2}{2} + \sum_{i=1}^{n} 2\rho_i \tilde{\phi}_i \hat{\phi}_i - \sum_{i=1}^{n} \frac{1}{2((2-\alpha)k_i^{\frac{1}{\alpha}})^2 \sigma_i^2} |\xi_i|^{4-2\alpha} \tilde{\phi}_i^2 \\ = & -\vartheta_1 \bar{V}^{\frac{1+\alpha}{2}} + \sum_{i=1}^{n} \frac{\sigma_i^2}{2} + \sum_{i=1}^{n} 2\rho_i \tilde{\phi}_i \hat{\phi}_i \end{aligned} \tag{14}$$

From $\tilde{\phi}_i$, we can obtain $\rho_i \tilde{\phi}_i \hat{\phi}_i \leq -\frac{\rho_i(2\nu_i-1)}{2\nu_i} \tilde{\phi}_i^2 + \frac{\rho_i \nu_i}{2} \phi_i^2$. Substituting it into (14) yields $\dot{V} \leq -\vartheta_1 \bar{V}^{\frac{1+\alpha}{2}} - \sum_{i=1}^{n} (\frac{\varpi_i}{o_i} \tilde{\phi}_i^2)^{\frac{\alpha+1}{2}} + \sum_{i=1}^{n} (\frac{\rho_i(2\nu_i-1)}{2\nu_i} \tilde{\phi}_i^2)^{\frac{\alpha+1}{2}} - \sum_{i=1}^{n} \frac{\varpi_i}{o_i} \tilde{\phi}_i^2 + \sum_{i=1}^{n} \frac{\rho_i \nu_i}{2} \phi_i^2 + \sum_{i=1}^{n} \rho_i \tilde{\phi}_i \hat{\phi}_i + \sum_{i=1}^{n} \frac{\sigma_i^2}{2}$. Thus, we have $\dot{V} \leq -\bar{\theta} V^{\frac{\alpha+1}{2}} + \phi_0$, where $\phi_0 = \sum_{i=1}^{n} (\frac{\rho_i(2\nu_i-1)}{2\nu_i} \tilde{\phi}_i^2)^{\frac{\alpha+1}{2}} + \sum_{i=1}^{n} \frac{\rho_i \nu_i}{2} \phi_i^2 + \sum_{i=1}^{n} \rho_i \tilde{\phi}_i \hat{\phi}_i + \sum_{i=1}^{n} \frac{\sigma_i^2}{2}$. If $\frac{\rho_i(2\nu_i-1)}{2\nu_i} \tilde{\phi}_i^2 > 1$, we have $(\frac{\rho_i(2\nu_i-1)}{2\nu_i} \tilde{\phi}_i^2)^{\frac{\alpha+1}{2}} + \rho_i \tilde{\phi}_i \hat{\phi}_i \leq \frac{\rho_i(2\nu_i-1)}{2\nu_i} \tilde{\phi}_i^2 + \rho_i \tilde{\phi}_i \hat{\phi}_i \leq \frac{\rho_i \nu_i}{2} \phi_i^2$, if $\frac{\rho_i(2\nu_i-1)}{2\nu_i} \tilde{\phi}_i^2 \leq 1$, we have $(\frac{\rho_i(2\nu_i-1)}{2\nu_i} \tilde{\phi}_i^2)^{\frac{\alpha+1}{2}} \Big|_{\frac{\rho_i(2\nu_i-1)}{2\nu_i} \tilde{\phi}_i^2 \leq 1} < (\frac{\rho_i(2\nu_i-1)}{2\nu_i} \tilde{\phi}_i^2)^{\frac{\alpha+1}{2}} \Big|_{\frac{\rho_i(2\nu_i-1)}{2\nu_i} \tilde{\phi}_i^2 > 1}$. Thus, we have $(\frac{\rho_i(2\nu_i-1)}{2\nu_i} \tilde{\phi}_i^2)^{\frac{\alpha+1}{2}} + \rho_i \tilde{\phi}_i \hat{\phi}_i \leq \frac{\rho_i \nu_i}{2} \phi_i^2$, which means $\phi_0 = \sum_{i=1}^{n} \rho_i \nu_i \phi_i^2 + \sum_{i=1}^{n} \frac{\sigma_i^2}{2}$.

Choose a constant ϱ satisfies $0 < \varrho \leq 1$, then we have

$$\dot{V} \leq -\varrho \bar{\theta} V^{\frac{\alpha+1}{2}} - (1-\varrho) \bar{\theta} V^{\frac{\alpha+1}{2}} + \phi_0 \tag{15}$$

Thus, $\dot{V} \leq -\varrho \bar{\theta} V^{\frac{\alpha+1}{2}}$ if $V^{\frac{\alpha+1}{2}} > \frac{\phi_0}{(1-\varrho)\bar{\theta}}$. Then by Lemma 2, we conclude that there exists a time $T_1^* \leq \frac{2V^{\frac{1-\alpha}{2}}(0)}{\varrho \bar{\theta}(1-\alpha)} < \infty$, such that $V^{\frac{\alpha+1}{2}}(t) \leq \frac{\phi_0}{(1-\varrho)\bar{\theta}}$ for all $t \geq T_1^*$, which means $V_0(t) \leq (\frac{\phi_0}{(1-\varrho)\bar{\theta}})^{\frac{2}{\alpha+1}}$ and $V_i(t) \leq (\frac{\phi_0}{(1-\varrho)\bar{\theta}})^{\frac{2}{\alpha+1}}, i \in \mathcal{V}, \forall t \geq T_1^*$.

At last, we give the bipartite steady-state errors estimations. Since $\mathcal{G}$ is connected, we obtain that for any nodes i, j, there exists a path $i = i_1, i_2, \ldots, i_s = j$ to connect i and j, then, we have $\sqrt{\Gamma}|x_i - \text{sign}(a_{ij})x_j| \leq \sqrt{|a_{i_1 i_2}|}|x_{i_1} - \text{sign}(a_{i_1 i_2})x_{i_2}| + \cdots +$

$\sqrt{|a_{i_{s-1}i_s}|}|x_{i_{s-1}} - \text{sign}(a_{i_{s-1}i_s})x_{i_s}|$, where $\Gamma = \min\{|a_{ij}|\}$. From Lemma 3 in [13], we can further obtain $\sqrt{|a_{i_1i_2}|}|x_{i_1} - \text{sign}(a_{i_1i_2})x_{i_2}| + \cdots + \sqrt{|a_{i_{s-1}i_s}|}|x_{i_{s-1}} - \text{sign}(a_{i_{s-1}i_s})x_{i_s}| \leq \sqrt{2(s-1)V_0(t)}$.Thus, for $t \geq T_1^*$, we have $|x_i - \text{sign}(a_{ij})x_j| \leq \frac{\sqrt{2(N-1)}}{\sqrt{\Gamma}}(\frac{\phi_0}{(1-\varrho)\bar{\theta}})^{\frac{1}{\alpha+1}}$. Further, we have $V_i(t) \geq \frac{\alpha 2^{\frac{(\alpha-1)(2-\alpha)}{\alpha}-1}}{(2-\alpha)k_i^{\frac{1}{\alpha}}}(v_i - v_i^*)^{\frac{2}{\alpha}}$, and for $t \geq T_1^*$, $|v_i - v_i^*| \leq (\frac{(2-\alpha)k_i^{\frac{1}{\alpha}}}{\alpha 2^{\frac{(\alpha-1)(2-\alpha)}{\alpha}-1}})^{\frac{\alpha}{2}}(\frac{\phi_0}{(1-\varrho)\bar{\theta}})^{\frac{\alpha}{\alpha+1}}$. For $t \geq T_1^*$, $|v_i^*| \leq k_i(2\lambda_{\max}(L))^{\frac{\alpha}{2}}(\frac{\phi_0}{(1-\varrho)\bar{\theta}})^{\frac{\alpha}{\alpha+1}}$ and $|v_i| \leq (\frac{(2-\alpha)k_i^{\frac{1}{\alpha}}}{\alpha 2^{\frac{(\alpha-1)(2-\alpha)}{\alpha}-1}})^{\frac{\alpha}{2}}(\frac{\bar{\eta}_0}{(1-\varrho)\bar{\theta}})^{\frac{\alpha}{\alpha+1}} + k_i(2\lambda_{\max}(L))^{\frac{\alpha}{2}}(\frac{\phi_0}{(1-\varrho)\bar{\theta}})^{\frac{\alpha}{\alpha+1}}$. Then, for $t \geq T_1^*$, we can obtain $|v_i - \text{sign}(a_{ij})v_j| \leq 2(\frac{(2-\alpha)k_i^{\frac{1}{\alpha}}}{\alpha 2^{\frac{(\alpha-1)(2-\alpha)}{\alpha}-1}})^{\frac{\alpha}{2}}(\frac{\phi_0}{(1-\varrho)\bar{\theta}})^{\frac{\alpha}{\alpha+1}} + 2k_i(2\lambda_{\max}(L))^{\frac{\alpha}{2}}(\frac{\phi_0}{(1-\varrho)\bar{\theta}})^{\frac{\alpha}{\alpha+1}}$. Thus, the bipartite errors will converge to the region Ω in finite time.

4 Numerical Results

The interactions between four agents are described over a signed undirected graph with $a_{12} = a_{21} = 0.1, a_{34} = a_{43} = 0.3, a_{13} = a_{31} = -0.2, a_{23} = a_{32} = -0.4$. The intrinsic nonlinear function $f_i(\cdot)$ is described as $f_1 = \sin(v_1) + 0.2v_1, f_2 = \sin(2v_2) + 0.2v_2, f_3 = \sin(3v_3) - 0.2v_3, f_4 = \sin(4v_4) - 0.2v_4$ [13]. The disturbances are chosen as $d_i(t) = 0.1\sin(it), i \in \mathcal{V}$. To perform simulations with the adaptive finite-time protocol (3) with update law (2), the control parameters are chosen as $\alpha = \frac{3}{5}, \kappa = 1, \kappa_1 = 1, \kappa_2 = 1, \kappa_3 = 1, o_i = 1, \rho_i = 0.1, \iota_i = 0.2, \sigma_i = 0.1, i \in \mathcal{V}$. The response curves of position and velocity states of all agents are given in Figs. 1 and 2, respectively.

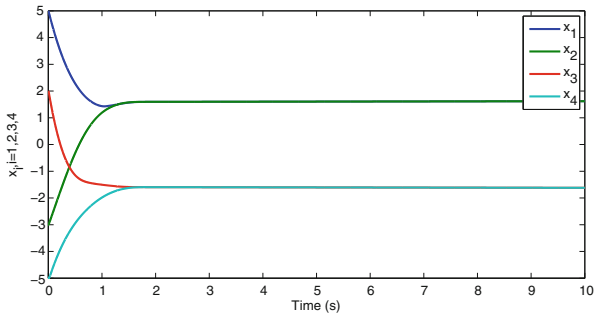

Fig. 1 The time responses of position states of all agents

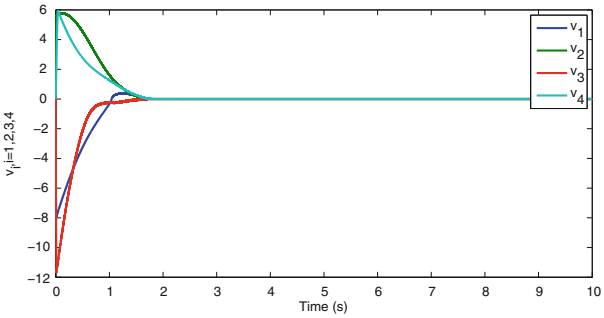

Fig. 2 The time responses of velocity states of all agents

5 Conclusion

In this paper, the adaptive finite-time bipartite consensus for second-order nonlinear multi-agent systems on coopetition networks is studied. Based on the finite-time stability theorem and adding a power integrator technique, a continuous adaptive distributed protocol with update law is designed. It is shown that the bipartite position and velocity errors of any two agents will converge to the desired small region in finite time.

Acknowledgments This work was supported by the National Basic Research Program of China (973 Program: 2012CB821201), and the NSFC (nos. 61603204, 61134005, 61221061, 61327807, 61573204, 61573203, 61501276).

References

1. Olfati-Saber R, Murray R (2004) Consensus problems in networks of agents with switching topology and time-delays. IEEE Trans Autom Control 49(9):1520–1533
2. Hong Y, Hu J, Gao L (2006) Tracking control for multi-agent consensus with an active leader and variable topology. Automatica 42(7):1177–1182
3. Li Z, Ren W, Liu X, Xie L (2013) Distributed consensus of linear multi-agent systems with adaptive dynamic protocols. Automatica 49(7):1986–1995
4. Wasserman S, Faust K (1994) Social Network Analysis: Methods and Applications, Cambridge. Cambridge Univ. Press, U.K
5. Altafini C (2013) Consensus problems on networks with antagonistic interactions. IEEE Trans Autom Control 58(4):935–946
6. Hu J, Zhu H (2015) Adaptive bipartite consensus on coopetition networks. Phys D 307(1):14–21
7. Valcher ME, Misra P (2014) On the consensus and bipartite consensus in high-order multi-agent dynamical systems with antagonistic interactions. Syst Control Lett 66:94–103
8. Bhat SP, Bernstein DS (2000) Finite-time stability of continuous autonomous systems. SIAM J Control Optim 38(3):751–766
9. Qian C, Lin W (2001) A continuous feedback approach to global strong stabilization of nonlinear systems. IEEE Trans Autom Control 46(7):1061–1079

10. Lu K, Xia Y (2013) Adaptive attitude tracking control for rigid spacecraft with finite time convergence. Automatica 49(12):3591–3599
11. Zhao L, Jia Y (2015) Finite-time attitude tracking control for a rigid spacecraft using time-varying terminal sliding mode techniques. Int J Control 88(6):1150–1162
12. Zhao Y, Duan Z, Wen G, Chen G (2015) Distributed finite-time tracking for a multi-agent system under a leader with bounded unknown acceleration. Syst Control Lett 81:8–13
13. Zhao L, Jia Y (2015) Finite-time consensus for second-order stochastic multi-agent systems with nonlinear dynamics. Appl Math Comput 270:278–290
14. Li S, Du H, Lin X (2011) Finite-time consensus algorithm for multi-agent systems with double-integrator dynamics. Automatica 47(8):1706–1712
15. Meng D, Jia Y, Du J (2015) Nonlinear finite-time bipartite consensus protocol for multi-agent systems associated with signed graphs. Int J Control 88(10):2074–2085
16. Meng D, Jia Y, Du J (2016) Finite-time consensus for multiagent systems with cooperative and antagonistic nteractions. IEEE Trans Neural Netw Learn Syst 27(4):762–770

Finite-Time Consensus Tracking for Second-Order Multi-agent Systems Without Relative Velocity Measurements

Ping Wang and Yingmin Jia

Abstract This paper considers the finite-time consensus tracking problem in directed networks of second-order multi-agent systems. Based on auxiliary system approach, a distributed control protocol is proposed for each follower, which only relies on the relative position measurements among the neighboring agents. Then, using homogeneous theory, sufficient conditions are derived to ensure that the states of the followers can track that of the leader in finite time under fixed topology. Moreover, the case under switching topology is also studied. Finally, numerical simulations are given to illustrate our theoretical results.

Keywords Second-order multi-agent systems · Finite-time · Consensus tracking · Homogeneous theory

1 Introduction

Recently, consensus tracking problem of multi-agent systems has received considerable attention and numerous interesting results have been obtained from different perspectives by many researchers. The objective of the consensus tracking is to design an appropriate consensus protocol guaranteeing that the states of the followers can track that of the leader.

Since many practical individual systems are of second-order dynamics, consensus tracking of second-order multi-agent systems has been widely investigated [1–6]. Note that most consensus protocols need both relative position and velocity measurements between neighboring agents. Unfortunately, velocity information of neighbor-

P. Wang (✉)
The Department of Mathematics and Physics, North China Electric Power University, Baoding 071003, China
e-mail: wangpinglh2014@126.com

Y. Jia
The Seventh Research Division, Beihang University (BUAA), Beijing 100191, China

Y. Jia et al. (eds.), *Proceedings of 2016 Chinese Intelligent Systems Conference*, Lecture Notes in Electrical Engineering 404, DOI 10.1007/978-981-10-2338-5_5

ing agents is not available in many practical situations. Furthermore, for practical systems, it is often required that consensus tracking can be achieved in finite time. Until now, there are some results about finite-time consensus tracking [7–12]. However, most existing results require that each topology of the systems be connected or have a spanning tree. In fact, the topology of the network may not always maintain connected or have a spanning tree because there might exist link failures or creations in a communication network of mobile agents. Therefore, it is more practical but challenging to investigate the finite-time consensus tracking problem of second-order multi-agent systems under switching topology, where only the union of the switching graphs has a spanning tree.

In this paper, we consider the finite-time consensus tracking problem in directed networks of second-order multi-agent systems under fixed and switching topologies, where the absence of relative velocity measurements is taken into account. The main contribution of this paper is twofold. First, we propose a unified control protocol without velocity measurements based on the auxiliary system approach. Second, we prove that finite-time consensus tracking can be achieved, respectively, under fixed and switching directed topologies, even when the union of the switching graphs across each bounded time internal has a spanning tree and the corresponding topology among the followers satisfies the detailed balance condition.

2 Problem Statement and Protocol Design

2.1 Problem Statement

Suppose that the multi-agent system consists of n followers and one leader. The dynamics of the ith follower is given by

$$\begin{aligned} \dot{x}_i(t) &= v_i(t), \\ \dot{v}_i(t) &= u_i(t), \end{aligned} \tag{1}$$

where $x_i(t), v_i(t), u_i(t) \in \mathbb{R}^m$ are the position, velocity and control input, respectively, and the leader's dynamics is described as follows:

$$\begin{aligned} \dot{x}_0(t) &= v_0(t), \\ \dot{v}_0(t) &= 0, \end{aligned} \tag{2}$$

where $x_0(t), v_0(t) \in \mathbb{R}^m$ are the position and velocity, respectively, of the leader. In this paper, we only consider one-dimensional space case, i.e., $m = 1$. With the aid of Kronecker product, we can easily obtain the high-dimensional case.

Definition 1 The multi-agent system is said to achieve finite-time consensus tracking, if for any initial states, there exist a protocol u_i and a finite-time T such that

$$\begin{aligned} &\lim_{t\to T^-} \|x_i(t) - x_0(t)\| = 0, \quad \lim_{t\to T^-} \|v_i(t) - v_0(t)\| = 0, \\ &x_i(t) = x_0(t), v_i(t) = v_0(t), \quad \forall i \in \mathscr{I}_n, \ \textit{if } t \geq T. \end{aligned} \tag{3}$$

2.2 Protocol Design

A unified control protocol without relative velocity measurements is proposed for each follower under fixed and switching topologies.

$$\begin{aligned} u_i(t) &= \sum_{j=1}^{n} a_{ij}(t)\varphi_1(\mathrm{sig}(x_j(t) - x_i(t))^{\alpha_1}) - b_i(t)\varphi_2(\mathrm{sig}(x_i(t) - x_0(t))^{\alpha_1}) + k_1\dot{y}_i(t), \\ \dot{y}_i(t) &= -k_2\varphi_3(\mathrm{sig}(y_i(t))^{\alpha_2}) + k_3\Big(\sum_{j=1}^{n} a_{ij}(t)\varphi_1(\mathrm{sig}(x_j(t) - x_i(t))^{\alpha_1}) \\ &\quad - b_i(t)\varphi_2(\mathrm{sig}(x_i(t) - x_0(t))^{\alpha_1})\Big), \end{aligned} \tag{4}$$

where $0 < \alpha_1 < 1$, $\alpha_2 = 2\alpha_1/(1+\alpha_1)$, and $k_i > 0, i = 1, 2, 3$. $a_{ij}(t)$ are adjacency elements of the corresponding interaction graph $\mathscr{G}_t$ and $b_i(t)$ are the corresponding adjacency weights between the follower i and the leader 0. The function $\mathrm{sig}(x)^\alpha = |x|^\alpha \mathrm{sign}(x)$, φ_k is a continuous odd function with $z\varphi_k(z) > 0 (\forall z \neq 0)$ and $\varphi_k(z) = c_k z + \mathrm{o}(z)$ around $z = 0$ for some $c_k > 0, k = 1, 2, 3$.

3 Main Results

In this section, with the aid of homogeneous theory [13], the finite-time consensus tracking problems for multi-agent systems (1) and (2) under fixed and switching topologies are investigated, respectively. First, we investigate the case with fixed topology, i.e., $\bar{\mathscr{G}}(t) = \bar{\mathscr{G}}$ for any time instant t.

3.1 Networks with Fixed Topology

Theorem 1 *Assume that the fixed graph $\bar{\mathscr{G}}$ has a spanning tree and the communication topology $\mathscr{G}$ among the followers satisfies the detailed balance condition. Then the second-order multi-agent system under protocol (4) can achieve finite-time consensus tracking.*

Proof The communication topology $\mathscr{G}$ among the followers satisfies the detailed balance condition, i.e., there exists a vector $\omega = [\omega_1, \omega_2, \dots, \omega_n]^{\mathrm{T}}$ with $\omega_i > 0, i = 1, 2, \dots, n$ such that $\omega_i a_{ij} = \omega_j a_{ji}$ for all $i, j \in \mathscr{I}_n$.

Under protocol (4), system (1) can be written as follows:

$$\begin{aligned}
\dot{x}_i(t) &= v_i(t),\\
\dot{v}_i(t) &= \sum_{j=1}^{n} a_{ij}\varphi_1(\mathrm{sig}(x_j(t) - x_i(t))^{\alpha_1}) - b_i\varphi_2(\mathrm{sig}(x_i(t) - x_0(t))^{\alpha_1}) + k_1\dot{y}_i(t),\\
\dot{y}_i(t) &= -k_2\varphi_3(\mathrm{sig}(y_i(t))^{\alpha_2}) + k_3\Big(\sum_{j=1}^{n} a_{ij}\varphi_1(\mathrm{sig}(x_j(t) - x_i(t))^{\alpha_1})\\
&\quad - b_i\varphi_2(\mathrm{sig}(x_i(t) - x_0(t))^{\alpha_1})\Big).
\end{aligned} \tag{5}$$

Let $\eta_i(t) = x_i(t) - x_0(t)$, $\eta_{n+i}(t) = v_i(t) - v_0(t)$, and $\eta_{2n+i}(t) = y_i(t)$, $i = 1, 2, \dots, n$. It follows from (2) and (5) that

$$\begin{aligned}
\dot{\eta}_i &= \eta_{n+i},\\
\dot{\eta}_{n+i} &= \sum_{j=1}^{n} a_{ij}\varphi_1(\mathrm{sig}(\eta_j - \eta_i)^{\alpha_1}) - b_i\varphi_2(\mathrm{sig}(\eta_i)^{\alpha_1}) + k_1\dot{\eta}_{2n+i},\\
\dot{\eta}_{2n+i} &= -k_2\varphi_3(\mathrm{sig}(\eta_{2n+i})^{\alpha_2}) + k_3\Big(\sum_{j=1}^{n} a_{ij}\varphi_1(\mathrm{sig}(\eta_j - \eta_i)^{\alpha_1})\\
&\quad - b_i\varphi_2(\mathrm{sig}(\eta_i)^{\alpha_1})\Big).
\end{aligned} \tag{6}$$

Denote $\eta(t) = [\eta_1(t), \eta_2(t), \dots, \eta_{3n}(t)]^{\mathrm{T}}$, and recall the fact that $\varphi_k(z) = c_k z + \mathrm{o}(z)$ around $z = 0$ for some $c_k > 0, k = 1, 2, 3$, we have that around the origin, system (6) can be written as

$$\begin{aligned}
\dot{\eta}_i &= \eta_{n+i} \triangleq f_i(\eta) + \hat{f}_i(\eta),\\
\dot{\eta}_{n+i} &\triangleq f_{n+i}(\eta) + \hat{f}_{n+i}(\eta),\\
\dot{\eta}_{2n+i} &\triangleq f_{2n+i}(\eta) + \hat{f}_{2n+i}(\eta), \quad \forall i \in \mathscr{I}_n,
\end{aligned} \tag{7}$$

where $f_i(\eta) = \eta_{n+i}, \hat{f}_i(\eta) = 0$, and

$$\begin{aligned}
f_{n+i}(\eta) &= (1 + k_1k_3)\Big(\sum_{j=1}^{n} c_1 a_{ij}\mathrm{sig}(\eta_j - \eta_i)^{\alpha_1} - c_2 b_i\mathrm{sig}(\eta_i)^{\alpha_1}\Big)\\
&\quad - k_1k_2c_3\mathrm{sig}(\eta_{2n+i})^{\alpha_2},\\
\hat{f}_{n+i}(\eta) &= (1 + k_1k_3)\Big(\sum_{j=1}^{n} a_{ij}\mathrm{o}(\mathrm{sig}(\eta_j - \eta_i)^{\alpha_1}) - b_i\mathrm{o}(\mathrm{sig}(\eta_i)^{\alpha_1})\Big)
\end{aligned}$$

$$
\begin{aligned}
&\quad - k_1 k_2 \mathrm{o}(\mathrm{sig}(\eta_{2n+i})^{\alpha_2}),\\
f_{2n+i}(\eta) &= k_3 \Big(\sum_{j=1}^{n} c_1 a_{ij} \mathrm{sig}(\eta_j - \eta_i)^{\alpha_1} - c_2 b_i \mathrm{sig}(\eta_i)^{\alpha_1} \Big) - k_2 c_3 \mathrm{sig}(\eta_{2n+i})^{\alpha_2},\\
\hat{f}_{2n+i}(\eta) &= k_3 \Big(\sum_{j=1}^{n} a_{ij} \mathrm{o}(\mathrm{sig}(\eta_j - \eta_i)^{\alpha_1}) - b_i \mathrm{o}(\mathrm{sig}(\eta_i)^{\alpha_1}) \Big)\\
&\quad - k_2 \mathrm{o}(\mathrm{sig}(\eta_{2n+i})^{\alpha_2}), \quad \forall i \in \mathscr{I}_n.
\end{aligned}
$$

In the following, we take three steps to prove the theorem.

Step 1. We prove that system (6) is globally asymptotically stable. Take the Lyapunov function V_1 for system (6) as follows:

$$
\begin{aligned}
V_1 = &\frac{1}{2} \sum_{i=1}^{n} \sum_{j=1}^{n} \int_0^{\eta_j - \eta_i} \omega_i a_{ij} \varphi_1(\mathrm{sig}(s)^{\alpha_1}) ds + \frac{1}{2} \sum_{i=1}^{n} \frac{k_1}{k_3} \omega_i \eta_{2n+i}^2 \\
&+ \sum_{i=1}^{n} \int_0^{\eta_i} \omega_i b_i \varphi_2(\mathrm{sig}(s)^{\alpha_1}) ds + \frac{1}{2} \sum_{i=1}^{n} \omega_i (\eta_{n+i} - k_1 \eta_{2n+i})^2.
\end{aligned} \tag{8}
$$

Since z and $\varphi_k(\mathrm{sig}(z)^{\alpha_1}), k = 1, 2$ have the same sign componentwise, it follows that $\int_0^{\eta_j - \eta_i} \omega_i a_{ij} \varphi_1(\mathrm{sig}(s)^{\alpha_1}) ds > 0$ for any $\eta_j - \eta_i \neq 0$ and $\int_0^{\eta_i} \omega_i b_i \varphi_2(\mathrm{sig}(s)^{\alpha_1}) ds > 0$ for any $\eta_i \neq 0$. Thus V_1 is positive definite with respect to $\eta_j - \eta_i$, η_i, η_{n+i}, and η_{2n+i} for any $i \neq j$, $i, j \in \mathscr{I}_n$, which implies that V_1 is a valid Lyapunov function for system (6).

Differentiating V_1 along the trajectory of the system (6) gives

$$
\begin{aligned}
\dot{V}_1 = &- \sum_{i=1}^{n} \sum_{j=1}^{n} \omega_i a_{ij} \varphi_1(\mathrm{sig}(\eta_j - \eta_i)^{\alpha_1}) \eta_{n+i} + \frac{k_1}{k_3} \sum_{i=1}^{n} \omega_i \eta_{2n+i} \dot{\eta}_{2n+i} \\
&+ \sum_{i=1}^{n} \omega_i b_i \varphi_2(\mathrm{sig}(\eta_i)^{\alpha_1}) \eta_{n+i} + \sum_{i=1}^{n} \omega_i (\eta_{n+i} - k_1 \eta_{2n+i})(\dot{\eta}_{n+i} - k_1 \dot{\eta}_{2n+i}) \\
= &- \frac{k_1 k_2}{k_3} \sum_{i=1}^{n} \omega_i \eta_{2n+i} \varphi_3(\mathrm{sig}(\eta_{2n+i})^{\alpha_2}) \leq 0.
\end{aligned}
$$

The last inequality comes from the fact that $\eta_{2n+i} \varphi_3(\mathrm{sig}(\eta_{2n+i})^{\alpha_2}) > 0$, for any $\eta_{2n+i} \neq 0, i \in \mathscr{I}_n$.

Denote the invariant set $S = \{\eta | \dot{V}_1 \equiv 0\}$. From $\dot{V}_1 \equiv 0$, we obtain that $\sum_{i=1}^{n} \omega_i \eta_{2n+i} \varphi_3(\mathrm{sig}(\eta_{2n+i})^{\alpha_2}) \equiv 0$, and then $\eta_{2n+i} \equiv 0, \forall i \in \mathscr{I}_n$. Together with (6), we have

$$
\sum_{j=1}^{n} a_{ij} \varphi_1(\mathrm{sig}(\eta_j - \eta_i)^{\alpha_1}) - b_i \varphi_2(\mathrm{sig}(\eta_i)^{\alpha_1}) = 0. \tag{9}
$$

Because the topology $\mathscr{G}$ among the followers satisfies the detailed balance condition, we have

$$\begin{aligned}&\sum_{i=1}^{n}\omega_i\eta_i\Big(\sum_{j=1}^{n}a_{ij}\varphi_1(\mathrm{sig}(\eta_j-\eta_i)^{\alpha_1})-b_i\varphi_2(\mathrm{sig}(\eta_i)^{\alpha_1})\Big)\\&=-\frac{1}{2}\sum_{i=1}^{n}\sum_{j=1}^{n}\omega_i a_{ij}(\eta_j-\eta_i)\varphi_1(\mathrm{sig}(\eta_j-\eta_i)^{\alpha_1})-\sum_{i=1}^{n}\omega_i b_i\eta_i\varphi_2(\mathrm{sig}(\eta_i)^{\alpha_1})\\&=0.\end{aligned}\tag{10}$$

Moreover, due to the fact that the graph $\bar{\mathscr{G}}$ has a spanning tree, we have $\eta_i=\eta_j=0,\forall i\neq j,i,j\in\mathscr{I}_n$. It follows from Lasalle's invariance principle that system (6) is globally asymptotically stable. That is,

$$\begin{aligned}&\lim_{t\to\infty}\|x_i(t)-x_0(t)\|=0,\\&\lim_{t\to\infty}\|v_i(t)-v_0(t)\|=0.\end{aligned}$$

Step 2. We show that the following reduced system of system (6)

$$\begin{aligned}&\dot{\eta}_i=f_i(\eta),\\&\dot{\eta}_{n+i}=f_{n+i}(\eta),\\&\dot{\eta}_{2n+i}=f_{2n+i}(\eta),\end{aligned}\tag{11}$$

is asymptotically stable and homogeneous of degree $\kappa=\alpha_1-1<0$ with dilation $(\underbrace{2,\dots,2}_{n},\underbrace{1+\alpha_1,\dots,1+\alpha_1}_{2n})$.

Take the Lyapunov function V_2 for system (11) as follows:

$$\begin{aligned}V_2=&\frac{1}{2}\sum_{i=1}^{n}\sum_{j=1}^{n}c_1\omega_i a_{ij}\frac{|\eta_j-\eta_i|^{1+\alpha_1}}{1+\alpha_1}+\frac{1}{2}\sum_{i=1}^{n}\frac{k_1}{k_3}\omega_i\eta_{2n+i}^2+\sum_{i=1}^{n}c_2\omega_i b_i\frac{|\eta_i|^{1+\alpha_1}}{1+\alpha_1}\\&+\frac{1}{2}\sum_{i=1}^{n}\omega_i(\eta_{n+i}-k_1\eta_{2n+i})^2,\end{aligned}\tag{12}$$

where V_2 is positive definite with respect to $\eta_j-\eta_i$, η_i, η_{n+i} and η_{2n+i} for any $i\neq j$, $i,j\in\mathscr{I}_n$.

Following the similar argument as in Step 1, it follows from Lasalle's invariance principle that system (11) is globally asymptotically stable.

Furthermore, based on the following fact

$$\epsilon^{1+\alpha_1}\eta_{n+i}=\epsilon^{\kappa+2}\eta_{n+i},\tag{13}$$

$$(1+k_1k_3)\Big(\sum_{j=1}^{n} c_1a_{ij}\mathrm{sig}(\epsilon^2\eta_j-\epsilon^2\eta_i)^{\alpha_1}-c_2b_i\mathrm{sig}(\epsilon^2\eta_i)^{\alpha_1}\Big)-k_1k_2c_3\mathrm{sig}(\epsilon^{1+\alpha_1}\eta_{2n+i})^{\alpha_2}$$
$$=\epsilon^{\kappa+1+\alpha_1}\Big[(1+k_1k_3)\Big(\sum_{j=1}^{n} c_1a_{ij}\mathrm{sig}(\eta_j-\eta_i)^{\alpha_1}-c_2b_i\mathrm{sig}(\eta_i)^{\alpha_1}\Big)-k_1k_2c_3\mathrm{sig}(\eta_{2n+i})^{\alpha_2}\Big], \tag{14}$$

and

$$k_3\Big(\sum_{j=1}^{n} c_1a_{ij}\mathrm{sig}(\epsilon^2\eta_j-\epsilon^2\eta_i)^{\alpha_1}-c_2b_i\mathrm{sig}(\epsilon^2\eta_i)^{\alpha_1}\Big)-k_2c_3\mathrm{sig}(\epsilon^{1+\alpha_1}\eta_{2n+i})^{\alpha_2}$$
$$=\epsilon^{\kappa+1+\alpha_1}\Big[k_3\Big(\sum_{j=1}^{n} c_1a_{ij}\mathrm{sig}(\eta_j-\eta_i)^{\alpha_1}-c_2b_i\mathrm{sig}(\eta_i)^{\alpha_1}\Big)-k_2c_3\mathrm{sig}(\eta_{2n+i})^{\alpha_2}\Big], \tag{15}$$

we know that system (11) is homogeneous of degree $\kappa=\alpha_1-1<0$ with dilation $(\underbrace{2,\ldots,2}_{n},\underbrace{1+\alpha_1,\ldots,1+\alpha_1}_{2n})$.

Step 3. We prove that $\lim\limits_{\epsilon\to 0}\dfrac{\hat{f}_i(\epsilon^2\eta_1,\ldots,\epsilon^2\eta_n,\epsilon^{1+\alpha_1}\eta_{n+1},\ldots,\epsilon^{1+\alpha_1}\eta_{3n})}{\epsilon^{\kappa+r_i}}=0, i\in\mathscr{I}_{3n}$, where $r_i=2, i\in\mathscr{I}_n$ and $r_i=1+\alpha_1, i\in\mathscr{I}_{3n}/\mathscr{I}_n$.

First,

$$\lim_{\epsilon\to 0}\frac{\hat{f}_i(\epsilon^2\eta_1,\ldots,\epsilon^2\eta_n,\epsilon^{1+\alpha_1}\eta_{n+1},\ldots,\epsilon^{1+\alpha_1}\eta_{3n})}{\epsilon^{\kappa+2}}=\lim_{\epsilon\to 0}\frac{0}{\epsilon^{\kappa+2}}=0,\ i\in\mathscr{I}_n, \tag{16}$$

Note that $\eta_i(t)\to 0$, $\eta_{n+i}(t)\to 0$ and $\eta_{2n+i}(t)\to 0, i\in\mathscr{I}_n$ as $t\to\infty$, then there exist a bounded constant $M>0$ and a time instant $t_0>0$, such that $|\eta_i(t)|\le M$, $|\eta_{n+i}(t)|\le M$ and $|\eta_{2n+i}(t)|\le M$ hold for any $t\ge t_0$.

$$\lim_{\epsilon\to 0}\frac{\hat{f}_{n+i}(\epsilon^2\eta_1,\ldots,\epsilon^2\eta_n,\epsilon^{1+\alpha_1}\eta_{n+1},\ldots,\epsilon^{1+\alpha_1}\eta_{3n})}{\epsilon^{\kappa+1+\alpha_1}}$$
$$=\lim_{\epsilon\to 0}\frac{\big\{(1+k_1k_3)[\sum_{j=1}^{n}a_{ij}\mathrm{o}(\epsilon^{2\alpha_1}\mathrm{sig}(\eta_j-\eta_i)^{\alpha_1})b_i\mathrm{o}(\epsilon^{2\alpha_1}\mathrm{sig}(\eta_i)^{\alpha_1})]-k_1k_2\mathrm{o}(\epsilon^{2\alpha_1}\mathrm{sig}(\eta_{2n+i})^{\alpha_2})\big\}}{\epsilon^{2\alpha_1}} \tag{17}$$
$$=0,\ \ i\in\mathscr{I}_n.$$

Similarly, we have

$$\lim_{\epsilon\to 0}\frac{\hat{f}_{2n+i}(\epsilon^2\eta_1,\ldots,\epsilon^2\eta_n,\epsilon^{1+\alpha_1}\eta_{n+1},\ldots,\epsilon^{1+\alpha_1}\eta_{3n})}{\epsilon^{\kappa+1+\alpha_1}}=0,\ \ i\in\mathscr{I}_n. \tag{18}$$

Moreover, $\hat{f}_i(0) = 0, \forall i \in \mathscr{I}_{3n}$. Thus, system (11) is globally finite-time stable, which implies that consensus tracking for systems (1) and (2) under protocol (4) can be achieved in finite time. This completes the proof.

3.2 Networks with Switching Topology

To describe the switching topology, a switching signal $\sigma(t)(\sigma$ for short):$[0, \infty) \to \Gamma$ is introduced, where Γ denotes the finite switching index set. Then the interaction graph at time instant t is denoted by $\bar{\mathscr{G}}_\sigma$. Consider an infinite sequence of nonempty, bounded and contiguous time intervals $[t_s, t_{s+1}), s = 0, 1, 2, \ldots$, with $t_0 = 0$ and $t_{s+1} - t_s \le T_1$ for some constant $T_1 > 0$. Suppose that in each interval $[t_s, t_{s+1})$ there is a sequence of nonoverlapping subintervals

$$[t_{s_0}, t_{s_1}), [t_{s_1}, t_{s_2}), \ldots, [t_{s_{m_s-1}}, t_{s_{m_s}})$$

with $t_{s_0} = t_s$, $t_{s_{m_s}} = t_{s+1}$ satisfying $t_{s_{k+1}} - t_{s_k} \ge T_2$, $0 \le k \le m_s - 1$, for some integer $m_s \ge 0$ and constant $T_2 > 0$ such that the communication topology $\bar{\mathscr{G}}_\sigma$ switches at t_{s_k} and it does not change during each subinterval $[t_{s_k}, t_{s_{k+1}})$. Obviously, there are at most $N = \lfloor T_1/T_2 \rfloor$ subintervals in each interval $[t_s, t_{s+1}), s = 0, 1, 2, \ldots$.

Theorem 2 *Assume that for any switching signal $\sigma(\cdot)$, the union of the switching graphs $\bar{\mathscr{G}}_{s_0}, \bar{\mathscr{G}}_{s_1}, \ldots, \bar{\mathscr{G}}_{s_{m_s-1}}$ across each internal $[t_s, t_{s+1}), s = 0, 1, 2, \ldots$ has a spanning tree and the corresponding topology among the followers satisfies the detailed balance condition. Then the second-order multi-agent system under protocol (4) can achieve finite-time consensus tracking.*

Proof The proof of Theorem 2 is similar to that of Theorem 1 and thus omitted.

4 Simulation Results

Consider a multi-agent system consisting of 5 followers and 1 leader with communication topologies shown in Fig. 1, where the weights are indicated on the edges. Agents 1–5 are followers and agent 0 is the leader. Let $\omega = [2, 1, 3, 1.5, 1]^{\mathrm{T}}$, the communication topologies $\mathscr{G}_i, i = 1, 2, 3$ among the followers satisfy the detailed balance condition. Note that the union of the topology $\bar{\mathscr{G}}_1$, $\bar{\mathscr{G}}_2$ and $\bar{\mathscr{G}}_3$ has a directed spanning tree.

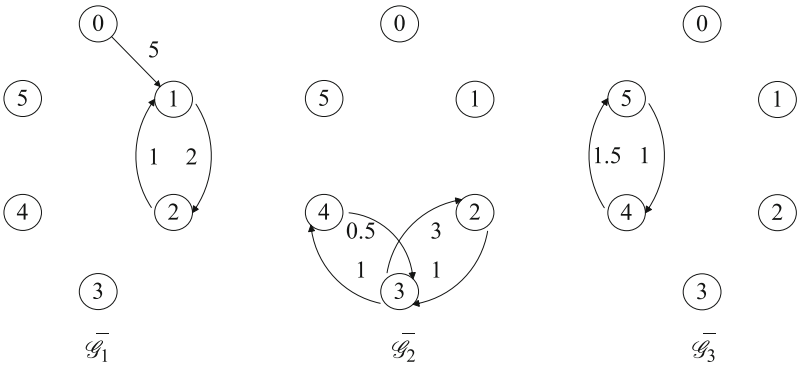

Fig. 1 Three directed graphs with 5 followers and 1 leader

Let $\varphi_k(x) = x, k = 1, 2, 3$, the dynamics of the followers is given as follows:

$$\begin{aligned}
\dot{x}_i(t) &= v_i(t),\\
\dot{v}_i(t) &= -k_1k_2\mathrm{sig}(y_i(t))^{\alpha_2} + (1+k_1k_3)\Big(\sum_{j=1}^{n} a_{ij}(t)\mathrm{sig}(x_j(t)-x_i(t))^{\alpha_1}\\
&\quad - b_i(t)\mathrm{sig}(x_i(t)-x_0(t))^{\alpha_1}\Big),\\
\dot{y}_i(t) &= -k_2\mathrm{sig}(y_i(t))^{\alpha_2} + k_3\Big(\sum_{j=1}^{n} a_{ij}(t)\mathrm{sig}(x_j(t)-x_i(t))^{\alpha_1}\\
&\quad - b_i(t)\mathrm{sig}(x_i(t)-x_0(t))^{\alpha_1}\Big).
\end{aligned} \tag{19}$$

Here, the parameters are $\alpha_1 = 0.9, \alpha_2 = 2\alpha_1/(1+\alpha_1) = 0.9474$ and $k_i = 1$, $i = 1, 2, 3$. Moreover, the initial states of the followers are given as $x(0) = [-30, -10, 10, 30, 60]^{\mathrm{T}}$, $v(0) = [-1, -2, 2, -3, 3]^{\mathrm{T}}$, and $y(0) = [0, 0, 0, 0, 0]^{\mathrm{T}}$. Correspondingly, the initial states of the leader 0 are $x_0(0) = 20$ and $v_0(0) = 1$, respectively. The communication topology switches every 0.1 s in the sequence $\bar{\mathcal{G}}_1 \to \bar{\mathcal{G}}_2 \to \bar{\mathcal{G}}_3 \to \bar{\mathcal{G}}_1 \to \ldots$. Figure 2 shows the state trajectories of the network switching among $\bar{\mathcal{G}}_1$, $\bar{\mathcal{G}}_2$ and $\bar{\mathcal{G}}_3$, from which we can see that consensus tracking can be achieved in finite time.

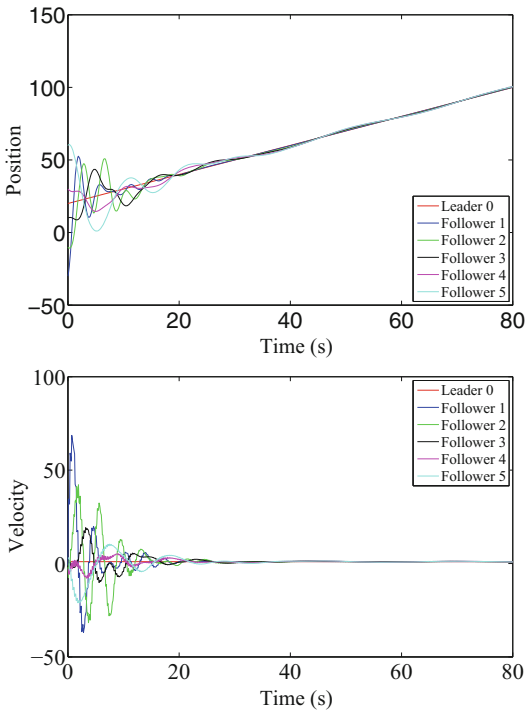

Fig. 2 The state trajectories of the network switching among $\bar{\mathcal{G}}_1$, $\bar{\mathcal{G}}_2$ and $\bar{\mathcal{G}}_3$

5 Conclusions

The finite-time consensus tracking problem in directed networks of second-order multi-agent systems is considered in this paper. Based on the auxiliary system approach, a unified protocol is proposed for the followers without relative velocity measurements. Sufficient conditions are derived to ensure that the consensus tracking can be achieved in finite time under fixed and switching topologies, respectively.

Acknowledgments The work was supported by the National 973 Program (Grant No. 2012CB821200 and 2012CB821201), the National Natural Science Foundation of China (Grant No. 61134005, 61221061 and 61327807), and the Fundamental Research Funds for the Central Universities 2016MS129.

References

1. Hong Y, Hu J, Gao L (2006) Tracking control for multi-agent consensus with an active leader and variable topology. Automatica 42(7):1177–1182
2. Hong Y, Chen G, Bushnell L (2008) Distributed observers design for leader-following control of multi-agent networks. Automatica 44(3):846–850

3. Hu J, Hong Y (2007) Leader-following coordination of multi-agent systems with coupling time delays. Phys A 374(2):853–863
4. Peng K, Yang Y (2009) Leader-following consensus problem with a varying-velocity leader and time-varying delays. Phys A 388(2–3):193–208
5. Zhu W, Cheng D (2010) Leader-following consensus of second-order agents with multiple time-varying delays. Automatica 46(12):1994–1999
6. Song Q, Cao J, Yu W (2010) Second-order leader-following consensus of nonlinear multi-agent systems via pinning control. Syst Control Lett 59(9):553–562
7. Bhat SP, Bernstein DS (2000) Finite-time stability of continuous autonomous systems. SIAM J Control Optim 38(3):751–766
8. Li S, Du H, Lin X (2011) Finite-time consensus algorithm for multi-agent systems with double-integrator dynamics. Automatica 47(8):1706–1712
9. Sun F, Guan Z (2013) Finite-time consensus for leader-following second-order multi-agent system. Int J Syst Sci 44(4):727–738
10. Lu X, Lu R, Chen S, Lu J (2013) Finite-time distributed tracking control for multi-agent systems with a virtual leader. IEEE Trans Circuits Syst I Regul Pap 60(2):352–362
11. Zheng Y, Zhu Y, Wang L (2014) Finite-time consensus of multiple second-order dynamic agents without velocity measurements. Int J Syst Sci 45(3):579–588
12. Zhang Y, Yang Y (2013) Finite-time consensus of second-order leader-following multi-agent systems without velocity measurements. Phys Lett A 377:243–249
13. Rouche N, Habets P, Laloy M (1977) Stability theory by Liapunov's direct methodright. Springer, New York

Inland Moving Ships Detection via Compressive Sensing and Saliency Detection

Pingping Lu, Qing Liu, Fei Teng, Langqi Mei and Jing Li

Abstract This paper presents an effective inland moving ships' detection method fused with compressive sensing and saliency detection to attack the challenge: when the ships detected suffer serious cavities due to their large size, relatively low speed, and uniform color. The background is composed of a K-SVD dictionary and a mean set of K-SVD coefficients associated to each pixel. To address the problem that the background and difference image are corrupted by the movement traces when ships sail into the first frame, the logical bitwise AND is performed between difference image and saliency map to get the exact result. Due to the use of K-SVD coefficients, the background is blurry. Then background update strategy is put forward to eliminate the movement traces and make the background more clearly. Finally, both qualitative and quantitative evaluations on several challenging inland video sequences demonstrate that the proposed algorithm outperforms several state-of-the-art methods in terms of efficiency and accuracy.

Keywords Compressive sensing · Saliency detection · Moving ships detection · Inland waterway · Background subtraction

1 Introduction

The intelligent video analysis in inland waterway closed circuit television (CCTV) video sequences has got increasing attention in the past few years. It provides some important information for us, such as traffic capacity, traffic quality, and accident rate. Moving ships detection plays a key role in CCTV intelligent video analysis.

P. Lu · Q. Liu (✉) · L. Mei · J. Li
School of Automation, Wuhan University of Technology,
Wuhan 430070, Hubei, China
e-mail: qliu2000@163.com

F. Teng
School of Energy and Power Engineering, Wuhan University of Technology,
Wuhan 430070, Hubei, China

Y. Jia et al. (eds.), *Proceedings of 2016 Chinese Intelligent Systems Conference*,
Lecture Notes in Electrical Engineering 404, DOI 10.1007/978-981-10-2338-5_6

The common and classical approaches for moving objects detection are divided into three main categories: optical flow, frame subtraction, and background subtraction (BS). Because CCTV video sequences are monitored by a fixed camera view and the background is relatively considered constant, background subtraction is the preferred method to segment moving ships. An important number of background subtraction approaches are proposed in the related literature with more or less success in different difficult cases. The paper [1] enhances the Gaussian Mixture Model (GMM) by adaptively determining the number of Gaussian distribution. It has better robustness to illumination variation, but there is still some noise for ripple. The GMM method do not consider spatial characteristics, Barnich et al. [2] present Visual Background Extractor (ViBe) which builds background in terms of time-space consistency. This technique has a good real-time performance. Nevertheless, the phony targets emerge from silhouette when moving objects go into the first frame, subsequently disappearing slowly. Motivated by [2], St-Charles et al. [3] improve Local Binary Similarity Segmenter (LOBSTER) for background subtraction followed background initialization mode of ViBe. However, ships detected undergo serious cavities due to their large size, relatively low speed, and uniform color.

The former approaches model background in spatial domain, Cevher et al. [4] reconstruct measured value differences which is obtained by subtracting measured value of background from measured value of original image in wavelet domain, and update the measured value of background. It requires the objects of interest occupy a small portion of the camera view, so it is not applicable to ships. Huang et al. [5] develop adaptive Dynamic Group Sparsity (AdaDGS) algorithm. It considers foreground as dynamic group sparse data. The method reconstructs foreground by dictionary and coefficient, and then update dictionary. It brings out infamous results in the case that a slow ship and a fast ship are traveling at the same time. While David et al. [6] do not change dictionary and model background by a mean set of coefficients. The constraint that the average of coefficients set satisfies Gaussian distribution eliminates the influence of dynamic backgrounds. However, there is no clear background update mechanism.

Parks et al. [7] point out that saliency detection is always determined as post-processing technique, which verifies a blob represents a valid foreground by checking it contains a certain percentage of pixels that are highly salient. But most frames contain only highly salient blobs. Teng et al. [8] fuse improved GMM and saliency detection via ITTI model. In the saliency map, surrounding parts that do not belong to object area may be detected.

Motivated by the above-mentioned discussions, we propose an inland moving ships' detection method fused with compressive sensing with saliency detection. The remainder of this paper is organized as follows: Sect. 2 describes our proposed framework in details. Section 3 conducts several experiments on challenging CCTV video sequences to illustrate the effectiveness of the proposed method. Finally, Sect. 4 presents a brief summary.

2 Inland Moving Ships Detection

The proposed method is summarized in Table 1. Following it, we will describe the main steps in Sects. 2.1–2.4 sequentially.

2.1 Background Subtraction Based on Compressive Sensing

The t-th frame $\boldsymbol{I}_t$ of video sequence consists of background $\boldsymbol{b}$, foreground $\boldsymbol{f}_t$ and some noise z_t: $\boldsymbol{I}_t = \boldsymbol{b} + \boldsymbol{f}_t + z_t$. Based on compressive sensing theory, background could be linearly represented by the atoms of dictionary $\boldsymbol{D}$: $\boldsymbol{b} = \boldsymbol{D}\alpha$. The dictionary is calculated by solving the minimization problem subjected to error ε via K-SVD algorithm [9]

$$\min_{\boldsymbol{D},A} \|\boldsymbol{A}\|_0 \text{ s.t.} \|\boldsymbol{Y} - \boldsymbol{D}\boldsymbol{A}\|_2 < \varepsilon \tag{1}$$

In the dictionary learning stage, in order to avoid the dictionary being corrupted by foreground pixels, m frames selected randomly from video sequence compose the training set, n patches ($bb \times bb$ neighbors of pixel) selected from each images of the training set and changed into column vector compose the original data set $\boldsymbol{Y}$. That is to say, $\boldsymbol{Y} \in R^{M \times N}$, $\boldsymbol{D} \in R^{M \times K}$, sparse coefficient matrix $\boldsymbol{A} \in R^{K \times N}$, where $M = bb^2$, $N = m \cdot n$.

Due to ships' large size, relatively low speed, and uniform color, pixel value is probable to remain the same for a long time, subsample of video sequence is not adopted and decomposition coefficients of the subsampled data set by orthogonal matching pursuit is not performed, instead of sparse coefficient matrix obtained in the dictionary learning stage directly. Hence, after classifying the column vectors of matrix $\boldsymbol{A}$ by pixel location, each pixel has a set of coefficients associated, $\{\alpha_{il}\alpha_i \in \boldsymbol{A}\}$ ($i = 1,\ldots,l$), where $l = \lfloor N/(w \cdot h) \rfloor$, w, h are the width and height of image,

Table 1 Basic flow of our algorithm

Set parameters:
Step 1: Set parameters, such as the number of atoms in dictionary K, patch size bb, the number of training image/patches m/n, error threshold for dictionary learning ε, threshold for background update T_1.
Model computation:
Step 2: Learn K-SVD dictionary and coefficients (see Eq. 1)
Step 3: Compute a mean set of coefficients (see Eq. 2)
Online segmentation phase:
For each frame
Step 4: Compute estimated background (see Eq. 3)
Step 5: Compute difference image (see Eq. 4) and impose threshold by Otsu algorithm on difference image
Step 6: Extract saliency map and impose threshold by improved Otsu algorithm on saliency map
Step 7: Perform a logical bitwise AND on saliency map and difference image (see Eq. 5)
Step 8: Update the mean set of coefficients
End For

Fig. 1 Results of background subtraction based on compressive sensing. From left to right: original frame, background, foreground, background-foreground binary image

respectively, Furthermore, to model estimated background $\boldsymbol{b}'$ with the mean set of coefficients α' and $\boldsymbol{D}$, and to compute difference image $\boldsymbol{f}_t'$ with $\boldsymbol{b}'$ and reconstructed image of the current frame $\boldsymbol{I}_t'$, as Eqs. 2–4.

$$\alpha^{'} = \frac{1}{l}\sum_{i=1}^{l}\alpha_i \tag{2}$$

$$\boldsymbol{b}^{'}(x,y) = \frac{1}{bb^2}\sum_{i=1}^{bb}\sum_{j=1}^{bb}\boldsymbol{D}\alpha'_{(i+x,j+y)} \tag{3}$$

$$\boldsymbol{f}_t^{'} = \left|\boldsymbol{I}_t^{'} - \boldsymbol{b}^{'}\right| \tag{4}$$

Finally, a global adaptive threshold on difference image will output the background-foreground binary map. As shown in Fig. 1, the location and hull of the ships are detected rough but fully, though the background and difference image are corrupted by the movement traces when ships sail into the first frame. Due to the use of K-SVD coefficients, the background is a little bit blurry. The foreground is corrupted by some branches and other noise. Later then the paper adopts saliency detection to obtain more accurate foreground and eliminates the movement traces of ships by updating background.

2.2 *Inland Saliency Extraction*

Motivated by the paper 8, this paper analyzes several advanced algorithms (ITTI, LC, FT, SR, HC, RC) mentioned in the paper [10]. As shown in Fig. 2, objects extracted by AC [11] method have clear and complete contours, with no cavities and other surrounding parts which do not belong to object area. The AC method not only has higher contrast between saliency region and non-saliency region, but also has low misdetection rate and less noise. The paper extracts the color and luminance features in CIELab color space, computes multi-scales saliency maps based on AC, and then fuses them to gain the final saliency map.

Finally, a global adaptive threshold based on an improved Otsu algorithm [12] is imposed on the saliency map to output the binary saliency map. The approach considers not only the distance between classes but also the distances of pixels in

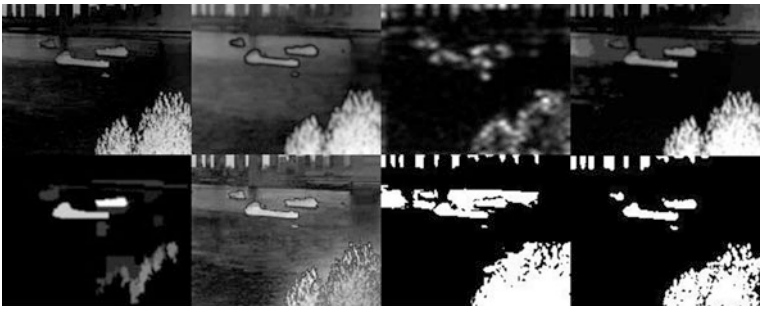

Fig. 2 Saliency detection results. The 1st row: LC, FT, SR, HC; The 2nd row: RC, AC, binary saliency maps segmented by Otsu and improved Otsu, respectively

one class, and imposes a constraint by Trough Stressed method to get more exact threshold. As shown in Fig. 2, compared with the result by Otsu algorithm, the result by improved Otsu algorithm is in a relatively noise-free environment.

2.3 The Integrated Strategy of Moving Ships Detection

The background subtraction based on compressive sensing usually detects the movement traces of ships and the edge of ships are vague, while inland saliency detection based on AC often extract all interested ships regardless of moving or static and the contours of ships are clear. The result of moving ships detection is performed after a logical bitwise AND on saliency map $\boldsymbol{S}_t$ and difference image $\boldsymbol{f}_t^{'}$ as Eq. 5 through synthesizing the advantage of the two approaches, as shown in Fig. 3.

$$\boldsymbol{f}_t = \boldsymbol{S}_t \cap \boldsymbol{f}_t^{'} \tag{5}$$

2.4 Background Update Mechanism

The result still has some noise as shown in Fig. 3; in order to achieve robust moving ship detection for a long time, online learning background is adapted to the

Fig. 3 Background update results. From left to right: the final result of first frame, background and the final result of the 100th frame, respectively

changes of background. So the paper adds a new background update scheme. In Sect. 2.1, the estimate background is determined by the dictionary $\boldsymbol{D}$ and the mean set of coefficients $\alpha^{'}$, we consider that dictionary remains the same and the mean set of coefficients gets updated. First, count the number,*Count*, of the pixels in the neighborhood which are foreground pixels. If it exceeds a certain threshold T_1, then update the coefficients set and mean coefficients of pixels in background. This could reduce the influence of noise and isolate pixels. β is learning rate, the larger the learning rate, the faster the background updates. The movement traces of ships in background will fade away gradually as shown in Fig. 3.

$$\alpha_t^{'}(x,y) = \begin{cases} (1-\beta)\alpha_{t-1}^{'}(x,y) + \beta\alpha_t(x,y), & Count > T_1 \\ \alpha_{t-1}^{'}(x,y), & Count \le T_1 \end{cases} \tag{6}$$

3 Experimental, Results and Discussion

3.1 Experimental and Results

In this section, we evaluate our approach with five state-of-the-art methods on six challenging CCTV video sequences. The five referenced approaches we compare with are GMM [1], ViBe [2], LOBSTER [3], AdaDGS [5], GMCA [6]. All parameters involved in the one considered for comparison are manually tuned to obtain the best result. The parameters of this paper are similar to GMCA: $m = 100$, $n = 1000$, $bb = 7$, $K = 200$, $\varepsilon = 0.1$, $T_1 = 3$.

The six video sequences are collected from local maritime bureau. The first sequence present two ships with fast and slow speed are traveling, and the camera shakes slightly in previous 50 frames. The second sequence represents an extreme case of dynamic scene with a large amount of ripple, the ships are traveling in the opposite direction and they suffer partial or even full occlusion some time later. The third sequence includes previous 267 frames without moving ships but a lot of ripple, the yacht gets into the scene from the 268th frame. The ship in the fourth sequence is so big and its speed is quite slow. This scene representing slow boats is easy to cause serious cavities. The ship in the fifth sequence which has change of scale enters into image in the bright light. In view of time cost, the size of images in all sequence is 128×160.

Figure 4 displays the qualitative comparison of our approach against state-of-the-art approaches on the considered video sequences. All ground truths are calibrated by manual. Our approach performs better than GMM in terms of noise removal for water ripple. In the case of the first, fourth, and fifth sequences our method clearly outperforms the ViBe, LOBSTER, AdaDGS in the camouflaged foreground areas. Our proposal apparently compensates cavities in the condition of the fourth and fifth sequences. The method has low misdetection rate for slow freighters.

Fig. 4 Comparative results on six video sequences. From left to right: test frame, ground truth, GMM, ViBe, LOBSTER, AdaDGS, GMCA, ours, respectively

Table 2 demonstrates some quantitative measures computed on the six sequences. For this purpose, 200 frames which are the 301th–500th frame in each sequence with corresponding ground truths are considered. The scores presented in Table 2 are the averages on those 200 frames. The measures we use are the ones presented in [13]. In most cases our approach scores much better than the considered state-of-the-art approaches. Otherwise, the numerical results are comparable, the score differences being very small.

3.2 Discussion

For modeling background, we used the K-SVD coefficients instead of decomposition coefficients by orthogonal matching pursuit. The background is a little bit blurry. But it causes that the ships detected more complete with no cavities. A global adaptive threshold instead of a fixed threshold enables us to automatically output background-foreground binary map. Meanwhile, this filtering stage removes some noise. However, there is still some movement traces of ships left in the foreground, and this is where saliency detection intervenes. The saliency map by AC algorithm and a threshold by improved Otsu algorithm detect the location of ships in current frame and remove water ripple. What is more, background update stage is adapted to the changes of background.

Because of the use of background subtraction, this approach has no clearly distinguishable difference when ships have similar color with other region. Saliency

Table 2 Quantitative scores

Sequence	Measures	GMM	ViBe	LOBSTER	AdaDGS	GMCA	Ours
1st	Recall	0.5731	0.5605	0.4840	0.4456	0.5673	**0.8110**
	Precision	0.2264	0.3353	0.4626	0.2671	0.1121	**0.6591**
	F-measure	0.3245	0.4196	0.4784	0.3340	0.1873	**0.7272**
2nd	Recall	0.4942	0.4719	0.0781	0.1149	0.6761	**0.8717**
	Precision	0.5343	0.5866	**0.8359**	0.1973	0.1846	0.7677
	F-measure	0.5135	0.5231	0.1429	0.1453	0.2899	**0.8164**
3rd	Recall	0.4068	**0.5712**	0.5072	0.1851	0.3989	0.4985
	Precision	0.5692	0.5281	**0.5815**	0.0644	0.4342	0.5245
	F-measure	0.4745	**0.5488**	0.5418	0.0956	0.4158	0.5112
4th	Recall	0.4023	0.8447	0.7828	0.2088	0.3321	**0.9638**
	Precision	0.3100	0.5240	0.7840	0.5913	0.0881	**0.8987**
	F-measure	0.3502	0.6468	0.7834	0.3086	0.1393	**0.9301**
5th	Recall	0.2367	0.5349	0.1163	0.5775	0.4130	**0.8406**
	Precision	0.2489	0.8055	0.8604	0.3126	0.2870	**0.9119**
	F-measure	0.2426	0.6429	0.2050	0.4056	0.3387	**0.8784**
6th	Recall	0.3400	0.3454	0.1036	0.8519	0.4445	**0.9400**
	Precision	0.4181	0.2034	0.2626	0.5263	0.2939	**0.9126**
	F-measure	0.3750	0.2560	0.1486	0.6506	0.4542	**0.9261**

detection identifies the most visually noticeable foreground object in the scene and focuses on such perceived important regions, it gets useless result when ships are very small that even people cannot see or they are not significant area compared with other object. There is no enough sequences to observe the result especially when a static ship starts moving or a moving ship becomes static after a period of time.

4 Conclusion

This paper improves the GMCA algorithm. First, we use K-SVD to set up blurry background model, and then fuse difference image and saliency map to get the exact result of initial frame. We also put forward background update strategy to eliminate ships' movement traces in background. Both visual comparison and numerical scores computed for these sequences prove that our approach yields better robustness than some state-of-the-art techniques, especially when ships are very big with relatively slow speed, the color of hull is approximately similar and moving ships sail into the initial frame.

Acknowledgments This work is supported by the National Natural Science Foundation of China under Grant No. 51279152 and the Independent Innovation Foundation of Wuhan University of Technology under Grant No. 155211005.

References

1. KaewTraKulPong P, Bowden R (2002) An improved adaptive background mixture model for real-time tracking with shadow detection. Video-based surveillance systems, pp 135–144
2. Barnich O, Van Droogenbroeck Marc M (2011) ViBe: a universal background subtraction algorithm for video sequences. IEEE Trans Image Process 20(6):1709–1724
3. St-Charles P-L, Bilodeau G-A (2014) Improving background subtraction using local binary similarity patterns. In: 2014 IEEE winter conference on applications of computer vision (WACV 2014), pp 509–515
4. Cevher V, Sankaranarayanan A, Duarte MF et al (2008) Compressive sensing for background subtraction. In: 10th European conference on computer vision (ECCV 2008), pp 155–168
5. Huang J, Huang X, Metaxas D (2009) Learning with dynamic group sparsity. In: 12th IEEE international conference on computer vision, pp 64–71
6. David C, Gui V (2013) Sparse coding and gaussian modeling of coefficients average for background subtraction. In: 8th international symposium on image and signal processing and analysis (ISPA), pp 230–235
7. Parks DH, Fels SS (2008) Evaluation of background subtraction algorithms with post-processing. In: IEEE 5th international conference on advanced video and signal based surveillance (AVSS 2008), pp 192–199
8. Teng F, Liu Q, Zhu L et al (2015) Ripple—driven ship detection in inland waterway CCTV system. Comput Simul 32(6):247–250 (in Chinese)
9. Aharon M, Elad M, Bruckstein A (2006) K-SVD: an algorithm for designing over-complete dictionaries for sparse representation. IEEE Trans Signal Process 54(11):4311–4322
10. Cheng M, Mitra NJ, Huang X et al (2015) Global contrast based salient region detection. IEEE Trans Pattern Anal Mach Intell 37(3):569–582
11. Achanta R, Francisco E, Patricia W et al (2008) Salient region detection and segmentation. In: Proceedings of the 6th international conference on computer vision systems (ICVS 2008), LNCS 5008
12. Li C, Zhang Z, Liu Z et al (2014) A novel fabric defect detection algorithm based on textural differential visual saliency model. J Shandong Univ (Engineering Science) 44(4):1–9 (in Chinese)
13. Goyette N, Jodoin P-M, Porikli F et al (2012) ChangeDetection.Net: a new change detection benchmark dataset. In: Proceedings of the 2012 IEEE computer society conference on computer vision and pattern recognition workshops (CVPRW 2012), pp 1–8

Robust Control of Piecewise Linear Switched System with Constrained Input and Ellipsoid

Zhilin Liu, Xin Yuan, Jun Zhang and Li Su

Abstract This paper deals with the uncertain linear discrete-time switched systems with constrained control input and ellipsoid. The piecewise linear systems is described as ellipsoid which can be characterized by a set of vector inequalities, thereby the constraint of LMIs (linear matrix inequalities) is released. In terms of LMIs, the perturbed impulsive switched system with constrained control input can be robust stabilized in Lyapunov theory. The simulation results verify the effectiveness of the proposed method.

Keywords Parameter perturbation · Switched system · Ellipsoid · LMI

1 Introduction

Hybrid systems are composed of discrete event dynamic systems and continuous time dynamic systems or discrete time dynamic systems, which interact on each other. Hybrid system exists widely in transportation, aviation scheduling, engineering and other fields. Hybrid system has extensive practical application background but it is difficult to deal with traditional control method. So hybrid system is one of hot issue in current control field. Switching system is an important branch of hybrid system, which consists of several subsystems and switching regular which

Z. Liu (✉) · X. Yuan · L. Su
College of Automation, Harbin Engineering University, Harbin 150001, China
e-mail: liuzhilin@hrbeu.edu.cn

X. Yuan
e-mail: yuanxin@hrbeu.edu.cn

L. Su
e-mail: suli406@hrbeu.edu.cn

J. Zhang
School of Electrical and Information Engineering,
Jiangsu University, Zhenjiang 212013, China
e-mail: jzhang@mail.ujs.edu.cn

Y. Jia et al. (eds.), *Proceedings of 2016 Chinese Intelligent Systems Conference*,
Lecture Notes in Electrical Engineering 404, DOI 10.1007/978-981-10-2338-5_7

decide each moment of effective subsystem. Many of the actual physical system can be described by switching system model, such as automobile steering system, robot control system. The switching system has aroused wide attention of scholars [1–5]. The study of the stability of the switched systems and design of controller has gained lots of achievements. Method of stability analysis of discrete linear switched systems mainly conclude common Lyapunov function, multiple Lyapunov function method and category Lyapunov function etc. [6, 7]. A common feature of these methods is that regard state transition conditions as the LMI constraints. Calculate the controller by solving a set of LMIs to construct the system stability constrained Lyapunov function. A set of subsystems can be described by the ellipsoids, and the ellipsoidal sets convert in the form of inequality or equations [8]. With this method, the continuous time state set is instead of a group of quadratic inequality [9], which will transform constrained LMIs into unconstrained LMIs, which makes it easy and fast to get LMI solution.

On the other hand, the system uncertainties and input constraints exist inevitably in the model. The performance of the system will become more complex even instability because of the input constraints and uncertainty of system parameter. In paper [10], considered the stability of switching system with parameter norm is bounded. Convert uncertain parameters LMI into the certain parameters LMI though elementary transformation of matrix [10]. In paper [11, 12], the authors analyzed the stability of system with input constraints in the method of LMIs, and designed the controller for the switched system. Parameters uncertainty and input constraints exist in the practical switching system at the same time, such as chemical process control and multi-controller dynamic system, which started to study this problem. Researches for the kinds of switched systems with input constraints and parameter perturbation are relatively small at present.

This paper studies for parameter perturbation linear switched discrete system which regard conditions of discrete event state transfer as state dependent and take LMIs as the tool of solving. A group of ellipsoidal sets which describe the discrete time state set of each subsystem is introduced. Considering the systems with norm bounded uncertainties and input constraints, we convert stability constraints and input constraints into easy form of LMIs. The algorithm of local stability controller in the sense of Lyapunov is given by piecewise Lyapunov function. The simulation examples show that method can stabilize discrete switched systems with parameter perturbation, satisfy the control input to the input constraints requirements and solve the controller easily.

Symbols in this article are illustrated as following: R^n represent real number space with n dimensions. I represent the identity matrix with corresponding dimension. '*' represent symmetrical structure. $\begin{bmatrix} H+S+* & * \\ T & R \end{bmatrix} = \begin{bmatrix} H+S+S^T & T^T \\ T & R \end{bmatrix}$ is true if H and R are symmetrical matrix.

2 System Description

Consider the linear switching discrete system with input constrained and parameter perturbation as follows:

$$x(k+1) = \left[\overline{A_i} \quad \overline{B_i}\right]\left[x(k) \quad u(k)\right]^T \tag{1}$$

where $x(k) \in R^n$ is state vector, $u(k) \in R^m$ is input of control, $\overline{A_i}, \overline{B_i} (i = 1, 2, \ldots, N)$ represent state matrix and input matrix respectively in subsystem of i. $N > 1$ is the number of subsystems. $\overline{A_i}$ and $\overline{B_i}$ are matrix with parameter perturbation as formula (2)

$$\left[\overline{A_i} \quad \overline{B_i}\right] = \left[A_i \quad B_i\right] + D_i F_i \left[E_{ai} \quad E_{bi}\right], i \in \overline{N} \tag{2}$$

In the formula (2), A_i, B_i, D_i, E_{ai} and E_{bi} are known constant matrix. F_i is unknown time-varying function matrix which satisfy the norm bounded constraints $F_i^T F_i \leq I$ (I is the identity matrix with appropriate dimensions).

State feedback controller for system (1) as following

$$u(k) = K_i x(k) \tag{3}$$

Substitute (3) into (1) gives

$$x(k+1) = \hat{A}_i x(k) \tag{4}$$

where

$$\hat{A}_i = A_i + B_i K_i + D_i F_i \left[E_{ai} \quad E_{bi} K_i\right] \tag{5}$$

Denote Ω_i as the state region where subsystem i is active at moment k. That means the i-th sub-system is working when the system states $x(k) \in \Omega_i$.

Denote that Ω_{ij} is a transfer of the domain for switching between the i-th sub-systems and j-th sub-system. Ω_{ij} is defined as $\Omega_{ij} = \{x(k) \in R^n | \exists k \geq 0, x(k) \in \Omega_i, x(k+1) \in \Omega_j, i, j \in \overline{N}\}$. The i-th subsystem can not transfer to the j-th subsystem when Ω_{ij} is an empty set. Generally, Ω_i is an ellipsoidal set which dimension is less than the dimension of the states space.

For the system (1) and a feedback controller (3), we get a piecewise Lyapunov function $V(k) = x^T(k) P_i x(k)$, $P_i = P_i^T > 0$, by solving a set of LMIs to address the following three questions to obtain the feedback controller to stabilize the system (1).

Question 1: When the system (1) do not switch $(x(k) \in \Omega_i, x(k+1) \in \Omega_i)$, we find a feedback controller to stabilize system (1).

Question 2: When the system is switching $\left(x(k) \in \Omega_i, x(k+1) \in \Omega_j\right)$, we find a feedback controller to stabilize system (1).

Question 3: When there is an input constraint, we find a feedback control law to ensure the stability of system (1).

Lemma 1 *The state region Ω_i can be described as same ellipsoids $\Omega_i \subseteq \varepsilon_i$, where $\varepsilon_i = \{x | ||E_i x + e_i|| \leq 1\}$. Denote the ellipsoid Ω_i as the quadratic inequalities (see [8])*

$$\begin{bmatrix} x(k) \\ 1 \end{bmatrix}^T \begin{bmatrix} E_i^T E_i & * \\ e_i^T E_i & -1 + e_i^T e_i \end{bmatrix} \begin{bmatrix} x(k) \\ 1 \end{bmatrix} \leq 0$$

More precisely, if $d_1 < C_i^T x < d_2$, then the degenerate ellipsoid is described by $E_i = 2C_i^T / (d_2 - d_1), e_i = -(d_2 + d_1)/(d_2 - d_1)$ and $e_i = -(d_2 + d_1)/(d_2 - d_1)$.

Lemma 2 [9] *For any given matrix Y, H, F and matrix E with appropriate dimension, where Y is a symmetric matrix, any F meet $F^T F \leq I$, if there is $Y + HFE + E^T F^T H^T < 0$, exists a only constant $\varepsilon > 0$ so that $Y + \varepsilon HH^T + \varepsilon^{-1} E^T E < 0$.*

3 Design of Control Method

3.1 Solving for Problem 1

Theorem 1 *Consider a switching system (1) with parameter perturbation, where $x(k) \in \Omega_i, x(k+1) \in \Omega_i$, if there is a symmetrical and positive definite matrix $Q_i = Q_i^T > 0$ and some positive scalars $\varepsilon_i > 0$, $\lambda_i > 0$, $0 \leq \eta \leq 1$, and a suitable dimension matrix Y_i, $i \in \overline{N}$, so as to satisfy LMI (6), the state feedback controller $u(k) = Y_i Q_i^{-1} x(k)$ enables switching system (1) asymptotically stable.*

$$\begin{bmatrix} (\eta - 1)Q_i & * & * & * \\ E_{ai}Q_i + E_{bi}Y_i & -\varepsilon_i & * & * \\ A_i Q_i + B_i Y_i & 0 & -Q_i + \varepsilon_i D_i D_i^T & * \\ E_i Q_i & 0 & 0 & \lambda_i^{-1}(I - e_i e_i^T) \end{bmatrix} < 0 \quad , i \in \overline{N} \tag{6}$$

Proof Using quadratic Lyapunov–Krasovskii function $V(k) = x^T(k) P_i x(k)$, for a given constant $0 \leq \eta \leq 1$, there exists $V(k) > 0$ and $V(k+1) - V(k) < -\eta V(k)$.

For

$$V(k+1) - V(k) = x^T(k+1) P_i x(k+1) - x^T(k) P_i x(k) \leq -\eta V(k) \tag{7}$$

Substituting (4) to (7) gives

$$\Delta V(k) = (\hat{A}_i x(k))^T P_i (\hat{A}_i x(k)) + (\eta - 1) x(k)^T P_i x(k) < 0$$

This is equivalent to

$$\begin{bmatrix} x(k) \\ 1 \end{bmatrix}^T \begin{bmatrix} \hat{A}_i^T P_i \hat{A}_i + (\eta - 1)P_i & 0 \\ 0 & 0 \end{bmatrix} \begin{bmatrix} x(k) \\ 1 \end{bmatrix} < 0$$

Referring to Lemma 1, we get

$$\begin{bmatrix} x(k) \\ 1 \end{bmatrix}^T \begin{bmatrix} E_i^T E_i & * \\ e_i^T E_i & -1 + e_i^T e_i \end{bmatrix} \begin{bmatrix} x(k) \\ 1 \end{bmatrix} \leq 0,$$

Use S-process [13] to obtain

$$\begin{bmatrix} x(k) \\ 1 \end{bmatrix}^T \begin{bmatrix} \hat{A}_i^T P_i \hat{A}_i + (\eta - 1)P_i & 0 \\ 0 & 0 \end{bmatrix} \begin{bmatrix} x(k) \\ 1 \end{bmatrix} - \lambda_i \begin{bmatrix} x(k) \\ 1 \end{bmatrix}^T \begin{bmatrix} E_i^T E_i & * \\ e_i^T E_i & -1 + e_i^T e_i \end{bmatrix} \begin{bmatrix} x(k) \\ 1 \end{bmatrix} < 0, \quad \lambda_i > 0, \text{I.e.}$$

$$\begin{bmatrix} \hat{A}_i^T P_i \hat{A}_i + (\eta - 1)P_i - \lambda E_i^T E_i & -\lambda E_i^T e_i \\ -\lambda e_i^T E_i & -\lambda(-1 + e_i^T e_i) \end{bmatrix} < 0$$

By using of Schur complement theory [14], we get

$$\hat{A}_i^T P_i \hat{A}_i + (\eta - 1)P_i - \lambda E_i^T E_i - \lambda E_i^T e_i (1 - e_i^T e_i)^{-1} e_i^T E_i < 0 \tag{8}$$

According to the matrix inversion formula

$$(1 - e_i^T e_i)^{-1} = 1 + e_i^T (I - e_i e_i^T)^{-1} e_i,$$

In Eq. (8) can be written as

$$\hat{A}_i^T P_i \hat{A}_i + (\eta - 1)P_i - \lambda E_i^T E_i - \lambda E_i^T e_i e_i^T E_i - \lambda E_i^T e_i e_i^T (I - e_i e_i^T)^{-1} e_i e_i^T E_i < 0 \tag{9}$$

This is equivalent to

$$\begin{aligned} &\hat{A}_i^T P_i \hat{A}_i + (\eta - 1)P_i - \lambda E_i^T (I + e_i e_i^T) E_i \\ &- \lambda_i (E_i^T - E_i^T (I - e_i e_i^T))(I - e_i e_i^T)^{-1} (E_i - (I - e_i e_i^T) E_i) < 0 \end{aligned}$$

This is equivalent to

$$\begin{aligned} &\hat{A}_i^T P_i \hat{A}_i + (\eta - 1)P_i - \lambda_i E_i^T (I + e_i e_i^T) E_i - \lambda E_i^T (I - e_i e_i^T)^{-1} E_i \\ &- \lambda E_i^T (I - e_i e_i^T) E_i + \lambda_i E_i^T E_i + \lambda_i E_i^T E_i < 0 \end{aligned}$$

So we get

$$\hat{A}_i^T P_i \hat{A}_i + (\eta - 1)P_i - \lambda_i E_i^T (I - e_i e_i^T)^{-1} E_i < 0 \tag{10}$$

By using of the Schur complement theory, in Eq. (10) can be written in the form of LMI (11) as follows

$$\begin{bmatrix} (\eta-1)P_i & \hat{A}_i^T & E_i^T \\ \hat{A}_i & -P_i^{-1} & 0 \\ E_i & 0 & \lambda_i^{-1}(I - e_i e_i^T) \end{bmatrix} < 0 \tag{11}$$

Substituting (5)–(11) gives

$$\begin{bmatrix} (\eta-1)P_i * & * & \\ A_i + B_i K_i & -P_i^{-1} & 0 \\ E_i & 0 & \lambda_i^{-1}(I - e_i e_i^T) \end{bmatrix} + \begin{bmatrix} 0 \\ D_i \\ 0 \end{bmatrix} F_i [E_{ai} + E_{bi} K_i \quad 0 \quad 0] +$$

$$[E_{ai} + E_{bi} K_i \quad 0 \quad 0]^T F_i^T \begin{bmatrix} 0 \\ D_i \\ 0 \end{bmatrix}^T < 0$$

By Lemma 2, there exists a constant $\varepsilon_i > 0$, $i \in \overline{N}$ to set up

$$\begin{bmatrix} (\eta-1)P_i * & * & \\ A_i + B_i K_i & -P_i^{-1} & 0 \\ E_i & 0 & \lambda_i^{-1}(I - e_i e_i^T) \end{bmatrix} + \varepsilon_i \begin{bmatrix} 0 \\ D_i \\ 0 \end{bmatrix} \begin{bmatrix} 0 \\ D_i \\ 0 \end{bmatrix}^T$$

$$+ \varepsilon_i^{-1} [E_{ai} + E_{bi} K_i \quad 0 \quad 0]^T [E_{ai} + E_{bi} K_i \quad 0 \quad 0] < 0,$$

this is equivalent to

$$\begin{bmatrix} (\eta-1)P_i + \varepsilon_i^{-1}(E_{ai} + E_{bi}K_i)^T (E_{ai} + E_{bi}K_i) & * & * \\ A_i + B_i K_i & -P_i^{-1} + \varepsilon_i D D^T & 0 \\ E_i & 0 & \lambda_i^{-1}(I - e_i e_i^T) \end{bmatrix} < 0,$$

By using of Schur complement theory two times, we get

$$\begin{bmatrix} (\eta-1)P_i & * & * & * \\ E_{ai} + E_{bi} K_i & -\varepsilon_{ij} & * & * \\ A_i + B_i K_i & 0 & -P_j + \varepsilon_{ij} D_i D_i^T & * \\ E_i & 0 & 0 & \lambda^{-1}(I - e_i e_i^T) \end{bmatrix} < 0 \tag{12}$$

Substituting $Q_i^{-1} = P_i$ and pre and post multiplying by diag $\{ Q_i \quad \begin{bmatrix} I & & \\ & I & \\ & & I \end{bmatrix} \}$ gives LMI (6).

3.2 Solving for Problem 2

Theorem 2 *Consider a parameter perturbation switching system (1), where* Ω_i *shows the corresponding operating region which is described by* $E_i x + e_i|| \leq 1$

If there exist $Q_i = Q_i^T > 0$, $Q_j = Q_j^T > 0$, *scalar* $\varepsilon_{ij} > 0$, $\lambda_i > 0$ *and the appropriate dimension matrix* Y_i, $K_i = Y_i Q_i^{-1}$, $i, j \in \overline{N}$ *so as to satisfy the following LMI,*

$$\begin{bmatrix} (\eta-1)Q_i & * & * & * \\ E_{ai}Q_i + E_{bi}Y_i & -\varepsilon_{ij} & * & * \\ A_i Q_i + B_i Y_i & 0 & -Q_j + \varepsilon_{ij} D_i D_i^T & * \\ E_i Q_i & 0 & 0 & \lambda_i^{-1}(I - e_i e_i^T) \end{bmatrix} < 0, i, j \in \overline{N}, \tag{13}$$

The state feedback controller enables parameter perturbation switching system (1) is asymptotically stable.

Proof We construct Lyapunov functions as $V(k) = x^T(k) P_i x(k)$, $V(k+1) = x^T(k+1) P_j x(k+1)$, $P_i = P_i^T > 0$, $P_j = P_j^T > 0$, $x(k) \in \Omega_i, x(k+1) \in \Omega_j$. The proof is similar to Theorem 1. Omitted.

3.3 Solving for Problem 3

Consider the common input constraints $||u||_2 \leq u_{\max}$. Use the Schur complement theory to get

$$\begin{bmatrix} Q_i & Y_i^T \\ Y_i & u_{\max}^2 I \end{bmatrix} \geq 0, i \in \overline{N} \tag{14}$$

The initial state $x(0)$ is located in the invariant set which meet $x^T(0) P_{r_0} x(0) \leq 1$, where $r_0 \in \bar{N}$ represents the initial work of the subsystem. Use the Schur complement theory to get

$$\begin{bmatrix} 1 & x^T(0) \\ x(0) & Q_{r_0} \end{bmatrix} \geq 0, Q_{r_0} = P_{r_0}^{-1} \tag{15}$$

3.4 Robust Control for Linear Switched Systems

Theorem 3 *For input parameter perturbation limited switching system (1), if there exist* $Q_i = Q_i^T > 0$, $Q_j = Q_j^T$, *and there exist some positive scalars number* $\varepsilon_{ij} > 0$, $\lambda_i > 0$, *and matrix* Y_i, $K_i = Y_i Q_i^{-1}$, $i, j \in \overline{N}$, *so as to satisfy LMI constraints (6), (13),*

(14), (15), the state feedback controller $u(k) = K_i x(k)$ *to make the system asymptotically stable and satisfies the input constraints.*

Proof Proved by Sects. 3.1, 3.2 and 3.3.

4 Simulation Results

4.1 Mathematical Model Simulation

There is a mathematical example for switched system in [14], where the system is described as follows:

$$x_{k+1} = \begin{cases} A_1 x_k + B_1 u_k & if \begin{bmatrix} 0 & 1 \end{bmatrix} x_k < 0 \\ A_2 x_k + B_2 u_k & if \begin{bmatrix} 0 & 1 \end{bmatrix} x_k \geq 0 \end{cases}$$

where $A_1 = \begin{bmatrix} 0.35 & -0.6062 \\ 0.6062 & 0.35 \end{bmatrix}$, $A_2 = \begin{bmatrix} 0.35 & 0.6062 \\ -0.6062 & 0.35 \end{bmatrix}$, $B_1 = B_2 = [0, 1]^T$, $x(0) = [4, -4]^T$, $|u| \leq 1$. In this paper we take parameter uncertainty into consider on the basis of system model in the literature [14] to get the new form as following: $\begin{bmatrix} \overline{A_i} & \overline{B_i} \end{bmatrix} = \begin{bmatrix} A_i & B_i \end{bmatrix} + D_i F_i \begin{bmatrix} E_{ai} & E_{bi} \end{bmatrix}$, $i = 1, 2$, in which $D_1 = \begin{bmatrix} 0.1 & 0.2 \\ 0.09 & 0.1 \end{bmatrix}$, $D_2 = \begin{bmatrix} 0.11 & 0.19 \\ 0.1 & 0.09 \end{bmatrix}$, $E_{a1} = \begin{bmatrix} 0.2 & 0.17 \\ 0.15 & 0.12 \end{bmatrix}$, $E_{a2} = \begin{bmatrix} 0.08 & 0.05 \\ 0.6 & 0.07 \end{bmatrix}$, $E_{b1} = E_{b2} = \begin{bmatrix} 0.1 \\ 0.09 \end{bmatrix}$, $F_i(k) = \sin(k)$ $(i = 1, 2)$, and $F_i^T(k) F_i(k) \leq I$.

The scope of the two subsystems are $\Omega_1 = \{x \in R^2 | -L < x_2 < 0\}$, $\Omega_2 = \{x \in R^2 | 0 < x_2 < L\}$ where $L = 100$. Firstly, according to Lemma 1, the $\Omega_{1,2}$ is described with two oval set, there are $E_{1,2} = [0, 0.01]$, $e_1 = 1$, $e_2 = -1$. In this paper, use of Theorem 3 to system simulation, Fig. 1 shows states of the track system, and Fig. 2 shows a control input. Figures 1 and 2 show that the system under the control of action move to stabilize after several switching steps, and control inputs satisfy the constraints requirements.

4.2 Simulation for Marine Surface Vessel

A switched model of marine surface vessel is described in [15] as follows:

$$\dot{x} = \begin{cases} A_1 x + B_1 \delta & -10 \leq \delta \leq 10 \\ A_2 x + B_2 \delta & 10 < |\delta| \leq 15 \end{cases}.$$

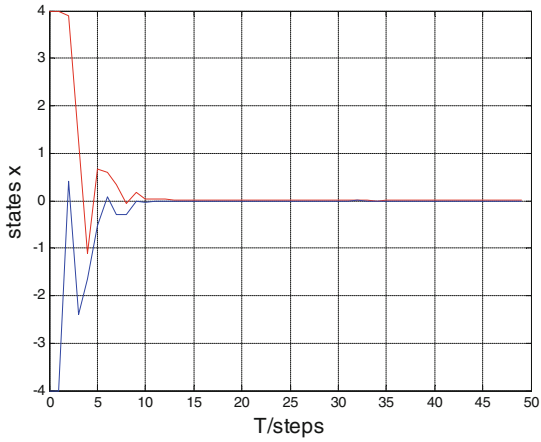

Fig. 1 States trajectory

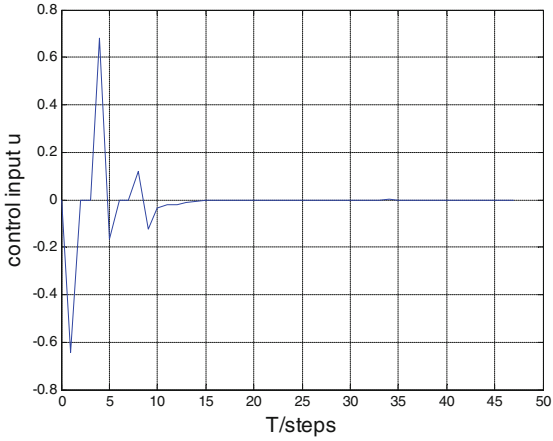

Fig. 2 Control input

where δ represents the steering angle as a control input simultaneously with input constraints $\delta \in [-15°, 15°]$. x is a 5-dimensional column vector as $x = [v \quad r \quad \psi \quad p \quad \varphi]^T$, including five state variables of surface craft, swaying speed v, yaw rate r, yaw angle ψ, roll angular velocity p, roll angle ϕ. If rudder angle δ is steered in the working region as $\delta \in [-10°, 10°]$, A_1 and B_1 is described as follows:

$$A_1 = \begin{bmatrix} -0.02276 & -2.7910 & 0 & 0.09211 & -0.1169 \\ -0.0009168 & 0.1068 & 0 & 0.009949 & 0 \\ 0 & 1 & 0 & 0 & 0 \\ 0.002032 & -0.3058 & 0 & 0.01982 & -0.04486 \\ 0 & 0 & 0 & 1 & 0 \end{bmatrix}$$

$$B_1 = [\,-0.05699 \quad 0.002838 \quad 0 \quad 0.004081 \quad 0\,]^T.$$

If rudder angle δ is steered in the working region as $\delta \in [\,-15^\circ \quad -10^\circ\,) \cup (\,10^\circ \quad 15^\circ\,]$, A_2 and B_2 is described as follows:

$$A_2 = \begin{bmatrix} -0.04062 & -0.1899 & 0 & -0.06664 & -0.09348 \\ 0.0001167 & -0.1468 & 0 & 0.007198 & -0.0008284 \\ 0 & 1 & 0 & 0 & 0 \\ 0.002594 & -0.3051 & 0 & -0.01434 & -0.04417 \\ 0 & 0 & 0 & 1 & 0 \end{bmatrix}$$

$$B_2 = [\,-0.04575 \quad 0.02279 \quad 0 \quad 0.003277 \quad 0\,]^T.$$

Taking into account the uncertainty of model parameters, we get the model of marine surface vessel with a parameter perturbation

$$\dot{x} = \begin{cases} A_{11}x + B_{11}\delta & -10 \le \delta \le 10 \\ A_{22}x + B_{22}\delta & 10 < |\delta| \le 15 \end{cases}.$$

where

$$A_{11} = A_1 + D_1 * F * E_{a1}, B_{11} = B_1 + D_1 * F * E_{b1},$$

$$A_{22} = A_2 + D_2 * F * E_{a2}, B_{22} = B_2 + D_2 * F * E_{b2}$$

$$E_{a1} = E_{a2} = \begin{bmatrix} -0.1108 & -1.3955 & 0 & -0.0461 & -0.0585 \\ 0.0015 & -0.0534 & 0 & 0.005 & 0 \\ 0 & 0.5 & 0 & 0 & 0 \\ 0.002 & -0.1529 & 0 & -0.0099 & -0.0224 \\ 0 & 0 & 0 & 0.5 & 0 \end{bmatrix},$$

$$E_{b1} = E_{b2} = [\,-0.0057 \quad 0.0004 \quad 0 \quad 0.0003 \quad 0\,]^T, F = \sin(t)$$

$$D_1 = D_2 = \begin{bmatrix} 0.1 & 0 & 0 & 0 & 0 \\ 0 & 0.1 & 0 & 0 & 0 \\ 0 & 0 & 0.1 & 0 & 0 \\ 0 & 0 & 0 & 0.1 & 0 \\ 0 & 0 & 0 & 0 & 0.1 \end{bmatrix},$$

Discrete above system and simulate the system using Theorem 3 of this article. Figure 3 shows a dynamic curve of control input. Figure 4 shows the dynamic curve of roll velocity v which is the first element in x state set. Figure 5 is dynamic curves of the other four elements in x state set. It is seen from Figs. 3, 4 and 5 that the system under the control of action move to stabilize after several switching and control input meet the constraints requirements.

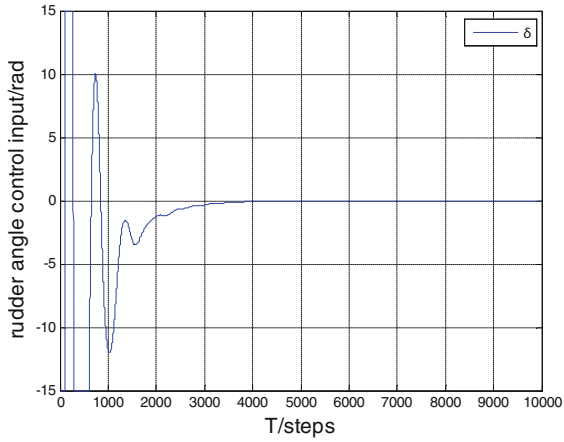

Fig. 3 Control input

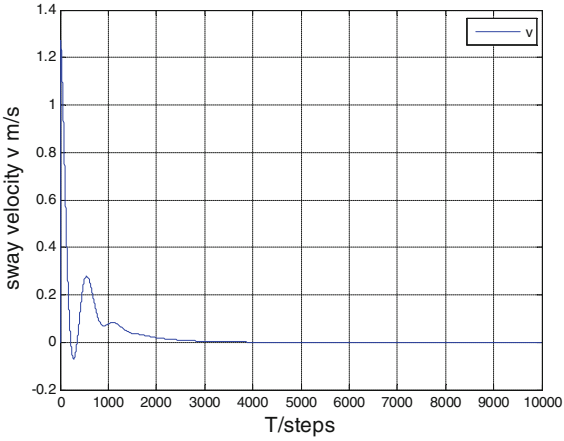

Fig. 4 Sway velocity

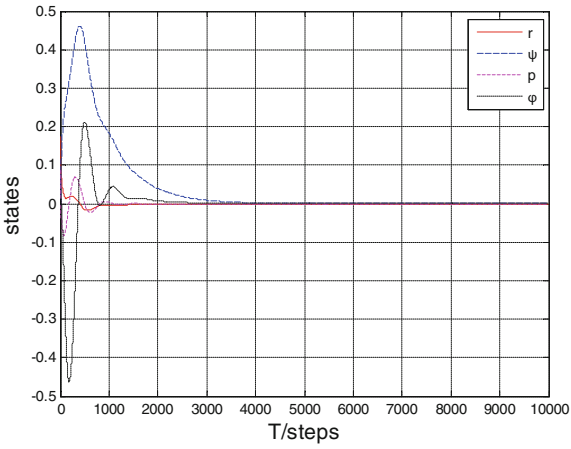

Fig. 5 States

5 Conclusion

In this paper, the design method of stability and controllers of a class of uncertain discrete switched linear systems with input constraints has been discussed. In LMIs solving tool, the discrete-time status of each set is described by a group of subsystems oval set combined with Lyapunov sense of stability constraints, form of LMIs given that robust stability sufficient condition and design method of controls of closed loop switched systems. While the common input constraints converted into LMIs, LMIs convex constraint ensure the feasibility of solving the controller. Finally, simulation examples demonstrate the effectiveness of the proposed method.

Acknowledgments This work is partially supported by National Natural Science Foundation of China (51379044, 61304060).

References

1. Xie DM, Wang L, Hao F, Xie GM (2003) Robust stability analysis and control synthesis for discrete-time uncertain switched systems. In: Proceedings of the 42nd IEEE conference on decision and control, Maui, pp 4812–4817
2. Hou L, Michel AN, Ye H (1996) Stability analysis of switched systems. In: Proceeding of 35th conference on decision and control, Kobe, pp 1208–1212
3. Liberzon D, Morse AS (1999) Basic problems in stability and design of switched systems. Control Syst Mag 19(5):59–70
4. Peleties P, Decarlo RA (1992) Asymptotic stability of m-switched systems using Lyapunov functions. In: Proceeding of 31st conference on decision and control, Tucson, pp 3438–3439
5. Li ZG, Wen CY, Soh YC (1999) Stability of perturbed switched nonlinear systems. In: Proceeding of the American control conference, San Diego, pp 2969–2973
6. Branicky MS (1998) Multiple Lyapunov functions and other analysis tools for switched and hybrid systems. IEEE Trans Autom Control 43(4):475–482
7. Daafouz J, Riedinger P, Iung C (2002) Stability analysis and control synthesis for switched systems: a switched Lyapunov function approach. IEEE Trans Autom Control 47 (11):1883–1887
8. Boyd S, El Ghaoui L, Feron E, Balakrishnan V (1994) Linear matrix inequalities in system and control theory. SIAM
9. Rodrigues Luis, Boyd Stephen (2005) Piecewise-affine state feedback for piecewise-affine slab systems using convex optimization. Syst Control Lett 54:835–853
10. Zhang Y, Duan G (2005) Guaranteed cost control for uncertain discrete-time switched systems with time-delay. In: Proceedings of the fourth international conference on machine learning and cybernetics, pp 1064–1068
11. Xia Yuanqing, Jia Yingmin (2003) Robust control of state delayed systems with polytopic type uncertainties via parameter-dependent Lyapunov functionals. Syst Control Lett 50:183–193
12. Et E, Kim DC, Park JH (1996) Robust controller design for uncertain systems with time delays: LMI approach. Automatica 32:229–1231

13. Jiang X, Tan D, Wang Y (2004) An LMI approach to stability of systems with severe time delay. IEEE Trans Autom Control 49(7):1192–1195
14. Lazar M, Heemels WPMH, Weiland S, Bemporad A (2004) Stabilization conditions for model predictive control of constrained PWA systems. In: 43rd IEEE conference on decision and control, vol 5, pp 4595–4600
15. Li Z, Sun J, Oh S (2009) Design, analysis and experimental validation of a robust nonlinear path following controller for marine surface vessels. To appear in Automatica

Fault Diagnosis Method of Wind Turbine Generators Based on Principal Component Feature Extraction

Feng Lv, Jing He, Zeyu Zhang, Lingyan Li and Xiyuan Ju

Abstract The operation process of the wind turbine generator is complex, the running state variables are many, and the variables are related to each other. It is difficult to achieve the expected results if the traditional fault diagnosis method is used. The fault diagnosis method based on principal component analysis (PCA) of the feature extraction of wind turbine generator is presented in this paper. The principal component model is established based on the normal working condition history data at first, and the control limits of Hotelling T^2 and SPE two statistics are obtained. The condition monitoring and fault location of generating sets are realized by comparing the statistics of real-time operation and the size of the threshold. The experimental simulation results of the operation data of the wind turbine generator show the effectiveness of the method.

Keywords PCA · Condition monitoring · Fault diagnosis · Wind turbine generators

1 Introduction

Synthesizing technology achievement of electronic computer, automatic control, optical fiber communication, power frequency ac, servo drive, precision testing and new mechanical structure, wind power generator system has the characteristics of high flexibility, high precision, and high automation. Because the operation of the generator is complex, and the operation state variables are many, and the variables

F. Lv · Z. Zhang · X. Ju
Electronic Department, Hebei Normal University, Shijiazhuang 050024, China

J. He (✉)
School of Automation, Northwestern Polytechnical University, Xi'an 710072, Shanxi, China
e-mail: hejing19920811@mail.nwpu.edu.cn

L. Li
Shijiazhuang Power Supply Company, Shijiazhuang 050010, China

Y. Jia et al. (eds.), *Proceedings of 2016 Chinese Intelligent Systems Conference*,
Lecture Notes in Electrical Engineering 404, DOI 10.1007/978-981-10-2338-5_8

are related to each other, it is difficult to achieve the expected results if the traditional fault diagnosis method is used, when the wind turbine is in trouble, traditional condition monitoring method can realize fault diagnosis, but it has some limitations. In most cases, the fault has occurred when the control system is issued. However, the whole system can do just automatically to the wind turbine down, to prevent further deterioration of the fault. But these can not reveal the monitoring time and its causes, and the fault often reached a certain level. On line monitoring and diagnosis system can overcome the above shortcomings, but the key is how to choose the appropriate condition monitoring method to realize the fault diagnosis of wind turbine, it is the main problem [1]. At present, in wind turbine, wavelet multi-scale analysis method can be used for the characteristics of fault signal extraction and the fault diagnosis realization [2]. Also, neural networks and support vector machines can be used to classify the fault characteristics and to realize the fault diagnosis and location [3]. In the literature [4], the relative principal component analysis method is used to establish wind turbine tower and its influencing factors between relationship models through the vibration of tower operation data mining analysis and to realize the fault diagnosis. For mechanical transmission parts, vibration signal spectrum analysis is used to monitor and diagnose the bearing faults [5, 6]. Current diagnostic methods mainly focus on the single signal of the wind generator or local fault diagnosis; there are few studies on the operation state multi-variable monitoring and fault diagnosis of wind turbine problem. Therefore, this paper presents a fault diagnosis method of wind turbine generator based on principal component analysis, the method does not need to consider complex industrial process model, through the historical data to establish the object model, and for these different data, it only needs to extract most of the useful data to represent the original data information, to eliminate the linear relationship between the variables, and to achieve dimensionality reduction. The performance monitoring and fault diagnosis of the system are realized by the feature extraction of the wind turbine.

2 Building the Principal Component Model

The object of the study of the PCA is that sample points multiply by variable type data matrix. The basic idea is that when the loss of the package information data is the minimum, lower the dimension of high variant space, pick up typical principal component, interpret the most change of the data, and divide the original data into two parts, which are system part and noise or error part.

If there are n sampling points and measured variables, $X = (x_1, x_2, \ldots, x_m)^T$, algorithms steps are as follows.

(1) Standardize the original data, then X is also used to express the data matrix and use the formula: $X = [X - Iu^T]D_\sigma^{-\frac{1}{2}}$. It is non-singular matrix in which all elements are 1. $u = [u_1, u_2, \ldots u_m]^T$ is the mean vector of the original data matrix-X. $D_\sigma = diag(\sigma_1^2, \sigma_2^2, \ldots \sigma_m^2)$ is the variance matrix of the original data matrix-X.

(2) According to the formula $R = (\mathrm{r}^{ij})^{m\times m} = X^T X/n$, we can calculate the covariance matrix of X.

(3) Calculate the first m eigenvalue: $\lambda_1 \geq \lambda_2 \geq \cdots \geq \lambda_m \geq 0$ and related feature vector $p_1, p_2, \ldots, p_m$. It is the principal component feature vector and also load vector, which represent the associated information among the variable.

(4) Representing the ith principal element

$$t_i = p_i^T X = p_{i1}x_1 + p_{i2}x_2 + \cdots + p_{im}x_m \tag{1}$$

The principal component vector represents the associated information of the sampled data.

(5) Pick up the number of the optimal principal component and use accumulative contribution rate to calculate the value of the pivot-a. The contribution of Pivot-t^i accounts for δ^i which is the proportion of each eigenvalue of correlative coefficient matrix-R in all eigenvalues. The accumulative contribution rate of the fist a principal element is η_a, which is the sum of the accumulative contribution rate of the fist a principal element.

$$\delta_\mathrm{i} = \frac{\lambda_i}{\sum_{j=1}^{m} \lambda_j} \tag{2}$$

$$\eta_a = \sum_{i=1}^{a} \delta_i = \frac{\sum_{i=1}^{a} \lambda_i}{\sum_{i=1}^{m} \lambda_i} \tag{3}$$

Generally, we can set the minimum value of accumulative contribution rate according to different needs. Accumulative contribution rate $\eta_a \geq 85\%$.

(6) The original data matrix can be reconstructed by extracted pivot model

$$X = \hat{X} + \tilde{X} = TP^T + \tilde{T}\tilde{P}^T \tag{4}$$

T and P are principal element score matrix and principal element load matrix, respectively. Column vectors of P are the first a feature vectors of R, respectively, $P = [p_1, p_2, \ldots, p_a]$. $\tilde{T}$ and $\tilde{P}$ are residue score matrix and residue load matrix, respectively and column vectors of $\tilde{P}$ are $(m–a)$ feature vectors, $\tilde{P} = [p_{a+1}, p_{a+2}, \ldots, p_m]$.

In practical application, if the residual matrix is ignored, it can also guarantee data integrity, so data-X can be approximately equal to

$$X \approx \mathrm{t}_1 p_1^T + t_2 p_2^T + \ldots + t_\mathrm{A} p_\mathrm{A}^T \tag{5}$$

3 Feature Extraction and Performance Detection of Principal Component Analysis

After the principal component model is established, we can use this data model to analyze and judge the real-time data of the new measurement. A new data matrix for real-time measurement of X, of course, is after the normalized data matrix, calculate the principal element measurement of the value of the new sample, similarly, X can be decomposed into two parts, then

$$X = \hat{X} + \tilde{X} \tag{6}$$

In the formula: $\hat{X} = PP^T X = CX$, C is projection matrix of corresponding principal component subspace. $\hat{X}$ is its projection. In the formula: $\tilde{X} = \tilde{P}\tilde{P}^T X = (I - C)X = \tilde{C}X$, I is unit matrix and $\tilde{C}$ is projection matrix of corresponding residual subspace of X. $\tilde{X}$ is its projection. The principal subspace is described in most of the information of all the data that the residual subspace is noise and fault measurement data, and the two are two orthogonal.

These results can be statistically tested, according to the test results, you can determine whether it is the process of failure or abnormal occurrence. There are two commonly used statistics: Hotelling T^2 and SPE.

(1) Hotelling's T^2: To measure the change of the sample vector mapping in the principal component space

$$T^2 = X^T P \Lambda^{-1} P^T X \le T_a^2 \tag{7}$$

In the formula: $\Lambda = diag\{\lambda_1, \ldots, \lambda_A\}$, T_a^2 is control limit of T^2 whose confidence is a. The formula is as follows:

$$T_a^2 = \frac{A(n^2-1)}{n(n-A)} F_{A,n-A;a} \tag{8}$$

$F_{A,n-A;a}$ is F distributed critical value whose confidence is a with A and n-A degree of freedom.

Visible, for statistics-T^2 is principal component subspace, which contains only information of principal component scores, embody the principal component

score vector is each sampling in the change trend and the amplitude deviations from the model, the characterization of PCA model interior changes. At the normal working condition, $T^2 \leq T_a^2$, however, when it is abnormal or fault, $T^2 > T_a^2$.

As mentioned above, the way based on statistics-T^2 can only detect some variable's change of principal component subspace. If one of the measured variables is not reflected well in the principal component model, the fault of these variables cannot be tested through this way. This case can be taken into consideration by analyzing the new measured variables of the residuals for fault detection, that is, the SPE statistic.

(2) SPE: To measure the change of the sample vector mapping in the residual space

$$SPE = \|\tilde{x}\|^2 = X^i(I - C)X^{i^T} = X^i\left(I - PP^T\right)X^{i^T} \quad (i = 1, 2, \ldots, n) \tag{9}$$

In the formula: i is the ith sample and I is a full rank matrix of 1 for all elements.

The formula of this control limit is

$$Q_\alpha = \theta_1\left[\frac{C_\alpha\sqrt{2\theta_2 h_0^2}}{\theta_1} + 1 + \frac{\theta_2 h_0(h_0 - 1)}{\theta_1^2}\right]^{\frac{1}{h_0}} \tag{10}$$

In the formula: $\theta_j = \sum_{j=a+1}^{m} \lambda_j \; j = 1, 2, 3; h_0 = 1 - \frac{2\theta_1\theta_3}{3\theta_2^2}a$ represents the number of principal element, m is the number of measurement, λ_j (j = a + 1, a + 2, …, m) is eigenvalue of covariance matrix from big to small, which is standardized by original variable data matrix and C_α is the statistic of α, which is confidence of normal distribution.

SPE is scalar in the residual subspace, which represents the every measured sample, relative to the extent of the deviation of principal component model. It is the measurement of data change outside the model and represents the change of the data against the principal component model's explanation. At the normal working condition, $\mathrm{SPE} \leq \mathrm{Q}^\alpha$, however, when it is abnormal or fault $\mathrm{SPE} > \mathrm{Q}^\alpha$. Statistics T^2 is for monitoring the changes of quality indexes; statistics SPE corresponding to the under reporting rate will be less (for non normal or unstable process).

When the two statistics exceed control limits, abnormal or fault happens, but it cannot obtain what were wrong or where the source problem is from the control chart of statistic. Separating the variable of fault, this text uses the technology of traditional contribution plots. It is a reflection of the various state variables on the impact of the two statistics, the histogram can obviously show the contribution of the size, by comparing the contribution of the percentage of the size, to be able to basically lock the source of failure. But the final and concert reason need to be determined further by technologists.

When SPE exceeds control limits, the contribution of the ith variable to statistic-SPE at the time j is:

$$SPE_{ij} = e_{ij}^2 = \left(\bar{x}_{ij} - x\right) \tag{11}$$

The ith variable to contribution value of statistic-SPE is:

$$CONTSPE_i = \left(\bar{x}_i - \hat{x}_i\right)^2 \tag{12}$$

4 Fault Diagnosis of Wind Turbine Based on Principal Component Analysis

We choose the SEC-W2000 generator real-time monitoring of a wind field measurement variable 40, for the 121 sampling points. Table 1 shows the measured variable parameters during the operation process.

Table 1 Measured variable of process of wind generator

Var	Description	Var	Description	Var	Description	Var	Description
1	Active power	11	wind velocity	21	Generator speed	31	Gear box temp
2	Reactive power	12	Average of 30 s	22	Stator U temp	32	Cool water temp of gear box
3	A phase voltage	13	Average of 10 min	23	Stator V temp	33	Cabin location
4	B phase voltage	14	Wind direction	24	Stator W temp	34	Out cabin temp
5	C phase voltage	15	Average of 60 s	25	Inlet temp	35	Cabin temp
6	A phase current	16	Rotor speed	26	Outlet temp	36	Cabin vibration sensor X
7	B phase current	17	Pitch angle	27	Free end axial temp	37	Cabin vibration sensor Y
8	C phase current	18	Pitch angle 1	28	Driving end axial temp	38	Valid value of cabin vibration
9	Line frequency	19	Pitch angle 2	29	High speed bearing temp	39	Twists and cable location
10	Power factor	20	Pitch angle 3	30	Low speed bearing temp	40	Generated energy

4.1 State Monitoring Procedure for Wind Turbine

The fault diagnosis process of wind turbine is shown in Fig. 1, mainly including discrete modeling and fault detection.

- Build the principal component model
  (1) At the normal condition of generator, we get a piece of process data and use these data to build training sample assemblies-X of principal component model, then standardize it. Processed data is also denoted by X.
  (2) Calculate the covariance matrix of X; $\sum = (\sigma_{ij})_{nXm}$, $\sigma_{ij} = \frac{1}{n-1} \sum_{k=1}^{n} (X_{ki} - \bar{X}_i)$.
  (3) Calculate eigenvalue of $\sum$: $\lambda_1 \geq \lambda_2 \geq \cdots \geq \lambda_m \geq 0$ and corresponding standardizing eigenvector $P_1, P_2 \ldots P_m$.
  (4) According to the CPV $\geq 85\,\%$ principles to determine the number of principal components A.
  (5) Construct the transformation matrix $P_A = [P_1, P_2 \ldots P_A]$.
  (6) Calculate the control limits of statistics T^2 and SPE at the confidence level of 95 %.
- Fault detection and diagnosis based on two statistics
  (1) Standard treatment for new detection sample X

$$\text{According to formula: } \begin{cases} t = \bar{X}_i P_k \\ \bar{X}_i = t_i \bar{P}_k^T = \bar{X}_k P_k P_k^T \\ e_i = \bar{X}_i - \hat{X}_i = \bar{X}_i (I - P_k P_k^T) \end{cases}$$

Calculate the principal component.

$$\text{And according to formula: } \begin{cases} T_i^2 = t_i D_k^{-1} t_i^T = \bar{X} P_k D_k^{-1} P_k^T X_i^T \\ Q = e_i \; e_i^T = \bar{X}_i \left(I - P_k P_k^T\right) \bar{X}_i^T \end{cases}$$

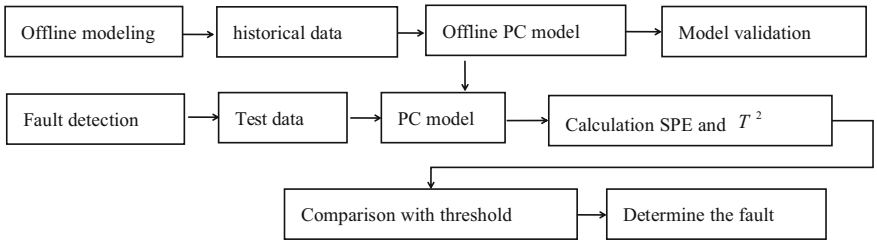

Fig. 1 Flow chart of fault diagnosis of wind turbine

Calculate two representative statistics of real-time monitoring of standardizing sample, make out the control chart and test the fault.

(2) If the process is abnormal, use contribution plot method to determine those variable, which mainly causes the fault.

4.2 Experiment and Simulation

We selected the 40 variables in real-time monitoring data of wing power generator system as the statistical magnitude to monitor variable, dopting normal data in 121 sampling sites respectively as training sample set and testing data. Among these data, we chose the first 89 to be normal, at the same time, leading malfunctions from the beginning of the 90 and continued to the end of the whole process. By applying MATLAB programming, we standardized the original data, finding out the covariance matrix. Then we ranked characteristic value and characteristic vector, and applied the variance contribution rate to get the number of the optimal principal. Figure 2 is the statistical magnitude of SPE and T^2. Their corresponding control limit is about the number 10. The curve recorded the statistical magnitude of all the sampling sites.

We can see that the two statistical magnitudes can both monitor the process of the experiment and have similar trends. When the malfunctions appeared in the

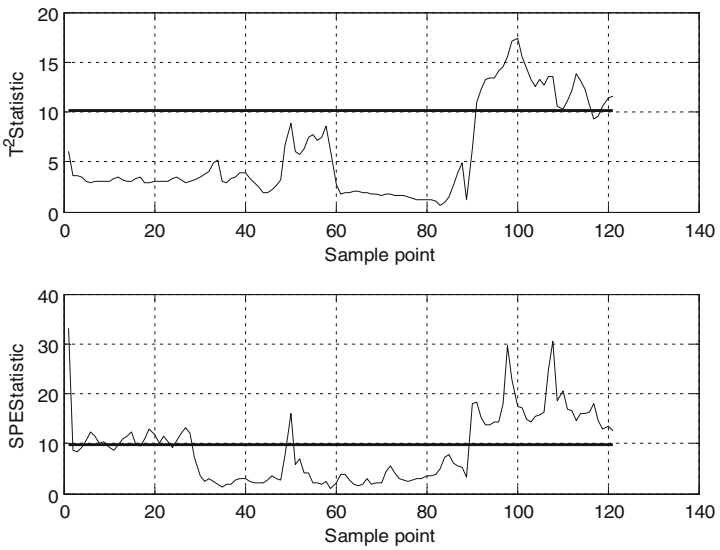

Fig. 2 Statistical monitoring process

90th sampling site, the statistical magnitude of the SPE and T^2 were both getting larger, even exceeding the control limit. The statistical magnitude Fig. 2 showed the fluctuation first appeared in the 90th sampling site. SPE and T^2 were no longer keeping stable in a proper level, but increased apparently, which saying the exception must have had occurred.

Besides, when testing out the malfunctions, the statistical magnitude of the SPE indicated that the sites after the 90th site were all apparently on the control limit and there were no underreporting. However, statistical magnitude of T^2 were below the control limit between the two sampling sites 117 and 118. It belongs to fault underreporting. That explained that the statistical magnitude of the SPE is more precise than and corresponding underreporting would be less.

Through the front analysis to determine the wind turbine generator fault. But exactly determining the fault still needs further positioning. So we randomly selected 100th sampling points to make a statistical contribution Fig. 3, looking for fault source, and to determine the location of the fault. See from Fig. 3 fault outlier SPE contribution plot, contribution to the SPE statistic maximum are 37 variables, also is to say no. 37 variables change model of the system stability has the greatest influence, from Table 1 can be seen, this variable is the cabin vibration sensor Y, can be convicted during the normal operation is mainly due to the cabin vibration sensor to detect transverse or longitudinal vibration led directly to the wind turbine fault.

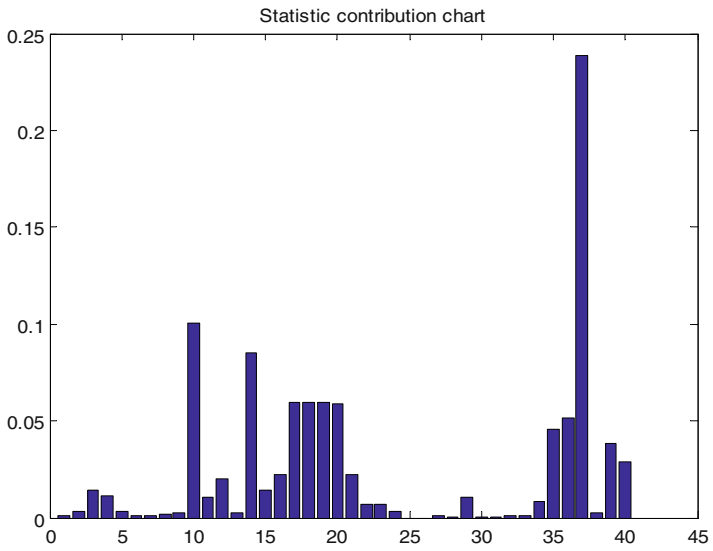

Fig. 3 100th sample points to the SPE contribution chart

5 Conclusion

Fault diagnosis, which is determined by principal component analysis, can extract the spatial main change information of original data without relying on process mechanism. It greatly reduces the dimension of original data space, eliminates the nonlinear connection of variables, and reduces noise influence ensuring that the loss of data information is least. The example of wind generator application testifies that the way based on extraction of principal component feature can react to abnormal change process and can also accurately reach the goal of performance test and fault diagnosis.

Acknowledgments This work is supported by National Natural Science Foundation of China under Grant (60974063, 61175059), and the Nature Science Foundation of Hebei under Contract (F2014205115), and the Education Department Project of Hebei under Contract (No: ZD2016053).

References

1. Chen X, Li J, Chen H (2011) Research and development of condition monitoring and fault diagnosis technology for wind turbine generator. J Mech Eng 47(9):45–52
2. Kechida R, Menacer A (2011) DWT wavelet transform for the rotor bars faults detection in induction motor. In: 2011 2nd international conference on electric power and energy conversion systems. IEEE, Sharjah, pp 1–5
3. Liu L, Wang A, Sha M et al (2011) Multi-class classification methods of cost-conscious LS-SVM for fault diagnosis of blast furnace. J Iron Steel Res 18(10):17–23, 33
4. Zhou J, Fang N, Guo P (2014) Wind turbine tower vibration monitoring and fault diagnosis based on principal component analysis. Electr Power Constr 35(8):125–129
5. Zhou J, Zhang B, Sheng Y (2011) Theoretical study and application of vibration monitoring of wind turbine. Wind Energy Source 3:66–69
6. Zhou D, Li G, Li Y (2011) Data driven industrial process fault diagnosis technology, Beijing

Transformer Internal Insulation Fault Diagnosis Based on RBF Neural Network Evolved by Immune Particle Swarm Optimization

Hao Li, Fuzhong Wang and Rui Wang

Abstract The reliability of the power transformer operation is directly related to the security of power system and the reliability of power supply. In order to improve the diagnosis accuracy of internal insulation fault in transformer, this paper proposes an algorithm of transformer internal insulation fault diagnosis which is based on RBF neural network evolved by immune particle swarm optimization by analyzing the internal insulation fault type of transformer and the content of dissolved gas in transformer oil composition. The paper focuses on the composition principle of transformer fault diagnosis based on RBF neural network. The method of determining the number of hidden layer of network center and the initial position based on artificial immune network algorithm is given. The method of network weight optimization based on particle swarm optimization algorithm is developed. And the simulation experiment is also given. The simulation results show that the proposed algorithm can effectively diagnose the transformer fault types and the diagnosis accuracy can reach above 90 %.

Keywords Power transformer · Fault diagnosis · RBF neural network · Artificial immune network · Particle swarm optimization

1 Introduction

Power transformer is one of the important equipment in power system. Diagnosing the internal insulation faults in power transformers correctly is of great significance to improve the security and reliability of power system operation [1]. The dissolved gas analysis (DGA) in transformer oil is one of the most effective methods to diagnose the oil immersed transformer with internal insulation faults. It can effectively detect transformer latent fault and the degree of faults development and

H. Li (✉) · F. Wang · R. Wang
School of Engineering and Automation,
Henan Polytechnic University, Jiaozuo 454000, Henan, China
e-mail: 1548905212@qq.com

Y. Jia et al. (eds.), *Proceedings of 2016 Chinese Intelligent Systems Conference*,
Lecture Notes in Electrical Engineering 404, DOI 10.1007/978-981-10-2338-5_9

prevent accidents caused by the faults [2]. Though the traditional three-ratio method and its improved method are simple and convenient in the engineering application, they expose the problems of coding not full and coding boundary too absolute. This often causes the miscarriage of justice or the leakage judgment and results of the fault diagnose accuracy rate are not very high. At present, in order to improve the accuracy of internal insulation fault diagnosis of transformer, many intelligent algorithms are introduced including artificial neural network [3–5], artificial immune algorithm [6], support vector machine [7], particle swarm algorithm, etc.

Neural network algorithm has many advantages including self-organization, self-learning ability, which is widely used in the field of pattern recognition and fault diagnosis. But neural network algorithm also has many defects such as needing large amount of training samples and training time. And it is also easy to fall into local minimum defects. Paper [3] used the BP neural network method to diagnose transformer faults. In order to improve the training speed of BP network, the author in this paper used the L-M algorithm to optimize the BP network and achieved good diagnostic results. In paper [8] the author used the immune ant algorithm to deal with the training data, which optimized RBF hidden layer parameters. In this paper, the author also used the least square algorithm to calculate the output weights of RBF network, which improved the network generalization ability and convergence speed. All of the above mentioned algorithms have played a very good role in guiding the application of neural network in fault diagnosis of transformer.

According to the analysis of internal insulation fault and its oil and gas components, this paper proposes a transformer fault diagnosis algorithm which combines artificial immune algorithm with particle swarm optimization algorithm to optimize the RBF neural network. First, this paper uses artificial immune network algorithm on the input of RBF neural network to determine the hidden layer of RBF center. Second, the paper uses the particle swarm optimization algorithm to optimize the weights of RBF network, which can simplify the structure of network, improve the generalization ability and convergence rate of network. Simulation results show that the method can effectively identify the fault types and improve the accuracy of fault diagnosis.

2 Internal Insulation Fault Type of Transformer and Its Oil and Gas Component

Insulation systems of power transformers usually use two kinds of basic insulation material: solid material (including insulating paper, laminated board, etc.) and liquid material (transformer oil). When the transformer is in the presence of latent

Table 1 Gas components produced by different fault types

Fault property	Fault type	Main gas	Secondary gas
Thermal fault	Oil overheating	CH_4, C_2H_4	H_2, C_2H_6
	Oil and paper overheating	CH_4, C_2H_4, CO, CO_2	H_2, C_2H_6
	Damp or bubbles in oil	H_2	–
	Natural aging	CO, CO_2	–
Electrical fault	The partial discharge of oil paper insulation	H_2, CH_4, CO	C_2H_2, C_2H_6, CO_2
	Spark discharge in oil	H_2, C_2H_2	–
	Electric arc in oil	H_2, C_2H_2	CH_4, C_2H_4, CO_2
	Arc in oil and paper	H_2, C_2H_2, CO, CO_2	CH_4, C_2H_4, C_2H_6

fault, these liquids or solid materials will decompose under the action of electricity and heat and produce some specific gas, which will dissolve in the transformer oil. The gases mainly included are H_2, CH_4, C_2H_6, C_2H_4, C_2H_2, CO, CO_2. The change of the characteristic gas content dissolved in oil is closely related to the development degree and the fault type of the transformer internal fault. The relationship between the characteristic gas and the internal insulation fault types of the transformer is shown in Table 1.

As can be seen from the Table 1, the internal insulation fault of power transformer can be divided into thermal fault and electrical fault. Thermal fault is mainly caused by the thermal stress caused by accelerated aging. Electrical failure is mainly due to the high electrical stress caused by insulation aging caused by internal fault. According to the energy density, the electrical failure can be divided into several different types: partial discharge (PD), low energy discharge (D1), and high energy discharge (D2).

According to the relationship between the type of dissolved gas in oil and the nature of internal insulation fault, the method of DGA uses the content of 7 kinds of characteristic gases dissolved in oil as the method to judge the insulation faults of transformer. Due to the dispersion of CO and CO_2 content and the data obtained in the field are often missing, hence this paper uses H_2, CH_4, C_2H_6, C_2H_4, C_2H_2, which are the kinds of gas as the characteristic gas.

According to the transformer oil dissolved gas analysis and judgment of the guidelines, this paper selects partial discharge (PD), low energy discharge (D1), high energy discharge (D2), low temperature overheat (T1), middle temperature overheat (T2), high temperature overheat (T3) a total of six kinds of patterns as the fault types to diagnosis.

3 Transformer Fault Diagnosis Model Based on RBF Neural Network

3.1 The Structure and Principle of Internal Insulation Fault Diagnosis Model of Transformer

RBF neural network is a kind of neural network with a strong biological background, which has strong function approximation ability. Each hidden layer neuron's transfer functions constitute a plane fitting of a basis function which is a local approximation network. That means in a local region of the input space exists only a small number of neurons, which are used to decide the output of the network. As the ability of the network learning speed and function approximation are strong, the RBF network is widely used in the fields of pattern recognition, function approximation and fault diagnosis. The RBF neural network is composed by three parts: input layer, hidden layer, and output layer. The fault diagnosis model of RBF network is shown in Fig. 1.

The main principle of RBF neural network is the nonlinear function of the network hidden layer unit. The RBF excitation function is used as the basis of the hidden layer unit. The basic form of the radial basis function is shown in the following (1).

$$s_j(x) = \phi_j(\|x - c_j\|), (j = 1, 2, \ldots, a) \tag{1}$$

In RBF neural network, the most commonly used radial basis function is the Gauss function because of its simple expression, good analysis performance, etc. Hence this paper uses the Gauss function as the radial basis function. The basic form is shown in the following (2).

$$\phi_j(\|x - c_j\|) = \exp\left[-\frac{(x - c_j)^T (x - c_j)}{\delta_j^2}\right] \tag{2}$$

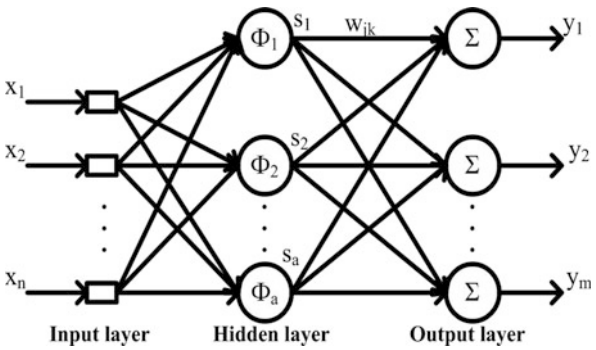

Fig. 1 Fault diagnosis model of RBF network

In formula, s_j is the output of the j unit in the hidden layer; $\phi(\cdot)$ is the basis functions; $\|x - c_j\|$ represents the Euclidean distance between the input vector x and the center vector c_j of the basis function; c_j is the center vector of the underlying function of the hidden layer; δ_j is the parameter of the first j basis function of the hidden layer; a is the number of nodes in the hidden layer.

The relationship between hidden layer and the output layer of the network achieves linear mapping. The output layer of the network realizes a linear combination of the hidden layer nodes, and its expression is shown in (3).

$$y_k = \sum_{j=1}^{a} \omega_{jk} \cdot s_j, (k = 1, 2, \ldots, m) \tag{3}$$

3.2 Design of Input and Output of Transformer Fault Diagnosis Model Based on RBF Neural Network

As can be seen from the structure of RBF network, the input of the network is a set of gas characteristics which corresponds to fault types. This paper selects five characteristic gases as the inputs of the network, they are H_2, CH_4, C_2H_6, C_2H_4, C_2H_2. Hence the number of input layer nodes in network is five. The outputs of the network are a vector which represents a kind of fault type. There are six fault models, hence the number of output layer in the network is six.

Assuming that there are a total of N group input data of the network $X = [x_1, x_2, \ldots, x_N]$, each of these elements $x_i = [x_{i1}, x_{i2}, x_{i3}, x_{i4}, x_{i5}]^T$ represents a set of fault data, the corresponding actual output is $Y = [y_{i1}, y_{i2}, y_{i3}, y_{i4}, y_{i5}, y_{i6}]^T$. As the relationship between hidden layer and output layer of RBF neural network is linear mapping, hence we can get the output layer of the network results expressions which is shown as follows according to the network structure shown in Fig. 1.

$$y_k = w_k^T \Phi = \sum_{j=1}^{a} w_{kj} \exp[-\frac{\|x - c_j\|^2}{\delta_j^2}], \quad (k = 1, \ldots, 6) \tag{4}$$

By analyzing (4), we can see that the key of construct RBF neural network fault diagnosis model lies in the two aspects. First, we need to use the input fault samples to determine hidden layer center vector and the number of hidden layer neuron. Second, we need to use the given training samples to train the weights of network hidden layer to the output layer. In RBF network, the computation of the network will increase if there are many centers of RBF network, which will result in a reduction of the network's generalization ability. Hence, it is key to select the appropriate number of RBF centers to build the network model. The common method used to solve the RBF network center algorithm are mainly the clustering algorithm, orthogonal least squares algorithm, etc. But these algorithms have

defects, such as clustering algorithms require a predefined cluster number, and the orthogonal least squares method will appear ill conditioned matrix when the quantity of input data is large [9]. In order to solve this problem, this paper uses the artificial immune network algorithm to process the training data, and then gets the number and location of the hidden layer center of the RBF network.

3.3 Determination of RBF Hidden Layer Center Based on Artificial Immune Network Algorithm

Artificial immune network algorithm is a new intelligent algorithm which simulates the biological immune system. It combines clone selection with immune suppression principle which simulates the role of the relationship between the mimic antigen and antibody. In the process of learning model of antigen, the antibody will be optimized constantly and finally will get the uniqueness of the characterizing antigen antibody [10]. In order to get the number of hidden layer center and the center vector of the network, this paper uses the principle of artificial immune network to process the sample data. The processing algorithm is shown as follows:

(1) Extraction of the original antigen set. This paper select five kinds of gas H_2, CH_4, C_2H_6, C_2H_4, C_2H_2 as the characteristic gas of the transformer. Hence, the content of these five kinds of characteristic gases are selected as the original antigen $x_i = [x_{i1}, x_{i2}, x_{i3}, x_{i4}, x_{i5}]$.

(2) Normalization of transformer fault gas characteristic value. Due to the analysis of the dissolved gas in the oil, the original gas data of the same fault type is different and the dimension is also different, which will affect the fault type [11]. Hence, this paper uses the following method to process the data.

$$x_{ip}^{'} = x_{ip} / \sum_{p=1}^{5} x_{ip}, (p = 1, 2, 3, 4, 5) \tag{5}$$

(3) Purification of transformer fault characteristic. In order to remove the similar individuals in the fault characteristic quantity, the characteristic quantity of the treated fault should be purified. The similarity degree of individual is characterized by Euclidean distance. Individual similarity is measured by c_v. An individual will be removed when the c_v is less than 0.01. N-dimensional Euclidean distance is shown as follows:

$$d(\overrightarrow{A}, \overrightarrow{B}) = sqrt \sum (a[i] - b[i])^2, (i = 1, 2, \ldots, n) \tag{6}$$

(4) Initialization of antibody set randomly. This paper selects a certain number N of the various types of failure mode from the sample randomly as the immune network initial antibody collection, which is expressed by Ab.

(5) Calculation of affinity. Calculate the affinity between the training sample $x_i^{'}$ and all the antibodies in initial antibody set Ab. The calculation formula of affinity is shown as follows: $\left(x_j \in Ab\right)$.

$$f_{ij} = \frac{1}{1 + \left\| x_i^{'} - x_j \right\|} \tag{7}$$

(6) Clone selection. According to the affinity vector f_i, this paper selects n the highest affinity antibody from antibody set Ab as a new antibody set $Ab_{\{n\}}$.

(7) Clone operation. This paper operates each antibody in the new antibody set $Ab_{\{n\}}$ and the number of N_c is determined by the following formula. The antibody set after clone operation is C_i.

$$N_c = \sum_{i=1}^{n} round(K_{scale} f_i) \tag{8}$$

(8) Mutation operation. Simulating the high frequency variation of somatic cells, the antibody set after mutation operation is C_i^*. The formula for variation operation is shown as follows, in this formula α is the learning rate, which is determined by affinity, the bigger the affinity is, the bigger the α is

$$c_j^* = c_j - \alpha(c_j - x_i^{'}). \tag{9}$$

(9) Calculate the affinity again. In paper we recalculate the affinity between $x_i^{'}$ and antibody set C_i^*. According to new affinity degree vector f_i from antibody set, this paper selects a maximum degree of $\xi\%$ antibody affinity and deletes antibody which affinity is less than a certain threshold σ_d.

(10) Immune suppression operation. We calculate the affinity between the various antibodies in the antibody set Ab^*, and remove the antibody whose affinity is greater than the specific threshold σ_s. Then update antibody set Ab^*.

(11) Repeat the above operation until the number of iterations is reached.

3.4 Particle Swarm Optimization Algorithm Based on RBF Network Weights

Particle swarm optimization algorithm is a new kind of optimization algorithm based on swarm intelligence. It is a kind of swarm intelligence optimization search which is realized by the cooperation and competition among groups [12]. Compared with other optimization algorithms such as genetic algorithm (GA), it is simple and easy to implement and also has stronger ability of local and global

optimization. Hence, the particle swarm optimization algorithm is used to optimize the connection weights of RBF network model.

In the particle swarm optimization algorithm, the models of position and velocity are used to search for a potential solution in the solution space. Suppose a group consisting of particles is flying at a certain speed in the solution space of the dimension (the dimension of each particle). Each particle is represented by its position and velocity vector, recorded as $P_i = (P_{i1}, P_{i2}, \ldots, P_{iR})$ and $V_i = (V_{i1}, V_{i2}, \ldots, V_{iR})$. The optimal value of each particle individual is recorded as $BestP_i$, the optimal value of the group search is denoted as $BestG_i$. The velocity and position of each particle are changed according to the following formula:

$$V_{id}^{k+1} = \omega V_{id}^{k} + C_1 R_1 (BestP_{id} - P_{id}^{k}) + C_2 R_2 (BestG_{id} - P_{id}^{k}) \tag{10}$$

$$P_{id}^{k+1} = P_{id}^{k} + V_{id}^{k+1} \tag{11}$$

In order to use particle swarm optimization algorithm to optimize the weights of the RBF neural network, the position vector of each particle is set as a set of weights of a RBF neural network. The particles are generated randomly. PSO algorithm is used to search the optimal position, when the objective function reaches the minimum value, which is shown that the best connection weights in the network are be found. Optimization algorithm of weight is shown as follows:

(1) Initialization of particle swarm. Set the number of particles as m, set the learning factor C_1, C_2, set the maximum number of iterations as $k_{\max}$, random particle position vector P_i, and velocity vector V_i;
(2) Calculate the fitness value of each particle. Calculate the fitness value of each particle through the output of the RBF neural network. Then record the individual and groups' extreme *BestP* and *BestG*. The fitness value of the whole network is evaluated as follows:

$$F_i = \frac{1}{N} \sum_{i=1}^{N} (Y_i^{'} - Y_i)^2. \tag{12}$$

In this formula, N is the number of training samples; $Y_i^{'}$ is the actual output of neural networks; Y_i is the expected output of neural network.
(3) Compare the fitness value of particle with the fitness value of the individual extreme *BestP*, take the best value as the new individual extreme *BestP*. Compare the fitness value of particle with the fitness value of the groups' extreme *BestG*, take the best value as a new global extreme population *BestG*;
(4) Update the position vector and velocity vector of the particles through the type (10) and (11);
(5) After reaching the maximum number of iterations $k_{\max}$ or the precision of network meet the requirements, stop iteration and output, otherwise the reversal to the step (2).

4 Simulation Analysis

4.1 Selection of Simulation Samples

In order to improve the accuracy of network training, this paper applies the value of dissolved gas in a certain transformer oil. This paper collects 300 groups of samples with known fault types and randomly selects 120 groups as the training set which contain each fault type. The rest of the 180 groups have been regarded as a test set to verify the performance of the algorithm in this paper.

4.2 Simulation Process

The input data of the artificial immune network algorithm is the training antigen set $x_i^{'} = [x_{i1}^{'}, x_{i2}^{'}, x_{i3}^{'}, x_{i4}^{'}, x_{i5}^{'}]$. After the artificial immune algorithm is processed, the outputs are the number and the initial location of the RBF network hidden layer center. This paper inputs 120 groups of fault samples into the artificial immune network algorithm in MATLAB and set the related parameters of network as follows. Purification threshold $c_v = 0.01$, the number of initial antibodies $N = 20$, optimal antibody selection $n = 6$, clone scale $K_{scale} = 10$, rate of reselection $\xi\,\% = 10\,\%$, threshold of clone selection $\sigma_d = 0.5$, threshold of immune suppression $\sigma_s = 0.15$. After the artificial immune principle, the number of the fault memory characteristic vector of the transformer is 11.

Then this paper uses the results of artificial immune network as the number and location of the initial hidden layer centers of RBF neural network, and uses particle swarm optimization algorithm to optimize the weights of the network. In this paper, we set the related parameters of PSO: group size $m = 40$, learning factors $C_1 = C_2 = 2$, maximum inertia factor $\omega_{\max} = 1.4$, minimum inertia factor $\omega_{\min} = 0.4$, maximum number of iterations $k_{\max} = 100$. In order to train the weights of the neural network, the fault type of the transformer should be encoded as the expected output of the RBF neural network, which is shown in Table 2. The actual output of the network is represented by the numerical value of 0 to 1 corresponding to the fault degree, the more close to 1, the numerical value is expressed as the occurrence of such failure.

Table 2 Fault type expected output code table

Fault type	Expected output
Low temperature overheat T1	1 0 0 0 0 0
Middle temperature overheat T2	0 1 0 0 0 0
High temperature overheat T3	0 0 1 0 0 0
Partial discharge PD	0 0 0 1 0 0
Low-energy discharge D1	0 0 0 0 1 0
High-energy discharge D2	0 0 0 0 0 1

Table 3 Diagnostic results

Fault type	Test number	Identify the corresponding fault						Wrong number	Diagnostic accuracy (%)
		T1	T2	T3	PD	D1	D2		
T1	34	31	3					3	91.2
T2	38	1	34	3				4	89.5
T3	43		3	40				3	93.0
PD	18				17	1		1	94.4
D1	25				2	23		2	92.0
D2	22				1	1	20	2	90.9

Table 4 Fault diagnosis examples of five groups of transformers

Group	φ (H_2)	φ (CH_4)	φ (C_2H_6)	φ (C_2H_4)	φ (C_2H_2)	Diagnostic results	Actual fault
1	167	238	105	485	9	T3	High temperature overheat caused by multi point grounding
2	59	10.4	4	10	12.7	PD	Low energy density board
3	86	110	18	92	7.4	T3	High temperature overheat
4	30	7.4	1.8	8.5	19	D1	Low energy discharge
5	335	67	18	143	170	D2	Internal arc discharge

4.3 Diagnostic Results

The remaining 180 groups of gas characteristics were used to test the diagnostic accuracy of the RBF network. The simulation results are shown in Table 3. There are 5 groups of typical fault cases of transformers. Here this paper lists the results of using the algorithm in Table 4.

In order to verify the accuracy of the method proposed in this paper in diagnosing transformer faults, this paper uses successively three-ratio method, BP neural network, and RBF neural network algorithm to diagnosis the collected failure data. Record the compared results in Table 5.

It is found that different fault types have different diagnostic accuracy from the results of Table 5. The accuracy rate of T2 is relatively low but also reach 89.5 %, the accuracy of T1, D1, and D2 is higher than T2, the average is about 91 %. The

Table 5 Comparison of diagnostic accuracy of different algorithms

Diagnostic algorithm	Test sample number	Correct number	Accuracy (%)
Three-ratio method	180	128	71.2
BP network	180	149	83.4
RBF network	180	141	78.3
Algorithm in paper	180	165	91.7

accuracy of T3 and PD are the highest, which can reach above 93 %. It is found that five sets of examples all obtain the correct results by using the algorithm in this paper from Table 4. It is found that compared with other algorithms, the proposed algorithm has higher diagnostic accuracy from Tables 3 and 5.

5 Conclusion

(1) This paper considers the dissolved gas content in transformer oil as the research object. And uses RBF neural network algorithm as the fault diagnosis model of transformer fault diagnosis. In order to improve the accuracy of transformer fault diagnosis, this paper introduces artificial immune network algorithm and particle swarm optimization algorithm on the basis of RBF neural network. This paper obtains the number of nodes in the hidden layer and the center vector of RBF neural network using the artificial immune network algorithm to process the fault data, which can simplify the network structure and improve the generalization ability of the network. This paper trains the weights of the network using the particle swarm optimization algorithm, which can improve the global convergence ability of the network.
(2) From the simulation results, it can be seen that combining artificial immune network algorithm with particle swarm optimization algorithm to optimize RBF neural network is a very effective method in the diagnosis of transformer insulation fault, which can effectively improve the transformer insulation faults diagnosis precision.

References

1. Zheng R, Zhao J, Zhao T et al (2011) Power transformer fault diagnosis based on genetic support vector machine and gray artificial immune algorithm. Proc CSEE 31(7):57–63
2. Wu X, Liu J, Liang Y et al (2007) Application of support vector machine in transformer fault diagnosis. J Xi'an Jiongtong Univ 41(6):722–726
3. Xiang W, Zhang H, Wang Y et al (2011) Application of BP neural network with L-M algorithm in power transformer fault diagnosis. Power Syst Protect Control 39(8)
4. Wang X, Li W, Zhang Y (2005) Application study of BP network used in the fault diagnosis of power transformer. High Voltage Eng 31(7):12–14
5. Chen J, Wen X, Lan L et al (2007) Fault diagnosis of power transformer by novel radial basis function neural network approach. High Voltage Eng 33(3):140–143
6. Zhou A, Zhang B, Zhang H (2007) Power transformer fault diagnosis by using the artificial immune classification algorithm. High Voltage Eng 33(8):77–80
7. Dong M, Y Meng, Xu C et al (2003) Fault diagnosis model for power transformer based on support vector machine and dissolved gas analysis. Proc CSEE 23(7):88–92
8. Li Q, He Y, Bao W (2010) Immune-ant algorithm based RBFNN for fault diagnosis of analog circuits. Chin J Sci Instrum 31(6):1255–1261

9. Ren J, Huang J (2010) Transformer fault diagnosis based on immune RBF neural network. Power Syst Protect Control 38(11):6–9
10. Xiong H, Sun C, Chen W et al (2006) Artificial immune network classification algorithm for fault diagnosis of power transformers. Autom Electr Power Syst 30(6):57–60
11. Zhao X, Tang X, Wang E et al (2013) Quantitative analysis of transformer oil dissolved gas using FTIR. Spectros Spectr Anal 33(9):2407–2410
12. Wang X, Wang T (2008) Power transformer fault diagnosis based on neural network evolved by particle swarm optimization. High Voltage Eng 34(11):2362–2367

Consensus Control for Multi-agent Networks with Mixed Undirected Interactions

Weili Niu, Deyuan Meng and Xiaolu Ding

Abstract This paper is concerned with the average consensus problem on multi-agent networks with undirected interactions which can be either static or dynamic. Notably, the multi-agent networks involving static and dynamic interactions are represented by graphs with edge weights in the form of real numbers and transfer functions. We propose a distributed consensus control algorithm based on the nearest neighbor rule. It is shown that the connectivity topology condition supplies a necessary and sufficient condition for all agents to achieve average consensus. Numerical simulations are provided to verify the effectiveness of the obtained results.

Keywords Average consensus · Multi-agent networks · Dynamic interactions

1 Introduction

Coordination control for multi-agent networks has attracted considerable attention owing to its wide applications in many areas, such as biological systems [1], vehicle systems [2], complex networks [3], and power networks [4]. An important research topic of multi-agent coordination is consensus since it plays a fundamental role in all related problems. By consensus, it needs all agents to agree on a common quantity [5].

W. Niu
School of Mathematics and Systems Science, Beihang University (BUAA),
Beijing 100191, China

W. Niu · D. Meng (✉) · X. Ding
The Seventh Research Division, Beihang University (BUAA),
Beijing 100191, China
e-mail: dymeng23@126.com

D. Meng · X. Ding
School of Automation Science and Electrical Engineering,
Beihang University (BUAA), Beijing 100191, China

Y. Jia et al. (eds.), *Proceedings of 2016 Chinese Intelligent Systems Conference*,
Lecture Notes in Electrical Engineering 404, DOI 10.1007/978-981-10-2338-5_10

In the literature, most results address consensus problems on multi-agent networks with static interactions (see [6–11]). Static interactions between agents denote that the information is directly communicated with each other, and the corresponding adjacency weights are usually represented by real numbers. However, in practice, many systems are subject to dynamic interactions, especially large-scale systems with interconnected storage elements [12]. Dynamic interactions between agents denote that the information is not directly communicated with each other but shared after it is dynamically processed via a system/filter, and the corresponding adjacency weights are represented by dynamic systems or transfer functions. Recently, consensus against dynamic interactions emerges as a hot topic. Consensus problems on multi-agent networks with dynamic interactions represented by positive real systems and stable LTI systems are addressed in [13, 14], respectively. Two consensus problems on directed dynamic multi-agent networks with application to the thermal processes in buildings and undirected dynamic multi-agent networks with application to the power networks are studied in [15]. These new studies have extended the consensus theory to more general multi-agent networks.

In this paper, we study the average consensus problem on multi-agent networks with both static and dynamic interactions. A new consensus algorithm that combines traditional static consensus algorithm and the dynamic consensus algorithm with dynamic weights designed in the form of transfer functions is proposed. We adopt analysis approaches both in the time domain and in the frequency domain. It is shown that the connectivity of the undirected graph plays a crucial role for the mixed multi-agent networks reaching average consensus.

The remainder of this paper is organized as follows. In Sect. 2, we introduce some preliminaries on graph theory and present the problem statement on dynamic consensus. Distributed dynamic consensus results are presented in Sect. 3 and simulation results are provided in Sect. 4 to demonstrate the dynamic average consensus performance. Finally, in Sect. 5, conclusions and future studies are given.

Notations: Throughout this paper, $\mathscr{I}_n = \{1, 2, \ldots, n\}$, $1_n = [1, 1, \ldots, 1]^T \in \mathbb{R}^n$, $\boldsymbol{I}$ and 0 denote the identity matrix and null matrix with appropriate dimensions, respectively, and diag$\{\cdot\}$ represents a block matrix with the off-diagonal elements are all zeros.

2 Problem Statement

2.1 Preliminaries

We use an undirected graph to model the information exchange among agents. A weighted undirected graph is denoted by a triple $G = (V, E, A)$, where $V = \{e_i : i \in \mathscr{I}_n\}$ is the vertex set, $E \subseteq \{(e_i, e_j) : e_i, e_j \in V\}$ is the edge set, and $A = (a_{ij}) \in \mathbb{R}^{n\times n}$ is the symmetric nonnegative adjacency weight matrix, which satisfies $a_{ij} > 0 \Leftrightarrow (e_i, e_j) \in E$ and $a_{ij} = 0$ otherwise. Moreover, $a_{ii} = 0$ is assumed for all $i \in \mathscr{I}_n$. The edge $(e_i, e_j) \in E$ denotes that e_i and e_j can receive information from

each other, and e_i and e_j are neighbors. The index set of neighbors of each agent e_i is denoted by $N_i = \{j : (e_i, e_j) \in E\}$. A path is a finite sequence of edges consisting of distinct vertices $e_{i_0}, e_{i_1}, \ldots, e_{i_j}$ such that $(e_{i_{k-1}}, e_{i_k}) \in E$ for $k = 1, 2, \ldots, j$. An undirected graph is said to be connected if there exists a path between every pair of distinct vertices.

2.2 Problem Description

Consider a mixed multi-agent network with $n + m$ agents, and the interaction topology among these $n + m$ agents is modeled by an undirected graph $\mathcal{G} = (\mathcal{V}, \mathcal{E}, \mathcal{A}(s))$, where $\mathcal{A}(s)$ is the symmetric adjacency weight matrix with entries in the form of real numbers and transfer functions. According to different interactions among agents, we divided the multi-agent networks into two separate subnetworks: a controlled network with n agents labeled 1 through n, and a controller network with m agents labeled 1 through m. If agents lie in the same networks, the interactions between them are static. Otherwise, if agents lie in different networks, the interactions between them are dynamic. A simple example of such mixed multi-agent networks is shown in Fig. 1, where the controlled and controller network have 6 agents and 4 agents, respectively.

The controlled network is associated with an undirected graph $\mathcal{G}^p = (\mathcal{V}^p, \mathcal{E}^p, \mathcal{A}^p)$, where $\mathcal{V}^p = \{v_i : i \in \mathcal{I}_n\}$, $\mathcal{E}^p \subseteq \{(v_i, v_j) : v_i, v_j \in \mathcal{V}^p\}$, and $\mathcal{A}^p = \left(a_{ij}^p\right) \in \mathbb{R}^{n\times n}$. The dynamics of each agent v_i are given by

$$\dot{x}_i(t) = \sum_{j\in\mathcal{N}_i^p} a_{ij}^p \left[x_j(t) - x_i(t)\right] + u_i^p(t), i \in \mathcal{I}_n \tag{1}$$

where $x_i(t) \in \mathbb{R}$ is the state of agent v_i, $u_i^p(t) \in \mathbb{R}$ is the control input or protocol to be designed according to the dynamic interactions between v_i and its neighbors in controller network, and $\mathcal{N}_i^p = \{j : (v_i, v_j) \in \mathcal{E}^p\}$.

Similarly, we consider the controller network be associated with an undirected graph $\mathcal{G}^c = (\mathcal{V}^c, \mathcal{E}^c, \mathcal{A}^c)$, where $\mathcal{V}^c = \{c_i : i \in \mathcal{I}_m\}$, $\mathcal{E}^c \subseteq \{(c_i, c_j) : c_i, c_j \in \mathcal{V}^c\}$, and $\mathcal{A}^c = \left(a_{ij}^c\right) \in \mathbb{R}^{m\times m}$. The dynamics of each agent c_i are given by

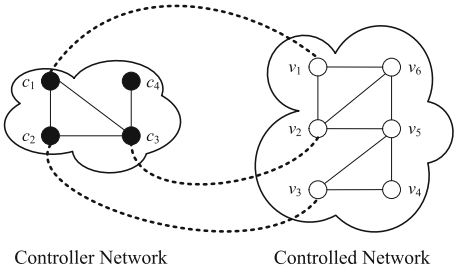

Fig. 1 An example of mixed undirected network, where *solid lines* denote the static interactions, and *dashed lines* denote the dynamic interactions

$$\dot{y}_i(t) = \sum_{j \in \mathscr{N}_i^c} a_{ij}^c \left[y_j(t) - y_i(t) \right] + u_i^c(t), i \in \mathscr{I}_m \tag{2}$$

where $y_i(t) \in \mathbb{R}$ is the state of agent c_i, $u_i^c(t) \in \mathbb{R}$ is the control input or protocol to be designed according to the dynamic interactions between c_i and its neighbors in controlled network, and $\mathscr{N}_i^c = \{j : (c_i, c_j) \in \mathscr{E}^c\}$.

The interactions between agents in different networks are achieved by the inputs $u_i^p(t)$ and $u_i^c(t)$ which fulfill the nearest neighbor rules. Let $U_i^p(s) = \mathscr{L}\left[u_i^p(t)\right]$ be the Laplace transform of $u_i^p(t)$, and let $U_i^c(s)$, $X_i(s)$, and $Y_i(s)$ be defined in the same way for $u_i^c(t)$, $x_i(t)$, and $y_i(t)$, respectively. We consider distributed dynamic consensus protocols in the form of

$$U_i^p(s) = \sum_{j \in \mathscr{N}_i^{cp}} g_{ij}^{cp}(s) \left[Y_j(s) - X_i(s) \right], i \in \mathscr{I}_n \tag{3}$$

$$U_i^c(s) = \sum_{j \in \mathscr{N}_i^{pc}} g_{ij}^{pc}(s) \left[X_j(s) - Y_i(s) \right], i \in \mathscr{I}_m \tag{4}$$

where $g_{ij}^{cp}(s)$ and $g_{ij}^{pc}(s)$ are dynamic weights to be designed, which satisfy $g_{ij}^{cp}(s) \neq 0$ if v_i can get dynamic information from c_j and $g_{ij}^{cp}(s) = 0$ otherwise, and $g_{ij}^{pc}(s) \neq 0$ if c_i can get dynamic information from v_j and $g_{ij}^{pc}(s) = 0$ otherwise. Also, in (3) and (4), $\mathscr{N}_i^{cp} = \{j : g_{ij}^{cp}(s) \neq 0\}$ and $\mathscr{N}_i^{pc} = \{j : g_{ij}^{pc}(s) \neq 0\}$.

The problem addressed in this paper is to enable the agents in mixed multi-agent networks to achieve consensus such that

$$\lim_{t \to \infty} \xi(t) = \xi_c, \forall \xi(t) \in \left\{ x_1(t), \ldots, x_n(t), y_1(t), \ldots, y_m(t) \right\} \tag{5}$$

where $\xi_c \in \mathbb{R}$ is a constant quantity. In particular, the multi-agent networks achieve the average consensus if $\xi_c = \frac{1}{n+m}\left(\sum_{i=1}^n x_i(0) + \sum_{j=1}^m y_j(0) \right)$, where $x_i(0)$ and $y_j(0)$ are initial states of $x_i(t)$ and $y_j(t)$, respectively.

3 Problem Analysis

3.1 Consensus Analysis

Let $x(t) = \left[x_1(t), x_2(t), \ldots, x_n(t) \right]^T$, and let $u^p(t)$, $y(t)$, $u^c(t)$ be denoted in the same way with $x(t)$. In this case, the consensus algorithm (1) and (2) can be written in a compact form as

$$\dot{x}(t) = -L^p x(t) + u^p(t) \tag{6}$$

$$\dot{y}(t) = -L^c x(t) + u^c(t), \tag{7}$$

where $L^p = \text{diag}\{\sum_{j\in\mathcal{N}_1^p} a_{1j}^p, \sum_{j\in\mathcal{N}_2^p} a_{2j}^p, \ldots, \sum_{j\in\mathcal{N}_n^p} a_{nj}^p\} - \mathcal{A}^p$ and $L^c = \text{diag}\{\sum_{j\in\mathcal{N}_1^c} a_{1j}^c, \sum_{j\in\mathcal{N}_2^c} a_{2j}^c, \ldots, \sum_{j\in\mathcal{N}_m^c} a_{mj}^c\} - \mathcal{A}^c$ are symmetric Laplacian matrix associated with $\mathcal{G}^p$ and $\mathcal{G}^c$, respectively.

For distributed dynamic consensus protocols (3) and (4), we design dynamic weights in the form of transfer functions as

$$g_{ij}^{cp}(s) = \frac{a_{ij}^{cp}}{s + k_i^p}, i \in \mathcal{I}_n, j \in \mathcal{I}_m; g_{ij}^{pc}(s) = \frac{a_{ij}^{pc}}{s + k_i^c}, i \in \mathcal{I}_m, j \in \mathcal{I}_n, \tag{8}$$

where $k_i^p > 0$, $a_{ij}^{cp} > 0$ if v_i can get dynamic information from c_j and $a_{ij}^{cp} = 0$ otherwise, $k_i^c > 0$, and $a_{ij}^{pc} > 0$ if c_i can get dynamic information from v_j and $a_{ij}^{pc} = 0$ otherwise.

Remark 1 Since the interactions between agents are undirected, it can easily be seen that the dynamic weights $g_{ij}^{cp}(s) = g_{ji}^{pc}(s)$ if there exist dynamic interactions between v_i and c_j, which implies that $k_i^p = k_j^c$, $a_{ij}^{cp} = a_{ji}^{pc} > 0, \forall i \in \mathcal{I}_n, j \in \mathcal{I}_m$.

With dynamic weights in (8), the control inputs $u_i^p(t)$ and $u_i^c(t)$ take the form of

$$\dot{u}_i^p(t) = -k_i^p u_i^p(t) + \sum_{j\in\mathcal{N}_i^{cp}} a_{ij}^{cp} \left[y_j(t) - x_i(t)\right], i \in \mathcal{I}_n \tag{9}$$

$$\dot{u}_i^c(t) = -k_i^c u_i^c(t) + \sum_{j\in\mathcal{N}_i^{pc}} a_{ij}^{pc} \left[x_j(t) - y_i(t)\right], i \in \mathcal{I}_m \tag{10}$$

which can be rewritten as

$$\dot{u}^p(t) = -K^p u^p(t) - D^{cp} x(t) + \mathcal{A}^{cp} y(t) \tag{11}$$

$$\dot{u}^c(t) = -K^c u^c(t) - D^{pc} y(t) + \mathcal{A}^{pc} x(t), \tag{12}$$

where $K^p = \text{diag}\{k_1^p, k_2^p, \ldots, k_n^p\}$, $D^{cp} = \text{diag}\{\sum_{j\in\mathcal{N}_1^{cp}} a_{1j}^{cp}, \sum_{j\in\mathcal{N}_2^{cp}} a_{2j}^{cp}, \ldots, \sum_{j\in\mathcal{N}_n^{cp}} a_{nj}^{cp}\}$, $\mathcal{A}^{cp} = \left(a_{ij}^{cp}\right) \in \mathbb{R}^{n\times m}$, $K^c = \text{diag}\{k_1^c, k_2^c, \ldots, k_m^c\}$, $D^{pc} = \text{diag}\{\sum_{j\in\mathcal{N}_1^{pc}} a_{1j}^{pc}, \sum_{j\in\mathcal{N}_2^{pc}} a_{2j}^{pc}, \ldots, \sum_{j\in\mathcal{N}_m^{pc}} a_{mj}^{pc}\}$, and $\mathcal{A}^{pc} = \left(a_{ij}^{pc}\right) \in \mathbb{R}^{m\times n}$. Clearly, we have $\mathcal{A}^{cp} = (\mathcal{A}^{pc})^T$, $D^{cp} 1_n = \mathcal{A}^{cp} 1_m$ and $D^{pc} 1_m = \mathcal{A}^{pc} 1_n$.

3.2 Main Result

Let $z(t) = \left[x^T(t), y^T(t)\right]^T$ and $u(t) = \left[(u^p(t))^T, (u^c(t))^T\right]^T$. By combining (6), (7) and (11), (12), we get

$$\dot{z}(t) = -Lz(t) + u(t) \tag{13}$$

$$\dot{u}(t) = -Ku(t) - Hz(t), \tag{14}$$

where $L = \begin{bmatrix} L^p & 0_{n\times m} \\ 0_{m\times n} & L^c \end{bmatrix}$, $K = \begin{bmatrix} K^p & 0_{n\times m} \\ 0_{m\times n} & K^c \end{bmatrix}$, and $H = \begin{bmatrix} D^{cp} & -\mathscr{A}^{cp} \\ -\mathscr{A}^{pc} & D^{pc} \end{bmatrix}$.

To achieve the primary objective of this paper, we proceed to analyze (13) and (14). Traditional convergence analysis of (13) and (14) generally collapses into checking the Hurwitz property of block matrix $C \triangleq \begin{bmatrix} -L & I \\ -H & -K \end{bmatrix}$. However, it is hard to testify, since the block matrix C does not have nice structure, such as diagonally dominant. We adopt a different analysis approach to addressing this issue, which is motivated by the proof of sufficiency of Theorem 3.1 in [16].

Let $Z(s) = \mathscr{L}[z(t)]$ and $U(s) = \mathscr{L}[u(t)]$ be the Laplace transform of $z(t)$ and $u(t)$, respectively. Taking Laplace transform of (13) and (14) gives that

$$sZ(s) - Z(0) = -LZ(s) + U(s) \tag{15}$$

$$sU(s) = -KU(s) - HZ(s) \tag{16}$$

Substituting (16) into (15) arrives at $Z(s) = \left[sI + L + (sI + K)^{-1}H\right]^{-1} Z(0)$. Now the consensus problem can be transformed into the stability problem of the transfer function matrix $G(s) = \left[sI + L + (sI + K)^{-1}H\right]^{-1}$.

Theorem 1 *For the multi-agent network given by (1) and (2) with undirected graph $\mathscr{G}$, let the control input $U^p(s)$ and $U^c(s)$ be applied with dynamic weights $g_{ij}^{cp}(s)$ and $g_{ij}^{pc}(s)$ satisfying $k_i^p = k_j^c = k, \forall i \in \mathscr{I}_n, j \in \mathscr{I}_m$. Then the multi-agent network achieves average consensus asymptotically if and only if $\mathscr{G}$ is connected.*

The proof of Theorem 1 depends on the Gershgorin's disc theorem [17] and the final value theorem [18], which is omitted here due to the page limitation.

4 Illustrative Simulations

Consider mixed multi-agent networks whose interaction topology among agents is shown in Fig. 1. Note that the undirected graph is connected. Without loss of generality, let the static adjacency weights (solid lines) be taken as 1, and let the dynamic adjacency weights (dashed lines) be taken as $g_{11}^{cp}(s) = g_{11}^{pc}(s) = \frac{1}{s+1}$, $g_{23}^{cp}(s) = g_{32}^{pc}(s) = \frac{3}{s+1}$, $g_{32}^{cp}(s) = g_{23}^{pc}(s) = \frac{2}{s+1}$. The initial states are given by $x(0) = [1, 2, 1.6, 2.5, 2.3, 2.7]^T$ and $y(0) = [1, 2, 3, 2.2]^T$. Simulation results of this mixed multi-agent networks with static and dynamic weights are shown in Fig. 2. It is clear from Fig. 2 that average consensus is achieved for all agents on 2.03. This illustration coincides with the statement of Theorem 1.

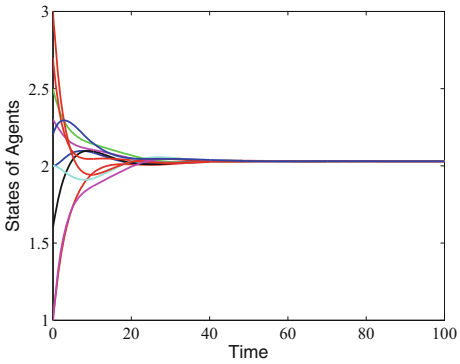

Fig. 2 Average consensus for multi-agent networks with mixed static and dynamic interactions

5 Conclusions

In this paper, average consensus problems on multi-agent networks with static and dynamic interactions have been discussed. We have proposed a new distributed consensus algorithm and have studied under what kind of topology conditions average consensus can be obtained. We adopt analysis approaches both in the time domain and in the frequency domain, which can provide an alternative way to deal with dynamic consensus problems on multi-agent networks. Simulations have been given to validate the effectiveness of our proposed consensus algorithm. Possible future research studies include dealing with multi-agent networks with directed static and dynamic interactions.

Acknowledgments This work was supported in part by the National Basic Research Program of China (973 Program) under Grant 2012CB821200 and Grant 2012CB821201, in part by the National Natural Science Foundation of China (NSFC) under Grant 61473010, Grant 61134005, Grant 61221061, Grant 61327807, Grant 61532006, and Grant 61320106006, in part by the Beijing Natural Science Foundation under Grant 4162036, and in part by the Fundamental Research Funds for the Central Universities.

References

1. Reynolds C (1987) Flocks, herds, and schools: a distributed behavioral model. Comput Graph 21(4):25–34
2. Fax JA, Murray RM (2004) Information flow and cooperative control of vehicle formations. IEEE Trans Autom Control 49(9):1465–1476
3. Ji Z, Hai L, Yu H (2015) Protocols design and uncontrollable topologies construction for multi-agent networks. IEEE Trans Autom Control 60(3):781–786
4. Teixeira A, Sandberg H, Johansson KH (2010) Networked control systems under cyber attacks with applications to power networks. In: Proceedings of the American control conference, pp 3690–3696
5. Olfati-Saber R, Fax A, Murray RM (2007) Consensus and cooperation in networked multi-agent systems. Proc IEEE 95(1):215–233

6. Jadbabaie A, Lin J, Morse AS (2003) Coordination of groups of mobile autonomous agents using nearest neighbor rules. IEEE Trans Autom Control 48(6):998–1001
7. Ren W, Beard RW (2005) Consensus seeking in multiagent systems under dynamically changing interaction topologies. IEEE Trans Autom Control 50(5):655–661
8. Olfati-Saber R, Murray RM (2004) Consensus problems in networks of agents with switching topology and time-delays. IEEE Trans Autom Control 49(9):1520–1533
9. Olfati-Saber R, Murray RM (2003) Consensus protocols for networks of dynamic agents. In: Proceedings of the American control conference, pp 951–956
10. Yucelen T, Egerstedt M (2012) Control of multiagent systems under persistent disturbances. In: Proceedings of the American control conference, pp 5264–5269
11. Ren W, Beard RW (2008) Distributed consensus in multi-vehicle cooperative control: theory and applications. Springer, London
12. Moore K, Vincent T, Lashhab F, Liu C (2011) Dynamic consensus networks with application to the analysis of building thermal processes. In: Proceedings of the IFAC world congress, pp 3078–3083
13. Oh KK, Lashhab F, Moore KL, Vincent TL, Ahn HS (2013) Consensus of positive real systems cascaded with a single integrator. Int J Robust Nonlinear Control 25(3):418–429
14. Wang J, Elia N (2008) Consensus over networks with dynamic channels. In: Proceedings of the American control conference, pp 2637–2642
15. Lashhab F (2012) Dynamic consensus networks: spectral properties, consensus and control. Dissertations and Theses, Colorado School of Mines
16. Cao Y, Ren W, Egerstedt M (2012) Distributed containment control with multiple stationary or dynamic leaders in fixed and switching directed networks. Automatica 48(8):1586–1597
17. Horn RA, Johnson CR (1991) Matrix analysis. Cambridge University Press, Cambridge, UK
18. Chen J, Lundberg KH, Lundberg DE, Bernstein DS (2007) The final value theorem revisited-Infinite limits and irrational functions. IEEE Control Syst Mag 27(3):97–99

Modeling and Simulation of Parafoil Systems in Wind Fields

Jin Tao, Qinglin Sun, Zengqiang Chen and Yingping He

Abstract Parafoil systems are a kind of flexible wing vehicle. In view that the vehicle flying at low altitude is more susceptible to wind fields, and considering that the parafoil canopy and the payload are regarded as rigid connection, a six degrees of freedom (DOF) dynamic model is established according to the Kirchhoff motion equation, which consists of three DOF for translational motion and three DOF for rotational motion. Moreover, the effects of wind fields on its flight performances are also discussed. The motion characteristics of parafoil systems under the horizontal constant wind field are studied by numerical simulation. Simulation results demonstrate that the established model can accurately characterize dynamic performances of parafoil systems in wind fields, which is high valuable in engineering applications.

Keywords Parafoil system · Dynamic model · Wind field · Flight characteristic

1 Introduction

A parafoil system is made up of a ram-air parafoil canopy and a payload. It is a kind of precision aerial delivery system with superior pneumatic performance, excellent gliding ability, and easy handling property. It now has been widely used in military, aerospace, and civil fields due to its excellent properties [1]. Over the last 50 years, researchers had done a lot of researches on dynamic modeling of parafoil systems. One of the first models was proposed by Goodrich who developed a three DOF

J. Tao · Q. Sun (✉) · Z. Chen
College of Computer and Control Engineering,
Nankai University, Tianjin 300350, China
e-mail: sunql@nankai.edu.cn

Y. He
Aerospace Life-Support Industries Ltd, Aviation Industry
Corporation of China, Xiangyang 441003, China

Y. Jia et al. (eds.), *Proceedings of 2016 Chinese Intelligent Systems Conference*,
Lecture Notes in Electrical Engineering 404, DOI 10.1007/978-981-10-2338-5_11

model to analyze the static and dynamic longitudinal stability of parafoil in 1975 [2]. Iacomini and Cerimele [3] explored the lateral and longitudinal aerodynamics for large-scale parafoil from the flight test data of NASA's X-38 parafoil program. Jann [4] proposed simple three and four DOF models based on ALEX parafoil flight test data. Tao et al. [5] used a three DOF motion model of parafoil system for planning optimal homing trajectories. Mortaloni et al. [6] addressed the development of a six DOF model of a low aspect ratio controllable parafoil-based delivery system which is equally suitable for modeling and simulation and for the design of guidance, navigation, and control algorithms. Barrows [7] mainly focused on calculations of the apparent mass of parafoil, and presented dynamic equations including nonlinear terms of a six DOF model. Xiong [8] also established a six DOF model for trajectory design and homing control. Considering the relative pitch and yaw motion between the parafoil and payload, Slegers [9], Yakimenko and Slegers [10], and Zhu et al. [11] applied the concept of coupling of moments between the payload and parafoil at the joining to build eight DOF model of parafoil system. Prakash and Ananthkrishnan [12] set up a nine DOF dynamic model of parafoil–payload system representing three of freedom each for rotational motion of the parafoil system, and three DOF for translational motion of the confluence point of the lines. Inspired by the above achievements, the full combined flexible system of parafoil and payload can be represented as an eight or nine DOF model depending on the specific harness connecting these two pieces together. Alternatively, it also can be modeled as a rigid body during flight only requiring six DOF, which is preferred in this paper.

Flying in a complicated environment, the parafoil system may encounter a sudden wind, which may cause severe influences on its aerodynamic performances, affect the desired trajectory, even lead to stall. So far, however, literatures that studied the effects of wind fields are merely to explore the influences on simple movements of parafoil systems, such as gliding and turning, comprehensive studies on wind effects are rather less.

Regarding the parafoil and the payload as a rigid body, a six DOF dynamic model of parafoil systems is established in terms of the Kirchhoff motion equation in wind fields. This paper emphasizes on effects of wind fields on its aerodynamics performances. Consequently, basic flight motions such as gliding, turning and flare landing in windy conditions are analyzed in simulations. The results verify the validity of the established dynamic model of parafoil systems.

2 Modeling of Parafoil Systems in Wind Fields

2.1 Wind Field Model

Constant winds often used for flight simulation are adopted to explore the effects of wind fields on flight characteristics of parafoil systems.

In the geodetic coordinate, the wind field can be expressed as

$$\boldsymbol{V}_v = [u_v, v_v, w_v]^T, \tag{1}$$

where subscript v denotes the velocity of wind, u, v, and w denote the component of $\boldsymbol{V}$ in x-, y-, and z-axes, respectively.

Project $\boldsymbol{V}_v$ into the body coordinate

$$[u_{v,p}, v_{v,p}, w_{v,p}]^T = \boldsymbol{T}_{e-p}[u_v, v_v, w_v]^T, \tag{2}$$

where $\boldsymbol{T}_{e\text{-}p}$ denotes the transformation matrix from the geodetic coordinate to the body coordinate.

Thus, the velocity $\boldsymbol{V}$ of the vehicle in the body coordinate is expressed as

$$\boldsymbol{V} = [u, v, w]^{\mathrm{T}} - [u_{v,p}, v_{v,p}, w_{v,p}]^T \tag{3}$$

2.2 Dynamic Model of Parafoil System

Before modeling, some reasonable hypothesis should be made to facilitate analysis:

(1) After the canopy has been inflated completely, its aerodynamic configuration keeps fixed without maneuvering.
(2) The parafoil and the payload are regarded as a rigid body, and the mass center of the canopy overlaps the aerodynamic pressure center.
(3) The payload is regarded as a revolutionary body, such that the lift of the payload is neglected, and only its aerodynamic drag force is considered.
(4) The ground is regarded as a plane.

The dynamic equations of parafoil system can be obtained by the momentum and angular momentum theorem, the total momentum and angular momentum are composed of two parts, one is produced by the real mass, and the other is generated by the apparent mass. The quantity of the apparent mass is associated with motion directions. However, the traditional rigid body dynamics equations often obscure the changes of the apparent mass under different coordinate frames, which may lead to incorrect results [13]. Accordingly, Kirchhoff motion equation is applied to describe dynamic equations of parafoil systems.

The motion equations of the parafoil system are expressed as

$$\frac{\partial \boldsymbol{P}_T}{\partial t} + \boldsymbol{W}^{\times}\boldsymbol{P}_T = \dot{P}_{a,O} + \dot{\boldsymbol{P}}_{r,O} + \boldsymbol{W}^{\times}\boldsymbol{P}_{a,O} + \boldsymbol{W}^{\times}\boldsymbol{P}_{r,O} = \boldsymbol{F}_{\text{aero}} + \boldsymbol{F}_{ex} \tag{4}$$

$$\begin{aligned}\frac{\partial \boldsymbol{H}_T}{\partial t}+\boldsymbol{W}^{\times}\boldsymbol{H}_T+\boldsymbol{V}_O^{\times}\boldsymbol{P}_T&=\dot{\boldsymbol{H}}_{a,O}+\dot{\boldsymbol{H}}_{r,O}+\boldsymbol{W}^{\times}\boldsymbol{H}_{a,O}\\&\quad+\boldsymbol{V}_O^{\times}\boldsymbol{P}_{a,O}+\boldsymbol{W}^{\times}\boldsymbol{H}_{r,O}+\boldsymbol{V}_O^{\times}\boldsymbol{P}_{r,O}\\&=\boldsymbol{M}_{\text{aero}}+\boldsymbol{M}_{ex},\end{aligned}\tag{5}$$

where $\boldsymbol{P}_T$ and $\boldsymbol{H}_T$ denote the total momentum and total angular momentum of the whole system, respectively; $\boldsymbol{V}$ and $\boldsymbol{W}$ denote the vectors of velocity and angle velocity of mass center, respectively; $\boldsymbol{F}$ and $\boldsymbol{M}$ denote the force and the moment, respectively. The subscript aero denotes aerodynamic force associated with the traditional aerodynamic force coefficients and static derivatives, the subscript *ex* denotes the external force except the aerodynamic force, but for parafoil systems, the only external force is gravity.

$\boldsymbol{F}_{\text{aero}}$, $\boldsymbol{F}_{ex}$, $\boldsymbol{M}_{\text{aero}}$, $\boldsymbol{M}_{ex}$ can be expressed as

$$\boldsymbol{F}_{\text{aero}}=\boldsymbol{F}_{\text{aero},p}+\boldsymbol{F}_{\text{aero},l}+\boldsymbol{F}_{\text{aero},f}\tag{6}$$

$$\boldsymbol{F}_{ex}=\boldsymbol{F}_{G,p}+\boldsymbol{F}_{G,l}\tag{7}$$

$$\boldsymbol{M}_{\text{aero}}=\boldsymbol{M}_{\text{aero},p}+\boldsymbol{M}_{\text{aero},l}+\boldsymbol{M}_{\text{aero},f}\tag{8}$$

$$\boldsymbol{M}_{ex}=\boldsymbol{M}_{G,p}+\boldsymbol{M}_{G,l}\tag{9}$$

where the subscript p, l, f, and G denote flap, parafoil canopy, payload, and gravity, respectively.

Then write

$$\dot{\boldsymbol{P}}_{a,O}+\dot{\boldsymbol{P}}_{r,O}=\boldsymbol{F}_{\text{aero}}+\boldsymbol{F}_{ex}-\boldsymbol{W}^{\times}\boldsymbol{P}_{a,O}-\boldsymbol{W}^{\times}\boldsymbol{P}_{r,O}\tag{10}$$

$$\dot{\boldsymbol{H}}_{a,O}+\dot{\boldsymbol{H}}_{r,O}=\boldsymbol{M}_{\text{aero}}+\boldsymbol{M}_{ex}-\boldsymbol{W}^{\times}\boldsymbol{H}_{a,O}-\boldsymbol{V}^{\times}\boldsymbol{P}_{a,O}-\boldsymbol{W}^{\times}\boldsymbol{H}_{r,O}-\boldsymbol{V}^{\times}\boldsymbol{P}_{r,O}\tag{11}$$

Define

$$\boldsymbol{F}_{r,nl}=-\boldsymbol{W}^{\times}\boldsymbol{P}_{r,O}=-\boldsymbol{W}^{\times}m_r\boldsymbol{V}\tag{12}$$

$$\boldsymbol{F}_{a,nl}=-\boldsymbol{W}^{\times}\boldsymbol{P}_{a,O}=-\boldsymbol{W}^{\times}\boldsymbol{M}_a\left(\boldsymbol{V}-(\boldsymbol{L}_{RO}^{\times}+\boldsymbol{L}_{PR}^{\times}\boldsymbol{S}_2)\boldsymbol{W}\right)\tag{13}$$

$$\boldsymbol{M}_{r,nl}=-\boldsymbol{W}^{\times}\boldsymbol{H}_{r,O}-\boldsymbol{V}^{\times}\boldsymbol{P}_{r,O}=-\boldsymbol{W}^{\times}\boldsymbol{J}_{r,O}\boldsymbol{W}-\boldsymbol{V}^{\times}m_r\boldsymbol{V}=-\boldsymbol{W}^{\times}\boldsymbol{J}_{r,O}\boldsymbol{W}\tag{14}$$

$$\begin{aligned}\boldsymbol{M}_{a,nl}&=-\boldsymbol{W}^{\times}\boldsymbol{H}_{a,O}-\boldsymbol{V}^{\times}\boldsymbol{P}_{a,O}\\&=\boldsymbol{W}^{\times}\left(\boldsymbol{S}_2\boldsymbol{L}_{PR}^{\times}+\boldsymbol{L}_{RO}^{\times}\right)\boldsymbol{M}_a\boldsymbol{V}-\boldsymbol{W}^{\times}\boldsymbol{J}_{a,O}\boldsymbol{W}+\boldsymbol{V}^{\times}\boldsymbol{M}_a(\boldsymbol{L}_{RO}^{\times}+\boldsymbol{L}_{PR}^{\times}\boldsymbol{S}_2)\boldsymbol{W},\end{aligned}\tag{15}$$

where the subscripts a and r denote the apparent mass and the real mass, respectively, and the subscript *nl* denotes the nonlinear force and moment. $\boldsymbol{J}$ denotes the momentum of inertia of the system, $\boldsymbol{S}$ denotes a choice matrix, $\boldsymbol{L}_{MN}^{\times}$ denotes the cross-product matrix of the corresponding distance vector from M to N.

Then the dynamic equation of the parafoil system can be expressed as

$$\begin{bmatrix} \dot{\boldsymbol{V}} \\ \dot{\boldsymbol{W}} \end{bmatrix} = [\boldsymbol{A}_r + \boldsymbol{A}_a]^{-1} \begin{bmatrix} \boldsymbol{F}_{\text{aero}} + \boldsymbol{F}_{ex} + \boldsymbol{F}_{r,nl} + \boldsymbol{F}_{a,nl} \\ \boldsymbol{M}_{\text{aero}} + \boldsymbol{M}_{ex} + \boldsymbol{M}_{r,nl} + \boldsymbol{M}_{a,nl} \end{bmatrix}, \tag{16}$$

where $\boldsymbol{A}_r$ and $\boldsymbol{A}_a$ denote the matrix form of real mass and apparent mass of the parafoil system, respectively.

3 Numerical Simulation Analysis

The simulation experiments are conducted based on a certain type of parafoil systems whose physical parameters are listed in Table 1.

The initial values of motions are set as follows: initial position $(x, y, z) = (0, 0, 2000\ \text{m})$, initial velocity $(u, v, w) = (15.9\ \text{m/s}, 0, 2.1\ \text{m/s})$, initial Euler angles $(\phi, \theta, \psi) = (0, 0, 0)$, and initial angular velocity $(p, q, r) = (0, 0, 0)$.

Aiming that the parafoil system is more susceptible to wind fields, the effects of transverse constant wind on gliding, turning, and flare landing are discussed below.

3.1 Gliding with Winds

The working condition is set as follows: after 50 s, when the vehicle is in stable state of gliding, the wind $\boldsymbol{V}_v = (0, 5\ \text{m/s}, 0)$ is added to the simulation environment. Simulation results are shown in Fig. 1.

It can be seen from Fig. 1a, b that the parafoil system glides steadily in the vertical plane and the trajectories both in the horizontal plane and 3D space are straight lines. Influenced by the transverse wind field, its horizontal trajectory is an inclined line, whose slope is a constant value and corresponding to its yaw angle. From (c), the velocities of x- and z-axes remain unchanged at 13.9 m/s and 4.5 m/s, respectively, the ultimate velocity of y-axis increases close to the wind speed. Thus

Table 1 Design parameters of the parafoil system

Parameters	Values/Units
Span	6.2/m
Chord	3.6/m
Area of canopy	21.0/m^2
Length of ropes	4.0/m
Rigging angle	10.0/°
Mass of canopy	20.0/kg
Mass of payload	80.0/kg
Characteristic area of payload	0.5/m^2
Characteristic area of flag	0.9/m^2

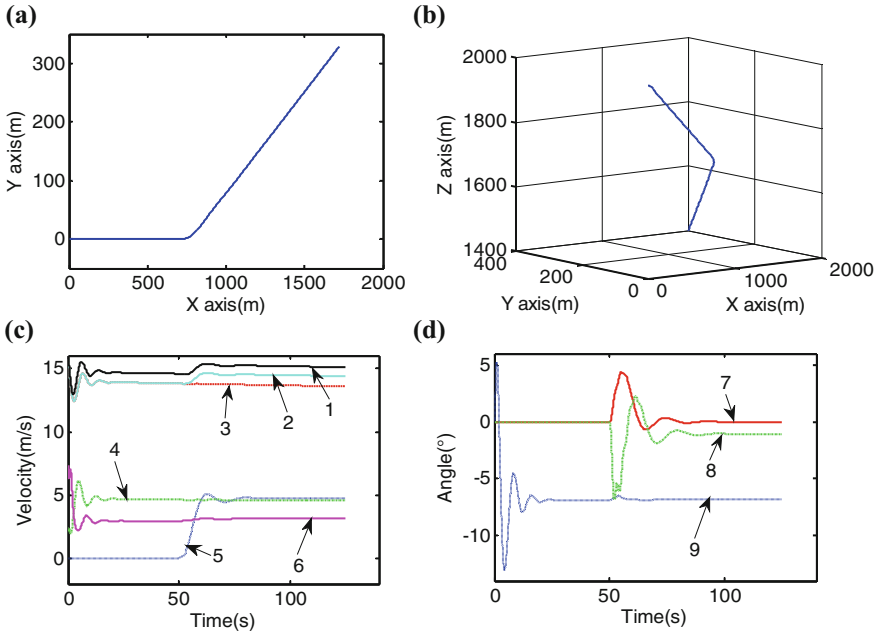

Fig. 1 Simulation results of gliding with winds: **a** trajectory in horizontal plane; **b** trajectory in 3D space; **c** velocities and gliding ratio in geodetic coordinate: 1 refers to resultant velocity, 2 refers to horizontal resultant velocity, 3 refers to velocity of x-axis, 4 refers to velocity of z-axis, 5 refers to velocity of y-axis, 6 refers to gliding ratio; **d** Euler angles: 7 refer to roll angle, 8 refers to yaw angle, 9 refers to pitch angle

the resultant velocity increases from 14.8 m/s to 15.4 m/s, but the gliding ratio stays unchanged at 3. From (d), we can observe that at the beginning of the wind, there exits large fluctuations in roll and yaw angles, but small changes in pitch angle. After stabilized, steady yaw trend is produced, the yaw angle is less than 1.5°. It is obvious that the parafoil system will drift with winds, the velocity and direction of drifting depend on the velocity and direction of the wind.

3.2 *Turning with Winds*

The working condition is set as: after 37.5 s, the left steering rope connected to the trailing edge of the parafoil canopy is pulled down by 20 %, after 50 s, when the system is in stable gliding state, the wind $\boldsymbol{V}_v = (0,\ 5\ \text{m/s},\ 0)^T$, is added to the simulation environment. The results are shown in Fig. 2.

As shown in Fig. 2, by the influence of wind, the horizontal trajectory is an upward spiral curve. The velocities of x- and y-axis sinusoidal fluctuate significantly. The velocity of z-axis fluctuates very slightly with sine functions. The

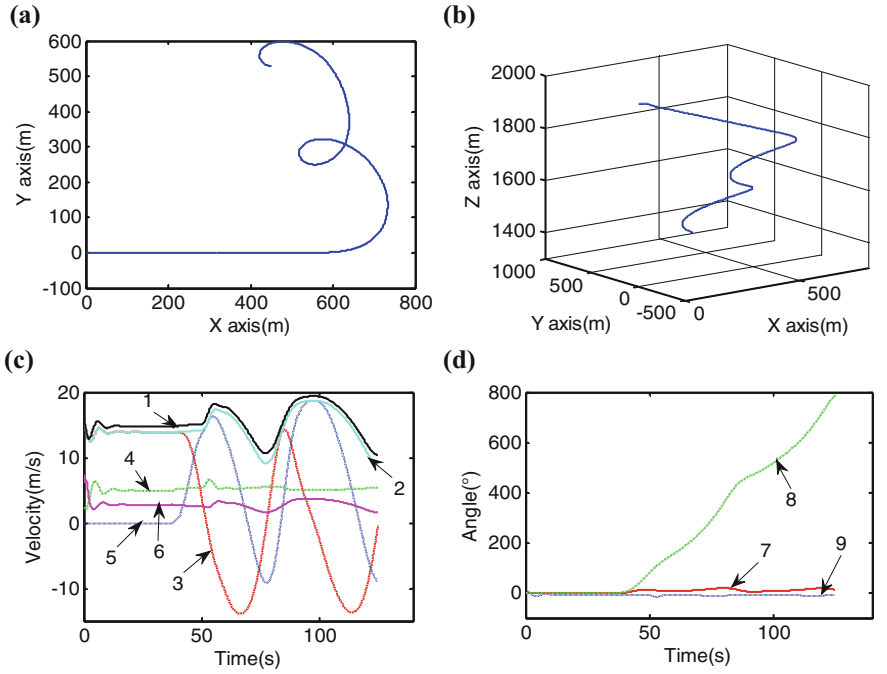

Fig. 2 Simulation results of turning with winds: **a** trajectory in horizontal plane; **b** trajectory in 3D space; **c** velocities and gliding ratio in geodetic coordinate: 1–6 indicate the same as Fig. 1c; **d** Euler angles: 7–9 indicate the same as Fig. 1d

resultant velocity fluctuates from 11.3 m/s to 20.5 m/s. The gliding ratio fluctuates from 1.7 to 3.6. From Fig. 1, roll and yaw angles fluctuate slightly with sine function, and continuous yaw trend is produced. It is said that the parafoil system also drifts with the wind, which can be used for identifying the speed and direction of wind field.

3.3 *Flare Landing with Winds*

The working conditions are set as follows: after 50 s, $\boldsymbol{V}_v = (5\ \text{m/s},\ 0,\ 0)$ and $\boldsymbol{V}_v = (-5\ \text{m/s}, 0, 0)$ are added to the simulation environment, separately. After 75 s as the system gliding steadily in the wind field, both steering ropes are pulled down by 100 % simultaneously and quickly, the simulation results are shown as Fig. 3.

It can be observed from Fig. 3a that for flare landing against wind, the minimum velocity will be more close to zero, so as to ensure the safety of recycled payloads. Whereas for flare landing following wind, see as Fig. 3b, the minimum velocity will be much larger. This may further explain that flying against wind is a necessary condition for flare landing.

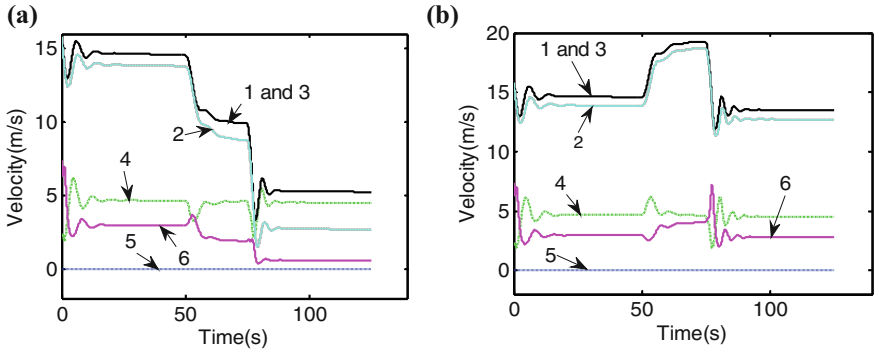

Fig. 3 Simulation results of flare landing with winds: **a** $\boldsymbol{V}_v = (5\ \text{m/s}, 0, 0)$; **b** $\boldsymbol{V}_v = (-5\ \text{m/s}, 0, 0)$. 1–6 indicate the same as Fig. 1c

4 Conclusion

In this paper, a nonlinear dynamic model of the parafoil system was built according to the Kirchhoff motion equation in the wind field. Regarding the parafoil and the payload as a rigid body, the model has six DOF, including three DOF of translational motion with the mass center and the other three DOF of rotational motion around the mass center. This modeling method considers the wind fields on aerodynamics performances of the parafoil system, and the modeling process is relatively simple, which provides significant hints for the research of parafoil systems. The basic motion characteristics of gliding, turning, and flare landing in the transverse constant wind were analyzed by simulations. The simulation results verified the validity of the established model.

Acknowledgments This work is supported by National Natural Science Foundation of China (No.61273138, 61573197), National Key Technology R&D Program (No.2015BAK06B04), Key Fund of Tianjin (No.14JCZDJC39300), and Key Technologies R&D Program of Tianjin (No.14ZCZDSF00022).

References

1. Rogers J, Slegers N (2013) Robust parafoil terminal guidance using massively parallel processing. J Guid Control Dyn 36(5):1336–1345
2. Goodrick TF (1975) Theoretical study of the longitudinal stability of high-performance gliding airdrop systems. In: Proceedings of the 5th aerodynamic deceleration systems conference, Albuquerque, NM. AIAA, USA, pp 1–9
3. Iacomini CS, Cerimele CJ (1999) Lateral-directional aerodynamics from a large scale parafoil test program. In: Proceedings of the 15th aerodynamic decelerator systems technology conference. Toulouse, France. AIAA, USA, 218–228

4. Jann T (2001) Aerodynamic model identification and GNC design for the parafoil-load system ALEX. In: Proceedings of the 16th AIAA aerodynamic decelerator systems technology conference and seminar, Boston, MA, USA. AIAA, USA, pp 21–24
5. Tao J, Sun QL, Zhu EL, Chen ZQ (2015) Quantum genetic algorithm based homing trajectory planning of parafoil system. In: Proceedings of the 34th chinese control conference, Hangzhou, China. IEEE, Piscataway, USA, pp 2523–2528
6. Mortaloni PA, Yakimenko OA, Dobrokhodov VN, Howard RM (2003) On the development of a six-degree-of-freedom model of a low-aspect-ratio parafoil delivery system. In: Proceedings of the 17th AIAA aerodynamic decelerator systems technology conference and semina, Monterey, California, USA. AIAA, USA, pp 1–10
7. Barrows TM (2002) Apparent mass of parafoils with spanwise camber. J Aircr 39(3):445–451
8. Xiong J (2005) Research on the dynamics and homing project of parafoil system. National University of Defense Technology, Changsha, China
9. Slegers N (2010) Effects of canopy-payload relative motion on control of autonomous parafoils. J Guid Control Dyn 33(1):116–125
10. Yakimenko O, Slegers N (2009) Using direct methods for terminal guidance of autonomous aerial delivery systems. In: Proceedings of the 2009 European control conference, Budapest, Hungary. IEEE, Piscataway, USA, pp 2372–2377
11. Zhu EL, Sun QL, Tan PL, Chen ZQ, Kang XF, He YP (2014) Modeling of powered parafoil based on Kirchhoff motion equation. Nonlinear Dyn 79(1):617–629
12. Prakash O, Ananthkrishnan N (2006) Modeling and simulation of 9-DOF parafoil-payload system flight dynamics. In: Proceedings of the AIAA atmospheric flight mechanics conference and exhibit, Keystone, Colorado. AIAA, USA, pp 21–24
13. Wang LR (1997) Parachute theory and application. Aerospace Press, Beijing, China (in Chinese)

Implementation of Intelligent Dynamic Tracking Monitoring System for Vehicle Transportation-in Hazardous Goods

Dekuan Liu

Abstract In order to put an end to malignant accident caused by leakage, loss, explosion, etc., of hazardous goods of vehicle in transportation process, this paper explores a kind of remote real-time dynamic track monitoring system. In the paper, it makes the anatomy of the reason resulted in malignant accidents, discusses the system architecture aimed at the conditions and trigger factors of malignant accidents caused, based on the combination between GPS positioning and GPRS communication, it designs the transceiver terminal of vehicle data acquisition and the functional modules such as communication, electronic map loading, database, monitoring alarm, etc., in monitoring center, and realizes a prototype of real-time dynamic track monitoring system. The preliminary test demonstrated that it could complete the remote dynamic tracking and monitoring function of transportation-in hazardous goods in vehicle. Research shows that it can provide effective technical support for security of transportation-in hazardous goods of vehicle.

Keywords Hazardous goods transportation · GPRS · Electronic map · B/S structure mode · Transportation-in monitoring

1 Introduction

In recent years, the serious accidents in leak, loss, and explosion caused by the vehicle mounted hazardous goods in transit have given people a serious lesson, and have aroused great concern from all walks of life [1–4]. The hazardous goods own the characteristic such as being flammable, explosive, toxic, corrosive, and radioactive, and it is extremely easy to cause fire, explosion, poisoning, radiation, and other major accidents in the course of transport if it is heated in case of fire, collision, vibration, friction, and other trigger factors [5–7]. In order to prevent the occurrence of malignant accident, it has important practical significance to carry out

D. Liu (✉)
International School, Chongqing Jiaotong University, Chongqing 400074, China
e-mail: 1751332285@qq.com

Y. Jia et al. (eds.), *Proceedings of 2016 Chinese Intelligent Systems Conference*,
Lecture Notes in Electrical Engineering 404, DOI 10.1007/978-981-10-2338-5_12

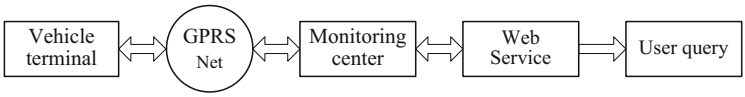

Fig. 1 Structure of tracking and monitoring system

the real-time tracking and monitoring of the vehicle hazardous goods in transit. Although many applications have been made in this area, and in view of the complexity of the problem [8–10], it is still necessary to conduct in-depth study.

2 System Structure of Real-Time Dynamic Tracking and Monitoring

The structure diagram of real-time dynamic tracking and monitoring system is shown in Fig. 1, and it is composed by the vehicle terminal, GPRS network, and monitoring center.

Monitoring center, GPRS network, and vehicle terminal are, respectively, responsible for the monitoring of hazardous goods vehicle, alarm, and scheduling, communication of monitoring center and vehicle terminal, and the test of vehicle operation, hazardous goods status, and GPS positioning parameters.

3 Monitoring System Design

Real-time dynamic tracking monitoring of vehicle hazardous goods in transit must have the following functions. ① Based on the GIS Web map, it can achieve the location of the transport vehicle GIS tracking. ② Based on vehicle terminal, it can achieve the information query such as kind of hazardous goods, transport vehicle number, and other hazardous goods state data. ③ Based on historical data storage, it can achieve the historical data query and track playback. ④ Based on the early warning of state parameters, it can achieve the threshold management and early warning of hazardous goods. ⑤ Based on a variety of control commands, it can achieve the relevant information management.

3.1 Vehicle Terminal System

Vehicle terminal state monitoring is not only involved in the state parameter of hazardous goods, and it is also related to the location of the vehicle, the state of the vehicle itself, and the state parameters of the vehicle. Geographic location-related

information data of vehicle terminal system can be obtained by GPS, and other state data information can be collected automatically by the vehicle terminal system. In view of the vehicle terminal state data, it includes the distribution in the compartment and also covers the environment parameters which are not with the wiring of the data collected such as temperature, etc. It is desirable to design a distributed status monitoring system based on WSN for wireless sensor networks, and therefore, it adopts the design of the wireless communication mode based on ZigBee and GPRS for data transmission. The local data collection and transmission is realized by ZigBee, and the remote data transmission of sensing data to the monitoring center is completed with the help of GPRS. ZigBee is suitable for automatic monitoring in the field of remote monitoring and control, and it is a kind of two-way wireless communication technology with close distance and low cost. WSN network hardware is achieved using 2.4 GHz band ZigBee device, and this can help to reduce costs and promote the applications, because it is a global unity without the application of the available frequency bands. The monitoring node includes 16 channels at a frequency of 2.4 GHz, its transmission distance is 10–75 m, and the data transmission rate is 250 kbps. As long as it configures the ZigBee monitoring nodes on the way of the vehicle terminal and vehicle, it can meet the requirements of vehicle terminal wireless networking and monitoring.

3.2 Design of Monitoring Center and Communication System

The communication system is responsible for establishing and maintaining the communication link, sending and receiving data among the vehicle terminals, and it is the information transmission channel of the monitoring center and the vehicle terminal. The monitoring center is responsible for specific functions needed to be realized.

The specific functions needed to be realized are as follows. ① Establishing communication link between the monitoring center and the mobile terminal, ② Receiving and checking the data transmitted by the vehicle terminal, ③ In accordance with the data encapsulation protocol, the vehicle terminal data is resolved to have the actual meaning of the data. ④ making the data analyzed to store into the classified ground database in accordance with the structure of the database table classification. ⑤ After monitoring center judging the receiving comprehensive data, it issues the corresponding prompt information to the vehicle terminal. In order to ensure the correctness of data transmission, the communication adopts TCP/IP protocol, and the communication between the monitoring center and the vehicle terminal adopts the real-time bidirectional transmission channel provided by TCP agreement. Although the GPRS network also has limitations on the TCP link, but network programming based on socket, the application does not need direct contact with the network interface to send and receive data packets.

3.3 System Database Design

The background database of the monitoring center carries the storage of the data information such as the hazardous goods and the vehicle state, and it is the information hub of the monitoring system. Monitoring system database must make the reasonable design according to the design principles such as reasonable organization, clear structure, low redundancy, easy to operate, easy maintenance, good expansibility, and so on. Monitoring system database is used to store basic information, GPS positioning and geographic information, and other data, in which, the basic information database is used to organize and store the attribute information of the related objects, including the data table such as warning threshold of hazardous goods, hazardous chemicals, transport vehicles, the driver status, and so on. GPS positioning database is used to store the latitude and longitude data information of hazardous goods transport vehicles, and it can also store the vehicle terminal position track, vehicle terminal number, vehicle terminal instruction sending and receiving information, alarm information, and other data tables. Geographic information database is used to organize and store the geographical distribution and other spatial data table of the hazardous goods in the way to monitor. Database access is realized through the data table, and the monitoring center database includes static and dynamic data tables, in which, the static data table is a long-term preservation of the system, and the contents of the general does not change. Dynamic data table is dynamically established in the vehicle transport of hazardous goods, and the content is continuously updated in real time. The relationship between the various data tables is distinguished in accordance with the "number", and the relations between them are shown in Fig. 2, in which, the static data table is represented by the black body line frame.

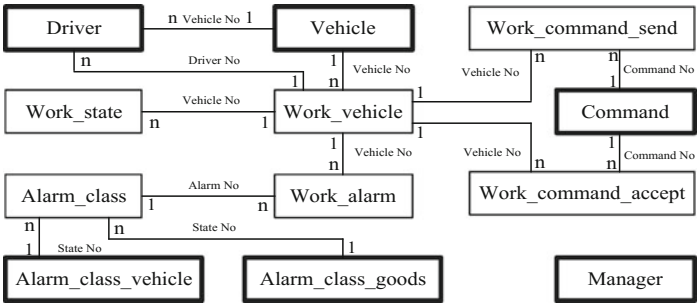

Fig. 2 Relationship between data tables

3.4 Electronic Map

Weighing the impact of various aspects of electronic map such as function, loading speed, cross-platform performance, ease of use, etc., and in order to realize the positioning and tracking of the vehicle terminal of hazardous goods, it adopts third-party GIS Web electronic map engine to design and construct the electronic map platform in the design. Because of its software system in the server side is equipped with the corresponding desktop GIS software, the client can send its desktop software support space query command directly to the server via Internet, and it can directly make positioning the transport vehicle display on the electronic map. With the aid of map matching technology, the monitoring system can correct all kinds of errors, and so that the hazardous goods vehicles accurately positioned on a certain road, more accurately displayed on the electronic map.

4 Monitoring System Implementation

Monitoring center carries on the function of real-time dynamic monitoring and historical data inquiry of hazardous goods vehicle state, among them, the latter is used to realize the tracing query of the historical data. The system adopts B/S structure mode to realize the real-time location of hazardous goods, the display of the state parameters, the historical data, and the track query, and the state parameters of the transport vehicle; the monitor center database selects server SQL 2000, and based on GPRS-Internet communication mode, it realizes the monitoring for sensor data acquisition, related commands issued, and remote office.

4.1 Information Management

The information management module is responsible for the management of users, vehicles, alarm, and control command information. After the user management module conducts to read the relevant parameters, configuration files, system initialization, and user logins verification process, the users own the right to use the system. The configuration file is WXPJC.ini.

[General]	
DSN = WXPJC	//Data source, the user can configure
UID = name	//Database logins user name
PWD = password	//Database logins password
[NET]	
IP = xxx.xx.xx.xxx	//Monitoring center server IP
Port = xxxx	//Communication port

Alarm management module deals with the operating management of data tables in alarm class, alarm class vehicle, and alarm class goods, and they are corresponding to the alarm definition column, vehicle status definition, and hazardous goods status column in the window. The module includes three submodules, they are, respectively, the vehicle information input, query, modification and deletion, and it defines the alarm state parameters used to manage the static information of all vehicles. Control command management module integrates the command definition, send command and dispatch information management functions into a window, and among them, the command definition management column is to manage the system command, and the send command and dispatch information management column is to send the system command and scheduling information to the target vehicle. The process of sending command (scheduling information) is that according to the vehicle number of the target vehicle, it first makes query IP address and port from data table work vehicle, then the command, along with the IP address and port number, is transmitted to the communication module, and stored in the work command send data table. Communication module based on IP address and port number finds the communication connection, it converts command to communication protocol format, and finally, it is sent to the target vehicle.

4.2 Real-Time Monitoring

The monitoring module has two functions of classification monitoring and alarm. Status information of hazardous goods and transport vehicles can be monitored in real time by classified monitoring according to the type of goods, the model of the vehicle, the container number, and the driver information. If the real-time status of hazardous goods and vehicles is abnormal, the alarm signs of the monitoring interface will be constantly flashing.

4.3 History Query

Historical inquiry is used for hazardous goods traceability for all kinds of information in the way, including the vehicle number and time, hazardous goods temperature, humidity, smoke, inclination, vibration and other records, logistics information, transport vehicle information, as well as tracing and querying for all alarm record, it can realize the online view of historical data information, and one of the monitoring interfaces is shown as in Fig. 3.

Fig. 3 Monitoring interface

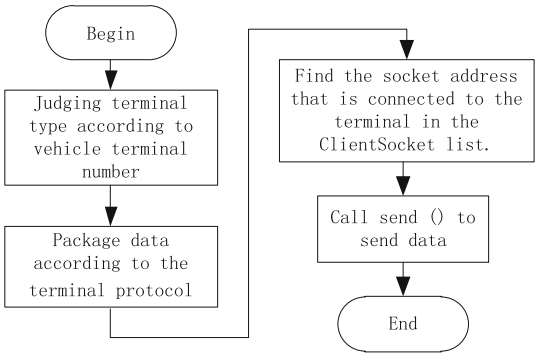

Fig. 4 Send data process for GPRS

4.4 GPRS Communication Implementation

Figure 4 describes the implementation process of command issued under the GPRS communication mode.

4.5 Implementation of GIS Web Platform

In the vehicle monitoring system of hazardous goods, with aid of related functions provided by Google Maps API, the monitoring center site can be combined with the satellite map of Google Maps, and it makes jointly implement the vehicle's trajectory description and positioning and other functions. The steps are that after the Google website is registered, according to the key provided by Google, the Maps Google can be embedded in the web page. In the process of generating a map, it calls the map code provided by Google into the user's web page, such as < script src="http: Maps.Google.com/MaPs?file = api&amp:v = 2&amp:key = abedefg"type=" text/JavaScript" > </script > < script type = "text/JavaScript" >, all the information used by Maps API Google are derived from the above link. With

the help of the code, it completes the map creation and center point establishment, embedded web maps are placed in div tags (map size and ID), and write it as a parameter to construction function of GMap2. Through call for Google Maps API, it can complete the call process for Google satellite map. Its code is as follows:

```
Var Map = new GMap2(docurnent.getElementById ("Map"));
Map.setCenter(new GLatLng (110,32), 15);
```

Maps Google has obvious advantages over the traditional map service system in aspects of response speed and ease use, and the application of maps Google in the monitoring system also has the advantage of maps Google application. It is worth noting that GIS Web platform implementation is only the use of the third party map engine implementation, and there is no GIS server in the monitoring center. In fact, the GIS Server is stored in the Google Company, that is, to say that the monitoring system does not have the map engine, and it just uses the map engine provided by the Google to complete the related GIS operation.

4.6 System Testing

After building a distributed state monitoring system based on WSN, the wireless sensor acquisition node of vehicle terminal and gateway node with GPS can be through the GPRS and monitoring center for data transceiver communications. If the sensor data acquisition is normal and communication is unimpeded,the user can log in monitoring center site with the user name and password, and check whether the monitoring data and the map acquisition are successful. Through the monitoring center sending the relevant control commands to the vehicle terminal, it can test whether the monitoring system is stable or not, and whether the working state of related communication system, GIS system, and the functional module is normal, and thereby it can test the feasibility, rationality, and availability of remote real-time tracking and monitoring system for the vehicle hazardous goods in transit.

5 Conclusions

With the continuous development of WSN technology, the popularity of GPRS communication technology, and the wide applications of maps Google satellite map, it is conducive to the development of hazardous goods transportation monitoring toward to the network monitoring direction. The system adopts the B/S structure pattern design, based on wireless sensor data acquisition of WSN, combined the monitoring center site with the maps Google satellite map, with aid of GPRS-Internet communication, the monitoring center can realize the real-time positioning of hazardous goods, display of the state parameters, query of historical

data, track, transport vehicle state parameters. It can effectively reduce the requirements of the system to the client, and is conducive to the realization of remote monitoring system for remote access. The test shows that the system design is feasible and reasonable, and the implementation of the system has a certain reference value for the design of similar systems.

References

1. Zongzhi WU, Meng USN (2006) Statistic analysis and countermeasure study on 200 transportation accidents of dangerous chemicals [J]. China J Saf Sci Technol 2(2):3–8
2. Ping LH, Du Yaohui J, et al (2008) Several problems in road hazardous materials transportation [J]. Mod Transp Technol 1(1):77–80
3. Yui QIN, Zhenqiang YAO (2008) A real time state monitoring system for hazardous goods in container [J]. Mach Des Res 24(6):98–101
4. Sheng MAO, Jiaming ZHOU, Mingxian WAMG (2005) Exploration and prospect of dynamic safety monitored control of transportable hazards [J]. China Saf Sci J 15(10):100–104
5. Hong-wei DONG, Guo-hua LI, Rong-hui CAO (2008) Design and development of realtime monitoring system for dangerous goods transport [J]. Railw Comput Appl 17(2):4–7
6. Zhang L (2010) Design of vehicle monitoring and warning system for dangerous goods in transit based on GPS GPRS and GIS [D]. JINAN: Shandong University of Technology (2010)
7. Chen G, Zhang Y, Yu Q et al (2009) Study and design of control system about dangerous goods delivery [J]. J Yunnan Univ (NATURAL SCIENCE EDITION) 31:150–155
8. Zhao J, LI Y, Xu C (2006) Introduction of ZigBee technology [J]. Commun Power Syst 27 (165):54–56
9. Akyildiz l, Su W, Sanakarasubramaniam Y et al (2002) Wireless sensor networks: a survey [J]. Comput Netw 38(4):393–422
10. Vlaga NR, Quddus MA, Bristow AL (2009) Developing an enhanced Weight-based topological map-matching algorithm for intelligent transport systems [J]. Trans Res Part C: Emerg Technol 17(6):672–683

Design on Embedded System in Parameter Measurement for Electric Power System

Dekuan Liu

Abstract In order to avoid out of whack in large-scale complex power system caused by the influence of artificial or natural factors, this paper explores the application of embedded system in electric power system measurement of electrical parameters. In the paper, it researches the related algorithm of the characteristic parameters in power system, takes the microcomputer line protection system of a 110 kV substation as an example, constructs the software and hardware platform of electric power parameter state monitoring system based on embedded microprocessor, and designs the hardware circuit and software control program. The system commissioning results demonstrates that the designed system can determine whether the fault of the related equipment, sends correctly the trip command to make the isolation between the fault equipment and the power system so as to protect the system from being damaged. The experiment results show that it is effective and available to electrical parameter test of the embedded system based on integrated testing method in the power system for guaranteeing the safe and stable operation of power system.

Keywords Embedded system · Parameter testing · Electric power system

1 Introduction

Once the power system is affected by man-made or natural factors to enter the abnormal operation state, and there may be a decline in the quality of power supply, power failure, or damage to electrical equipment, or even personal casualties and other accidents. Therefore, the relay protection device is an important means to ensure the stable operation of power system. In power system, electrical parameter measurement is the most important, the literature [1, 2] have made a comprehensive study on this, and a lot of research results have been achieved in the online

D. Liu (✉)
International School, Chongqing Jiaotong University, Chongqing 400074, China
e-mail: 1751332285@qq.com

Y. Jia et al. (eds.), *Proceedings of 2016 Chinese Intelligent Systems Conference*,
Lecture Notes in Electrical Engineering 404, DOI 10.1007/978-981-10-2338-5_13

detection and calculation of single parameter [3–7]. In order to improve the intelligentized and networked level of relay protection device, combined with engineering practice, the following is to conduct some discussion of the relevant technology for the embedded system in the power system electrical parameters measurement based on embedded Linux system.

2 Algorithm of System Characteristic Parameter

2.1 Two-Point Multiplication Algorithm

Taking the calculation of voltage parameters as an example, it assumes voltage sampling, respectively, to be u1 and u2 corresponding to the sampling time n1 and n2, and in which, if the phase difference between sampling time n1 and n2 is π/2, ω is angular frequency, and T is the sine wave period, then Eq. (1) is satisfied.

$$\omega T(n_2 - n_1) = \pi/2 \tag{1}$$

From which, it can derive the RMS value U of voltage and initial phase $\alpha 1\nu$, shown as in Eqs. (2) and (3).

$$2U^2 = u_1^2 + u_2^2 \tag{2}$$

$$tg\alpha_{1v} = u_1/u_2 \tag{3}$$

That is to say that if two sine instantaneous values separated by π/2 are known, then it can calculate the RMS value and phase.

In power system, it is necessary to carry out distance protection, and therefore the impedance must be measured. If the current and voltage i1, u1, and $i2$, $u2$ at sampling time $n1$ and $n2$ can be measured simultaneously at the same time, it can find the current RMS value and the phase angle α11 at sampling time $n1$, shown as in Eqs. (4) and (5).

$$2I^2 = i_1^2 + i_2^2 \tag{4}$$

$$tg\alpha_{11} = i_1/i_2 \tag{5}$$

From which, it can calculate the complex impedance modulus z and modulus angle αz,shown as in Eqs. (6) and (7).

$$z = \sqrt{u_1^2 + u_2^2}/\sqrt{i_1^2 + i_2^2} \tag{6}$$

$$a_z = \alpha_{1v} - \alpha_{11} = tg^{-1}(u_1/u_2) - tg^{-1}(i_1/i_2) \tag{7}$$

The algorithm is based on sine wave calculation, and the algorithm itself has no error. The algorithm adopts two sampling values separated by π/2, the length of the data window is only 1/4 cycle of power frequency, and the time delay is 5 ms. In fact, the algorithm has nothing to do with the sampling frequency, but it must be matched with the digital filter. Because of the power grid signal cannot be pure sine wave, so the sampling frequency is generally determined by the selected filter. The algorithm has more calculation of multiplication and division, so the calculation workload is rather large. It is worth to point out that the length of the data window can be arbitrarily valued, two sampling points are not necessarily separated by π/2, and only the calculation is slightly more complex.

2.2 Recursive Fast Fourier Algorithm

The algorithm is as an auxiliary algorithm of differential full wave filtering Fourier algorithm, the computation workload is relatively small. Recursive fast Fourier algorithm has more application in the liquid crystal display real-time calculation, because it can be measured by the order of data. After obtaining the new sample data, it can adopt the recursive algorithm to correct the original valuation, and its valuation correction and data sampling is carried out simultaneously [8].

The discrete Fourier transform is defined as Eq. (8), in which, $x(n)$ ($n = 0, 1, \ldots, N-1$) is the discrete time signal for the corresponding sampling.

$$X(k) = \frac{1}{N}\sum_{n=0}^{N-1} x(n)e^{-j(2\pi/N)kn} \tag{8}$$

In Eq. (8), $k = 0, 1, \ldots, N-1$. Based on Eq. (8), the fundamental component of data $x(n)$ obtained from the sampling is defined as Eq. (9).

$$\begin{aligned} X(1) &= \frac{1}{N}\sum_{n=0}^{N-1} x(n) \times W_N^n \\ &= \frac{1}{N}\left[x(0) \times W_N^0 + x(1) \times W_N^1 + \cdots + x(N-1) \times W_N^{N-1}\right] \end{aligned} \tag{9}$$

In Eq. (9), $W_N = e^{-j(2\pi/N)}$.

In accordance with the same method, it moves a data after the sampling point, and by means of the transformation definition Eqs. (8) and (10) can be got.

$$\begin{aligned} X'(1) &= \frac{1}{N}\sum_{n=0}^{N-1} x(n) \times W_N^n \\ &= \frac{1}{N}\left[x(1) \times W_N^0 + x(2) \times W_N^1 + \cdots + x(N) \times W_N^{N-1}\right] \end{aligned} \tag{10}$$

Equation (10) is the Fourier transform of a sampling point $x(n)$ after shifting a sampling point, and compared Eq. (9) with Eq. (10), Eq. (11) can be obtained.

$$X'(1) = [X(1) - x(0)] \times W_N^{-1} + x(N) \times W_N^{N-1} \tag{11}$$

From Eq. (11), it can be seen that it only needs the computation of a complex number, a real number addition, and two times of multiplication, hence the computation of the recursive fast Fourier algorithm is significantly reduced.

3 Hardware Platform Design

Taking a certain 110 kV microcomputer line protection system as an example, the designed hardware platform of embedded electrical parameters monitoring system is shown as in Fig. 1.

3.1 Main Module of Protection Monitor

The working process of the microcomputer protection device is mainly completed by the main module, and the function structure of the main module is shown in Fig. 2. After through the conversion of the low-voltage signal to send the main module, the MCF5282 microprocessor runs and makes the signal sampling, and completes the software function of prior arrangement of all kinds of numerical calculation, analysis, and processing. If the state of the object to be protected is abnormal (such as any fault), the microprocessor MCF5282 can send out the tripping action signal of the drive circuit breaker by the switch output circuit of the microprocessor so as to protect the system. At the same time, it makes protection action information to send directly to the host computer and management templates, and makes the record, saves the data, and alarms for operators by data communication mode. Because the embedded platform is universal, although the protection of the transformer is not the same in power systems (such as transformers, motors,

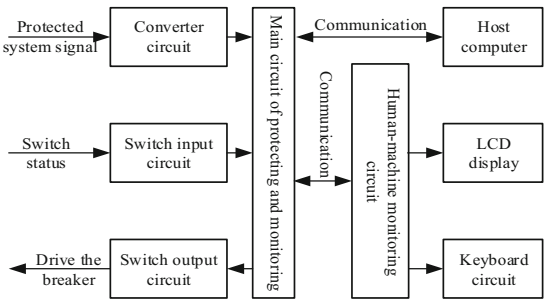

Fig. 1 Hardware platform structure of monitoring system

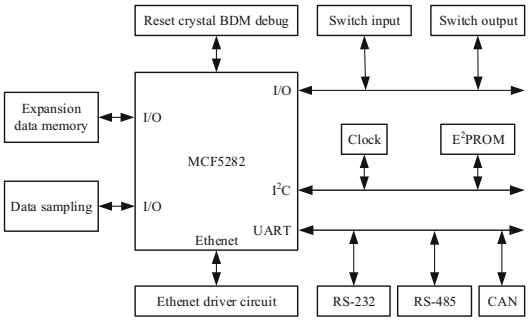

Fig. 2 Structure of main module

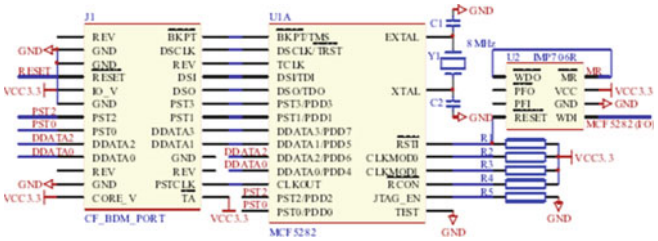

Fig. 3 MCF5282 single-mode circuit diagram

or other control equipment), as long as the corresponding functional software can be changed, then it can complete the protection function.

The main module of the MCF5282 is a 32-bit RISC microprocessor, as shown in Fig. 3. In order to reduce the peripheral devices of MCF5282 and improve the reliability of the main template, the operation of single chip mode is adopted, and it uses I/O port or functional port to exchange with external information.

3.2 Analog Input Circuit

The voltage and current converter of the unit input module is used for converting the relevant signal into a low-voltage signal which is sampled by A/D of the MCF5282 microprocessor, and the forming circuit of voltage square wave is used to detect the voltage frequency, frequency difference, and phase difference. In order to get a better signal, the AC and DC components of the analog input channel are, respectively, configured by the RC and RLC passive filter circuit.

3.3 Switch Input and Output Circuit

The switching signal input and output signal are designed on the main template. Among them, the switch input via the optical isolation chip TLP521 sends to I/O

port of MCF5282. Through the driver, the signal output by the MCF5282 microprocessor controls the relay action in the output template.

3.4 Man–Machine Interface Module

The module directly deals with the human–computer interaction, and the interface circuit is composed of data communications, keyboard, LCD, USB print interface, and other parts. In view of the fact that the performance requirements are high, the single chip adopts the LPC2294 of ARM7 kernel. LCP2294 is a 16/32-bit ARM7TDMI-S microcontroller, and its unique acceleration structure and the 128-bit width of the storage interface can be run at the maximum clock rate of 32-bit code. If it strictly controls the size of the code, using the 16-bit thumb mode, it would reduce the size of the code more than 30 % in the case of very small performance loss.

4 Software System Design

4.1 Software Main Frame

Figure 4 shows the main frame of the software system, and the task is that if the relevant conditions are satisfied, then it calls the corresponding subfunction module to execute the functional module task that meets the relevant conditions of [9, 10]. Its working process is simply described as follows. First, the microprocessor MCF5282 makes the setting up of itself environment and working conditions, such as the I/O port, "watchdog" and peripheral initialization. Second, it makes the judgment for the sampling interrupt time, if the sampling interrupt time is reached, then it conducts the analog sampling, and otherwise it conducts the hardware self-test judgment. After completing the analog sampling, the system reads out the tuning parameters from the EEPROM, and calculates the electrical parameters. According to the calculation results, it can judge whether the fault occurs, and if a fault occurs, then it issues a warning or enters a fault processor. It can be seen that in the main program loop, only when the function module meets the preset condition, the main program executes the function module, and otherwise the main program is forced to transfer into the next function module. In fact, not all operations must be performed every time. From the above it can find that in the program, the reading of each electrical parameter A/D sampling result and data exchange communication are completed through the corresponding interrupt program.

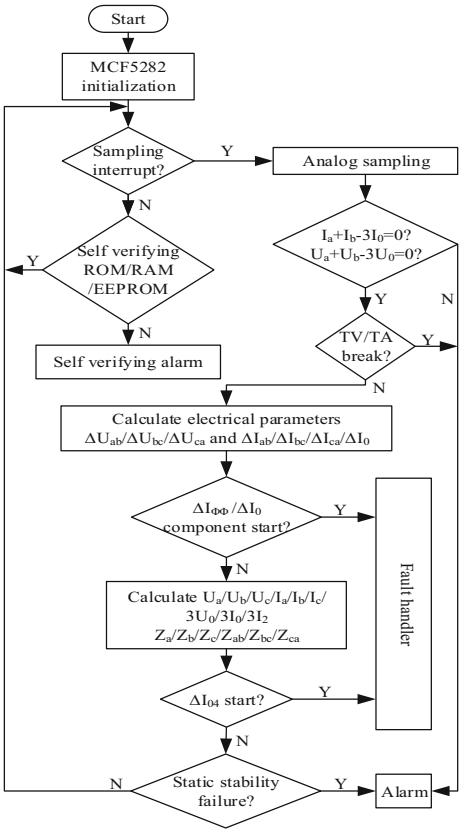

Fig. 4 Main frame of software

4.2 Design A/D Interrupt Program

Figure 5 is the interrupt processing flowchart of various electrical parameters of the A/D conversion. Taking a substation as an example, there is a total of 24 channels including 8 DC channels and 16 AC channels. After the conversion is completed to be generated interrupt, the AC channel A/D conversion is started by the timer cycle. The counter pointl is used to store the sampling number of measured parameters for a complete cycle of 24 points. When a complete cycle sampling is completed, the sign of adflag is 2, its pointl count is 24, and it shows that the main program can call its measurement parameters of the calculation subroutine. From Fig. 5, it can be seen that when adflag is only 1 the new A/D sample value can be saved, and when the measurement parameters are calculated the new A/D sampling values cannot covered that it is using to calculate the conversion results. After calculating the measured parameters of a cycle, the main program will automatically set the adflag to be 1. It shows that the measurement parameter calculation of a cycle has been completed, and the counter pointl is cleared so as to store the A/D conversion results of the next cycle. The time to execute the interrupt program is as short as

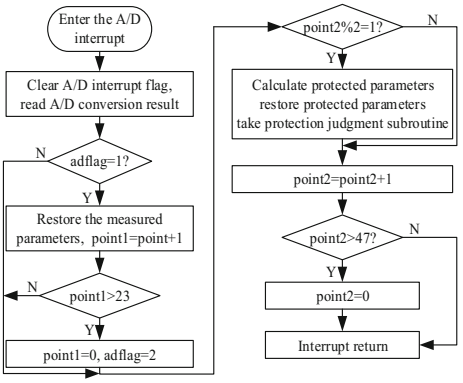

Fig. 5 Interrupt processing flow

possible, and it facilitates CPU to have more time to deal with other tasks. For this purpose, point2 is used for storing sampling number of statistical parameters in the program design. When it is odd number of sampling, it calls the protection subroutine to calculate and save the protection parameters. When it is an even number of sampling, it does not make any measurement data processing, and after through a period of idling, the counter point2 automatically resets.

4.3 Design of Man–Machine Interface Programming

The above has been mentioned, and the man–machine interface module function, (such as print processing, keyboard processing, LCD display, etc.) is mainly completed by the ARM7 kernel LPC2294. Here, it is worth noting that the mutual data communication is completed with the help of executing the interrupt, and the human–machine interface program is shown as in Fig. 6.

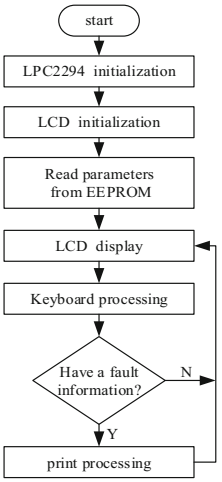

Fig. 6 Programming of man–machine interface

5 Conclusions

Electrical parameter measurement is the precondition to judge whether the power system is safe and stable, and now the parameter measurement is developing toward to integrated automation, networking, and intelligent development. Above taking a 110 kV microcomputer line protection system as an example, explored the electrical characteristic parameter algorithm of power system based on embedded platform, designed the embedded system hardware platform and software main frame, and gave the relevant program block flow. The experiments online with the scheduling center host computer show that the designed protection measurement system can be used to modify the electrical parameters of power system, correctly controls the switching operation of the system, and the operation speed is fast, the error is not greater than 0.1 %. When the sampling points are selected as 24 points in a cycle, the fast response time protection is in 1.67 ms, and it can fast isolate the fault equipment so as to protect the electric power system from being damaged.

References

1. Kemi Q, Changqing L (2005) Synthetic performance comparison of algorithm for microprocessor-based protections [J]. Electr Power Autom Equip 25(5):43-45
2. Zhou J (2006) Design on novel microcomputer protection system based on embedded system [D]. Chongqing University, Chongqing
3. Xue Pan (2011) Transmission line parameter online calculating method research [D]. Chongqing University, Chongqing
4. Zhao D (2010) Research on transmission line power frequency parameters [D]. Southwest Jiaotong University, Chendu
5. Liu Y, Hui J, Yang H et al (2012) Research on the criterion of the existence of genuine power system interharmonics [J]. Proc CSEE 32(28):76–82
6. Yuan W, Wang B, Guo H et al (2015) Online parameters calculation sensitivity analysis of transmission lins based on synchronous measurements [J]. Shanxi Electr Power 43(4):36–39
7. Jinrui Tang (2014) Research on on-line inspection and accurate fault location methods for power lines [D]. Huazhong University of Science and Technology, Wuhan
8. Wang J, Yang M, Yanchao JI et al (2003) A recursive fast Fourier transform of single harmonic component [J]. RELAY 31(5):14–15
9. Xiao-ping CHEN (2006) The research and application of the supervising system of power quality based on embedded [D]. Hunan University, Changsha
10. Yan H (2007) Study of feed switch based on ARM embedded network control system [D]. Anhui University of Science and Technology. Huainan

Virtual Actuators for Attitude Control Based on Variable-Speed Control Moment Gyros

Kebei Zhang, Dayi Wang and Liang Tang

Abstract A steering law avoiding singularity by virtual actuators for variable-speed control moment gyros (VSCMGs) is proposed in this paper. Using virtual actuator to extend VSCMGs Jacobian matrix, this method can guarantee the pseudo-inverse solution of VSCMGs steering law always exists. At the same time, the null motion of VSCMGs is adopted to make sure that the VSCMGs gimbal angles always get away from the singularity and the VSCMGs rotor velocities tend towards to expect speed. The proposed steering law is demonstrated through numerical simulation for large angle attitude maneuver control.

Keywords Variable-speed control moment gyros · Virtual actuators · Steer law

1 Introduction

In the near future, the new generation spacecraft will require rapid attitude maneuver capability to accomplish various missions. Control moment gyros (CMGs) along with the reaction wheels (RWs) are regarded as an effective and perfect torque generator for attitude stability and attitude maneuver. The CMGs can generate relatively large control torque due to its large torque amplification capability. The reaction wheel can generate exactly torque for highly attitude stability. Adopting both the CMGs and RWs capability, the variable-speed control moment gyros (VSCMGs) are designed for generating large torque and exactly torque.

K. Zhang · D. Wang (✉) · L. Tang
Beijing Institute of Control Engineering, Beijing 100190, China
e-mail: dayiwang@163.com

D. Wang · L. Tang
Science and Technology on Space Intelligent Control Laboratory, Beijing 100190, China

Y. Jia et al. (eds.), *Proceedings of 2016 Chinese Intelligent Systems Conference*,
Lecture Notes in Electrical Engineering 404, DOI 10.1007/978-981-10-2338-5_14

However, one drawback of the VSCMGs is the steering law suffering from the singularity problem. Thus, a practical and reliable steering law for VSCMGs is needed for engineering in spacecraft attitude control.

Many literatures discuss the singularity avoidance steering law for VSCMGs. The Moore–Penrose pseudoinverse (MP) solution has been tried as an exact solution for VSCMGs steering law [1–6]. The null motion method of CMGs was used to avoidance the singularity. It has been believed that addition of null motions is beneficial to VSCMGs for avoiding hyperbolic singularity. The VSCMGs singularity is analyzed in [1, 2] and it turns out that the drawback of pseudoinverse steering law is that, it cannot pass though the elliptic singularity. Professor Frederick in [3] developed a hybrid steering law to avoid hyperbolic internal singularity and or elliptic singularities. Lee and Bang in [4] developed singularity avoidance optimal approach for VSCMGs. The steering law is based on a constrained optimization by minimizing a cost function which consists of a singularity index and a kinetic energy term. The steering law can overcome the wheel velocity saturation problem during the operation of VSCMGs clusters. Leeghim et al. [5, 6] designed new CMGs steering law in which one-step predicted singularity index was used to avoid singularity. The proposed predicted singularity approach ultimately leads to an optimized solution of gimbal rates with performance improvement to avoid singularity by robust gradient null vectors. The above predicted singularity index steering law was used in [7] to design VSCMGs one-step predicted singularity steering law. It turns out that the predicted steering law that used to avoidance singularity in VSCMGs is equivalent to a general solution including the null motion method. The proposed optimal steering law for VSCMGs can deal with the RWs wheel saturation during the operations of VSCMGs clusters as well as add null motion to avoid the singularity. Jay and Schaub [8] implements singularity avoidance null motion for VSCMG. The method is based on tracking the range of the transverse axes instead of calculating the rank of VSCMGs control projecting matrix. Virtual actuators technical are used in [9] to develop CMG singularity avoidance steering law. When CMGs is approximate to singularity, the singular vector is used to extend dimension of Jacobian matrix. The singular vector is perpendicular to the command torque. Thus, the extended dimension matrix is always full ranked and the MP inverse always exists. The singular direction avoidance (SDA) is further examined and modified by Tao and Saburo in [10]. It confirms that the modified SDA steering has a clearer geometric meaning and shares a similar ability to escape singularity.

In this paper, we first introduce the focus of attention and study for VSCMGs steering law in Sect. 1. Second, the VSCMGs singularity is analyzed and the steering law based on virtual actuator is designed in Sect. 2. Simulation results are shown in Sect. 3 and conclusions are given in Sect. 4.

2 Steering Law for VSCMGs

2.1 VSCMGs Dynamics

The most used pyramid-type VSCMGs clusters are introduced and shown in Fig. 1. There are four VSCMGs in pyramid configuration. The total angular moment of pyramid configuration is closing to sphere so that the VSCMGs clusters can output 3-D torque. The total angular moment $\boldsymbol{H}$ and the output torque $\boldsymbol{T}_c$ of VSCMGs are given as

$$H = H(\boldsymbol{\delta}, \boldsymbol{\Omega}) = \sum_{i=1}^{4} h_{\text{cmgi}} + \sum_{i=1}^{4} h_{rwi} \tag{1}$$

$$\begin{cases} T_c = H = \frac{\partial H}{\partial \boldsymbol{\delta}} \boldsymbol{\delta} + \frac{\partial H}{\partial \boldsymbol{\Omega}} \boldsymbol{\Omega} = C(\boldsymbol{\delta})\boldsymbol{\delta} + D(\boldsymbol{\Omega})\boldsymbol{\Omega} \\ T_{c0} = C(\boldsymbol{\delta})\boldsymbol{\delta} \\ T_{c1} = D(\boldsymbol{\Omega})\boldsymbol{\Omega} \end{cases} \tag{2}$$

Here T_c is the command torque, T_{c0} is the torque generated by CMGs, T_{c1} is the torque generated by RWs. The variable $\boldsymbol{\delta} = [\delta_1 \quad \delta_2 \quad \delta_3 \quad \delta_4]^T$ is a 4-D gimbal angle column vector for CMGs and the variable $\boldsymbol{\delta} = [\delta_1 \quad \delta_2 \quad \delta_3 \quad \delta_4]^T$ is a 4-D gimbal angle column vector for CMGs. The matric C is the CMGs Jacobian matrix. The variable $\boldsymbol{\Omega} = [\Omega_1 \quad \Omega_2 \quad \Omega_3 \quad \Omega_4]^T$ is the RWs velocity column vector and the variable $\boldsymbol{\Omega} = [\Omega_1 \quad \Omega_2 \quad \Omega_3 \quad \Omega_4]^T$ is the RWs acceleration column vector. The matric $\boldsymbol{D}$ is the Jacobian matrix of RWs.

The most used MP pseudoinverse steering law can be illustrated as follows:

$$x_T = \begin{bmatrix} \boldsymbol{\delta} \\ \boldsymbol{\Omega} \end{bmatrix} = WQ^T \left(QWQ^T\right)^{-1} T_c \tag{3}$$

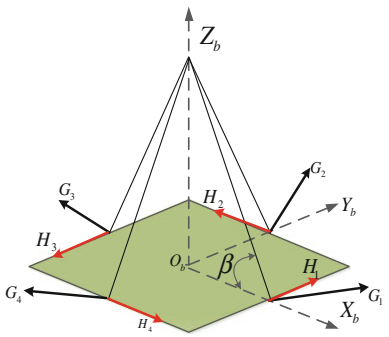

Fig. 1 Pyramid configuration

Here $Q = [C \quad D]$ and the weighted matrix $\boldsymbol{W}$ is designed as

$$W = \begin{bmatrix} I_{4\times4} & \mathbf{0}_{4\times4} \\ \mathbf{0}_{4\times4} & \omega_1 e^{-\omega_2 K} I_{4\times4} \end{bmatrix} \tag{4}$$

Here the variables ω_1, ω_2 are designed parameters. The parameter $K = \sigma_3/\sigma_1$ can be calculated by the minimum singular value σ_3 and maximum singular σ_1 of Jacobian matrix $\boldsymbol{C}$.

Based on the theory of SVD, the Jacobian matrix $\boldsymbol{C}$ can be decomposed into the production of three special matrices

$$C = U\Lambda V^T = \sum_{i=1}^{3} \sigma_i U_i V_i^T \tag{5}$$

Here $U = [U_1 \quad U_2 \quad U_3] \in R^{3\times3}$ and $V = [V_1 \quad V_2 \quad \cdots \quad V_n] \in R^{n\times n}$ are unitary matrices. The following equations are satisfied: $U^T U = V^T V = I_{3\times3}$. The matrix $I_{3\times3}$ represents the 3-D identify matrix. $\Lambda = [S \quad \mathbf{0}_{3\times1}]$, $S = \mathrm{diag}(\sigma_1 \quad \sigma_2 \quad \sigma_3)$ and $\sigma_1 > \sigma_2 > \sigma_3$ are singular value of Jacobian matrix $\boldsymbol{C}$.

2.2 Singularity Analysis and Steering Law

When the VSCMGs are closing to singular, the 3-D torque unit axis vectors ***x***-***y***-***z*** remains on the same plane. The rank of Jacobian matrix $\boldsymbol{C}$ is less than 3. The inverse of $\boldsymbol{Q}$ does not exist. VSCMGs cannot generate torque along the singular vector $\boldsymbol{C}_s$, which is perpendicular the torque axis plane. As illustrated in Fig. 2, the command torque cannot be generated by the VSCMGs when the torque unit axis vectors ***x***-***y***-***z*** remain on the same plane because none of the available torque vectors orthogonal to the ***x***-***y***-***z*** plane.

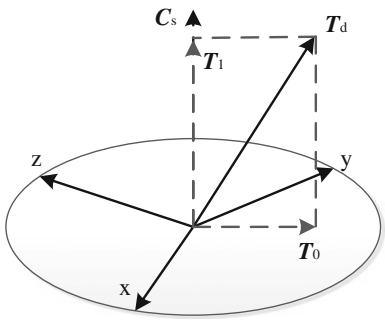

Fig. 2 Singular configuration and vector *C*s

It is assumed that there exists a virtual actuator which the unit torque axis vector is parallel to the singular vector $\boldsymbol{C}_s$. The singular vector can be defined as

$$c_s = x \times y \quad \text{or} \quad y \times z \tag{6}$$

Then, any 3-D command torques can be generated. The existence for Moore–Penrose pseudoinverse solution in Eq. 2 can be guaranteed. The new Jacobian matrix of CMGs is extended by the virtual actuator. The expanded matrix is then defined as

$$\boldsymbol{C} = [\, C \quad h_s c_s \,] \tag{7}$$

Here the h_s represents the magnitude of virtual actuator angular moment. The Jacobian matrix $\boldsymbol{Q}$ in Eq. 3 is consisted as $Q = [\, \boldsymbol{C} \quad D \,]$.

Then the command gimbal rate of extended CMGs is given by

$$\dot{\boldsymbol{\delta}} = [\, \boldsymbol{\delta} \quad \boldsymbol{\delta}_{c_s} \,]^T = \boldsymbol{C}^T \left(C \hat{C}^T \right)^{-1} \mathrm{T}_{c0} \tag{8}$$

Here $\boldsymbol{\delta}_{c_s}$ is the corresponding virtual gimbal rate. The existence of $\dot{\boldsymbol{\delta}}$ is guaranteed since the rank of $\boldsymbol{C}$ is always three. Then, the error torque generated by virtual actuator is given as

$$\Delta \mathrm{T}_{c0} = h_s c_s \boldsymbol{\delta}_{c_s} \tag{9}$$

The error torque generated by virtual actuator can be compensated by the RWs. The extra compensation torque generated by RWs can be calculated as

$$\Delta \mathrm{T}_{c0} = D(\boldsymbol{\Omega}) \Delta \boldsymbol{\Omega} \tag{10}$$

The RWs extra velocity is given as

$$\Delta \boldsymbol{\Omega} = D^T \left[D D^T \right]^{-1} h_s c_s \boldsymbol{\delta}_{c_s} \tag{11}$$

Then, the resolve for command torque in Eq. 3 is given as

$$x = \begin{bmatrix} \boldsymbol{\delta} \\ \boldsymbol{\Omega} + \Delta \boldsymbol{\Omega} \end{bmatrix} \tag{12}$$

2.3 Null Motion Steering Law

It is confirmed that null motion often does a favor for VSCMGs to escape the singularity. The local gradient null motion for VSCMGs, which is presented in [11, 12] is given by

$$x_N = \begin{bmatrix} \boldsymbol{\delta}_N \\ \boldsymbol{\Omega}_N \end{bmatrix} = \left[I_8 - WQ^T \left(QWQ^T \right)^{-1} Q \right] d \tag{13}$$

To effectively avoid VSCMGs singularity, the vector $\boldsymbol{d}$ should be selected appropriately. The method to select $\boldsymbol{d}$ is briefly explained as follows:

Let K in the Eq. 4 denote a measure of the singularity of the matrix $\boldsymbol{C}$ as a function of the gimbal angles. The null motion steering law and vector $\boldsymbol{d}$ in Eq. 13 should be selected to keep singular measurement K larger in order to avoid any singularity. The null motion steering law does not have any effect on the generated output torque. The vector $\boldsymbol{d}$ is selected as [11]

$$d = \alpha(1 - K) \begin{bmatrix} \left(\frac{\partial K}{\partial \boldsymbol{\delta}} \right) \\ \boldsymbol{\Omega}_f - \boldsymbol{\Omega} \end{bmatrix} \tag{14}$$

Here $\boldsymbol{\Omega}_f$ is the RWs balance velocity. The method to calculate the item $\frac{\partial K}{\partial \boldsymbol{\delta}}$ is illustrated in [13] and shown as follows:

$$\frac{\partial K}{\partial \boldsymbol{\delta}} = \frac{1}{\sigma_1} \frac{\partial \sigma_3}{\partial \boldsymbol{\delta}} - \frac{\sigma_3}{\sigma_1^2} \frac{\partial \sigma_1}{\partial \boldsymbol{\delta}} \tag{15}$$

$$\frac{\partial \sigma_i}{\partial \boldsymbol{\delta}} = - \begin{bmatrix} U(:,i)^T \bullet \boldsymbol{\Lambda}(:,1) \bullet V(1,i) \\ U(:,i)^T \bullet \boldsymbol{\Lambda}(:,2) \bullet V(2,i) \\ U(:,i)^T \bullet \boldsymbol{\Lambda}(:,3) \bullet V(3,i) \\ U(:,i)^T \bullet \boldsymbol{\Lambda}(:,4) \bullet V(4,i) \end{bmatrix} \quad i = 1, 3 \tag{16}$$

Here $U(:,i)$ is ith column of matrix $\boldsymbol{U}$. The $V(j,i)$ is the jth row and ith column of matrix $\boldsymbol{V}$.

3 VSCMGs Maneuver Simulation

To demonstrate the proposed steering laws, spacecraft three axis attitude maneuver simulation is conducted and VSCMGs ability to escape singularity is also examined in this section. The parameters used in simulation are illustrated in Table 1.

The time responses for spacecraft attitude, including Euler angle, angular velocity, gimbal angle, and so on are shown in Figs. 3 and 4. The spacecraft angular velocity is approximating to zeros after 40 s. Two cases are conducted in order to

Table 1 Simulation parameter

Item	Parameter
Spacecraft inertia	$\boldsymbol{I}$ = diag(560, 600, 600) (kgm/s^2)
Initial attitude	(roll, pitch, yaw) = [20, −30, 30] (°)
Desired attitude	(roll, pitch, yaw) = [0, 0, 0] (°)
Singular gimbal angle	$\boldsymbol{\delta}(0)$ = [85, 5, −95, −5] (°)
Initial gimbal rate	$\boldsymbol{\delta}'(0)$ = [0, 0, 0, 0] (°/s)
RWs rate	$\boldsymbol{\Omega}(0)$ = [3900, 3900, 3900, 3900] (r/min)
RWs moment	$\boldsymbol{H}(0)$ = [16.25, 16.25, 16.25, 16.25] (Nms)
PID controller	[K_p, K_i, K_d] = [616, 0.02, 693]
Maximum gimbal rate	δ′max = 57.3 (°/s)
Maximum RWs torque	Tmax = 0.06 (Nm)
ω_1	50
ω_2	0.1
α	0.2

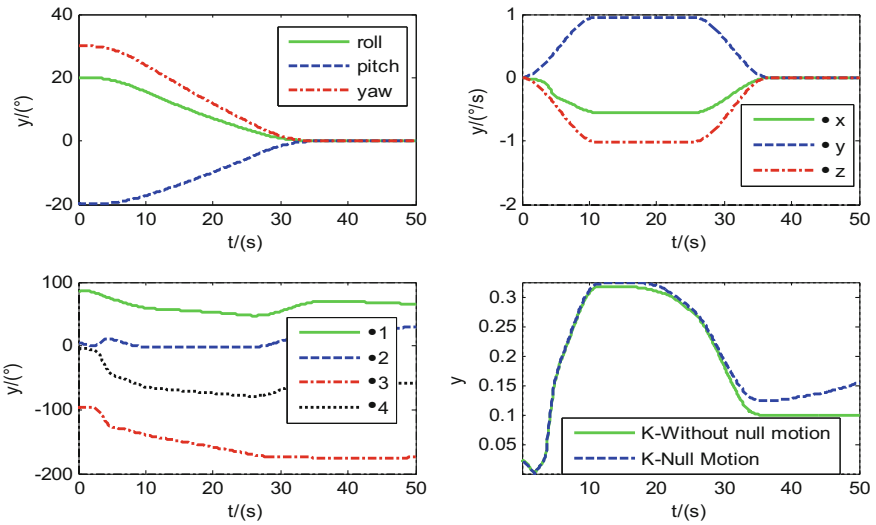

Fig. 3 Attitude simulation result with null motion steering law

compare the singular measurement K and the steer law ability to escape singularity. In the first case, the null motion steer law is not added to the command steer law and the second case the null motion steer law is used.

Two cases are conducted in attitude maneuver simulation. The first case is that only the command steering law in Eq. 3 is used. Both command steering law and null motion steering law are used in second case. As shown in Fig. 3, the attitude large angle maneuver is done when the initial VSCMGs gimbal angles are closing to singular. It confirms that the virtual actuator steer law can successfully steer the

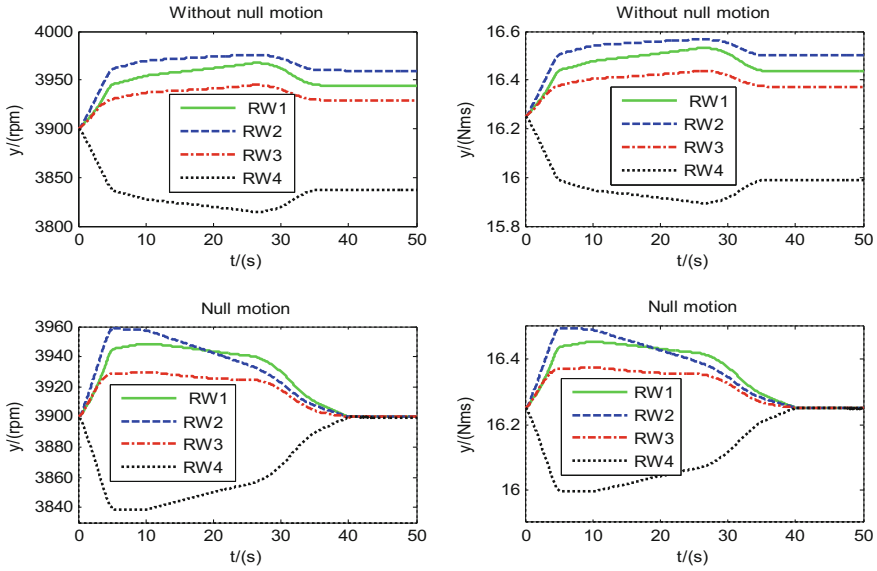

Fig. 4 Comparison results of RWs with/without null motion

gimbal to escape the singular while they meet requirement of the attitude maneuver command torque. The lower right in Fig. 3 shows that the singular measurement K is increasing when the null motion steering law is added. The upper two in Fig. 4 show that the RWs velocity and angle moment cannot keep to the expect speed. The lower two show that the RWs velocity and angle moment can keep to the balance value. It is also proved that the null motion steering law in Eq. 14 is working.

4 Conclusion

In this paper, the virtual actuators technique to solve the singularity problem of VSCMGs is studied and tested in attitude maneuver simulation. When the VSCMGs initial condition is closing to singularity, the virtual actuators can also generate the torque so that the large angle attitude maneuver can be realized. Two cases are conducted in attitude maneuver in order to show the detail of singular K. It confirms that null motion steer law is conducive to increase the K. The new approach presented in this paper can be explored towards escaping singular for VSCMGs.

References

1. Yoon H, Tsiotras P (2004) Singularity analysis of variable-speed control moment gyros [J]. J Guid Control Dyn 27(3):374–386
2. Leve F (2014) Evaluation of steering algorithm optimality for single-gimbal control moment gyroscopes [J]. IEEE Trans Control Syst Technol 22(3):1130–1134
3. Leve F, Fitz CN (2010) Hybrid steering logic for single-gimbal control moment gyroscopes [J]. J Guid Control Dyn 33(4):1202–1212
4. Lee H, Bang H (2007) Singularity avoidance of variable speed control moment gyros by optimization approach [J]. J Astronaut Sci 55(1):67–84
5. Leeghim H, Bang H, Park JO (2009) Singularity avoidance of control moment gyros by one-step ahead singularity index [J]. Acta Astronaut 64(9):935–945
6. Leeghim H, Lee IH, Lee DH (2009) Singularity avoidance of control moment gyros by predicted singularity robustness: ground experiment [J]. IEEE Trans Control Syst Technol 17 (4):884–891
7. Lee H, Lee IH (2005) Optimal steering laws for variable speed control moment gyros [C]. In: AIAA guidance, navigation, and control conference and exhibit vol 2005. pp 1–11
8. Jay M, Schaub H (2009) Simplified singularity avoidance using variable-speed control moment gyroscope null motion [J]. J Guidance Control Dyn 32(6):1938–1943
9. Park JO, Young ID (2010) Singularity avoidance of CMGs by virtual actuators [J]. Int J Control Autom Sys 8(4):891–895
10. Tao M, Saburo M (2011) Modified singular-direction avoidance steering for control moment gyros [J]. J Guid Control Dyn 34(6):1915–1919
11. Schaub H, Junkins JL (2000) Singularity avoidance using null motion for variable speed control moment gyros [J]. J Guid Control Dyn 23(1):11–16
12. Kasai S, Kojima H (2013) Gain-scheduled steering control law for variable speed control moment gyros [C]. In: AIAA guidance, navigation and control conference. Boston, USA, 19–23 Aug 2013
13. Junkin JL, Kim Y (1993) Introduction to dynamic and control of flexible structures [M]. AIAA, New York, pp 48–49

Modeling and Control of a Rail-Type Mobile Robotic Work Platform

Sheng Shi, Xiaobin Li and Haiyan Sun

Abstract The longitudinal displacement of a rail-type mobile robotic work platform based on semi-active suspension system is modeled, and the unknown disturbance noise in the model is separated. As for the control method, we use the state feedback control of linear quadratic regulator and add the filter of H∞ minimum error state estimation to filter the unknown process and measurement noise. Besides, the difference between Kalman filter and H∞ filter is analyzed based on the power spectral density. Eventually, the anti-interference performance of two filters is compared by means of simulation.

Keywords A rail-type mobile robot · Platform · Modeling and control

1 Introduction

As an indispensable part of intelligent manufacturing, the mobile operation of industrial robotic equipment is more and more widely used in practical field. Along with the improvement of production precision, in addition to improve the positioning and working accuracy of the industrial robot equipment itself, it is also need more precision and real-time positioning and control for the rail-type mobile platform which is rigidly connected with robot.

According to current research, due to the simple model and the control method, the positioning error of industrial rail-type mobile work platform is in the centimeter range. It is impossible for robot which only relies on the error compensation ability of itself to fully meet the higher precise requirement which is in the millimeter range.

S. Shi · X. Li (✉)
School of Electrical and Electronic Engineering, Shanghai Institute of Technology, Shanghai 201418, China
e-mail: lixiaobinauto@163.com

H. Sun
School of Ecological Technology and Engineering, Shanghai Institute of Technology, Shanghai 201418, China

Y. Jia et al. (eds.), *Proceedings of 2016 Chinese Intelligent Systems Conference*, Lecture Notes in Electrical Engineering 404, DOI 10.1007/978-981-10-2338-5_15

There are accuracy problems of work platform positioning in many yields, such as pushing coke lathe, coke-educing carrier, coke quenching car, coal conveyor using encoder to locate in the metallurgical industry, high-speed industrial production line and the industrial robot working on the rail-type mobile platform [1].

To solve the above problems, the industrial mobile platform should be effectively modeled and improved. After that, the advanced control method is utilized to restrain the random disturbance in the system so as to realize the high precision positioning of mobile platform.

As to the research of mobile platform modeling, Weia et al. [2] uses the acceleration sensor to model the error of rail vehicles in vertical direction. A comprehensive stress analysis of the train and a dynamic model of 31 degrees of freedom is established by Kim et al. [3]. In the study of control strategy, the fuzzy control strategy is adopted to analyze position compensation of the lateral, vertical, and angle error respectively [4]. Eski [5] researches a robust neural network control method to solve the disturbance problems. In the research of disturbance restrain, Zolotas uses the Kalman filter to eliminate the error caused by the random disturbance of the rail [6].

In this study, the rail-type mobile platform is modeled, the random disturbance of model is filtered and the error of longitudinal error is corrected through the H∞ filter and the linear quadratic optimal control. These studies indicate that mobile platform model based on improved mode can not only achieve efficient location tracking, but also obtain better robustness on filtering performance compared to the traditional Kalman filter.

2 Modeling

In the actual industrial robot operation and manufacturing field, a relatively simple mechanical structure is generally used as the track moving operation platform including roller, track, etc. The more advanced work platform is added as a passive way of suspension, shock absorber, and damper to the roller. This way, which can meet the general requirements of industrial production, have the advantage of low price and simple structure. But as to the industrial field of higher positioning accuracy requirements, such as welding robot, robotic ultraprecision machining, this structure cannot greatly eliminate the disturbance error of mobile operation platform.

This study intends to solve the coke oven cleanup problem of industrial robotic equipment. Through the analysis of the characteristics of industrial machine cleaning coke oven, referencing [4, 7, 8] and combining with the requirements of mobile industrial production based on robotic, a rail-type mobile robotic work platform is constructed as shown in Fig. 1.

This platform is designed to describe work condition of longitudinal direction based on the single-direction and main function of industrial robot. On the other hand, not only bogies, suspension and damper, which are indispensable in the passive suspension system, but also the semi-active control suspension structure, i.e.,

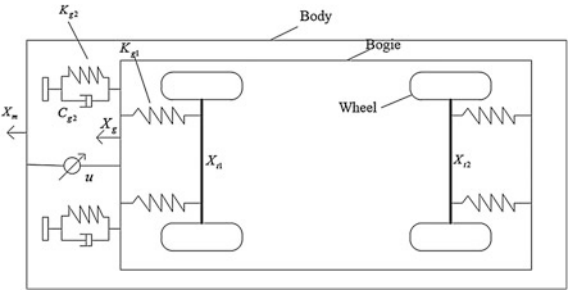

Fig. 1 The structure of model

Table 1 Parameters of model

Parameters	Definitions
K_{g1}	Primary suspension spring stiffness
C_{g2}	Secondary suspension damping coefficients
K_{g2}	Secondary suspension spring stiffness
m_c	Car body mass
m_g	Bogies mass
X_m	Longitudinal displacement of car body
X_g	Longitudinal displacement of bogies
X_{t1}	Longitudinal displacement of 1st wheel-set
X_{t2}	Longitudinal displacement of 2nd wheel-set
u	Control

adding semi-active suspension structure as controller, are adopted to reduce errors caused by external factors of rail, environment, and other uncertainties (Table 1).

Through the force analysis of platform body and the bogies, the dynamic equation was established as followed:

$$\begin{aligned} m_c\ddot{X}_m &= -2K_{g2}(X_m - X_g) - 2C_{g2}(\dot{X}_m - \dot{X}_g) + u \\ m_b\ddot{X}_g &= -2K_{g1}[2X_g - (X_{t1} + X_{t2})] - 2K_{g2}(X_g - X_m) - 2C_{g2}(\dot{X}_g - \dot{X}_m) - u \end{aligned} \tag{1}$$

let $x = \begin{bmatrix} X_m & \dot{X}_m & X_g & \dot{X}_g \end{bmatrix}^T$, then dynamic Eq. (1) can be transformed into state space expression

$$\dot{x} = Ax + B_1(X_{t1} + X_{t2}) + B_2u$$
$$y = H_1x + v$$
$$A = \begin{bmatrix} 0 & 1 & 0 & 0 \\ -\frac{2K_{g2}}{m_c} & -\frac{2C_{g2}}{m_c} & \frac{2K_{g2}}{m_c} & \frac{2C_{g2}}{m_c} \\ 0 & 0 & 0 & 1 \\ \frac{2K_{g2}}{m_b} & \frac{2C_{g2}}{m_b} & -\frac{4K_{g1}+2K_{g2}}{m_b} & -\frac{2C_{g2}}{m_b} \end{bmatrix} \quad B_1 = \begin{bmatrix} 0 \\ 0 \\ 0 \\ \frac{2K_{g1}}{m_b} \end{bmatrix} \quad B_2 = \begin{bmatrix} 0 \\ \frac{1}{m_c} \\ 0 \\ -\frac{1}{m_b} \end{bmatrix}$$
$$H_1 = \begin{bmatrix} 1 & 0 & 0 & 0 \end{bmatrix}$$

where u denotes control input, y denotes the measurement output, v denotes the measurement noise.

In addition, $(x_{t1}+x_{t2})$ denotes the sum of longitudinal displacement of two wheelsets, and because of its formation is related to the rail itself and various environmental factors, with unpredictable randomness, it can be considered as unknown process noise ω.

3 Control Strategy

3.1 Linear Quadratic Optimal Control

It may exist as linear optimal control method if the system is linear and controllable. Assuming this control strategy satisfies the quadratic performance index, it can realize the optimal tracking and regulation [9].

If we ignore the noise temporarily and just consider tracking problems of systems. Equation (2) can be transformed into a standard linear quadratic state equation

$$\begin{aligned} \dot{x}_s &= Ax_s + B_2 u \\ y_s &= H_1 x_s \end{aligned} \tag{3}$$

If the system is linear and controllable, there is a state feedback control strategy $u = -K_l x$

If the value of K_l can minimize the quadratic performance index [6]

$$J = \lim_{t \to \infty} E\{\int_0^t [x^T M_l x + u^T N_l u] d\tau\} \tag{4}$$

and K_l satisfies the following Riccati equation:

$$A^T P - P B_2 N_l^{-1} B_2^T P + M_l + \dot{P} + PA = 0 \tag{5}$$

then the linear quadratic optimal control is

$$u = -N_l^{-1} B_2 P x \tag{6}$$

where M_l denotes state weighting matrix and N_l is control weighted matrix, as well as symmetric matrix of positive definite, P is time-variable matrix and the boundary conditions are satisfied, then $\dot{P} = 0$ and there exists P which lets $K_l = N_l^{-1} B_2 P$.

3.2 H∞ Filter [10–13]

According to Eq. (2), the system state equation driven by noise is given as followed:

$$\begin{aligned} \dot{x} &= Ax + B_1\omega \\ y &= H_1x + v \\ z &= H_2x \end{aligned} \tag{7}$$

where $H_2 = [1 \quad 0 \quad 0 \quad 0]$, $\|\omega\|^2 < \infty$, $\|v\|^2 < \infty$, which means these two noises have finite energy, and z is estimated output, then the observer

$$\begin{aligned} \dot{x}_o &= K_i(y - y_o) + Ax_o \\ y_o &= H_1x_o \\ z_o &= H_2x_o \end{aligned} \tag{8}$$

where $\hat{x}, \hat{y}, \hat{z}$ are estimated value of x, y, z respectively, K_i is gain value of filter.

Equation (7) subtracts Eq. (8), the state equation of estimated error is

$$\begin{aligned} \dot{x}_r &= B_1\omega - K_iv + (A - K_iH_1)x_r \\ e &= z - z_o = H_2x_r \end{aligned} \tag{9}$$

where $x_r = x - x_o, \breve{\omega} = [\omega \quad v]^T$

The performance index of H∞ is

$$I = \sup_{0 \neq \breve{\omega} \in L_2} \frac{\|e\|_2^2}{\|\breve{\omega}\|_2^2} \leq \gamma^2 \tag{10}$$

where γ is positive constant.

Then the main problem can be considered as guaranteeing stability of the system and finding out the K_i which can minimize γ.

According to the above conditions and zero initial condition, there exists $X \geq 0$, which satisfies the equation

$$B_1B_1^T + XA^T - X(H_1^TH_1 - \gamma^{-2}H_2^TH_2)X + AX = 0 \tag{11}$$

where $X(\gamma^{-2}H_2^TH_2 - H_1^TH_1) + A$ is stable matrix.

$$K_i = XH_1^T$$

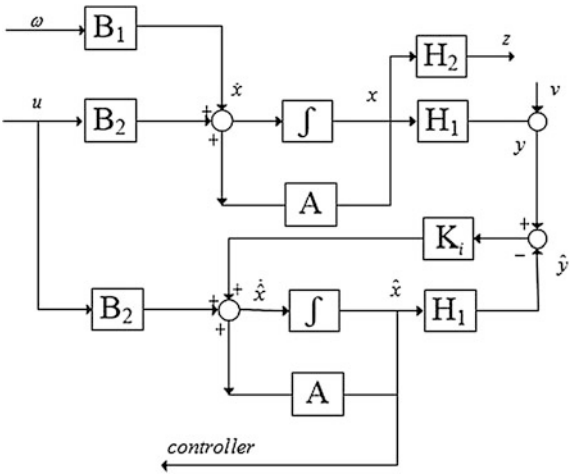

Fig. 2 The structure of system

3.3 Structure of System

In the light of above tracking and filtering strategies, Fig. 2 indicates the system block diagram.

In Fig. 2, the structure is similar to linear quadratic Gauss control (LQG). The difference is that the value of K_i is obtained by algorithm of H∞ filter and it will be analyzed through the power spectral density in the next section.

3.4 Comparison of the Two Filters

(1) From the conditions of filtering, Kalman filter is based on the minimum estimation of variance and it should be built on the basis of the known mathematical model. H∞ filter can be obtained better result by unknown power spectral density or statistic characteristics of noise, which the parameters of filter can be adjusted just through Riccati equations.

(2) The structure of filter is shown in Fig. 3.
The Eq. (11) is simplified as follows:

$$XH_2^T\gamma^{-2}H_2X = -AX - XA^T + XsE - B_1B_1^T + XH_1^TH_1X + sEX \tag{12}$$

If $K_i = XC_1^T$, The Eq. (12) can be transformed into Eq. (13).

$$XH_2^T\gamma^{-2}H_2X = K_iK_i^T + (sE - A)X + X(sE - A^T) - B_1B_1^T \tag{13}$$

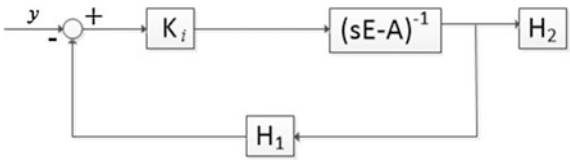

Fig. 3 The structure of filter

Equation (13) is left multiplied by $H_1(sE-A)^{-1}$ and right multiplied by $(-sE-A^T)^{-1}H_1^T$,

$$H_1(sE-A)^{-1}XH_2^T\gamma^{-2}H_2X(-sE-A^T)^{-1}H_1^T = D(s)\tilde{D}(s) - G_y \tag{14}$$

where E is identity matrix of 4×4,

$$D(s) = H_1(sE-A)^{-1}K_i + E, \tilde{D}(s) = D^T(-s)$$
$$G_y = H_1(sE-A)^{-1}B_1B_1^T(-sI-A^T)^{-1}H_1^T + \mathrm{E}$$

According to conclusions of the least mean square deviation in [14], $D(s)$ is return difference ratio matrix, G_y is power spectral density. If $D(s)\tilde{D}(s) = G_y$, the filter can obtain the minimum estimation of variance which is the basis of the Kalman filter. If and only if $\gamma \to \infty$, H∞ is regarded as Kalman filter, i.e., Kalman filter is a special form of H∞.

Above all, theoretically, because the value of γ is related to the robust performance and the filter performance, when the filter is the minimum estimation of variance, the robustness is poor and when the value of γ is minimum, the result is the opposite. Therefore, the appropriate choice of filter can make the filter possess a smaller estimation of variance and strong robustness, so as to meet the requirements of the rail-type mobile robotic platform.

4 Experiment and Result

If the value of parameter is shown as followed:

$$K_{g1} = 100000\ N/m,\ K_{g2} = 10100000\ N/m,\ C_{g2} = 25000\ Ns/m,$$
$$m_c = 67000\ \mathrm{kg},\ m_b = 10000\ \mathrm{kg}$$

and in the Eq. (4), the value is $Q = diag([2\times 10^8, 10^8, 10^3, 10])$, $R = 10^{-11}$

Then $K_l = 10^9[4.45203.1677 - 0.00270.0009]$

(1) The measurement noise and process noise are all set to be Gaussian distributed noise of zero means and covariance that is equal to 1. If $\gamma = 10$ which is chosen based on the stability and the structure of Fig. 4, we can obtain the following simulation,

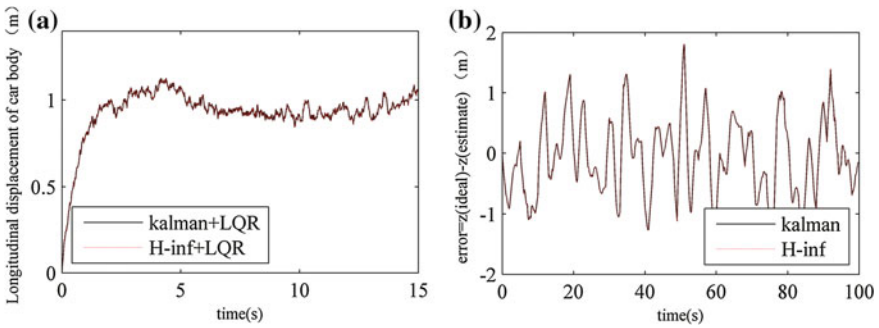

Fig. 4 Comparison on two filters processing with white noise. **a** Tracking comparison, **b** the difference between ideal output and estimated output

Figure 4 indicates that when the means and covariance of noise is respectively 0 and 1, the tracking and filtering effect of combining Kalman filter with linear quadratic optimal control is very similar to the one of combining H∞ filter with linear quadratic optimal control. Even during period of middle, performance of Kalman filter is better.

(2) The measurement noise and process noise are all set to be Gaussian distributed noise. The means of process and measurement noise are all zero and covariance are respectively, 0.5 and 0.2^2. If $\gamma = 5$ which is chosen based on the stability and Fig. 5, we can obtain the following simulation:
Experimental results of Fig. 5 shows that when the noise covariance is smaller, the robustness of the Kalman filter and the filter performance is significantly worse than that of the H∞ filter.

(3) If the measurement noise and process noise are limited energy instead of Gaussian noise, which the noise function is $\omega = 0.707\ \sin(t)e^{-10t}$; $v = 0.2\ \sin(t)e^{-5t}$, the simulation is shown as followed, Fig. 6.

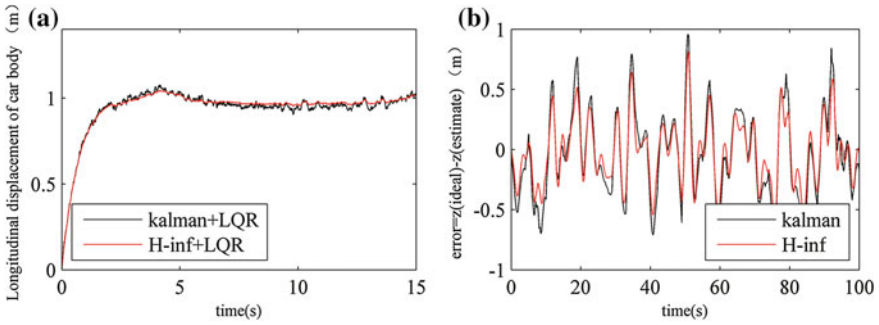

Fig. 5 Comparison on two filters processing with white noise. **a** Tracking comparison, **b** the difference between ideal output and estimated output

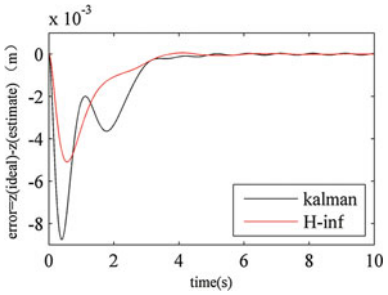

Fig. 6 Comparison of error on two filters with finite energy

The comparison of these two filters indicates that when the noise is the finite energy signal, H∞ filter has a more distinguished effect of decrease error between the estimated value and the ideal value.

5 Conclusion

The precision of the mobile platform plays an important role on the operation of the mobile robot. In this study, robotic platform of single-direction mobile is modeled by using characteristics of the semi-active suspension system. Besides, the H∞ filter and the linear quadratic optimal control method is designed for tracking simulation and anti-interference simulation. Eventually, the comparison of these two filters reflect the fact that H∞ filter has a more distinguished effect of decrease error between the estimated value and the ideal value if the covariance of white noise is smaller or the noise possesses uncertain limited energy. The result of experiment has a high value for applications on coke oven cleaning robot using rail-type mobile platform.

References

1. Wei Tian, Dongqi Mei, Pengcheng Li, Yuanfan Zeng, Peng Hong, Wei Zhou (2015) Determination of optimal samples for robot calibration based on error similarity[J]. Chin J Aeronaut 28(3):946–953
2. Weia Xiukun, Liub Feng, Jiaa Limin (2016) Urban rail Track condition monitoring based on in-service vehicle acceleration measurements[J]. Measurement 80:217–228
3. Kim Pilkee, Jung Jeehyun, Seok Jongwon (2011) A parametric dynamic study on hunting stability of full dual-bogie railway vehicle[J]. Int J Precis Eng Manuf 12(3):505–519
4. Sezer S, Atalay AE (2011) Dynamic modeling and fuzzy logic control of vibrations of a railway vehicle for different track irregularities[J]. Simul Mod Pract Theory 19:1873–1894
5. Eski I (2009) Vibration control of vehicle active suspension system using a new robust neural network control system[J]. Simul Mod Pract Theory 17:778–793

6. Zolotas AC (2002) Advanced control strategies for tilting trains[D]. Loughborough University, pp 1–2 44
7. Yang M (2002) Investigation of semi-active suspension for locomotive lateral dynamic performance[D]. South Jiaotong University, pp 1–94
8. Zhang B, Zhang J, Wang C (2011) Notice of retraction research on semi-active control of high speed railway vehicle based on neural network-PID control[J]. In: IEEE 2011 Seventh International Conferenc on Natural Computation, pp 673–676
9. Anderson BDO, Moore JB (1990) Optimal control: linear quadratic methods[J]. Prentice-Hall Inc., pp 35–67
10. NagPal KM, Khargonekar PP (1991) Filtering and smoothing in An H∞setting. IEEE Trans Autom Control[J] 36(2):152–166
11. U.SHAKED. H∞-Minimum Error State Estimation of Linear Stationary Processes[J]. Transactions on Automatic Control, 1990, 35(5):554– 558
12. Bernstein DS, Haddad W (1989) Steady state kalman filtering with an H∞error bound[J]. Syst Control Lert 12(1):9–16
13. Shaked U (1976) A transfer function solution of the L.Q.G. control problem[J]. In: IEEE Conference on Decision & Control Including Symposiumon Adaptive Processes. pp 354–360
14. Shaked U (1976) A general transfer function approach to Linear stationary filtering and steady-state optimal control problems[J]. IEEE Int J Control 24(6):741–770

Modeling and Control of Rail Type Suspended Conveyor for Electrolytic Aluminum Anode Casting

Sheng Shi, Xiaobin Li and Haiyan Sun

Abstract The dynamic equation of rail type suspended conveyor for electrolytic aluminum anode casting is established as controlled plant. Besides, hierarchical sliding mode control (HSMC) is utilized to track the displacement of conveyor driving unit for anode casting and, meanwhile, realize the smooth control for swing angle of loading hook and ferrophosphorus ladle container without extra force on them. Simulation studies the control of conveyor for electrolytic aluminum anode casting in various conditions and cycle operation test of factory production process, indicating that the anode casting process of conveying can be stably, effectively, and smoothly controlled and has good robustness.

Keywords Electrolytic aluminum anode casting · Rail type suspended conveyor · Cycle operation test · Modeling and control

1 Introduction

In the process of electrolytic aluminum anode assembly, the anode casting is a crucial link, which it will incredibly difficult for rail type suspended conveyor to positioning precisely causing the instability of conveyor and inaccuracy of reaching the location of the work area because of the high temperature and conveying of reciprocating motion within the process of electrolytic aluminum anode casting.

Now the rail type suspended conveyor for anode casting is mainly composed of a driving device, tensioning device, traction chain (driving chain), traction and bearing track, pusher, lifting, rotating mechanism and loading car. The conveying system is

S. Shi · X. Li (✉)
School of Electrical and Electronic Engineering, Shanghai Institute of Technology, Shanghai 201418, China
e-mail: lixiaobinauto@163.com

H. Sun
School of Ecological Technology and Engineering, Shanghai Institute of Technology, Shanghai 201418, China

Y. Jia et al. (eds.), *Proceedings of 2016 Chinese Intelligent Systems Conference*, Lecture Notes in Electrical Engineering 404, DOI 10.1007/978-981-10-2338-5_16

mainly controlled by force limiter, car retarder, limit switch, proximity switch, encoding card, address reader and Programmable Logic Controller (PLC). In the practical production, in light of inertia and nonlinear characteristics of force limiter, car retarder, strength of chain, accurate positioning of rail type suspended conveyor for anode casting is exceedingly difficult to be realized in the case of hanging ferrophosphorus ladle container of 1.2 t and moving at the speed of 35 mm/s. This study intends to improve the existing control system of rail type suspended conveyor and now it has realized the accurate positioning during conveying process. Besides, the system can cooperate with the industrial robot placed on the ground to charge and cast material precisely and safely. This kind of automatic production structure will highly avoid the waste of the working area, and ensure the safety of the staff.

To solve the above problems, rail type suspended conveyor should be effectively modeled and controlled by advanced method so as to reach each work station precisely and stably and overcome perturbation of parameters in the controlled model which is imposed by instability of ferrophosphorus mass or other irresistible environmental factors. These abilities can bring the system strong robustness, accuracy, and anti-swing ability.

Currently there is little research on rail type suspended conveyor for electrolytic aluminum anode. Just the similar model, suspended crane, can be searched. As to the modeling of suspended conveyor, Sawodny and Briechle [1] studies overhead crane model based on two-dimensional pendulum angle model. The nonlinear model of two-dimensional angle is simplified to a linear model to facilitate controller design by Tanaka and Kouno [2]. Arena and Casalotti [3] builds a three-dimensional swing angle model of full-motion and the change of suspended line length is taken into account. In addition, in terms of control strategies, Zhang and Man [4] establishes the adaptive tracking strategy based on Lyapunov equation and the relatively complete uncertainty variables are considered. A passive control method for double pendulum model is built through Lyapunov equation based on the conservation of energy [5]. Blajer and Kolodziejczyk [6] introduces the intelligent obstacle avoidance strategy into three-dimensional crane in order to realize the path planning of crane.

This study references the specific structure of suspended conveyor and establishes the dynamic model based on the Lagrange equation. Meanwhile, the swing angle of loading hook and ferrophosphorus ladle container are taken into account. Multilayer sliding mode control is used to make the rail type suspended conveyor smoothly track the path, and then the simulation of the general cycle of electrolytic aluminum anode casting is done. Through the above work, the effectiveness and robustness of the controller for type suspended conveyor have been demonstrated.

2 Dynamics Modeling

In the factory of electrolysis aluminum assemble, the driving unit of suspended conveyor is composed of motor, reducer and some transmission devices. Tension control just depends on the force limiter, i.e., when the force output is too large, the

power supply will be cut off to ensure the safety of the operation of the system. While the ferrophosphorus ladle container and loading hook, without any force control, is driven by the driving device carrying the hanging chain. The moving stability of container and hook should be considered since the container is loaded with high-temperature workpiece, ferrophosphorus, or other dangerous items. Based on the above points, and combined with the structure of rail type suspended conveyor, the dynamic model is shown in Fig. 1 (Table 1).

The $x-y$ coordinate system is built based on the overhead rail in Fig. 1. Positive direction of Y axis is above the overhead rail and the right side of midpoint of rail is positive direction of X axis. The kinetic energy of system is

$$E = 0.5m_0\dot{x}^2 + 0.5m_1(\dot{x}_1^2 + \dot{y}_1^2) + 0.5m_1(\dot{x}_2^2 + \dot{y}_2^2) + 0.5J_1\dot{\varphi}_1 + 0.5J_1\dot{\varphi}_1 \tag{1}$$

where (x_1, y_1) and (x_2, y_2) respectively denote the coordinate values of the center of gravity of loading hook and ferrophosphorus ladle container.

$$\begin{aligned} &x_1 = \lambda_1 \sin\varphi_1 + x, y_1 = -\lambda_1 \cos\varphi_1 \\ &x_2 = (\lambda_1 + \lambda_1^{'})\sin\varphi_1 + \lambda_2 \sin\varphi_2 + x, y_2 = -\lambda_2 \cos\varphi_2 - (\lambda_1 + \lambda_1^{'}) \cos\varphi_1 \end{aligned} \tag{2}$$

The potential energy of system is

$$H = (m_2 g(\lambda_1 + \lambda_1^{'}) + m_1\lambda_1 g)(1 - \cos\varphi_1) + m_2 g(\lambda_1 + \lambda_1^{'})(1 - \cos\varphi_2) \tag{3}$$

According to the Lagrange equation

Table 1 Parameters of model

Parameters	Definitions
φ_1	The angle between the hanging rope and the y axis
φ_2	The angle between the y axis and the line connecting container gravity and loading hook
m_0	Driving unit mass
m_1	Loading hook mass
m_2	Container mass
λ_1	Distance between the center of gravity of loading hook and driving unit
$\lambda_1^{'}$	Distance between the center of gravity of loading hook and the connection of loading hook and container
λ_2	Distance between the center of gravity of container and the connection of loading hook and container
J_1	Load hook moment of inertia
J_2	Container moment of inertia
f	Friction of rail
F	Driving force of driving unit
x	Longitudinal displacement of driving unit

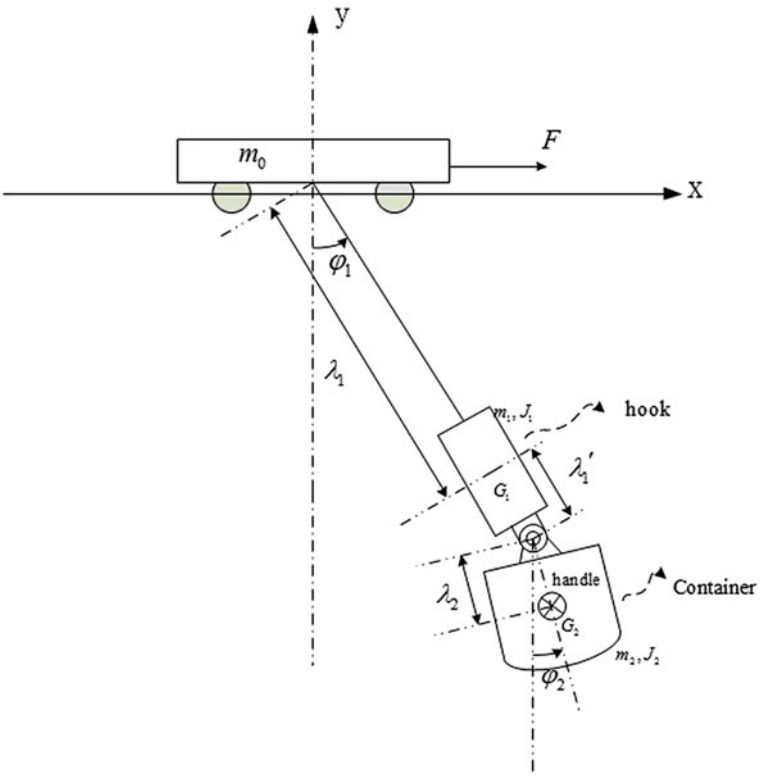

Fig. 1 Model of conveyor

$$\frac{\mathrm{d}\frac{\delta E}{\delta \dot{a}}}{\mathrm{d}t} - \frac{\delta E}{\delta a} + \frac{\delta H}{\delta a} = u \quad (\text{where } a = [x, \varphi_1, \varphi_2]^T, u = [F - f, 0, 0]^T) \tag{4}$$

By substituting Eq. (1) and (3) into (4), the dynamic equation can be obtained

$$M(a)\ddot{a} + Q(a, \dot{a})\dot{a} + G(a) = u \tag{5}$$

where

$$M(a) = \begin{pmatrix} m_0 + m_1 + m_2 & (m_1\lambda_1 + m_2(\lambda_1 + \lambda_1^{'}))\cos\varphi_1 & m_2\lambda_2\cos\varphi_2 \\ (m_1\lambda_1 + m_2(\lambda_1 + \lambda_1^{'}))\cos\varphi_1 & m_1\lambda_1^2 + m_2(\lambda_1 + \lambda_1^{'})^2 + J_1 & m_2\lambda_2(\lambda_1 + \lambda_1^{'})\cos(\varphi_1 - \varphi_2) \\ m_2\lambda_2\cos\varphi_2 & m_2\lambda_2(\lambda_1 + \lambda_1^{'})\cos(\varphi_1 - \varphi_2) & m_2\lambda_2^2 + J_2 \end{pmatrix}$$

$$Q(a, \dot{a}) = \begin{pmatrix} 0 & -(m_1\lambda_1 + m_2(\lambda_1 + \lambda_1^{'}))\sin\varphi_1\dot{\varphi}_1 & -m_2\lambda_2\sin\varphi_2\dot{\varphi}_2 \\ 0 & 0 & m_2\lambda_2(\lambda_1 + \lambda_1^{'})\sin(\varphi_1 - \varphi_2)\dot{\varphi}_2 \\ 0 & -m_2\lambda_2(\lambda_1 + \lambda_1^{'})\sin(\varphi_1 - \varphi_2)\dot{\varphi}_1 & 0 \end{pmatrix}$$

$$G(a) = \begin{bmatrix} 0 & (m_1 g\lambda_1 + m_2 g(\lambda_1 + \lambda_1^{'}))\sin\varphi_1 & m_2 g\lambda_2\sin\varphi_2 \end{bmatrix}^T, u = [F - f \quad 0 \quad 0]^T = [F_s \quad 0 \quad 0]^T$$

To clearly describe the role of F_s played in each variables of $a=[x,\varphi_1,\varphi_2]^T$, Eq. (5) can be transformed into the following system of nonlinear form

$$\ddot{x}=B_0+A_0F_s,\ \ddot{\varphi}_1=B_1+A_1F_s,\ \ddot{\varphi}_2=B_2+A_2F_s \tag{6}$$

where

$$A_0=\frac{1}{m_0+m_1+m_2},\ A_2=\frac{\cos\varphi_2}{m_2\lambda_2\cos^2\varphi_2-(\lambda_2+J_2/m_2\lambda_2)(m_0+m_1+m_2)}$$

$$A_1=\frac{\cos\varphi_1(m_1\lambda_1+m_2(\lambda_1+\lambda_1^{'}))}{(m_1\lambda_1+m_2(\lambda_1+\lambda_1^{'}))^2\cos^2\varphi_1-(m_1\lambda_1^2+m_2(\lambda_1+\lambda_1^{'})^2+J_1)(m_0+m_1+m_2)}$$

$$B_0=\frac{\begin{pmatrix}-(m_1\lambda_1+m_2(\lambda_1+\lambda_1^{'}))\cos\varphi_1\ddot{\varphi}_1-m_2\lambda_2\cos\varphi_2\ddot{\varphi}_2\\+(m_1\lambda_1+m_2(\lambda_1+\lambda_1^{'}))\sin\varphi_1\dot{\varphi}_1^2+m_2\lambda_2\sin\varphi_2\dot{\varphi}_2^2\end{pmatrix}}{m_0+m_1+m_2}$$

$$B_1=\frac{\begin{pmatrix}(m_2\lambda_2(\lambda_1+\lambda_1^{'})(m_0+m_1+m_2)\cos(\varphi_1-\varphi_2)-m_2\lambda_2(m_1\lambda_1+m_2(\lambda_1+\lambda_1^{'}))\cos\varphi_1\cos\varphi_2)\ddot{\varphi}_2\\+(m_1\lambda_1+m_2(\lambda_1+\lambda_1^{'}))^2\sin\varphi_1\cos\varphi_2\dot{\varphi}_1^2\\+((m_1\lambda_1+m_2(\lambda_1+\lambda_1^{'}))m_2\lambda_2\cos\varphi_1\sin\varphi_2+m_2\lambda_2(\lambda_1+\lambda_1^{'})\sin(\varphi_1-\varphi_2)(m_0+m_1+m_2))\dot{\varphi}_2^2\\+(m_1\lambda_1+m_2(\lambda_1+\lambda_1^{'}))(m_0+m_1+m_2)g\sin\varphi_1\end{pmatrix}}{(m_1\lambda_1+m_2(\lambda_1+\lambda_1^{'}))^2\cos^2\varphi_1-(m_1\lambda_1^2+m_2(\lambda_1+\lambda_1^{'})^2+J_1)(m_0+m_1+m_2)}$$

$$B_2=\frac{\begin{pmatrix}((m_0+m_1+m_2)(\lambda_1+\lambda_1^{'})\cos(\varphi_1-\varphi_2)-(m_1\lambda_1+m_2(\lambda_1+\lambda_1^{'}))\cos\varphi_1\cos\varphi_2)\ddot{\varphi}_1\\+((m_1\lambda_1+m_2(\lambda_1+\lambda_1^{'}))\sin\varphi_1\cos\varphi_2-(\lambda_1+\lambda_1^{'})\sin(\varphi_1-\varphi_2))\dot{\varphi}_1^2\\+m_2\lambda_2\cos\varphi_1\sin\varphi_2\dot{\varphi}_2^2\\+(m_0+m_1+m_2)g\sin\varphi_2\end{pmatrix}}{m_2\lambda_2\cos^2\varphi_2-(\lambda_2+J_2/m_2\lambda_2)(m_0+m_1+m_2)}$$

3 Control Law

3.1 HSMC Control [7]

HSMC is multilayer slide mode method and each layer of slide mode has its own function [8]. First of all, the first layer of multilayer is defined as follows:

$$\begin{aligned}&s_0=w_0(x-x_{ref})+(\dot{x}-\dot{x}_{ref}),\ s_1=w_1(\varphi_1-\varphi_{1ref})+(\dot{\varphi}_1-\dot{\varphi}_{2ref})\\&s_2=w_2(\varphi_2-\varphi_{2ref})+(\dot{\varphi}_2-\dot{\varphi}_{2ref})\end{aligned} \tag{7}$$

where w_0,w_1,w_2 denote the positive weight parameter to be chosen. $x_{ref},\varphi_{1ref},\varphi_{2ref}$ are the ideal trajectory which are tracked by each variables of $a=[x,\varphi_1,\varphi_2]^T$. Furthermore, x_{ref} is predefined curve or step function and φ_{1ref} and φ_{2ref} are equal to zero according to the goal of study. If moving phase points approach and reach the switch surface of first layer, according to [9], $\dot{s}_0,\dot{s}_1,\dot{s}_2$ are equal to zero. Second, the second layer is written as follows:

$$H = q_0 s_0 + q_1 s_1 + q_2 s_2 \tag{8}$$

where q_0, q_1, q_2 are the weight parameters to be chosen. Now we should find out the F_s which can make the phase points to reach the switch surface of second layer, move along the switch surface, and then arrive at the origin, i.e., the second layer is asymptotically stable. F_s is obtained based on the Lyapunov stability criterion, assuming the Lyapunov function, $L = 0.5H^2 \geq 0$, and then we can obtain,

$$\dot{L} = H\dot{H} = H(q_0 \dot{s}_0 + q_1 \dot{s}_1 + q_2 \dot{s}_2) \tag{9}$$

By substituting Eqs. (6) and (7) into (9),

$$\begin{aligned}\dot{L} = H((&q_0 B_0 + q_1 B_1 + q_2 B_2 + q_0 w_0 \dot{x} + q_1 w_1 \dot{\varphi}_1 + q_2 w_2 \dot{\varphi}_2 - (q_0 \ddot{x}_{ref} + q_0 w_0 \dot{x}_{ref})) \\ &+ (q_0 A_0 + q_1 A_1 + q_2 A_2) F_S)\end{aligned} \tag{10}$$

Let

$$\dot{L} = -c_1 H^2 - c_2 |H| \quad \text{where } c_1 > 0, c_2 > 0 \tag{11}$$

If Eq. (11) < 0, the second layer is asymptotically stable according to Lyapunov stability criterion, then

$$F_s = -\frac{\begin{pmatrix} c_2 \mathrm{sgn}(H) + c_1 H + q_0 B_0 + q_1 B_1 + q_2 B_2 \\ + q_0 w_0 \dot{x} + q_1 w_1 \dot{\varphi}_1 + q_2 w_2 \dot{\varphi}_2 - (q_0 \ddot{x}_{ref} + q_0 w_0 \dot{x}_{ref}) \end{pmatrix}}{(q_0 A_0 + q_1 A_1 + q_2 A_2)} \tag{12}$$

where $\mathrm{sgn}(H) = \begin{cases} 1 & H > 0 \\ 0 & H = 0 \\ -1 & H < 0 \end{cases}$ and $H\mathrm{sgn}(H) = |H|$

3.2 Proof of Stability

Equation (11) shows the second layer is asymptotically stable. According to the stability proof of multilayer slide mode control on Single-Pendulum Crane in [10]: In view of this study, based on Lasalle invariance principle, if $t \to \infty$, the maximum invariant set is

$$\left\{H \in R^3 | \dot{L} \leq 0\right\} \cap \left\{H = q_0 s_0 + q_1 s_1 + q_2 s_2 = 0 \, or \, \dot{H} = q_0 \dot{s}_0 + q_1 \dot{s}_1 + q_2 \dot{s}_2 = 0\right\}$$

And because $H = q_0 s_0 + q_1 s_1 + q_2 s_2$ is asymptotically stable, the first step is that the phase points will go into the neighborhood of the zero point of the

three-dimensional coordinate which is composed of three slide mode functions in Eq. (7). Then, the second step is that $[x - x_{\text{ref}}, \dot{x} - \dot{x}_{\text{ref}}, \varphi_1, \dot{\varphi}_1, \varphi_2, \dot{\varphi}_2]$ will all tend to zeros, which means Eq. (7) is asymptotically stable. Above all, the system is asymptotically stable.

4 Simulation and Result

The parameters of rail type suspended conveyor for electrolytic aluminum anode casting are $m_0 = 20\,\text{kg}$, $m_1 = 10\,\text{kg}$, $m_2 = 300\,\text{kg}$, $\lambda_1 = 5\,\text{m}$, $\lambda_1^{'} = 0.4\,\text{m}$, $\lambda_2 = 0.5\,\text{m}$. Besides, f, J_1, J_2 is defined as the uncertain perturbation of system.

(1) If the driving unit tracks the S-shape smooth curve [11],

$$x_{\text{ref}} = \frac{p}{2} + \frac{k_1^2}{4k_2}(\ln\ \cosh(2k_2 t/k_1 - \delta) - \ln\ \cosh(2k_2 t/k_1 - \delta - 2pk_2/k_1^2)) \qquad (13)$$

where $p = 1$ is positional parameter which means that when $t \to \infty$, the x_{ref} is equal to p; $k_1 = 0.4, k_2 = 0.2$ is respectively maximum rising velocity and acceleration of x_{ref}; $\delta = 2$ is regulative initial velocity of x_{ref}. On the other hand, the weight parameters of controller is chosen as follows:

$$c_1 = 0.8, c_2 = 0.35, w_0 = 0.007, w_1 = 150, w_2 = 50.2, q_0 = 1000, q_1 = -100, q_2 = 0.37$$

Figure 2 shows simulation of eight variables when tracking x_{ref}. Figure 2a indicates that, with the exception of rising time, the simulation of driving unit tracking x_{ref} is perfect, which non-overshoot is so important to meet the requirements of the precise robotic operation. Figure 2b, c reflect the fact that the swing range of loading hook is from −0.01249 rad to +0.01046 rad approximately and that of ferrophosphorus ladle container is from −0.0123 rad to +0.01048 rad. The swing range of the system is really small to rail type suspended conveyor [10] and they are equal to zero when the state of system is stable. Figure 2d shows that when conveyor movement tends to stable, F also tends to stable.

(2) If the x_{ref} and parameters of controller are not changed,

case 1 $m_0 = 15\,\text{kg}$, $m_1 = 5\,\text{kg}$, $m_2 = 200\,\text{kg}$, $\lambda_1 = 3\,\text{m}$, $\lambda_1^{'} = 0.3\,\text{m}$, $\lambda_2^{'} = 0.4\,\text{m}$

case 2 $J_1 = 1\,\text{N m}^2$, $J_2 = 5\,\text{N m}^2$

case 3 $f = 0.05\,\text{sgn}(\dot{x})$.

The above four figures reflect the fact that when parameters of model inevitably exist perturbation, the system can quickly restore the original state. Figures 3, 4 and 5 indicate that the main variables of systems do not appear to be affected (Fig. 6).

(3) Electrolytic aluminum anode casting process is simulated in Fig. 7.

In Fig. 7, P1 is position of anode casting. P2 and P3 is respectively Charging area1 and Charging area2. P1, P2, and P3 are four meters apart. Each workstation

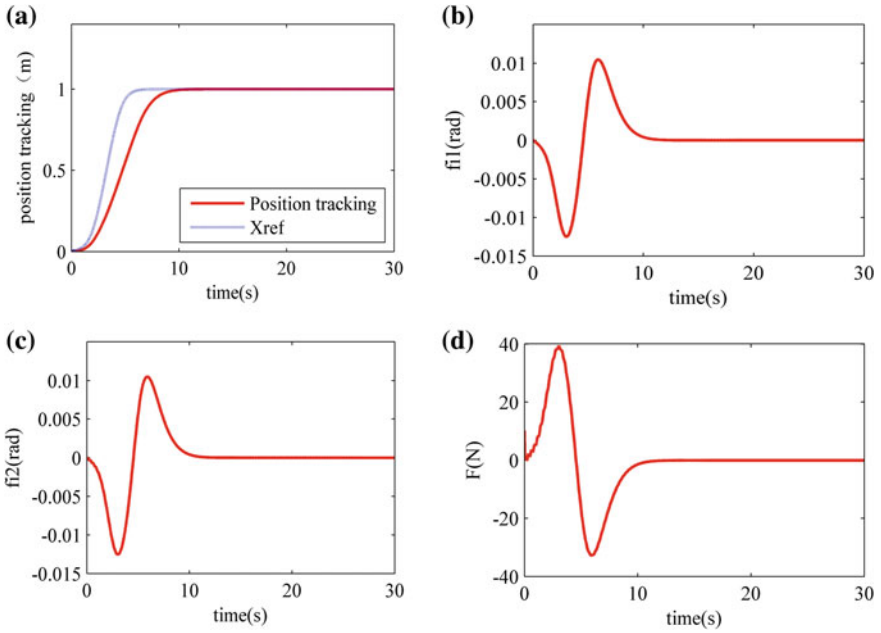

Fig. 2 Simulation of eight variables when tracking Xref. **a** Position tracking, **b** Angle of loading hook, **c** Angle of ferrophosphorus ladle container, **d** Input F

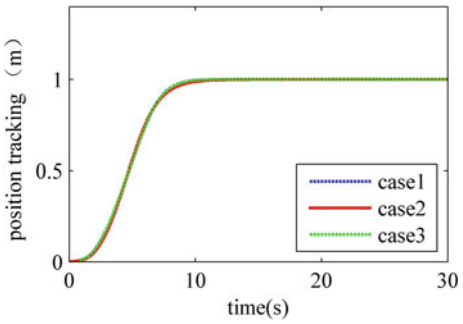

Fig. 3 Position tracking with perturbation

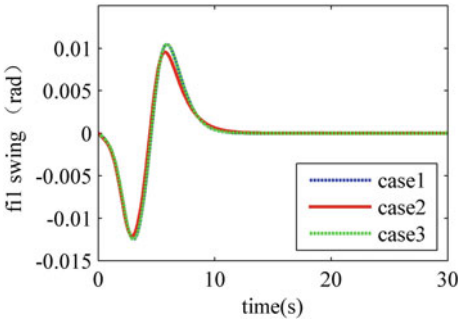

Fig. 4 Angle of loading hook with perturbation

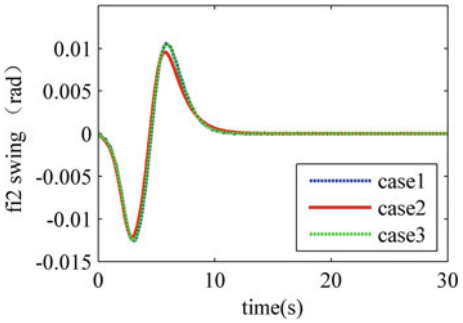

Fig. 5 Angle of ferrophosphorus ladle container with perturbation

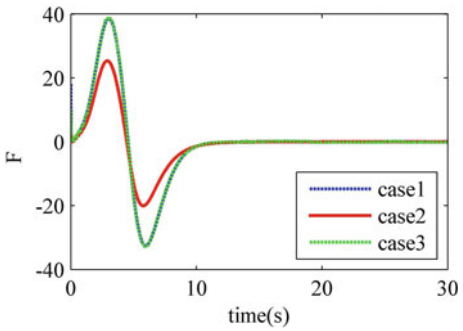

Fig. 6 Input F with perturbation

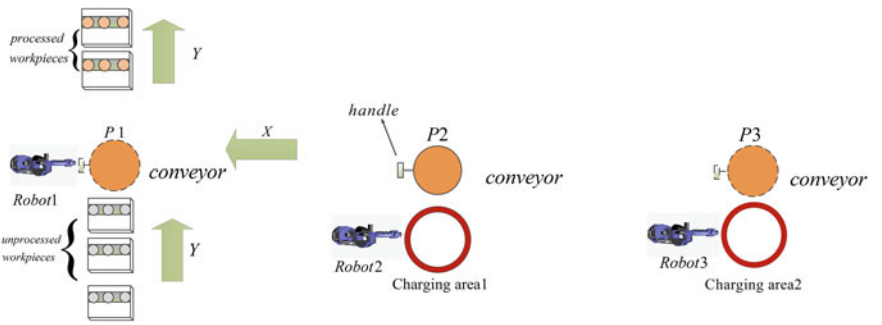

Fig. 7 Top view of working process

has an industrial robot for casting and charging. One operational cycle of rail type suspended conveyor is listed as follows:

X1: After receiving the material in P2, the conveyor moves 4 meters to P1 along the positive direction of X axis.

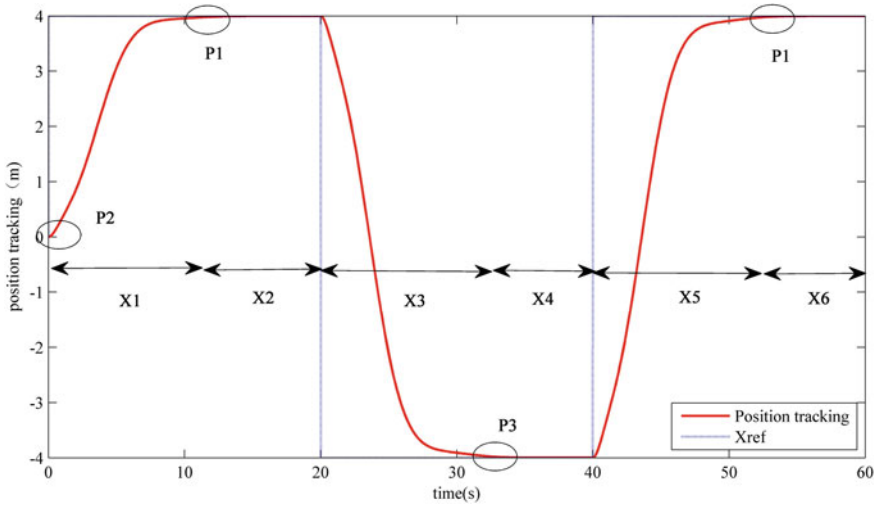

Fig. 8 Position tracking of working process

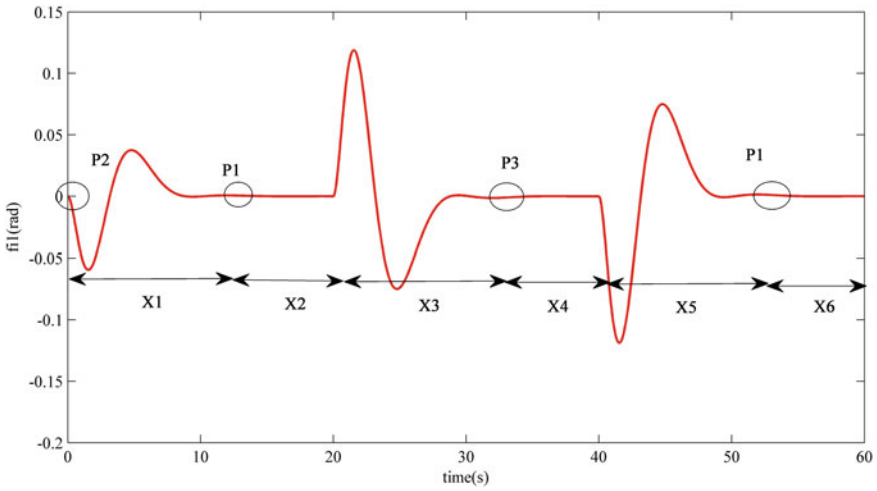

Fig. 9 Loading hook swing of working process

X2: Start the casting of workpiece1.

X3: After finishing the casting of workpiece1, the conveyor moves 8 meters to P3 along the reverse direction of X axis.

X4: Start charging in P3.

X5: After receiving the material in P3, the conveyor moves 8 meters to P1. along the positive direction of X axis.

X6: Start the casting of workpiece2.

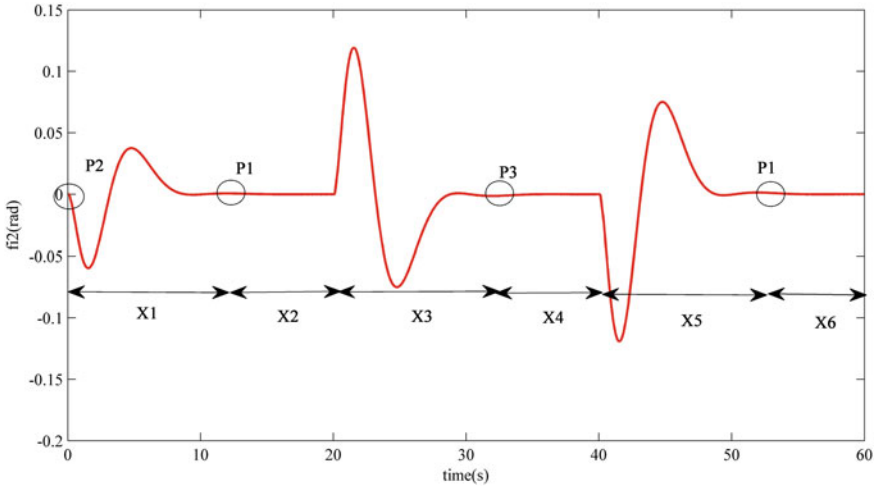

Fig. 10 Ferrophosphorus ladle container swing of working process

Finished.

It can be seen that the ideal tracking trajectory is square wave. The weight parameters of controller is chosen as follows:

$$c_1 = 1, c_2 = 0.001, w_0 = 0.37, w_1 = 400, w_2 = 100, q_0 = 8, q_1 = -0.4, q_2 = 1$$

The simulation of each variable on one operational cycle of rail type suspended conveyor is shown in Figs. 8, 9, 10 and 11. They indicate that although the direction of movement and state has changed many times, the system can still come

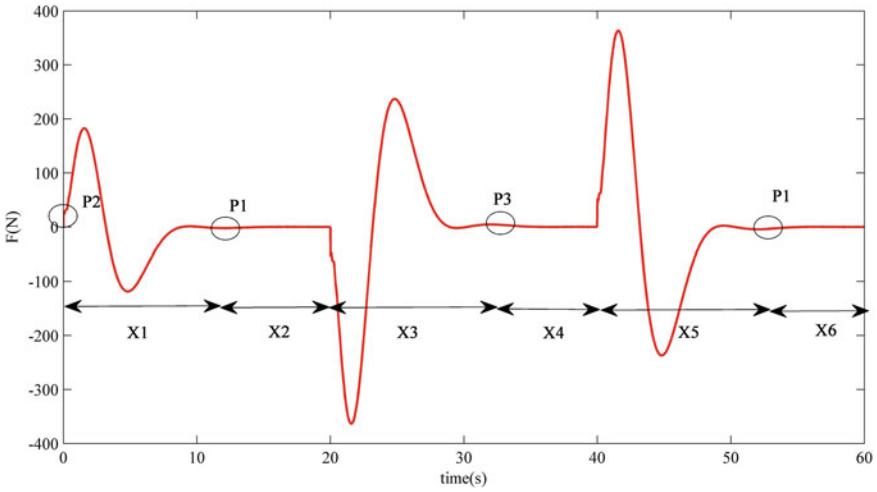

Fig. 11 Input F of working process

to steady-state in a relatively short time. Besides, when the displacement of driving unit is between −4 m and +4 m, φ_1 and φ_2 can still be kept from –0.15 rad to +0.15 rad.

5 Conclusion

Currently, the manual mode and under-actuated control is widely used in the process of rail type conveying for electrolytic aluminum anode casting, which this mode will bring a number of environmental and safety issues on staff and equipment operation. In this study, the rail type suspended conveyor is taken as the controlled plant. Initially, the locomotion process has been analyzed and the dynamic model was established based on the Lagrange equation. Furthermore, the HSMC control is utilized to rail type conveying for electrolytic aluminum anode casting. Eventually, the cycle experiments of reliability and stability working process have been made in many cases. These results show the satisfactory effect on tracking ability of system and anti-swing ability of ferrophosphorus ladle container and loading hook. On the other hand, the robustness and stability of system which can meet the requirement of controlling the conveying of electrolytic aluminum anode casting have a high value for application.

References

1. Sawodny O, Briechle K (1999) Damping of tilt oscillations of loads in automated crane systems. In: IEEE control conference (ECC), pp 889–894
2. Tanaka S, Kouno S (1998) Automatic measurement and control of the attitude of crane lifters Lifter-attitude measurement and control. Control Eng Pract 6(9):1099–1107
3. Arena A, Casalotti A (2015) Dynamics of container cranes: three-dimensional modeling, full-scale experiments, and identification. Int J Mech Sci 93:8–21
4. Zhang M, Man X (2016) Adaptive tracking control for double-pendulum overhead cranes subject to tracking error limitation, parametric uncertainties and external disturbances. Mech Syst Signal Process 76–77:15–32
5. Guo W*, Liu D (2004) Passivity-based-control for double-pendulum-type overhead cranes. In: IEEE Region 10 conference, 2004, vol 4, pp 546–569
6. Blajer W, Kolodziejczyk K (2007) Motion planning and control of gantry cranes in cluttered work environment. IET Control Theory Appl 1(5):1370–1379
7. Tuan LA, Lee S-G (2013) Sliding mode controls of double-pendulum crane systems. J Mech Sci Technol 27 (6):1863–1873
8. Saridis GN (1983) Intelligent robotic control. IEEE Trans Autom Control 28(5):547–557
9. Utkin V, Guldner J, Shi J (2009) Sliding mode control in electromechanical systems, 2nd edn. Taylor & Francis, pp 1–355
10. Qian D, Yi J (2016) Hierarchical sliding mode control for under-actuated cranes. Springer, Berlin, pp 1–166
11. Fang Y (2012) A motion planning-based adaptive control method for an underactuated crane system. IEEE Trans Control Syst Technol 20(1):241–248

Composite DOBC and H_∞ Control for Stochastic Systems with Disturbances

Linqing Zhang and Xinjiang Wei

Abstract Composite disturbance observer-based control (DOBC) and H_∞ control scheme is proposed for a class of stochastic systems with nonlinear dynamics and multiple disturbances. The stochastic disturbance observer based on pole placement is constructed to estimate disturbance which is generated by an exogenous system. Then, composite DOBC and H_∞ controller is designed to ensure that the composite system is mean-square stable and its H_∞ performance satisfies a prescribed level. A numerical example validates the feasibility and effectiveness of the approach.

Keywords Stochastic system · Multiple disturbances · Disturbance observer-based control · H_∞ control

1 Introduction

Disturbance observer-based control approach was established in the late 1980s and has been used in many control engineering systems against disturbances [1–5]. The basic idea is to estimate disturbance by disturbance observer, and then compensate disturbance by combining a feedforward compensator and control laws. In [6], single-input single-output (SISO) nonlinear systems with external disturbances which were limited to be constant or harmonic signals have been considered. In [7], the DOBC approaches were proposed for a class of multiple-input multiple-output (MIMO) nonlinear systems with nonlinear dynamics and neutral stable disturbances. In [8], the DOBC methods were extended to a class of stochastic systems. Recently, composite DOBC and other control approaches have been proposed to achieve the multiple disturbances attenuation and rejection performance. For instance, composite DOBC and H_∞ control was proposed for MIMO continuous models in [9]. Composite DOBC and fuzzy control was presented for continuous MIMO nonlinear systems in [10]. In [11], Composite hierarchical anti-disturbance control (CHADC) method was proposed for nonlinear systems with multiple disturbances. CHADC

L. Zhang (✉) · X. Wei
School of Mathematics and Statistics Science, Ludong University, Yantai 264025, China
e-mail: 17862824221@163.com

Y. Jia et al. (eds.), *Proceedings of 2016 Chinese Intelligent Systems Conference*,
Lecture Notes in Electrical Engineering 404, DOI 10.1007/978-981-10-2338-5_17

can make full use of disturbance characteristic to complete anti-disturbance performance. In [12], New disturbances compensation and rejection methods were studied based on DOBC technique for the various nonlinear systems, and have been widely applied in the process control, mechanical control, and the aeronautic engineering.

On the other hand, the stochastic H_∞ control for stochastic systems have been investigated by many researchers. For example, the H_∞ scheme for uncertain stochastic systems with delay was proposed in [13]. The robust H_∞ method for uncertainty impulsive stochastic system under sample measurements was presented in [14]. However, composite DOBC and H_∞ control for stochastic systems with multiple disturbances are not given enough attention.

The purpose of this paper is to propose a composite DOBC and H_∞ control scheme for a class of stochastic systems with disturbances. The main contributions of this paper are as follows. Composite DOBC and H_∞ control scheme is extended from nonlinear systems to a class of stochastic systems, and it can improve control accuracy and achieve satisfactory system performance compared with pure DOBC method.

Notations: For matrices $M_1, M_2, M_1 < 0$ means that M_1 is a negative definite matrix. $diag\{M_1, M_2\}$ stands for a black diagonal matrix; $\lambda_{min}(M_1)$ and $\lambda_{max}(M_1)$ are minimum and maximum of matrix M_1 eigenvalues; (Ω, F, F_t, P) is a complete probability space with a natural filtration F_t and $E\{\cdot\}$ be the mathematical expectation operator with respect to probability measure; $*$ represents the symmetric form of matrix;

2 Formulation of the Problem

The following stochastic system with disturbances is described as

$$\begin{aligned} dx(t) = &\{A_0 x(t) + F_0 f_0(x(t), t) + H_0[u(t) + d_0(t)] \\ &+ H_1 d_1(t)\}dt + B_0 x(t) dW(t) \end{aligned} \tag{1}$$

where $x \in R^n$, $u \in R^m (m < n)$ are the system state and the control input, respectively. $A_0 \in R^{n\times n}$, and $H_0 \in R^{n\times m}$, $H_1 \in R^{n\times p}$, $B_0 \in R^n$ are the coefficient matrices. $F_0 \in R^{n\times q}$ are weighting matrices. The Borel measurable and bounded nonlinear functions $f : R^q \times R_+ \longrightarrow R^q$ satisfy Assumption 2. $d_0(t) \in R^m$ is supposed to satisfy Assumption 1. $d_1(t) \in R^p$ is the external disturbance which is assumed in the H_2-norm. $W(t)$ is a zero-mean scalar Wiener process (Brownian Motion) on (Ω, F, F_t, P) with $E[W(t)] = 0$ and $E[W^2(t)] = dt$.

Assumption 1 The disturbance $d_0(t)$ can be generated by the following exogenous system

$$\begin{aligned} dw(t) &= Gw(t)dt + H_2\delta(t)dt \\ d_0(t) &= Vw(t) \end{aligned} \tag{2}$$

where $G \in R^{r\times r}, H_2 \in R^{r\times r}$ and $V \in R^{m\times r}$ are proper known matrices. $\delta \in R^l$ is the additional disturbance which results from the perturbations and uncertainties in the exogenous system. It is also supposed that $\delta(t)$ belongs to H_2-norm.

Assumption 2 The nonlinear functions $f_0(x(t), t)$ are locally Lipschitz in $x(t) \in R^n$ with $f(0, t) = 0$, there exists a constant weighting matrix U_0 which satisfies

$$\|f_0(x_1(t), t) - f_0(x_2(t), t)\| \leq \|U_0(x_1(t) - x_2(t))\| \tag{3}$$

Assumption 3 (A_0, H_0) is controllable and (G, H_0V) is observable.

3 Composite DOBC and H_∞ Control

In this section, we suppose that all the system states are available, f_0 are known and Assumptions 1–3 hold. A stochastic observer will be designed to estimate the disturbance $d_0(t)$. Then the new control method which combines the DOBC with H_∞ control abbreviated as DOBPH_∞C is proposed such that the disturbance can be rejected and the mean-square stability of the composite system can also be guaranteed.

3.1 Stochastic Disturbance Observer (SDO)

In this section, the stochastic disturbance observer is formulated as

$$\begin{cases} \hat{d}_0(t) = V\hat{w}(t) \\ \hat{w}(t) = v(t) - Lx(t) \\ dv(t) = (G + LH_0V)[V(t) - Lx(t)]dt \\ \qquad\quad + L[A_0x(t) + F_0f_0(x(t), t) + H_0u(t)]dt \end{cases} \tag{4}$$

where $\hat{w}(t)$ is the estimation of $w(t)$, and $v(t)$ is the auxiliary variable. Define the estimation error $e_w(t) = w(t) - \hat{w}(t)$. Based on (1), (2), and (4), it can be obtained that

$$de_w(t) = (G + LH_0V)e_w(t)dt + H_2\delta(t)dt + LH_1d_1(t)dt + LB_0x(t)dW(t) \tag{5}$$

Since (G, H_0V) can be observed, we can place the poles at an arbitrarily chosen location by adjusting L in (5) to satisfy the performance requirement for SDO.

In the following, the controller can be constructed as

$$u(t) = -\hat{d}_0(t) + Kx(t) \tag{6}$$

Substituting (6) into (1), the closed-loop system is given by

$$\begin{aligned} dx(t) = &[(A_0 + H_0K)x(t) + F_0f(x(t), t) + H_0Ve_w(t) \\ &+ H_1d_1(t)]dt + B_0x(t)dW(t) \end{aligned} \tag{7}$$

Combining (5) and (7), the composite system is described as

$$\begin{cases} d\bar{x}(t) = [A\bar{x}(t) + Ff(\bar{x}(t), t) + HD(t)]dt + B\bar{x}(t)dW(t) \\ z(t) = C\bar{x}(t) \end{cases} \tag{8}$$

where

$$\bar{x}(t) = \begin{bmatrix} x(t) \\ e_w(t) \end{bmatrix}, A = \begin{bmatrix} A_0 + H_0K & H_0V \\ 0 & G + LH_0V \end{bmatrix}, F = \begin{bmatrix} F_0 \\ 0 \end{bmatrix},$$
$$f(\bar{x}(t), t) = f_0(x(t), t), H = \begin{bmatrix} H_1 & 0 \\ LH_1 & H_2 \end{bmatrix}, B = \begin{bmatrix} B_0 & 0 \\ LB_0 & 0 \end{bmatrix}, D(t) = \begin{bmatrix} d_1(t) \\ \delta(t) \end{bmatrix}$$

The reference output is denoted as $z(t) = C\bar{x}(t)$ with weighting matrices $C = \begin{bmatrix} C_1 & C_2 \end{bmatrix}$. For $f(\bar{x}(t), t)$, it can be shown that

$$\|f(\bar{x}(t), t)\| \leq \|U\bar{x}(t)\|$$

where

$$U = \begin{bmatrix} U_0 & 0 \\ 0 & 0 \end{bmatrix}$$

With the above formulations, the main objective is to estimate $d_0(t)$ with stochastic disturbance observer, and compute a composite DOBC and H_∞ controller such that (8) is stable and satisfies the following requirement:
1. The composite system in (8) with $D(t) = 0$ is mean-square stable.
2. Under the zero initial condition, the system (8) satisfies the following inequality:

$$\|z(t)\|_{E_2} < \gamma \|D(t)\|_{E_2} \tag{9}$$

for all nonzero $D(t) \in L_2[0, \infty)$, where $\gamma > 0$ is a prescribed scalar, and $\|z(t)\|_{E_2} = (E\int_0^\infty |z(t)|^2 dt)^{1/2}$.

3.2 Composite DOBC and H_∞ Control

In this section, we aim to design K such that (8) is mean-square stable and satisfies the performance of anti-disturbance attenuation.

Theorem 1 *For given parameters $\lambda > 0, \gamma > 0$, if there exist $Q_1 > 0, Q_2 > 0$, and R_1 satisfying*

$$\begin{bmatrix} M_1 & F_0 & H_1 & 0 & Q_1B_0^T & Q_1B_0^TL^T & Q_1C_1^T & Q_1U_0^T & H_0VQ_2 \\ * & -\frac{1}{\lambda^2}I & 0 & 0 & 0 & 0 & 0 & 0 & 0 \\ * & * & -\gamma^2 I & 0 & 0 & 0 & 0 & 0 & H_1^TL^T \\ * & * & * & -\gamma^2 I & 0 & 0 & 0 & 0 & H_2^T \\ * & * & * & * & -Q_1 & 0 & 0 & 0 & 0 \\ * & * & * & * & * & -Q_2 & 0 & 0 & 0 \\ * & * & * & * & * & * & -I & 0 & C_2Q_2 \\ * & * & * & * & * & * & * & -\lambda^2 I & 0 \\ * & * & * & * & * & * & * & * & M_2 \end{bmatrix} < 0 \tag{10}$$

where

$$M_1 = A_0Q_1 + Q_1A_0^T + H_0R_1 + R_1^TH_0^T,$$
$$M_2 = GQ_2 + Q_2^TG^T + LH_0VQ_2 + Q_2^TV^TH_0^TL^T.$$

Then, by designing SDO (5) with gain L and DOBC law (6) with gain $K = R_1Q_1^{-1}$, the composite system (8) is mean-square stable in the absence of disturbance $D(t)$, and satisfies $\|z(t)\|_{E_2} < \gamma\|D(t)\|_{E_2}$.

Proof For the system (8) with $D(t) = 0$, consider the following Lyapunov function

$$V(\bar{x}(t)) = \bar{x}^T(t)P\bar{x}(t) + \frac{1}{\lambda^2}\int_0^t [\|U\bar{x}(s)\|^2 - \|f(\bar{x}(s), s)\|^2]ds \tag{11}$$

Define

$$P = \begin{bmatrix} P_1 & 0 \\ 0 & P_2 \end{bmatrix} = \begin{bmatrix} Q_1^{-1} & 0 \\ 0 & Q_2^{-1} \end{bmatrix} > 0 \tag{12}$$

based on (8), (11) and (12), we have

$$\begin{aligned} LV(\bar{x}(t), t) &= \bar{x}^T(t)(PA + A^TP + B^TPB)\bar{x}(t) + \bar{x}^T(t)PFf(\bar{x}(t), t) \\ &\quad + f^T(\bar{x}(t), t)F^TP\bar{x}(t) + \frac{1}{\lambda^2}\bar{x}^T(t)U^TU\bar{x}(t) - \frac{1}{\lambda^2}f^T(\bar{x}(t), t)f(\bar{x}(t), t) \\ &= \begin{bmatrix} \bar{x}(t) \\ f(\bar{x}(t), t) \end{bmatrix}^T \Omega_0 \begin{bmatrix} \bar{x}(t) \\ f(\bar{x}(t), t) \end{bmatrix} \end{aligned} \tag{13}$$

where

$$\Omega_0 = \begin{bmatrix} PA + A^T P + B^T PB + \frac{1}{\lambda^2} U^T U & PF \\ F^T P & 0 \end{bmatrix} < 0.$$

Now, the expectation of (13) can be seen that

$$E\{LV(\bar{x}(t))\} \leq \lambda_{min}(\Omega_0) E\{\|\bar{x}(t)\|^2\} \tag{14}$$

Let $\alpha = -\frac{\lambda_{min}(\Omega_0)}{\lambda_{max}(P)} > 0$ and $\beta = E\{\bar{x}^T(0) P \bar{x}(0)\} > 0$, such that

$$E\{\|\bar{x}(t)\|^2\} \leq \frac{\beta}{\lambda_{min}(P)} e^{-\alpha t} \tag{15}$$

$$\lim_{t \to \infty} E\{\|\bar{x}(t)\|^2\} = 0 \tag{16}$$

So the mean-square stability of the system (8) with $D(t) = 0$ is proved.

To establish the H_∞ performance under the zero initial condition, we consider the following auxiliary function

$$\begin{aligned} J(t) &= E \int_0^t [z^T(s) z(s) - \gamma^2 D^T(s) D(s)] ds \\ &= E \int_0^t [z^T(s) z(s) - \gamma^2 D^T(s) D(s) + LV(\bar{x}(s), s)] ds - EV(\bar{x}(t), t) \\ &\leq E \int_0^t [z^T(s) z(s) - \gamma^2 D^T(s) D(s) + LV(\bar{x}(s), s)] ds \\ &= E \int_0^t \begin{bmatrix} \bar{x}(s) \\ f(\bar{x}(s), s) \\ D(s) \end{bmatrix}^T \Omega_1 \begin{bmatrix} \bar{x}(s) \\ f(\bar{x}(s), s) \\ D(s) \end{bmatrix} ds \end{aligned} \tag{17}$$

in which $V(\bar{x})$ is denoted in (11), and

$$\Omega_1 = \begin{bmatrix} PA + A^T P + B^T PB + \frac{1}{\lambda^2} U^T U + C^T C & PF & PH \\ F^T P & -\frac{1}{\lambda^2} I & 0 \\ H^T P & 0 & -\gamma^2 I \end{bmatrix}. \tag{18}$$

Now, we will prove that if (11) holds, then $\Omega_1 < 0$.

Based on Schur complement, $\Omega_1 < 0$ is equivalent to $\Omega_2 < 0$, where

$$\Omega_2 = \begin{bmatrix} \Pi_1 & P_1H_0V & P_1F_0 & P_1H_1 & 0 & P_1B_0^T & P_1B_0^TL^T & C_1^T & U_0^T \\ * & \Pi_2 & 0 & P_2LH_1 & P_2H_2 & 0 & 0 & C_2^T & 0 \\ * & * & -\frac{1}{\lambda^2} & 0 & 0 & 0 & 0 & 0 & 0 \\ * & * & * & -\gamma^2 I & 0 & 0 & 0 & 0 & 0 \\ * & * & * & * & -\gamma^2 I & 0 & 0 & 0 & 0 \\ * & * & * & * & * & -P_1^{-1} & 0 & 0 & 0 \\ * & * & * & * & * & * & -P_2^{-1} & 0 & 0 \\ * & * & * & * & * & * & * & -I & 0 \\ * & * & * & * & * & * & * & * & -\lambda^2 I \end{bmatrix} \tag{19}$$

with

$$\Pi_1 = P_1A_0 + A_0^TP_1 + P_1H_0K + K^TH_0^TP_1,$$
$$\Pi_2 = P_2G + G^TP_2 + P_2LH_0V + V^TH_0^TL^TP_2$$

$\Omega_2 < 0$ is pre-multiplied and post-multiplied by matrix $diag\{Q_1, Q_2, I, I, I, I, I, I, I\}$, then by exchanging rows and columns, we can obtain (10).

4 Simulation Example

In this section, we give a numerical example to demonstrate the effectiveness of the proposed method. Consider the system (8) with the following parameters:

$$A_0 = \begin{bmatrix} -2.2 & 1.5 \\ 0 & 1.2 \end{bmatrix}, H_0 = \begin{bmatrix} -1.5 \\ 2 \end{bmatrix}, H_1 = \begin{bmatrix} 1.2 \\ 1 \end{bmatrix}, B_0 = \begin{bmatrix} 0.1 & 1 \\ 0 & 1 \end{bmatrix}, F_0 = \begin{bmatrix} 1 \\ 0.5 \end{bmatrix},$$
$$C_1 = \begin{bmatrix} 0.5 & 0.1 \end{bmatrix}, C_2 = \begin{bmatrix} 0.4 & 0.2 \end{bmatrix}, G = \begin{bmatrix} 0 & 2 \\ -2 & 0 \end{bmatrix}, V = \begin{bmatrix} 2 & 0 \end{bmatrix},$$
$$d_2(t) = \frac{2}{5 + 10t}, H_2 = \begin{bmatrix} 0.4 \\ 0.6 \end{bmatrix}.$$

Assume $\lambda = 1, \gamma = 10, U_0 = diag\{0, 1\}$. The initial value of the state is taken to be $x(0) = [-1, 1]^T$. Suppose that $f_0 = sin(2\pi * 5t)x_2(t)$.

By placing the poles J at $[-5, -6]$ in (5), it can be computed that

$$L = \begin{bmatrix} 1.3200 & -1.7600 \\ 1.5600 & -2.0800 \end{bmatrix}.$$

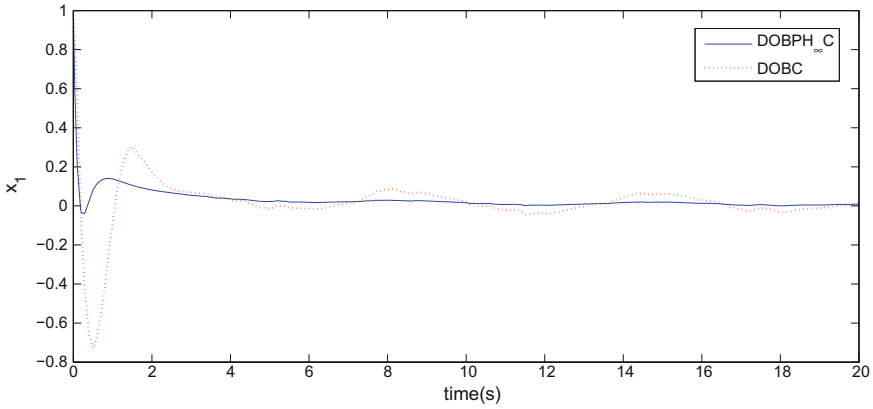

Fig. 1 The comparison of system state x_1 between the DOBC and the DOBP$H_\infty C$

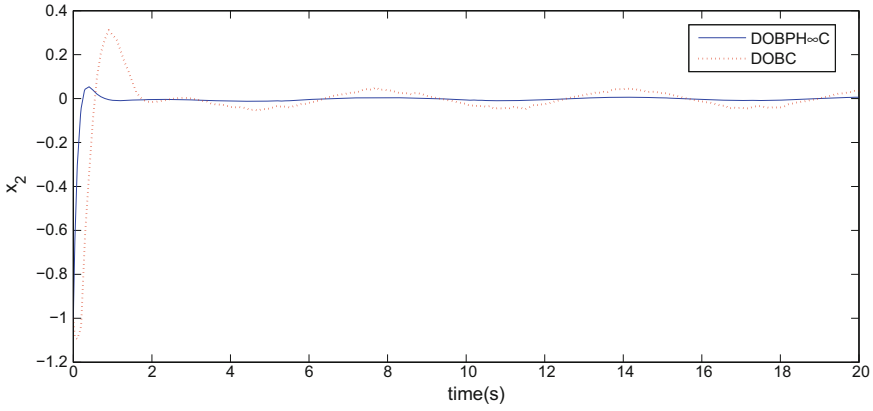

Fig. 2 The comparison of system state x_2 between the DOBC and the DOBP$H_\infty C$

According to Theorem 1, we can obtain

$$R = \begin{bmatrix} 37.9093 & -54.4370 \end{bmatrix},$$
$$K = \begin{bmatrix} -1.8771 & -9.8850 \end{bmatrix}$$

Figures 1 and 2 demonstrate the comparison of system performance between the DOBC approach and the DOBPH_∞C scheme. Figure 3 shows the estimation error for system disturbance using DOBPH_∞C approach. Figure 4 illustrates the trajectory of DOBPH_∞C control. The simulation results show that although there are multiple disturbances in the stochastic system, the disturbance rejection performance is improved by the presented DOBPH_∞C in comparison with the pure DOBC method.

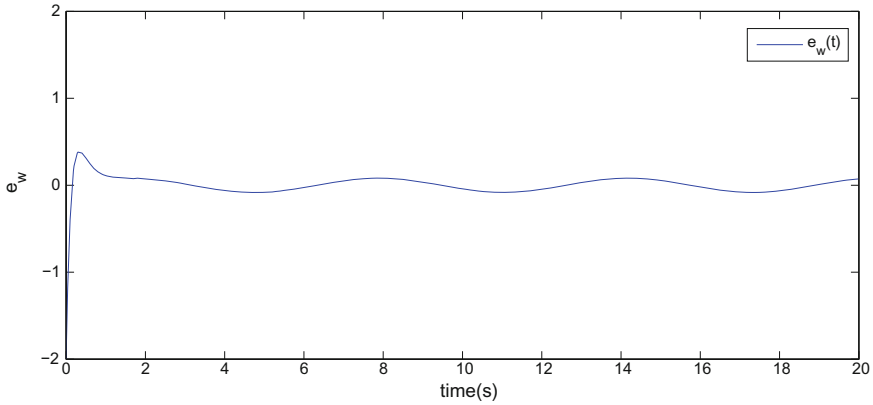

Fig. 3 Estimation error for disturbance using DOBPH_∞C strategy

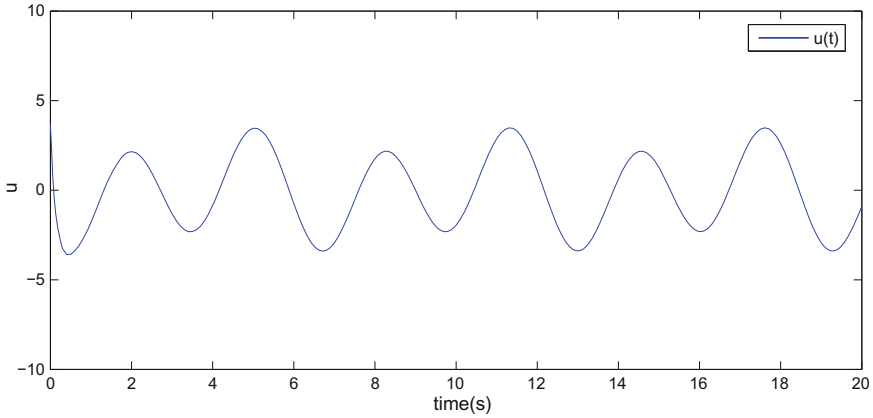

Fig. 4 The trajectory of control input with DOBPH_∞C

5 Conclusions

Composite disturbance observer-based control (DOBC) and H_∞ control for a class of stochastic systems with nonlinearity and disturbances are considered in this paper. The stochastic disturbance observer based on pole placement is constructed and integrated with conventional H_∞ control laws to achieve anti-disturbance performance. One of the challenging works for further research is how to design disturbance observer to estimate $d_0(t)$ with unknown parameters.

References

1. Nakao M, Ohnishi K, Miyachi K (1987) A robust decentralized joint control based on interference estimation. In: Proceedings of the IEEE international conference on robotics and automation, pp 326–331
2. Chan SP (1995) A disturbance observer for robot manipulators with application to electronic components assembly. IEEE Trans Ind Electron 42:487–493
3. Iwasaki M, Shibata T, Matsui N (1999) Disturbance-observer-based nonlinear friction compensation in the table drive systems. IEEE/ASME Trans Mechatron 4(1):3–8
4. Ishikawa J, Tomizuka M (1998) Pivot friction compensation using an accelerometer and a disturbance observer for hard disk. IEEE/ASME Trans Mechatron 3:194–201
5. Bodson M, Jensen JS, Douglas SC (2001) Active noise control for periodic disturbances. IEEE Trans Control Syst Technol 9(1):200–205
6. Chen WH (2004) Disturbance observer based control for nonlinear systems. IEEE/ASME Trans Mechatron 9:706–710
7. Guo L, Chen WH (2005) Disturbance attenuation and rejection for systems with nonlinearity via DOBC approach. Int J Robust Nonlinear Control 15:109–125
8. Wei XJ, Wu ZJ, Hamid RK (2016) Disturbance observer-based anti-disturbance control for a class of stochastic systems. Automatica 162:105–109
9. Wei XJ, Guo L (2010) Composite disturbance-observer-based control and H_∞ control for complex continuous models. Int J Robust Nonlinear Control 20(1):106–118
10. Wei XJ, Chen N (2014) Composite hierarchical anti-disturbance control for nonlinear systems with DOBC and fuzzy control. Int J Robust Nonlinear Control 24:362–373
11. Guo L, Cao SY (2013) Anti-disturbance control for systems with multiple disturbances. CRC Press, New York
12. Li SH, Yang J, Chen WH, Chen XS (2014) Disturbance observer based control: methods and applications. CRC Press
13. Xu SY, Chen TW (2003) Robust H_∞ control for uncertain stochastic systems with state delay. IEEE Trans Autom Control 47(12):942–956
14. Xu SY, Chen TW (2003) Robust H_∞ control filtering for uncertain impulsive stochastic systems under sampled measurements. Automatica 5:95–112

Estimation for a Class of Unknown Frequency Disturbance Using Two-Step Nonlinear Disturbance Observer

Lingxia Ran and Xinjiang Wei

Abstract This paper proposes an estimation strategy of two-step disturbance observer to unknown frequency disturbance existing in a class of nonlinear systems. Two-step disturbance observer is designed to estimate the disturbance and guarantee the disturbance estimation error system is asymptotically stable. A number simulation example is given to demonstrate the correctness and effectiveness of the presented method.

Keywords Unknown frequency disturbance · Disturbance observer · Two-step disturbance observer · Nonlinear system

1 Introduction

Disturbances widely exist in modern industrial control system, such as measurable noise, environmental interference, mechanical and electrical system of the friction and load change, the error caused by the sensor and actuator, and so on. Disturbance is one of the important factors that causes adverse influence on system performance. Disturbance attenuation, compensation, and rejection have been a hot research spot of control problem [1]. Disturbance attenuation is an important way for anti-disturbance control, which mainly includes the internal model control [2], the output regulation theory [3], the active disturbance rejection control [4], the disturbance observer based control (DOBC) [5–7], and so on. For linear systems, the internal model control and output regulation theory can be used to compensate disturbance which satisfies certain neutral stability conditions. The active disturbance rejection control (ADRC) offsets the disturbance through the observation of it. Since the control observed by it is the equivalent lumped disturbance whose using range is quite extensive while the design of controller is relatively complex. Thus it is

L. Ran (✉) · X. Wei
School of Mathematics and Statistics Science, Ludong University,
Yantai 264025, China
e-mail: ranlingxia666@163.com

Y. Jia et al. (eds.), *Proceedings of 2016 Chinese Intelligent Systems Conference*,
Lecture Notes in Electrical Engineering 404, DOI 10.1007/978-981-10-2338-5_18

conservative on the control accuracy. Disturbance observer based control (DOBC) appeared in the 1980s and was put forward first by Japanese scholars Nakao et al. [8]. The basic ideas of DOBC are to design the disturbance observer to estimate external disturbance and to compensate the disturbance in the feedforward channel. Monograph [9] and monograph [10] expound systematically the basic principle of DOBC approach and the latest research achievement. Monograph [9] proposes a composite hierarchical anti-disturbance control (CHADC) strategy through the combination of DOBC with other control methods for the system with multiple source disturbance. CHADC is a kind of exact anti-disturbance control (EADC), which make full use of disturbance information to obtain better anti-disturbance performance. In Monograph [10], the basic principle of DOBC control strategy and new progress in theory and practical application of current DOBC are introduced. The new method based on the DOBC which includes the disturbance estimation and compensation is proposed for various disturbance systems with constant, harmonic, higher order, and it is applied to the motion control, process control, flight control, etc.

In reference [11], a new design for observers of external deterministic disturbances is developed, which is useful in constructing parametrized disturbance models for wide classes of linear system on a unified basis. Literature [12] considers a class of strict feedback linear time invariant system with unknown frequency disturbance, using the adaptive backstepping control method to offset disturbance, and the closed-loop system is asymptotically stable. In reference [13], a class of manipulator system with unknown frequency sinusoidal disturbance, designing two-step disturbance observer to estimate the disturbance is described. Based on the above researches, this paper considers a class of nonlinear system as the research object, and interferes with the description of the range to expand of a class of unknown frequency condition.

2 Problem Formulation

The following nonlinear system with unknown disturbances is described as

$$\begin{cases} \dot{x}(t) = f(x(t)) + g(x(t))\, d(t) \\ y(t) = h(x(t)) \end{cases} \tag{1}$$

where $x(t) \in \mathbb{R}^n$, $d(t) \in \mathbb{R}$, and $y(t)$ are the state vector,the unknown disturbance and the system output, respectively. It is assumed that $f(x(t))$, $g(x(t))$, $h(x(t))$ are smooth and differentiable functions in terms of $x(t)$.

Assumption 1 The disturbance $d(t)$ can be described by the following exogenous system:

$$\begin{aligned} \dot{w}(t) &= Aw(t) \\ d(t) &= Cw(t) \end{aligned} \tag{2}$$

where $w(t) \in \mathbb{R}^n$ is the state of the exogenous system, $A \in \mathbb{R}^{m\times m}$ and $C \in \mathbb{R}^{1\times m}$ are unknown matrices. (A, C) is observable. A has all its eigenvalues on the imaginary axis and $C = [c_1, c_2, \ldots, c_m]$ is constant vector. Generally, the exogenous system (2) is deemed to be neutral stable.

Remark 1 In many cases, disturbances can be formulated as dynamic systems with unknown parameters and initial conditions. Thus, the model (2) can be applied to describe some kinds of disturbances in engineering applications. It is shown that harmonic disturbances with unknown frequency, amplitude, and phase are special cases of this model (2), and the coefficient matrices A, C are described as follows

$$A = \begin{bmatrix} 0 & a \\ a & 0 \end{bmatrix}, \; C = [c \;\; 0] \tag{3}$$

where $a > 0$ represents the frequency of harmonic disturbances.

In this paper, we need to structure the nonlinear disturbance observer for the unknown disturbances so that the disturbances can be estimated. It can be guaranteed that the disturbance estimation error system is asymptotically stable.

3 Two-Step Nonlinear Disturbance Observer (TSNDO)

Before the design of TSNDO, some definition and preliminary result are required, which are stated as follows:

According to relevant references [14, 15], there is a unique constant vector $\theta \in \mathbb{R}^n$ for any Hurwitz matrix $N \in \mathbb{R}^{n\times n}$ such that the disturbance $d(t)$ can be presented in the form

$$d = \theta^T \varphi + \theta^T \delta \tag{4}$$

where $\varphi \in \mathbb{R}^n$, the system satisfies

$$\dot{\varphi} = N\varphi + Ld \tag{5}$$

where (N, L) is controllable, $\dot{\delta} = N\delta$, $\delta(0) = Mw(0) - \varphi(0)$, and $\theta^T = CM^{-1}$.

The matrix M is a solution to the Sylvester matrix equation

$$MA - NM = LC \tag{6}$$

Introducing auxiliary variable $\xi = \varphi + \delta$, the disturbance can be presented in the form

$$d = \theta^T \xi \tag{7}$$

$$\dot{\xi} = G\xi + Ld \tag{8}$$

If N and L are selected as follow

$$N = \begin{bmatrix} 0 & 1 & & \\ \vdots & & \ddots & \\ 0 & & & 1 \\ -n_0 & -n_1 & \cdots & -n_{n-1} \end{bmatrix}, \; L = \begin{bmatrix} 0 \\ 0 \\ \vdots \\ 1 \end{bmatrix} \tag{9}$$

where $N \in \mathbb{R}^{n\times n}$ is Hurwitz matrix, (N, L) is controllable, $n_0, n_1, \ldots, n_{n-1}$ are unknown constant.

In order to estimate the unknown disturbance $d(t)$, two-step nonlinear disturbance observer is designed.

The design of first-step nonlinear disturbance observer

$$\hat{\xi} = \eta + \psi(x) \tag{10}$$

$$\dot{\eta} = N\eta + N\psi(x) - \frac{\partial \psi}{\partial x} f(x) \tag{11}$$

$$\frac{\partial \psi}{\partial x} g(x) = L \tag{12}$$

where $\hat{\xi}$ is the estimation of ξ, η and $\psi(x)$ are auxiliary vectors as the state of the first-step nonlinear disturbance observer.

The estimation error of ξ is denoted as $e_\xi = \xi - \hat{\xi}$. Based on (10)–(12), its derivative gains

$$\begin{aligned} \dot{e}_\xi &= \dot{\xi} + \dot{\eta} + \dot{\psi}(x) \\ &= N\xi + Ld(t) - N\eta - N\psi(x) + \frac{\partial \psi}{\partial x} f(x) - \frac{\partial \psi}{\partial x}(f(x) + g(x)d(t)) \\ &= N\xi + Ld(t) - N\eta - N\psi(x) + \frac{\partial \psi}{\partial x} f(x) - \frac{\partial \psi}{\partial x} f(x) - \frac{\partial \psi}{\partial x} g(x)d(t) \\ &= N(\xi - \eta - \psi(x)) \\ &= Ne_\xi \end{aligned} \tag{13}$$

The construction of second-step nonlinear disturbance observer

$$\hat{\theta} = z + p \tag{14}$$

$$\dot{z} = -s\hat{\xi}^T N\hat{\xi} - s\hat{\xi}^T L\hat{\xi}^T\hat{\theta} \tag{15}$$

$$p = \frac{1}{2} s\hat{\xi}^T\hat{\xi} \tag{16}$$

where $s \in \mathbb{R}^n$ satisfying $s\hat{\xi}^T = \hat{\xi}L^T$. z and p are auxiliary vectors. $\hat{\theta}$ is the estimation of θ.

Differentiating estimation error $e_\theta = \hat{\theta} - \theta$, we obtain the following error model

$$\dot{e}_\theta = \dot{\hat{\theta}} - \dot{\theta} = \dot{z} + \dot{p} - \dot{\theta} = -s\hat{\xi}^T L e_\theta^T \hat{\xi} + s\hat{\xi}^T L \theta^T e_\xi \tag{17}$$

Based on the two-step disturbance observer, the following result can be obtained.

Theorem 1 *Consider nonlinear system (1) with disturbance (2) under Assumption 1. By designing the two-step disturbance observer (10)–(12) and (14)–(16), if there exists a positive definite matrix P, two scalars $\lambda > 0$ and $\varepsilon > 0$ satisfying*

$$N^T P + PN + \lambda I < 0 \tag{18}$$

$$\|\theta\|^2 + 4\varepsilon = 4\lambda \tag{19}$$

the estimation error system of disturbance consisting of the plant (13) and (17) is asymptotically stable.

Proof Based on construction of the first-step disturbance observer, the disturbance (2) describe as

$$d(t) = \theta^T \hat{\xi} + \theta^T e_\xi \tag{20}$$

combining the estimation error system of disturbance consisting of the plant (13) and (17), consider the Lyapunov function candidate $V(t)$ as

$$V(t) = \frac{1}{2} e_\theta^T e_\theta + e_\xi^T P e_\xi \tag{21}$$

By differentiating $V(t)$ with respect to time, it can be shown that

$$\dot{V}(t) = e_\theta^T \dot{e}_\theta + \dot{e}_\xi^T P e_\xi + e_\xi^T P \dot{e}_\xi \tag{22}$$

Substitution of (13) and (17) into (22) yields

$$\begin{aligned}
\dot{V}(t) &= e_\theta^T \dot{e}_\theta + \dot{e}_\xi^T P e_\xi + e_\xi^T P \dot{e}_\xi \\
&= e_\theta^T (-s\hat{\xi}^T L e_\theta^T \hat{\xi} + s\hat{\xi}^T L \theta^T e_\xi) + e_\xi^T (N^T P + PN) e_\xi \\
&< -e_\theta^T \hat{\xi} L^T L \hat{\xi}^T e_\theta + e_\theta^T \hat{\xi} L^T L \theta^T e_\xi - \lambda e_\xi^T e_\xi \\
&\le -e_\theta^T \hat{\xi} L^T L \hat{\xi}^T e_\theta + \| e_\theta^T \hat{\xi} L^T \| \| L \theta^T \| \| e_\xi \| - \lambda e_\xi^T e_\xi \\
&\le -\| e_\theta^T \hat{\xi} L^T \|^2 + \| e_\theta^T \hat{\xi} L^T \| \| L \| \| \theta^T \| \| e_\xi \| - \lambda \| e_\xi \|^2 \\
&= -\| e_\theta^T \hat{\xi} L^T \|^2 + \| e_\theta^T \hat{\xi} L^T \| \| \theta^T \| \| e_\xi \| - \lambda \| e_\xi \|^2 \\
&= -\| e_\theta^T \hat{\xi} L^T \|^2 + \| e_\theta^T \hat{\xi} L^T \| \| \theta \| \| e_\xi \| - \lambda \| e_\xi \|^2 \\
&= -\| e_\theta^T \hat{\xi} L^T \|^2 - \lambda \| e_\xi \|^2 + 2\left(\frac{\|\theta\|}{2} \| e_\xi \|\right) \| e_\theta^T \hat{\xi} L^T \|
\end{aligned} \tag{23}$$

Using the Young inequality acquire,

$$\begin{aligned}\dot{V}(t) &< -\|e_\theta^T\hat{\xi}L^T\|^2 - \lambda\|e_{\tilde{\xi}}\|^2 + 2(\frac{\|\theta\|}{2}\|e_{\tilde{\xi}}\|)\|e_\theta^T\hat{\xi}L^T\| \\ &\leq -\|e_\theta^T\hat{\xi}L^T\|^2 - \lambda\|e_{\tilde{\xi}}\|^2 + \|e_\theta^T\hat{\xi}L^T\|^2 + (\frac{\|\theta\|^2}{4})\|e_{\tilde{\xi}}\|^2 \\ &= -(\|e_\theta^T\hat{\xi}L^T\|^2 + \|e_\theta^T\hat{\xi}L^T\|^2) + (\frac{\|\theta\|^2}{4} - \lambda)\|e_{\tilde{\xi}}\|^2 \\ &= (\frac{\|\theta\|^2}{4} - \lambda)\|e_{\tilde{\xi}}\|^2 \end{aligned} \tag{24}$$

$\dot{V}(t) < -\varepsilon\|e_{\tilde{\xi}}\|^2$ can be guaranteed by (19), then $\dot{V}(t) < 0$. Hence, the result.

Remark 2 The disturbance estimation is $\hat{d}(t) = \hat{\theta}^T\hat{\xi}$, what is more, the disturbance estimation error is denoted as $e = d - \hat{d}$. so we can obtain estimation error of disturbance

$$e = \theta^T e_{\tilde{\xi}} - e_\theta^T\hat{\xi} \tag{25}$$

$e_\theta \to 0$, $e_{\tilde{\xi}} \to 0$, as $t \to \infty$, and $\dot{\hat{\xi}} = N\xi + Ld$. N is Hurwitz matrix. θ is an unknown constant vector, L is chosen in (9) and disturbance is bounded, so $e \to 0$ ($t \to \infty$). It is given to demonstrate the effectiveness of TSNDO.

4 Simulation Example

To show the efficiency of the proposed scheme, a numerical simulation is given in this paper. The second-order nonlinear system is described as follows:

$$\begin{cases} \dot{x}_1 = -x_1^2 - x_1x_2 + x_2 \\ \dot{x}_2 = -x_2^3 + x_2^2 + x_1x_2 - x_1 - 6x_2 + (1 + \sin^2 x_1)d(t) \\ y = x_1 + x_2 \end{cases} \tag{26}$$

where $x = [x_1, x_2]^T$ *and*y are the system states and output, respectively. what is more, $d(t)$ is assumed to be an unknown harmonic disturbance described by (2) with

$$A = \begin{bmatrix} 0 & 15.6 \\ -10 & 0 \end{bmatrix},\ C = [19.86\ \ 0],\ N = \begin{bmatrix} 0 & 1 \\ -66 & -10 \end{bmatrix},\ L = \begin{bmatrix} 0 \\ 1 \end{bmatrix}$$

Based on Theorem 1 we can select $\lambda = 100$ and $\psi(x) = [6; x_2]$. Moreover, in the simulation of state and the initial value of secondary variables are as follows:

$x_1(0) = 16.8$, $x_2(0) = 50$, $z(0) = [0.982; 11.123]$, $\eta(0) = [-16.757; -48.456]$

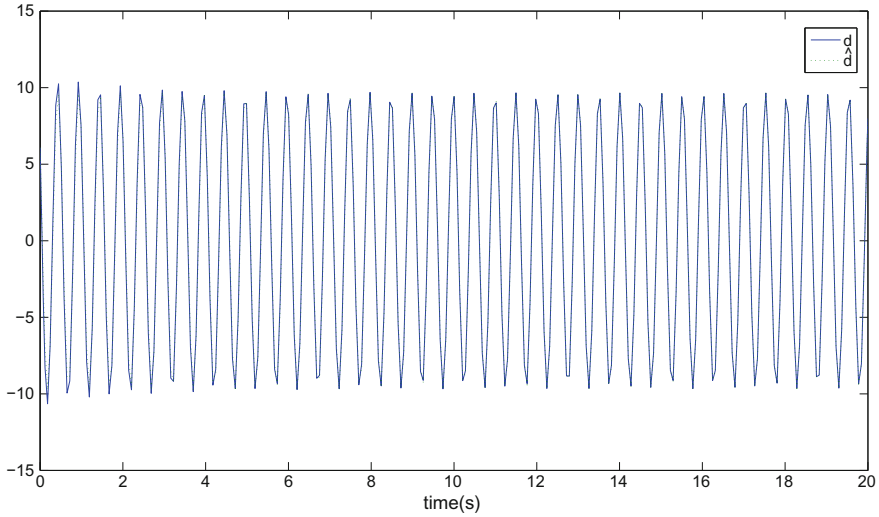

Fig. 1 The response curves are d (*solid line*) and $\hat{d}$ (*dash line*)

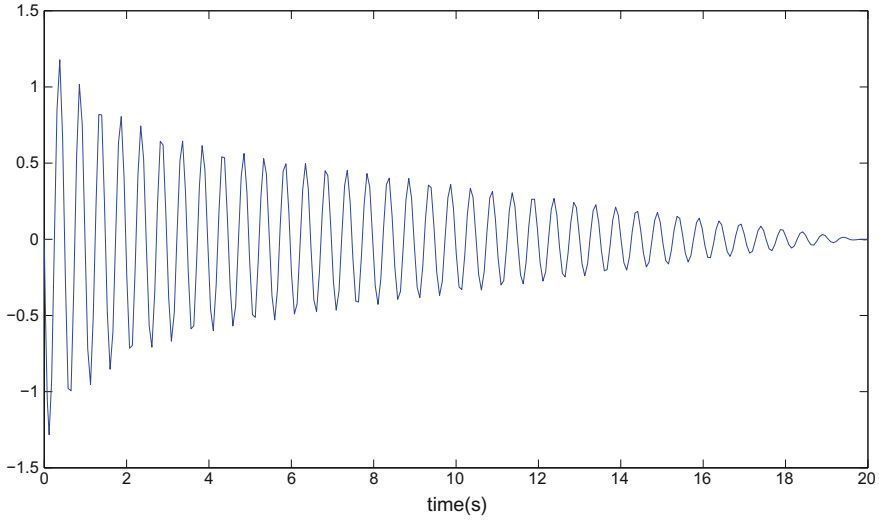

Fig. 2 The estimation error of disturbance using TSNDO

The simulation results are shown in Figs. 1 and 2.

Figures 1 and 2 illustrate disturbance estimation response curve and disturbance estimation error response curve, respectively. The simulation results show that although the disturbance frequency, amplitude, and initial phase are unknown, two-step disturbance observer can still well estimate disturbance and make disturbance estimation error for the asymptotic stability.

5 Conclusions

This paper shows that the proposed TSNDO scheme is an effective estimation disturbance approach for a class of general nonlinear systems subject to unknown disturbance. Theoretic results obtained for the TSNDO scheme can guarantee asymptotic stability of the disturbance eliminate error. However, the disturbance is single disturbance in this paper. In practical engineering, many complex systems can be affected by multiple disturbances. One of the challenges for further research is to find a novel anti-disturbance control approach for a class of general nonlinear system with multiple unknown disturbances.

References

1. Peng J, Chen X (2013) A survey of modeling and control of piezoelectric actuators. Modern Mech Eng 03(1):1–20
2. Harnefors L, Nee H (1998) Model-based current control of AC machines using the internal model control method. IEEE Trans Ind Appl 34(1):133–141
3. Byrnes CI, Priscoli FD, Isidori A (1990) Output regulation of nonlinear systems. IEEE Trans Autom Control 35(2):131–140
4. Yi H, Xue W (2014) Active disturbance rejection control: methodology and theoretical analysis. ISA Trans 53(4):963–976
5. Chen W (2004) Disturbance observer based control for nonlinear systems. IEEE/ASME Trans Mechatron 51(12):706–710
6. Wei X, Chen N (2014) Composite hierarchical anti-disturbance control for nonlinear systems with DOBC and fuzzy control. Int J Robust Nonlinear Control 24:362–373
7. Guo L, Chen WH (2005) Disturbance attenuation and rejection for systems with nonlinearity via DOBC approach. Int J Robust Nonlinear Control 15:109–125
8. Nakao M, Ohnishi K, Miyachi K (1987) A robust decentralized joint control based on interference estimation. In: Proceedings of the IEEE international conference on robotics and automation, pp 326–331
9. Guo L, Cao S (2013) Anti-disturbance control for systems with multiple disturbances. CRC Press
10. Li S, Yang J, Chen W et al (2014) Disturbance observer-based control:methods and applications. CRC press
11. Nikiforov VO (2004) Observers of external deterministic disturbances. I. Objects with known parameters. Autom Remote Control 65(10):1531–1541
12. Basturk HI, Krstic M (2014) State derivative feedback for adaptive cancellation of unmatched disturbances in unknown strict-feedback LTI systems. Automatica 50(10):2539–2545
13. Wen X, Guo L, Zhang Y (2011) Estimation of unknown sinusoidal disturbances using two-step nonlinear observer. In: Proceedings of the 30th Chinese control conference, pp 22–24
14. Nikiforov VO (1998) Adaptive non-linear tracking with complete compensation of unknown disturbances. Eur J Control 4(2):132–139
15. Nikiforov VO (2001) Nonlinear servo-compensation of unknown external disturbances. Automatic 37(10):1647–1653

Containment Consensus of Multi-agent Systems with Communication Noises

Fusheng Wang and Hongyong Yang

Abstract Containment control of multi-agent systems with switching topologies and communication noises is studied. In order to attenuate the effect of noises, containment control algorithm with multiple leaders is presented, where a positive time-varying gain is employed in the protocol. The stability of control algorithm is studied with the assumption that communication topology is jointly connected. Some constraint conditions of multi-agent systems are derived with the aid of modern control theory and stochastic analysis. Simulation results are provided to verify the correctness and effectiveness of the conclusion.

Keywords Containment control · Multi-agent systems · Communication noise

1 Introduction

Recently, cooperative control of multi-agent systems has attracted great attentions in the fields of control theory, mathematics, computer science, etc. Due to communication noises and disconnected topologies emergence in practical applications, distributed cooperative problem are more complex and difficult.

Containment control has been paid much more attention [1–3], which aims to control followers eventually converging to a target area formed by the leaders. In [4], distributed containment control of multi-agent systems with measurement noises was considered, and a stochastic approximation type and consensus-like algorithm was proposed. In [5], containment control problem for multi-agent systems with transmission noises was studied, and some sufficient conditions were derived to guarantee the mean square containment. In [6], containment of first-order and second-order multi-agent systems with communication noises was investigated. By using graph theory and stochastic analysis, containment control was investigated, and many mean square convergences were derived [7]. In [8], the distributed

F. Wang · H. Yang (✉)
School of Information and Electrical Engineering, Ludong University, Yantai 264025, China
e-mail: hyyang@yeah.net

Y. Jia et al. (eds.), *Proceedings of 2016 Chinese Intelligent Systems Conference*,
Lecture Notes in Electrical Engineering 404, DOI 10.1007/978-981-10-2338-5_19

containment tracking control for multiple leaders system under directed Markovian switching network topologies was investigated, and some necessary and sufficient conditions were presented for the containment tracking in the asymptotic unbiased mean square sense.

In this paper, distributed coordination control problem for multi-agent systems with multiple leaders and communication noises is studied. By applying modern control theory and stochastic analysis, the convergence of control algorithm for multi-agent systems with jointly connected topologies is studied.

2 Preliminaries

Let $G=(V,E)$ be an undirected graph of order n, where $V=\{v_1, v_2, \ldots, v_n\}$ is the set of nodes, $E=\{(v_i,v_j): v_i, v_j \in V\}$ is the set of edges. If $(v_j,v_i)\in E$, then v_j is the neighbor of v_i. The neighbors set of node v_i is denoted by $N_i=\{v_j\in V|(v_i,v_j)\in E, j\neq i\}$. A path from v_i to v_j is denoted by $\pi_{i,j}=\{(v_{i1},v_{i2}),(v_{i2},v_{i3}),\ldots,(v_{im-1},v_{im})\}$, where $v_{i1}=v_i, v_{im}=v_j$ and $(v_{ik},v_{ik+1})\in E$, $k\in\{1,2,\cdots,m-1\}$. If there is a path between any distinct pair of nodes then the undirected graph is said to be connected. The union of a collection of graphs $G_1, G_2, \cdots, G_m$ with the same node set V, is defined as the graph G_{1-m} with the node set V and edge set equalling to the union of the edge sets of all of the graphs. Moreover, $G_1, G_2, \cdots, G_m$ is jointly connected if its union graph G_{1-m} is connected.

The weighted adjacency matrix $A=[a_{ij}]\in\mathbb{R}^{n\times n}$ of undirected graph G satisfies $a_{ij}\geq 0$, where $a_{ij}>0$ if $(v_i,v_j)\in E$, $a_{ij}=0$ otherwise. The Laplacian matrix corresponding to the undirected graph G is defined as $L=[l_{ij}]\in\mathbb{R}^{n\times n}$, where l_{ij} is defined as follows:

$$l_{ij}=\begin{cases} -a_{ij}, & i\neq j,\\ \sum\limits_{j\in N_i} a_{ij}, & i=j. \end{cases}$$

Definition 1 Let $X=\{x_1,x_2,\cdots,x_m\}$ be a set in a real vector space $V\subseteq\mathbb{R}$. The convex hull $CO(X)$ of the set X is denoted as

$$CO(X)=\{\sum_{i=1}^{m}\alpha_i x_i | x_i\in X, \alpha_i\in\mathbb{R}, \alpha_i\geq 0,$$

Consider an infinite sequence of nonempty, bounded and contiguous time intervals $[t_r,t_{r+1})$, $r=1,2,\cdots$, with $t_1=0$ and $t_{r+1}-t_r\leq T_a$ for some constant $T_a>0$. In each interval $[t_r,t_{r+1})$ there is a sequence of subintervals $[t_{r,j},t_{r,j+1})$, $j=1,2,\cdots,m_r$ with $t_{r,1}=t_r$ and $t_{r,m_r+1}=t_{r+1}$ satisfying $t_{r,j+1}-t_{r,j}\geq T_b$, $j=1,2,\cdots,m_r$ for some integer $m_r\geq 1$ and given constant $T_b>0$. Such that the communication topology described by $G_{r,j}$ switches at $t_{r,j}$ and it does not change

during each subinterval $[t_{r,j}, t_{r,j+1})$. Let $\sigma(t): [0, +\infty) \to \Gamma$, $\Gamma = \{1, 2, \cdots, N\}$ (N denotes the total number of all possible topologies), be a piecewise constant switching function. $G_{\sigma(t)}$ denotes the information topology of multi-agent systems at time t, and its Laplacian is denoted by $L_{\sigma(t)}$.

3 Mean Square Containment Control of Multi-agent Systems

Suppose that multi-agent systems with m leaders and $n-m$ followers have the following dynamics

$$\dot{x}_i(t) = u_i(t), \quad i = 1, 2, \cdots, n. \tag{1}$$

where $x_i(t) \in \mathbb{R}$, $u_i(t) \in \mathbb{R}$ are the state and the control input of the ith agent, respectively.

Suppose the information of agent i receiving from its neighbor agent j is corrupted by the additive communication noise $\sigma_{ij}\mu_{ij}(t)$, where $\mu_{ij}(t)$ is the standard white noise and $\sigma_{ij} > 0$ is the finite noise intensity, satisfying $\mu_{ij}(t) = \mu_{ji}(t)$, $\sigma_{ij} = \sigma_{ji}$. Then the real information that agent i receives from agent j is $\xi_{ij}(t) = x_j(t) + \sigma_{ij}\mu_{ij}(t)$. It is also assumed that $\{\mu_{ij}(t) | i = 1, \cdots, n;\ j = 1, \cdots, n\}$ are mutually independent, that is, $E\{\mu_{ij}(t)\mu_{kl}(t)\} = 0, \forall \{i, j\} \neq \{k, l\}$.

Definition 3 ([9]). The mean square containment problem of multi-agent systems with communication noises is said to be solved if for any initial states $(x_1(0), \cdots, x_n(0))^{\mathrm{T}} \in \mathbb{R}^n$, there exist deterministic variables $x_i^* \in Co_L \triangleq Co\{\hat{x}_1, \cdots \hat{x}_m\} = \{\sum_{j=1}^{m} \alpha_j \hat{x}_j | \alpha_j \geq 0, \sum_{j=1}^{m} \alpha_j = 1\}$ (Co_L denotes the convex hull spanned by the leaders' final states $\hat{x}_j \triangleq \lim_{t \to \infty} x_j(t)$, $j = 1, \cdots, m$) such that $\lim_{t \to \infty} |x_i(t) - x_i^*| = 0$, $i = m+1, m+2, \cdots, n$.

Considering the case of stationary leaders, and suppose the control protocol of first-order multi-agent systems is

$$u_i(t) = b(t) \sum_{j \in N_i} a_{ij}(t)(\xi_{ij}(t) - x_i(t)), \tag{2}$$

where $b(t) > 0$ is a continuous time-varying function.

Definition 4 $L = \begin{bmatrix} 0_{m \times m} & 0_{m \times (n-m)} \\ L_1 & L_2 \end{bmatrix}$ is the Laplacian matrix of graph G, where $L_1 \in \mathbb{R}^{(n-m) \times m}$, $L_2 \in \mathbb{R}^{(n-m) \times (n-m)}$.

According to Definition 4, the system (1–2) can be written as

$$\dot{x}(t) = -b(t)Lx(t) + b(t)H\mu(t) \tag{3}$$

where $x(t) = [x_1(t), x_2(t), \cdots, x_n(t)]^{\mathrm{T}}$, and $\mu(t) = [\mu_1^{\mathrm{T}}(t), \mu_2^{\mathrm{T}}(t), \cdots, \mu_n^{\mathrm{T}}(t)]^{\mathrm{T}}$ is the n^2 dimensional standard white noise vector, $\mu_i(t) = (\mu_{i1}(t), \cdots, \mu_{in}(t))^{\mathrm{T}}$, $H = diag(E_1, \cdots, E_n)$, $E_i = (a_{i1}\sigma_{i1}, \cdots, a_{in}\sigma_{in})$, $i = 1, \cdots, n$.

By the knowledge of stochastic process, the standard white noise is the generalized mean square derivative of standard Brownian motion. Then this stochastic system is equivalent to the following *Itô* stochastic differential equation

$$\begin{cases} dx_L(t) = 0_{m\times 1} \\ dx_F(t) = -b(t)(L_1 x_L(t) + L_2 x_F(t))dt + b(t)H_2 dW(t) \end{cases} \tag{4}$$

where $x_L(t) = (x_1(t), x_2(t), \cdots, x_m(t))^{\mathrm{T}}$, $x_F(t) = (x_{m+1}(t), \cdots, x_n(t))^{\mathrm{T}}$, and $W(t)$ is an $n(n-m)$ dimensional standard Brownian motion, $H_1 = diag(E_1, \cdots, E_m) = 0_{mn\times m}$, $H_2 = diag(E_{m+1}, \cdots, E_n) \in \mathbb{R}^{(n-m)\times n(n-m)}$.

Before further discussion, the following three conditions are presented for first-order multi-agent systems.

(A1) The communication topologies of multi-agent systems, in each interval $[t_r, t_{r+1}), r = 1, 2, \cdots,$ are jointly connected;

(A2) There exists a connectivity subset for multi-agent systems in each nonoverlapping time intervals $[t_{r,j}, t_{r,j+1}) \subset [t_r, t_{r+1}), j = 1, 2, \cdots, m_r$. For each follower, there exists at least one leader that has a path to the follower in this subset;

(A3) $\int_0^{\infty} b(t)dt = \infty$.

Lemma 1 ([9]). *For undirected graph G, if condition (A2) holds, then L_2 is positive definite, $-L_2^{-1}L_1$ is a nonnegative matrix and the sum of the entries in every row equals to 1.*

Let $\tilde{x}_F(t) = x_F(t) + L_2^{-1}L_1 x_L(t)$, then Eq. (4) can be written as

$$\mathrm{d}\tilde{x}_F(t) = -b(t)L_2\tilde{x}_F(t)\mathrm{d}t + b(t)H_2\mathrm{d}W(t) \tag{5}$$

Lemma 2 *Let $\hat{x}_L = \lim_{t\to\infty} x_L(t) = [\hat{x}_1, \cdots, \hat{x}_m]^{\mathrm{T}}$, if $\lim_{t\to\infty} \tilde{x}_F(t) = 0$, then the mean square containment control of the multi-agent system can be achieved.*

Proof From Lemma 1 and Definition 2, we can know $-L_2^{-1}L_1$ is a nonnegative matrix and the sum of the entries in every row equals to 1. Then $-L_2^{-1}L_1\hat{x}_L$ is located in the convex hull formed by those stationary leaders, where $\hat{x}_L = \lim_{t\to\infty} x_L(t) = [\hat{x}_1, \cdots, \hat{x}_m]^{\mathrm{T}}$. Thus, if $\lim_{t\to\infty} \tilde{x}_F(t) = 0$, i.e., $\lim_{t\to\infty} x_F(t) = -L_2^{-1}L_1\hat{x}_L$, then the containment control of multi-agent systems can be achieved. □

Lemma 3 *Consider the following differential equation*

$$\dot{y}(t) = -b(t)\Delta_s(\lambda)y(t) \tag{6}$$

where $y(t) = (y_1(t), y_2(t), \cdots, y_s(t))^{\mathrm{T}}$, $\Delta_s(\lambda) = \mathrm{diag}\{\lambda_1, \cdots, \lambda_s\} \in \mathbb{R}^{s\times s}$, $\lambda_k > 0$, $k = 1, 2, \cdots s$. *The state transition matrix of (6) is*

$$\Phi(t, t_0) = diag\{\phi_{\lambda_1}(t, t_0), \cdots, \phi_{\lambda_s}(t, t_0)\} \tag{7}$$

where $\phi_{\lambda_k}(t, t_0) = e^{-\lambda_k \int_{t_0}^{t} b(\tau)d\tau}$, $k = 1, 2, \cdots s$.

Suppose the communication graph G_σ on subinterval $[t_{r,j}, t_{r,j+1})$ has n_σ connected subgraphs G_σ^i, $i = 1, 2, \cdots, n_\sigma$, and each connected subgraph G_σ^i has d_σ^i nodes, where $\{1, \cdots, d_{\sigma L}^i\}$ represents the set of leaders, $\{d_{\sigma L+1}^i, \cdots, d_\sigma^i\}$ represents the set of followers. The Laplacian matrix of subgraph G_σ^i is denoted by L_σ^i. Then there exists a orthogonal matrix U_σ such that

$$U_\sigma^{\mathrm{T}} L_\sigma U_\sigma = \mathrm{diag}\{L_\sigma^1, L_\sigma^2, \cdots, L_\sigma^{n_\sigma}\} \tag{8}$$

$$U_\sigma^{\mathrm{T}} H_\sigma U_\sigma = \mathrm{diag}\{E_{\sigma 1}^1, E_{\sigma 2}^2, \cdots, E_{\sigma d_\sigma^i}^{n_\sigma}\} \tag{9}$$

$$U_\sigma^{\mathrm{T}} H_{\sigma 2} U_\sigma = \mathrm{diag}\{E_{\sigma d_{\sigma L}^i+1}^1, E_{\sigma d_{\sigma L}^i+2}^2, \cdots, E_{\sigma d_\sigma^i}^{n_\sigma}\} \tag{10}$$

$$x_F(t)U_\sigma = (x_{\sigma F}^1(t), x_{\sigma F}^2(t), \cdots, x_{\sigma F}^{n_\sigma}(t))^{\mathrm{T}} \tag{11}$$

$$x_L(t)U_\sigma = (x_{\sigma L}^1(t), x_{\sigma L}^2(t), \cdots, x_{\sigma L}^{n_\sigma}(t))^{\mathrm{T}} \tag{12}$$

$$W(t)U_\sigma = (W_\sigma^1(t), W_\sigma^2(t), \cdots, W_\sigma^{n_\sigma}(t))^{\mathrm{T}} \tag{13}$$

where $L_\sigma^i = \begin{bmatrix} 0_{d_{\sigma L}^i \times d_{\sigma L}^i} & 0_{d_{\sigma L}^i \times (d_\sigma^i - d_{\sigma L}^i)} \\ L_{\sigma 1}^i & L_{\sigma 2}^i \end{bmatrix}$, $E_{\sigma k}^i = (a_{k1}\sigma_{k1}, \cdots, a_{kd_\sigma^i}\sigma_{kd_\sigma^i})$, $k = 1, \cdots, d_\sigma^i$, $i = 1, 2, \cdots, n_\sigma$.

According to the above description, Eq. (5) can be written as

$$d\tilde{x}_F(t) = -b(t)L_{\sigma 2}\tilde{x}_F(t)\mathrm{d}t + b(t)H_{\sigma 2}\mathrm{d}W(t) \tag{14}$$

The system (14) can be transformed into the following subsystems dynamic in each subinterval $[t_{r,j}, t_{r,j+1})$

$$d\tilde{x}_{\sigma F}^i(t) = -b(t)L_{\sigma 2}^i\tilde{x}_{\sigma F}^i(t)dt + b(t)H_{\sigma 2}^i dW_\sigma^i(t) \tag{15}$$

where $\tilde{x}_{\sigma F}^i(t) = x_{\sigma F}^i(t) + L_{\sigma 2}^{i-1}L_{\sigma 1}^i x_{\sigma L}^i(t)$, $x_{\sigma L}^i(t) = (x_{\sigma 1}^i(t), \cdots, x_{\sigma d_{\sigma L}^i}^i(t))^{\mathrm{T}}$, $x_{\sigma F}^i(t) = (x_{\sigma d_{\sigma L}^i+1}^i(t), \cdots, x_{\sigma d_\sigma^i}^i(t))^{\mathrm{T}}$, $L_{\sigma 2}^i \in \mathbb{R}^{(d_\sigma^i - d_{\sigma L}^i)\times(d_\sigma^i - d_{\sigma L}^i)}$, $L_{\sigma 1}^i \in \mathbb{R}^{(d_\sigma^i - d_{\sigma L}^i)\times d_{\sigma L}^i}$,

$H^i_{\sigma 2} = \mathrm{diag}(E^i_{\sigma d^i_{\sigma L}+1}, \cdots, E^i_{\sigma d^i_\sigma}) \in \mathbb{R}^{(d^i_\sigma - d^i_{\sigma L}) \times d^i_\sigma (d^i_\sigma - d^i_{\sigma L})}$, $E^i_{\sigma k} = (a_{k1}\sigma_{k1}, \cdots, a_{kd^i_\sigma}\sigma_{kd^i_\sigma})$, $k = 1, \cdots, d^i_\sigma$, and $W^i_\sigma(t)$ is an $d^i_\sigma(d^i_\sigma - d^i_{\sigma L})$ dimensional standard Brownian motion, $i = 1, 2, \cdots, n_\sigma$.

Theorem 1 *Consider first-order dynamic system (1) with n followers and m leaders under switching topologies. Suppose conditions (A1), (A2) and (A3) hold, and then control protocol (2) can solve the mean square containment control of first-order multi-agent systems with communication noises and dynamical topologies.*

Proof There exists a transformation matrix P such that

$$P^{-1} L^i_{\sigma 2} P = \Lambda \tag{16}$$

where $\Lambda = diag\{\lambda_1, \cdots \lambda_{d^i_\sigma - d^i_{\sigma L}}\}$ is the diagonal matrix of $L^i_{\sigma 2}$, $\lambda_l > 0$, $l = 1, \cdots, (d^i_\sigma - d^i_{\sigma L})$.

According to Lemma 3, the state transition matrix of (15) is

$$\Phi(t, t_{r,j}) = P diag\{\phi_{\lambda_1}(t, t_{r,j}), \cdots, \phi_{\lambda_{d^i_\sigma - d^i_{\sigma L}}}(t, t_{r,j})\} P^{-1} \tag{17}$$

If Conditions (A2) and (A3) hold, it is obtained from Lemma 3, for any $t \in [t_{r,j}, t_{r,j+1})$

$$\lim_{t \to \infty} \Phi(t, t_{r,j}) = 0_{(d^i_\sigma - d^i_{\sigma L}) \times (d^i_\sigma - d^i_{\sigma L})} \tag{18}$$

The solution of *Itô* stochastic differential Eq. (15) in each subinterval $[t_{r,j}, t_{r,j+1})$ can be written as

$$\tilde{x}^i_{\sigma F}(t) = \Phi(t, t_{r,j}) \tilde{x}^i_{\sigma F}(t_{r,j}) + Y^i_\sigma(t) \tag{19}$$

where $Y^i_\sigma(t) = \int_{t_{r,j}}^t b(\tau) \Phi(t, \tau) H^i_{\sigma 2} dW^i_\sigma(\tau)$, $t \in [t_{r,j}, t_{r,j+1})$.

The second-order moment matrix of $Y^i_\sigma(t)$ satisfies $E(Y^i_\sigma(t) Y^{iT}_\sigma(t)) = \int_{t_{r,j}}^t b^2(\tau) \Phi(t, \tau) H^i_{\sigma 2} H^{i\mathrm{T}}_{\sigma 2} \Phi^{\mathrm{T}}(t, \tau) d\tau$, and each element of $E(Y^i_\sigma(t) Y^{i\mathrm{T}}_\sigma(t))$ is a linear combination of the following terms

$$\eta_{\lambda_l} = \int_{t_{r,j}}^t b^2(\tau) \phi^2_{\lambda_l}(t, t_{r,j}) d\tau \tag{20}$$

where $t \in [t_{r,j}, t_{r,j+1})$, $l = 1, \cdots, (d^i_\sigma - d^i_{\sigma L})$.

According to Lemma 3 and condition (A3), we have $\lim_{t \to \infty} \phi^2_{\lambda_l}(t, t_{r,j}) = \lim_{t \to \infty} e^{-2\lambda_l \int_{t_{r,j}}^t b(\tau) d\tau} = 0$. Based on Eq. (20), we get $\lim_{t \to \infty} \eta_{\lambda_l} = 0$,

i.e., $\lim_{t\to\infty} E(Y_\sigma^i(t)Y_\sigma^{i\mathrm{T}}(t))=0$. We obtain $\lim_{t\to\infty} Y_\sigma^i(t)=0$ from Definition 3. Therefore, we have $\lim_{t\to\infty} \tilde{x}_{\sigma F}^i(t)=0$ as $t\to+\infty$ from (19), then $\lim_{t\to\infty} x_{\sigma F}^i(t)=-L_{\sigma 2}^{i-1}L_{\sigma 1}^i x_{\sigma L}^i(t)$.

Furthermore, in any subinterval $[t_{r,j},t_{r,j+1})\subset[t_r,t_{r+1})$, $j=1,2,\cdots,m_r$, $\lim_{t\to+\infty} x_{\sigma F}^i(t)=-L_{\sigma 2}^{i-1}L_{\sigma 1}^i x_{\sigma L}^i(t)$, $i=1,2,\cdots,n_\sigma$. Therefore, in the connected portion of multi-agent systems in the subinterval $[t_{r,j},t_{r,j+1})$ and $[t_{r,j+1},t_{r,j+2})$, i.e., in the subinterval $[t_{r,j},t_{r,j+2})$, $\lim_{t\to+\infty} x_{\sigma F}^{i'}(t)=-L_{\sigma 2}^{i-1'}L_{\sigma 1}^{i'}x_{\sigma L}^{i'}(t)$ still holds, $i=1,2,\cdots,n_\sigma^{'},t\to\infty$. Since all agents are jointly connected in each $[t_r,t_{r+1})$, according to condition (A1), $\lim_{t\to\infty} x_F(t)=-L_2^{-1}L_1\hat{x}_L$ by induction, where $\hat{x}_L$ denotes the states of stationary leaders. From Lemma 2, the containment control of multi-agent systems with communication noises can be achieved. □

4 Simulations

In this section, we consider two dynamic switching topologies shown in Fig. 1, where connection weight of each edge is 1. Suppose communication topology of multi-agent systems randomly is switched among $G1$ to $G4$ at $t=kT$, $k=0,1,\cdots$, $T=0.5\,s$.

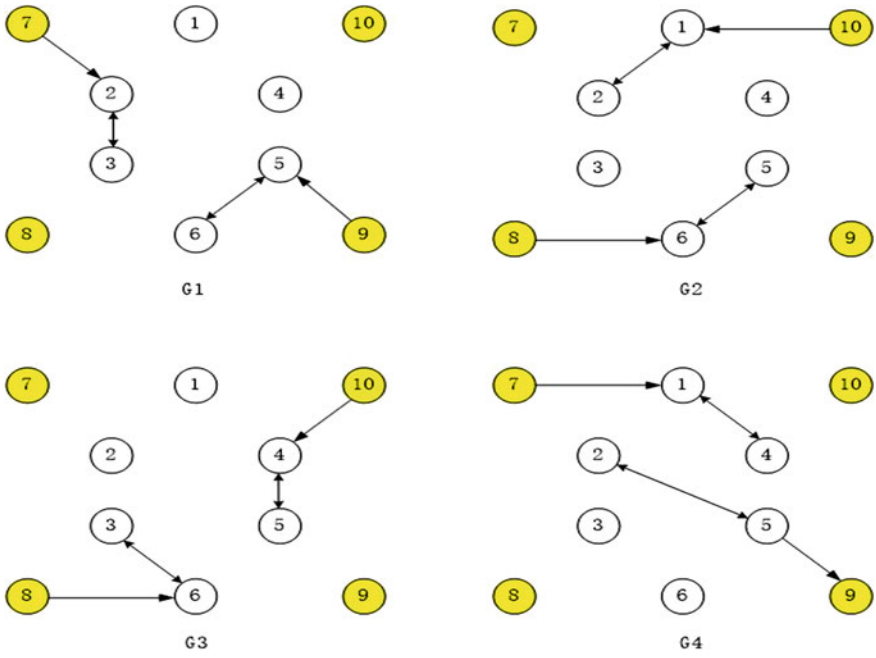

Fig. 1 Communication topology of the multi-agent systems

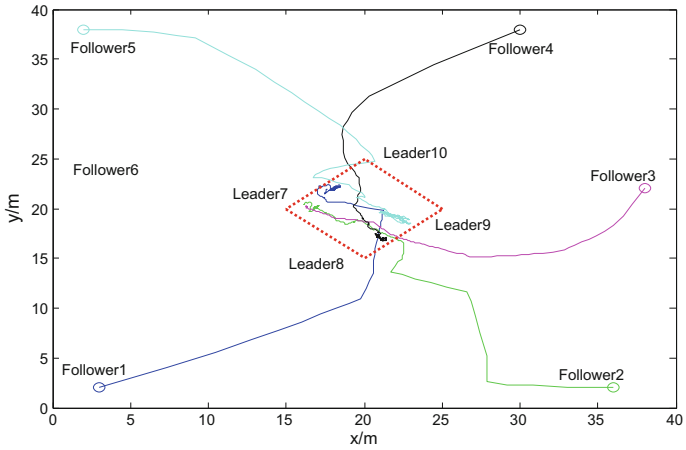

Fig. 2 State trajectories of multi-agent system

We consider four leaders and six followers, whose communication topology is shown in Fig. 1. The initial states of followers and leaders are taken $x_1(0) = (3, 2)$, $x_2(0) = (36, 2)$, $x_3(0) = (38, 22)$, $x_4(0) = (30, 38)$, $x_5(0) = (2, 38)$, $x_6(0) = (2, 22)$; $x_7 = (15, 20)$, $x_8 = (20, 15)$, $x_9 = (25, 20)$, $x_{10} = (20, 25)$, respectively. Simulation results are given in Fig. 2, where followers can asymptotically converge to the plane area formed by four leaders.

5 Conclusion

In this paper, two distributed containment control problems for multi-agent systems with communication noises are studied, and two control algorithms of first-order systems with multiple stationary leaders and jointly connected topologies are proposed. By applying modern control theory and algebraic graph theory, the convergences of distributed containment control algorithms are analyzed on stochastic analysis. Finally, some simulation examples are given to verify the correctness and effectiveness of the conclusion. The mean square containment control for discrete-time systems will be our future work.

Acknowledgments This work is supported by Chinese Scholarship Council (CSC), the National Natural Science Foundation of China (No. 61273152).

References

1. Lin P, Jia YM (2011) Multi-agent consensus with diverse time-delays and jointly-connected topologies. Automatica 47(4):848–856

2. Yang HY, Guo L, Zou HL (2012) Robust consensus of multi-agent systems with time-delays and exogenous disturbances. Int J Control Autom Syst 10(4):797–805
3. Cao YC, Ren W, Egerstedt M (2012) Distributed containment control with multiple stationary or dynamic leaders in fixed and switching directed networks. Automatica 48(8):1586–1597
4. Tang ZJ, Huang TZ, Shao JL (2012) Containment control of multiagent systems with multiple leaders and noisy measurements. In: Abstract and applied analysis. Hindawi Publishing Corporation
5. Liu S, Xie LH, Zhang HS (2013) Mean square containment control of multi-agent systems with transmission noises. Acta Automatica Sinica 39(11):1787–1795
6. Wang YP, Cheng L, Hou ZG et al (2014) Containment control of multi-agent systems in a noisy communication environment. Automatica 50(7):1922–1928
7. Miao GY, Li T (2015) Mean square containment control problems of multi-agent systems under Markov switching topologies. Adv Differ Equ 2015(1):1–10
8. Li WQ, Xie LH, Zhang JF (2015) Containment control of leader-following multi-agent systems with Markovian switching network topologies and measurement noises. Automatica 51:263–267
9. Meng ZY, Ren W, You Z (2010) Distributed finite-time attitude containment control for multiple rigid bodies. Automatica 46(12):2092–2099

Sensor Fault Diagnosis Using Ensemble Empirical Mode Decomposition and Extreme Learning Machine

J. Ji, J. Qu, Y. Chai, Y. Zhou and Q. Tang

Abstract An algorithm using Ensemble Empirical Mode Decomposition (EEMD) and Extreme Learning Machine (ELM) for the detection and classification of sensor fault is presented in this paper. Under this method, the standardized sensor signal is decomposed through EEMD into the original signal, several Intrinsic Mode Functions (IMFs), and residual signal. Then, the variance, reduction ratio and normalized total energy of each IMF and residual are calculated as the sensor fault features. Subsequently, the feature vectors are input into the Extreme Learning Machine (ELM), which is utilized as the classifier for the detection and identification of sensor faults. The fault diagnosis simulation result of the carbon dioxide sensor indicates that this method can not only be effectively applied to the fault diagnosis of carbon dioxide sensors but also provide reference for the fault diagnosis of other sensors.

Keywords Ensemble empirical mode decomposition (EEMD) · Extreme learning machine (ELM) · Intrinsic mode functions (IMFs) · Variance · Energy

1 Introduction

Sensor is not only an indispensable part in any measurement and control system, but also one of the parts most prone to failure. Once the sensor fails due to the cascading effect of the system, it is likely to cause the fault to spread throughout the system, and the consequences could be disastrous. Therefore, sensor fault detection and identification are of extreme importance to improve safety and reliability of system operations.

The process of sensor fault detection and identification is a process of pattern recognition essentially. In the pattern recognition problems, Huang et al. proposed extreme learning machine (ELM) algorithm [1]. This algorithm can not only help

J. Ji · J. Qu (✉) · Y. Chai · Y. Zhou · Q. Tang
School of Automation, Chongqing University, Chongqing 400044, China
e-mail: qujianfeng@cqu.edu.cn

Y. Jia et al. (eds.), *Proceedings of 2016 Chinese Intelligent Systems Conference*,
Lecture Notes in Electrical Engineering 404, DOI 10.1007/978-981-10-2338-5_20

avoid the risk of falling into local optimum, but also greatly improve the network learning speed and generalization performance. The recognition effect of the ELM depends on the effectiveness of the extracted feature, so how to extract the fault features and identify the condition from the signals are the key steps in the fault diagnosis of sensor. The time–frequency analysis method is applied to the feature extraction of sensor fault signals by scholars at home and abroad. As shown in Reference [2], the sensor output signal is performed by wavelet transform (WT). The change rates of energy before and after signal failure are calculated to detect various faults of the pressure sensor on different scales. As can be seen from Reference [3], wavelet packet decomposition is utilized to extract the energy of each node, and the RBF (Radial Basis Function) neural network to diagnose sensor fault. As an automatic decomposition and fully data adaptive method, EMD [4] provides an efficient analysis method for nonstationary and nonlinear signals. Besides, EMD [5] method was considered as a major breakthrough in 2000, and it has been successfully applied in the field of gas detection since then [6]. But one of its important defects is mode mixing. In order to solve this problem, Ensemble Empirical Mode Decomposition (EEMD), an improved version of EMD, has been proposed by Wu and Huang [7], and has been widely applied in fault diagnosis [8, 9]. In this paper, the variance, reduction ratio, and normalized total energy of each IMF and residual are calculated as the feature vector by EEMD method.

A sensor fault diagnosis method based on EEMD and ELM is presented in this paper. The complete algorithm includes the following steps: (1) EEMD is applied to decompose the standardized sensor signals into several IMFs and a residual signal. (2) Their variance characteristics are calculated as the part signal features by selecting the first four IMF components and final residual. (3) In order to strengthen the fault feature of IMF components, the reduction thresholds of IMFs and residual are calculated to facilitate cut processing, and obtain the reduction ratios of each IMF component and the residual item. (4) Constructing feature vectors acquired by calculating the normalized total energy of IMFs and residual item is input into the ELM for classification. The rest of the content of this paper is arranged as follows: In Sect. 2, the fundamental principles of EEMD, fault feature extraction method, and ELM will be illustrated. In Sect. 3, data acquisition simulation experiment and analysis will be demonstrated. Finally, the conclusion is drawn in Sect. 4.

2 Methodology

Fault diagnosis process for sensor includes both fault feature extraction and fault classification. The former is the most important part in fault diagnosis. In accordance to the extracted feature, different fault types are classified. The proposed algorithm flow chart of the whole fault diagnosis is described in Fig. 1.

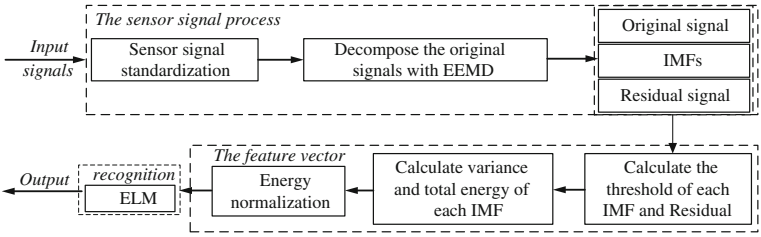

Fig. 1 Block diagram of the proposed method

2.1 Ensemble Empirical Mode Decomposition (EEMD)

The principle of EEMD [10] method is to make use of the Gauss white noise with the statistical characteristics of uniform frequency distribution. EEMD is an improved version of the EMD algorithm, which not only retains the advantages of EMD, but also has the ability to effectively suppress mode aliasing and improve the accuracy of signal analysis. The specific decomposition steps and principles are as follows [11, 12]:

(1) Add the random Gauss white noise $n_j(t)$ with a mean value of zero to the original vibration signal $x(t)$ under the condition of constant standard deviation, to obtain the decomposed signal $x_j(t)$.

$$x_j(t) = x(t) + n_j(t) \tag{1}$$

Wherein, $x_j(t)$ is the noise-added signal, $j = 1, 2, 3, \ldots, M$, and M is the number of trials. The size of Gauss white noise will directly affect the signal EEMD modal aliasing extinction effect.

(2) Decompose the newly generated gas signal $x_j(t)$ into some IMFs through the original EMD algorithm.

$$x_j(t) = \sum_{i=1}^{N} c_{j,i}(t) + r_{Nj}(t) \tag{2}$$

Wherein, i is the number of IMFs, $i = 1, 2, 3, \ldots, N$, $c_{j,i}(t)$ represents the IMFs $(c_{j,1}, c_{j,2}, \ldots, c_{j,N})$ which contain different frequency bands, and $r_{Nj}(t)$ signifies the final residue, which presents the mean trend of signal.

(3) Repeat Steps 1 and 2 for M times with a different white noise series each time to obtain an ensemble of IMFs.

$$[\{c_{1,i}(t)\}, \{c_{2,i}(t)\}, \ldots, \{c_{M,i}(t)\}] \tag{3}$$

Wherein, $i = 1, 2, 3, \ldots, N$.

(4) Calculate the ensemble means of the corresponding IMFs of the decompositions as the final result

$$c_i(t) = \frac{1}{M} \sum_{k=1}^{M} c_{k,i}(t) \tag{4}$$

Wherein, $c_i(t)$ is the i-th IMF decomposed through EEMD, while $k = 1, 2, \ldots, M$ and $i = 1, 2, 3, \ldots, N$.

2.2 Fault Feature Extraction Method

In order to ensure that the extracted features are not affected by the amplitude of the output signal of the sensor, the signal is normalized before the EEMD decomposition. The specific feature extraction steps are as follows:

(1) Make the sensor signals X standardized.

$$\hat{X} = D^{-1}[X - E(X)] \tag{5}$$

Wherein, X represents the output signal of the sensor, $E(X)$ indicates the mean value of X, and D denotes the standard deviation of X.

(2) Decompose $\hat{X}$ into some IMFs and residual signal through the EEMD algorithm and extract the first four IMFs, which are represented by F_1, F_2, F_3, F_4, respectively. F_5 signifies the residual signal.

(3) Calculate the variance D_i of F_1, F_2, F_3, F_4 and residual F_5 to extract the fault features of the sensor.

$$D_i = \sum_{j=1}^{m} \frac{F_i^2}{m} - \left(\sum_{j=1}^{m} \frac{F_i}{m} \right)^2, \quad i = 1, 2, \ldots, k \tag{6}$$

(4) Reduce the IMF component and the residual term, and calculate the cutoff threshold of each IMF component and residual to enhance the fault characteristics of the IMF component

$$ThrF_{\mathrm{i}} = \sqrt{\frac{1}{m}\sum_{j=1}^{m} F_{i,j}^2} \tag{7}$$

Wherein, m indicates the lengths of the IMF component and the residue, $F_{i,j}$ the j-th value of the i-th component of the IMF, and $F_{5,j}$ the j-th value of the residual component. Then reduce each IMF component and residual item as follows, and calculate the reduction ratio of each IMF component and residual term.

$$\bar{F}_{i,j} = \begin{cases} F_{i,j} & \left|F_{i,j}\right| \geq |ThrF_i| \\ 0 & \left|F_{i,j}\right| < |ThrF_i| \end{cases} \tag{8}$$

$$CutF_i = \frac{Num\left(\bar{F}_{i,j} \neq F_{i,j}\right)}{m} \tag{9}$$

Wherein, $\bar{F}_{i,j}$ is the IMF component and the residual term after the reduction, and $CutF_i$ the reduction ratio of the corresponding component, i.e., the ratio of the number of points to be cut to the total number of points.

(5) Calculate the normalized total energy EF_i of each IMF component and the residual items, as well as the total cutting ratio $\Delta CutF$ for pattern classification.

$$EF_i = \int \left|\bar{F}_i\right|^2 dt = \sum_{j=1}^{m} \left|\bar{F}_{i,j}\right|^2 \tag{10}$$

$$\Delta EF_i = \frac{EF_i}{\sqrt{\sum_{i=1}^{5} |EF_i|^2}} \tag{11}$$

$$\Delta CutF = \frac{1}{5}\sum_{i=1}^{5} CutF_i \tag{12}$$

(6) Construct feature vector T for sensor fault diagnosis, where

$$T = [\Delta EF_1, \Delta EF_2, \Delta EF_3, \Delta EF_4, \Delta EF_5, \Delta CutF, D_1, D_2, D_3, D_4, D_5] \tag{13}$$

2.3 Extreme Learning Machine (ELM)

After the completion of the above EEMD and feature extraction, Extreme Learning Machine (ELM) is applied to complete sensor fault classification and identification. Recently, a least square based learning algorithm named Extreme Learning Machine (ELM) has been developed for single hidden layer feedforward networks (SLFNs) [13].

Suppose that there are N training samples (x_i, t_i), in which the input sample is $x_i = [x_{i1}, x_{i2}, \cdots, x_{in}]^T \in R^n$ and the output sample $t_i = [t_{i1}, t_{i2}, \cdots, t_{im}]^T \in R^m$, and SLFNs output with $L(L \leq N)$ hidden layer nodes, then the activation function of $g(x)$ is as follows [14, 15]:

$$\sum_{i=1}^{L} \beta_i g_i(x_j) = \sum_{i=1}^{L} \beta_i g(w_i \cdot x_j + b_i) = o_j, j = 1, 2, \cdots, N \tag{14}$$

Wherein, $w_i = [w_{i1}, w_{i2}, \cdots, w_{in}]^T$ denotes the weight vector of the i-th hidden layer neurons and the input neurons, $\beta_i = [\beta_{i1}, \beta_{i2}, \cdots, \beta_{im}]^T$ that of the i-th hidden layer neurons and the output neurons, and b_i the deviation of the i-th hidden layer neurons.

As a new unsupervised and fast learning algorithm, ELM is not only effective but also simple and easy to use. It only requires the activation function to be infinite-order differentiable and needs to set the number of hidden nodes in the network and incentive function before training rather than the input weights of the network and the bias of the hidden layer nodes. The unique optimal solution is obtained by solving the minimum norm least square solution of linear equations, and the whole training process is completed at one time.

3 Experiments and Analysis

3.1 Data Collection

To evaluate the effectiveness of the feature extraction methods for sensor, a flow chart of data acquisition is considered and shown in Fig. 2. Produced by British City Technology, the sensor utilized in this experiment has been calibrated in advance. To generate the required dataset, the gas in the environment is pumped

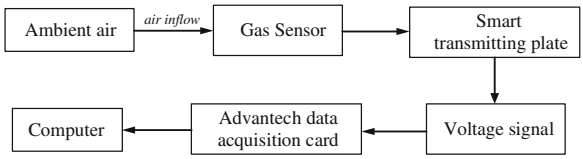

Fig. 2 Flow chart of data acquisition

into the reaction chamber first for full contact with the sensor. Then, the output of the sensor is converted to the available voltage corresponding to the concentration of the target gas through a transmission plate. Finally, Advantech data acquisition card is adopted to collect the voltage signals of smart transmitting plate and convert the voltage value into its concentration value. The data of this experiment is collected at a room temperature of $25 \pm 2\,^{\circ}\mathrm{C}$ and a relative humidity of 50 %. Each type of the dataset consists of 100,000 recordings (time series sequences) collected over a period of 13 days. A total of 50 sample data are collected from each type, with each datum containing 2000 points.

According to the structural characteristics and the online usage of the sensor, sensor faults can be divided into six types: bias, precision degradation, drift, complete failure, drift and bias, as well as precision degradation and bias.

3.2 Signal Decomposition

In EEMD, the number of ensemble M and the noise amplitude c are the two parameters that need to be determined, and (M, c) should be selected carefully. To make the EEMD effective, c should not be too small. Otherwise, it may not introduce the change of extrema that the EMD relies on. It should be noticed that the number of ensemble should increase as the amplitude of noise increases so as to reduce the contribution of added noise in the decomposed results. In this study, EEMD is employed to decompose the sensor signal. After testing some pairs of (M, c), a satisfying result could be achieved when $M = 100$ and $c = 20$ %. Hence, these two parameters are set as $M = 100$ and $c = 20$ % in this study. To acquire the fault feature vectors, EEMD is first applied to decompose the sensor signals into several IMFs and a residual. And the sensor signals are also decomposed through EMD, and different IMF components and residual are obtained. It can be observed that the modes take on a set of amplitude modulation and frequency modulation signals fluctuating from the highest frequency to the lowest.

3.3 Fault Feature Extraction

To illustrate the effect of the method proposed in this paper, an experimental comparison between EMD and EEMD is carried out. First, six different signals after standardization are decomposed through EMD. Later, the variance, normalized energy and reduction ratio of the three kinds of features are extracted, respectively, to construct sensor feature vector T1. From Formula (13), it can be seen that feature vector T1 contains a total of 11 different features. In order to make it easy to see the effect of the distribution of the characteristics, this section only selects three features of them for comparison and analysis. Figure 3a displays the distribution results of the three features. Similarly, the six kinds of signals to be classified after

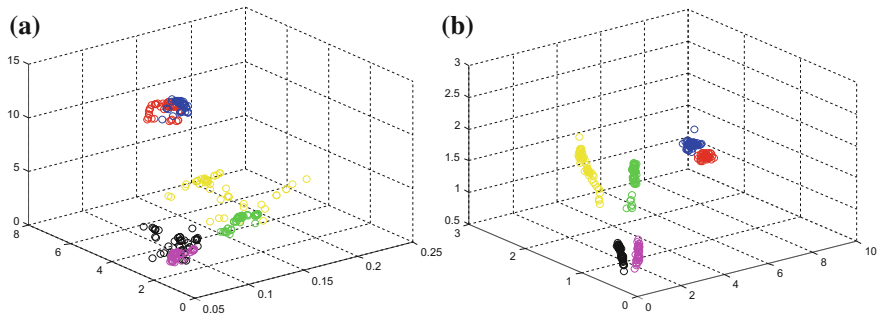

Fig. 3 Scatter plot of the three features for the EMD and EEMD results

standardization are decomposed through EEMD to calculate sensor feature vector T2. Then, three features from the vector T2 are chosen to compare the experimental result. Figure 3b shows the distribution results of the three features from the selected feature vector.

From Fig. 3, it can be seen that EMD has poor performance of characteristic distribution and obviously two classes of overlap. In comparison, EEMD can obtain a clearer separation on the mapping. Consequently, EEMD can identify each fault accurately for the feature samples. Extracting the variance, normalized energy and reduction ratio of the sensor signal can clearly help classify the different faults.

3.4 State Classification Based on ELM

State classification for recognizing the operating states of sensor can be done based on EEMD and ELM. The feature vector is obtained by the formula (13) and input into ELM in this experiment. State classification results based on ELM are shown in Figs. 4 and 5, from which it can be seen that the actual outputs of ELM are extremely consistent with the target outputs even under variable conditions. By comparing the EMD-ELM and EEMD-ELM, Fig. 4 shows that the result of the extracted features through the EEMD decomposition is more suitable for fault classification. Likewise, the comparison of EEMD-SVM and EEMD-ELM reveals that the classification results of ELM are better compared with SVM, which is unaffected by the number of training samples. Thus, the proposed method combining EEMD with ELM is able to efficiently realize sensor fault diagnosis under variable conditions.

In order to display the superiority of ELM, a comparison is made to show the performances of SVM and ELM. Detailed comparison results are shown in Table 1, in which 50 experiments are given to calculate the mean values of running time and classification accuracy in order to facilitate the comparison. As can be seen, the

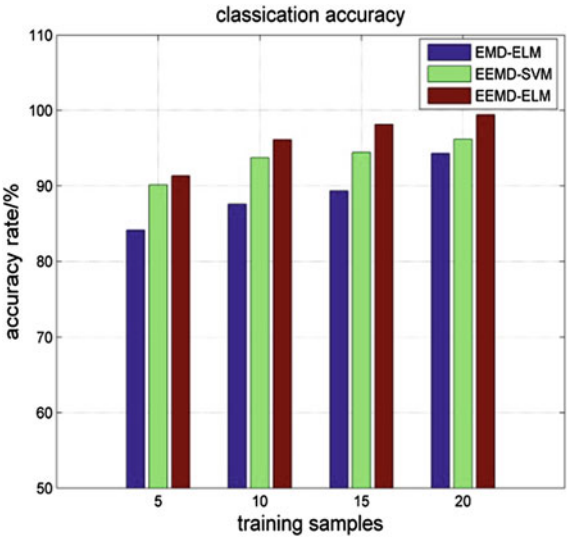

Fig. 4 Classification results of experiment

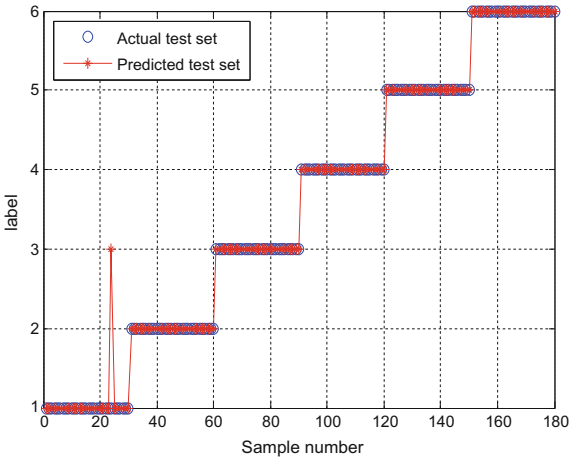

Fig. 5 Classification result of ELM

Table 1 Classification results of SVM and ELM

Test samples	Running time (s)		Classification accuracy (%)	
	SVM	ELM	SVM	ELM
180	2.3775	0.2818	93.75	99.48

average time consumed by ELM is 0.2818 s, and the average classification accuracy of ELM is 99.48 %. The SVM method is obviously more time consuming and less accurate than the other methods. As a result, both the purposes of improving the accuracy of pattern recognition and reducing model complexity can be achieved by EEMD-ELM.

4 Conclusions

In order to fully extract the fault signal of sensor, this paper proposes a new sensor fault diagnosis method based on EEMD and ELM. This approach first decomposes the standardized signal through EEMD into the original signal, several IMFs and the residual signal, and calculates their variances. Then, each component of IMF after decomposition is cut to calculate the reduction ratio and the normalized total energy. Subsequently, the feature vector obtained via the above calculation is constructed to carry out fault classification through ELM algorithm. The sensor data in the experiment are adopted to validate the proposed method. The results show that EEMD is suitable for nonlinear and nonstationary signal processing, and the proposed approach obviously improves the fault classification performance of sensor and outperforms the other traditional approaches such as EMD and SVM.

Acknowledgments This research is supported by the National Nature Science Foundation of China (No. 61374135), the National Natural Science Foundation of Chongqing (No. cstc2016jcyjA0504).

References

1. Huang GB, Zhu GY, Siew CK (2006) Extreme learning machine: theory and applications. Neurocomputing 70(1–3):489–501
2. Zhang J, Yan Y (2001) A wavelet-based approach to abrupt fault detection and diagnosis of sensor. IEEE Trans Instrum Meas 50(5):1389–1396
3. Liu H, Tian H-Q, Pan D-F, Li Y-F (2013) Forecasting models for wind speed using wavelet, wavelet packet, time series and artificial neural networks. Appl Energy 107:191–208
4. Huang NE, Shen Z, Long SR et al (1998) The empirical mode decomposition and the Hilbert spectrum for nonlinear and non-stationary time series analysis. Proc R Soc London A: Math Phys Eng Sci. R Soc 454:903–995
5. Huang NE, Shen Z, Long SR (1999) A new view of nonlinear water waves: the Hilbert Spectrum 1. Annu Rev Fluid Mech 31(1):417–457
6. Xie Q, Li J, Gao X et al (2009) Real time infrared gas detection based on a modified EMD algorithm. Sens Actuators B: Chem 136(2):303–309
7. Wu Z, Huang NE (2009) Ensemble empirical mode decomposition: a noise-assisted data analysis method. Adv Adapt Data Anal 1(01):1–41
8. Zhang X, Zhou J (2013) Multi-fault diagnosis for rolling element bearings based on ensemble empirical mode decomposition and optimized support vector machines. Mech Syst Signal Process 41(1):127–140
9. Lei Y, He Z, Zi Y (2011) EEMD method and WNN for fault diagnosis of locomotive roller bearings. Expert Syst Appl 38(6):7334–7341
10. Guo W, Peter WT (2013) A novel signal compression method based on optimal ensemble empirical mode decomposition for bearing vibration signals. J Sound Vib 332(2):423–441
11. Zhang X, Liang Y, Zhou J (2015) A novel bearing fault diagnosis model integrated permutation entropy, ensemble empirical mode decomposition and optimized SVM. Measurement 69:164–179
12. Yu Y, Li W, Sheng D et al (2015) A novel sensor fault diagnosis method based on modified ensemble empirical mode decomposition and probabilistic neural network. Measurement 68:328–336

13. Cao J, Lin Z, Huang GB et al (2012) Voting based extreme learning machine. Inf Sci 185(1):66–77
14. Wong PK, Yang Z, Vong CM et al (2014) Real-time fault diagnosis for gas turbine generator systems using extreme learning machine. Neurocomputing 128:249–257
15. Tian Y, Ma J, Lu C et al (2015) Rolling bearing fault diagnosis under variable conditions using LMD-SVD and extreme learning machine. Mech Mach Theory 90:175–186

A New Quantum-Behaved PSO: Based on Double δ-Potential Wells Model

Zhaoqing Xie, Qing Liu and Lanqing Xu

Abstract In this paper, a new QPSO based on double δ-potential wells model (QPSO-DPW) is proposed. The algorithm contains three components: the global best position, the particle position relative to the mean individual best positions, and the particle position relative to global best position. This strategy restrains the particle premature convergence and fall into local convergence. Several classical nonlinear functions are employed to test the effectiveness of QPSO-DPW. The results demonstrate good performance in convergence speed and the global searching ability when compared with other recent variants of the PSO.

Keywords Quantum-behaved · Particle swarm optimization · Potential well

1 Introduction

The Quantum-behaved Particle Swarm Optimization (QPSO) was inspired by the Quantum Dynamics and first proposed by Sun [1]. A lot of research work has been done on QPSO, such as Guiding Quantum Particle Swarm Optimizer incorporating Immune algorithm (GQPSOI) [2], Hybrid Chaotic Quantum-behaved Particle Swarm Optimization (HCQPSO) [1], decentralized form of quantum-inspired particle swarm optimization (DFQPSO) [3], multi-objective quantum-behaved particle swarm optimization (IMOQPSO) [4], etc. Based on QPSO, we proposed a new QPSO which is based on double δ-potential wells model (QPSO-DPW), By analyzing the properties of particle in potential well in terms of quantum mechanics, we find it has three different bound states in the iteration space. The first state is the particle X in the potential well around point P (pbset) as the center of aggregation,

Z. Xie (✉)
School of Energy and Power Engineering, Wuhan University of Technology, Wuhan 430070, China
e-mail: youzicha2012@163.com

Q. Liu · L. Xu
School of Automation, Wuhan University of Technology, Wuhan 430070, China

Y. Jia et al. (eds.), *Proceedings of 2016 Chinese Intelligent Systems Conference*, Lecture Notes in Electrical Engineering 404, DOI 10.1007/978-981-10-2338-5_21

the second state is the particle X around point G (gbset) as the center of aggregation, in addition to the particle X, the pbest particle P also considered converging to point G (gbest). We propose two different particles binding state models. The new algorithm retains the ability of stochastic global searching and has better global convergence and very strong self-adaptive ability with environment.

The rest of the paper is organized as follows. In Sect. 2 we describe the QPSO algorithms. In Sect. 3, we introduce two different δ-potential well models on QPSO, and then present QPSO-DPW algorithm. In Sect. 4, we present simulation parameters and results and an evaluation of DPW-QPSO. Finally, In Sect. 5, conclusions and future work are presented.

2 QPSO Algorithm

In [5], Clerc and Kennedy proved that if the upper coefficients r_1, r_2, c_1, c_2 are properly selected, $x_{ij}(t)$ will converge to $p_{ij}(t)$, whose coordinates are

$$p_{ij}(t) = \varphi_{ij}(t) \cdot P_i(t) + \left(1 - \varphi_{ij}(t)\right) \cdot G_j(t) \quad \varphi_{ij}(t) \sim U(0,1) \tag{1}$$

The particle moves around and toward to point $p_{ij}(t)$, from the point view of dynamics, particle must be in binding state to guarantee convergence, moving in an attraction potential field whose center is point $p_{ij}(t)$, correspondingly, we can establish a quantitative and attractive δ-potential well model to bind the particles. In [1], Jun Sun proved the particle converges to the center of potential point $p_{ij}(t)$, the potential energy of the particle in one-dimensional δ-potential well is represented as

$$V(x) = -V_0\delta(X-p) = -V_0\delta(Y_1) \quad Y_1 = X - p \tag{2}$$

By solving the Schrödinger equation, the probability density function Q is given by

$$Q(y) = |\psi(y)|^2 = \frac{1}{L} e^{-2|y|/L} \tag{3}$$

which describes particles appearing at position y relative to p, if we set $Q(y) \sim U(0,1)$, then the position of particles can be measured by

$$X = p \pm \frac{L}{2} \ln(1/u) \quad u \sim U(0,1) \tag{4}$$

The position of particle i at $(t+1)$th iteration in QPSO is updated as follows [6]

$$x_{ij}(t+1) = p_{ij}(t) \pm \alpha \cdot \left|C_j(t) - x_{ij}(t)\right| \cdot \ln\frac{1}{u_{ij}(t)} \tag{5}$$

$$C_j(t) = \frac{1}{M}\sum_{i=1}^{M} P_i(t) = \left(\frac{1}{M}\sum_{i=1}^{M} p_{i1}(t), \frac{1}{M}\sum_{i=1}^{M} p_{i2}(t), \ldots, \frac{1}{M}\sum_{i=1}^{M} p_{in}(t)\right) \quad (6)$$

where the pbest and gbest are computed as follows:

$$P_i(t) = \begin{cases} X_i(t) & f(X_i(t)) < f(P_i(t-1)) \\ P_i(t-1) & f(X_i(t)) \geq f(P_i(t-1)) \end{cases} \quad (7)$$

$$G_j = P_g(t), g = \arg\min_{1 \leq i \leq M}(f(P_i(t))) \quad (8)$$

where $C_j(t)$ means the mean of the best individual positions of all particles which replace $p_{ij}(t)$ can be more effective. α is called contraction-expansion coefficient which can be tuned to control the convergence speed of the algorithm.

3 QPSO-DPW Algorithm

As aforementioned QPSO-DPW, we present two different particle binding state models as follows.

3.1 Particle in Two δ-Potential Wells Model

When particle X converges to P then it converges to G at the same time. We establish one-dimensional δ-potential well around point P and G, as shown in Fig. 1.

Respectively, the potential energy as

$$V_1(x) = -V_0\delta(X-P) = -V_0\delta(Y_1) \quad Y_1 = X - P \quad (9)$$

$$V_2(x) = -V_0\delta(X-G) = -V_0\delta(Y_2) \quad Y_2 = X - G \quad (10)$$

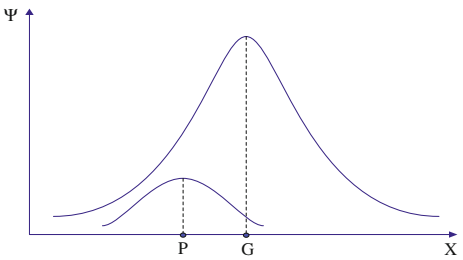

Fig. 1 Particle in two δ-potential wells model

According to formula (3), the position X relative to P and G as

$$x_{pij}(t+1) = p_{ij}(t) \pm \frac{L_1}{2} \cdot \ln \frac{1}{u_{ij}(t)} \tag{11}$$

$$x_{gij}(t+1) = G_j(t) \pm \frac{L_2}{2} \cdot \ln \frac{1}{u_{ij}(t)} \tag{12}$$

The position X can be defined as

$$x_{ij}(t+1) = \varphi_{ij}(t) \cdot x_{pij}(t+1) + \left(1 - \varphi_{ij}(t)\right) \cdot x_{gij}(t+1)\, \varphi_{ij}(t) \sim U(0,1) \tag{13}$$

Thus

$$x_{ij}(t+1) = \varphi_{ij}(t) \cdot P_{ij}(t) + \left(1 - \varphi_{ij}(t)\right) \cdot G_j(t) \pm \frac{L}{2} \ln \frac{1}{u_{ij}(t)} \tag{14}$$

where $L_1 = L_2 = L$, compare to the upper (5), the final result of this model has the same meaning with QPSO.

3.2 Double δ-Potential Wells Model

When particle X converges to P then it converges to G at the same time (Fig. 2).

The potential energies are as

$$V_1(x) = -V_0\delta(X-p) = -V_0\delta(Y_1) \quad Y_1 = X - p \tag{15}$$

$$V_2(x) = -V_0\delta(p-G) = -V_0\delta(Y_2) \quad Y_2 = p - G \tag{16}$$

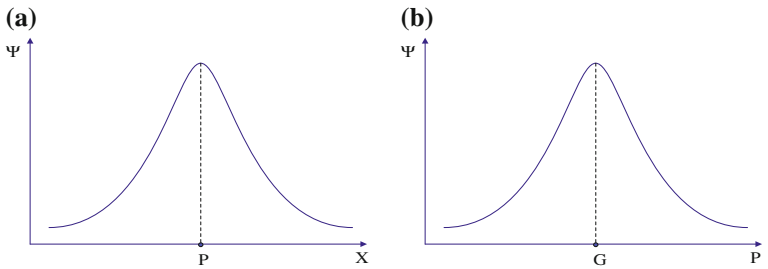

Fig. 2 Double δ-potential wells model. **a** Particle converges to individual best position. **b** Individual best particle converges to global best position

The position X can be defined as

$$x_{ij}(t+1) = G_j(t) \pm \frac{L_1}{2} \ln \frac{1}{u_{ij}(t)} \pm \frac{L_2}{2} \ln \frac{1}{u_{ij}(t)} \tag{17}$$

We define

$$L_1 = \alpha \left| C_j(t) - x_{ij}(t) \right| \cdot \ln \frac{1}{u_{ij}(t)} \tag{18}$$

$$L_2 = \beta \left| G_j(t) - x_{ij}(t) \right| \cdot \ln \frac{1}{u_{ij}(t)} \tag{19}$$

The position X can be defined as

$$x_{ij}(t+1) = G_j(t) \pm \alpha \left| C_j(t) - x_{ij}(t) \right| \cdot \ln \frac{1}{u_{ij}(t)} \pm \beta \left| G_j(t) - x_{ij}(t) \right| \cdot \ln \frac{1}{u_{ij}(t)} \tag{20}$$

where α is the contraction-expansion coefficient which can be tuned to control the convergence speed of particles emergence to the meaning best position, β is the contraction-expansion coefficient which can be tuned to control the convergence speed of particles emergence to the global best position.

3.3 Comparison

The particle of QPSO-DPW whose position update equation in (20) also has three major components, the differences between the above three different algorithms are as follows [7, 8]:

(1) The first component: The $p_{ij}(t)$ of QPSO weighs the pbest and gbest ratio which can make sure particles convergent to attractor P, the $G_j(t)$ of QPSO-DPW records the best position ever found by all particles which can accelerate particle convergences to global rapidly.
(2) The second component: The $\left| C_j(t) - x_{ij}(t) \right|$ of QPSO selects the average best position of all particles, which is referred to as "shared information" or "group knowledge." QPSO-DPW in this component is the same as QPSO.
(3) The third component: the $\left| G_j(t) - x_{ij}(t) \right|$ of QPSO and QPSO-DPW are the same meaning, which belongs to social cognitive part, reflects the information sharing between particles.

We can include that QPSO and QPSO-DPW allow particles to profit both from their own discoveries as well as the discoveries of the swarm as a whole, mixing local and global information uniquely for each particle in each iteration, they both are concerned about co-evolution and knowledge sharing.

According to the formulations above, the following procedure can be used for implementing the QPSO-DPW, the algorithm pseudocode is as follows:

Initial:

Step1: Initialize the swarm by assigning a random position in the problem hyperspace to each particle.
Step2: Initialize pbest, gbest, and the fitness values.

Iteration:

While $t < T$ (T is the max generation)
  for $i = 1$ to M
    Step3: Evaluate the fitness function for each particle.
    Step4: For each individual particle, compare the particle's fitness value with its pbest. The pbest is computed according to (7).
    Step5: Calculate the gbest according to (8).
    Step6: Update the gbest and the current position.
    Step7: Calculate the mean best according to (6).
    Step8: Generate the random number.
    for $i = 1$ to N
    Step9: Update the position of particle according to (20).
    End for
    Step10: Update the fitness value of particle i.
  End for
End while

Output: Step11: Select final solution with best evaluate index.

4 Experimental Results

4.1 Test Functions

In the experiments, four-dimensional benchmark functions with different properties are chosen to test QPSO-DPW's performance (Table 1). The equations are listed below

4.2 Sensitivity to Control Parameters

In our experiments, the variation method of linear reduction with the change of the iteration number is adopted in the control parameters. α and β are determined as

$$\alpha = \beta = (\alpha_0 - \alpha_1) \cdot (G_{\max} - t) / G_{\max} + \alpha_1 \tag{21}$$

Table 1 Test function and parameter configuration

F	Mathematic expression	Initial range	$f_{\min}$
Griewank	$f(x)=\frac{1}{4000}\sum_{i=1}^{n}x_i^2-\prod_{i=1}^{n}\cos\left(\frac{x_i}{\sqrt{i}}\right)+1$	$-600\le x_i\le 600$	0
Rastrigrin	$f(x)=\sum_{i=1}^{n}\left[x_i^2-10\cos(2\pi x_i)+10\right]$	$-5.12\le x_i\le 5.12$	0
Rosenbrock	$f(x)=\sum_{i=1}^{n}\left[100\left(x_{i+1}-x_i^2\right)+(x_i-1)^2\right]$	$-30\le x_i\le 30$	0
Sphere	$f(x)=\sum_{i=1}^{n}x_i^2$	$-100\le x_i\le 100$	0

where $\alpha_0>\alpha_1$, α_0 and α_1 are the initial control value and the end control value respectively, $G_{\max}$ is the total number of iterations, t is the current number of iterations. We set $\alpha_0=1$ and $\alpha_1=0.5$.

4.3 Results

As in [9], for each function, three different dimension sizes, 10, 20, and 30 are tested. The corresponding maximum generations are 1000, 1500, and 2000 respectively, and the population size is set to 20, 40, and 80. We choose the mean best fitness, standard deviation, and convergence times to compare (Tables 2, 3, 4, and 5). The experiment results are as follow tables.

Through the analysis of table data shows that the QPSO-DPW algorithm has a strong ability of global optimization. For Griewank Function, QPSO-DPW has higher fitness accuracy and convergence speed, in 20 populations and 20 dimensions, the convergence has been realized. For Rastrigrin Function, QPSO and PSO do not get the optimal solution, but QPSO-DPW shows excellent performance, in

Table 2 Experimental values for Griewank function

P	D	G	QPSO			QPSO-DPW			PSO		
			Mean	St.Dev	n	Mean	St.Dev	n	Mean	St.Dev	n
20	10	1000	0.1838	0.1347	1000	0.0234	0.0762	840	0.0643	0.2874	1000
	20	1500	0.0437	0.0422	1375	0.0077	0.0016	1074	0.0599	0.2679	1500
	30	2000	0.0120	0.0043	1259	0.0083	0.0013	1452	0.0548	0.2451	2000
40	10	1000	0.1224	0.0955	1000	0.0065	0.0022	617	0.0245	0.1095	1000
	20	1500	0.0220	0.0136	1292	0.0074	0.0023	1046	0.0404	0.1805	1500
	30	2000	0.0153	0.0093	1170	0.0072	0.0020	1371	0.0542	0.2424	2000
80	10	1000	0.0838	0.0743	1000	0.0070	0.0022	703	0.0163	0.0731	1000
	20	1500	0.0170	0.0124	1204	0.0078	0.0014	934	0.0099	0.0442	1500
	30	2000	0.0124	0.0052	1212	0.0079	0.0018	1402	0.0536	0.2397	2000

Table 3 Experimental values for Rastrigrin function

P	D	G	QPSO			QPSO-DPW			PSO		
			Mean	St.Dev	n	Mean	St.Dev	n	Mean	St.Dev	n
20	10	1000	7.4805	4.4116	1000	0.0075	0.0021	726	2.0140	9.0070	1000
	20	1500	17.8823	9.1916	1500	0.0076	0.0014	1197	3.2075	14.3444	1500
	30	2000	40.3947	21.5696	2000	0.0083	0.0012	1667	4.3053	19.2540	2000
40	10	1000	6.0945	4.1070	1000	0.0080	0.0014	672	0.7462	3.3372	1000
	20	1500	13.2951	8.8933	1500	0.0082	0.0020	1123	1.2136	5.4274	1500
	30	2000	22.6855	6.1164	2000	0.0078	0.0016	1530	2.7271	12.1960	2000
80	10	1000	2.8170	2.4749	1000	0.0075	0.0019	605	0.8955	4.0046	1000
	20	1500	10.8525	6.7026	1500	0.0080	0.0015	1081	1.6954	7.5822	1500
	30	2000	18.9472	12.7890	2000	0.0080	0.0017	1491	3.0842	13.7930	2000

Table 4 Experimental values for Rosenbrock function

P	D	G	QPSO			QPSO-DPW			PSO		
			Mean	St.Dev	n	Mean	St.Dev	n	Mean	St.Dev	n
20	10	1000	6.4090	1.7173	1000	7.6108	0.2338	1000	12.7093	56.8376	1000
	20	1500	33.4467	32.0712	1500	17.6796	0.2686	1500	31.4622	140.7031	1500
	30	2000	58.1192	46.6087	2000	27.8290	0.3080	2000	25.2040	112.7157	2000
40	10	1000	6.8361	4.2061	1000	7.3314	0.1474	1000	0.4816	2.1539	1000
	20	1500	31.4469	33.9511	1500	17.3883	0.1852	1500	51.6630	231.0438	1500
	30	2000	46.0095	45.3339	2000	27.4588	0.2878	2000	120.3963	538.4286	2000
80	10	1000	4.6891	1.2205	1000	7.2036	0.1303	1000	0.4330	1.9362	1000
	20	1500	19.6564	17.5665	1500	17.2392	0.1200	1500	7.5854	33.9228	1500
	30	2000	29.8979	19.4430	2000	27.2948	0.0954	2000	56.7790	253.9233	2000

Table 5 Experimental values for Sphere function

P	D	G	QPSO			QPSO-DPW			PSO		
			Mean	St.Dev	n	Mean	St.Dev	n	Mean	St.Dev	n
20	10	1000	0.0082	0.0015	271	0.0077	0.0019	529	0.3948	1.7657	1000
	20	1500	0.0087	0.0008	688	0.0082	0.0011	1005	0.0581	0.2597	1500
	30	2000	0.0089	0.0010	1110	0.0083	0.0019	1429	0.0360	0.1607	2000
40	10	1000	0.0081	0.0016	256	0.0079	0.0012	443	0.0000	0.0000	431
	20	1500	0.0087	0.0013	633	0.0078	0.0020	945	0.0941	0.4210	1500
	30	2000	0.0090	0.0010	1071	0.0084	0.0015	1353	0.1849	0.8268	2000
80	10	1000	0.0082	0.0014	195	0.0077	0.0015	400	0.0000	0.0000	9
	20	1500	0.0084	0.0010	603	0.0080	0.0016	864	0.0128	0.0571	1500
	30	2000	0.0089	0.0007	1036	0.0081	0.0013	1271	0.0316	0.1413	2000

20 population and 10 dimension, the optimal solution is found. For Rosenbrock Function, the improvements are not so remarkable, but it is still better than the other two algorithms under all conditions. For Sphere function, we can see that the accuracy of QPSO-DPW is higher than QPSO and PSO, but the convergence speed is lower than QPSO, can always converge to an optimal solution and the accuracy is higher than QPSO and PSO obviously. Thus, on the whole, the global convergence ability of QPSO-DPW is indeed improved obviously.

5 Conclusion

In this paper, QPSO has been extended based on Double δ-potential wells model. In the model, the mean best individual positions and the best global positions two attractors increase the ability of global searching and better global convergence accuracy. Although we present a method of parameter control, it is only one of self-adaption methods. Further research would investigate the sensitivity of parameters into QPSO-DPW to increase its intelligence of search.

References

1. Sun J, Feng B, Xu W (2004) Particle Swam Optimization with Particles Having Quantum Behavior. IEEE, pp 325–331
2. Liu F, Li D, Jin Q (2014) Neighborhood immune based guiding quantum particle swarm optimizer. IEEE, pp 2091–2096
3. Fang W et al (2016) A decentralized quantum-inspired particle swarm optimization algorithm with cellular structured population. Inf Sci 330:19–48
4. Li Y et al (2015) Overlapping community detection through an improved multi-objective quantum-behaved particle swarm optimization. J Heuristics 21(4):549–575
5. Clerc M, Kennedy J (2002) The particle swarm—explosion, stability, and convergence in a multidimensional complex space. IEEE Trans Evol Comput 58–73
6. Turgut OE (2016) Hybrid chaotic quantum behaved particle swarm optimization algorithm for thermal design of plate fin heat exchangers. Appl Math Model 40(1):50–69
7. Boeringer DW, Werner DH (2004) Particle swarm optimization versus genetic algorithms for phased array synthesis. IEEE Trans Antennas Propag 52(3):771–779
8. Del Valle Y, Venayagamoorthy GK, Mohagheghi S, Hernandez JC, Harley RG (2008) Particle swarm optimization: basic concepts, variants and applications in power systems. IEEE Trans Evol Comput 170–195
9. Liu J, Sun J, Xu W (2006) Quantum-Behaved Particle Swarm Optimization with Immune Operator. Springer, Berlin, pp 77–83

Bearing Fault Diagnosis Based on Hilbert Marginal Spectrum and Supervised Locally Linear Embedding

Zhanqiang Xing, Jianfeng Qu, Yi Chai, Yanxia Li and Qiu Tang

Abstract A bearing vibration signal is nonlinear and nonstationary, with multiple components and multifractal properties. A bearing fault diagnosis method based on Hilbert marginal spectrum (HMS) and supervised locally linear embedding (SLLE) is proposed for the first time in this paper. HMS is introduced for feature extraction from faulty bearing vibration signals. Then SLLE is proposed for the dimensionality reduction of high-dimensional fault feature, which is more effective than other reducing dimension methods, such as principle component analysis (PCA), multidimensional scaling (MDS), and locally linear embedding (LLE). Finally, the support vector machine (SVM) is applied to achieve the bearing fault diagnosis according to the extracted feature vector. The results show that the proposed method improves the fault diagnostic and classification performance significantly.

Keywords Bearing fault diagnosis · Hilbert marginal spectrum · Supervised locally linear embedding · Support vector machine

1 Introduction

As an important part of mechanical equipment, bearing plays a very important role in maintaining the normal operation [1]. The faults of rolling bearings often lead to a decline in productivity and even cause huge economic loss. Thus, it is important to keep the rolling bearing working in good state via condition monitoring and fault diagnosis. Fault diagnosis is mainly divided into two parts, faults recognition and faults classification. As a critical part of faults recognition, feature extraction method should extract the most distinctive feature to reduce the feature dimension [2] and classify. And the effective classifier is needed to obtain higher diagnostic accuracy and reduce the time consumed.

Z. Xing · J. Qu (✉) · Y. Chai · Y. Li · Q. Tang
School of Automation, Chongqing University, Chongqing 400044, China
e-mail: qujianfeng@cqu.edu.cn

Y. Jia et al. (eds.), *Proceedings of 2016 Chinese Intelligent Systems Conference*,
Lecture Notes in Electrical Engineering 404, DOI 10.1007/978-981-10-2338-5_22

Due to the complexity of rotating machinery systems, the vibration signals of rolling bearings are nonlinear and nonstationary. Several popular time-frequency analysis methods about fault feature extraction of bearings have been suggested in the literature, such as the short-time Fourier transform (STFT) [3], the wavelet transform (WT) [4] and the Wigner-Ville distribution (WVD) [5]. In the short-time Fourier transform, the time and frequency of the window function could not achieve optimal at the same time that restrict the application of STFT. The performance of WT mainly depends on the measured signal. Meanwhile, the WVD is limited by the presence of cross-term interference.

Recently, the Hilbert-Huang transform (HHT) method is applied to the nonlinear, nonstationary data analysis. The empirical mode decomposition (EMD) decomposes the original signal to obtain the intrinsic mode function (IMF) [6]. Then the Hilbert transform is applied to each IMF to obtain the amplitude and frequency. The EMD method can decompose any type of signals without any basic function preselection with its own time scale characteristics. Based on its own time scale characteristics, the EMD method can decompose any type of signals without any basic function preselection. Therefore, it has an extremely significant advantage in processing nonstationary and nonlinear data and can decompose a complicated signal into some IMFs. Meanwhile, the decomposed IMFs contain the local characteristics of the original signal at different time scales. Hilbert marginal spectrum (HMS) analysis is based on HHT, and possesses the advantage of HHT [7].

For the dimensionality reduction of fault feature extraction, the classical methods are only effective on linear data such as principal component analysis (PCA) [8], linear discriminate analysis (LDA) [9] and locality preserving projection (LPP) [10]. It is difficult to extract feature for nonlinear data using those methods. The manifold learning, a nonlinear dimensionality reduction method such as isometric feature mapping (Isomap) [11], locally linear embedding (LLE) [12], can effectively approximate the low-dimensional input space and have been applied to rotating machinery fault diagnosis. However, when LLE is applied to faults recognition, the LLE ignore the classification information and reduce the diagnostic accuracy [13].

In this study, a novel hybrid model based on HMS, SLLE, and SVM is presented for bearing fault diagnosis. First, the vibration signal is decomposed into some IMFs by EMD and the HMS is applied to obtain the high-dimensional features. Next, the manifold learning of SLLE is used to reduce features to improve the accuracy and reduce the calculation time of the classification. Finally, the low-dimensional fault feature vectors are fed into the trained SVM to identify the fault type.

This paper is organized as follows: Sect. 2 is the introduction of HHT, SLLE, and SVM, Sect. 3 shows the case study performed to validate the method, and Sect. 4 concludes the paper.

2 Methods

Bearings fault diagnosis includes fault feature extraction and fault classification. According to the extracted feature, the fault is classified [14]. The proposed fault feature extraction technique is described in Fig. 1.

2.1 Hilbert-Huang Transform and Its Marginal Spectrum

The HHT consists of EMD and Hilbert spectral analysis. The method of EMD based on time series data is empirical, intuitive, direct, and adaptive. Therefore, any nonlinear and nonstationary signal can be decomposed into a set of IMFs to obtain the amplitude and frequency modulated signals. The signal $x(t)$ can be decomposed as:

$$x(t) = \sum_{i=1}^{n} c_i(t) + r_n(t) \tag{1}$$

where n is the number of intrinsic modes, $c_i(t)$ is the ith IMF, and $r_n(t)$ is the final residual which represents the average trend of the signal.

The Hilbert transform is applied to every IMF to compute instantaneous frequency and amplitude [15]. For any IMF $c_i(t)$, its Hilbert transform $\hat{c}(t)$ is defined as:

$$\hat{c}(t) = \frac{1}{\pi} p \int_{-\infty}^{+\infty} \frac{c(\tau)}{t-\tau} d\tau \tag{2}$$

where p is the Cauchy principal value. Then, the analytic signal $z(t)$ can be defined as:

$$z(t) = c(t) + j\hat{c}(t) = \alpha(t) e^{j\phi(t)} \tag{3}$$

The amplitude $\alpha(t)$ and instantaneous phase $\phi(t)$ are defined as:

$$\alpha(t) = \sqrt{c(t)^2 + \hat{c}(t)^2} \tag{4}$$

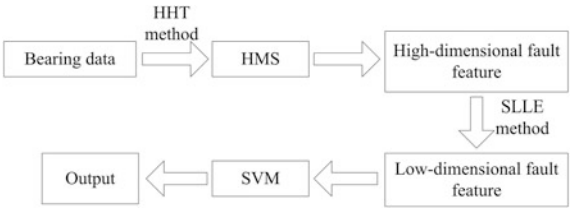

Fig. 1 Block diagram of the proposed method

$$\phi(t) = \arctan \frac{\hat{c}(t)}{c(t)} \tag{5}$$

According to the instantaneous phase $\phi(t)$ the instantaneous frequency $w(t)$ can be denoted as:

$$w(t) = \frac{d\phi(t)}{dt} \tag{6}$$

The original signal can be written in the following form:

$$X(t) = \mathrm{Re} \sum_{i=1}^{n} a_i(t) \exp(j \int w_i(t)dt) \tag{7}$$

The frequency-time distribution of the amplitude is defined as the Hilbert-Huang spectrum, $H(w,t)$. The marginal spectrum $h(w)$ can be defined as:

$$h(w) = \int_0^T H(w,t)dt \tag{8}$$

The marginal spectrum offers a measure of total amplitude contribution from each frequency value [16].

2.2 Supervised Locally Linear Embedding Algorithm

Using the HMS analysis method, the feature vectors are calculated from the bearing vibration signal. The dimension of the feature vectors is too high, so the SLLE algorithm is applied to obtain the low-dimensional feature vectors to improve the accuracy and reduce the calculation time of the classification.

The LLE algorithm is an unsupervised method of nonlinear mapping from high-dimensional space to low-dimensional space. Given a set of data, $X = \{x_1, x_2, \ldots x_n\}$ is in a high-dimensional input data space representing feature vectors. The objective of LLE is to map a low-dimensional representation of the data X. The LLE algorithm mainly contains three steps [17]:

Step 1: Finding the k-nearest neighbors for each point x_i in $R^D, I = 1, 2, \ldots n$ by using the Euclidean distance.

Step 2: Assuming that each sample x_i can be reconstructed by the k-nearest neighbors. Compute the reconstruct weights w_{ij} of each input sample, $w_{ij} > 0$ and $\sum_j w_{ij} = 1$. The reconstruction error is defined as:

$$\varepsilon(W) = \sum_{i=1}^{n} \left\| x_i - \sum_{j=1}^{n} w_{ij} x_j \right\|^2 \tag{9}$$

Step 3: Computing the coordinates of each x_i in the low-dimensional space. The low-dimensional output space Y can be computed by minimizing the cost function:

$$\phi(Y) = \left\| y_i - \sum_{j=1}^{n} w_{ij} y_j \right\|^2 \tag{10}$$

With the constraints: $\sum_{i=1}^{N} y_i y_i^T / N = I_{d \times d}$, $\sum_{i=1}^{N} y_i = 0$, where $y_i \in R^d$ is the output sample vector, and I is an identity matrix. To find the matrix Y, we can define a matrix M as follows:

$$M = (I - W)^T (I - W) \tag{11}$$

The d bottom eigenvectors of M is associated to the d smallest nonzero eigenvalues and make up the matrix Y.

The LLE is an unsupervised learning method which does not the category information of training samples. To improve the recognition ability, the class label information is integrated in LLE. Supervised LLE (SLLE) [18] is introduced to increase the distance between samples of different classes by reducing the distance within class. A distance between samples x_i and x_j from different classes was added to modify only the first step of the original LLE, while keeping the other two steps unchanged [19]. The redefined distance between samples is as follows:

$$\Delta' = \Delta + \alpha \max(\Delta)(1 - \delta(x_i, x_j)) \tag{12}$$

where Δ' is the distance integrated with the class label information, $\Delta = \left\| x_i - x_j \right\|$ is the original distance between samples and $\max(\Delta) = \max_{x,j} \left\| x_i - x_j \right\|$ is the maximum distance between samples. If x_i and x_j belong to different classes, $\delta(x_i, x_j) = 1$ otherwise $\delta(x_i, x_j) = 0$. a is a parameter to adjust the distance between point sets. When $\alpha = 0$, SLLE is equivalent to the original unsupervised LLE.

3 Experiments and Analysis

3.1 Bearing Fault Data

An experimental analysis on bearing fault diagnosis was present to evaluate the effectiveness of the proposed method. The bearing vibration data were provided by the Bearing Data Center of the Case Western Reserve University (CWRU) [20].

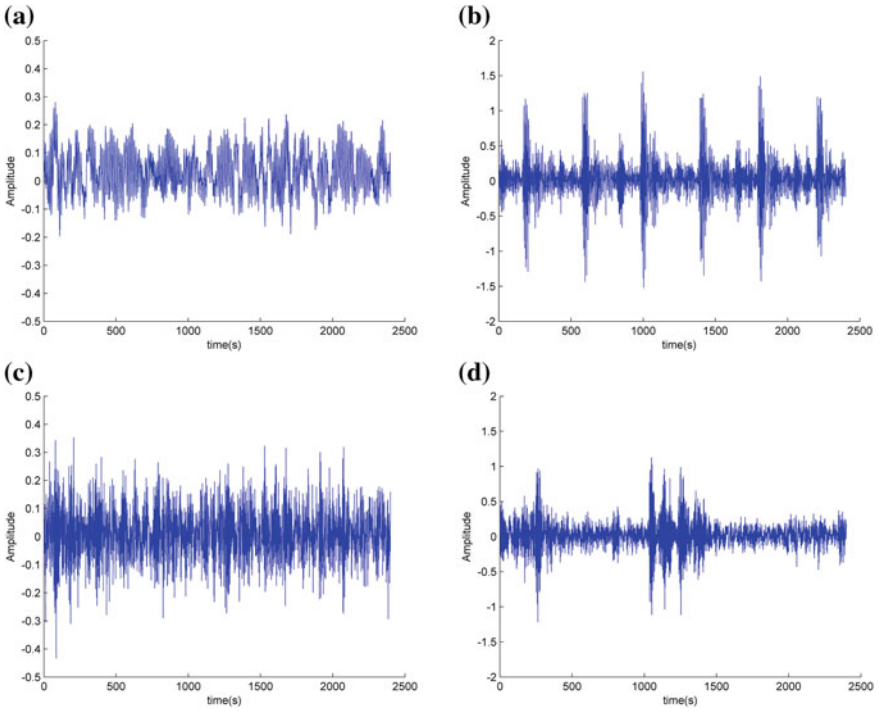

Fig. 2 The vibration signal waveforms of **a** the normal, inner-race fault, **b** outer-race fault, **c** and rolling element fault, **d** signal

The four types of the vibration signal (normal, inner-race, outer-race, and rolling element) were collected at 12,000 sample/s. The motor drives the input shaft and the output shaft drive the loads of 0 and 3 horsepower (corresponding to motor speeds of 1797 and 1720 r/min). Three levels of fault severity 7, 14, and 21 mils were injected into the test bearings. In this study, the length of each original collected signal is about 120,000, and 50 samples for each vibration condition are extracted. The vibration signal waveforms of the different fault types are shown in Fig. 2.

3.2 Feature Extraction Based on Hilbert-Huang Transform

To acquire the fault feature vectors, EMD is used to decompose the vibration signals of the different fault types into IMFs, as shown in Fig. 3. The subsignals are a series of amplitude and frequency modulation signals and the frequency is reduced. Then based on Hilbert-Huang transform, further analyses of the bearings signal can be made to obtain the significant feature.

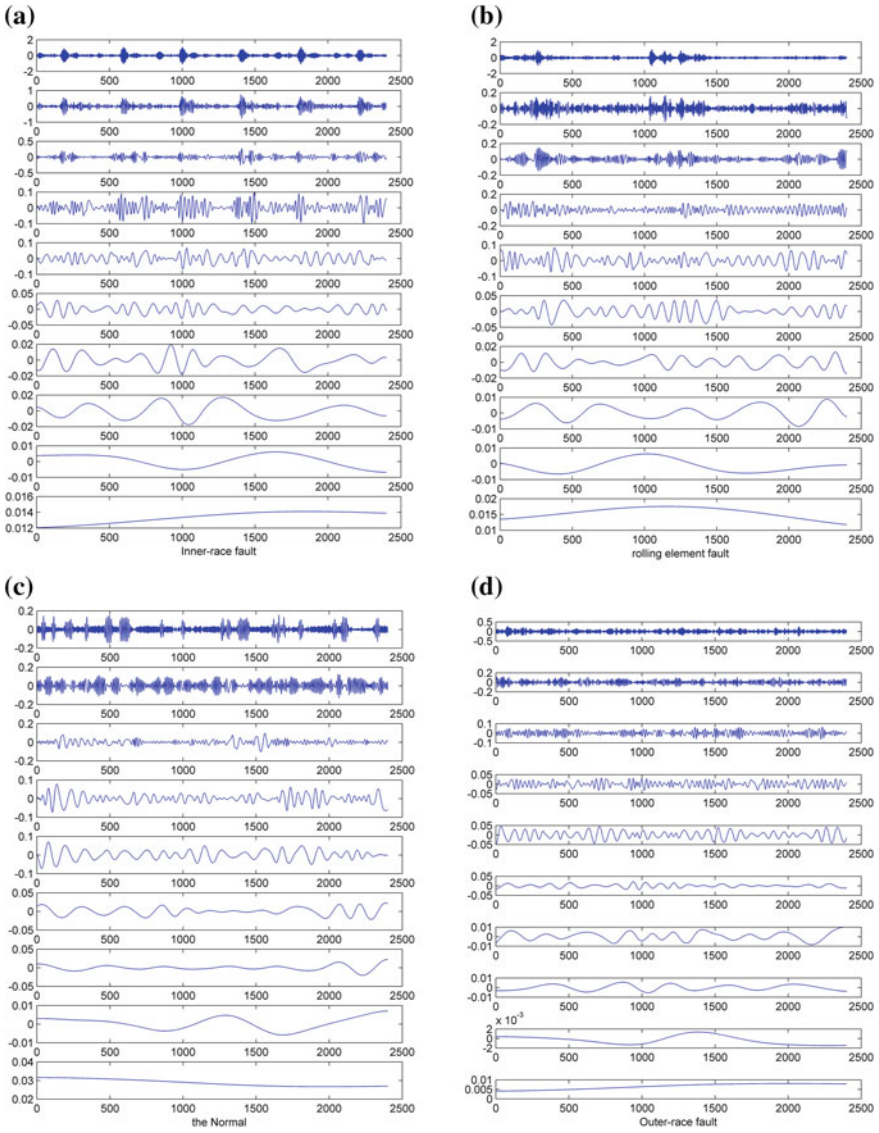

Fig. 3 IMFs of the vibration signal obtained by EMD: **a** the normal; **b** the inner-race fault; **c** the out-race fault; **d** the rolling element fault

The plots of the HMS analysis method applied to the IMFs of the raw vibration signals are shown in Fig. 4. Compared among the four figures, the qualitative distinction of the different fault types is obtained. According to the Hilbert-Huang spectrum, it is clearly observed from the figures that the amplitudes and the distributions of the frequencies of the different faults samples are quite different. With

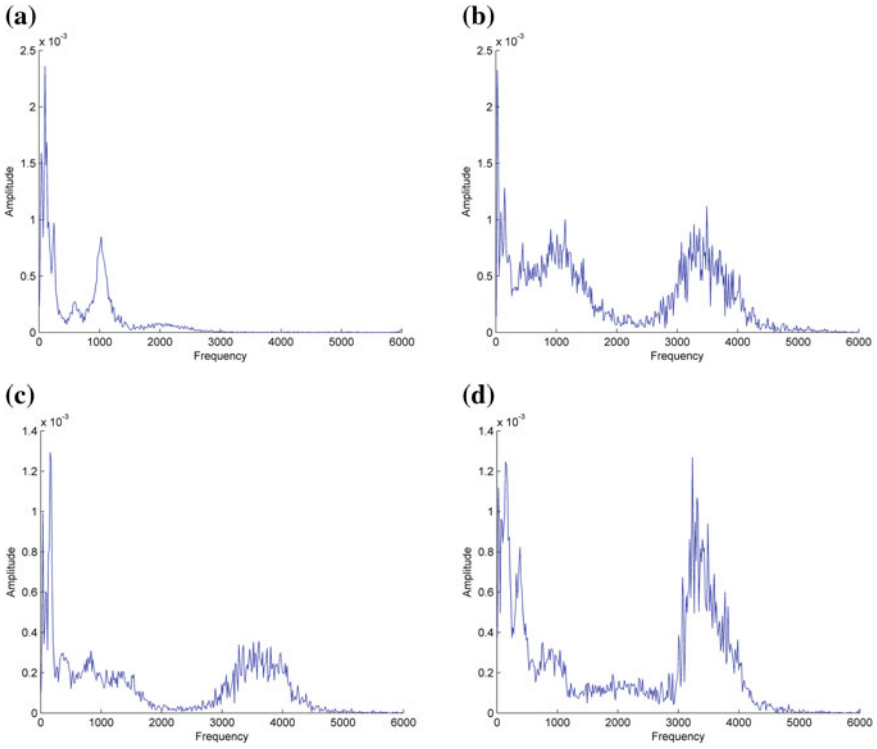

Fig. 4 The HMS of **a** the normal, **b** inner-race fault, **c** outer-race fault, **d** rolling element fault signal

these obtained spectrums, the energy beyond 2000 Hz is considered to be the noise signal. We extract the feature of the vibration signals from the energy spectrum below 2000 Hz. Therefore, with the same level of fault severity and the same load, 200 samples are obtained, $N = 200$. Meanwhile, 136 features are obtained for each fault sample.

3.3 Feature Dimension Reduction Based on SLLE

The traditional diagnosis methods that these feature values of the HMS analysis method are directly input into the diagnosis model is difficult to meet the needs of complex fault diagnosis for bearing fault diagnosis. Based on the manifold learning method, the high-dimensional features are input into SLLE for nonlinear dimensionality reduction. In order to verify the validity of the SLLE method, a comparison with PCA, MDS and LLE was made to evaluate its dimensionality reduction performance. The optimal parameters of SLLE d, k, and are respectively,

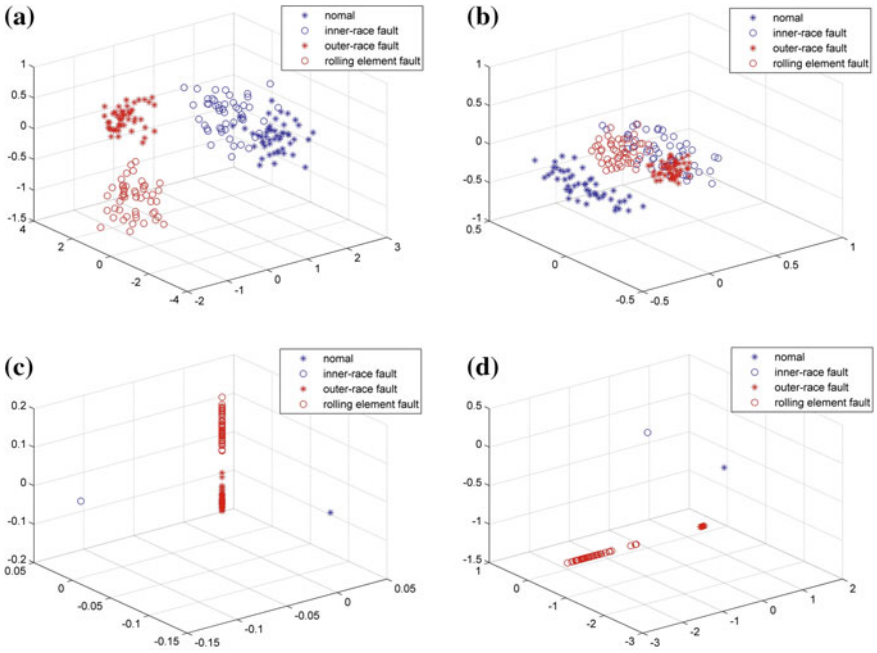

Fig. 5 Feature dimension reduction to rolling bearing multi-domain feature in the dataset of 0 horsepower with fault diameters of 7 mils: **a** Mapping with PCA; **b** Mapping with MDS; **c** Mapping with LLE; **d** Mapping with SLLE

set to 3, 14, and 0.01. The experimental results with the four methods are shown in Fig. 5, where it can be seen that the classification performance of PCA and MDS are poor. The classification accuracy of LLE is close to SLLE, but when SLLE is applied, the fault can be separated and gathered better. We will discuss this in detail in the following paragraphs.

3.4 State Classification Based on SVM

State classification for recognizing the operating states of rolling bearing can be done based on the fault feature vectors obtained by HMS and LLE methods. 80 samples are regarded as training sample, and the other 120 samples are regarded as testing sample. State classification results based on SVM are shown in Table 1, from which we can see that even under variable conditions, the actual output of SVM are extremely consistent with the target outputs. Thus, the proposed method combining HMS and SLLE with SVM is able to efficiently realize the fault diagnosis of rolling bearings under variable conditions. A comparison is made to show the performance of MDS, LTSA, and LLE. Detailed results of the comparison are

Table 1 State classification results based on SVM using SLLE

Sequence	Severity (in)	Load (hp)	No. of categories	Average accuracy (%)
1	0.007	0	4	100
2		3	4	100
3	0.014	0	4	99.52
4		3	4	99.71
5	0.021	0	4	100
6		3	4	99.73

Table 2 Classification results of MDS, LLE, and SLLE

	MDS	LLE	SLLE
Running time/s	0.8281	0.4895	0.3052
Average accuracy (%)	96.52	99.08	99.82

shown in Table 2, in which six examples are given to calculate the mean values of running time and classification accuracy in order to make the comparison. As we can see, the average consumed time by SLLE is 0.3052 s, and the average classification accuracy of SLLE is 99.82 %. The MDS method is obviously more time-consuming and less accurate than the other methods. Although LLE and SLLE are comparable, SLLE still has advantages in both running time and classification accuracy. However, the classification accuracies of the three methods are all higher than 95 %, because the fault feature vectors have good separability, which in turn verifies the effectiveness of the proposed feature extraction method.

4 Conclusions

To fully extract the features of the bearings vibration signal, a novel fault diagnosis method based on HMS and SLLE is proposed in this study. The approach first performs the Hilbert marginal spectrum for feature extraction from faulty bearing vibration signals. Then the supervised locally linear embedding (SLLE) method solves the problem of mapping the high-dimensional feature into a low-dimensional fault feature space. Finally, the SVM is applied to the fault classification. The effectiveness of the proposed fault diagnosis method is verified by using the bearing data. The results show that the proposed approach has a strong advantage over the other traditional methods.

Acknowledgments This research is supported by the National Nature Science Foundation of China (No.61374135), the National Natural Science Foundation of Chongqing (No.cstc2016jcyjA0504) and Chongqing University Postgraduates Innovation Project (No.CYS15027).

References

1. Goswami DY, Zhao Y (2009) Proceedings of ISES World Congress 2007 (Vol. 1–Vol. 5): Solar Energy and Human Settlement. Springer Science and Business Media
2. Jiang L, Xuan J, Shi T (2013) Feature extraction based on semi-supervised kernel marginal fisher analysis and its application in bearing fault diagnosis. Mech Syst Sig Process 41 (1):113–126
3. Chen Y, Zhao Y, Yu G et al (2015) A fault diagnosis method based on ITD and LSSVRCGSO for roller bearings. J Comput Inf Syst 11(10):3469–3476
4. Yang Y, Yuan C, Wang J et al (2014) Day-ahead electricity demand forecasting method based on SOM, WT and PSO-LSSVM algorithm. J Comput Inf Syst 10(5):2203–2210
5. Shi L, Zhang Y, Mi W (2011) Application of Wigner-Ville-distribution-based spectral kurtosis algorithm to fault diagnosis of rolling bearing. J Vibr Meas Diagn 31(1):27–31
6. Huang NE (2014) Hilbert-Huang transform and its applications. World Scientific
7. Wang B, Wang Z, Xu J (2012) A new coal-rock interface recognition method based on Hilbert marginal spectrum distribution characteristics. J Comput Inf Syst 8(19):8137–8142
8. Jolliffe IT (2010) Principal component analysis, series: springer series in statistics, 2nd edn. Springer, New York, NY, USA
9. Borg I, Groenen P (2005) modern multidimensional scaling: theory and applications, 2nd edn. Springer: New York, NY, USA, pp 207–212
10. Wong WK, Zhao HT (2012) Supervised optimal locality preserving projection. Pattern Recogn 45(1):186–197
11. Zhang Y, Li B, Wang Z et al (2013) Fault diagnosis of rotating machine by isometric feature mapping. J Mech Sci Technol 27(11):3215–3221
12. Wang J (2012) Locally linear embedding. In: Geometric structure of high-dimensional data and dimensionality reduction. Springer, Berlin Heidelberg, pp 203–220
13. Zhang Y, Li B, Wang W et al (2014) Supervised locally tangent space alignment for machine fault diagnosis. J Mech Sci Technol 28(8):2971–2977
14. Zhao B, Jia X (2015) Fault diagnosis for turntable based on rough sets-neural network. J Comput Inf Syst 11(10):3545–3551
15. Huang NE (2014) Hilbert-Huang transform and its applications. World Scientific
16. Fu K, Qu J, Chai Y et al (2015) Hilbert marginal spectrum analysis for automatic seizure detection in EEG signals. Biomed Sig Process Control 18:179–185
17. Ahmed S, Islam MR, Azam MS (2009) Bangla hand written digit recognition using supervised locally linear embedding algorithm and support vector machine. In: 12th international conference on computers and information technology ICCIT'09. IEEE, pp 390–393
18. McClure KS, Gopaluni RB, Chmelyk T et al (2013) Nonlinear process monitoring using supervised locally linear embedding projection. Ind Eng Chem Res 53(13):5205–5216
19. Zhang S, Li L, Zhao Z (2010) Speech emotion recognition based on supervised locally linear embedding. In: 2010 international conference on communications, circuits and systems (ICCCAS). IEEE, pp 401–404
20. Loparo KA Bearings vibration data set, Case Western Reserve University. http://www.eecs.case.edu/laboratory/beaing/

Salient Region Detection Using Multilevel Image Features

Qichang Duan, Si Li and Mingxuan Mao

Abstract In this paper, we propose a novel salient region detection approach. First, segment the original image into a set of superpixels to extract patch level features using low-level features in the patch. Next, global level features like element uniqueness and color contrast are created by previous patch level features. And then both patch level and global level features are gathered to a region to create region level features. Finally, all three level features are utilized to train support vector machines (SVM) classifier, and the trained SVM classifier is used to compute saliency map. The experiment results on the datasets show that the approach we propose performs outstanding in several state-of-the-art approaches.

Keywords Element uniqueness · Color contrast · Saliency detection · SLIC · SVM

1 Introduction

The primary goal of computer vision is to understand the surrounding environment utilizing images and videos. In this field, there are three critical works which are correct perception of the main object in the scene, outline recognition of the objects, and access to environmental context of the objects. In order to achieve this goal, saliency detection in the images is the most basic step. Thus, it has turned into an active field in computer vision on account of its various applications, such as image retargeting, object recognition, and object detection.

Salient region detection approaches can be usually classified into two groups, which are top-down and bottom-up [1]. Bottom-up approach is stimulus and data-driven, which utilizes lots of low-level features [2], such as texture, intensity and color, since salient objects have strong contrast in comparison with the background. Nowadays, in order to value saliency, many approaches [1, 3, 4] use color

Q. Duan · S. Li (✉) · M. Mao
School of Automation, Chongqing University, Chongqing 400044, China
e-mail: lee88688@163.com

Y. Jia et al. (eds.), *Proceedings of 2016 Chinese Intelligent Systems Conference*,
Lecture Notes in Electrical Engineering 404, DOI 10.1007/978-981-10-2338-5_23

contrast features along with other high-level features which are called color distribution and uniqueness, since salient objects are spatial compact rather than widely spread background in the image. Except for these features, center prior [1] is another useful feature, which can evaluate salient objects center with color contrast and position.

Currently, more and more approaches are using multiple level detection methods, which however operate on either global level [4, 5], region level [6, 7] or patch level [1]. Patch level features usually called low-level features like color, edge, and texture would usually fail to suppress background noises and cannot highlight a salient object more uniformly [8]. While region level features may solve this difficulty a little when smaller salient objects are in the image. If a salient object is large enough, global level features can figure out the entire salient object. However, it may ignore the small part of the salient object and highlight large background texture leading to degraded performance.

In order to solve the aforementioned issues, we propose a novel saliency detection approach. We combine patch level, region level, and global level features together and use SVM (Support Vector Machine) classifier to composite the final saliency map. Currently, there are rare region level features in previous works. On the contrary, a lot of patch level and global level features are present and it can be used to create relative region level features.

2 Proposed Approach

In order to get abstracted patch level, region level, and global level features of an image, our method first use SLIC algorithm [9] to segment the input image into a cluster of patches, which is an edge-preserving superpixel segmentation result. And then, these superpixels are used to extract patch level, region level and global level features which can be utilized to learn and estimate visual saliency. Figure 1 demonstrates the main features involved in the proposed approach.

2.1 Frequency Saliency Feature

In frequency domain, low-frequency parts represent the outline and basic compositional region, while high-frequency parts are texture and noise. The saliency detection would like to emphasize the largest silent objects and disregard texture and noise. So the low-and high-frequency cutoff value ω_{lc} and ω_{hc}, respectively would be considered to have well-defined boundaries and avoid noise. We choose DoG band-pass filter the same as [10] to get frequency information between ω_{hc} and ω_{lc}.

DoG filter is widely applied in edge detection because of the fact that it can be used to obtain an approximation of the Laplacian of Gaussian when the radio of the

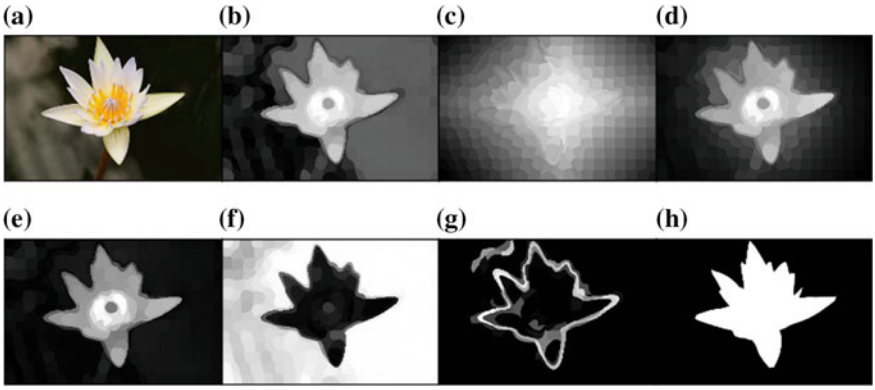

Fig. 1 Main features that have be used in the proposed approach. **a** Original image. **b** Frequency saliency feature map. **c** Center focus feature map. **d** Global color contrast feature map. **e** Element uniqueness feature map. **f** Element distribution feature map. **g** Edge feature map. **h** Ground truth

standard deviation of the Gaussians ($\sigma_1 : \sigma_2$) are 1.6:1 [11]. The DoG filter is given by:

$$Dog\,(x,y) = G(x,y,\sigma_1) - G(x,y,\sigma_2) \tag{1}$$

where $G(x,y,\sigma) = \frac{1}{2\pi\sigma^2} e^{-\frac{x^2+y^2}{2\sigma^2}}$. Let us define $\sigma_1 = \rho\sigma$ and $\sigma_2 = \sigma$, where ρ is a constant at 1.6 which is a perfect edge detector. On the contrary one DoG filter with fixed ρ has narrow bandwidth. The summation over DoG could fix.

$$\begin{aligned} F_N &= \sum_{n=0}^{N-1} G\left(x,y,\rho^{n+1}\sigma\right) - G(x,y,\rho^n\sigma), \\ &= G\left(x,y,\sigma\rho^N\right) - G(x,y,\rho) \end{aligned} \tag{2}$$

where $N \geq 0$, the bandwidth of filter is decided by $K = \rho^N$. In order to keep more frequencies, K is derived to infinity, and therefore, $G(x,y,\sigma\rho^N)$ are the average feature of the image. So the frequency feature of each pixel could be calculated as:

$$f(x,y) = \left\| I_\mu - I_{\omega hc}(x,y) \right\| \tag{3}$$

where I_μ is the average feature of the image and $I_{\omega hc}$ is computed by Gaussian blur in Lab color space, x, y is the pixel of the position in the image, $\|\cdot\|$ is the L_2 norm. Therefore, each superpixel frequency feature is:

$$S_i^1 = \frac{1}{K} \sum_{i=1}^{K} f(x_i, y_i), \tag{4}$$

where the pixel (x_i, y_i) is in the superpixel i.

2.2 Center Focus Feature

According to Gestalt laws [12], human's visual system may grasp one or several attention centers in the scene [13]. Generally, an image have just one salient object called central object which can attract human's attention and this phenomenon is known as center focus. None-salient objects are distributed around the salient object and thus spatial position play an important role in it. Objects which are close to salient center would stand more out. So we use frequency saliency feature as weight to calculate spatial center of the image. Hence it is:

$$S_{i,x}^2 = \frac{\sum_{i=1}^{W}\sum_{j=1}^{H} S_{ij}^1 \cdot i}{\sum_{i=1}^{W}\sum_{j=1}^{H} S_{ij}^1}, S_{i,y}^2 = \frac{\sum_{i=1}^{W}\sum_{j=1}^{H} S_{ij}^1 \cdot j}{\sum_{i=1}^{W}\sum_{j=1}^{H} S_{ij}^1}, \tag{5}$$

where W, H are the image's weight and height, S_{ij}^1 is the frequency saliency feature of the image in the pixel at position (i,j).

2.3 Global Color Contrast Feature

The color contrast between a patch and its surroundings can be a very important factor for visual saliency. Color contrast can be local and global. Local contrast is concentrated on contrast between center and surroundings and the saliency value is the greater the difference the greater the contrast. Conversely, global contrast focuses more on contrast between one region and the whole image sense.

Local contrast is computational efficiency due to its limited surroundings, while global contrast may cost expensive on computation in $O(N^2)$ (N is the pixels' number) time order. Thus, we use superpixels to accelerate our computing. When calculating global contrast, use mean value of the pixels in the superpixel to supplants pixels in it, which can be decreased in $O(n^2)$ (n is the superpixels' number) time order where $n \ll N$.

Visual color contrast is also involved in spatial position. If a region with high contrast with its surroundings would be more attracted. For every superpixel, the feature is calculated as (6). Let d_{color} be the distance between two superpixels' mean color feature in Lab color space. d_{pos} is the distance between two superpixels' mean spatial position.

$$\begin{aligned} d(p_i, p_j) &= \frac{d_{color}(p_i, p_j)}{(1 + d_{pos}) \cdot \alpha} \\ S_i^3 &= 1 - e^{-\frac{1}{N}\sum_{j=1}^{N} d(p_i, p_j)} \end{aligned} \tag{6}$$

where $\alpha = 5$ in our experiments. N is superpixel's number used to search for all superpixels in the image to calculate global color contrast.

2.4 Element Uniqueness and Distribution Feature

Element uniqueness and distribution [4] are designed for the contrast measure among patches such as superpixels and they are also global features. They are all comprised of color and spatial position and similarly we use average color and spatial position to represent each superpixels.

Element Uniqueness evaluate how different each superpixel is from others, mainly it measures rareness of each superpixel. Thanks to the segmentation, textures and noise on the pixel level can be restrained due to average and color discontinuities cannot stay sharply because of SLIC's edge-preserving segmentation. And it is defined as:

$$\begin{aligned} S_i^4 &= \sum_{j=1}^{N} \left\| c_i - c_j^2 \right\| \omega_{ij}^{(p)} \\ \omega_{ij}^{(p)} &= \frac{1}{Z_i} e^{-\frac{1}{2\sigma_p^2}\left\| p_i - p_j \right\|^2} \end{aligned} \tag{7}$$

where c_i, c_j are color vector in Lab color space and Z_i is normalization factor. In our experiments, we choose $\sigma_p = 20$.

Element distribution measures its existence somewhere in other superpixels of the image. A compact object which means that the segment's spatial with low variance of its color corresponding to other segments should be more salient. And spatially widely distributed segments should be less salient than a compact object. Thus, the element distribution is defined as:

$$\begin{aligned} S_i^5 &= \sum_{j=1}^{N} \left\| p_j - \mu_i \right\|^2 \omega_{ij}^{(c)} \\ \omega_{ij}^{(c)} &= \frac{1}{Z_i} e^{-\frac{1}{2\sigma_c^2}\left\| c_i - c_j \right\|^2}, \mu_i = \sum_{j=1}^{N} \omega_{ij}^{(c)} p_j, \end{aligned} \tag{8}$$

where $\sigma_c = 20$ in our experiments.

2.5 Training SVM Classifier

Except the features that we are introduced above, we also extract other practical features to assist in locating salient objects. Table 1 shows all these features and their levels and they are extracted as either patch level or global level feature. So we

Table 1 All features and there levels

Feature name	Feature level
Mean color in lab color space	Patch level and region level
Mean position	
Edge	
Relative size	Patch level
Frequency saliency	Region level and global level
Element distribution	
Color contrast	
Element uniqueness	
Center focus	Global level

use the superpixel and its neighbors to create the region and the region feature value is the mean value of superpixels in the region.

Every superpixel S_i is represented by 22-dimensional feature vector as demonstrated in Table 1. The label of each individual superpixel, in which true represents a salient superpixel while false is not, is calculated as:

$$P(S_i) = \begin{cases} 1, t_i/(t_i + f_i) \geq \beta \\ 0, t_i/(t_i + f_i) < \beta \end{cases}, \tag{9}$$

where $P(S_i)$ is the salient probability of S_i. f_i and t_i are the quantity of false and true positives, respectively, which are calculated by the ground truth of pixels' number in the superpixel S_i. We use $\beta = 0.9$ in our experiments. In our method, we use SLIC algorithm to segment image into 300 superpixels and then use the features in Table 1 as input and the $P(S_i)$ as label in training SVM classifier.

3 Experimental Result

We compare our algorithm on the three of most widely used datasets MSRA-1000 dataset [10] and SED-100 dataset [14]. MSRA-1000 dataset is the one of the most popular datasets for salient object detection. SED-100 dataset consists of 100 images and it is a subset of the SED dataset, where each image has only one salient object. We compare our approach with seven state-of-the-art methods, which are AC [15], FT [10], GC [3], HC [5], LC [16], RC [5] and SF [4]. In order to implement our experiment, we eventually select 5 images in MSRA-1000 dataset to train the SVM classifier.

3.1 Evaluation Criterion

For a state-of-the-art method in each dataset, we adopt four evaluation methods to evaluate the performance, which are F-measure with adaptive threshold, precision-recall (PR) curve, mean absolute error (MAE) score and area under ROC

curve (AUC) score. Usually the saliency map is often a grayscale map and can be easily normalized to [0, 255]. For a saliency map S, with the help of the threshold it can be converted to a binary mask B. Precision and Recall are computed by comparing ground truth G with B. It is defined as:

$$Precision = \frac{|B \cap G|}{|B|}, Recall = \frac{|B \cap G|}{|G|} \tag{10}$$

In this definition, it is found that the key step in evaluation is the binarization of the saliency map. In our paper we use 2 popular ways. First, Achanta et al. [10] proposed an adaptive threshold method with image-dependent property, which is defined as:

$$T_a = \frac{2}{W \times H} \sum_{x=1}^{W} \sum_{y=1}^{H} S(x, y), \tag{11}$$

where H and W are the saliency map's height and width, respectively. The second way is using fixed threshold from 0 to 255. Every threshold can compute a pair of recall and precision, and then combine them to compose a precision-recall curve. By using the adaptive threshold, we can obtain binarized maps of each of approaches to calculate precision and recall from the same ground-truth. The F-Measure using mean of the precision and recall is computed as:

$$F_\beta = \frac{\left(1 + \beta^2\right) Precision \times Recall}{\beta^2 \times Precision \times Recall} \tag{12}$$

where β^2 is set to 0.3 the same as that in [10]. Area under ROC curve (AUC) score considers the consistency between the saliency map and its ground-truth, while mean absolute error (MAE) score are evaluating a continuous saliency map and its binary ground-truth, and it is defined as:

$$MAE = \frac{1}{W \times H} \sum_{x=1}^{W} \sum_{y=1}^{H} |S(x, y) - G(x, y)|, \tag{13}$$

where H and W are the saliency map's height and width respectively.

3.2 Quantitative Evaluation

The performance of precision-recall curve of the proposed method presents best, which means it can suppress the background noise more efficiently, except in SOD dataset which is the same as RC method. And Fig. 2a shows that the proposed method gets nearly 100 % precision rate for higher thresholds. Figures 2b and 3b

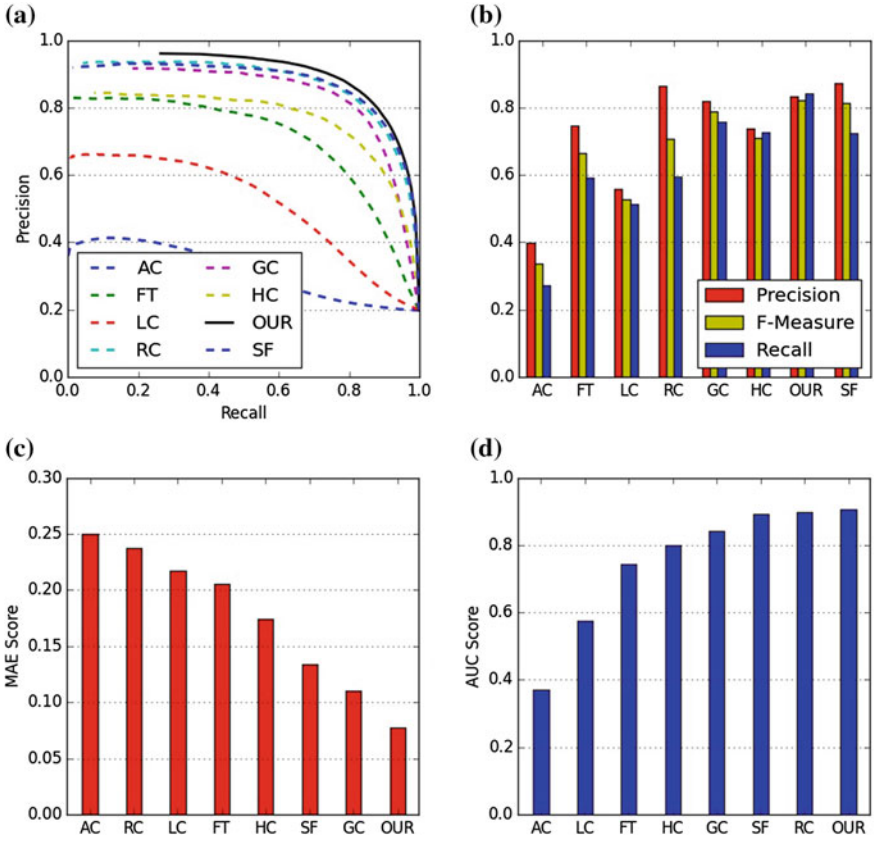

Fig. 2 Comparison of evaluation result with 7 state-of-the-art methods on MSRA-1000 dataset. **a** Average precision-recall curve with fixed thresholding. **b** Precision, F-Measure and recall value with adaptive thresholding. **c** Mean absolute error (MAE) score of different approaches. **d** Area under ROC curve (AUC) score of different approaches

show that our method performs not well enough on precision rate, but our F-Measure and recall are significantly higher than other methods in two datasets. Figures 2c and 3c show that our method excels other methods compared with us in terms of MAE score, which gives better estimate of difference between ground truth and saliency map, and can be much lower than other methods in MSRA-1000 and SED-100 dataset. From Figs. 2d and 3d, we can know that the AUC score of our method basically is the same as the best of the other method and behaves unsatisfying.

Figure 4 shows the comparison of saliency maps of different methods. It is seen that the saliency map of our method can be so much like the ground truth. Due to the SVM classifier, our method can clearly identify foreground and background and pick out the saliency object.

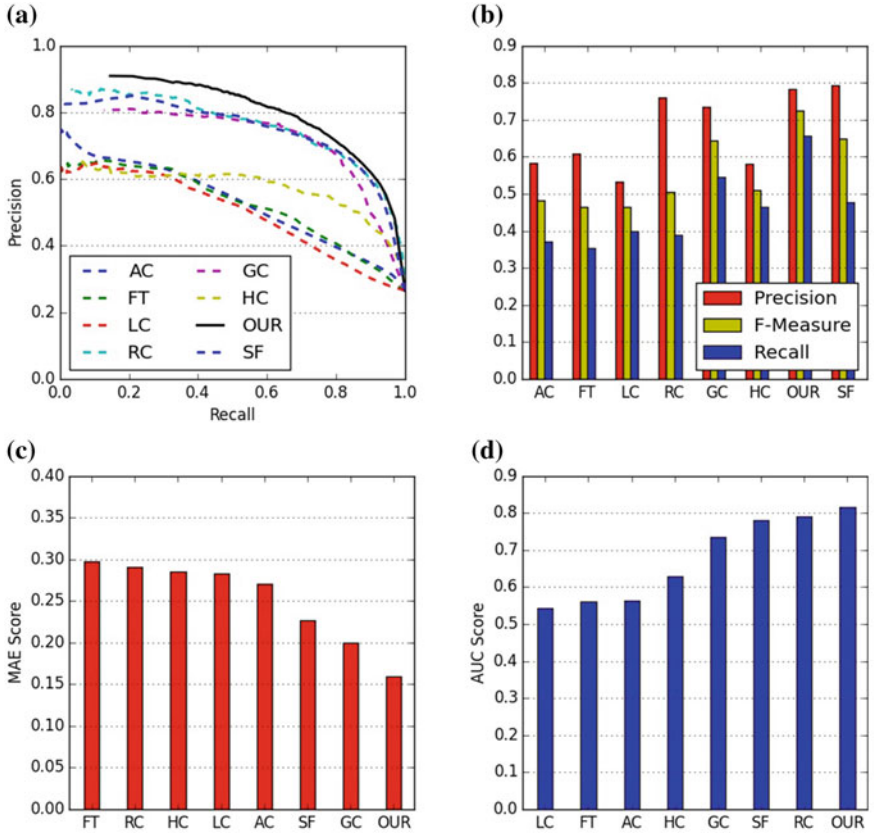

Fig. 3 Comparison of evaluation result with 7 state-of-the-art methods on SED-100 dataset. **a** Average precision-recall curve with fixed thresholding. **b** Precision, F-Measure and recall value with adaptive thresholding. **c** Mean absolute error (MAE) score of different approaches. **d** Area under ROC curve (AUC) score of different approaches

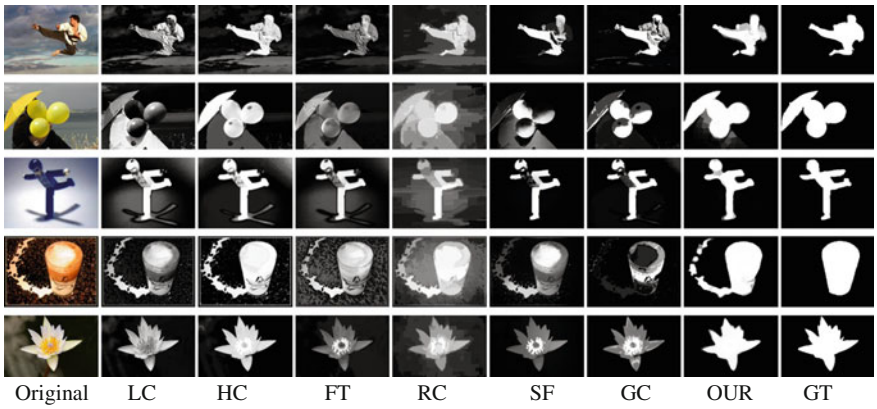

Fig. 4 Example saliency maps of different methods

4 Conclusion

In this paper, we propose a novel salient region detection approach using multilevel features to train SVM classifier which is used for the product of the saliency map. The proposed approach performs outstanding compared with existing methods, and presents robust performance for different datasets even if we choose the same feature images in MSRA-1000 dataset, and performs well on suppressing background non-salient objects. Further works include analysis and simplification of the features, improvement of the computational efficiency and the precision of the prediction.

References

1. Fu K, Gong C, Yang J et al (2013) Superpixel based color contrast and color distribution driven salient object detection. Sig Process Image Commun 28(10):1448–1463
2. Itti L, Koch C, Niebur E (1998) A model of saliency-based visual attention for rapid scene analysis. IEEE Trans Pattern Anal Mach Intell 11:1254–1259
3. Cheng MM, Warrell J, Lin WY et al (2013) Efficient salient region detection with soft image abstraction. In: Proceedings of the IEEE International Conference on Computer vision, pp 1529–1536
4. Perazzi F, Krähenbühl P, Pritch Y et al (2012) Saliency filters: Contrast based filtering for salient region detection. In: IEEE conference on computer vision and pattern recognition (CVPR). IEEE, pp 733–740
5. Cheng M, Mitra NJ, Huang X et al (2015) Global contrast based salient region detection. Pattern Anal Mach Intell IEEE Trans 37(3):569–582
6. Yu JG, Zhao J, Tian J et al (2014) Maximal entropy random walk for region-based visual saliency. Cybern IEEE Trans 44(9):1661–1672
7. Ren Z, Gao S, Chia LT et al (2014) Region-based saliency detection and its application in object recognition. Circuits Syst Video Techno IEEE Trans 24(5):769–779
8. Kannan R, Ghinea G, Swaminathan S (2015) Salient region detection using patch level and region level image abstractions. Sig Process Lett IEEE 22(6):686–690
9. Achanta R, Shaji A, Smith K et al (2012) SLIC superpixels compared to state-of-the-art superpixel methods. Pattern Anal Mach Intell IEEE Trans 34(11):2274–2282
10. Achanta R, Hemami S, Estrada F et al (2009) Frequency-tuned salient region detection. In: IEEE conference on computer vision and pattern recognition, CVPR 2009. IEEE, pp 1597–1604
11. Mart DC (1982) A computational investigation into the human representation and processing of visual information
12. Hartmann GW (1935) Gestalt psychology: A survey of facts and principles
13. Koffka K (2013) Principles of Gestalt psychology. Routledge
14. Alpert S, Galun M, Brandt A et al (2012) Image segmentation by probabilistic bottom-up aggregation and cue integration[J]. Pattern Anal Mach Intell IEEE Trans 34(2):315–327
15. Achanta R, Estrada F, Wils P et al (2008) Salient region detection and segmentation. In: Computer vision systems. Springer, Berlin Heidelberg, pp 66–75
16. Zhai Y, Shah M (2006) Visual attention detection in video sequences using spatiotemporal cues. In: Proceedings of the 14th annual ACM international conference on Multimedia. ACM, pp 815–824

Leader-Following Consensus Problem of Fractional-Order Multi-agent Systems with Perturbation

Zhiyong Yu, Haijun Jiang and Cheng Hu

Abstract In this paper, the consensus problem of fractional-order multi-agent systems (FOMAS) with perturbation is considered. Both undirected and directed communication topologies are considered for FOMAS, where the fractional order $0 < \alpha < 2$. By using the fractional-order stability theory and the inequality techniques, some consensus criteria are obtained. Besides, an example is given for illustration.

Keywords Consensus · Multi-agent systems · Fractional-order · Perturbation

1 Introduction

The consensus was proposed a long time ago [1]. Broadly speaking, consensus refers to reaching an agreement regarding certain quality of interests among some agents. For all agents, sharing information with each other, or consulting multiple experts as presented in [2] makes the decision makers more confident. In recent years, inspired by this idea, similar strategy has been implemented in multi-agent systems (MAS). Consensus algorithms of single integrator dynamic systems have been discussed in [3, 4]. The consensus algorithms of double-integrator dynamics [5] and high-order dynamic systems [6] also have been considered.

Consensus phenomena, in reality, are widely existed in biology, engineered systems, social science, etc. At present, most of studies of consensus are confined to systems with integer-order dynamics. As a matter of fact, many phenomena can naturally be explained by fractional-order dynamics. For example, (1) Food seeking and chemotaxis behavior of microbes. (2) Flying vehicles operating in high-speed flow of dust storm, rain, or snow. (3) Ground vehicles moving on muddy road, grass, carpet, sand, etc. To the best of our knowledge, the consensus of fractional-order systems

Z. Yu · H. Jiang (✉) · C. Hu
College of Mathematics and System Sciences, Xinjiang University,
Urumqi 830046, China
e-mail: jianghaijunxju@163.com

Y. Jia et al. (eds.), *Proceedings of 2016 Chinese Intelligent Systems Conference*,
Lecture Notes in Electrical Engineering 404, DOI 10.1007/978-981-10-2338-5_24

was first investigated in [7] and further studied in [8]. Moreover, some protocols about the consensus of FOMS were proposed in [9–13].

Leader-following consensus problem is a very interesting topic of consensus. The leader is regarded as a special agent, whose dynamics is independent of all others. However, the follower agents can receive information form the leader and follow the leader's state. It was said that the configuration of leader–follower, which was found in many biological systems, is an energy saving mechanism [14], and can also enhance the communication and orientation of the flock. In [15, 16], the leader-following consensus of FOMAS was investigated using feedback control and adaptive pinning control. Up to now, the problem of FOMAS with perturbation has rarely been investigated in the open literatures.

In this paper, the consensus of FOMAS with perturbation is studied. The main contributions of the paper are twofold: (1) We consider the leader-following consensus of FOMAS via feedback control with perturbation, in which perturbation is variable with respect to time. Moreover, both undirected and directed communication topologies are considered, respectively. (2) The fractional order $0 < \alpha < 2$ is studied for the FOMAS.

The rest of this paper is organized as follows. In Sect. 2, some preliminaries are presented. In Sect. 3, consensus of FOMAS over undirected topology is studied. In Sect. 4, the consensus of FOMAS with directed communication topology is considered. In Sect. 5, an example is presented for illustration. Conclusions are given in Sect. 6.

Notations Throughout the paper, I_n represents the identity matrix with dimension n, For a real symmetric matrix P, $P > 0$ represents that P is a positive definite matrix. $\|\cdot\|$ refers to the Euclidean norm. $Sym\{Y\}$ denotes the expression $Y + Y^T$.

2 Preliminaries

In the paper, Caputo fractional operator is adopted to analyze the asymptotic consensus. The definition of Caputo fractional derivative of function $f(t)$ with order α is presented by [19]:

$$ {}_0^C\mathcal{D}_t^\alpha f(t) = \frac{1}{\Gamma(n-\alpha)} \int_0^t \frac{f^{(n)}(\tau)}{(t-\tau)^{\alpha-n+1}} d\tau, $$

where $n-1 < \alpha < n$, $n \in \mathbf{Z}^+$, and $\Gamma(\cdot)$ is the Gamma function. A simple notation D^α is used to replace the Caputo fractional derivative operator ${}_0^C\mathcal{D}_t^\alpha$.

Consider a group of multi-agent system with N followers and a leader. The dynamics of the ith follower is given by

$$ D^\alpha x_i = Ax_i + \mathcal{U}_i, i = 1, 2, \ldots, N, \tag{1} $$

where $0 < \alpha < 2$, $x_i \in R^n$ is the state. $\mathcal{U}_i \in R^n$ is the control input. The dynamics of the leader, labeled as $i = 0$, is given by

$$D^{\alpha} x_0 = A x_0, \tag{2}$$

where $0 < \alpha < 2$, $x_0 \in R^n$ is the state of the leader.

Definition 1 ([15]) The leader-following consensus of systems (1) and (2) is said to be reached if, for any initial conditions,

$$\lim_{t \to \infty} \|x_i(t) - x_0(t)\| = 0, i = 1, 2, \ldots, N.$$

It is well known that the perturbation always exists in the process of information transmission. There is few reports in the open literature investigation the consensus of FOMAS via feedback control with perturbation. Hence, we propose the following control protocol and the input $\mathcal{U}_i$ is designed as

$$\mathcal{U}_i = \sum_{j \in N_i} a_{ij}(x_j - x_i) + (B + \Delta B)(x_0 - x_i), \tag{3}$$

where $B \in R^{n \times n}$ represents feedback control gain matrix, ΔB is the control perturbation matrix. Suppose that the control perturbation is given by:

$$\Delta B = MF(t)N, \tag{4}$$

where M and N are known matrices. $F(t)$ is unknown time-varying matrix, which satisfies the following condition

$$F(t)F(t)^T \leq I_n. \tag{5}$$

Remark 1 In (3), each agent can be regarded as a node of the graph, then $x_i \in R^n$ denotes the state of node v_i, $\mathcal{A} = [a_{ij}]_{N \times N}$ with $a_{ij} \geq 0$ represents the weighted adjacency matrix. $a_{ij} > 0$ if there exists information pass from node v_j to node v_i and $a_{ij} = 0$, otherwise. In the paper, $\mathcal{G} = (G, x)$ with $x = (x_1^T, x_2^T, \ldots, x_N)^T$ denotes a network composed by state value $x \in R^{nN}$ and communication graph G. The Laplacian matrix $L = [\ell_{ij}]$ with respect to the graph G is defined as $\ell_{ii} = \sum_{j \neq i} a_{ij}$ and $\ell_{ij} = -a_{ij}$ for $i \neq j$. Let $\bar{\mathcal{G}}$ represents the network of leader-following FOMAS (1) and (2) with input (3).

Define the error vector $e_i = x_i - x_0$, then error system can be rewritten as

$$D^{\alpha} e_i = A e_i + \sum_{j \in N_i} a_{ij}(e_j - e_i) - (B + \Delta B)e_i, i = 1, 2, \ldots, N. \tag{6}$$

Combination with the Kroncker product, the system (6) is written as:

$$D^{\alpha}\mathbf{e} = (I_N \otimes (A - B - \Delta B) - L \otimes I_n)\mathbf{e}, \tag{7}$$

where $\mathbf{e} = (e_1^T, \ldots, e_N^T)^T \in R^{nN}$. The consensus of systems (1) and (2) via the controller (3) can be achieved if the error system (7) is global asymptotical stability.

3 Network with Fixed and Undirected Topology

We focus on investigating the consensus of the network over undirected graph. In order to obtain our main results, we make the following assumption.

Assumption 1 The network $\bar{\mathcal{G}}$ contains a directed spanning tree with root v_0 and the subnetwork $\mathcal{G}$ is undirected.

Theorem 1 *Under Assumption 1, the leader-following consensus of FOMAS (1) and (2) via protocol (3) is achieved if*

$$|arg(\xi_j)| > \frac{\alpha\pi}{2}, j = 1, 2, \ldots, n, \tag{8}$$

where ξ_j are eigenvalues of matrix $A - (B + \Delta B)$ and $0 < \alpha < 2$.

Proof Let $\lambda_1, \ldots, \lambda_N$ denote the eigenvalues of the $-L$. Since L is the Laplacian matrix of graph G, so all λ_i are non-positive real numbers, which are sorted out in decreasing order as

$$0 = \lambda_1 \geq \lambda_2 \geq \cdots, \geq \lambda_N. \tag{9}$$

Then, according to Lemma 3 in [17], all eigenvalues of $(I_N \otimes (A - B - \Delta B) - L \otimes I_n) \in R^{nN \times nN}$ have the form $\lambda_i + \xi_j$ for $i = 1, 2, \ldots, N$, and $j = 1, 2, \ldots, n$. Because ξ_j satisfies inequality (8) and λ_i is non-positive real number. Then, $\lambda_i + \xi_j$ also satisfies inequality (8). Based on Lemma 2.5 in [12], the system (7) is stable. Consequently, leader-following consensus of FOMAS (1) and (2) is achieved.

Although some sufficient criteria are obtained for achievement of the consensus in Theorem 1, which is more complicated in implementation since the perturbation ΔB is a variable. So, it main applies to theoretical analysis. Consequently, the following theorem is proposed.

Theorem 2 *Under Assumption 1, the leader-following consensus of FOMAS (1) and (2) with protocol (3) is achieved if there exist a constant $\varepsilon > 0$, a matrix $P > 0$ and a matrix Q satisfying the following condition:*

case *(1).* $0 < \alpha \leq 1$

$$\begin{pmatrix} Q + Q^T + \varepsilon MM^T & PN^T \\ \star & -\varepsilon I \end{pmatrix} < 0, \tag{10}$$

case *(2).* $1 < \alpha < 2$

$$\begin{pmatrix} \Pi & I_2 \otimes (PN^TNP + MM^T)^{\frac{1}{2}} \\ \star & -\varepsilon I \end{pmatrix} < 0, \tag{11}$$

where

$$\Pi = \theta_1 \otimes Q + \theta_2 \otimes Q^T + \varepsilon \left(I_2 \otimes (MM^T + PN^TNP) \right),$$

with

$$\theta_1 = \begin{pmatrix} \sin\theta & \cos\theta \\ -\cos\theta & \sin\theta \end{pmatrix} \theta_2 = \begin{pmatrix} \sin\theta & -\cos\theta \\ \cos\theta & \sin\theta \end{pmatrix}, \theta = \pi - \frac{\alpha\pi}{2}.$$

Moreover, the control gain B is given by

$$B = A - QP^{-1}.$$

Proof When $0 < \alpha \leq 1$, based on Lemma 2 in [10], the asymptotical stability of system (7) holds if and only if

$$\sum_{i=1}^{2}\sum_{j=1}^{2} Sym\left\{\theta_{ij} \otimes [(I_N \otimes (A - B - \Delta B) - L \otimes I_n)\tilde{P}_{ij}]\right\} < 0, \tag{12}$$

where $\tilde{P}_{i1} > 0$, $i = 1, 2$. $P_{i2}, i = 1, 2$ are two skew-symmetric matrices which satisfy

$$\begin{pmatrix} P_{11} & P_{12} \\ -P_{12} & P_{11} \end{pmatrix} > 0, \begin{pmatrix} P_{21} & P_{22} \\ -P_{22} & P_{21} \end{pmatrix} > 0.$$

Set

$$\tilde{P}_{11} = \tilde{P}_{21} = I_N \otimes P, P_{12} = P_{22} = 0, \tag{13}$$

where $P > 0$. According to Lemma 2 in [10], one obtains that if

$$\sum_{i=1}^{2} Sym\left\{\theta_{i1} \otimes [I_N \otimes (A - B - \Delta B)P - L \otimes P]\right\} < 0, \tag{14}$$

where

$$\theta_{11} = \begin{pmatrix} \sin(\frac{\alpha\pi}{2}) & -\cos(\frac{\alpha\pi}{2}) \\ \cos(\frac{\alpha\pi}{2}) & \sin(\frac{\alpha\pi}{2}) \end{pmatrix}, \theta_{21} = \begin{pmatrix} \sin(\frac{\alpha\pi}{2}) & \cos(\frac{\alpha\pi}{2}) \\ -\cos(\frac{\alpha\pi}{2}) & \sin(\frac{\alpha\pi}{2}) \end{pmatrix},$$

then system (7) is asymptotically stable.

Let

$$AP - BP = Q, Q - \Delta BP = \Xi. \tag{15}$$

Since

$$\begin{aligned}&\sum_{i=1}^{2} Sym\left\{\theta_{i1} \otimes [I_N \otimes (A - B - \Delta B)P - L \otimes P]\right\}\\ =&\begin{pmatrix} 2\sin(\frac{\alpha\pi}{2}) I_N \otimes (\Xi + \Xi^T) & 0 \\ 0 & 2\sin(\frac{\alpha\pi}{2}) I_N \otimes (\Xi + \Xi^T) \end{pmatrix}\\ &-\begin{pmatrix} 2\sin(\frac{\alpha\pi}{2}) & 0 \\ 0 & 2\sin(\frac{\alpha\pi}{2}) \end{pmatrix} \otimes \left[(L \otimes P) + (L \otimes P)^T\right],\end{aligned}$$

$\sin(\frac{\alpha\pi}{2}) > 0$ for $0 < \alpha < 1$, and $L \otimes P \geq 0$, it obtains that

$$\sum_{i=1}^{2} Sym\{\theta_{i1} \otimes [I_N \otimes (A - B - \Delta B)P - L \otimes P]\} < 0,$$

if

$$Q + Q^T - (\Delta BP + P\Delta B^T) < 0. \tag{16}$$

It is well known that for any real scalar $\varepsilon > 0$

$$\Delta BP + P\Delta B^T \leq \varepsilon MM^T + \frac{1}{\varepsilon}(PN^T NP). \tag{17}$$

Substituting inequality (17) into inequality (16), one has

$$\sum_{i=1}^{2} Sym\{\theta_{i1} \otimes [I_N \otimes (A - B - \Delta B)P - L \otimes P]\} < 0,$$

if

$$Q + Q^T + \varepsilon MM^T + \frac{1}{\varepsilon}(PN^T NP) < 0. \tag{18}$$

Using Schur complement lemma in [20], it can be easily seen that inequality (18) is equivalent to (10).

When $1 < \alpha < 2$, base on Theorem 8 in [18], the asymptotical stability of system (7) holds if there exists a matrix $P > 0$, such that

$$\begin{pmatrix} (\Xi + \Xi^T)\sin\theta & (\Xi - \Xi^T)\cos\theta \\ * & (\Xi + \Xi^T)\sin\theta \end{pmatrix} < 0, \tag{19}$$

where $\theta = \pi - \frac{\alpha\pi}{2}$, $\Xi = (A - B - \Delta B)P$.

Let

$$AP - BP = Q, \qquad (A - B - \Delta B)P = \Xi. \tag{20}$$

Since

$$\begin{pmatrix} (\Xi + \Xi^T)\sin\theta & (\Xi - \Xi^T)\cos\theta \\ * & (\Xi + \Xi^T)\sin\theta \end{pmatrix} = \theta_1 \otimes \Xi + \theta_2 \otimes \Xi^T,$$

where

$$\theta_1 = \begin{pmatrix} \sin\theta & \cos\theta \\ -\cos\theta & \sin\theta \end{pmatrix} \theta_2 = \begin{pmatrix} \sin\theta & -\cos\theta \\ \cos\theta & \sin\theta \end{pmatrix}, \theta = \pi - \frac{\alpha\pi}{2},$$

Then, it can be concluded by Theorem 8 in [18] that if

$$\theta_1 \otimes \Xi + \theta_2 \otimes \Xi^T < 0, \tag{21}$$

then error system (7) is asymptotically stable.

$$\theta_1 \otimes \Xi + \theta_2 \otimes \Xi^T = \theta_1 \otimes Q + \theta_2 \otimes Q^T + (-\theta_1 \otimes \Delta BP - \theta_2 \otimes P\Delta B^T). \tag{22}$$

From inequality (5) and $\theta_i\theta_i^T = I_2,\ i = 1, 2$, it directly follows that for any scalar $\varepsilon > 0$,

$$\begin{aligned} &-\theta_1 \otimes \Delta BP - \theta_2 \otimes P\Delta B^T \\ &\le \varepsilon \left[I_2 \otimes (MM^T + PN^TNP)\right] + \frac{1}{\varepsilon}\left[I_2 \otimes (PN^TNP + MM^T)\right]. \end{aligned} \tag{23}$$

substituting inequality (23) into Eq. (22), one has

$$\begin{aligned} &\theta_1 \otimes (Q - \Delta BP) + \theta_2 \otimes (Q^T - P\Delta B^T) \\ &< \theta_1 \otimes Q + \theta_2 \otimes Q^T + \varepsilon[I_2 \otimes (MM^T + PN^TNP)] \\ &+ \frac{1}{\varepsilon}[I_2 \otimes (PN^TNP + MM^T)]. \end{aligned} \tag{24}$$

Following from inequality (24), the inequality (21) holds if

$$\theta_1 \otimes Q + \theta_2 \otimes Q^T + \varepsilon \left[I_2 \otimes (MM^T + PN^TNP)\right] + \frac{1}{\varepsilon}\left[I_2 \otimes (PN^TNP + MM^T)\right] < 0. \tag{25}$$

Using Schur complement lemma in [20], it is obtained that inequality (25) is equivalent to the linear matrix inequality (11). This completes the proof.

4 Networks with Fixed and Directed Topology

In this section, we focus on investigating the consensus of the network with directed topology.

Assumption 2 The network $\bar{\mathcal{G}}$ contains a directed spanning tree with root v_0 and the subnetwork $\mathcal{G}$ is directed.

Theorem 3 *Under Assumption 2, the leader-following consensus of FOMAS (1) and (2) via protocol (3) can be achieved if*

$$|arg(\lambda_i + \xi_j)| > \frac{\alpha\pi}{2}, \qquad i = 1, \ldots .N,\ j = 1, \ldots, n, \tag{26}$$

where λ_i and ξ_j are eigenvalues of matrix $-L$ and $A - (B + \Delta B)$, respectively, and $0 < \alpha < 2$.

Proof The proof is similar to Theorem 1, thus the details are omitted.

Theorem 4 *Under Assumption 2, the leader-following consensus of FOMAS (1) and (2) with protocol (3) is achieved if there exist a constant $\varepsilon > 0$, a matrix $P > 0$ and a matrix Q satisfying the following condition:*
case *(1).* $0 < \alpha \leq 1$

$$\begin{pmatrix} I_N \otimes (Q + Q^T + \varepsilon MM^T) - (L + L^T) \otimes P & I_N \otimes PN^T \\ \star & -\varepsilon I \end{pmatrix} < 0. \tag{27}$$

case *(2).* $1 < \alpha < 2$

$$\begin{pmatrix} \Pi & I_{2N} \otimes (PN^T NP + MM^T)^{\frac{1}{2}} \\ \star & -\varepsilon I \end{pmatrix} < 0, \tag{28}$$

where

$$\Pi = \theta_1 \otimes [(I_N \otimes Q) - (L \otimes P)] + \theta_2 \otimes [(I_N \otimes Q^T) - (L^T \otimes P)] + \varepsilon I_{2N} \otimes (MM^T + PN^T NP),$$

with

$$\theta_1 = \begin{pmatrix} sin\theta & cos\theta \\ -cos\theta & sin\theta \end{pmatrix},\ \theta_2 = \begin{pmatrix} sin\theta & -cos\theta \\ cos\theta & sin\theta \end{pmatrix}, \qquad \theta = \pi - \frac{\alpha\pi}{2}.$$

Moreover, the control gain B is given by $B = A - QP^{-1}$.

Proof The proof is similar to Theorem 2, thus the details are omitted.

5 Numerical Simulations

A numerical example is presented to show the effectiveness and feasibility of our results.

Consider the multi-agent system (1) and (2) with protocol (3), in which there are three followers in multi-agent system (1) and

$$A = \begin{pmatrix} 0.3 & 0 \\ 0 & 0.25 \end{pmatrix}, M = \begin{pmatrix} 1 & 0 \\ 0 & 1.2 \end{pmatrix}, F(t) = \begin{pmatrix} \sin x_{i1}(t) & 0 \\ 0 & \sin x_{i2}(t) \end{pmatrix}, N = \begin{pmatrix} 0.5 & 0 \\ 1 & 1/2 \end{pmatrix}.$$

The network with fixed topology and coupling weight satisfies $a_{12} = 0.6$ $a_{21} = 0.4$, $a_{32} = 0.5$, and other elements are zero. Then, the consensus can be achieved by choosing feasible control gain as shown in Figs. 1, 2, 3 and 4.

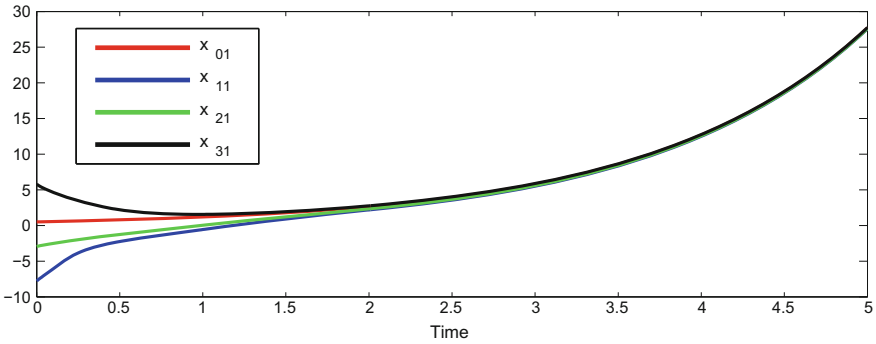

Fig. 1 The states of x_{i1}, $\alpha = 0.9$

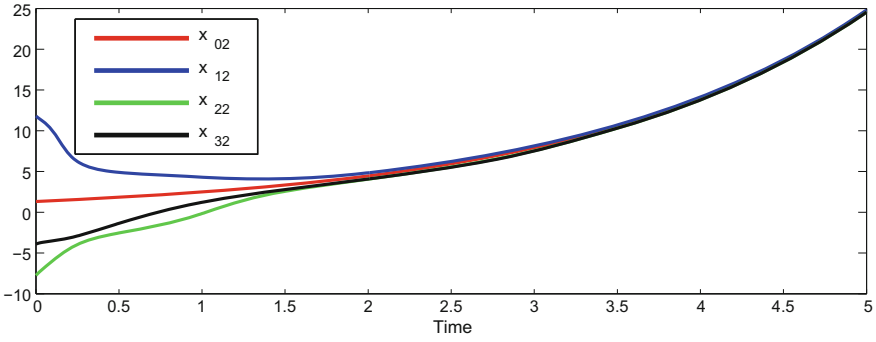

Fig. 2 The states of x_{i2}, $\alpha = 0.9$

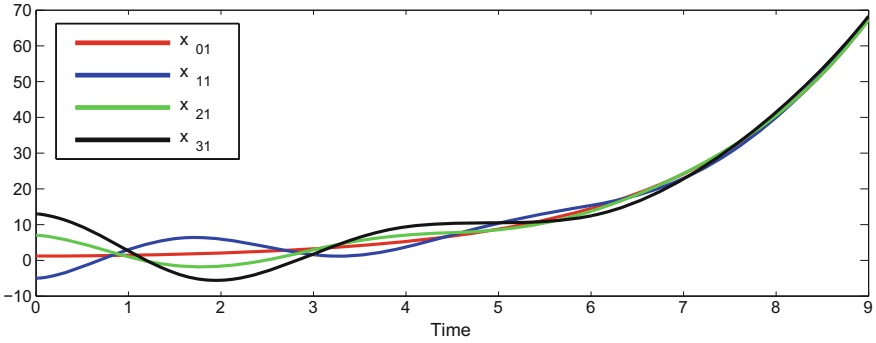

Fig. 3 The states of x_{i1}, $\alpha = 1.8$

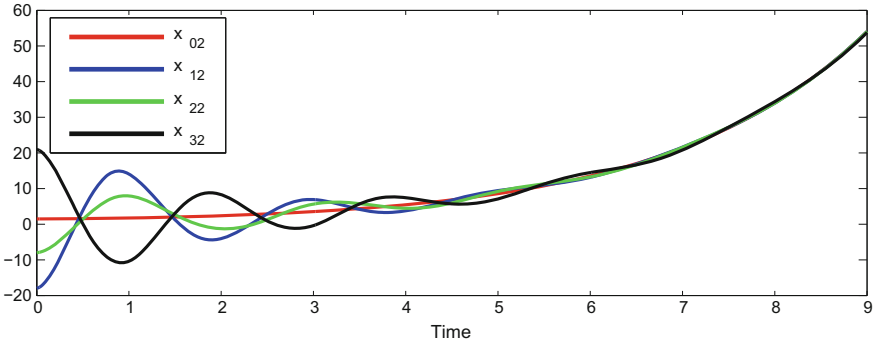

Fig. 4 The states of x_{i2}, $\alpha = 1.8$

6 Conclusion

In this paper, the leader-following consensus problems of linear FOMAS over undirected and directed communication topology via feedback control with perturbation are investigated. By using fractional-order stability theory and LMI techniques, some sufficient criteria are derived to ensure the consensus. An example is presented for illustration.

Acknowledgments This work was supported by National Natural Science Foundation of Peoples Republic of China (Grants No. 61164004, No. 61473244, No. 11402223).

References

1. DeGroot M (1974) Reaching a consensus. J Am Stat Assoc 69(345):118–121
2. Winkler R (1968) The consensus of subjective probability distributions. Manag Sci 15(2): 61–75

3. Chen F, Chen Z, Xiang L, Liu Z, Yuan Z (2009) Reaching a consensus via pinning control. Automatica 45(5):1215–1220
4. Olfati-Saber R (2007) Consensus and cooperation in networked multi-agent systems. Proc IEEE 95(1):215–233
5. Sun Y, Wang L (2009) Consensus problems in networks of agents with dobble-integrator dynamics and time-varying delays. Int J Control 82(10):1937–1945
6. Liu Y, Jia Y (2010) Consensus problem of high-order multi-agent systems with external disturbances: an H_∞ analysis approach. Int J Robust Nonlinear Control 20(14):1579–1593
7. Cao Y, Li Y, Chen Y (2008) Distributed coordination algorithems for multiple fractional-order systems. In: IEEE conference on decision and control, pp 9–11
8. Cao Y, Li Y, Ren W, Chen Y (2010) Distributed coordination of networked fractional-order systems. IEEE Trans Syst Man Cybern 40(2):362–370
9. Song C, Cao J (2013) Consensus of fractional-order linear systems. In: 9th Asian control conference (ASCC), pp 1–4
10. Yin X, Yue D, Hu S (2013) Consensus of fractional-order heterogeneous multi-agent systems. IET Control Theory Appl 7(2):314–322
11. Shen J, Cao J (2012) Necessary and sufficient conditions for consensus of delayed fractional-order systems. Asian J Control 14(6):1690–1697
12. Li H (2012) Observer-type consensus protocol for a class of fractional-order uncertain multi-agent systems. Abstr Appl Anal. doi:10.1155/2012/672346
13. Bai J, Wen G, Rahmani A, Yu Y (2015) Distributed formation control of fractional-order multi-agent systems with absolute damping and communication delay. Int J SystSci 46(13): 2380–2392
14. Hammel D (1995) Formation flight as an energy saving mechanism. Israel J Zool 41(3): 261–278
15. Yu Z, Jiang H, Hu C (2015) Leader-following consensus of fractional-order multi-agent systems under fixed topology. Neurocomputing 149:613–620
16. Yu Z, Jiang H, Hu C, Yu J (2015) Leader-following consensus of fractional-order multi-agent systems via adaptive pinning control. Int J Control 88(9):1746–1756
17. Wang J, Ma Q, Zeng L (2013) Observer-based synchronization in fractional-order leader-follower complex networks. Nonlinear Dyn 73(1):921–929
18. Sabatier J, Moze M, Farges C (2010) LMI stability conditions for fractional order systems. Comput Math Appl 59(5):1594–1609
19. Kilbas A, Srivastava H, Trujillo J (2006) Theory and appliciations of fractional differential equations. Elsevier, The Netherlands
20. Boyd S, Ghaoui L, Feron E, Balakrishnan V (1994) Linear matrix inequalities in system and control theory. SIAM, Philadelphia

Distributed Control for Formation Switch of Fixed Wing MAVs

Wanrong Huang, Yanzhen Wang, Hai Yang, Xiaodong Yi and Xuejun Yang

Abstract We propose a distributed control approach for formation switch of fixed wing micro aerial vehicles (MAVs). First, a multilayer system framework is designed for distributed formation control of fixed wing MAVs. Then, a specific control algorithm is proposed for on-the-fly formation switch. During the entire formation switching process, constraints such as a safe inter-MAV distance can be satisfied, by applying position-based dynamics on the conceptual centers around which the MAVs circle. The effectiveness of the proposed approach is demonstrated by comparative experiments in a realistic robot simulator.

Keywords Swarm robotics · Fixed wing MAV · Formation switch · Distributed control

1 Introduction

In recent years, teams of micro aerial vehicles (MAVs) have attracted great interests from research community, for their application potentials in various areas, such as surveillance in border patrol [1], environmental monitoring in vegetation protection, search, and rescue missions during a natural disaster [2]. Although most existing research work focuses on helicopters or quadrotors, fixed wing MAVs have much more potentials in real-world applications, especially in outdoor environments. Fixed wing MAVs can achieve considerably higher speed and have much longer battery life, and hence much larger coverage and more sustainability. Moreover, they have better robustness to wind disturbances in complex environments.

W. Huang · Y. Wang (✉) · H. Yang · X. Yi · X. Yang
State Key Laboratory of High Performance Computing (HPCL),
College of Computer, National University of Defense Technology,
137 Yanwachi Street, Changsha, 410073 Hunan, People's Republic of China
e-mail: yanzhenwang@hotmail.com

Y. Jia et al. (eds.), *Proceedings of 2016 Chinese Intelligent Systems Conference*,
Lecture Notes in Electrical Engineering 404, DOI 10.1007/978-981-10-2338-5_25

A great challenge involved in dealing with fixed wing MAVs is the reduced maneuverability. Limits could be derived from the aircraft physics. A fixed wing MAV cannot hover and has to maintain a sufficiently large forward speed to produce enough lift [3]. Besides, the turning radius of fixed wing MAVs will be always large due to the limited turning rate [4]. These kinematic properties present the main challenge to achieve control of fixed wing MAVs.

As a key problem in applications of swarm and multi-robot systems, formation control has been extensively studied in the past few years. Some work develops collision-free and obstacle-avoiding formation algorithms. In [5], a decentralized control strategy is introduced to let a group of robots create a desired geometric formation and avoid collisions. [6] present a control framework for achieving encirclement of a target using a multi-robot system and discuss about maintenance of a safe inter-robot distance briefly. Typically, these algorithms are designed for ground robots or rotary-wing MAVs, and cannot be directly applied to fixed wing MAVs.

In [7], a novel guidance logic for multi-agent fixed wing unmanned aerial systems using a moving mesh method is proposed. A fleet of a fixed wing MAVs move in formation safely based on artificial potential field method by keeping a settled geometric model in [8]. [9] proposes a method for controlling a swarm of fixed wing MAVs to organize in an equilateral triangles with their neighbors and keep communication link quality on a desired level by expanding or shrinking the formation uniformly. Nevertheless, it does not consider modification of the underlying structure of the formation on the fly.

In this paper, we focus on the on-the-fly formation switch problem of fixed wing MAVs. The contribution of this paper is twofolds. First, a multilayer distributed formation control system for fixed wing MAVs is designed and implemented. Second, a distributed control algorithm for formation switch of fixed wing MAVs using position-based dynamics (PBD) [10] is proposed. This algorithm is implemented as a controller, among other type of controllers, in the framework. Its effectiveness in formation switch control with safe inter-MAV distance constraints is demonstrated by comparative experiments in a realistic simulator.

2 Preliminaries

2.1 Kinematics of Fixed Wing MAVs

The kinematics of a fixed wing MAV is modeled as follows.

$$\begin{cases} \dot{x} = u_1 cos\psi \\ \dot{y} = u_1 sin\psi \\ \dot{\psi} = u_2 \end{cases} \tag{1}$$

where u_1 is the linear velocity control input in the horizontal direction, u_2 is the angular velocity in the horizontal direction, $[x, y]^T$ is the position of the MAV, and ψ is yaw of the MAV.

Obviously, fixed wing MAVs must maintain a sufficiently large forward speed to avoid stalling. Therefore, an MAV have to circle around a static or low-speed target, in order to keep in proximity to it.

2.2 Virtual Agents

Similar to the approach in [9], we define a virtual agent (VA) for each MAV to circle around, so that the relatively slower formation switch motion can be captured by the VA, while the MAVs can still stay airbourne. As a result, the complex formation control of fixed wing MAVs is decoupled into two independent parts: motion of MAVs which needs to obey the fixed wing aircraft kinematics, and motion of VAs as holonomic systems.

As depicted by Fig. 1, when VAs are steadily converging to a formation, MAVs also need to synchronize their phase angles according to the corresponding VAs with their neighbors, in order to faithfully reproduce the same formation.

2.3 Problem Formulation

Consider a system of n MAVs, represented by $MAVs = \{MAV_1, \ldots, MAV_n\}$. The set $VAs = \{VA_1, \ldots, VA_n\}$ contains the corresponding VAs. The initial position of VA_i is $\mathbf{s}_i$, and its goal position after formation switch is $\mathbf{g}_i$. Denote the position of VA_i in the inertial world frame by $\mathbf{p}_i$, the position of MAV_i in the inertial world frame by $\mathbf{p}_i^{mav}$.

The first part of the problem is to figure out a way, in which the VAs moving gradually moving toward their targets, while maintaining a safe inter-VA distance to avoid potential collision of MAVs. The second part of the problem is to figure out how the MAVs can control their motion to follow the corresponding VAs, while reproduce the formation of the VAs.

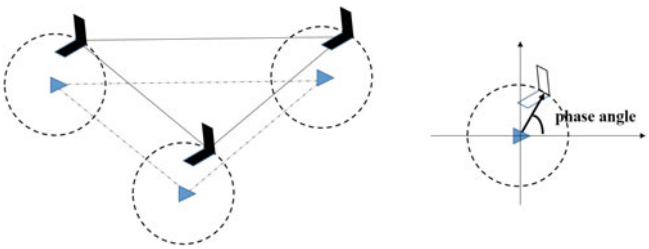

Fig. 1 Example of a three-MAV team with the VAs shown in *blue triangles*

There are also several constraints need to be satisfied during the formation switching process. First, any pair of MAVs must be collision-free at any time:

$$||\mathbf{p}_i^{mav} - \mathbf{p}_j^{mav}|| \geq threshold_{safe}, \forall j \tag{2}$$

Second, fixed wing MAVs always need to maintain a forward speed in order to remain airborne and cannot exceed a maximum speed due to engine limits:

$$0 < v_{min} \leq u_1 \leq v_{max} \tag{3}$$

Third, fixed wing MAVs cannot suddenly change direction due to the limitations in the bank angle:

$$|u_2| \leq \omega_{max} \tag{4}$$

3 Proposed Method

This section presents a detailed description about the proposed distributed control approach for formation switch of fixed wing MAVs, as well as the design choices of the prototype system implemented.

3.1 System Overview

As shown in Fig. 2, the prototype system for interactive formation control of fixed wing MAVs is organized in a layered structure, in order to transform high-level for-

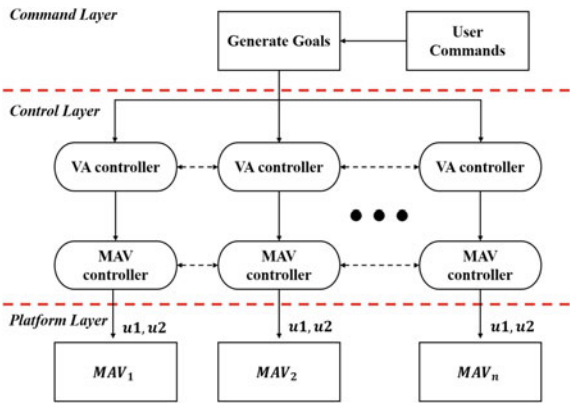

Fig. 2 System architecture

mation switch commands from the user to decentralized velocity commands for each individual MAV.

The *command layer* receives user inputs and generate goals for VAs accordingly. The core of the system is the *control layer*, which is further subdivided into two sublayers, namely the *VA controller* and the *MAV controller*. The *platform layer* converts the linear and angular velocity commands generated by the control layer into low-level flight control signals to MAV hardwares, no matter they are physical or simulated.

3.2 MAV Controller

In order to make the MAVs circle around their corresponding VAs respectively, the MAV controller for each individual MAV generates velocity commands for the low-level control system according to a commanded air speed v_c, and radius r_d. The motion is controlled using a Lyapunov vector field [11] $\mathbf{f}(x_r, y_r)$ to calculated desired horizontal velocity $[\dot{x}_d, \dot{y}_d]$:

$$\begin{aligned}\mathbf{f}(x_r, y_r) &= \begin{bmatrix}\dot{x}_d \\ \dot{y}_d\end{bmatrix} \\ &= \frac{v_0}{r(r^2 + r_d^2)} \begin{bmatrix}x_r(r^2 - r_d^2) + y_r \cdot 2rr_d \\ y_r(r^2 - r_d^2) - x_r \cdot 2rr_d\end{bmatrix}\end{aligned} \tag{5}$$

where r is the relative distance between MAV and its virtual agent, $r^2 = \mathbf{p}_r^T \mathbf{p}_r, \mathbf{p}_r = ||\mathbf{p}^{mav} - \mathbf{p}||$.

It can be shown that the desired speed at any point in this vector field is given by v_0, direction by $\psi_d = arctan2(\dot{y}_d/\dot{x}_d)$. The MAV controller can be implemented as follows.

$$\begin{cases} u_1 = v_c \\ u_2 = -K_\omega < \psi, \psi_d > + \dot{\psi}_d \end{cases} \tag{6}$$

where $e = < \psi, \psi_d >$ is the heading angle error, K_ω is a turning rate gain.

It is easy to prove that the MAV controller (Eq. 6) satisfies the speed and turn rate constraints. The speed u_1 is prescribed by the user and satisfies the constraint (Eq. 3) controllably. As for the turn rate constraint, from Eq. 5, it is obtained that:

$$\dot{\psi}_d = \frac{4v_0 r_d r^2}{(r^2 + r_d^2)^2} \tag{7}$$

where $\dot{\psi}_d$ has a maximum value at $r = r_d$, and $\dot{\psi}_{dmax} = \frac{v_0}{r}$. The maximum value of $-K_\omega < \psi, \psi_d >$ is $K_\omega \pi$. So we can conclude that u_2 is bounded.

In order to guarantee the MAVs maintain approximately the same formation as that of the VAs, we take the approach described in [9] to synchronize their orientation with their neighbors. Specifically, the forward speed of the MAV is adjust within an allowed range:

$$u_1 = v_c + K_\theta \sum_{j \in N_i^{mav}} sin(\theta_j - \theta_i) \tag{8}$$

where N_i^{mav} is the set of neighbors of MAV_i it can exchange information with, θ_j and θ_i are the phase angles of MAV_j and MAV_i, respectively.

3.3 VA Controllers

The main contribution of this paper is the design of VA controllers, which are responsible for converting the high-level formation switch commands into VA motions. Specifically, we propose three strategies for VA control in this paper.

Suppose that all the line segments connecting the start and goal positions, s_i and g_i, for the VAs are intrinsically collision-free. In this case, VA_i can simply move with a constant velocity directly heading toward its goal. This simple controller is named *Uniform Straight Line Motion* or *USLM*, whose implementation is described in Algorithm 1, where v_i^{va} is the prescribed constant speed of VA_i, and Δt is the timestep of the control loop.

Algorithm 1 USLM controller for VA_i

1: **while** $!(||\mathbf{g}_i - \mathbf{p}_i|| \leq 10^{-5})$ **do**
2: $\quad \mathbf{p}_i = \mathbf{p}_i + v_i^{va} \Delta t \frac{\mathbf{g}_i - \mathbf{s}_i}{||\mathbf{g}_i - \mathbf{s}_i||}$
3: **end while**

Obviously, the collision-free assumption does not hold for most cases, and the USLM controller would probably result in crashes of MAVs. Therefore, we further applied the position-based dynamics approach [10] into the VA controller, which is consequently named *PBD*, to maintain a safe inter-VA distance.

As mentioned in Sect. 3.2, MAV controllers make each MAV synchronize its phase angle with its neighbors, so that the distance between each pair of MAVs will always approximately equal to the corresponding inter-VA distance. Therefore, we add a constraint of a safe distance, which should be kept between each VA and its neighbors, into the PBD controller. Theoretically, the safe distance must be greater than the diameter of the MAV D_m, which can be defined as the maximum distance between any two points on the outline of the MAV.

Given the initial positions $\{\mathbf{s}_i\}$ and goal positions $\{\mathbf{g}_i\}$ of the VAs, the implementation of the PBD controller can be described by Algorithm 2. Note that the weight w_i is independently defined for each VA to determine how much the VA gets involved

in avoiding a collision, δ is how much the VA proceed in one time step, and *threshold* is the predefined safe distance.

Algorithm 2 PBD controller for VA_i

1: receive information from other virtual agents
2: **while** not all j satisfied $||\mathbf{g}_j - \mathbf{p}_j|| \leq 10^{-5}$ **do**
3: $\quad \mathbf{p}_i = \mathbf{p}_i + \delta(\mathbf{g}_i - \mathbf{p}_i)$
4: $\quad$ **for** $j = 1 : n \quad and \quad j \neq i$ **do**
5: $\quad\quad$ **if** $||\mathbf{p}_j - \mathbf{p}_i|| < threshold$ **then**
6: $\quad\quad\quad \mathbf{p}_i = \mathbf{p}_i - \frac{w_j}{w_i + w_j}(threshold - ||\mathbf{p}_j - \mathbf{p}_i||)\frac{\mathbf{p}_j - \mathbf{p}_i}{||\mathbf{p}_j - \mathbf{p}_i||}$
7: $\quad\quad$ **end if**
8: $\quad$ **end for**
9: **end while**

A feedback based on the degree of synchronization of the MAVs can be added into the PBD controller to further improve the formation quality during the switching process. We call the new controller a *PBD with Feedback* (PBD-F) controller. The degree of synchronization is defined by accumulating the inter-MAV phase angle differences:

$$K_{sync} = \frac{\sum_j \sum_i < \theta_i, \theta_j >}{2\pi(n-1)}$$

Then, we attenuate the speed of VA motion δ in Line 3 of Algorithm 2 by the factor $(1 - K_{sync})$. Obviously, if the MAVs do not synchronize well, a smaller factor $(1 - K_{sync})$ will slow down the speed of the VAs to give the MAVs more time to adjust.

4 Experimental Results

4.1 Experiment Setup

We have implemented the proposed control approach as a package in the Robot Operating System (ROS) [12], and conducted several experiments in Gazebo [13], a realistic 3D robot simulator with support for dynamics. The *hector_quadrotor* package [14] in ROS is used to facilitate the simulation. Although *hector_quadrotor* is originally aimed at quadrotors, we impose the fixed wing kinematics in Eq. 1 as a constraint to each virtual MAVs in the simulation.

Small-scale formation switch experiments with three MAV were first conducted to test the performance of the proposed methods. As shown in Fig. 3, three MAVs taking off from different locations, $\{[-3,-1]^T, [0,-3]^T, [3,-1]^T\}$, are commanded to circle around corresponding VA positions, $\{\mathbf{s}_1 = [-1,0]^T, \mathbf{s}_2 = [0,-2]^T, \mathbf{s}_3 = [1,0]^T\}$ at first. When they successfully reach the desired formation and cir-

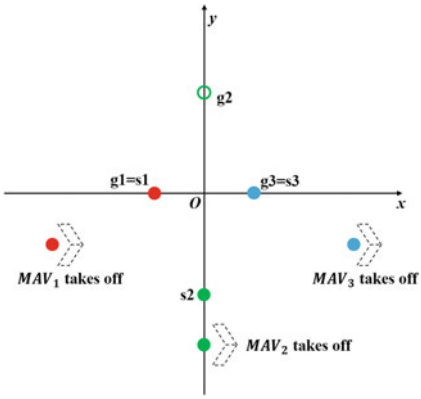

Fig. 3 Setup of the small-scale formation experiment

cle around corresponding VAs in synchronization, goals of VAs in the new formation, $\{\mathbf{g}_1 = [-1, 0]^T, \mathbf{g}_2 = [0, 2]^T, \mathbf{g}_3 = [1, 0]^T\}$, are assigned to the MAVs. Obviously, MAV_2 needs to get through the zone between MAV_1 and MAV_3, in order to reach its goal in the new formation. Trajectories of all MAVs during the formation switching process are captured and used as a qualitative indicator. Furthermore, the minimum inter-MAV distance, $d_{min} = min||\mathbf{p}_j - \mathbf{p}_i||, \forall j \neq i$, is recorded to quantitatively measure the effectiveness in collision avoidance. Note that values of some parameters are scaled down proportionally to accommodate the relatively small simulation world. For all the following results, we use $v^{mav} = 0.5\,\mathrm{m/s}, rd = 1.0\,\mathrm{m}$, $K_\theta = 1.0, K_\omega = 0.05$.

Finally, formation switch of a team of MAVs with a relatively larger scale was simulated to qualitatively demonstrate the feasibility of the proposed methods for problems closer to real-world applications. During the experiment, ten fixed wing MAVs are commanded to switch between different formations, each resembling an Latin letter.

4.2 Comparative Experiments

Figure 4 shows trajectories of the three MAVs, using formation control approaches with USLM, PBD, and PBD-F controllers, respectively. Parameters for the USLM controller are set to $v_2^{va} = 0.1\,\mathrm{m/s}, \Delta t = 0.01\,\mathrm{s}$. The flight path of MAV_2 is like a standard spiral towards $\mathbf{g}_2$ through two circles, which are the paths of other two vehicles. In simulation with PBD controller, the values of weights are $w_1 = w_2 = w_3 = 1.0$ while $\delta = 0.00016$ and $threshold = 1.8\,\mathrm{m}$. As shown in Fig. 4b, we can divided the whole process into two stages. In the first stage, MAV_2 is "pushed" by MAV_1 and MAV_3 and slowly performs a spiral flight path along VA_2's trajectory towards $\mathbf{g}_2$. Meanwhile, MAV_2 "pushed" MAV_1 and MAV_3 out of their goals to "squeeze" through them. And then, after crossing x-axis, MAV_2 quickly forwards to circle around $\mathbf{g}_2$

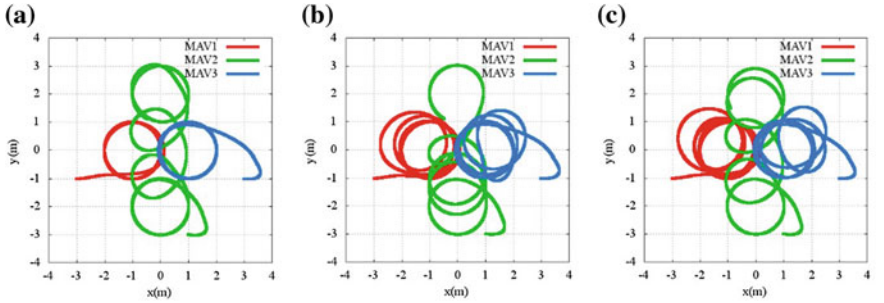

Fig. 4 Resulting trajectories of the three MAVs, using **a** USLM controller, **b** PBD controller, and **c** PBD-F controller, respectively

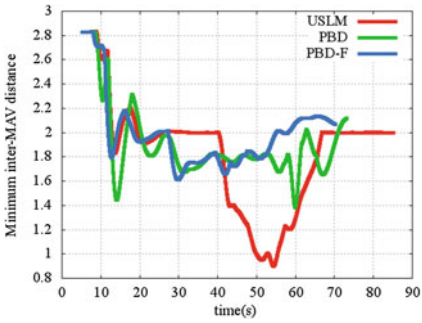

Fig. 5 Comparison of minimum inter-MAV distances during formation switch using different controllers

while MAV_1 and MAV_3 fly back to circle $\mathbf{g}_1, \mathbf{g}_3$. Parameter setting when using PBD-F controller in this simulation is $\delta = 0.0001, w1 = w3 = 1.0, w2 = 10.0$. The results in Fig. 4c show that the trajectory of MAV_2 is more like the one in Fig. 4a, and more smoothly than the one in Fig. 4b.

Figure 5 shows minimum inter-MAV distances in these simulations. The minimum distance measure with USLM is above 0.9 m all the time, with PBD above 1.4 m and with PBD-F above 1.6 m. These are all greater than $D_m = 0.45$ m no matter which controller is used. Compared with USLM and PBD cases, PBD-F approach has the most safety allowance as d_{min} is more strictly greater than the safer threshold to avoid colliding.

4.3 Parameters

To evaluate the effect of different parameter values on the performance of the approach, PBD controllers with different choices of parameter values were applied to solve the formation switch problem depicted by Fig. 3. Figure 6 plots the resulting minimum inter-MAV distances for different parameter groups.

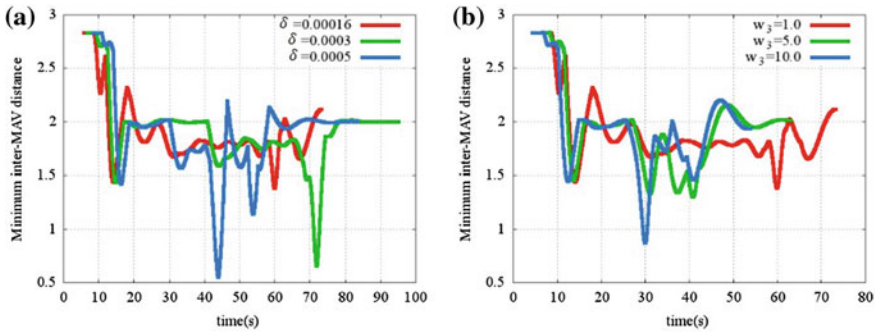

Fig. 6 Effects on the minimum inter-MAV distance of **a** different δ with uniform weighting, i.e., $w1 = w2 = w3$, and **b** different weighting schemes with a fixed $\delta = 0.00016, w1 = w3 = 1.0$, respectively

As shown in Fig. 6a, larger values for δ introduce larger oscillations into the inter-MAV distances and may lead to violation of the safe inter-MAV distance constraints during the formation switch, although the goal formation could be achieved more rapidly. On the other hand, giving MAVs with larger position changes during the formation switch a larger weight would also speed up the process, as shown in Fig. 6b.

4.4 Stress Test

We also run a medium-scale simulations consisting of 10 MAVs to test the performance of our approach in stress. Initially, positions of all VAs together resemble the character "*C*" from a bird's eye view. We assign a series of goals to the VAs

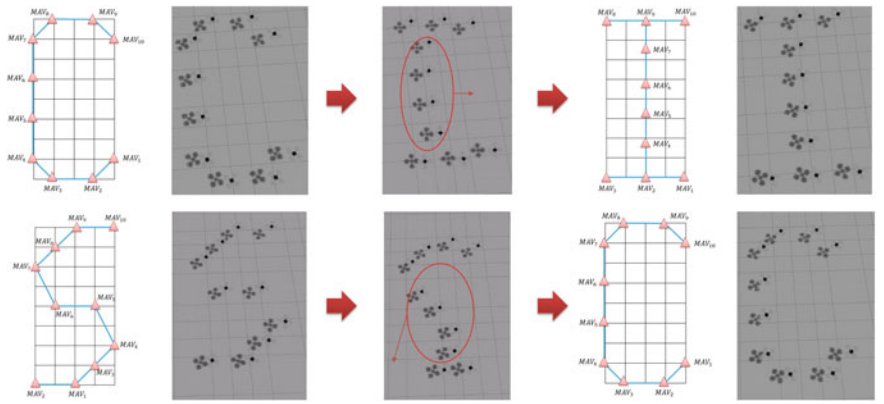

Fig. 7 Setup and snapshots of the medium-scale formation experiment

so that the resulting formation would resemble characters "*I*," "*S*," and "*C*" in turn. As shown in Fig. 7, this experiment shows that our technique is still feasible in a simulated problem closer to real-world applications.

5 Conclusions

This paper presents a distributed control approach for formation switch of fixed wing MAVs. We designed and implemented a multilayer system framework for distributed formation control, and propose a specific control algorithm for on-the-fly formation switch of fixed wing MAVs. Based on position-based dynamics approaches, our algorithm can satisfy the inter-MAV distance constraints during the entire formation switching process. To validate the proposed approach, we conducted several comparative experiments and stress test in a realistic simulator. We observe that MAVs are able to follow instructions given by the user to transform formation. In comparative experiments, it is shown that the PBD-F controller outperforms other two controllers in satisfying the safe inter-MAV distance constraint. The stress test demonstrates that our method is well suited for relatively larger scale systems in practical applications. In the future, we will focus on adding real-time controllers in our framework considering 3D scenarios and run real MAVs experiments in outdoor environment. Another interesting direction is to exploit more advanced approaches for mesh generation or deformation [15, 16] in computational geometry and computer graphics to improve the formation control quality.

Acknowledgments This work was partially supported by National Science Foundation of China under Grant No. 61303185, University Grants from NUDT under No. ZDYYJCYJ20140601 and 434513322532, and HPCL Grants under No. 201502-01.

References

1. Swaminathan S, Phillips M, Likhachev M (2015) Planning for multi-agent teams with leader switching. In: IEEE international conference on robotics and automation, pp 5403–5410
2. Karamouzas I, Guy SJ (2015) Prioritized group navigation with formation velocity obstacles. In: IEEE international conference on robotics and automation, pp 5983–5989
3. Lawrence DA, Frew EW, Pisano WJ (2008) Lyapunov vector fields for autonomous unmanned aircraft flight control. J Guid Control Dyn 31(31):1220–1229
4. Hauert S, Leven S, Varga M, Ruini F (2011) Reynolds flocking in reality with fixed-wing robots: communication range vs. maximum turning rate. In IEEE/RSJ international conference on intelligent robots and systems, pp 5015–5020
5. Falconi R, Sabattini L, Secchi C, Fantuzzi C, Melchiorri Clau-dio (2015) Edge-weighted consensus-based formation control strategy with collision avoidance. Robotica 33(1):81–83
6. Franchi A, Stegagno P, Oriolo G (2015) Decentralized multi-robot encirclement of a 3d target with guaranteed collision avoidance. Auton Robots 40(2):1–21
7. Kim AR, Keshmiri S, Huang W, Garcia G (2015) Guidance of multi-agent fixed-wing aircraft using a moving mesh method. In: International conference for unmanned arial systems

8. Benghezal A, Louali R, Bazoula A, Chettibi T (2015) Path planning of fixed wing UAVs formation. In: First international conference on new technologies of information and communication
9. Varga M, Basiri M, Heitz G, Floreano D (2015) Distributed formation control of fixed wing micro aerial vehicals for area coverage. In: Proceedings of 2015 IEEE/RSJ international conference on intelligent robots and systems (IROS 2015). IEEE, pp 669–674
10. Müller M, Heidelberger B, Hennix M, Ratcliff J (2006) Position based dynamics. In: Third workshops in virtual reality interactions and physical simulation (VRIPHYS 2006). The Eurographics Association, pp 71–80
11. Frew EW, Lawrence DA, Dixon C, Elston J, Pisano WJ (2007) Lyapunov guidance vector fields for unmanned aircraft applications. In: 2007 American control conference, pp 371–376
12. Quigley M, Conley K, Gerkey BP, Faust J, Foote T, Leibs J, Wheeler R, Ng AY (2009) Ros: an open-source robot operating system. In: ICRA workshop on open source software
13. Gazebo. http://gazebosim.org/. Accessed 25 April 2016
14. Hector quadrotor—ROS Wiki. http://wiki.ros.org/hector_quadrotor. Accessed 25 April 2016
15. Xu K, Zhang H, Cohen-Or D, Xiong Y (2009) Dynamic harmonic fields for surface processing. Comput Graph 33(3):391–398
16. Chen X, Xiong Y (2008) 2d finite element mesh generation over planar domain byoptimized bisection refinement. In Proceedings of 2008 international pre-olympic congress on computer science. World Academic Press, pp 81–87

Research of Variable Cycle Engine Modeling Technologies

Shaochang Wang, Jiqiang Wang, Bo Jiang and Xiaolong He

Abstract A component level mathematical model of double bypass variable cycle engine (VCE) was built with a reference to the modeling method of two-spool-turbofan engine. The model of fan was developed with separated characteristic of fan tip and hub sections. The model of core drive fan stage (CDFS) model was built to work under single bypass mode and double bypass mode. The model was able to run as steady mode and transient mode. During the calculating process of the dynamic co-working equations, the method of volume dynamics was used in order to avoid the iterative calculations. In single bypass mode, it represents higher thrust and smaller bypass ratio, which is fit for the high-speed flight. In double bypass mode, it shows lower thrust and bigger bypass ratio, which is fit for the low-speed flight.

Keywords Variable cycle engine · Component level model · Volume dynamics

1 Introduction

With five generations of research in 100 years, modern aviation engine technologies has become full-fledged. The SFC (specific fuel consumption) and the thrust weight ratio of engine has been constantly improved. The performance of the aircraft is greatly increased at the same time [1]. In the field of military aviation, along with the expansion of aircraft fighter envelope and complexity of flight mission, traditional fixed geometry, or few adjustable geometry engines could not meet the flight and endurance requirements. In this case, variable cycle engine (VCE) shows great potential [2].

GE has been studied on VCE for more than 50 years. It has always been a leader in this area [3]. Its F120 engine is the first one that validated by flight test [4]. This

S. Wang · J. Wang (✉) · B. Jiang · X. He
Jiangsu Province Key Laboratory of Aerospace Power System, Nanjing University of Aeronautics and Astronautics, Nanjing 210016, China
e-mail: jiqiang.wang@nuaa.edu.cn; jiqiang_wang@hotmail.com

Y. Jia et al. (eds.), *Proceedings of 2016 Chinese Intelligent Systems Conference*, Lecture Notes in Electrical Engineering 404, DOI 10.1007/978-981-10-2338-5_26

paper describes a concept of component level mathematical model of double bypass variable cycle engine (VCE), which is built based on the advanced graphical simulation environment MATLAB/SIMULINK.

2 Configuration of Variable Cycle Engine

The configuration of variable cycle engine is shown as Fig. 1. The engine includes several main components: forward fan, CDFS, HPC, combustor, HPT, LPT, mixer, afterburner, and nozzle. It also contains three variable valves: mode selector valve, front variable bypass injector (FVABI), rear variable bypass injector (RVABI). The mode selector valve and RVABI are initiative regulating valves while FVABI is passive regulating valve.

There are two typical working mode: single bypass mode and double bypass mode.

Single bypass mode: when accelerating, climbing and supersonic cruise, close the mode selector valve and RVABI, FVABI passively closed, most of the air goes through the core duct. The engine performs like a single bypass turbojet engine (high thrust) while the bypass ratio decreases.

Double bypass mode: when subsonic cruise and taking off, open the mode selector valve and RVABI, the air from forward fan goes to CDFS and first bypass duct, respectively. The air from CDFS also separates into two parts. One goes inside and the other one goes to second bypass duct. The engine performs like a turbofan cycle engine to reach the purpose of reduce off specific fuel consumption and noise while bypass ratio increases.

3 Model of Forward Fan

This model has a forward fan fit with a separation between the tip and the hub of the fan [5]. When the selector valve opens, the air goes through both the tip and the hub of fan. When closed, most of the air goes through the hub of fan. The model of

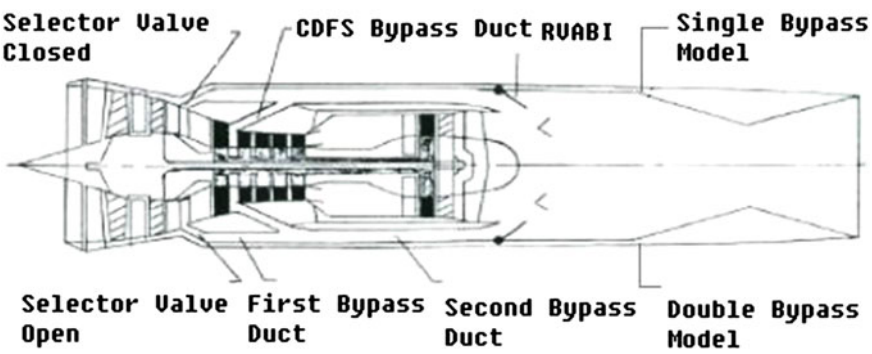

Fig. 1 Configuration of variable cycle engine

forward fan has to be built by interpolation method because of lack of experiments. This paper introduces a simplified method to get their characteristic curves by bringing in two factors of proportionality (X_1, X_2) [6].

Define:

$$Q_{f1,cor} = X_1 * Q_{f,cor}$$
$$Q_{f2,cor} = X_2 * Q_{f,cor}$$

Then, the characteristic curves approximatively calculated. X_1 represents the tip of fan, which is equal to 0.33. X_2 represents the hub of fan, which is equal to 0.67.

4 Model of the Mode Selector Valve

First bypass duct stays after the forward fan. Its real area depends on the angle of the mode selector valve (∂_{msv}). If assume that flow of fan tip is known, than flow of first bypass duct is able to achieve.

$$Q_{13} = \partial_{msv} * Q_f$$
$$P_{13} = \sigma_{msv} * P_{14}$$

5 Co-working Equations

As show in Fig. 2, during the calculating process of the dynamic co-working equations based on flow and power balance, the method of volume dynamics was used in order to avoid the iterative calculations.

Equations based on volume dynamics:

$$\dot{P}_{225} = \frac{(Q_{16} - Q_{225}) \cdot R \cdot T_{16}}{V_{\mathrm{I}}}$$
$$\dot{P}_{41} = \frac{(Q_3 - Q_{41}) \cdot R \cdot T_3}{V_{\mathrm{II}}}$$
$$\dot{P}_{45} = \frac{(Q_{42} - Q_{45}) \cdot R \cdot T_{42}}{V_{\mathrm{III}}}$$
$$\dot{P}_7 = \frac{(Q_6 - Q_7) \cdot R \cdot T_6}{V_{\mathrm{IV}}}$$
$$\dot{P}_{125} = \frac{(Q_{13} - Q_{125}) \cdot R \cdot T_{13}}{V_{\mathrm{V}}}$$
$$\dot{P}_9 = \frac{(Q_7 - Q_9) \cdot R \cdot T_7}{V_{\mathrm{VI}}}$$

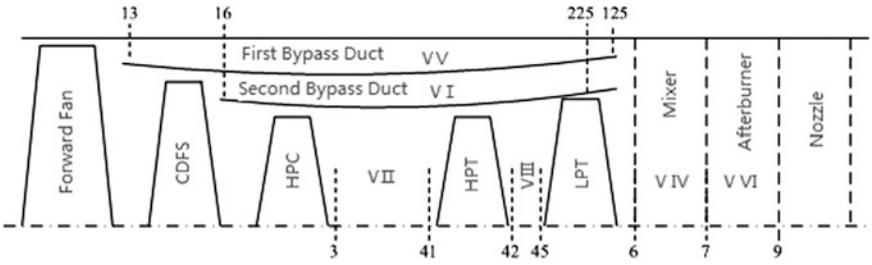

Fig. 2 Volume design of variable cycle engine

Equations based on rotor dynamics:

$$\frac{dn_l}{dt} = \frac{(\eta_{lt} H_{lt} - H_{\text{fan}})}{\left[n_l J_1 \left(\frac{\pi}{30}\right)^2\right]}$$

$$\frac{dn_h}{dt} = \frac{(\eta_{ht} H_{ht} - H_{\text{cdfs}} - H_{\text{com}})}{\left[n_h J_2 \left(\frac{\pi}{30}\right)^2\right]}$$

Eight initial guess were chosen to solve the equations. They are pressure ratio of fan tip ($\pi_{f,1}$), pressure ratio of fan hub ($\pi_{f,2}$), pressure ratio of CDFS (π_{cdfs}), pressure ratio of compressor (π_{com}), pressure ratio of HPT ($\pi_{t,h}$), pressure ratio of LPT ($\pi_{t,l}$), speed of HPR (n_h), speed of LPR (n_l).

6 Design Parameters of Variable Cycle Engine

As show in Table 1, state of idol (H = 0, Ma = 0) was chosen as the design parameters of variable cycle engine.

7 Simulation

To get different performance characteristics of two typical operation mode, two typical working points of the flight envelope were selected. They are supersonic cruise (H = 11 km, Ma = 1.6), subsonic cruise (H = 11 km, Ma = 0.8), respectively. Then simulate two working modes based on the model, conclusion is shown as Table 2.

As show in Table 2, when working under condition of subsonic cruise and same thrust, sfc of double bypass mode is 22.9 % smaller than single bypass mode. When working under condition of supersonic cruise and same low pressure rotor speed, thrust of single bypass mode is 27.8 % bigger than double bypass mode. But, sfc of

Table 1 Design parameters of variable cycle engine

Parameter	Double bypass	Single bypass
n_l/%	100	100
n_h/%	100	100
$\pi_{f,1}$	3	3
$\pi_{f,2}$	3.2	3.2
η_f	0.8	0.8
π_{cdfs}	1.3	1.3
η_{cdfs}	0.88	0.88
π_{com}	6	6
η_{com}	0.88	0.88
$\pi_{t,h}$	3	3
$\eta_{t,h}$	0.9	0.9
$\pi_{t,l}$	2.14	1.91
$\eta_{t,l}$	0.9	0.9
W_f/(kg/s)	1.1440	1.1440
W_{fb}/(kg/s)	1.7630	2.0341
A_8/m^2	0.2307	0.2051
T_{t4}/K	1700	1800

Table 2 Comparison of performance parameters under two typical operation modes

		Performance parameters of engine					
Operating condition	Operation mode	F/N	sfc/(kg/Nh)	T_{t4}/K	B	n_l/%	n_h/%
Subsonic	Single bypass	14492	0.3689	1491.9	0.2527	0.970	0.982
	Double bypass	14492	0.2842	1485.6	0.8215	0.982	0.988
Supersonic	Single bypass	17827	0.5179	1762.4	0.1361	0.885	0.980
	Double bypass	13952	0.3481	1538.7	0.7821	0.885	0.992

single bypass mode is 44.5 % bigger than double bypass mode. According to this conclusion, performance of VCE is better in single bypass mode when under condition of supersonic cruise and double bypass mode when under condition of subsonic cruise.

VCE changes its operation mode by mode selector valve. When engine was in the state of ground, simulation of changing from single bypass mode to double bypass mode was made.

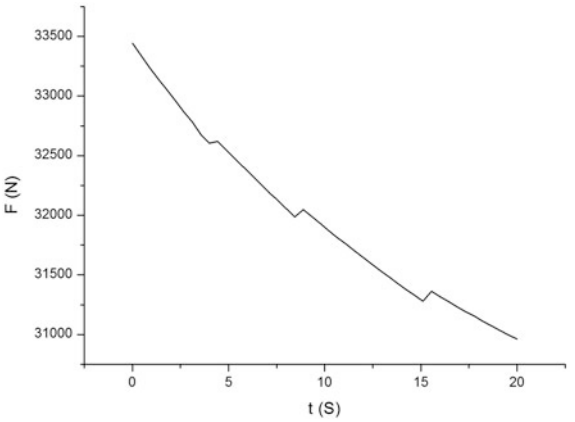

Fig. 3 Changes of thrust in the process of conversion

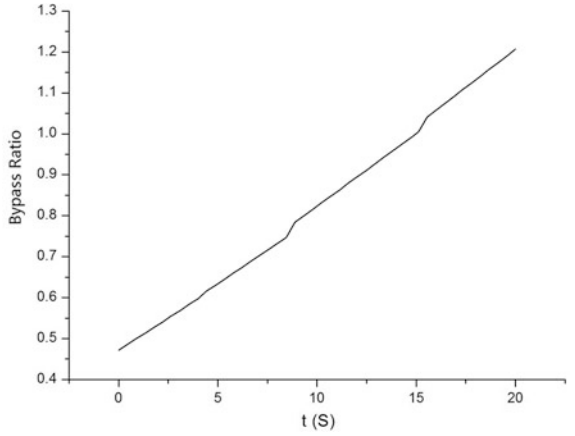

Fig. 4 Changes of bypass ratio in the process of conversion

As show in Fig. 3, thrust grows smaller as well as operation mode changes from double bypass mode to single bypass mode.

As show in Fig. 4, bypass ratio grows bigger as well as operation mode changes from double bypass mode to single bypass mode.

8 Conclusion

This paper describes a concept of component level mathematical model of double bypass variable cycle engine (VCE), which contains mode selector valve. Besides, this model has a forward fan fit with a separation between the tip and the hub of the fan. Results show that this model enables switching of working modes. Its performance characteristic is fit for different working condition.

There are several deficiencies of this model, such as characteristic curves of fan tip and hub are not accurate, influence of flow during the process of conversion is ignored, influence of core flow by bypass flow is ignored, et al.

References

1. Ballal DR, Zelina J (2004) Progress in aeroengine technology. J Aircr 41(1)
2. Changde F (2004) Variable cycle engines. Gas Turbine Exp Res 17(3):1–5
3. Hongxia L (2015) Development of variable cycle engine in GE. Aeroengine 41(2):94–98
4. Yanling Y, Chunfeng H (2012) Research on advanced variable cycle engine. Aeronaut Manuf Technol 23/24:106–109
5. Vyvey P, Bosschaerts W, Villace VF et al (2011) Study of an airbreathing variable cycle engine. 2011–5758
6. John R (1975) Real-time simulation of F100-PW-100 turbofan engine using the hybrid computer. NASA TMX-3261

An Improved Kernel K-means Clustering Algorithm

Yang Liu, Hong Peng Yin and Yi Chai

Abstract Kernel K-means is an extended method of K-means, which identifies nonlinearly separable clusters. However it still exits limitations, the one is which repeatedly sets different initial positions to find better local minima, the other is that it can only for linear separable data clustering. In order to overcome this issue, in this paper we propose an improved global kernel k-means. The proposed algorithm adds one cluster at every stage and generates the next centric point at next stage to avoid the unnecessary calculation. Experimental result shows that the proposed algorithm does not depend on initialization which identifies nonlinearly separable cluster, meanwhile, because of the incremental nature and search procedure, the poor local minima is avoided. Moreover, an improvement is put forward to decrease the computational complexity that does not significantly affect the accuracy of classification.

Keywords K-means · Global K-means · Kernel K-means · Global kernel K-means

1 Introduction

Cluster analysis is a process which divides concrete or abstract data set into several groups or classes. It is wildly used in data mining, image segmentation, pattern recognition, space remote sensing technology, feature extraction, signal compression, and many other fields, and has got many satisfactory results [1, 2]. K-means is commonly an algorithm used in clustering. Different groups are separated by different cluster centers which are obtained according to the classified error calculated

Y. Liu (✉) · H.P. Yin · Y. Chai
College of Automation, Chongqing University, Chongqing 400030, China
e-mail: 415138364@qq.com

H.P. Yin
Key Laboratory of Dependable Service Computing in Cyber Physical Society, Ministry of Education, Chongqing 400030, China

Y. Jia et al. (eds.), *Proceedings of 2016 Chinese Intelligent Systems Conference*, Lecture Notes in Electrical Engineering 404, DOI 10.1007/978-981-10-2338-5_27

by the sum of the squared Euclidean distances between each data point and the corresponding cluster center. The algorithm has two serious constraints. First of all, the results of clustering depend heavily on the positions of the initial cluster centers, resulting in local minimum; Second, it can only handle linearly separable clusters.

For the first limitation, in order to find a good enough local minima, the initial positions of the centers of the clusters are randomly placed to different locations. This process always starts lots of time. But there is no basis for the number of restarts, we always decide the number according to experience and whether the minimum is optimal is never confirmed. In order to overcome this limitation, the global k-means algorithm proposed by [3], they use the k-mean algorithm as the local search process. The global k-mean algorithm solves all the problems as m-clustering intermediate 1, … M, k-means cluster. M cluster solution is the establishment of uncertainty, so it is not dependent on the initial conditions, and the minimum value is found in the near optimal [1].

The kernel k-means [4, 5] is an extension of the traditional k-algorithm, Data from the input space is mapped to a high-dimensional feature space by kernel function and minimize errors in the clustering feature space. Therefore, nonlinear separated clusters in the input space overcome the second limitation of k-means.

The global kernel k-means [6] combines the kernel method and global k-means algorithm. In order to solve the problem of high-computational complexity, [7, 8] proposed a scheme to accelerate. Although global kernel k-means algorithm solves two limitations of traditional k-means algorithm, it still exists some unnecessary calculation. In this paper, we improve the unnecessary calculation, which is further in the second quarter.

2 Methodologies

In this section, First, the kernel k-means and global kernel k-means method are discussed. Second, the improvement of global kernel k-means is proposed in this paper.

2.1 Kernel K-means

Kernel k-means [4] is the extension of the standard k-means algorithm. Suppose a data set $X = \{x_1, \ldots x_N\}$, $x_n \in R^d$. The objective function is shown in Eq. (1) defines a kernel matrix $K \in R^{N \times N}$, and by computing the squared Euclidian distances in Eq. (1) without mapping the original data to feature space using Eq. (2). Notice that in Eq. (1) cluster centers m_j in the feature space cannot calculate directly. The kernel functions $K = \phi(x_i)^T \phi(x_j) = K_{ij}$ directly provide the inner products in the feature space without calculating the transformation function ϕ.

$$E(m_1, \cdots m_M) = \sum_{i=1}^{N} \sum_{j=1}^{M} R_i \left\| \phi(x_i) - m_j \right\|^2, \tag{1}$$

where $m_j = \frac{\sum_{i=1}^{N} R_i \phi(x_i)}{\sum_{k=1}^{N} \sum_{l=1}^{N} R_k R_l}$

$$\left\| \phi(x_i) - m_j \right\|^2 = K_{ii} - \frac{2 \sum_{j=1}^{N} R_j K_{ij}}{\sum_{j=1}^{N} R_i} + \frac{\sum_{j=1}^{N} \sum_{l=1}^{N} R_l R_j K_{jl}}{\sum_{j=1}^{N} \sum_{l=1}^{N} R_j R_l}, \tag{2}$$

where $R_i = 1$ if x_i is true and 0 otherwise, the kernel function $K(x_i, x_j) = K_{ij}$ is used to directly provide the inner products in the feature space without explicitly defining transformation $\phi(x_i)$, m_j is centroid, $E(m_1, \cdots m_M)$ is the sum of the squared Euclidean distances between each data point x_i and the centroid m_j.

Kernel k-means can handle the nonlinearly separable clusters well, but it still has one limitation: due to the algorithm procedure is the same as k-means, thus, it's need to depend on the initialization of k-means.

2.2 Global Kernel K-means

Global Kernel k-means is proposed by Likas [7], which builds on the global k-means and the kernel k-means. Global kernel k-means maps the data to feature space which has the same effect as kernel k-means does. The initial center point of the algorithm is always center of mass, and by using kernel k-means algorithm to calculate the next center point. At each procedure, the center point adds incrementally and deterministically. So the trapped of poor local minima and the problem initial cluster centers can be avoided. Although global kernel k-means has the benefit of global k-means and kernel k-means, the computational cost is complex. Likas proposed a method to improving the complexity of the global kernel k-means. The main idea of algorithm is same as the fast global k-means proposed in [3]. In order to decrease the complexity, they define a weight w_k^n to evaluate the next center point. They calculate the $F_k^n \le F_{k-1}^* - w_k^n$ as boundary of the final clustering error when the k-th cluster is initialized to the point x_n. F_{k-1}^* is the clustering error corresponding to the k-1 problem and w_k^n measures the reduction of the min error and it is denoted in Eq. (3), where d_{k-1}^i defines the squared distance between x_i and the center in feature space after calculating the $k-1$ clustering problem. We use initialization for the k-th cluster the point x_n that maximizes: w_k^n

$$w_n^k = \sum_{i=1}^{N} \max\left(d_{k-1}^i - \left\| \phi(x_n) - \phi(x_i) \right\|^2, 0 \right) \tag{3}$$

where $\left\| \phi(x_n) - \phi(x_i) \right\|^2 = K_n K_n + K_i K_i - 2 K_n K_i$

Above process speeds up the global kernel k-means, but it still has some trivial calculation. The more detail is discussed in next section.

2.3 Improved Global Kernel K-means

The scheme to lower the complexity of the global kernel k-means still has bottleneck constraint when dataset is huge. According to (3), every point computes the weight b_k^n. That is obviously needless, because the point that is close to central point cannot be the next center. Thus, this kind of point should be ignoring to calculate weight $\|\phi(x_n) - \phi(x_i)\|^2$. In order to reduce this kind of trivial calculation, we define the $L_i = \frac{1}{N}\sum_{j=1}^{N} d_j^N$ as the mean distance of each dataset point in the feature space. We employ L_i and (4) to eliminate the points near the central point.

$$f_i = H(d_k - L_i) \tag{4}$$

where $L_i = \frac{1}{N}\sum_{j=1}^{N} d_j^N$, $H(x)$ is Heaviside function.

Equation (4) calculates the point that out of the mean of distance, we can improve the (3) to (5). If the dataset point is close to the central point, (4) is 0, otherwise is 1. When we compute b_k^n, the result of (4) provides the information that weather the point is nearby center.

$$b_k^n = \sum_{i=1}^{N} \max\left(d_{k-1}^i - f_i\|\phi(x_n) - \phi(x_i)\|^2, 0\right) \tag{5}$$

The complexity of improved global kernel k-means algorithm is significantly lower than global kernel k-means. In addition the low computational cost could take our algorithm as a very good alternative method for graph cut optimization, if weights are specified in the same way as in [9–12], causes it also computes near optimal solutions.

3 Results

This paper adopts a classical actual data set of UCI [13] wine as experimental data to validate the performance of the algorithm. The Wine data set consists of 178 samples, each sample consisted of 13 attributes, and these attributes are alcohol, malic acid content, ash content, the ash alkalinity, magnesium content, total phenol content, flavonoids, phenolic content, anthocyanin content, color, hue, dilution, and praline. According to the 13 attributes of the samples, we could divide them into three types of wine label for 1, 2, and 3.

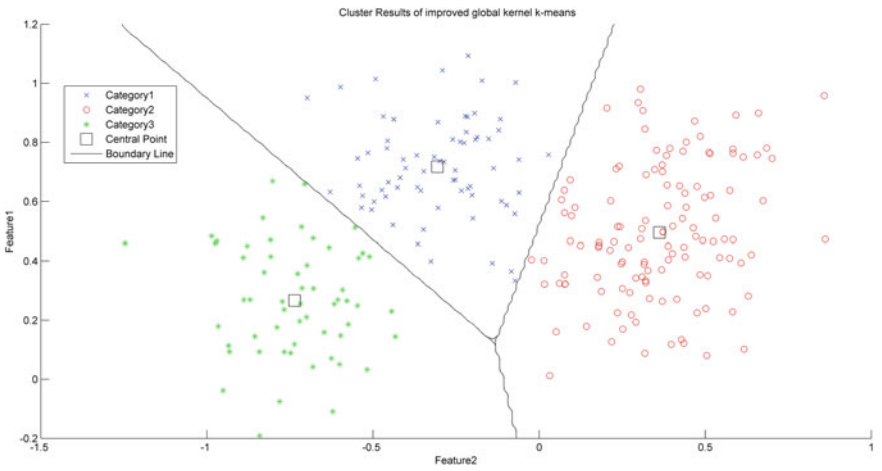

Fig. 1 Cluster results of improved global kernel k-means

Table 1 Result for wine dataset using improved algorithm, Global *k*-means, and Global kernel *k*-means

	Global *k*-means	Global kernel *k*-means	Improved algorithm
MSE	3.55	3.49	3.40
Run time	0.63	0.18	0.10

In the experiment, we use improved algorithm global kernel k-means algorithm, global k-means algorithm to cluster, respectively 178 samples from wine data, and compared clustering results with the sample itself category, and got the accuracy of clustering algorithm, in order to improve the reliability, each experiment was repeated for three times. In addition, the number of level of each attribute with a sample is not exactly the same, so data should be normalized before using it.

Clustering analysis of the experimental results shows in Fig. 1.

In order to estimate different methods, we use the mean squared clustering error (MSE) of the dataset point to their closest mean. Table 1 shows the result of that, where we also consider the corresponding execution times (in seconds).

Our experiments indicate that the performance of the improved global kernel k-means is faster than global kernel k-means in many cases.

4 Conclusions and Discussions

We describe the improved global kernel k-means clustering algorithm, the algorithm that maps data points from input space to a higher dimensional feature space through a kernel function and optimizes the clustering error in the feature space by

locating near optimal minima. The main advantage of our method is combined the global kernel k-means algorithm procedure, meanwhile, the computational cost of improved global kernel k-means algorithm is lower than original algorithm.

Acknowledgment This research is supported by the National Natural Science Foundation of China (Grant No. 61203084 and 61374135) and the National Natural Science Foundation of Chongqing China (cstc2011jjA40013)

References

1. Jain AK, Murty MN, Flynn PJ (1999) Data clustering: a survey. ACM Comput Surv 31:264–323
2. Murty MN, Jain AK, Flynn PJ (1999) Data clustering: a review. ACM Comput Surv 31 (3):264–323
3. Likas A, Vlassis N, Verbeek JJ (2003) The global *k*-means clustering algorithm. Pattern Recogn 36(2):451–461
4. Scholkopf B, Smola A, Muller K-R (1998) Nonlinear component analysis as a kernel eigenvalue problem. Neural Comput 10:1299–1319
5. Lozano JA, Pena JM, Larranaga P (1999) An empirical comparison of four initialization methods for the k-means
6. Milligan GW, Cooper MC (1985) An examination of procedures for determining the number of clusters in a data set. Psychometrika 50:159–179
7. Likas, Vlassis M, Verbeek J (2003) The global k-means clustering algorithm. Pattern Recogn 36(2):451–461
8. Vlassis N, Likas A (2002) A greedy EM algorithm for Gaussian mixture learning. Neural Process Lett 15:77–87
9. Dhillon IS, Guan Y, Kulis B (2004) Kernel *k*-means, spectral clustering and normalized cuts. In: Proceedings of 10th ACM knowledge discover and data mining conference, pp 551–556
10. Dhillon IS, Guan Y, Kulis B (2004) A unified view of kernel *k*means, spectral clustering and graph cuts. University of Texas at Austin, Technical Report TR-04-25
11. Dhillon IS, Guan Y, Kulis B (2007) Weighted graph cuts without eigenvectors: a multilevel approach. IEEE Trans Pattern Anal Mach Intell 29(11):1944–1957
12. Ng AY, Jordan M, Weiss Y (2001) On spectral clustering: analysis and an algorithm. In: Proceedings of neural information processing systems
13. Machine learning repository (2013) Center for machine learning and intelligent system. http://archive.ics.uci.edu/ml/datasets.html

Metal Magnetic Memory Signal Denoising for Stress Concentration Zone

Shengzhen Zhu, Jun Zhang and Zhenfa Bi

Abstract The method of metal magnetic memory (MMM) was developed for early fault diagnosing of ferromagnetic materials. MMM signal is a weak-field detect signal, where the Earth's magnetic field acts as the stimulus instead of an artificial magnetic field, and can be easily affected by the various factors such as environment interference and electronic noise. This paper is aimed to denoise metal magnetic memory signal and extract the feature of stress concentration zone. An efficient algorithm is proposed for detection of stress concentration zone based on wavelet and teager energy operator (TEO). This algorithm employs wavelet transform, to decompose the MMM signal into sub-band signal. In each of the critical sub-band signals, the mask construction is obtained by smoothing the TEO of corresponding wavelet coefficients that is applied to enhance the discriminability of signal components against those of noise. The multiscale related feature is extracted for the low signal-to-noise ratio signals that accurately determines the stress concentration. Finally, the proposed method is proved to be effective through the experimental data.

Keywords MMM stress concentration · Signal feature · Singularity · Peak-peak values · Wavelet analysis

This work is supported by National Natural Science Foundation (51405303), Postdoctoral fund of Jiangsu Province (1301175C) Priority Academic Program Development of Jiangsu Higher Education Institutions.

S. Zhu · J. Zhang (✉)
Electrical and Information Engineering College, Jiangsu University, Zhenjiang 212013, China
e-mail: jzhang@mail.ujs.edu.cn

Z. Bi
Shanghai Institute of Technology, Shanghai 201620, China

Y. Jia et al. (eds.), *Proceedings of 2016 Chinese Intelligent Systems Conference*, Lecture Notes in Electrical Engineering 404, DOI 10.1007/978-981-10-2338-5_28

1 Introduction

Currently in the area of NDT (nondestructive testing), the main methods such as ultrasonic inspection, magnetic particle inspection, X-ray, and eddy current testing possess a high detection rate of testing the preexisting defects, but for the early detection and diagnosis of the equipment defects, these methods cannot perform well and detect the initiation stage cracks easily. The local stress concentration of metal structures and micro-cracks mainly results in the failure of mechanical structures and equipment as well as the accidents. Hence, it is very important to identify the most dangerous stress concentration zone timely and accurately together with preventing the work pieces from being damaged.

The MMM technique is nonconventional NDT method [1, 2], its basic principle is to record and analyze the leakage magnetic field by defecting the stress concentration when the metal parts are in magnetic field of earth. It is not only fit to inspect the existing defect (crack, porosity, inclusion, etc.) but also defect the stress concentration and early failure. Due to its advantages of cost-effective, easy-operating and time-saving, and high sensibility, the MMM technique has received extensive attention in various industry fields, such as power machinery, pressure vessels, boilers, pipelines, etc. The fundamental difference of this technique from traditional ones is not required in special magnetization because the natural magnetization formed at manufacturing and working of products is used. MMM method can be used for both at operation of the object to be examined and at its repair [3].

In addition, MMM technique is a weak-field detect, which is a kind of natural geomagnetic signal. The evaluation of stress concentration zones and macro-defects is based on magnetic field gradient on length: MMM signal of industrial filed acquisition contains various noise and disturbance, the magnetic field gradient is very difficult to accurately extract. It leads to misjudgment of stress concentration, which restricts the application of the MMM method. Based on the above discussion, the magnetic memory signals must be denoised to enhance the SNR of MMM signal and the effectiveness of extracting gradient characteristics. In the literature [4–8], respectively from the experiment and application, the feature of magnetic memory signal had been discussed, but MMM signal extraction was rarely studied from complicated noise. The traditional time domain filter cannot preserve the distortion characteristics of the MMM signal. In this paper according to the nonstationarity and singularity of the MMM signal, the signal by wavelet transform is decomposed into different sub-band signals, and signal energy is enhanced by TEO operator, Simultaneously multiscale observations accurate determine stress concentration zone, the new threshold function denoising is proposed for denosing. Finally, through oilfield casing experiment verify the feasibility of magnetic memory test, and the effectiveness of the proposed signal processing method.

2 Mechanism of MMM Testing

Method of MMM is method of a nondestructive inspection based on registration and analysis of distribution of self-magnetic leakage fields arising on products and equipment in stress concentration zones and metal defects. At that, self-magnetic leakage field reflects irreversible change of a magnetization in a direction of maximal stresses action from working loads. Also SMLF reflect structural and technological heredity of products and welded joints after their manufacturing and cooling in a weak magnetic field. A natural magnetization and aftereffect, which appears as magnetic memory of metal to actual strains and structural changes in products and equipment metal, are used in the MMM method. The relationship between the scattered magnetic leakage fields of H_p and the changes of mechanical stress $\Delta\sigma$(MPa) of ferromagnetic members under test is formulated as [1, 2]

$$H_p = \frac{\lambda^{\mathrm{H}}}{\mu_0}\Delta\sigma, \tag{1}$$

where λ^{H} is an irreversible component in magneto elastic effect, and it is a function based on mechanical stress, the intensity and temperature of the external magnetic field; $\mu_0 = 4\pi \times 10^{-7}$ is the permeability of vacuum. The magnetic leakage component $H_P(y)$ perpendicularly oriented to the surface changes to its polarity and its $H_P(x)$ reaches the maximum (see Fig. 1) for the stress concentration zones. MMM method is unique NDT method to detect stress concentration zones and defects on the surface and in the deep layers of metal within 1mm in express-inspection mode.

In the MMM technology, normal and tangential component of magnetic leakage fields Hp, and magnetic field gradient on length (dHp/dx) are key characters. This is power diagnosis company of Russia company's patent technology, is applied in more than 20 countries. In the ideal experiment, MMM signal has high signal-to-noise ratio, the stress concentration is easy to confirm for the MMM signal referring to Fig. 1. As the actual acquired MMM signal is obviously much more complicated than what is depicted in Fig. 1, signal is seriously deteriorated by various noise and disturbance, it is difficult to extract the magnetic field gradient of MMM signal, so we make the error to determine the stress concentration stress by gradient in industrial environment

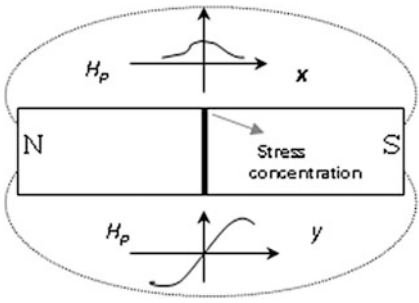

Fig. 1 Principle diagram of MMM testing

testing. Therefore, the signal processing is necessary, and the signal feature extraction method is proposed in this paper.

3 MMM Signal Analysis

In magnetic memory testing, the sensor acquisition MMM signal contains various kinds of interference and noise. Figure 2 is a collection of MMM signal, Fig. 3 is the spectral analysis. The results show that signal energy is concentrated in low frequency, and noise is generated in high frequency, which is derived from the measurement noise and probe jitter. The magnetic memory signal belongs to random signal, with has non-stationary characteristics.

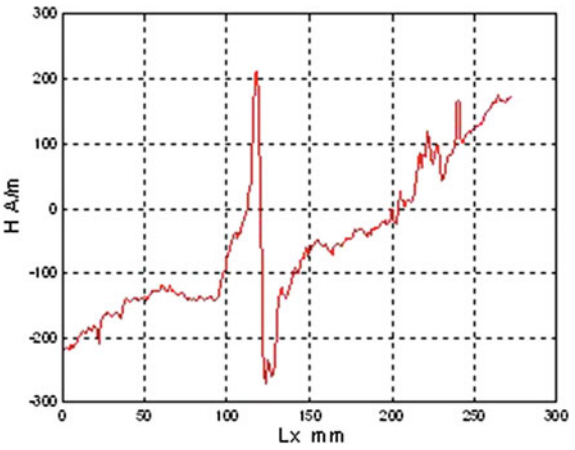

Fig. 2 Acquired MMM signal

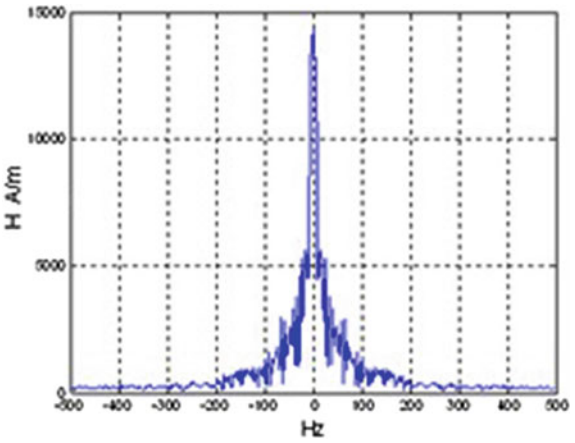

Fig. 3 Signal spectrum of MMM signal

MMM is a weak spatial signal in low frequency. As a result, if digital smoothing is used to the data, short disturbance signal and insignificant outlier may exist in testing data. In order to make signal amplitude to have high fidelity and prevent increasing new quantization step which can avoid quantization noise, so moving, median, and smoothing filter is selected. Besides, system's real-time demand is also satisfied. Its output is

$$y(m) = \text{median}[x(m), x(m-1), x(m-2)] \tag{2}$$

where $y(m)$is the output of smoothing filter, $x(m)$ is the input signal sequence, median is the median function. After preprocessing the MMM signal $y(m)$ contains more random noise, the traditional time filter is difficult to extract useful signal edge. The next section is using wavelet transform signal processing.

4 Singularity Detection of MMM

From engineering experiments and the mechanism of metal magnetic memory, it is known that the magnetic memory signal of stress concentration or micro-damage area often appears as the local singular point and irregular mutation part(maximum value) [7], possessing the quite important information which is one of the significant features of the signal as shown in Fig. 1. Wavelet analysis has good time–frequency localization features, so it could provide a way of describing the signals singularity. Different from the conventional wavelet transform, the second generation wavelet transform uses a general construction of the lifting scheme which has given up the translation and the dilation.

For MMM signal $f(t)$ which contains noise, the model in wavelet domain is

$$y(t_i) = f(t_i) + \sigma \cdot n(t_i) \quad i = 0, 1, \ldots \mathrm{N} \tag{3}$$

where $n(t)$ represents Gaussian white noise, σ indicates noise intensity, and t_i shows discrete time. The purpose is to obtain the original signal $f(t)$ from the polluted observing data $y(t)$. It is extremely important for the magnetic memory signal in that the identification of the stress concentration location of the casing in engineering is usually based on the $f(t)$ gradient maximum value and passing zero features proposed by Energodiagnostika Co. Ltd. If the data contains noise, the obtained gradient value will seriously deviate from its true value, then it is impossible to identify the stress concentration zone. The disadvantages of the method have been mentioned in literature [6], meanwhile it is also explained in the following data experiments.

First, it is significant to identify the location of stress concentration zone exactly. In this section, multiscale height correlation of magnetic memory wavelet energy is combined with its gradient maximum value feature to identify the stress concentration zone together. In order to highlight the magnetic memory signal generated by the stress concentration and distinguish the noise from the useful signal easily,

Teager energy operator of wavelet coefficients is adopted to enhance the local energy [8]:

$$\overline{\mathrm{WT}(j,k)} = \mathrm{WT}^2(j,k) - \mathrm{WT}(j,k+1).\mathrm{WT}(j,k-1), \tag{4}$$

where $\mathrm{WT}(j,k)$ represents wavelet coefficient, 2^j indicates decomposition scale and $k=0, \ldots, \mathrm{N}$. From the feature of the noise and signals wavelet decomposition, it is known that wavelet transform of the noise at different scales is not related with the height, local modulus maximum of adjacent scales almost appears at the same position and shows the same sign. It means that the wavelet transform of the signal does not decay a lot or remain unchanged with the changes of scales.

The product of wavelet coefficients of the two adjacent scales enhances the effect of magnetic memory signal as well as the sharply decrease of the noise. The wavelet coefficients energy product of two adjacent scales in the wave transform is defined as following. The definition of wavelet coefficients energy product of two adjacent scales in the wave transform is

$$P_j^k = \overline{\mathrm{WT}(j,k)}.*\overline{\mathrm{WT}(j+1,k)}\, j = 1,2,3 \tag{5}$$

In the formula, .* represents the product of two vectors or two matrix dots. We observe the enhanced wavelet energy (4) and P_j^k (5) in multi angle and look for maximum peak value related with the scale and height. In the meantime, we combine the gradient maximum value (passing zero) feature of the magnetic memory signal, the corresponding location of the stress concentration could be identified in the end.

In order to extract gradient feature and evaluate the casing life accurately, the signal needs to be denoised after locating the stress concentration. New method based on domain to denoise signal is proposed here to make the MMM signal of concentration zone more explicit and reduce noise substantially. Detail processing signal is

$$\bar{d}_i^k = \begin{cases} d_i^k\left(1 - \frac{\alpha_k^2}{M_{k,i}^2}\right) & \left(M_{k,i}^2 \geq \alpha_k^2\right) \\ 0 & \left(M_{k,i}^2 < \alpha_k^2\right) \end{cases} \tag{6}$$

$$M_{k,i}^2 = \left(d_i^k\right)^2 + \left(d_{i+1}^k\right)^2 \tag{7}$$

$$\alpha_k = \sqrt{2\sigma_k^2 \mathrm{In}(\mathrm{N})} \tag{8}$$

where k is wavelet decomposition level, N is signal length, σ_k is standard deviation of k noise [9–11].

5 Experimental Data

In experiments, MMM technology can not only detect abnormal stress concentration, but also the appeared cracks, the difference lies in the magnetic memory signal gradient of the cracks and the larger signal peak-peak value.

If we load 160kN pressure near the center of 1 m casing periodically, slight deformation obviously appears on the casing by observation through a magnifying glass. If we only use qualitative rules of Energodiagnostika Co. Ltd (gradient maximum value and passing zero) to determine the stress concentration zone, the disturbance will be too big. As shown in Fig. 5, there are many maximum value areas. It is difficult to judge which area is the real stress concentration and misjudgment will be caused. So we need the adoption of wavelet analysis method to eliminate misdirection. Description: abscissa in Figs. 4 and 5 represents the space distance measured in mm and abscissa in Figs. 6 and 7 shows the collected data which is collected at every 2 mm by system. The signal collected at the edge of the region 0–40 and 450–470 will be ignored as shown in Figs. 6 and 7. The arrival of the sensor at the edge of the casing caused the sudden change of the signal (magnetic memory signal boundary effect).

Data processing: choose function db4 and choose layer 4 as the decomposition level. Figures 6 and 7 indicate the energy product chart of enhanced wavelet coefficients and two adjacent scales wavelet coefficients, respectively. Through a large number of experiments, we can know the signal always shows the singularity and the energy mainly exists at the low frequency stage with the appearance of the stress concentration zone. The result is that peak-peak value energy in the regions of 200–250, 250–270, 430–450, and 450–470 as shown in the fourth decomposition energy (low frequency) in Fig. 4 is larger, only the signal singularity peak value at the sampling points of 200–250 and 450–470 is not related with the scale and

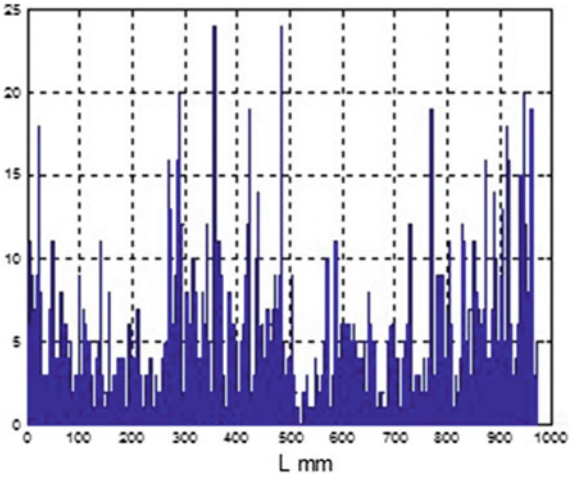

Fig. 4 MMM signal

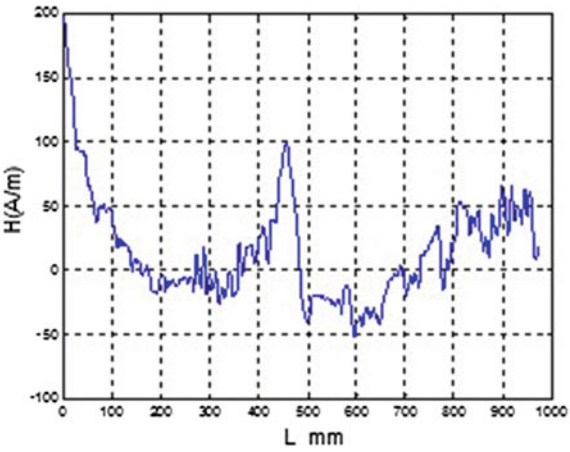

Fig. 5 MMM signal gradient

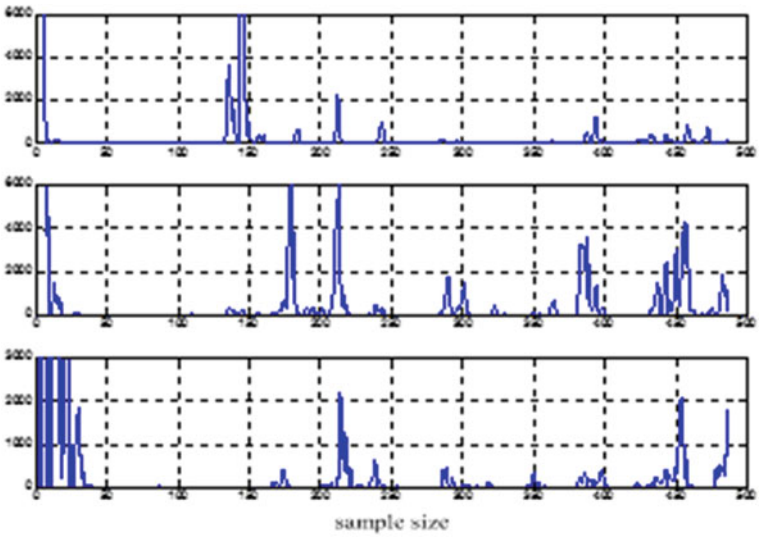

Fig. 6 Enhanced wavelet coefficient energy chart

height, the value does not decay a lot or remains unchanged with the increasing scale. The different scales at the two sampling-points sometimes are big while sometimes are small, therefore the consistence is not good. Combining with Fig. 7, the relevant and larger amplitude product of adjacent scales appears at the point of 220 and 450, we ignore the product at the point of 450 as it is at the edge; and it can be determined the sampling point of 200–250 is the stress concentration zone which is consistent with the testing results.

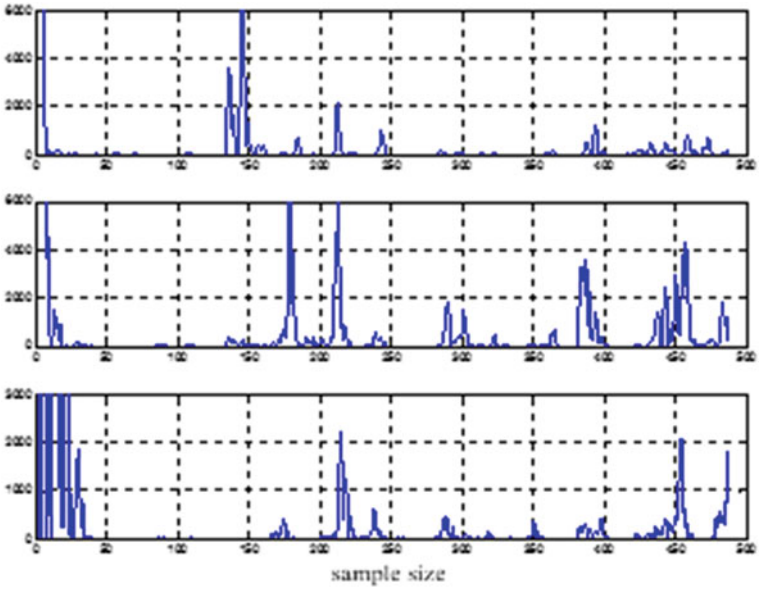

Fig. 7 Energy product chart of two adjacent scales wavelet coefficients

6 Conclusion

MMM technique is an effective method of providing the early diagnosis about stress concentration of the metal parts, and it can locate the position of the existing metal defects quickly. The MMM signal is vulnerable to the external noise and disturbance, so its application is limited. In order to determine the stress concentration accurately, an efficient algorithm is proposed for detection of stress concentration zone based on wavelet and teager energy operator, the multiscale related feature is extracted for the low signal-to-noise ratio signal. The feasibility of the proposed algorithm is validated by experimental data.

References

1. Doubov AA (1998) Screening of weld quality using the metal magnetic memory. Weld World 41:196–199
2. Dubov N, Sergey K (2013) The metal magnetic memory method application for online monitoring of damage development in steel pipes and welded joints specimens. Weld World 57:123–136
3. Xiao-meng L, Hong-sheng D, Shi-wu B (2014) Research on the stress-magnetism effect of ferromagnetic materials based on three-dimensional magnetic flux leakage testing. NDT & E Int 62(5):50–54

4. Sablik MJ, Wilhelmus JG, Smith K (2010) Modeling of plastic deformation effects in ferromagnetic thin films. IEEE Trans Magn 46(2):491–494
5. Jun Z, Biao W, Bingyu J (2006) Signal processing for metal magnetic memory testing of borehole casing based on wavelet transform. Acta Petrol Ei Sinica 27(2):137–140
6. Yang H, Yihua K, Wenxiang L, Shuzi Y (2000) Some algorithms for nondestructive testing of wire ropes—signal pre-processing and character extraction. Nondestr Test 22(11):483–488
7. Xiaoyong Z, Yinzhong Y (2004) Multi-fault diagnosis method based on Mallat pyramidal algorithms wavelet analysis. Control and Decis 19(5):592–594
8. Kaiser JF (1990) On a simple algorithm to calculate the energy of a signal, China Mechanical ICASSP. Academies Press, Albuquerque, pp 381–384
9. Chan TF, Hao-Min Z (2007) Total variation wavelet thresholding, J Sci Comput 32(2):315–341
10. Krommveh J, Jian-wei MA (2010) Tetrolet shrinkage with anisotropic total var-iation minimization for image approximation, Sig Process 90(8):2529–2539
11. Om H, Biswas M (2012) An improved image denoising method based on wave-let, J Sig Inf Process 3(1):109–116
12. Mallat SG, Hwang WL (1992) Singularity detection and processing with wave-lets, IEEE Trans IT 38(2):617–643

3D Velocity Measurement of High-Speed Rotating Sphere Based on the Monocular Vision Servo System

Yunfeng Ji, Zhihao Shi, Jie Ren, Chaoli Wang, Yanni Shen and Xiaojun Huang

Abstract The information processed by monocular vision is a target object that projects from 3D to 2D. So restoring the depth information has a significant influence on the prediction of target trajectory and subsequent control decision. This paper proposes an algorithm based on monocular vision, which can be used to calculate 3D velocity of high-speed rotating sphere, this will be applied to vision recognition of table tennis robot, and play an important role in robots' motion plan and decision control. The experimental results of the proposed algorithm are verified with little error, which proves the feasibility of the proposed method.

Keywords Monocular vision · Rotating sphere · 3D velocity

1 Introduction

Using the camera visual sensors to obtain image sequences in the natural space, analyzing the features of target objects, resolving the geometry relations between the target and the camera, and finding the space locations and posture is to achieve the estimation and analysis of object motion. This is an old and vital importance research subject in the field of computer vision, also has a wide application background. There are some ways to locate the targets such as monocular vision, binocular stereo vision and stereo vision. Stereo vision is based on the principle of stereo disparity, using different images to generate a deep sense, and getting the

Y. Ji · Z. Shi · J. Ren (✉) · X. Huang
China Table Tennis College, Shanghai University of Sport, Shanghai 200438, China
e-mail: jyf123456789@126.com

C. Wang
Control Science and Engineering,
University of Shanghai for Science and Technology, Shanghai 200093, China

Y. Shen
Department of Publishing and Communication,
Shanghai Publishing and Printing College, Shanghai 200093, China

Y. Jia et al. (eds.), *Proceedings of 2016 Chinese Intelligent Systems Conference*,
Lecture Notes in Electrical Engineering 404, DOI 10.1007/978-981-10-2338-5_29

changeable parameters of the field target movements and postures through the geometric relationship between binocular camera and the object [1]. General speaking, to got the goal in traditional sense of 3D information needs binocular or more cameras. Taking many factors into account in the measurement, such as the costs, time, calculations and so on, the monocular camera has a great practical value for the spatial measurement of the target.

Monocular camera in theory can only be taken the 2D information of the target, that is the plane information, so making use of the targets' related movement characteristics and information. NAOKI YAMAGUTI puts forward a new method of monocular visual measurement, the principle is to gather the known movement tracks of object, which change the proportion of two images before and after, and then, calculating the distance between lens and target [2]. Shi Chunqin and others measure objects under different texture, shows the algorithm has good performance under different texture. On this basis, the SAXENA predicts the depth information based on a model of more images [3].

Most researches based on monocular vision apply to measure straight distance, robot navigation and positioning, parts finishing, Applications hardly used in the sphere rotation speed yet. Ball velocity measurement commonly used in the table tennis robots, because Rotary is a very important information of table tennis. The robot must judge the rotation of the table tennis, if it wants to hit table tennis accurately. A. Nakashima and others measure the rotation of the labeled ball by high-speed vision. In addition to use tags to measure rotation, some estimate the rotation through the analysis of the table tennis movement. Matsushima M and others use the method of empirical study, mainly adopting LWR (locally weighted linear regression) to make a track prediction and get the information about the rotation. Matsushima et al. [4], Leung et al. [5], Qing and Zongwu [6] make the force analysis of table tennis, and establish a parameter model to forecast the flight track by iteration, which contains the fuzzy rotation information.

So far, there is no scholar proposed a method without labeled to measure the 3D velocity of sphere rotation. In this paper, the main research object is the velocity and direction of sphere rotation, with using the features in the sphere rotation, the author propose the method of measurement about spheres' three-dimensional velocity by monocular camera, and verify the effectiveness of algorithm by some experiments.

2 Measure the Rotating Speed of the Sphere

2.1 The Model of Sphere Rotation

In this paper, we use a monocular camera to shoot the rotating sphere, and calculate the rotating speed and direction of the ball by the rotation features of the rotating sphere. Analyzing the features of rotating ball first, as shown in Fig. 1.

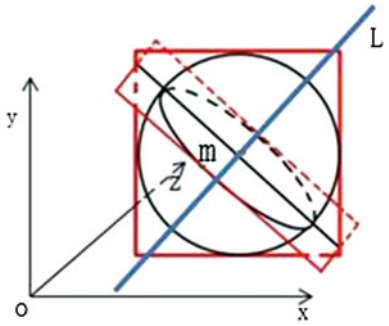

Fig. 1 The model of sphere rotation

In the space coordinate *o-xyz*, two black circles represent a sphere. Solid circle represents the sphere projected on the plane of *x-o-y*, and the dotted circle represents a circle formed on any section of a sphere. Two red boxes represent the section of two circles. It is known that two planes' intersection will produce a cross line in the space, two plane intersections in the picture is the black line in the middle. And the intersection of two circular cross sections is the diameter of dotted circle, defined *m*, It is also a part of the two planes' intersection.

2.2 Decomposition of Three Dimensional Velocity of the Sphere

High-speed rotating sphere will rotated along axis, which through the center of the sphere, so the direction problem of 3D velocity of the high-speed rotating sphere can be transformed into the problem of the space position of the rotating shaft. It is assumed that the rotating direction of the sphere rotates along the dotted circle. The rotating axis of the sphere is the line *L* of the perpendicular bisector, which is vertical to the diameter m in the cross section of dashed circle.

As shown in Fig. 2, the high speed rotating sphere is projected onto the *x-o-y* plane, and the sphere can be obtained in the new coordinate system, x'-o'-y'. At this point, the space coordinates of solid circle remain unchanged, and the dotted cicle in the space coordinates will be projected into an ellipse in the plane. In addition, the axis of rotation in space will be projected onto a plane x'-o'-y', and become the mid perpendicular (L') of long axis (m') of the ellipse.

Thus, the problem that the rotation axis (*L*) of the rotating sphere in the space positions transformed into two problems as followed.

(1) The location of the line (L') in the plane (x'-o'-y')
(2) The included angle between the line (L') and the plane(x'-o'-y').

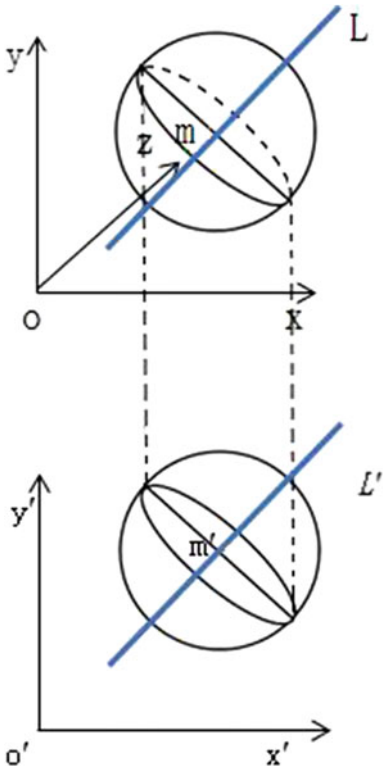

Fig. 2 Decomposition of three dimensional velocity of the sphere

2.3 Solving the Direction of the Axis of Rotation

2.3.1 The Location of the Line (L') in the Plane (x'-o'-y')

The problem about the location of the line (L') in the plane(x'-o'-y') can be converted into the solution of angle built by long axis (m') of the ellipse and X axis, and center coordinates in the ellipse.

For any ellipses, we can use its general equation $A\,x^2 + Bxy + C\,y^2 + Dx + Ey + 1{=}0$, there are five coefficient, A, B, C, D, E, that means if we can find the coordinates of any five points on the ellipse, we can solve the general equation of the ellipse. For example, in the determination of the table tennis rotation, we could use the trademark center above the balls as the object of the recognition, and then record the each positions of the center of the trademark in the 5 frame images. It is assume that the coordinates of the arbitrary five positions on the ellipse are found, set as (x_n, y_n), $n = 1, 2, 3, 4, 5$, then we can get the following equations:

$$\begin{cases} Ax_1^2 + Bx_1y_1 + Cy_1^2 + Dx_1 + Ey_1 + 1 = 0 \\ Ax_2^2 + Bx_2y_2 + Cy_2^2 + Dx_2 + Ey_2 + 1 = 0 \\ Ax_3^2 + Bx_3y_3 + Cy_3^2 + Dx_3 + Ey_3 + 1 = 0 \\ Ax_4^2 + Bx_4y_4 + Cy_4^2 + Dx_4 + Ey_4 + 1 = 0 \\ Ax_5^2 + Bx_5y_5 + Cy_5^2 + Dx_5 + Ey_5 + 1 = 0 \end{cases} \tag{1}$$

The solution of the Eq. (1) is solved by MATLAB software to obtain the system value, and then the ellipse general equation will be got, thereby the angle with the ellipse axis (m') and the X axis and center point coordinate of ellipse are calculated. Assume that

$$F(x, y) = Ax^2 + Bxy + Cy^2 + Dx + Ey + 1 \tag{2}$$

Because the ellipse belongs to the center curve, the position (x_0, y_0) in the center coordinate can be represented as follows:

$$\frac{\partial F}{\partial x}(x_0, y_0) = 0, \quad \frac{\partial F}{\partial y}(x_0, y_0) = 0 \tag{3}$$

F(x, y) is substituted into the Eq. (3) for calculating the Eq. (4)

$$\begin{cases} 2Ax_0 + By_0 + D = 0 \\ Bx_0 + 2Cy_0 + E = 0 \end{cases} \tag{4}$$

From Eq. (4), the following equation can be given:

$$\begin{cases} x_0 = \frac{BE - 2CD}{4AC - B^2} \\ y_0 = \frac{BD - 2AE}{4AC - B^2} \end{cases} \tag{5}$$

From Eq. (5), the center coordinate of the ellipse (x_0, y_0) can be given.

Assuming the inclination angle of the x-axis and the axis of the ellipse is β, the original coordinate is rotated angel β along the X axis. If any point in the coordinate is assumed (x_1, y_1), the new point in the new coordinate can be given (x_1', y_1'), According to related transformation in analytic geometry, it can be represented as follows

$$\begin{cases} x_1 = x_1' \cos\beta - y_1' \sin\beta \\ y_1 = x_1' \sin\beta + y_1' \cos\beta \end{cases} \tag{6}$$

Assume $F(x) = 0$, the Eq. (6) is substituted into it, and then it can be calculated as follows

$$A'x_1'^2 + B'x_1'y_1' + C'y_1'^2 + D'x_1' + E'y_1' + 1 = 0 \tag{7}$$

where,

$$\begin{cases} A' = A\cos^2\beta + B\sin\beta\cos\beta + C\sin^2\beta \\ B' = 2(C-A)\sin\beta\cos\beta + B(\cos^2\beta - \sin^2\beta) \\ C' = A\sin^2\beta - B\sin\beta\cos\beta + C\cos^2\beta \\ D' = D\cos\beta + E\sin\beta \\ E' = -D\sin\beta + E\cos\beta \end{cases} \tag{8}$$

If the included angle β need to be calculated, the coordinate axis rotates angle β, at this point, the coefficient B' of $x_1'y_1'$ is 0. It follows that

$$2(C-A)\sin\beta\cos\beta + B(\cos^2\beta - \sin^2\beta) = 0 \tag{9}$$

By using two angle formula, one may write

$$(C-A)\sin 2\beta + B\cos 2\beta = 0 \tag{10}$$

which is equivalent to

$$\tan 2\beta = \frac{B}{A-C} \tag{11}$$

Then, the value of angle β between Long axis (m') of the ellipse and the X axis can be given.

$$\beta = \frac{1}{2}\arctan\frac{B}{A-C} \tag{12}$$

2.3.2 The Included Angle Between the Line (L') and the Plane (x'-o'-y')

From the perspective of a monocular camera, a circle that lies on the plane with an angel α to the camera plane will be identified as an ellipse. The main reason is the original circle on the plane projected onto the camera view, thereby causing the image distortion. The minor axis of the ellipse is formed as the original diameter, which projected onto a new plane.

As shown in Fig. 3, assumed the prospective plane of cameras is x_1-o-y_1, the angle between prospective plane of cameras and the plane of the circle is α. As a result, three slides of the projected triangle are a, b, c respectively, and the original diameter c, which projected on the plant (x_1-o-y_1), is the minor axis (b) of ellipse. It follows that

$$\cos\alpha = \frac{b}{c} \tag{13}$$

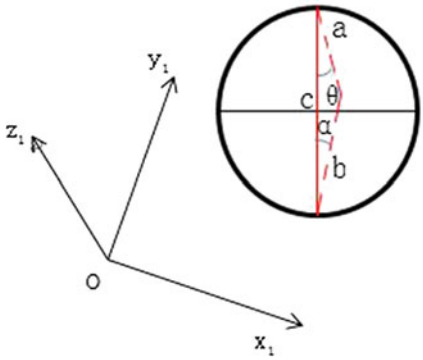

Fig. 3 The included angle between the line ($L^{'}$) and the plane(x'-o'-y')

The included angle α is the angle between line $L^{'}$ and the plane x'-o'-y', the sides of the triangle b and c are the ellipse's long axis and short axis, which are defined as $a^{'}$ and $b^{'}$ respectively. It can be obtained as

$$\alpha = \arccos\frac{b^{'}}{a^{'}} \tag{14}$$

Hence, this can be transformed to solved problems of elliptic long axis and short axis. According to results above, the ellipse center coordinate is (x_0, y_0). It is assumed that the line through the center coordinate and X axis, which is formed the angle ϕ, then the parametric equation of the line can be given as follows:

$$\begin{cases} x = x_0 + t\ \cos\varphi \\ y = y_0 + t\ \sin\varphi \end{cases} \tag{15}$$

where t is the parameter, φ is the angle between the straight line and the x-axis.

Assume $F(x) = 0$, the Eq. (15) is substituted into it, and then it can be calculated as follows:

$$\begin{aligned} &\left(A\cos^2\varphi + B\sin\varphi\cos\varphi + C\sin^2\varphi\right)t^2 \\ &\quad + [(2Ax_0 + By_0 + D)\cos\varphi + (Bx_0 + 2Cy_0 + E)\sin\varphi]t + H = 0, \end{aligned} \tag{16}$$

where,

$$H = Ax_0^2 + Bx_0y_0 + Cy_0^2 + Dx_0 + Ey_0 + 1 \tag{17}$$

Putting the known center coordinate above into Eq. (15). It can be obtained as

$$H = \frac{B^2 - 4AC + AE^2 + CD^2 - BDE}{B^2 - 4AC} \tag{18}$$

Assumed two roots of Eq. (16) are t_1, t_2, The geometric meaning of the parameters $|t|$ shows that a length of string through the center point (x_0, y_0) is given

$$|t_1 - t_2| = \sqrt{(t_1 + t_2)^2 - 4t_1 t_2} \tag{19}$$

Easy to know

$$t_1 + t_2 = 0 \tag{20}$$

Thus, it can be gotten

$$|t_1 - t_2| = 2\sqrt{-t_1 t_2} \tag{21}$$

By Weber's theorem, it can be obtained

$$t_1 t_2 = \frac{H}{A\cos^2\varphi + B\sin\varphi\ \cos\ \varphi + C\ \sin^2\varphi} \tag{22}$$

Thus, it can be gotten

$$|t_1 - t_2| = 2\sqrt{\frac{-H}{A\ \cos^2\varphi + B\sin\varphi\cos\varphi + C\sin^2\varphi}} \tag{23}$$

The inclination can be obtained by the Eq. (23). Because the long and short axis of the ellipse are its the longest and the shortest string, respectively.

When $A\ \cos^2\varphi + B\sin\varphi\cos\varphi + C\sin^2$ takes the extreme value, then it is the long and short axis of the ellipse.

Assume $A\cos^2\phi + B\sin\phi\cos\phi + C\sin^2$, it can be obtained

$$G = \frac{A(\cos 2\phi + 1)}{2} + \frac{B\sin 2\phi}{2} + \frac{C(1 - \cos 2\phi)}{2} \tag{24}$$

For simplicity, it can be gotten

$$G = \frac{A + C}{2} + \frac{\sqrt{(A - C)^2 + B^2}}{2}\sin\left(2\phi + \arctan\frac{A - C}{B}\right) \tag{25}$$

Easy to know

$$-1 \le \sin\left(2\phi + \arctan\frac{A - C}{B}\right) \le 1 \tag{26}$$

then, it can be gotten

$$\begin{cases} G_{\max} = \frac{A+C}{2} + \frac{\sqrt{(A-C)^2+B^2}}{2} \\ G_{\min} = \frac{A+C}{2} - \frac{\sqrt{(A-C)^2+B^2}}{2} \end{cases} \tag{27}$$

Hence, the long axis and short axis of ellipse can be calculated as follows:

$$\begin{cases} a' = 2\sqrt{\frac{-2H}{A+C-\sqrt{(A-C)^2+B^2}}} \\ b' = 2\sqrt{\frac{-2H}{A+C+\sqrt{(A-C)^2+B^2}}} \end{cases} \tag{28}$$

According the Eq. (14), (18) and (28), the formula of the angle α between the line L' and the plant x'-o'-y' can be gotten as follows:

$$\alpha = \arccos\sqrt{\frac{A+\mathrm{C}-\sqrt{(\mathrm{A}-\mathrm{C})^2+B^2}}{A+C+\sqrt{(\mathrm{A}-\mathrm{C})^2+B^2}}} \tag{29}$$

2.4 Solving the Rotation Velocity

So far, the direction of sphere rotation has been solved, the next is to address the issue of rotation velocity. Precise calculation method is to first calculate the arc distance of the same point motion in any two frame images,and then divided by the time between two frame images, that is the rotation velocity. In the high speed rotating sphere, the curve distance between two points can be approximated to the straight line, which can greatly reduce the amount of calculation and shorten the time. This paper selects a point with five consecutive elliptical trajectory, in order to reduce the error, which selects the average distance between each point.

According to the foregoing, we can see the oval coordinates of any five points (x_n, y_n), $n = 1, 2, 3, 4, 5$, The rotation speed of the ball is V, the interval between two frames is t,and the ratio between the actual size of the object and the pixel size of the image is k

$$v = \frac{k\sum_{n=1}^{4}\sqrt{(x_{n+1}-x_n)^2+(y_{n+1}-y_n)^2}}{4t} \tag{30}$$

3 Experimental Verification

A high-speed camera is used to shoot a marker rotating sphere, and obtain the coordinates of points by Kinovea software, which is verified via the model. Then the 5 consecutive coordinates of the same point on the sphere. To simplify the sphere model, we try to select the center plane coordinate system on the shaft. As shown in Fig. 4.

Selecting five coordinates (67, −25), (31, −58), (2, −64), (−30, −58), (−61, −35), and substituting into the elliptic equation respectively, it can be obtained by matlab

$$\begin{cases} A = 1.7948e-4 \\ B = 9.1191e-6 \\ C = 2.0961e-4 \\ D = 3.4943e-4 \\ E = -2.2000e-3 \end{cases} \tag{31}$$

The center coordinate can be calculated as (−1.107, −2.645) by Using above models, and the angle showed as follows:

$$\beta = 8.42^\circ \tag{32}$$

$$\alpha = 22.76^\circ \tag{33}$$

Because the selected center point is closed to coordinate axis as possible, the ideal value of angle β is 0. Measuring the center point may be allowed to have some errors in the acceptable range.

$$\alpha = \arcsin\frac{112.5 - 87.5}{62.5} \tag{34}$$

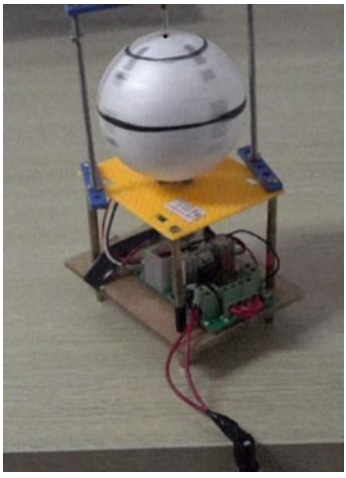

Fig. 4 The experimental device

It can be calculated

$$\alpha = 23.58^{\circ} \tag{35}$$

Error is small in the actual calculation, within the acceptable range.

4 Conclusion and Suggestion

This paper proposes a algorithm that monocular vision discerns the 3D velocity and size of sphere rotation. A rotation parameter equation is established at the coordinate of the 5-frame image in the high speed camera according to any marked points on the sphere.

Finally, the three-dimensional velocity and the size of the sphere rotation are obtained by the rotation feature information, and the validity of the algorithm is verified by experiments. At present, the algorithm is mainly used in the table tennis trajectory recognition and prediction. In the case of ensuring the accuracy of the recognition, it plays an important role in the movement planning and action decision making in the subsequent stage of table tennis robot. This is direction of author's efforts in the future. We hope to improve the accuracy of image recognition and apply the algorithm to the table tennis robot more effectively, so as to complete the task of accurately strike.

References

1. Lingfu Kong, Qiaona Liu (2012) Motion parameters estimation Of 3D object based on the monocular camera [J]. J Yanshan Univ 36(4):310–315
2. Yamaguti N, Shunichiro OE, Terada K (1997) Method of distance measurement by using monocular camera [C]. SICE 97. In: Proceedings of the 36th SICE annual conference. International session papers, pp 1255–1260
3. Saxena A, Chung SH, Ng A (2006) Learning depth from single monocular images [J]. Adv Neural Inf Process Syst
4. Matsushima M, Hashimoto T, Takeuchi M (2005) A learning approach to robotic table tennis [J]. IEEE Trans Robot 21(4):767–771
5. Leung H, Wang HQ, Cao CX (2006) An improved locally weighted regression for a converter re-vanadium prediction modeling [C]. In: The 6th world congress on intelligent control and automation, Dalian, pp 151–1519
6. Qing Rui, Zongwu Hu (1998) Simulation of table tennis track prediction with LWR learning [J]. Robotics 20(5):373–377
7. Yamaguti N, Shunichiro OE, Terada K (2006) A distance measurement method available to texture surface by using complex-log mapping [C]. In: Industrial Electronics, control and instrumentation, 1997, IECON 97. 23rd international conference, pp 1142–1147
8. Chunqin Shi, Liyan Zhang (2010) Monocular measurement in binocular measurement system with instantaneous random illumination [J]. Optics Precision Eng 18(1):257–264

9. Nakashima A, Ogawa Y (2011) Robotic table tennis based on physical models of aerodynamics and rebounds [C]. In: IEEE international conference: robotics and biomimetics (ROBIO)
10. Nakashima A, Tsuda Y, Liu C, Hayakawa Y (2010) A real-time measuring method of translational/rotational velocity of a table tennis ball. In: Proceeding of 5th IFAC symposium on mechatronic systems, pp 732–738
11. Liu C, Hayakawa Y, Nakashima A (2011) A registration algorithm for on-line measuring the rotational velocity of a table tennis ball. In: Proceeding of IEEE/RSJ international conference on intelligent robots and systems
12. Yanlong H, De X, Min T (2011) Trajectory prediction of spinning ball for ping-pong player robot [C]. In: 2011 IEEE/RSJ international conference on intelligent robots and systems, San Francisco, 2011, pp 3434–3439
13. Xiaopeng C, Ye T, Qiang H (2010) Dynamic model based ball trajectory prediction for a robot ping-pong player [C]. In: The 2010 IEEE international conference on robotics and biomimetics, Tianjin, 2010, pp 603–608
14. Sun L, Liu JT, Wang YS (2009) Ball's flight trajectory prediction for table-tennis game by humanoid robot [C]. In: IEEE international conference on robotics and biomimetics, Guilin, 2009, pp 1136–1141
15. Yanqing Ren, Zaojun Fang (2014) Spinning pattern classification of table tennis ball's flying trajectory based on fuzzy neural network [J]. Control Decis 29(2):263–269
16. Genlin Lv (1986) Analytic geometry [M]. Higher Education Press, Beijing

Observer-Based Event-Triggered Consensus Tracking Control of Multi-agent Systems

Jiahuan Lu and Lin Li

Abstract The leader-following consensus problem of multi-agent systems with general linear dynamics is investigated in this paper. Only one leader is considered and the communication topology among the followers is undirected. A novel consensus protocol based on observer and event-triggered mechanism is proposed. Based on the protocol, a sufficient condition is obtained by using common Lyapunov function method. This condition can guarantee that each follower agent can track the leader. Finally, a numerical example is given to demonstrate the effectiveness of the proposed scheme.

Keywords Event-triggered control · Leader-following consensus · Multi-agent systems · Observer

1 Introduction

In recent decades, cooperative control problems of multi-agent systems (MAS) have been causing great attention in control areas due to the rapid development of embedded system, computer network and communication technology [1–3]. Consensus problems, as a hot issue in cooperative control of MAS, which is to design a control scheme for agents so that all agents can reach a common state of interest [4, 5]. In many real applications, agents may need to track an assigned point or signal to complete a special task, which is called leader-following consensus and is one of the most important topics in consensus control. In [6], Jadbabaie et al. considered a leader-following consensus problem and proved that if the topology is jointly connected, then, the followers can track the leader as times goes on. Ni et al. [7] studied

J. Lu · L. Li (✉)
Department of Control Science and Engineering, University of Shanghai for Science and Technology, Shanghai 200093, China
e-mail: lilin0211@163.com

Y. Jia et al. (eds.), *Proceedings of 2016 Chinese Intelligent Systems Conference*, Lecture Notes in Electrical Engineering 404, DOI 10.1007/978-981-10-2338-5_30

the leader-following consensus problem of higher order multi-agent systems under fixed and switching topologies, meanwhile, the distributed controllers were designed to solve the leader-following consensus problem.

Above these papers, to reach the consensus, the continuous communication between agent and neighbors must be kept, which need more unnecessary resources. However, in some practical applications, the limited resources will be consumed soon with the constantly communication. Motivated by the limitation, the event-triggered control is developed [8–10]. In [8], the leader-following consensus for second-order MAS with event-triggered consensus was discussed. Zhou et al. [10] considered a combinational measurements to leader-following exponential consensus of general linear MAS with event-triggered control. Moreover, it is quite difficult to detect the real-time states in some engineering applications, so, designing an estimator for each agent to estimate the agents' states is very significant [9, 11–13]. In [11], authors considered an observer-based control protocol which was related to the relative output information. On the basis of the [11], Li et al. [12] designed a reduced-order observer-based scheme for continuous and discrete systems.

There are lots of literatures studying the consensus control of general linear MAS with leader-following scheme, event-triggered mechanism or estimator-based method. However, to the best of authors' knowledge, there are few works on the event-based leader-following consensus control under the assumption that the real-time states cannot be measured. In this paper, we consider the observer-based event-triggered control for leader-following consensus with general linear MAS. First, the common observers are designed for each agent to estimate the states. Second, based on the estimates, an appropriate event-triggering function is proposed. Finally, it is shown that the leader-following consensus can be reached under the proposed observer-based and event-triggered scheme.

Notations: I_N denotes the identity matrix of N order, 1_N denotes the column vector with all entries equal to one. $\|x\|$ and $\|A\|$ are the Euclidean norm of a vector x and a matrix A, respectively. If a real matrix $Q > 0$, that is to say, the matrix Q is positive definite. The superscript T of a vector or a matrix represents the transpose of it. The symbol $\otimes$ means the Kronecker product.

2 Preliminaries and Problem Statement

The topology of this paper is modeled by an undirected graph $\mathcal{G} = (\mathcal{V}, \mathcal{E}, \mathcal{A})$, where $\mathcal{V} = \{v_1, v_2, ..., v_N\}$ is the set of nodes, $\mathcal{E} = \mathcal{V} \times \mathcal{V}$ is the set of edges, and a weighted adjacency matrix $\mathcal{A} = (a_{ij}) \in R^{N\times N}$, in which, the entry $a_{ij} \geq 0$. If edge $(v_i, v_j) \in \mathcal{E}$, then node v_j is called a neighbor of node v_j and $a_{ij} > 0$. Then the neighbor index set of agent v_i can be denoted by $\mathcal{N}_i = \{j|(v_j, v_i) \in \mathcal{E}\}$. Then the in-degree matrix of $\mathcal{G}$ is defined by $\Delta = diag\{\Delta_1, \Delta_2, ..., \Delta_N\}$, where $\Delta_i = \sum_{j\in\mathcal{N}_i} a_{ij}$. The Laplacian matrix of the graph is defined as $L = \Delta - \mathcal{A}$, suppose the graph $\mathcal{G}$ is connected, then we can find that the matrix L has a zero eigenvalue and the corresponding eigenvector is 1_N.

In this paper, we consider a multi-agent system with N follower agents and a leader agent. The dynamics of each follower agent is

$$\begin{cases} \dot{x}_i(t) = Ax_i(t) + Bu_i(t) \\ y_i(t) = Cx_i(t), \qquad i = 1, 2, ..., N, \end{cases} \tag{1}$$

where $x_i(t) \in R^n$ is the state, $u_i(t) \in R^m$ is the control input, and $y_i(t)$ is the measured output, and A, B, C are known constant matrices with appropriate dimensions. It is assumed that the pair (A, B) and (C, A) are stabilizable and detectable, respectively.

The leader is described as

$$\begin{cases} \dot{x}_0(t) = Ax_0(t) \\ y_0(t) = Cx_0(t), \end{cases} \tag{2}$$

where $x_0(t) \in R^n$ is the state of leader, which is independent of followers' states.

Considering the difficulty of reaching the states of agents, we consider the following observer

$$\begin{cases} \dot{\tilde{x}}_i(t) = A\tilde{x}_i(t) + Bu_i(t) + G(\tilde{y}_i(t) - y_i(t)) \\ \tilde{y}_i(t) = C\tilde{x}_i(t), \end{cases} \tag{3}$$

where $\tilde{x}_i \in R^n$ is the observer state, G is the observer gain matrix.

Based on the Eq. (3), design the event-triggered and leader-following consensus protocol as

$$u_i(t) = K[\sum_{j \in N_i} a_{ij}(\tilde{x}_j(t_k) - \tilde{x}_i(t_k)) + d_i(x_0(t_k) - \tilde{x}_i(t_k))], t \in [t_k, t_{k+1}), \tag{4}$$

where K is the control gain matrix to be determined and t_k is the kth event instant for each agent.

The leader-following consensus of system (1) and (2) is said to be achieved, if with the control input (4), the close-loop system satisfies

$$\lim_{t \to \infty} \|x_i(t) - x_0(t)\| = 0, \qquad \forall i, j \in \mathcal{I}, i \neq j$$

for any initial condition $x_i(0)$.

Before giving the main result, we should list one useful lemma.

In the undirected topology, let $D = diag(d_1, d_2, ..., d_N)$ be the leader adjacency matrix of union graph $\bar{\mathcal{G}} = \mathcal{G} \cup \{0\}$, and $H = L + D$, then the following lemma holds.

Lemma 1 ([13]) *The matrix H has nonnegative eigenvalues $\lambda_1, \lambda_2, ..., \lambda_N$ and the matrix H is positive definite if and only if the union graph $\bar{\mathcal{G}}$ is connected.*

3 Main Result

Theorem 1 *Consider system (1) and (2) with the observer (3) and control protocol (4), and assume that the communication graph $\bar{\mathcal{G}}$ is connected, the pair (A, B) is stabilizable and pair (C, A) is detectable. Given a positive scalar α, if there exists a positive definite matrix Q and an appropriate positive scalar μ, such that the following Riccati inequality*

$$QA + A^T Q - 2\mu QBB^T Q + \alpha I_n < 0, \tag{5}$$

holds. Then, N follower agents can track the leader agent from any initial conditions, when the triggering function is designed as

$$f(e(t), \hat{x}(t)) = \|e(t)\| - \beta \frac{\alpha}{2\|H \otimes QBB^T Q\|} \|\hat{x}(t)\|, \tag{6}$$

where $\beta \in (0, 1)$.

Constructing the matrix K in consensus protocol (4) as

$$K = B^T Q \tag{7}$$

Proof Denote

$$\begin{cases} \hat{x}_i(t) = \tilde{x}_i(t) - x_0(t) \\ \varepsilon_i(t) = \tilde{x}_i(t) - x_i(t), \qquad i = 1, 2, ..., N \end{cases} \tag{8}$$

then, the dynamics of $\hat{x}_i(t)$ is

$$\begin{aligned} \dot{\hat{x}}_i(t) = A\hat{x}_i(t) + BK[\sum_{j \in N_i} a_{ij}(\tilde{x}_j(t_k) - \tilde{x}_i(t_k)) + d_i(x_0(t_k) - \tilde{x}_i(t_k))] \\ + GC(\tilde{x}_i(t) - x_i(t)) \end{aligned} \tag{9}$$

Define the measurement error $e_i(t)$ of current state and triggering state as

$$e_i(t) = \hat{x}_i(t_k) - \hat{x}_i(t). \tag{10}$$

Substituting (10) into (9), then one has

$$\begin{aligned} \dot{\hat{x}}_i(t) =& A\hat{x}_i(t) + BK[\sum_{j \in N_i} a_{ij}((e_j(t) - e_i(t)) + (\hat{x}_j(t) - \hat{x}_i(t))) \\ & - d_i(e_i(t) + \hat{x}_i(t))] + GC\varepsilon_i(t) \qquad t \in [t_k, t_{k+1}) \end{aligned} \tag{11}$$

which can be written in compact form

$$\begin{aligned}\dot{\hat{x}}(t) = &((I_N \times A) - (H \otimes BK))\hat{x}(t) - (H \otimes BK)e(t) \\ &+ (I_N \otimes GC)\varepsilon(t)\end{aligned} \tag{12}$$

From (3) and (1), we can find

$$\dot{\varepsilon}_i(t) = (A + GC)\varepsilon_i(t). \tag{13}$$

If the observer feedback matrix G is designed to make $A + GC$ Hurwitz, then $\varepsilon_i(t)$ will approach zero asymptotically. From (12) and (13), we can find that the estimation error $\varepsilon(t)$ is decoupled from the dynamics $\hat{x}(t)$, thus, the stability of (12) is equivalent to the stability of the following system:

$$\dot{\hat{x}}(t) = ((I_N \times A) - (H \otimes BK))\hat{x}(t) - (H \otimes BK)e(t) \tag{14}$$

Considering the following Lyapunov function

$$V(t) = \hat{x}^T(t)(I_N \otimes Q)\hat{x}(t),$$

where $Q > 0$.

Differentiating $V(t)$ along the solution of (14), we have

$$\begin{aligned}\dot{V}(t) = &2\hat{x}^T(t)(I_N \otimes QA - H \otimes QBK)\hat{x}(t) \\ &- 2\hat{x}^T(t)(H \otimes QBK)e(t)\end{aligned} \tag{15}$$

It follows from (6) that

$$\dot{V}(t) = \underbrace{2\hat{x}^T(t)(I_N \otimes QA - H \otimes QBB^TQ)\hat{x}(t)}_{\textit{the first part}} \underbrace{-2\hat{x}^T(t)(H \otimes QBB^TQ)e(t)}_{\textit{the second part}} \tag{16}$$

Dividing (16) into two parts, and now we will analyze the first part.

According to Lemma 1, since H is symmetric, there exists an orthogonal matrix $T \in R^{N\times N}$, such that

$$THT^T = \Lambda = diag(\lambda_1, ..., \lambda_N),$$

where Λ is an upper triangular matrix, the elements on the primary diagonal are the eigenvalues of matrix H. Then, with the assumption that $\bar{\mathcal{G}}$ is connected in Theorem 1, we know that $\lambda_i, i = 1, ..., N$ are all positive. Setting $\hat{x}(t) = (T \otimes I_n)\zeta(t)$, then, the first part of (16) becomes

$$\begin{aligned}
&\hat{x}^T(t)[I_N \otimes (QA + A^TQ) - 2H \otimes QBB^TQ]\hat{x}(t) \\
\leq &\sum_{i=1}^{N} \zeta_i^T(t)((QA + A^TQ) - 2\lambda_1 QBB^TQ)\zeta_i(t) \\
\leq &\sum_{i=1}^{N} \zeta_i^T(t)((QA + A^TQ) - 2\mu QBB^TQ)\zeta_i(t) \\
\leq &-\alpha \sum_{i=1}^{N} \zeta_i^T(t)\zeta_i(t) \\
\leq &-\alpha\|\hat{x}(t)\|^2,
\end{aligned} \tag{17}$$

where μ is chosen sufficiently small such that $\mu < \lambda_1$.

It is easy to see that the second part of (16) satisfies

$$\begin{aligned}
&-2\hat{x}^T(t)(H \otimes QBB^TQ)e(t) \\
\leq &2\|H \otimes QBB^TQ\|\|\hat{x}(t)\|\|e(t)\|
\end{aligned} \tag{18}$$

Combining (17) and (18), we can get

$$\begin{aligned}
\dot{V}(t) &\leq -\alpha\|\hat{x}(t)\|^2 + 2\|H \otimes QBB^TQ\|\|\hat{x}(t)\|\|e(t)\| \\
&= -\|\hat{x}(t)\|(\alpha\|\hat{x}(t)\| - 2\|H \otimes QBB^TQ\|\|e(t)\|)
\end{aligned} \tag{19}$$

Enforcing the triggering condition (7) as

$$\|e(t)\| \leq \beta \frac{\alpha}{2\|H \otimes QBB^TQ\|}\|\hat{x}(t)\|, \tag{20}$$

with $0 < \beta < 1$, we have

$$\dot{V}(t) \leq \alpha(\beta - 1)\|\hat{x}(t)\|^2 < 0. \tag{21}$$

Therefore system (14) is globally asymptotically stable, which means that all agents follow the leader.

In the following, we will show that Zeno behavior can be excluded. For any interval $t \in [t_k, t_{k+1})$, computing the time derivative of $\frac{\|e(t)\|}{\|\hat{x}(t)\|}$,

$$\frac{d}{dt}\frac{\|e(t)\|}{\|\hat{x}(t)\|} \leq (1 + \frac{\|e(t)\|}{\|\hat{x}(t)\|})\frac{\|\dot{\hat{x}}(t)\|}{\|\hat{x}(t)\|}$$

Defining the notion $y(t) = \frac{\|e(t)\|}{\|\hat{x}(t)\|}$, then we have

$$\dot{y}(t) \leq (1 + y(t))\frac{\|\dot{\hat{x}}(t)\|}{\|\hat{x}(t)\|} \tag{22}$$

It follows from (12) that

$$\|\dot{\hat{x}}(t)\| \leq \|I_N \otimes A + H \otimes BK\|\|\hat{x}(t)\| + \|H \otimes BK\|\|e(t)\| + \|I_N \otimes GC\|\|\varepsilon(t)\| \tag{23}$$

It can be observed from (23) that $\|\hat{x}(t)\|$ will not approach zero unless $\|\varepsilon(t)\|$ approaches zero. Thus, there exists a finite positive scalar γ such that $\frac{\|\varepsilon(t)\|}{\|\hat{x}(t)\|} < \gamma$. Substituting (23) into (22), we can get

$$\dot{y}(t) \leq (1 + y(t))(p + qy(t)), \tag{24}$$

where

$$\begin{cases} p = \|I_N \otimes A + H \otimes BK\| + \gamma\|I_N \otimes GC\| \\ q = \|H \otimes BK\| \end{cases} \tag{25}$$

So that $y(t)$ holds the bound $y(t) \leq \phi(t, \phi_0)$, where $\phi(t, \phi_0)$ is the solution of $\dot{\phi}(t) = (1 + \phi(t))(p + q\phi(t))$, $\phi(0, \phi_0) = \phi_0$. Therefore the inter-event times are bounded from below by the time τ that satisfies event-triggered condition, i.e., $\phi(\tau, 0) = \frac{\|e(t)\|}{\|\hat{x}(t)\|} = \beta\frac{\alpha}{2\|H \otimes QBB^TQ\|} = h$. Moreover, the solution of the above differential equation is $\phi(\tau, 0) = \frac{pe^{(p-q)(t+c)}-1}{1-qe^{(p-q)(t+c)}}$. Then, we obtain the below time

$$\tau = \frac{1}{p-q} \ln \frac{p(h+1)}{p+qh}. \tag{26}$$

Then, we can find that, whatever $p > q$, or $p < q$, the value of τ are both larger than zero, so we can conclude that the inter-event time intervals are nontrivial, that is to say the Zeno behavior is not exist.

4 Simulation Example

Assume that the network of four followers and one leader, the communication graph $\bar{\mathcal{G}}$ given in Fig. 1.

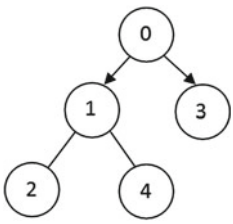

Fig. 1 Communication topology

The dynamics of the followers and the leader and the Laplacian matrix of the topology are

$$A = \begin{bmatrix} 0 & 1 \\ -1 & 0 \end{bmatrix}, \quad B = \begin{bmatrix} 0 \\ 1 \end{bmatrix}, \quad C = \begin{bmatrix} 1 & 0 \end{bmatrix}, \quad L = \begin{bmatrix} 2 & -1 & 0 & -1 \\ -1 & 1 & 0 & 0 \\ 0 & 0 & 0 & 0 \\ -1 & 0 & 0 & 1 \end{bmatrix},$$

and the leader adjacency matrix $D = diag(1, 0, 1, 0)$, then $\lambda_1 = 0.2679$.

Given the observer feedback matrix G and control gain matrix K as follows

$$G = \begin{bmatrix} -7.8180 \\ -15.3777 \end{bmatrix}, \quad K = \begin{bmatrix} 0.8199 & 2.6061 \end{bmatrix}.$$

Consider the random initial state and select the parameters $\alpha = 2, \beta = 0.5$, which satisfy the conditions in Theorem 1. Figure 2 shows the Leader–follower tracking

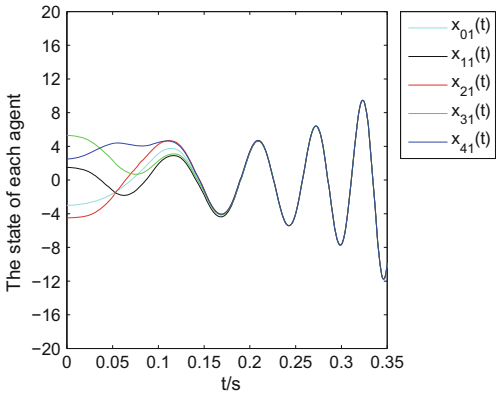

Fig. 2 Leader–follower tracking trajectories of each agent's first state

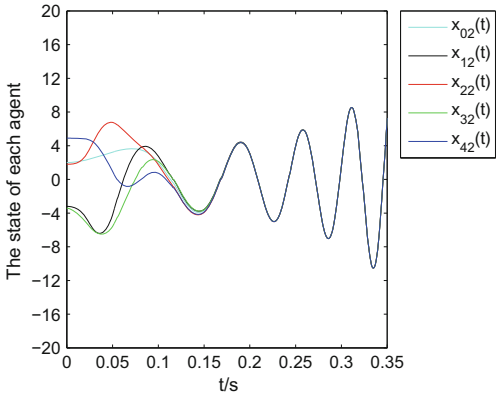

Fig. 3 Leader–follower tracking trajectories of each agent's second state

trajectories of each agent's first state, and Fig. 3 shows the Leader–follower tracking trajectories of each agent's second state.

From the simulation results, we can find that under the protocol (4), the leader-following problem has been solved.

5 Conclusion

The leader-following consensus problem for general linear multi-agent systems is addressed in this paper. Considering the impossibility of achieving the all states of agents, the state observers are adopted. A novel event-triggered scheme based on the observer states is then proposed. Finally, the simulation example is illustrated to demonstrate the effectiveness of proposed control strategy.

References

1. Olfati-Saber R, Murray R (2004) Consensus problems in networks of agents with switching topology and time-delays. IEEE Trans Autom Control 49(9):1520–1533
2. Yang Y, Wang C (2013) Obstacle avoidance method for mobile robots based on improved artificial potential field method and its implementation on MATLAB. J Univ Shanghai Sci Technol 35(5):496–500
3. Wei Y, Han Y (2010) Modeling and simulation of intersection based on multi-agents and fuzzy control strategy. J Univ Shanghai Sci Technol 32(3):259–263
4. Olfati-Saber R, Murray R (2003) Consensus protocols for networks of dynamic agents. Am Control Conf 2:951–956
5. Ren W, Beard RW (2005) Consensus seeking in multiagent systems under synamically changing interaction topologies. IEEE Trans Autom Control 50(5):655–661
6. Jadbabaie A, Lin J, Morse AS (2003) Coordination of groups of mobile autonomous agents using nearest neighbor rules. IEEE Trans Autom Control 48(6):988–1001
7. Ni W, Cheng D (2010) Leader-following consensus of multi-agent systems under fixed and switching topologies. Syst Control Lett 59(3–4):209–217
8. Hu J, Cheng G, Li H (2011) Distributed event-triggered tracking control of second-order leader-follower multi-agent systems. In: The 30th Chinese control conference. Yantai, China, pp 4819–4824, 22–24 Jul 2011
9. Zhang H, Feng G, Yan H, Chen Q (2014) Observer-based output feedback event-triggered control for consensus of multi-agent systems. IEEE Trans Ind Electron 61(9):4885–4894
10. Zhou B, Liao X (2015) Leader-following exponential consensus of general linear multi-agent systems via event-triggered control with combinational measurements. Appl Math Lett 40:35–39
11. Li Z, Duan Z (2010) Consensus of multiagent systems and synchronization of complex networks: a unified viewpoint. IEEE Trans Circuits Syst 57(1):213–224
12. Li Z, Liu X, Lin P, Ren W (2011) Consensus of linear multi-agent systems with reduced-order observer-based protocols. Syst Control Lett 60(7):510–516
13. Cheng TH, Kan Z, Shea JM, Dixon WE (2014) Decentralized event-triggered control for leader-follower consensus. In: The 53th IEEE conference on decision and control. Los Angeles, California, USA, pp 1244–1249, 15–17 Dec 2014

An Asynchronous Linear-Threshold Innovation Diffusion Model

Qi Zhang, Kuiying Deng and Tianguang Chu

Abstract We consider a linear-threshold innovation diffusion model in asynchronous networks, wherein the *positive* vertices hold supporting attitude towards the innovation and accelerate the diffusion whereas the *negative* vertices oppose it and obstruct the diffusion. A more realistic assumption made in this work is that the attitudes of the vertices (i.e. positive or negative) are changeable. The diffusion begins from a small subset of active nodes and propagates towards the whole network through random transmitting delays along each edge. The vertices outside of the initial active set would be activated and keep forever in active status once the difference of the positive and negative signals they receive from their neighbors exceed a certain threshold. The attitudes of these active nodes would change if the difference of the received positive and negative signals reaches given thresholds. Under these assumptions, our model can exhibit an interesting phenomenon: whenever the initial active set surpasses a certain size, the diffusion process propagates to a specific proportion instead of all the vertices. Experiments on Erdős-Rényi networks verify that the theoretical estimations match closely with the experimental results.

Keywords Bootstrap percolation · Social networks · Diffusion of innovation · Asynchronous transmitting

Q. Zhang · T. Chu (✉)
College of Engineering, Peking University, Beijing
100871, People's Republic of China
e-mail: chutg@pku.edu.cn

Q. Zhang
e-mail: zhang_qi@pku.edu.cn

K. Deng
Department of Engineering Mechanics, Hebei University,
Baoding 071002, China
e-mail: rossdeng@pku.edu.cn

Y. Jia et al. (eds.), *Proceedings of 2016 Chinese Intelligent Systems Conference*,
Lecture Notes in Electrical Engineering 404, DOI 10.1007/978-981-10-2338-5_31

1 Introduction

Most existing bootstrap percolation process based on the *linear threshold model* [1] can be described as follows. A deterministically or randomly selected subset of vertices are activated in the beginning, with others staying in inactive status. Then the diffusion process propagates in rounds, where the inactive vertices would turn into active once it receives k active signals from their neighbors and after that remain active forever. Upon the bootstrap percolation problem, a number of research has been conducted on graph models including trees [2], multidimensional grids [3], random regular graphs [4, 8], Erdős-Rényi graphs [5], and power-law graphs [6, 7].

Typically, many previous bootstrap percolation models assume that the diffusion process propagates synchronously (i.e., each edge requires the equal unit time to transmit the information), and each vertex would be activated once it has k active neighbors at any round. Although the synchronous manner might make more sense in describing the central unit phenomena exhibited in some technological networks (e.g., sensor networks), it is actually rare to present in many networks, e.g., social and neural networks. Moreover in most studies, all vertices are assumed to facilitate the diffusion without obstruction, under which the phenomena of *all-or-nothing* is usually observed. However in real social networks, not all individuals would positively promote the diffusion of innovation in a market.

In this paper, we extend the classical bootstrap percolation model by making more realistic assumptions on it to capture the activation phenomenon. To be specific, we assume that the diffusion evolves in the asynchronous manner, where random time delays sampled from an exponential distribution would be drawn for the information to transmit between individuals. The linear threshold model is adopted here to describe the status variance of the vertices. Furthermore, the attitudes of the vertices are assumed to be changeable. For brevity, we refer to our model as bootstrap percolation with changeable attitudes (BP-C) model. Based on it, we intend to understand to what extent the process of the innovation propagates in networks and under what conditions the initial outbreak would spread into a nontrivial proportion of the vertices. We find that the BP-C processes sometimes exhibit *normalization* instead of "all-or-nothing" phenomena, and when the process is explosive and the initial active set meet certain requirements, the normalization phenomena always exist. Experimental results on Erdős-Rényi networks verify the theoretical estimations.

1.1 Preliminaries

Denote $G = (V, E)$ as a finite graph, and we define the asynchronous (k, r, τ)-*BP-C process* on G as follows. During the diffusion process, all inactive vertices would become active whenever they get k more positive than negative signals from their active neighbors, and then keep in the active status forever. This means that the active vertex will always send signals to their neighbors. The attitudes of the active

vertices (i.e., positive or negative) depend on not only the initial reactions (i.e., positive with probability $1-\tau$ and negative with probability τ) but also their neighbors (i.e., positive if r more positive than negative signals are obtained, and negative if r more negative than positive signals are received with $r > k$). At the time instant t, we denote $\Gamma^+(v,t)$ and $\Gamma^-(v,t)$ as the number of v's active positive and negative neighbors at the time instant t, and thus $\Gamma(v,t) = \Gamma^+(v,t) + \Gamma^-(v,t)$ can be defined as the total number of active neighbors v has until time t.

For a graph model $G = (V, E)$ of size n, the BP-C process on G starting from $A \subset V$ is defined to be (b, η, δ)-*explosive* for some set $S \subseteq V$ if there exist $b \in \mathbb{N}$ and $\eta, \delta > 0$ such that with probability at least $(1-\delta)$, no less than $(1-\eta)|S|$ vertices $v \in S$ have no active neighbors at time $t = t(v)$ but at least b active neighbors at time $t + \eta$. Clearly, the adjective *explosive* here is used to indicate that the activating process takes place quickly in the graph.

2 Main Results

Based on the definition of the BP-C process, we introduce our main results in this section. Instead of "all-or-nothing" occurred in most classical bootstrap percolation models, we prove the normalization phenomena in the proposed BP-C model.

2.1 Estimation of Active Vertices

For the final active vertices, we find that for a graph model $G = (V, E)$ of size n, if the BP-C process on G starting from $A \subset V$ is (b, η, δ)-explosive for $S \subseteq V$ with $|S| \geq b_S$ and $|A \cap S| \leq \eta|S|$, then with probability at least $1-\varepsilon$ that the BP-C process is (b_S, b, η, δ)-normalizing, i.e., for every $\varepsilon > 0$ there exist positive constants b_S, b, η, δ that the BP-C process terminates with $(\alpha \pm \varepsilon)|S|$ active vertices in S, where α can be roughly estimated by

$$\alpha = \min\left\{\left(\frac{1-(\tau-\beta)}{\tau-\beta}\right)^k, 1\right\}, \tag{1}$$

where

$$\beta = \tau \times \min\left\{\left(\frac{1-\tau}{\tau}\right)^r, 1\right\}. \tag{2}$$

The above results can be derived as follows. Note that if the attitudes of the vertices are unchangeable, the ratio of the negative to positive vertices is always around $\tau/(1-\tau)$ since the attitudes of all the vertices can be illustrated by the binomial variables following $\mathrm{Bin}(s, \tau)$ and independent with each other. However, the assumption

is that the attitudes of the vertices would change with their neighbors, and thus the variables of their attitudes are actually dependent with each other. But we can still prove that the final ratio of negative to positive vertices can be roughly computed by $(\tau')/(1-\tau')$ with $\tau' = \tau - \beta$.

The estimation of β would be analyzed in the next section. For any vertex $v \in V$, when the activation threshold is reached at time t, i.e., $\Gamma^+(v,t) - \Gamma^-(v,t) = k$, it takes the probability $1-\tau'$ to be positive and τ' to be negative. Since the initial attitudes of the vertices are independent with each other, $\Gamma_s^+(v)$ and $\Gamma_s^-(v)$ can be regarded to follow the binomial distribution $\mathrm{Bin}(s, \tau')$. Since every vertex takes random exponentially distributed time to transmit the signals to its neighbors, we here denote $X_i(v)$ as the i-th signal received by v, and $Z_i(v) := X_1(v) + X_2(v) + \cdots + X_i(v)$ as the sum of the first i signals v obtained. Clearly, v will be activated once $Z_i(v)$ reaches k. We can see that the probability of $X_1(v) = 1$ is $1-\tau'$. But when i grows large, $Z_i(v)$ cannot be tackled by a random walk any more since the proportion of the remaining positive/negative signals would deviate from $1-\tau'/\tau'$ by relatively large biases. But we can prove that if $Z_i(v)$ has not reached k when i grows large, then with high probability that $Z_i(v)$ has already been far-away from the threshold and difficult to reach it anymore. Therefore, $(Z_i(v))_{i\in\mathbb{N}}$ roughly follows a random walk with bias τ', by which we can arrive at the conclusion of the final active vertices. The proof details are omitted due to the restriction of space. Note that (1) and (2) are just rough estimations, we would present a heuristic algorithm on the random walk process to give better estimations in future.

2.2 Proportion of Positive Active Vertices

For the active positive vertices, we can prove that for a graph model $G = (V, E)$ of size n, if the BP-C process on G starting from $A \subset V$ is (b, η, δ)-explosive for $S \subseteq V$ with $|S| \geq b_S$ and $|A \cap S| \leq \eta|S|$, then with probability at least $1-\varepsilon$ that the BP-C process is (b_S, b, η, δ)-normalizing, i.e., for every $\varepsilon > 0$ there exist positive constants b_S, b, η, δ that the BP-C process terminates with $\{[1+\beta-\tau]\alpha \pm \varepsilon\}|S|$ active positive vertices in S, where α can be roughly estimated by (1) and $0 < \beta < 1$ can be roughly estimated by (2).

It can be easily drawn that with high probability that the number of initial positive reactions of all the active vertices is in the range of $(1 \pm \xi)(1-\tau)\alpha$. On the other hand, once a vertex v is activated, it means that $(Z_i(v))_{i\in\mathbb{N}}$ reaches k within the first i signals and v has the probability of $1-\tau$ to be positive and τ to be negative. If it chooses to be positive (with probability $1-\tau$), we can yield that with high probability it would remain positive instead of changing into negative attitude because $k + r$ more negative than positive signals are required to be received to change v from the positive into the negative side. Since the early signals v has received roughly follow the biased random walk, having received k more positive than negative signals from the early-arriving signals indicates that it will take a very small probability to receive

$k + r$ more negative than positive signals. On the other hand, if v chooses to be negative (with probability τ), it would change into positive sider if it receives $r - k$ more positive than negative signals. Thus we can roughly estimate the number of vertices that would change from negative into positive attitude by $\beta * n$, which actually determines the final proportion of the positive and negative vertices and further influences on the bias of the random walk process. Based on the above analysis, we can arrive at the rough estimation of the positive active vertices' amount.

3 Experiments

In this section, we simulate the BP-C processes on Erdős-Rényi networks and compare the obtained percolation results with our theoretical predictions. Specifically, we first select a subset of vertices in random to establish the initial active set, and keep the other vertices in inactive status. Then, each active vertex sends a signal to all of its neighbors where the signals need exponentially distributed times (with expectation 1) to travel along the edges. With time proceeds, an inactive vertex turns into active once it receives k more positive than negative signals, and then takes the probability τ to choose negative as its initial attitude and $1 - \tau$ to be positive. They would keep active forever but their attitudes would change if the difference between positive and negative signals surpasses the threshold r. Finally, we will check if the normalization phenomenon arises. In experiments, we simulate the BP-C processes for different values of τ ranging from 0.1, 0.2 to 0.9. For each value of τ we run the diffusion process 20 times and report the average results.

The generated Erdős-Rényi graph $G(n, p)$ is determined by $n = 100000$, $p = 0.001$. We set the size of initial set as $a_0 = 5000$, the activation threshold as $k = 4$, and the attitude changing threshold as $r = 10$. The percolation results are shown in Fig. 1a, b, where the green dashed lines are the theoretical estimations and the blue solid lines denote the average experimental results, with the error bars indicating the standard deviations of 20 trials. Besides, the percolation ratio (among all of the vertices) and positive ratio (among the active vertices) comparisons in displayed in Fig. 1c, d, where the ratios are computed as follows:

$$\text{percolation ratio} = \frac{\#\{\text{active vertices}\} - a_0}{n - a_0}, \tag{3}$$

$$\text{positive percolation ratio} = \frac{\#\{\text{active positive vertices}\}}{n}, \tag{4}$$

where #{active vertices} in (3) means the number of active vertices, and similarly #{active positive vertices} in (4) indicates the number of active positive vertices. From Fig. 1a–d, it can be seen that the normalization phenomena do exist and our estimations are close to the experimental results.

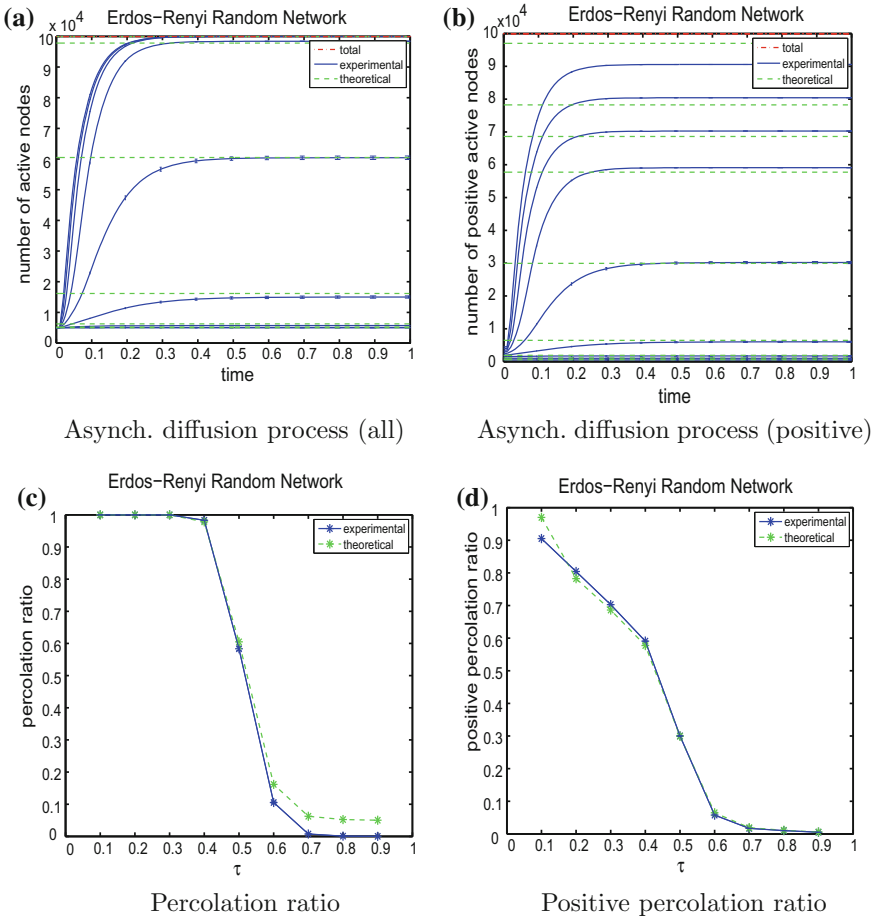

Fig. 1 Asynchronous BP-C processes on Erdős-Rényi networks. The *red dot dash lines* are total number of vertices, the *blue solid lines* indicate the experimental results, and the *green dash lines* represent the theoretical estimations

4 Concluding Remarks

We have discussed about the BP-C processes in this work. Different from many existing bootstrap percolation models, we make more realistic assumptions on it including the transmitting and status changing rules. Instead of the "all-or-nothing" phenomena encountered frequently in most classical bootstrap percolation processes, we find an interesting normalization phenomenon in the activating process and conduct theoretical analysis about it. The theoretical proof of the normalizing percolation results of the BP-C processes as well as the required percolation time would be presented elsewhere in future.

Acknowledgments This work was supported by NSFC (No. 61273111, No. 61673027), National Basic Research Program of China (973 Program, No. 2012CB821200), and the recruitment program of excellent talents in Hebei University (No. 2014-304).

References

1. Kempe D, Kleinberg J, Tardos E (2003) Maximizing the spread of influence through a social network. In: Proceedings of ACM International Conference on Knowledge Discovery and Data Mining, pp 137–146
2. Balogh J, Peres Y, Pete G (2006) Bootstrap percolation on infinite trees and non-amenable groups. Comb Probab Comput 15(5):715–730
3. Balogh J, Bollobás B, Duminil-Copin H, Morris R (2012) The sharp threshold for bootstrap percolation in all dimensions. Trans Am Math Soc 364(5):2667–2701
4. Balogh J, Pittel B (2007) Bootstrap percolation on the random regular graph. Random Struct Algorithms 30(1–2):257–286
5. Lelarge M (2012) Diffusion and cascading behavior in random networks. Games Econ Behav 75(2):752–775
6. Amini H, Fountoulakis N (2014) Bootstrap percolation in power-law random graphs. J Stat Phys 155(1):72–92
7. Aizenman M, Lebowitz J (1988) Metastability effects in bootstrap percolation. J Phys A 21(19):3801–3813
8. Janson S, Luczak T, Turova T, Vallier T (2012) Bootstrap percolation on the random graph $G(n,p)$. Ann Appl Probab 22(5):1989–2047

Deconvolution Estimation Problem for Measurement-Delay Systems with Packet Dropping

Zhenhua Duan, Xinmin Song and Xuehua Yan

Abstract This paper addresses the optimal deconvolution estimation problem for measurement-delay systems over a network subject to random packet dropout, which is modeled by independent and identically distributed Bernoulli processes. First, the state estimator problem is solved by utilizing the reorganized innovation analysis approach, which is given in the linear minimum mean square error sense (LMMSE). Then, the noise estimator is obtained based on the state estimator and the projection formula. Last, we provide a numerical example to declare that our proposed estimation approach is effective.

Keywords Time delay · Packet dropping · Reorganized innovation · Riccati equation · Projection formula

1 Introduction

Recently, the problem of deconvolution estimation for linear systems has attracted much attention due to its extensive applications in image processing [1], oil exploration [2, 3] and so on. The precursory work on the deconvolution problems can be traced back to [2], which contains the study of white noise estimation according to the Kalman filter approach. As for the deconvolution estimation problems, another approach based on the modern time series analysis method is presented in [4], which includes both the input white noise estimator and measurement white noise estimator. However, communication networks are usually unreliable and may lead to time delay and packet dropout, so that many results about time delay and packet dropout

Z. Duan · X. Song (✉)
School of Information Science and Engineering, Shandong Normal University, Jinan 250014, China
e-mail: xinminsong@sina.com

X. Yan
School of Electrical Engineering, University of Jinan, Jinan 250022, China

Y. Jia et al. (eds.), *Proceedings of 2016 Chinese Intelligent Systems Conference*, Lecture Notes in Electrical Engineering 404, DOI 10.1007/978-981-10-2338-5_32

are presented in [5–17]. For the time delay problems, the authors apply the state augmentation approach to solve time delay problem in [5, 6]. There is another approach in [7], where the authors use the partial difference Riccati equation approach to deal with time delay problem.

We retrospect the pioneer work on the Kalman filter about packet losses to [8], in which the author uses the statistics of the unobserved Bernoulli process to describe the observation uncertainty and to derive the estimator. In [9], the sensor measurements are encoded together and sent over the network in a single packet, so that the Kalman filter receives either the complete observation if the packet is received or none of the observation if the packet is lost. In [10], the measurements are transmitted to the filter via two communication channels, while the authors consider the measurements may be sent through different communication channels in the networked filter systems in [11], thus [11] is more general than [10]. Some results about multiple packet dropout have been published in [12–17].

For nonlinear stochastic systems with multi-step transmission delays, multiple packet dropouts and correlated noises, the authors study the recursive estimations by using the innovation analysis approach in [15], in which the noises are assumed to be one-step autocorrelated and cross-correlated. In [16], the multiple packet dropouts phenomenon is considered to be random and is described by a binary switching sequence, which obeys a conditional probability distribution. The authors calculate the recursive estimators based on an innovation analysis method and the orthogonal projection theorem.

In previous works about time delay and packet dropout, the authors have dealt with time delay problem using the partial difference Riccati equation approach or the state augmentation approach. While, those approaches may bring tremendous computation when time delay d_{l-1} is large. The authors have used a scalar independent and identically distributed (i.i.d) Bernoulli process to describe the packet dropout phenomenon. In the real word, scalar can not satisfy realistic. Stimulated by above works about measurement dropout and time delay systems, we will investigate deconvolution estimation for discrete-time systems with measurement delay and packet dropout in this paper. According to the projection formula and the reorganized innovation analysis approach, the state estimation is first obtained. Then, we gain the white noise estimation on the basis of the state estimation obtained above. The major contributions of this paper are as follows: (i) we describe the multiplicative noise using a diagonal matrix dropout, which is described by an independent and identically distributed (i.i.d) Bernoulli process. A closed-form result is gained using the Hadamard product flexibly. (ii) according to the reorganized innovation analysis approach, we derive the optimal state estimator and noise estimator utilizing l Raccati difference equations and one Lyapunov difference equation. When the delay d_{l-1} is large, our proposed approach is more efficient than the classical augmentation approach in [5, 6] and partial difference Riccati equation approach in [7].

The organization of this paper is following. In Sect. 2, we put forward the problem formulae, some assumptions and remarks. In Sect. 3, we deduce the optimal state estimation according to the reorganized innovation analysis approach. Then,

we obtain the white noise estimation based on the optimal state estimation gained above and the projection formula. A numerical example is given to explain the effectiveness of our approach in Sect. 4. Finally, some conclusions are provided in Sect. 5.

Notation: From beginning to end in this paper, the superscripts "−1" and "T" represent the inverse and transpose of a matrix. $\mathcal{R}^n$ denotes an Euclidean space of n-dimension. $\mathcal{R}^{n\times m}$ means the linear space of all $n \times m$ real matrices. The measurement sequence $\{y(0), \ldots, y(k)\}$ can be represented as $\mathcal{L}\left\{y(s)_{s=0}^{k}\right\}$. $\odot$ denotes the Hadamard product. The diagonal matrix with diagonal elements $\lambda_1, \ldots, \lambda_n$ is expressed as $diag\{\lambda_1, \ldots, \lambda_n\}$. In addition, the mathematical expectation operator is denoted as E.

2 Problems Statement and Preliminary

Consider the linear system following

$$x(k+1) = Ax(k) + n(k), \tag{1}$$

$$y_i(k) = \xi_i(k)B_i x(k-d_i) + v_i(k), k \geq d_i, i = 0, \ldots, l-1, \tag{2}$$

here $x(k) \in \mathcal{R}^n$ is an unknown state and $y_i(k) \in \mathcal{R}^{m_i}$ is delayed measurement, respectively. $n(k)$ and $v_i(k)$ are white Gaussian noises with zero mean and covariances $E\{n(k)n^T(j)\} = Q\delta_{k,j}, E\{v_i(k)v_i^T(j)\} = R_i\delta_{k,j}$ respectively. Here, $\delta_{k,j}$ is the Kronecker function. We describe the packet dropout phenomenon with the mutually uncorrelated and identically distributed (i.i.d.) Bernoulli random variables $\xi_{ij}(k)$, in the m_i channels with $Pr\{\xi_{ij}(k) = 1\} = \alpha_{ij}$, $Pr\{\xi_{ij}(k) = 0\} = 1 - \alpha_{ij}$. d_i satisfies that $0 = d_0 < d_1 < \cdots < d_{l-1}$. The initial state $x(0)$ is a random vector with zero mean and covariance matrix $D(0)$. The random process $n(k)$, $v_i(k)$, $\xi_i(k)$ for all k and the initial state $x(0)$ are uncorrelated mutually.

Let

$$y(k) = \begin{cases} y_0(k), & 0 \leq k < d_1, \\ \vdots & \\ \begin{bmatrix} y_0(k) \\ \vdots \\ y_i(k) \end{bmatrix}, & d_i \leq k < d_{i+1}, \\ \vdots & \\ \begin{bmatrix} y_0(k) \\ \vdots \\ y_{l-1}(k) \end{bmatrix}, & d_{l-1} \leq k. \end{cases} \tag{3}$$

Problem For the given measurements $\{y(k)\}_{k=0}^{N}$, find a LMMSE estimator $\hat{x}(k \mid k)$ of $x(k)$ and $\hat{n}(k \mid k+T)$ of $n(k)$, such that

$$E\{[n(k) - \hat{n}(k \mid k+T)][n(k) - \hat{n}(k \mid k+T)]^T\}$$

is minimized. Note that $T = 0$ is the filter, $T > 0$ is the smoother and $T < 0$ is the predictor.

Remark 1 From the distribution of $\xi_{ij}(k)$, it is readily to deduce that $E\{\xi_{ij}(k)\} = \alpha_{ij}$, $E\{(\xi_{ij}(k) - \alpha_{ij})^2\} = \alpha_{ij}(1 - \alpha_{ij})$, $E\{\xi_{ij}(k)(1 - \xi_{ij}(k))\} = 0$, $E\{[\xi_{ij}(k) - \alpha_{ij}][\xi_{il}(s) - \alpha_{il}]\} = \alpha_{ij}(1 - \alpha_{ij})\delta_{k,s}\delta_{j,l}$. $E\{\xi_{ij}(k)\xi_{il}(s)\} = \alpha_{ij}\alpha_{il}$ for $k \neq s$ or $j \neq l$.

Remark 2 In the previous references, the authors usually use a scalar independent and identically distributed (i.i.d) Bernoulli process to describe the packet dropout phenomenon. In this paper, we describe the packet dropout via a diagonal matrix independent and identically distributed (i.i.d) Bernoulli process, which is more realistic. Regarding to the time delay systems, one can use the state augmentation approach to solve the optimal state estimation and white noise estimation problems, but the state augmentation approach may bring tremendous computational when the delay d_{l-1} is large. Therefore, in this paper we will deduce the problem of deconvolution estimation using the reorganized innovation analysis approach to avoid tremendous computation.

3 Main Results

In this section, we will present an analytical solution to the optimal state estimation and the white noise estimation according to the projection formula.

Lemma 1 ([18]) *Let $\sigma = diag\{\sigma_1, \ldots, \sigma_n\}$ and $\rho = diag\{\rho_1, \ldots, \rho_m\}$ be two diagonal stochastic matrices, and A be any $n \times m$ matrix. Then*

$$E\{\sigma A \rho\} = \begin{bmatrix} E\{\sigma_1\rho_1\} & \cdots & E\{\sigma_1\rho_m\} \\ \vdots & \ddots & \vdots \\ E\{\sigma_n\rho_1\} & \cdots & E\{\sigma_n\rho_m\} \end{bmatrix} \odot A. \tag{4}$$

3.1 Design of the Optimal State Estimator

In the next, we first provide an optimal state estimator, which will lead to the optimal white noise estimator. We note that $y_i(k)$ is an additional measurement of the state $x(k - d_i)$, which is gained at time instant k with time delay d_i, so the measurement $y(k)$ contains time delay when $k \geq d_i$. On the basis of [19], the linear space $\{y(s)_{s=0}^{k}\}$ includes the same information as

$$\mathcal{L}\left\{\{Y_{l-1}(s)\}_{s=0}^{k-d_{l-1}},\ldots,\{Y_0(s)\}_{s=k-d_1+1}^{k}\right\},$$

where the new observations

$$Y_{l-1}(s)=\begin{bmatrix} y_0(s) \\ \vdots \\ y_{l-1}(s+d_{l-1}) \end{bmatrix}, 0\le s\le k-d_{l-1}, \tag{5}$$

$$\vdots$$

$$Y_i(s)=\begin{bmatrix} y_0(s) \\ \vdots \\ y_i(s+d_i) \end{bmatrix}, k-d_{i+1}+1\le s\le k-d_i, \tag{6}$$

$$\vdots$$

$$Y_0(s)=y_0(s), k-d_1+1\le s\le k. \tag{7}$$

Obviously, $Y_0(s)$, $Y_1(s)$,…, $Y_{l-1}(s)$ satisfy

$$Y_i(s)=H_i x(s)+V_i(s), i=0,1,2,\ldots,l-1, \tag{8}$$

where $H_i=diag\{\xi_0(s),\xi_1(s+d_1),\ldots,\xi_i(s+d_i)\}\bar{B}_i$, and

$$\bar{B}_i=\left[B_0^T,B_1^T,\ldots,B_i^T\right]^T,\ V_i(s)=\left[v_0^T(s),v_1^T(s+d_1),\ldots,v_i^T(s+d_i)\right]^T.$$

Obviously the new measurements $Y_0(s)$, $Y_1(s),\ldots,Y_i(s)$ are delay-free and the associated measurement noises $V_0(s)$, $V_1(s),\ldots,V_i(s)$ are white noises with zero mean and covariance matrices $R_{V_0(s)}=R_0$, $R_{V_1(s)}=diag\{R_0,R_1\},\ldots,R_{V_i(s)}=diag\{R_0,R_1,\ldots,R_i\}$. The filter $\hat{x}(k\mid k)$ is the projection of $x(k)$ onto the linear space of

$$\mathcal{L}\left\{\{Y_{l-1}(s)\}_{s=0}^{k-d_{l-1}},\ldots,\{Y_i(s)\}_{s=k-d_{i+1}+1}^{k-d_i},\ldots,\{Y_0(s)\}_{s=k-d_1+1}^{k}\right\}.$$

In order to compute the projection, we define the innovation sequence as follows:

$$\varepsilon(s,i)=Y_i(s)-\hat{Y}(s,i), i=0,1,2,\ldots,l-1, \tag{9}$$

where $\hat{Y}(s,i)$ is the projection of $Y_i(s)$ onto the linear space of

$$\mathcal{L}\left\{\{Y_{l-1}(m)\}_{m=0}^{k-d_{l-1}},\ldots,\{Y_i(m)\}_{m=k-d_{i+1}+1}^{s-1}\right\}.$$

From (8)–(9), the innovation sequence is given as follows

$$\begin{aligned}\varepsilon(s,i)=&diag\{\xi_0(s)-\phi_0,\ldots,\xi_i(s)-\phi_i\}\bar{B}_i x(s)\\&+diag\{\phi_0,\phi_1,\ldots,\phi_i\}\bar{B}_i\tilde{x}(s,i)+V_i(s),\end{aligned} \tag{10}$$

here $\phi_i = diag\{\alpha_{i1}, \alpha_{i2}, \ldots, \alpha_{im_i}\}$, $\tilde{x}(s,i) = x(s) - \hat{x}(s,i)$, the definition of $\hat{x}(s,i)$ is same to $\hat{Y}(s,i)$. We know that white noises $\varepsilon(s,0)$, $\varepsilon(s,1), \ldots, \varepsilon(s,l-1)$ are independent. Conveniently, we define that

$$\begin{aligned} P_i(s) &= E\{\tilde{x}(s,i)\tilde{x}^T(s,i)\}, \\ D(s) &= E\{x(s)x^T(s)\}. \end{aligned}$$

Based on (10) and Lemma 1, the recognized innovation covariance matrices are calculated by

$$\begin{aligned} R_{\varepsilon(s,i)} &= E\{diag\{\xi_0(s) - \phi_0, \ldots, \xi_i(s) - \phi_i\}\bar{B}_i x(s)x^T(s)\bar{B}_i{}^T \\ &\quad diag\{\xi_0(s) - \phi_0, \ldots, \xi_i(s) - \phi_i\} \\ &\quad + diag\{\phi_0, \phi_1, \ldots, \phi_i\}\bar{B}_i\tilde{x}(s,i)\tilde{x}^T(s,i)\bar{B}_i^T \\ &\quad diag\{\phi_0, \phi_1, \ldots \phi_i\}\} + diag\{R_0, R_1, \ldots, R_i\} \\ &= diag\{\phi_0, \phi_1, \ldots, \phi_i\}\bar{B}_i P_i(s)\bar{B}_i^T diag\{\phi_0, \phi_1, \ldots, \phi_i\} \\ &\quad + diag\{R_0, R_1, \ldots, R_i\} \\ &\quad + diag\{\Pi_0, \Pi_1, \ldots, \Pi_i\} \odot \left(\bar{B}_i D(s)\bar{B}_i^T\right), \end{aligned} \tag{11}$$

where

$$\Pi_i = \begin{bmatrix} \alpha_{i1}(1-\alpha_{i1}) & 0 & \cdots & 0 \\ 0 & \alpha_{i2}(1-\alpha_{i2}) & \cdots & 0 \\ \vdots & \vdots & \ddots & \vdots \\ 0 & 0 & \cdots & \alpha_{im_i}(1-\alpha_{im_i}) \end{bmatrix}.$$

Now, we deduce the covariance matrices of one-step ahead state estimation error using the lemma as follows.

Lemma 2 *The covariance matrices $P_i(s+1)$ submits to the Riccati difference equations following,*

$$\begin{aligned} P_i(s+1) &= AP_i(s)A^T + Q - AP_i(s)\bar{B}_i^T diag\{\phi_0, \phi_1, \ldots, \phi_i\} \\ &\quad R_{\varepsilon(s,i)}^{-1} diag\{\phi_0, \phi_1, \ldots, \phi_i\}\bar{B}_i P_i(s)A^T, \end{aligned} \tag{12}$$

$$P_{l-1}(0) = D(0), \tag{13}$$

$$P_i(k - d_i + 1) = P_{i-1}(k - d_i + 1), \tag{14}$$

where $R_{\varepsilon(s,i)}$ is the one in (11), and $D(s+1)$ can be calculated using

$$D(s+1) = AD(s)A^T + Q \tag{15}$$

with initial value $D(0)$.

Proof According to (1), it is readily to yield (15). On the basis of projection formula, $\hat{x}(s+1,i)$ is calculated

$$\begin{aligned}\hat{x}(s+1,i) &= proj\{x(s+1) \mid \{\varepsilon(m,l-1)\}_{m=0}^{k-d_{l-1}}, \ldots, \{\varepsilon(m,i)\}_{m=k-d_{i+1}+1}^{s}\} \\ &= A\hat{x}(s,i) + E\{x(s+1)\varepsilon^T(s,i)\}R_{\varepsilon(s,i)}^{-1}\varepsilon(s,i) \\ &= A\hat{x}(s,i) + K_P(s,i)\varepsilon(s,i), \end{aligned} \tag{16}$$

here $K_P(s,i) = AP_i(s)\bar{B}_i^T diag\{\phi_0, \phi_1, \ldots, \phi_i\}R_{\varepsilon(s,i)}^{-1}$. From (1) and (16), one has that

$$\tilde{x}(s+1,i) = A\tilde{x}(s,i) + n(s) - K_P(s,i)\varepsilon(s,i). \tag{17}$$

Therefore, the prediction error covariance is obtained by

$$\begin{aligned}P_i(s+1) &= E\{\tilde{x}(s+1,i)\tilde{x}^T(s+1,i)\} \\ &= AP_i(s)A^T + Q - AP_i(s)\bar{B}_i^T diag\{\phi_0, \phi_1, \ldots, \phi_i\}R_{\varepsilon(s,i)}^{-1} \\ &\quad diag\{\phi_0, \phi_1, \ldots, \phi_i\}\bar{B}_i P_i(s)A^T, \end{aligned}$$

which is (12). On the basis of the definitions of $\hat{x}(k-d_i+1,i)$, we have $\hat{x}(k-d_i+1,i) = \hat{x}(k-d_i+1,i+1)$. The proof is accomplished. ∇

Now, we introduce the filter according to the projection formula in Hilbert space.

Theorem 1 *In view of the system (1)–(2), the filter $\hat{x}(k \mid k)$ can be computed by*

$$\hat{x}(k \mid k) = \hat{x}(k,0) + P_0(k)B_0^T\phi_0 R_{\varepsilon(k,0)}^{-1}\varepsilon(k,0), \tag{18}$$

where, we calculate the estimation $\hat{x}(k,0)$ by

$$\hat{x}(s+1,0) = A\hat{x}(s,0) + K_P(s,0)\varepsilon(s,0) \tag{19}$$

with initial value $\hat{x}(k-d_1+1,0) = \hat{x}(k-d_1+1,1)$. $\hat{x}(k-d_1+1,i)$ is gained by

$$\hat{x}(s+1,i) = A\hat{x}(s,i) + K_P(s,i)\varepsilon(s,i) \tag{20}$$

with $\hat{x}(k-d_i+1,i) = \hat{x}(k-d_i+1,i+1)$. And one calculates $\hat{x}(k-d_{l-1}+1,l-1)$ by

$$\hat{x}(s+1,l-1) = A\hat{x}(s,l-1) + K_P(s,l-1)\varepsilon(s,l-1) \tag{21}$$

with initial value $\hat{x}(0,l-1) = 0$.

Proof Because $\hat{x}(k \mid k)$ is the projection of $x(k)$ onto the linear space of

$$\mathcal{L}\left\{\{\varepsilon(s,l-1)\}_{s=0}^{k-d_{l-1}}, \ldots, \{\varepsilon(s,i)\}_{s=k-d_{i+1}+1}^{k-d_i}, \ldots, \{\varepsilon(s,0)\}_{s=k-d_1+1}^{k}\right\},$$

according to the projection theory, one has

$$\begin{aligned}\hat{x}(k \mid k) &= proj\{x(k) \mid \{\varepsilon(s, l-1)\}_{s=0}^{k-d_{l-1}}, \ldots, \{\varepsilon(s,i)\}_{s=k-d_{i+1}+1}^{k-d_i}, \ldots, \\ &\quad \{\varepsilon(s,0)\}_{s=k-d_1+1}^{k}\} \\ &= \hat{x}(k,0) + P_0(k)B_0^T\phi_0 R_{\varepsilon(k,0)}^{-1}\varepsilon(k,0), \end{aligned} \tag{22}$$

therefore, (18) is proved. The proof of (19) and (20) can be yielded from (16). The proof is finished. ∇

Remark 3 Applying the reorganized innovation approach, we have deduced the optimal filter by calculating Riccati equations (12) and one Lyapunov equation (15) of $\mathbf{n} \times \mathbf{n}$ dimension. On the other hand, if we let

$$X(k) = \left[x^T(k), x^T(k-d_1), \ldots, x^T(k-d_{l-1})\right]^T_{(\mathbf{d_{l-1}+1})\mathbf{n}\times\mathbf{1}},$$

the delayed measurement equation (2) can be converted into a delay-free equation. Further, the LMMSE estimator can be designed in terms of one Lyapunov equation and one Riccati equation of $(\mathbf{d_{l-1}} + \mathbf{1})\mathbf{n} \times (\mathbf{d_{l-1}} + \mathbf{1})\mathbf{n}$ dimension. Hence the high dimension Riccati equation related to the augmentation approach is avoided.

3.2 Design of the Optimal White Noise Estimator

We can export the optimal white-noise estimator $\hat{n}(s \mid s+T)$ according to the innovation sequences $\varepsilon(0), \varepsilon(1), \ldots, \varepsilon(s+T)$. When $T \leq 0$, it can be observed that $n(s)$ is independent of $\varepsilon(0), \varepsilon(1), \ldots, \varepsilon(s+T)$. Then the estimator $\hat{n}(s \mid s+T)$ is 0. When $N > 0$, the optimal input white-noise smoother $\hat{n}(s \mid s+T)$ is defined following

$$\hat{n}(s \mid s+T) = \hat{n}(s \mid s+T-1) + E\{n(s)\varepsilon^T(s+T,i)\}R_{\varepsilon(s+T,i)}^{-1}\varepsilon(s+T,i), \tag{23}$$

where $E\{n(s)\varepsilon^T(s+T,i)\}R_{\varepsilon(s+T,i)}^{-1}$ is to be determined, such that

$$E\{[n(s) - \hat{n}(s \mid s+T)][n(s) - \hat{n}(s \mid s+T)]^T\}$$

is minimized. On the basis of the projection formula, we can calculate the optimal recursive input white-noise smoother $\hat{n}(s \mid s+T)$.

Theorem 2 *Consider the system (1)–(2), the optimal recursive input white-noise smoother is given following*

$$\hat{n}(s \mid s+T) = \hat{n}(s \mid s+T-1) + M_n(s+T,i)\varepsilon(s+T,i), T = 1, 2 \ldots, \tag{24}$$

the initial value $\hat{n}(s \mid s) = 0$*, and the smoother gain* $M_n(s+T)$ *satisfies the equation as follows*

$$\begin{aligned} M_n(s+1,i) &= Q\bar{B}_i^T diag\{\phi_0, \phi_1, \ldots, \phi_i\} R_{\varepsilon(s+1,i)}^{-1}, \\ M_n(s+T,i) &= Q\prod_{l=1}^{T-1}\{\Psi_p^T(s+l,i)\}\bar{B}_i^T diag\{\phi_0, \phi_1, \ldots, \phi_i\} R_{\varepsilon(s+T,i)}^{-1}, T>1 \\ \Psi_p(s,i) &= A - K_p(s,i) diag\{\phi_0, \phi_1, \ldots, \phi_i\}\bar{B}_i. \end{aligned}$$

The covariance matrix $P_n(s+T)$ *is derived following*

$$P_n(s+T) = P_n(s+T-1) + M_n(s+T,i) R_{\varepsilon(s+T,i)} M_n^T(s+T,i) \tag{25}$$

with initial value $P_n(s) = 0$.

Proof Using the projection formula, one obtains

$$\begin{aligned} \hat{n}(s \mid s+T) = \hat{n}(s \mid s+T-1) \\ + E\{n(s)\varepsilon^T(s+T,i)\} R_{\varepsilon(s+T,i)}^{-1} \varepsilon(s+T,i) \end{aligned} \tag{26}$$

where $E\{n(s)\varepsilon^T(s+T,i)\} R_{\varepsilon(s+T,i)}^{-1}$ is determined. We know that

$$\begin{aligned} \varepsilon(s+T,i) &= Y_i(s+T) - \hat{Y}_i(s+T) \\ &= diag\{\xi_0(s+T) - \phi_0, \ldots, \xi_i(s+T) - \phi_i\}\bar{B}_i x(s+T) \\ &\quad + diag\{\phi_0, \phi_1, \ldots, \phi_i\}\bar{B}_i \tilde{x}(s+T,i) + V_i(s+T) \end{aligned} \tag{27}$$

$$\begin{aligned} \tilde{x}(s+1,i) &= x(s+1,i) - \hat{x}(s+1,i) \\ &= A\tilde{x}(s,i) + n(s) - K_p(s,i)\varepsilon(s,i) \\ &= \Psi_p(s,i)\tilde{x}(s,i) + n(s) \\ &\quad - K_p(s,i)[diag\{\xi_0(s) - \phi_0, \ldots, \xi_i(s) - \phi_i\}\bar{B}_i x(s) \\ &\quad + V_i(s)] \end{aligned} \tag{28}$$

here, $\Psi_p(s,i) = A - K_p(s,i) diag\{\phi_0, \phi_1, \ldots, \phi_i\}\bar{B}_i$. From (28), $\tilde{x}(s+T,i)$ is derived as follows

$$\begin{aligned} \tilde{x}(s+T,i) = \Psi_i(s+T,s)\tilde{x}(s,i) + \sum_{l=s+1}^{s+T} \Psi_i(s+T,l)[n(l-1) \\ - K_p(l-1,i)(diag\{\xi_0(l-1) - \phi_0, \ldots, \xi_i(l-1) - \phi_i\} \\ \bar{B}_i x(l-1) + V_i(l-1))], T>1, \end{aligned} \tag{29}$$

where,

$$\Psi_i(s+T,s+T) = I,$$
$$\Psi_i(s+T,l) = \Psi_p(s+T-1,i)\ldots\Psi_p(l,i), l < s+T.$$

Putting (28), (29) into (27), one has

$$\begin{aligned}\varepsilon(s+1,i) = {} & diag\{\phi_0,\phi_1,\ldots,\phi_i\}\bar{B}_i\{\Psi_p(s,i)\tilde{x}(s,i)+n(s)\\ & -K_p(s,i)[diag\{\xi_0(s)-\phi_0,\ldots,\xi_i(s)-\phi_i\}\bar{B}_i x(s)\\ & +V_i(s)]\}+V_i(s+1)\\ & +diag\{\xi_0(s+1)-\phi_0,\ldots,\xi_i(s+1)-\phi_i\}\bar{B}_i x(s+1),\\ \varepsilon(s+T,i) = {} & diag\{\phi_0,\phi_1,\ldots,\phi_i\}\bar{B}_i\{\Psi_i(s+T,s)\tilde{x}(s,i)+\sum_{l=s+1}^{s+T}\Psi_i(s+T,l)\\ & [n(l-1)-K_p(l-1,i)(diag\{\xi_0(l-1)-\phi_0,\ldots,\xi_i(l-1)-\phi_i\}\\ & \bar{B}_i x(l-1)+V_i(l-1))]\}+V_i(s+T)+diag\{\xi_0(s+T)-\phi_0,\ldots,\\ & \xi_i(s+T)-\phi_i\}\bar{B}_i x(s+T), T>1.\end{aligned}$$

From above equations, it is readily to obtain

$$\begin{aligned}E\{n(s)\varepsilon^T(s+1,i)\} &= Q\bar{B}_i^T diag\{\phi_0,\phi_1,\ldots,\phi_i\},\\ E\{n(s)\varepsilon^T(s+T,i)\} &= Q\prod_{l=1}^{T-1}\{\Psi_p^T(s+l,i)\}\bar{B}_i^T diag\{\phi_0,\phi_1,\ldots,\phi_i\}, T>1.\end{aligned}$$

Considering that $R_{\varepsilon(s+T,i)}$ is invertible, we define

$$\begin{aligned}M_n(s+1,i) &= Q\bar{B}_i^T diag\{\phi_0,\phi_1,\ldots,\phi_i\}R^{-1}_{\varepsilon(s+1,i)},\\ M_n(s+T,i) &= Q\prod_{l=1}^{T-1}\{\Psi_p^T(s+l,i)\}\bar{B}_i^T diag\{\phi_0,\phi_1,\ldots,\phi_i\}R^{-1}_{\varepsilon(s+T,i)}, T>1.\end{aligned}$$

Next, we begin to derive the expression of $P_n(s+T)$. According to (24), $\tilde{n}(s \mid s+T)$ is gained by

$$\tilde{n}(s \mid s+T) = \tilde{n}(s \mid s+T-1) - M_n(s+T,i)\varepsilon(s+T,i), \tag{30}$$

so one gets (25). The proof is finished. ∇

Remark 4 According to projection formula and the optimal state estimator in Theorem 1, one can gain the smoother in Theorem 2 directly. What has we finished in this paper is the state estimator and white noise estimator for finite horizon, while the

related work for infinite horizon has not been finished. In the future, we will solve the problems about state estimator and white noise estimator for infinite horizon under the condition that A is a stable matrix.

4 Numerical Example

Consider the following linear measurement-delay systems

$$x(k+1) = \begin{bmatrix} 0.2 & 0.12 \\ 0.4 & 0.18 \end{bmatrix} x(k) + n(k), \tag{31}$$

$$y_0(k) = \xi_0(k) \begin{bmatrix} 1 & 1.5 \\ 2 & 1 \end{bmatrix} x(k) + v_0(k), \tag{32}$$

$$y_1(k) = \xi_1(k) \begin{bmatrix} 1.2 & 1.4 \\ 2.3 & 1.8 \end{bmatrix} x(k-d) + v_1(k), \tag{33}$$

with $x(0) = \begin{bmatrix} -1 \\ 1 \end{bmatrix}$, $\hat{x}(0,1) = \begin{bmatrix} 0 \\ 0 \end{bmatrix}$, $D(0) = P(0) = \begin{bmatrix} 1 & -1 \\ -1 & 1 \end{bmatrix}$, $\phi_0 = diag\{0.85, 0.73\}$, $\phi_1 = diag\{0.79, 0.89\}$, $R_0 = R_1 = I_{2\times 2}$, $Q = \begin{bmatrix} 1 & 1 \\ 1 & 1 \end{bmatrix}$. $n(k)$, $v_0(k)$ and $v_1(k)$ are white noises with zero mean and covariances Q, R_0 and R_1, respectively. We adopt d = 15, N = 100 in this simulation.

Primarily, according to Theorem 1, we give the simulation results in Figs. 1 and 2, where we can observe that the filter with additional measurement-delay channel

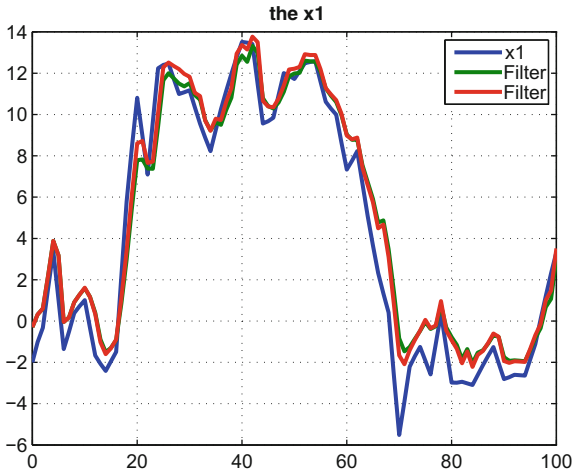

Fig. 1 The first state component $x_1(k)$ and the filter $\hat{x}(k \mid k)$

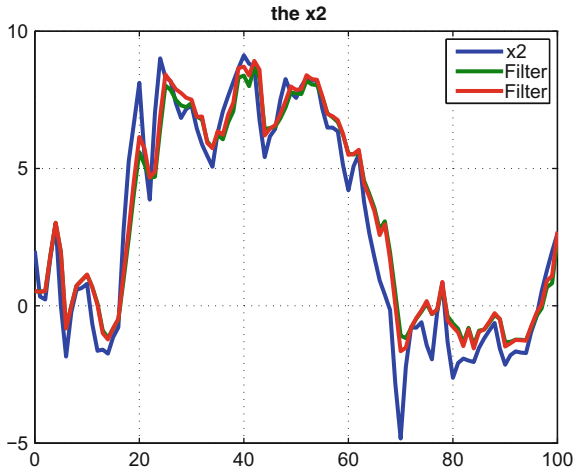

Fig. 2 The second state component $x_2(k)$ and the filter $\hat{x}(k \mid k)$

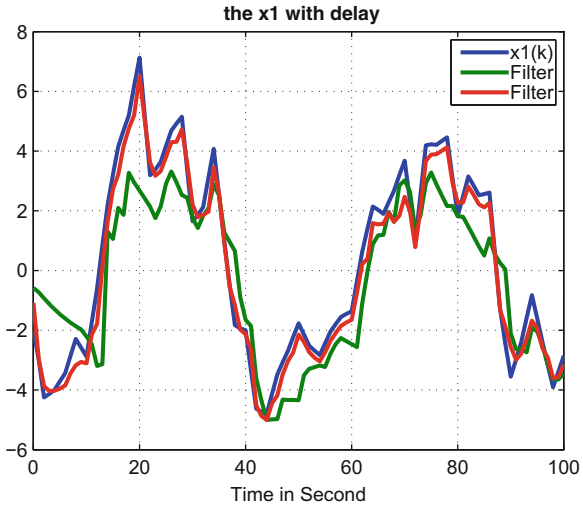

Fig. 3 The first state component $x_1(k)$ and the filter $\hat{x}(k \mid k)$

represented by red line tracks the true state $x(k)$ better than the filter without measurement-delay channel shown by green line. It suggests that the information coming from the measurement-delay channel is also important.

Then, we consider the influence of different packet dropping rate case,

$$\begin{aligned} &Case\ 1: \phi_0 = diag\{0.45, 0.43\}, \phi_1 = diag\{0.37, 0.5\}, \\ &Case\ 2: \phi_0 = diag\{0.83, 0.75\}, \phi_1 = diag\{0.78, 0.9\}. \end{aligned}$$

The results are appeared in Figs. 3 and 4, where the filter for case 1 is represented by green line and the filter for case 2 is shown by the red line. It is shown in Figs. 3

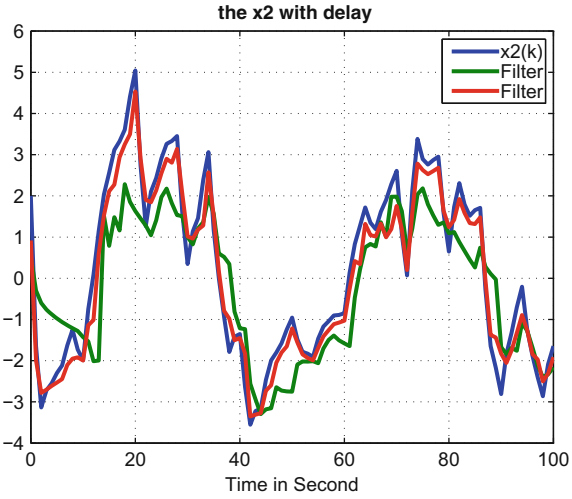

Fig. 4 The second state component $x_2(k)$ and the filter $\hat{x}(k \mid k)$

and 4 that the filter for case 2 tracks the true state better. The reason is that the filter in case 2 is gained with more information than the filter in case 1.

5 Conclusion

In this paper, we have investigated the LMMSE state estimation and noise estimation for discrete-time system with time delay and random packet loss, which is modeled by an independent and identically distributed Bernoulli process. First, the optimal state estimator has been designed by using the reorganized innovation analysis approach. The solution to state estimator has been provided by calculating l Riccati difference equations and one Lyapunov difference equation. Next, an optimal input white-noise estimation has been put forward based on innovation analysis approach and state estimation mentioned above. Finally, a numerical example has been offered to show the effectiveness of the proposed approach. These works about the state estimator and noise estimator are only for finite horizon. In the future, we will solve problems about the state estimator and noise estimator for infinite horizon under the condition that A is a stable matrix.

Acknowledgments This work is supported in part by the Shandong Provincial Key Laboratory for Novel Distributed Computer Software Technology, the Excellent Young Scholars Research Fund of Shandong Normal University, and the National Natural Science Foundation of China (61304013).

References

1. Sadreazami H, Ahmad MO, Swamy MNS (2015) A robust multiplicative watermark detector for color images in sparse domain. IEEE Trans Circuits Syst II: Express Briefs 62(12):1159–1163
2. Mendel JM (1977) White-noise estimators for seismic date processing in oil exploration. IEEE Trans Autom Control 22(5):694–706
3. Mendel JM (1981) Minimun variance deconvolution. IEEE Trans Geosci Remote Sens 19(3):161–171
4. Deng Z, Zhang H, Liu S, Zhou L (1996) Optimal and self-tuning white noise estimators with application to deconvolution and filtering problem. Automatica 32(2):199–216
5. Xiao L, Hassibi A, How JP (2000) Control with random communication delays via a discrete-time jump system approach. In: Proceedings of the American Control Conference, pp 2199–2204
6. Wu X, Song X, Yan X (2015) Optimal estimation problem for discrete-time systems with multi-channel multiplicative noise. Int J Innov Comput Inf Control 11(6):1881–1895
7. Song IY, Kim DY, Shin V, Jeon M (2012) Receding horizon filtering for discrete-time linear systems with state and observation delays. IET Radar Sonar Navig 6(4):263–271
8. Nahi NE (1969) Optimal recursive estimation with uncertain observation. IEEE Trans Inf Theory 15(4):457–462
9. Sinopoli B, Schenato L, Franceschetti M, Poolla K, Jordan M, Sastry S (2004) Kalman filtering with intermittent observations. IEEE Trans Autom Control 49(9):1453–1464
10. Liu X, Goldmith A (2004) Kalman filtering with partial observation losses. In: Proceeding of the 43rd IEEE Conference on Decision and Control, pp 4180–4186
11. Gao S, Chen P (2014) Suboptimal filtering of networked discrete-time systems with random observation losses. In: Mathematical Problems in Engineering
12. Zhang H, Song X, Shi L (2012) Convergence and mean square stability of suboptimal estimator for systems with measurement packet dropping. IEEE Trans Autom Control 57(5):1248–1253
13. Han C, Wang W (2013) Deconvolution estimation of systems with packet dropouts. In: Proceeding of the 25th Chinese Control and Decision Conference, pp 4588–4593
14. Sun S (2013) Optimal linear filters for discrete-time systems with randomly delayed and lost measurements with/without time stamps. IEEE Trans Autom Control 58(6):1551–1556
15. Wang S, Fang H, Tian X (2015) Recusive estimation for nonlinear stochastic systems with multi-step transmission delay, multiple packet droppouts and correlated noises. Signal Process 115:164–175
16. Feng J, Wang T, Guo J (2014) Recursive estimation for descriptor systems with multiple packet dropouts and correlated noises. Aerosp Sci Technol 32(1):200–211
17. Li F, Zhou J, Wu D (2013) Optimal filtering for systems with finite-step autocorrelated noises and multiple packet dropouts. Aerosp Sci Technol 24(1):255–263
18. Horn RA, Johnson CR (1991) Topic in Matrix Analysis. Cambridge University Press, New York
19. Zhang H, Xie L, Zhang D, Soh YC (2004) A reorganized innovation approach to linear estimation. IEEE Trans Autom Control 49(10):1810–1814

Adaptive Dynamic Surface Control for Dual-Motor Driving System with H∞ Performance

Minlin Wang and Xuemei Ren

Abstract In this paper, a novel adaptive tracking control method is proposed for the dual-motor driving system (DDS) with parameter uncertainties and external disturbances. The DDS is a multi-variable, nonlinear and strong-coupling system which increases the difficulty of the controller design. To handle this problem, a set of alternative state variables is introduced to transform the DDS into a strict feedback form. Based on the transformed system, an adaptive controller is constructed by integrating the H ∞ technique into the dynamic surface control to guarantee that the output tracking error satisfies the H ∞ performance. More importantly, the designed controller cannot only attenuate the influences of external disturbances on the system output, but also have a strong robustness for system parameter variations. Simulation results are conducted to validate the effectiveness of the proposed method.

Keywords Dual-motor driving system · Adaptive control · H ∞ performance · Dynamic surface control

1 Introduction

With the development of technology, servo system has been widely used in the industry and military, which usually employs one motor to drive the load. However, for the large inertia and power servo system, signal-motor driving system cannot meet the requirement of the driving force and power. Thus, the control method for the dual-motor driving system has drawn a wide attention and successfully applied in the radar antenna system [1] and the artillery control system [2]. The difficulties existing in this control system are the parameter uncertainties and the external disturbances which may degrade the control performance of DDS [3]. To overcome these difficulties, many robust control techniques have been proposed. Li [4]

M. Wang · X. Ren (✉)
School of Automation, Beijing Institute of Technology, Beijing 100081, China
e-mail: xmren@bit.edu.cn

Y. Jia et al. (eds.), *Proceedings of 2016 Chinese Intelligent Systems Conference*,
Lecture Notes in Electrical Engineering 404, DOI 10.1007/978-981-10-2338-5_33

presented a robust adaptive sliding mode control scheme for a class of uncertain nonlinear systems with fast transient performance. Guan [5] proposed a nonlinear adaptive robust control method for a single-rod electro-hydraulic actuator with unknown nonlinear parameters. In order to obtain a high control performance of a turntable servo system, Zhang [6] developed an adaptive robust controller based on the dynamic surface control approach. Although the above approaches can guarantee the boundedness of the tracking error by Lyapunov theory, the effect of the external disturbances is rarely analyzed.

To attenuate the effect of the external disturbances on the system output, Sun [7] firstly integrated the H ∞ control into the backstepping controller design. This method can not only achieve the asymptotic stability of tracking error but also make the system satisfy the H ∞ performance. However, the backstepping algorithm needs repetitive differentiations for the nonlinear components of the model, which will significantly increase the complexity of the controller design due to the "differential explosion". To deal with this drawback, this paper presents an adaptive controller which combines the dynamic surface control with the H ∞ technique. The external disturbances considered here do not conform to the unmatched conditions, which are suppressed by introducing another feedback term into the controller design. Thus, the H ∞ tracking performance and robust stability can be achieved for the control system based on the Lyapunov stability theorem.

2 Dynamic Model of a Dual-Motor Driving System

Without losing generality, the mechanical dynamics of dual-motor driving system [3] can be described by

$$\begin{cases} J_i\ddot{\theta}_i + b_i\dot{\theta}_i + T_i = u_i \\ J_m\ddot{\theta}_m + b_m\dot{\theta}_m = \sum_{i=1}^{2} T_i \end{cases}, \tag{1}$$

where θ_i, $\theta_m (i = 1, 2)$ are the motor angular position and the load angular position, J_i, J_m represent the motor inertia and the load inertia, b_i, b_m represent the motor viscous friction coefficient and the load viscous friction coefficient, u_i is the control input, T_i denotes the transmission torque between the motor and the load.

The backlash nonlinearity considered here uses the dead-zone model expressed as

$$T_i = kf(z_i(t)) = \begin{cases} k(z_i(t) - \alpha) & z_i(t) \geq \alpha \\ 0 & |z_i(t)| < \alpha \\ k(z_i(t) + \alpha) & z_i(t) \leq -\alpha \end{cases}, \tag{2}$$

where $z_i(t) = \theta_i - \theta_m, k > 0$ is the stiffness coefficient and $2\alpha > 0$ is the backlash width parameter. Then, $f(z_i(t))$ in Eq. (2) can be rewritten as:

$$f(z_i(t)) = z_i(t) + d_\alpha(z_i(t)), \tag{3}$$

$$\text{where} \quad d_\alpha(z_i(t)) = \begin{cases} -\alpha & z_i(t) \geq \alpha \\ -z_i(t) & |z_i(t)| < \alpha \\ \alpha & z_i(t) \leq -\alpha \end{cases}. \tag{4}$$

Define the load angular position, load angular velocity, motor angular position and motor angular velocity as the state variables, i.e., $[x_1, x_2, x_{3i}, x_{4i}]^T = [\theta_m, \theta_m, \theta_i, \theta_i]^T$, the DDS can be expressed in a state space form as

$$\begin{cases} \dot{x}_1 = x_2 + d_1(t) \\ \dot{x}_2 = -\frac{b_m}{J_m} x_2 + \frac{k}{J_m} \sum_{i=1}^{2} (x_{3i} - x_1) + \frac{k}{J_m} \sum_{i=1}^{2} d_\alpha(z_i) + d_2(t) \\ \dot{x}_{3i} = x_{4i} + d_{3i}(t) \\ \dot{x}_{4i} = \frac{1}{J_i} u_i - \frac{b_i}{J_i} x_{4i} - \frac{k}{J_i} (x_{3i} - x_1) - \frac{k}{J_i} d_\alpha(z_i) + d_{4i}(t) \\ y = x_1 \end{cases}, \tag{5}$$

where $d_1(t), d_2(t), d_{3i}(t), d_{4i}(t) \in L_2$ are the external disturbances.

Since all the motors in DDS are the same, we can assume that $J = J_1 = J_2, b = b_1 = b_2$. By defining the state variables as $x_3 = \sum_{i=1}^{2} x_{3i}$, $x_4 = \sum_{i=1}^{2} x_{4i}$ and the control $u = \sum_{i=1}^{2} u_i$, we rewrite the system (5) in a strict feedback form as

$$\begin{cases} \dot{x}_1 = x_2 + d_1 \\ \dot{x}_2 = x_3 + f_1 + d_2 \\ \dot{x}_3 = x_4 + d_3 \\ \dot{x}_4 = J^{-1} u + f_2 + d_4 \\ y = x_1 \end{cases}, \tag{6}$$

where $f_1 = w_1^T \phi_1 = \left[-\frac{k}{J_m} \quad -\frac{b_m}{J_m} \quad (\frac{k}{J_m} - 1) \right] \left[2x_1 - \sum_{i=1}^{2} d_\alpha(z_i) \quad x_2 \quad x_3 \right]^T$, $f_2 = w_2^T \phi_2 = \left[-\frac{k}{J} \quad -\frac{b}{J} \right] \left[x_3 + \sum_{i=1}^{2} d_\alpha(z_i) - 2x_1 \quad x_4 \right]^T$, $d_3 = \sum_{i=1}^{2} d_{3i}$ and $d_4 = \sum_{i=1}^{2} d_{4i}$.

The control objective of this paper can be stated as: for any given $\gamma > 0$, find an adaptive controller u and positive storage function V such that the following dissipativity inequality holds for any final time $T > 0$:

$$V(T) - V(0) \leq \int_0^T (\gamma^2 \|d\|^2 - \|e_1\|^2) dt, \tag{7}$$

where $e_1 = y - y_d$, d is external disturbance given in the latter and the L_2 gain from the disturbance to the output of the system is smaller than or equal to γ, where γ is a disturbance attenuation constant.

3 Adaptive Controller Design

As mentioned before, the control objective of this section is to design an adaptive tracking controller with a prescribed H ∞ performance (7). For system (6), the surface error is defined as

$$e_i = x_i - \alpha_{i-1}, \quad (i = 1, 2, 3, 4) \tag{8}$$

where $\alpha_0 = y_d$ is the reference trajectory and $\alpha_1, \alpha_2, \alpha_3$ are the virtual control inputs which will be given later on by the first order filter.

Define the boundary layer error as

$$y_j = \alpha_j - \alpha_j^*, \quad (j = 1, 2, 3) \tag{9}$$

where α_j^* is the stabilizing function which will also be designed later on. The design procedure for the adaptive dynamic surface controller is derived below.

Step1: According to the system (6), the derivative of the tracking error e_1 is obtained as

$$\dot{e}_1 = x_2 + d_1 - \dot{y}_d. \tag{10}$$

Consider the first Lyapunov function as

$$V_1 = \frac{1}{2} e_1^2, \tag{11}$$

then its derivative along the solution (10) is

$$\begin{aligned} \dot{V}_1 &= e_1(x_2 + d_1 - \dot{y}_d) \\ &= e_1(e_2 + y_1 + \alpha_1^* + d_1 - \dot{y}_d). \end{aligned} \tag{12}$$

To make (12) negative definite, α_1^* is selected as

$$\alpha_1^* = -c_1 e_1 - \frac{e_1}{(2\gamma_1)^2} + \dot{y}_d, \tag{13}$$

where $c_1 > 0$ and $\gamma_1 > 0$ are designed constants. Substituting (13) into (12) yields

$$\begin{aligned}\dot{V}_1 &= e_1(e_2 + y_1 - c_1 e_1 - \frac{e_1}{(2\gamma_1)^2} + d_1) \\ &= -c_1 e_1^2 + e_1(e_2 + y_1) - \frac{e_1^2}{(2\gamma_1)^2} + d_1 e_1 \\ &\le -c_1 e_1^2 + e_1(e_2 + y_1) + \gamma_1^2 d_1^2.\end{aligned} \tag{14}$$

Step2: Let α_1^* pass through a first-order filter as follows:

$$T_1\dot{\alpha}_1 + \alpha_1 = \alpha_1^*, \alpha_1(0) = \alpha_1^*(0), \tag{15}$$

where T_1 is a time constant. The second Lyapunov candidate is chosen as

$$V_2 = V_1 + \frac{1}{2}e_2^2 + \frac{1}{2}y_1^2 + \frac{1}{2}\tilde{w}_1^T \mathrm{P}_1^{-1}\tilde{w}_1, \tag{16}$$

where $P_1 > 0$ is the diagonal constant matrix and $\tilde{w}_1 = w_1 - \hat{w}_1$ is the estimated error vector, then its derivative is computed as

$$\begin{aligned}\dot{V}_2 &= \dot{V}_1 + e_2\dot{e}_2 + y_1\dot{y}_1 - \tilde{w}_1^T \mathrm{P}_1^{-1}\dot{\hat{w}}_1 \\ &= \dot{V}_1 + e_2(x_3 + f_1 + d_2 - \dot{\alpha}_1) + y_1\dot{y}_1 - \tilde{w}_1^T \mathrm{P}_1^{-1}\dot{\hat{w}}_1 \\ &= \dot{V}_1 + e_2\left(e_3 + y_2 + \alpha_2^* + w_1^T\phi_1 + d_2 - \dot{\alpha}_1\right) + y_1\dot{y}_1 - \tilde{w}_1^T \mathrm{P}_1^{-1}\dot{\hat{w}}_1.\end{aligned} \tag{17}$$

If we choose the stabilizing function and the adaptive law as

$$\alpha_2^* = -c_2 e_2 - \frac{e_2}{(2\gamma_2)^2} - \hat{w}_1^T\phi_1 + \dot{\alpha}_1, \tag{18}$$

$$\dot{\hat{w}}_1 = P_1 e_2 \phi_1, \tag{19}$$

where $c_2 > 0$ and $\gamma_2 > 0$ are designed constants, (17) can be rewritten as

$$\begin{aligned}\dot{V}_2 &= \dot{V}_1 + e_2(e_3 + y_2) - c_2 e_2^2 - \frac{e_2^2}{(2\gamma_2)^2} + d_2 e_2 - \frac{y_1^2}{T_1} - y_1\dot{\alpha}_1^* \\ &\le -c_1 e_1^2 - c_2 e_2^2 + e_1(e_2 + y_1) + e_2(e_3 + y_2) \\ &\quad + \gamma_1^2 d_1^2 + \gamma_2^2 d_2^2 - \frac{y_1^2}{T_1} - y_1\dot{\alpha}_1^*.\end{aligned} \tag{20}$$

Step3: Let α_2^* pass through another first-order filter as follows:

$$T_2\dot{\alpha}_2+\alpha_2=\alpha_2^*,\alpha_2(0)=\alpha_2^*(0), \tag{21}$$

where T_2 is a time constant. The third Lyapunov candidate is chosen as

$$V_3=V_2+\frac{1}{2}e_3^2+\frac{1}{2}y_2^2, \tag{22}$$

whose derivative is shown as

$$\begin{aligned}\dot{V}_3&=\dot{V}_2+e_3\dot{e}_3+y_2\dot{y}_2\\&=\dot{V}_2+e_3(x_4+d_3-\dot{\alpha}_2)+y_2\dot{y}_2\\&=\dot{V}_2+e_3\left(e_4+y_3+\alpha_3^*+d_3-\dot{\alpha}_2\right)+y_2\dot{y}_2.\end{aligned} \tag{23}$$

If we choose the stabilizing function

$$\alpha_3^*=-c_3e_3-\frac{e_3}{(2\gamma_3)^2}+\dot{\alpha}_2, \tag{24}$$

where $c_3>0$ and $\gamma_3>0$ are designed constants, (24) can be rewritten as

$$\begin{aligned}\dot{V}_3&=\dot{V}_2+e_3(e_4+y_3)-c_3e_3^2-\frac{e_3^2}{(2\gamma_3)^2}+d_3e_3-\frac{y_2^2}{T_2}-y_2\dot{\alpha}_2^*\\&\le-c_1e_1^2-c_2e_2^2-c_3e_3^2+e_1(e_2+y_1)+e_2(e_3+y_2)+e_3(e_4+y_3)\\&+\gamma_1^2d_1^2+\gamma_2^2d_2^2+\gamma_3^2d_3^2-\frac{y_1^2}{T_1}-y_1\dot{\alpha}_1^*-\frac{y_2^2}{T_2}-y_2\dot{\alpha}_2^*.\end{aligned} \tag{25}$$

Step4: Let α_3^* pass through another first-order filter as follows:

$$T_3\dot{\alpha}_3+\alpha_3=\alpha_3^*,\alpha_3(0)=\alpha_3^*(0), \tag{26}$$

where T_3 is a time constant. The final Lyapunov candidate is selected as

$$V=V_3+\frac{1}{2}e_4^2+\frac{1}{2}y_3^2+\frac{1}{2}\tilde{w}_2^T\mathrm{P}_2^{-1}\tilde{w}_2+\frac{1}{2pJ}\tilde{J}^2 \tag{27}$$

where $P_2>0$ is the diagonal constant matrix, $\tilde{w}_2=w_2-\hat{w}_2$ is the estimated error vector, $p>0$ is an adaptive gain coefficient and $\tilde{J}=J-\hat{J}$ is the estimated error of J, then its derivative is computed as

$$\begin{aligned}\dot{V} &= \dot{V}_3 + e_4\dot{e}_4 + y_3\dot{y}_3 - \tilde{w}_2^T \mathrm{P}_2^{-1}\dot{\hat{w}}_2 - \frac{1}{pJ}\tilde{J}\dot{\hat{J}} \\ &= \dot{V}_3 + e_4\left(J^{-1}u + f_2 + d_4 - \dot{\alpha}_3\right) + y_3\dot{y}_3 - \tilde{w}_2^T \mathrm{P}_2^{-1}\dot{\hat{w}}_2 - \frac{1}{pJ}\tilde{J}\dot{\hat{J}}.\end{aligned} \tag{28}$$

The final control law can be specified as

$$u = \hat{J}u' = \hat{J}\left(-c_4 e_4 - \frac{e_4}{(2\gamma_4)^2} - \hat{w}_2^T\phi_2 + \dot{\alpha}_3\right) \tag{29}$$

with its adaptive laws

$$\dot{\hat{w}}_2 = P_2 e_4 \phi_2, \quad \dot{\hat{J}} = -p e_4 u', \tag{30}$$

where $\hat{J}$ is the estimated value of J, $c_3 > 0$ and $\gamma_3 > 0$ are designed constants. Substituting control (29) and its adaptive law (30) into (28), one has

$$\begin{aligned}\dot{V} &= \dot{V}_3 - c_4 e_4^2 - \frac{e_4^2}{(2\gamma_4)^2} + d_4 e_4 - \frac{y_3^2}{T_3} - y_3\dot{\alpha}_3^* \\ &\le -c_1 e_1^2 - c_2 e_2^2 - c_3 e_3^2 - c_4 e_4^2 + e_1(e_2 + y_1) + e_2(e_3 + y_2) + e_3(e_4 + y_3) \\ &\quad + \gamma_1^2 d_1^2 + \gamma_2^2 d_2^2 + \gamma_3^2 d_3^2 + \gamma_4^2 d_4^2 - \frac{y_1^2}{T_1} - y_1\dot{\alpha}_1^* - \frac{y_2^2}{T_2} - y_2\dot{\alpha}_2^* - \frac{y_3^2}{T_3} - y_3\dot{\alpha}_3^*.\end{aligned} \tag{31}$$

As $\dot{\alpha}_1^* = -(c_1 + \frac{1}{(2\gamma_1)^2})(x_2 + d_1 - \dot{y}_d) + y_d$, $\dot{\alpha}_2^* = -(c_2 + \frac{1}{(2\gamma_2)^2})(x_3 + f_1 + d_2 - \dot{\alpha}_1) - \dot{\hat{w}}_1^T\phi_1 - \hat{w}_1^T\dot{\phi}_1 + \ddot{\alpha}_1$ and $\dot{\alpha}_3^* = -(c_3 + \frac{1}{(2\gamma_3)^2})(x_4 + d_3 - \dot{\alpha}_2) + \ddot{\alpha}_2$ are all bounded, there exists a positive constant $\beta_i (i = 1, 2, 3)$ such that $\left\|\dot{\alpha}_1^*\right\| \le \beta_i$.

Using Young's inequalities $|e_i e_{i+1}| \le \frac{e_i^2}{2} + \frac{e_{i+1}^2}{2}$, $|e_i y_i| \le \frac{e_i^2}{2} + \frac{y_i^2}{2}$ and $|\beta_i y_i| \le \frac{\gamma^2}{4} + \frac{\beta_i^2 y_i^2}{\gamma^2}$ in (31) yields

$$\begin{aligned}\dot{V} &\le -(c_1 - 1)e_1^2 - (c_2 - \frac{3}{2})e_2^2 - (c_3 - \frac{3}{2})e_3^2 - (c_4 - \frac{1}{2})e_4^2 \\ &\quad - (\frac{1}{T_1} - \frac{1}{2} - \frac{\beta_1^2}{\gamma^2})y_1^2 - (\frac{1}{T_2} - \frac{1}{2} - \frac{\beta_2^2}{\gamma^2})y_2^2 - (\frac{1}{T_3} - \frac{1}{2} - \frac{\beta_3^2}{\gamma^2})y_3^2 \\ &\quad + \gamma_1^2 d_1^2 + \gamma_2^2 d_2^2 + \gamma_3^2 d_3^2 + \gamma_4^2 d_4^2 + \frac{3}{4}\gamma^2,\end{aligned} \tag{32}$$

where $\gamma = \max[\gamma_1 \quad \gamma_2 \quad \gamma_3]$.

By defining $c_1^* = c_1 - 1, c_2^* = c_2 - \frac{3}{2}, c_3^* = c_3 - \frac{3}{2}, c_4^* = c_4 - \frac{1}{2}$ and $T_i^* = (\frac{1}{T_i} - \frac{1}{2} - \frac{\beta_i^2}{\gamma^2})$, one obtains

$$\dot{V} \le -\sum_{i=1}^{4} c_i^* e_i^2 - \sum_{i=1}^{3} T_i^* y_i^2 + \gamma^2 \sum_{i}^{4} (d_i^2 + \frac{3}{4}) \le -c_1^* e_1^2 + d^T \gamma^2 d, \tag{33}$$

where $d = \begin{bmatrix} d_1 & d_2 & d_3 & d_4 & \sqrt{3}/2 \end{bmatrix}^T$.

If we choose the parameter $c_1^* > 1$ and integrate (33) from $0 \to T$, it yields

$$V(T) - V(0) \le -c_1^* \int_0^T \|e_1\|^2 dt + \gamma^2 \int_0^T \|d\|^2 dt \le \int_0^T (\gamma^2 \|d\|^2 - \|e_1\|^2) dt, \tag{34}$$

which indicates that the H ∞ performance (7) is achieved.

4 Simulation Results

In this section, simulation results are performed to demonstrate the tracking performance of the proposed method for the dual-motor driving system. The system parameters for simulation are selected as $J = 0.5, b = 0.5, J_m = 2$, $b_m = 2, k = 1, \alpha = 0.2$ and the external disturbances are selected as $d_1 = 1 + \sin(t), d_2 = 0.5 + \exp(-2t), d_3 = -0.8 + 0.6\cos(2t), d_4 = 0.3$.

The controller parameters are selected based on the stability requirement for the control system, i.e., $c_i^* > 0, T_i^* > 0$ and $\gamma > 0$, etc. To obtain the best performance of the control system, the control parameters are given through a trial-and-error method as $c_1 = 2, c_2 = 8, c_3 = 20, c_4 = 25, T_1 = T_2 = T_3 = 0.1, P_1 = \text{diag}\,(0.4, 0.2, 0.4)$, $P_2 = \text{diag}\,(0.001, 0.006)$, $p = 0.001$.

The sampling time/interval is 0.001 s, and the initial values of system states are $x_1(0) = 0, x_2(0) = 0, x_3(0) = 0, x_4(0) = 0, \hat{w}_1(0) = \begin{bmatrix} -2 & -3 & 1 \end{bmatrix}$,

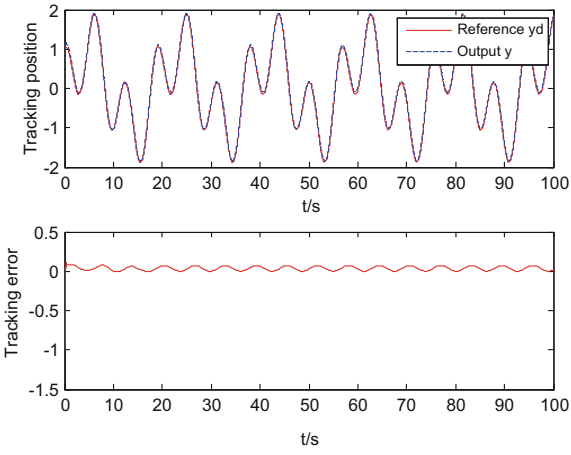

Fig. 1 Tracking performance for $\gamma = 0.2$

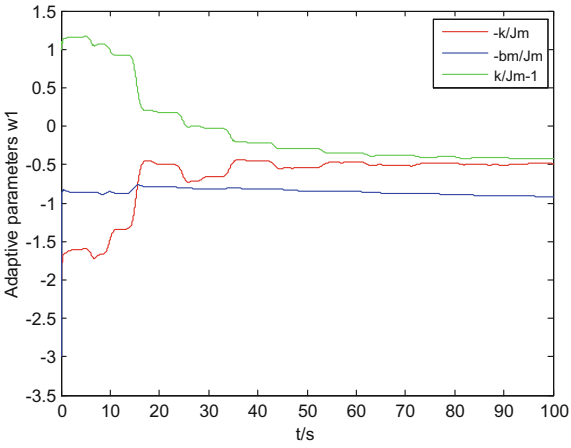

Fig. 2 Adaptive parameters of w_1

$\hat{w}_2(0) = [-1 \quad -2], \hat{J}(0) = 1$. A sinusoidal signal $y_d = \sin(\frac{1}{3}t) + \cos(t)$ is employed as the reference.

It can be seen from Fig. 1 that the proposed control system exhibits very good tracking performance under the conditions of uncertain parameters and time-varying external disturbances. Figure 2 shows that the estimated parameters will converge to the true value after a period time.

5 Conclusions

This paper presents a novel adaptive control scheme for the dual-motor driving system in the presence of parameter uncertainties and external disturbances. The proposed controller integrates the H ∞ control into the dynamic surface controller design which guarantees that the H ∞ performance is satisfied. Simulation results indicate that the uncertain parameters are estimated and the good tracking performance is achieved.

References

1. Gawronski W, Beech-Brandt JJ, Ahlstrom HG et al (2001) Torque-bias profile for improved tracking of the Deep Space Network antennas. IEEE Antennas Propag Mag 42(6):35–45
2. Tao G, Ma X, Ling Y (2001) Optimal and nonlinear decoupling control of systems with sandwiched backlash [J]. Automatica 37(2):165–176
3. Zhao H (2011) Backstepping adaptive control of dual-motor driving servo system[J]. Control Theory Appl 28(5):745–751
4. Li P, Zheng ZQ (2012) Robust adaptive second-order sliding-mode control with fast transient performance. IET Control Theory Appl 6(2):305–312

5. Guan C, Pan S (2008) Nonlinear adaptive robust control of single-rod electro-hydraulic actuator with unknown nonlinear parameters. IEEE Trans Control Syst Technol 16(3):434–445
6. Zhang G, Chen J, Lee Z (2010) Adaptive robust control for servo mechanisms with partially unknown states via dynamic surface control approach. IEEE Trans Control Syst Technol 18 (3):723–731
7. Sun LY, Tong S, Liu Y (2011) Adaptive backstepping sliding mode, control of static var compensator. IEEE Trans Control Syst Technol 19(5):1178–1185

Stabilization of a Class of Uncertain Nonlinear System via Fractional Sliding Mode Controller

Yuxiang Guo and Baoli Ma

Abstract In this paper, a novel fractional sliding mode control scheme is suggested to stabilize a second-order uncertain nonlinear system. The proposed sliding manifolds, which will converge to the origin in finite time by utilizing a classical quadratic Lyapunov function, ensures the reduction of the chattering phenomenon during the control process. Based on Lyapunov's stability theorem, the closed-loop system can be stabilized to the origin in the future time. Some results about the control and stabilization of such nonlinear systems, when the fractional sliding mode controller is used, are illustrated in this paper. Finally, an example with numerical simulations is provided to show the validity and feasibility of the proposed method.

Keywords Caputo derivative · Integer-order dynamical systems · Fractional sliding manifold · Stable

1 Introduction

The theory of integrals and derivatives of fractional order has attracted increasing attentions in the last decades. It is usually introduced to design the different controllers for the practical engineering problems, such as, fractional order-PI$^{\lambda}$D$^{\mu}$ controllers [1, 2], fractional-order adaptive controllers [3, 4] fractional-order adaptive high gain controllers [5, 6], and so on. As we all know, the sliding mode control (SMC) method for the nonlinear dynamical systems [7–9] has been studied extensively due to its robustness and simplicity. Meanwhile, many improved SMC schemes [10–12] were applied widely in mechanical systems, electrical circuit systems, and other control systems, we will not go into much detail here. With the development of fractional calculus, many authors devised fractional-order SMC scheme for fractional dynamical systems [13–15] that ensures the trajectory going

Y. Guo (✉) · B. Ma
School of Automation Science and Electrical Engineering,
Beijing University of Aeronautics and Astronautics, Beijing 100191, China
e-mail: yuxiangguo@buaa.edu.cn

Y. Jia et al. (eds.), *Proceedings of 2016 Chinese Intelligent Systems Conference*,
Lecture Notes in Electrical Engineering 404, DOI 10.1007/978-981-10-2338-5_34

into the sliding manifold within a finite time and decaying towards zero in the future time. Recently, Refs. [16, 17] have introduced fractional-order SMC technique with Riemann–Liouville derivatives to integer-order dynamical systems. It is well known that Caputo fractional derivative is frequently used in engineering disciplines since its initial conditions take the forms more similar to the traditional integer-order derivatives. Then how to design a fractional sliding mode controller with Caputo derivative, such that it can control and stabilize integer-order dynamical systems by using a classical quadratic Lyapunov function candidate.

Motivated by the previous works, in this paper, a novel fractional SMC scheme with Caputo derivative for controlling a coupled second-order nonlinear system will be constructed. It is found that the state trajectories of the system could reach the sliding manifold $s(t) = 0$ in finite time by choosing a classical quadratic Lyapunov function. Based on Lyapunov's stability theorem, the reduced-order system will be stabilized to the origin in the future time. Two main theorems about such results in this paper are illustrated. It should be pointed out in the proof of the obtained results, some limitations are overcome, when non-smooth function as a Lyapunov function candidate is used. An example with numerical simulations is provided to show the validity and feasibility of the proposed method.

Notations: $\mathbb{R}^+$ and $\mathbb{Z}^+$ are the sets of positive real and integer numbers, respectively, while $\mathbb{R}$ denotes the real numbers. $\mathbb{R}^n$ represents the n-dimensional Euclidean space. For a vector $x = [x_1, x_2, \dots, x_n]^T \in \mathbb{R}^n$, let us use $\|x\|_2 = \sqrt{\sum_{i=1}^{n} |x_i|^2}$ to denote the Euclidean norm of vector x. We denote by $L_p(\mathbb{R}^+), (1 \le p \le \infty)$ the set of those Lebesgue complex-valued measurable functions on $\mathbb{R}^+$. ${}^C D^\alpha$ and ${}_0 I_t^\alpha$ denote the Caputo fractional derivative of fractional-order $\alpha \in \mathbb{R}^+$ and Riemann–Liouville fractional integral of order $\alpha \in \mathbb{R}^+$ on $[0, t]$, respectively.

2 Preliminaries

In this section, we recall several basic definitions and properties of fractional operators which will be needed later. More detailed information related to fractional operators can be found in the literature [18, 19]. Without loss of generality, the lower limit of all fractional integrals and derivatives is supposed to be zero throughout the paper.

Definition 1 Let $x(t)$ be a continuous function on an interval $[0, b]$. The Riemann–Liouville fractional integral of order $\alpha \in \mathbb{R}^+$ is defined as

$$ {}_0 I_t^\alpha x(t) = \frac{1}{\Gamma(\alpha)} \int_0^t (t-\tau)^{\alpha-1} x(\tau) d\tau, \quad (t > 0,\ \alpha > 0), \tag{1} $$

where Γ is the Gamma function $\Gamma(s) = \int_0^{+\infty} t^{s-1} e^{-t} dt$.

Definition 2 The Caputo fractional derivative with order $\alpha \in \mathbb{R}^+$ of function $x(t)$ is defined by

$$ {}_0^C D_t^\alpha x(t) = \frac{1}{\Gamma(n-\alpha)} \int_0^t (t-\tau)^{n-\alpha-1} x^{(n)}(\tau) d\tau, \quad (t > 0), \tag{2} $$

where $0 < n-1 < \alpha \leq n$, $x^{(n)}(\tau)$ denotes the n-th derivative of x with respect to τ. Furthermore, when $0 < \alpha < 1$, it holds

$$ {}_0^C D_t^\alpha x(t) = \frac{1}{\Gamma(1-\alpha)} \int_0^t (t-\tau)^{-\alpha} x'(\tau) d\tau = {}_0 I_t^{1-\alpha} x'(t), \quad (t > 0), \tag{3} $$

Property 1 ([19]) *Let* $x(t) \in L_1(\mathbb{R}^+)$. *If* $0 < \alpha < 1$, *then*

$$ {}_0^C D_t^\alpha ({}_0 I_t^\alpha x(t)) = x(t), \quad (t > 0). $$

Property 2 ([20]) *If* $0 < \alpha < 1$, *for Caputo fractional derivative, then*

$$ {}_0^C D_t^{1-\alpha} ({}_0^C D_t^\alpha x(t)) = {}_0^C D_t^\alpha ({}_0^C D_t^{1-\alpha} x(t)) = x'(t). $$

Property 3 ([19]) *The fractional integration operator* ${}_0 I_t^\alpha$ *is bounded in* $L_p[0, b]$, $(1 \leq p \leq \infty)$ *and satisfies*

$$ \| {}_0 I_t^\alpha x(t) \|_p \leq K \| x(t) \|_p, \quad \left(K = \frac{b^{Re(\alpha)}}{Re(\alpha)|\Gamma(\alpha)|}, Re(\alpha) > 0, \alpha \in C\right). $$

3 Main Results

3.1 Problem Statement

A coupled second-order nonlinear system is expressed as

$$ \begin{cases} \dot{x}_1(t) = x_2(t), \\ \dot{x}_2(t) = f(t,x) + g(x)u + h(t,x), \end{cases} \tag{4} $$

where $x(t) = [x_1(t), x_2(t)]^T$ is the state of system, $g(x) \neq 0$ is a smooth nonlinear function of x, u is a control input of the system, $f(t,x)$ represents the nonlinear function of the system, $h(t,x)$ denotes the model uncertainties and external disturbances of the system. For the convenience of study, we assume that any influence of the past process history which has not been taken into account can effectively be merged into the 'perturbation term' $h(t,x)$ that satisfies $\|h(t,x)\| \leq {}_0 I_t^{1-\alpha} \delta_h t^\alpha$ and $\| {}_0^C D_t^{1-\alpha} h(t,x) \| \leq \delta_h t^\alpha$, where $\alpha \in (0,1)$ is a real constant and δ_h is a known positive constant.

Besides, since fractional calculus has the memory, calculation of the fractional derivative of variable $x(t)$ requires the information of all the variable past on an infinite time interval. In the present paper, it is assumed that the initialization function $x(t)$ of fractional-order systems involving Caputo derivative is a constant function of time (or null), and $x(t) = x(0^+)$ for $t \leq 0$. For a comprehensive treatment of the initialization issue of fractional derivatives, the reader may consult the literature [21, 22]. In the rest of this section, a novel fractional sliding mode control scheme and its stability analysis are proposed, respectively.

3.2 Design of Fractional Sliding Mode Controller

The following fractional sliding manifold with Caputo derivative is proposed

$$s(t) = \beta_0 I_t^{\alpha} x_1(t) + \gamma {}_0^C D_t^{1-\alpha} x_1(t) + {}_0^C D_t^{1-\alpha} x_2(t), \tag{5}$$

where $\alpha \in (0, 1)$, β and γ are real positive constants.

Taking Caputo type fractional derivative from both sides of (5), according to Properties 1 and 2, one gets

$${}_0^C D_t^{\alpha} s(t) = \beta x_1(t) + \gamma \dot{x}_1(t) + \dot{x}_2(t). \tag{6}$$

Substituting (4) into (6) results in:

$${}_0^C D_t^{\alpha} s(t) = \beta x_1(t) + \gamma x_2(t) + f(t, x) + g(x)u + h(t, x). \tag{7}$$

Now, we want to design a robust control law that constrains the motion of the system to the surface $s(t) = 0$ in a given finite time. Once the trajectory reaches the manifold, it cannot go away from it in the subsequent time. To this end, the following control law is proposed.

$$u = \frac{-1}{g(x)} \begin{pmatrix} \beta x_1(t) + \gamma x_2(t) + f(t, x) + {}_0 I_t^{1-\alpha} \delta_h t^{\alpha} \\ + \varepsilon {}_0 I_t^{1-\alpha} \text{sign}^q s(t) + \sigma {}_0 I_t^{1-\alpha} s(t) \end{pmatrix}, \tag{8}$$

where $\text{sign}^q s(t) = \text{sgn}(s(t))|s(t)|^q$, $q \in (0, 1)$ is a real constant, ε and σ are real positive switching coefficients.

Since the motion of the system consists of a reaching phase and a sliding phase, we start by proving that the state trajectory $x(t)$ converges to the sliding surface $s(t) = 0$. Subsequently, the following theorem is presented.

Theorem 1 *Suppose that system (4) is controlled by the feedback control law (8), then all the state trajectories of this system will converge to the sliding manifold* $s(t) = 0$ *within the finite time* $T_r \leq \frac{1}{\sigma(1-q)} \ln(1 + \frac{\sigma}{\varepsilon} \|s(0)\|_2^{1-q})$, *where* $\|\cdot\|_2$ *represents the Euclidean norm.*

Proof Let us consider the following Lyapunov function candidate, which is positive definite.

$$V = \frac{1}{2}s^2(t).$$

Taking the time derivative from both sides of Lyapunov function candidate, one has

$$\dot{V} = s(t)\dot{s}(t) = s(t){}_0^C D_t^{1-\alpha}({}_0^C D_t^{\alpha} s(t)). \tag{9}$$

Substituting (7) and (8) into (9), we have

$$\begin{aligned}\dot{V} &= s(t){}_0^C D_t^{1-\alpha}(h(t,x) - {}_0 I_t^{1-\alpha}\delta_h t^{\alpha} - \varepsilon {}_0 I_t^{1-\alpha}\text{sign}^q s(t) - \sigma {}_0 I_t^{1-\alpha} s(t)) \\ &\leq -\varepsilon |s(t)|^{q+1} - \sigma(s(t))^2. \end{aligned} \tag{10}$$

Consequently, one gets

$$\dot{V} \leq -\varepsilon |s(t)|^{q+1}.$$

Rewriting the above inequality, we obtain that

$$\dot{V} \leq -\varepsilon \|s(t)\|_2^{q+1}.$$

Thus by [23, Theorem 8], it can be concluded that all trajectories will asymptotically converge to the sliding manifold $s(t) = 0$.

From the formula (10), one gets

$$\dot{V} = \frac{dV}{dt} \leq -\varepsilon |s(t)|^{q+1} - \sigma(s(t))^2 = -\varepsilon (2V)^{\frac{q+1}{2}} - \sigma(2V).$$

Hence it can be concluded that

$$\begin{aligned} dt &\leq -\frac{dV}{\varepsilon(2V)^{\frac{q+1}{2}} + \sigma(2V)} = -\frac{1}{2}\frac{(2V)^{-\frac{1}{2}} d(2V)}{\varepsilon(2V)^{\frac{q}{2}} + \sigma(2V)^{\frac{1}{2}}} \\ &= -\frac{d(2V)^{\frac{1}{2}}}{\varepsilon(2V)^{\frac{q}{2}} + \sigma(2V)^{\frac{1}{2}}} = -\frac{d\|s(t)\|_2}{\varepsilon\|s(t)\|_2^q + \sigma\|s(t)\|_2} \\ &= -\frac{\|s(t)\|_2^{-q} d\|s(t)\|_2}{\varepsilon + \sigma\|s(t)\|_2^{1-q}} = -\frac{1}{\sigma(1-q)}\frac{d(\sigma\|s(t)\|_2^{1-q})}{\varepsilon + \sigma\|s(t)\|_2^{1-q}}. \end{aligned} \tag{11}$$

Taking integral of both sides of formula (11) from 0 to t_r and let $s(t_r) = 0$, we have

$$t_r \leq -\frac{1}{\sigma(1-q)} \int_0^{t_r} \frac{d(\sigma \|s(t)\|_2^{1-q})}{\varepsilon + \sigma \|s(t)\|_2^{1-q}} = -\frac{1}{\sigma(1-q)} \ln(\varepsilon + \sigma \|s(t)\|_2^{1-q}) \Big|_0^{t_r}$$
$$= \frac{1}{\sigma(1-q)} \ln(1 + \frac{\sigma}{\varepsilon} \|s(0)\|_2^{1-q}).$$

Let T_r be the finite time that it is taken to travel from $s(0) \neq 0$ to $s(t_r) = 0$ for any arbitrary initial time zero. From the above results, it is clear that the system states will reach the sliding mode $s = 0$ within the finite time T_r, which satisfies

$$T_r = t_r - 0 \leq \frac{1}{\sigma(1-q)} \ln(1 + \frac{\sigma}{\varepsilon} \|s(0)\|_2^{1-q}).$$

This completes the proof.

Remark 1 If ε is chosen large enough, the convergence time of system can be significantly shorter, which implies that the trajectory of system has a faster rate at the crossing of the sliding surface $s(t) = 0$. As for a parameter σ, it may have the same effect in the improved convergence performance of the system.

Remark 2 It should be noted that the new proposed fractional sliding mode surface (5) and control law (8) overcome the singularity problem in the conventional terminal sliding mode methods.

Under the obtained sliding surface Eq. (5) and the control law (8), the system dynamics is governed by the following nonlinear differential equation

$$\begin{cases} \dot{x}_1(t) = x_2(t), \\ \dot{x}_2(t) = h(t,x) - \beta x_1(t) - \gamma x_2(t) - \varepsilon\, {}_0I_t^{1-\alpha} \text{sign}^q s(t) - \sigma\, {}_0I_t^{1-\alpha} s(t) - {}_0I_t^{1-\alpha} \delta_h t^\alpha \end{cases} \tag{12}$$

Then, the stabilization problem of system (4) is equivalent to analyze the stability of the origin $x(t) = 0$ of system (12). In what follows, we investigate the globally asymptotic stability of this system state.

Theorem 2 *Under the obtained sliding surface Eq.* (5) *and the control law* (8)*, the closed-loop system* (4) *is globally uniformly asymptotically stable.*

Proof Let us consider the following Lyapunov function candidate, which is positive definite.

$$L = \frac{1}{2}\beta x_1^2(t) + \frac{1}{2} x_2^2(t).$$

Taking the time derivative of the above formula, one has

$$\begin{aligned}
\dot{L} &= \beta x_1(t)\dot{x}_1(t) + x_2(t)\dot{x}_2(t) \\
&= \beta x_1(t)x_2(t) + x_2(t)(h(t,x) - \beta x_1(t) - \gamma x_2(t) - \varepsilon\, {}_0I_t^{1-\alpha}\mathrm{sign}^q s(t) - \sigma_0 I_t^{1-\alpha} s(t) - \delta_{h0} I_t^{1-\alpha} t^{\alpha}) \\
&= -\gamma x_2^2(t) - x_2(t)\left[\frac{1}{\Gamma(1-\alpha)}\int_0^t \frac{\varepsilon \mathrm{sign}^q s(\tau) + \sigma s(\tau)}{(t-\tau)^{\alpha}} d\tau\right] + x_2(t)(h(t,x) - \delta_{h0} I_t^{1-\alpha} t^{\alpha}) \\
&\le -\gamma x_2^2(t) + |x_2(t)|\left[\frac{1}{\Gamma(1-\alpha)}\int_0^t \frac{\varepsilon |s(\tau)|^q + \sigma |s(\tau)|}{(t-\tau)^{\alpha}} d\tau\right] \qquad (13)
\end{aligned}$$

Note that, once the trajectory reaches the sliding surface within the finite time t_r, it stays in the manifold $s = 0$ for all future time, as seen from the formula (10); that is, $s(\tau) = 0$ for $\tau \in [t_r, +\infty)$. Therefore, for all $t > t_r \ge 0$, one has

$$\begin{aligned}
\int_0^t \frac{\varepsilon |s(\tau)|^q + \sigma |s(\tau)|}{(t-\tau)^{\alpha}} d\tau &= \int_0^{t_r} \frac{\varepsilon |s(\tau)|^q + \sigma |s(\tau)|}{(t-\tau)^{\alpha}} d\tau + \int_{t_r}^t \frac{\varepsilon |s(\tau)|^q + \sigma |s(\tau)|}{(t-\tau)^{\alpha}} d\tau \\
&= \int_0^{t_r} \frac{\varepsilon |s(\tau)|^q + \sigma |s(\tau)|}{(t-\tau)^{\alpha}} d\tau. \qquad (14)
\end{aligned}$$

By the proof of Theorem 1, it is clear to see that the variable s satisfies the following equation

$$\dot{s}(t) = -\varepsilon \mathrm{sign}^q s(t) - \sigma s(t). \qquad (15)$$

Then, for any $s(0) \neq 0$ and $t > 0$, the condition $s\dot{s} \le 0$ in the set $\{|s| \le |s(0)|\}$ makes it positively invariant. Hence, it follows from (13) and (14) that

$$\begin{aligned}
\dot{L} &\le -\gamma x_2^2(t) + |x_2(t)|\left[\frac{\varepsilon |s(0)|^q + \sigma |s(0)|}{\Gamma(1-\alpha)}\int_0^{t_r} \frac{d\tau}{(t-\tau)^{\alpha}}\right] \\
&= -\gamma x_2^2(t) + |x_2(t)|\left[\frac{\varepsilon |s(0)|^q + \sigma |s(0)|}{\Gamma(2-\alpha)}[t^{1-\alpha} - (t-t_r)^{1-\alpha}]\right]
\end{aligned}$$

For any $t > t_r \ge 0$ and $\alpha \in (0,1)$, one gets $t^{1-\alpha} = (t_r + t - t_r)^{1-\alpha} \le t_r^{1-\alpha} + (t-t_r)^{1-\alpha}$. Then

$$\begin{aligned}
\dot{L} &\le -\gamma x_2^2(t) + |x_2(t)|\left[\frac{\varepsilon |s(0)|^q + \sigma |s(0)|}{\Gamma(2-\alpha)} t_r^{1-\alpha}\right] \\
&= -\gamma(1-\theta)x_2^2(t) - \gamma\theta x_2^2(t) + |x_2(t)|\left[\frac{\varepsilon |s(0)|^q + \sigma |s(0)|}{\Gamma(2-\alpha)} t_r^{1-\alpha}\right]
\end{aligned}$$

where $\theta \in (0,1)$ is a real constant. Thus, for any $|x_2| \ge \frac{(\varepsilon |s(0)|^q + \sigma |s(0)|) t_r^{1-\alpha}}{\gamma\theta\Gamma(2-\alpha)}$, one obtains

$$\dot{L} \le -\gamma(1-\theta)x_2^2(t) \le 0$$

If, let us view the variable s as a input of the system (12). Then it can be concluded that the unforced system (12) is globally asymptotically stable. Subsequently, from $\|x\| \geq |x_2| \geq \frac{(\varepsilon|s(0)|^q+\sigma|s(0)|)t_r^{1-\alpha}}{\gamma\theta\Gamma(2-\alpha)}$, we can show that the system (12) is input-to-state stable. Again using the Eq. (15), for any $s(0) \neq 0$ and $t > 0$, it follows from the proof of Theorem 1 that this system is globally finite-time stable which implies that the system is also globally uniformly asymptotically stable. According to [24, Lemma 4.7], the origin of the cascade system (12) and (15) is globally uniformly asymptotically stable. So far, we achieve global stabilization of the second-order nonlinear system (4) by applying the new fractional sliding surface (5). This completes the proof.

Remark 3 Although this fractional-order SMC scheme is proposed for control and stabilization of integer-order systems, it still works on fractional-order dynamical systems.

4 An Illustrative Example

In this section, to verify and demonstrate the effectiveness of the proposed scheme, let us consider the following controlled Duffing forced-oscillation system

$$\begin{cases} \dot{x}_1 = x_2, \\ \dot{x}_2 = -0.3x_2 - x_1^3 + 0.04\sin(0.1t) + u, \end{cases} \tag{16}$$

where u is control input of system.

According to the scheme of the proposed fractional SMC, the sliding mode surface is designed as follows.

$$s = \beta {}_0I_t^{0.5}x_1 + \gamma {}_0^C D_t^{0.5}x_1 + {}_0^C D_t^{0.5}x_2,$$

where β and γ are real positive constants. Note that

$${}_0^C D_t^{0.5}0.04\sin(0.1t) = 0.004 {}_0I_t^{0.5}\cos(0.1t) \leq \frac{0.004}{\Gamma(1.5)}t^{\frac{1}{2}}$$

Consequently, applying the ideas of this controller design, we obtain

$$u = f(x_1, x_2) - \beta x_1 - \gamma x_2 - \frac{0.004}{\Gamma(1.5)} {}_0I_t^{0.5}t^{\frac{1}{2}} - \varepsilon\,\mathrm{sgn}(s) {}_0I_t^{0.5}|s|^q - \sigma {}_0I_t^{0.5}s,$$

where $f(x_1, x_2) \triangleq 0.3x_2 + x_1^3$, $q \in (0, 1)$ is a real constant, ε and σ represent the corresponding switching gains.

The parameters of the sliding manifold s are chosen as $\beta = 2$, $\gamma = 3$, while the control parameters of controller u are selected as $\varepsilon = 1$, $\sigma = 2$, $q = 0.3$. Figure 1a,

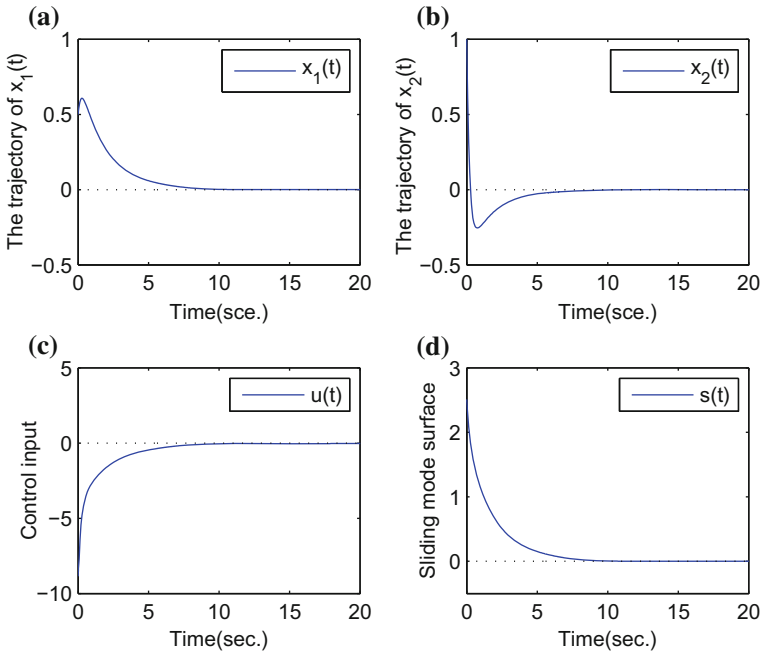

Fig. 1 Evolution of the system states, control input and sliding surface with the initial value $(x_1(0), x_2(0)) = (0.5, 1)$

b show that the states $x_1(t)$ and $x_2(t)$ of system can converge to zero as time t tends to infinity when the initial condition $(x_1(0), x_2(0)) = (0.5, 1)$. During the controller design of fractional SMC scheme, we introduce the terms $-\varepsilon\, {}_0I_t^{1-\alpha}\text{sign}^q s(t) - \sigma {}_0I_t^{1-\alpha} s(t)$; that is, from the proof of Theorem 2, one has

$$|{}_0I_t^{1-\alpha}(\varepsilon \text{sign}^q s(t) + \sigma s(t))| \leq \int_0^t \frac{\varepsilon|s(\tau)|^q + \sigma|s(\tau)|}{\Gamma(1-\alpha)(t-\tau)^\alpha} d\tau \leq \frac{\varepsilon|s(0)|^q + \sigma|s(0)|}{\Gamma(2-\alpha)} t^{1-\alpha}.$$

Consequently, there exist many α, t such that, for any $t \geq 1$, $\frac{\varepsilon|s(0)|^q+\sigma|s(0)|}{\Gamma(2-\alpha)} t^{1-\alpha} \leq (\varepsilon|s(0)|^q + \sigma|s(0)|)t$, which implies that the amplitude of the switching component will be smaller in the presence of the control switching. The simulation results are shown in Figs. 1c, d, and 2. More detailed illustration can be found in the literature [16, Remark 4.]. Those simulation results illustrate that the proposed method has been quite effective for control and stabilization integer-order nonlinear systems, using fractional sliding mode controller.

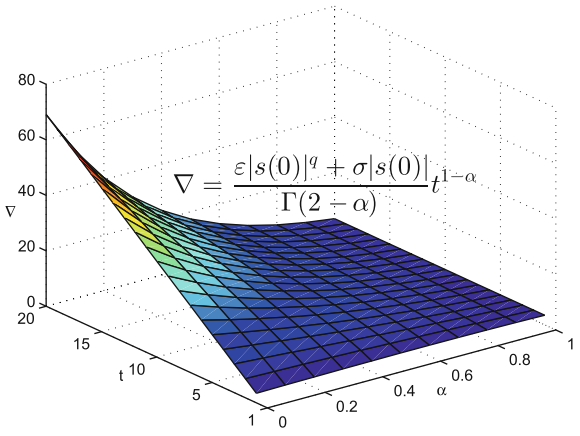

Fig. 2 Relationship between ∇ and α, t as parameters $\varepsilon = 1$, $\sigma = 2$, $q = 0.3$ and the initial value $|s(0)| = 1.2$

5 Conclusions

In this paper, a novel fractional sliding mode controller is suggested to stabilize a coupled second-order nonlinear systems with the model uncertainties and external disturbances. By taking a classical quadratic Lyapunov function, it can be concluded that the state trajectories of the controlled system reach the sliding manifold $s(t) = 0$ in finite time. The proposed sliding manifold ensures the reduction of the chattering phenomenon during the control process. Based on Lyapunov's stability theorem, the closed-loop system can be stabilized to the origin in the future time. It is pointed out that a novel fractional sliding mode controller is proposed for stabilization of integer-order dynamical systems by utilizing the smooth function as Lyapunov function candidate. Finally, an example is provided to show the validity and feasibility of the proposed method.

Acknowledgments This work was supported by the National Science and Technology Major Project (No. 2012CB821202), the National Nature Science Foundation (No. 61327807, No. 61573034).

References

1. Charef A (2006) Analogue realisation of fractional-order integrator, differentiator and fractional PI$^{\lambda}$D$^{\mu}$ controller. IEE Proc Control Theroy A. 153:714–720
2. Bettou K, Charef A, Mesquine F (2008) A New Design Method for Fractional PI$^{\lambda}$D$^{\mu}$ Controller. Int J Sci Tech Autom Control Comput Eng 2:414–429
3. Aguila-Camacho N, Duarte-Mermoud MA (2013) Fractional adaptive control for an automatic voltage regulator. ISA Trans 52:807–815
4. Ladaci S, Charef A (2006) On fractional adaptive control. Nonlinear Dyn 43:365–378
5. Ladaci S, Loiseau JJ, Charef A (2008) Fractional order adaptive high-gain controllers for a class of linear systems. Commun Nonlinear Sci Numer Simul 13:707–714

6. Figuigui E (2009) Application of fractional adaptive High-Gain controller to a LEO (Low Earth Orbit) satellite. In: International Conference on Computers Industrial Engineering, pp 1850–1856
7. Utkin V (1992) Sliding Modes in Control and Optimization. Springer Verlag, Berlin
8. Edwards C, Spurgeon S (1998) Sliding mode control: theory and applications, CRC Press
9. Yang L, Yang JY (2011) Nonsingular fast terminal sliding-mode control for nonlinear dynamical systems. Int J Robust Nonlinear 21:1865–1879
10. Yu SH, Yu X, Shirinzadeh B, Man Z (2005) Continuous finite-time control for robotic manipulators with terminal sliding mode. Automatica 41:1957–1964
11. Jin M, Lee J, Chang PH, Choi C (2009) Practical nonsingular terminal sliding-mode control of robot manipulators for high-accuracy tracking control. IEEE Trans Ind Electron 56:3593–3601
12. Xu SSD, Chen CC, Wu ZL (2015) Study of nonsingular fast terminal sliding-mode fault-tolerant control. IEEE Trans Ind Electron 62(6):3906–3913
13. Yang N, Liu C (2013) A novel fractional-order hyperchaotic system stabilization via fractional sliding-mode control. Nonlinear Dyn 74:721–732
14. Wang Z, Huang X, Shen H (2012) Control of an uncertain fractional order economic system via adaptive sliding mode. Neurocomputing 83:83–88
15. Chen L, Wu R, He Y, Chai Y (2015) Adaptive sliding-mode control for fractional-order uncertain linear systems with nonlinear disturbances. Nonlinear Dyn 80:51–58
16. Yin C, Chen YQ, Zhong S (2014) Fractional-order sliding mode based extremum seeking control of a class of nonlinear systems. Automatica 50:3173–3181
17. Ullah N, Wang SP, Khattak MI, Shafi M (2015) Fractional order adaptive fuzzy sliding mode controller for a position servo system subjected to aerodynamic loading and nonlinearities. Aerosp Sci Technol 43:381–387
18. Podlubny I (1998) Fractional differential equations: an introduction to fractional derivatives, fractional differential equations, to methods of their solution and some of their applications, Academic press
19. Kilbas AAA, Srivastava HM, Trujillo JJ (2006) Theory and applications of fractional differential equations, Elsevier Science Limited
20. Li C, Deng W (2007) Remarks on fractional derivatives. Appl Math Comput 187:777–784
21. Sabatier J, Merveillaut M, Malti R, Oustaloup A (2010) How to impose physically coherent initial conditions to a fractional system? Commun Nonlinear Sci Numer Simul 15:1318–1326
22. Sabatier J, Farges C, Oustaloup A (2014) Fractional systems state space description: some wrong ideas and proposed solution. J Vib Control 20:1076–1084
23. Li Y, Chen YQ, Podlubny I (2009) Mittag-Leffler stability of fractional order nonlinear dynamic systems. Automatica 45:1965–1969
24. Khalil HK (2002) Nonlinear Systems, 3rd edn. Prentice Hall, New Jersey

B-SIFT: A Simple and Effective SIFT for Real-Time Application

Yiliu Feng, Yafei Liu and Hengzhu Liu

Abstract SIFT is the one of the most famous algorithm in image matching for its robustness of scale changes, rotation changes, view changes and light changes. However, it is too complex to compute and match. This paper introduces a binary descriptor which can be computed using a simple intensity difference of relatively few bits, and proposes an efficient and effective algorithm named B-SIFT. Compared to complex 128-vector descriptors in SIFT, the binary descriptor is used as the local invariant features which is easy to compute and match. Experimental results based on open datasets demonstrate that B-SIFT obtains 1–2 orders of magnitude speed-up while preserving competitive discriminant ability.

Keywords SIFT · Binary descriptor · Real-time · Image matching

1 Introduction

Image matching plays an important role in computer vision, such as virtual reality (VR), stereo correspondence, image retrieval, and object tracking. Hence lots of methods have been proposed to solve this problem. The methods based on image local invariant features, which can work well under scale change, view change and rotation, have been turned out to be more suitable for image matching. SIFT (*Scale-Invariant Features*) [1] is one of the most famous algorithms that uses local invariant features as it is invariant to image scaling and rotation, and partially invariant to the changes in illumination and 3D camera viewpoint. However, the high dimensionality of SIFT descriptor constraint its speed, which makes SIFT cannot be well applied in the real-time environment, especially the descriptors

Y. Feng (✉) · Y. Liu · H. Liu
College of Computer Science, National University of Defense Technology, Changsha 410073, China
e-mail: 329436764@qq.com

Y. Jia et al. (eds.), *Proceedings of 2016 Chinese Intelligent Systems Conference*, Lecture Notes in Electrical Engineering 404, DOI 10.1007/978-981-10-2338-5_35

Table 1 The percentage of execution time for every step in SIFT

Unit	Time (*ms*)	Rate (%)
Gaussian	93	1.10
DoG	21	0.24
Keypoint detection	6	0.71
Orientation	326	3.86
Descriptor computing	7767	91.85
Matching	189	2.24
Total	8456	100

computing step occupies nearly 90 % execution time, which is shown in Table 1. Based on the Amdahl law we confirm that the descriptors computing is the bottleneck of SIFT.

In the paper, we propose a B(binary)-SIFT algorithm based on an efficient and efficient descriptor named binary descriptor. The binary descriptor can be obtained by directly computing binary strings from image patches in which every bits is computed by comparing the intensities of pairs of points in the fixed location. In the meantime, comparing strings can be done by calculating the Hamming Distance through XOR or bit count operation which is extremely fast. The experimental results show that B-SIFT obtains competitive performance, especially provides a factor of 2 speed-up in descriptor computing than SIFT. Therefore the proposed B-SIFT can be well applied in real-time applications.

2 Related Work

The SIFT descriptor is a 128-vector with highly discriminant, but it is relatively hard to compute and match, which constraints SIFT cannot be applied in real-time applications such as object tracking that need to keep track of many points.

To solve the problem of high complexity in SIFT, people have done much research work to improve the performance. Ke et al. use PCA (*Principal Component Analysis*) [2] to reduce the dimension of SIFT descriptor from 128 to 20, whereas PCA needs to compute the descriptors first and has little loss in discriminate. Bay et al. proposes SURF [3] based on local gradient histogram which uses integral images to accelerate the computation. SURF can obtain good matching performance by only using 64 dimensions, however SURF is still too complex to be applied in the real-time applications. The BRIEF [4] first proposes to use a binary descriptor for image matching. The binary descriptor consists of a binary string, which reflects the image intensity comparisons at random predetermined pixel locations. However the BRIEF is very sensitive to image rotation and scale changes which restrict its applying to general tasks. Rublee et al. propose an Oriented Fast and Rotated BREIF (ORB) [5] which assign an orientation to every keypoint makes ORB is insensitive to image rotation but is still sensitive to scale change.

In this paper, we combine the advantages of SIFT and BRIEF and propose a fast and effective image matching algorithm named B-SIFT. The results of experiment demonstrate that B-SIFT is much faster than the SIFT while preserving competitive discriminative power.

3 B-Sift

Our approach first detects keypoint in scale space to obtain the ability of scale invariant, and then we compute the orientation for every keypoint based on Moment. Finally, we compute the binary descriptors for every keypoint.

3.1 Keypoint Detection

We first construct a scale space for the input image through Gaussian filter. The scale space consists of n octaves and m intra-octaves. In this paper, we define n = 4, m = 5. Difference-of-Gaussian (DOG) can be computed from difference of two nearby scales in the same octaves, and then we find the extreme points in DOG space as keypoint. More details can be found in [1].

3.2 Orientation Assign

As one keypoint may have multiple orientations in SIFT, which leads to multiple keypoints records in the same pixel location and constraint the speed. We propose to use Moment to computer the orientation of a keypoint, by which every point only owns one orientation. The efficiency of Moment is revealed in [6].

3.3 Binary Descriptor Computing

SIFT descriptor is a 128-vector with highly discriminant which makes it robust to scale changes, rotations and viewpoint changes, but it is too complex to apply in real-time applications. Binary descriptor computes binary strings by comparing the intensities of an image patch.

Given an image patch $p(S \times S)$, the response function is defined as

$$t(p; x, y) = \begin{cases} 1, & p(x) < p(y) \\ 0, & otherwise \end{cases}$$

in which p(x) means the intensity at pixel x. If we select N pairs of pixels in an image patch, and then an N-bits binary string will be obtained.

$$f_N(p) = \sum_{1 \le i \le D} 2^{i-1} t(p; x, y)$$

in which N = 256. The location of the N pairs of pixel is prefixed through the greedy selection [5].

We can use the Hamming distance to compute the similarity between two binary descriptors.

4 Performance Evaluation and Comparison

We implement our proposed B-SIFT on a PC equipped with an i5 3.2 GHz CPU and 4 GB memory, and verify it based on the dataset of Mikolajczyk's [7] which includes varying image changes, for example scale changes, rotations and light changes. Each change has six images. ***n/m*** means the reference image and the match image are the n^{th} and the m^{th} image of a specified change, respectively. For each image change, we compare B-SIFT with the conventional SIFT in terms of runtime and number of matching points.

The dataset can be download from
http://www.robots.ox.ac.uk/~vgg/research/affine.

As shown in Table 2, we can find that the runtime between SIFT and our proposed B-SIFT in Gaussian, DOG and Keypoint detection steps are nearly the

Table 2 Every stage time comparison of various changes between B-SIFT and SIFT. The first column has the images used to match. The total means the whole execution time of SIFT and B-SIFT. The no. in the last column is the number of total matched points. The rest number are the operation time (*ms*) of every step in SIFT and B-SIFT

Image	Unit	Gaussian	DoG	Detection	Orientation	Descriptor	Total	No.
Boat 1/2	B-SIFT	93	16	33	**103**	**79**	**323**	76
	SIFT	92	16	42	319	7672	8141	51
Graf 1/2	B-SIFT	90	16	29	**108**	**91**	**289**	47
	SIFT	93	17	28	342	30719	31199	76
Bike 1/2	B-SIFT	94	16	25	**38**	**16**	**189**	77
	SIFT	96	16	29	202	2934	3177	104
Ubc 1/6	B-SIFT	92	14	30	**69**	**33**	**238**	140
	SIFT	94	17	33	249	13149	13542	544
Noise 1/6	B-SIFT	90	16	24	**35**	**14**	**179**	53
	SIFT	91	16	26	187	3469	3789	63
Light 1/2	B-SIFT	89	15	29	**34**	**13**	**180**	61
	SIFT	94	16	29	182	2175	2496	73

same, because the two different algorithms use the same method in these three steps. However, the B-SIFT uses the Moment in Orientation step to compute the main orientation, which saves the runtime.

In the Keypoint descriptor step, our B-SIFT is much faster than the SIFT, which leads to a holistic speed-up than the SIFT. And more the keypoints the higher speed-up, even under the case that the number of matched point of our method is more than the original SIFT, such as Boat1/2.

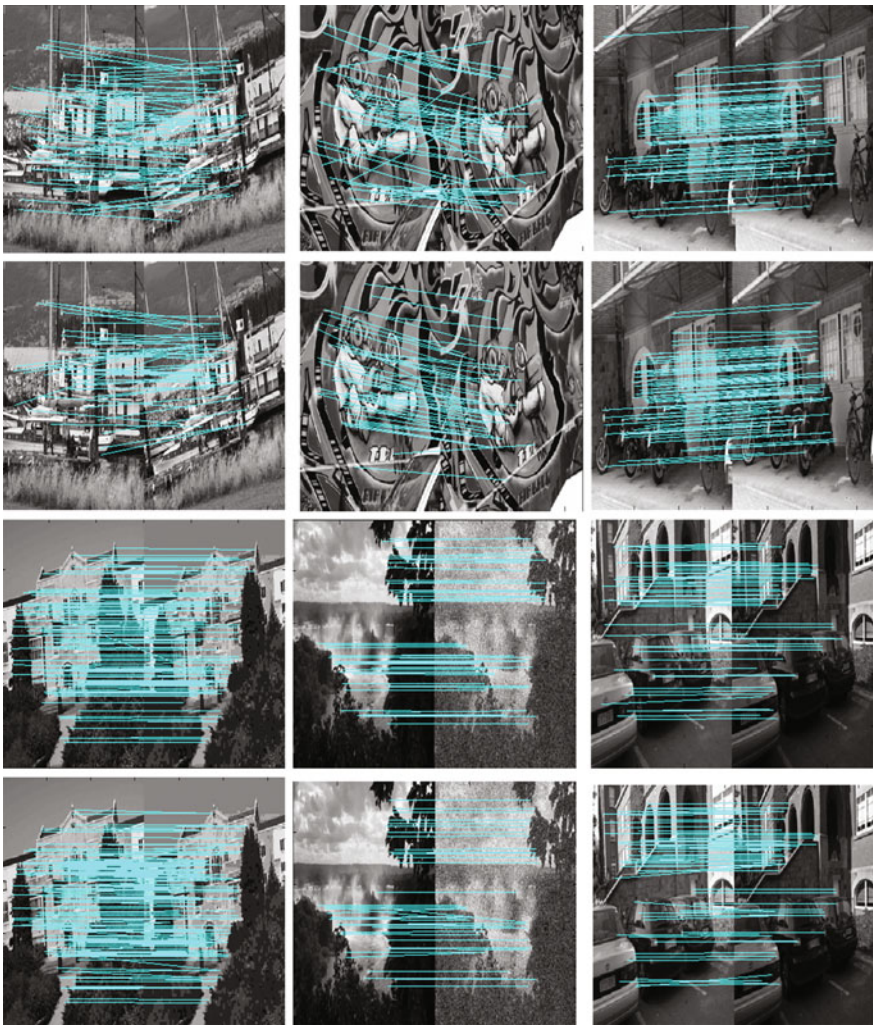

Fig. 1 Comparison of match results between B-SIFT and SIFT, the odd rows are our results, the even rows are SIFT results. From *left to right* and *top end down* the change are: Scale change and Rotation change, Viewpoint change, Image blur, Compression artifacts, Noise, illumination change

In many cases, the SIFT has more matched keypoints than the B-SIFT, but it does not mean the SIFT owns more effective matched keypoints. The reason is that, in the orientation assignment step of SIFT, peaks in the orientation histogram correspond to dominant directions of local gradient. The highest peak in the histogram is first detected, and then other local peaks within 80 % of the highest peak are used to create the new keypoint. Therefore, the same keypoints with multiple peaks will count repeatedly. In B-SIFT, as we use Moment, only one orientation is computed for every keypoints, which accelerates the descriptor computation step.

As shown in Table 2 and Fig. 1, compared to the SIFT, our approach B-SIFT has competitive performance in Scale change and Rotation change, Viewpoint change, Image blur, Compression artifacts, Noise and Illumination change while providing two orders of magnitude speed-up in descriptor compute and one order of magnitude speed-up in total SIFT respectively.

5 Conclusion

This paper has proposed an effective algorithm based on the SIFT named B-SIFT for image matching. Compared to the 128-vector SIFT, the B-SIFT uses binary strings to describe the image patch centered at keypoints which outperforms better speed while sacrificing few discrimination. In the meantime, as the B-SIFT calculates the binary strings by comparing the intensities of two fixed pixels, the B-SFIT cannot work in textureless region, which restricts its application. In the future, we will continue the research work on binary descriptors to resolve this problem and try to embed it in the mobile devices.

References

1. Lowe DG (2004) Distinctive image features from scale-invariant keypoints. Int J Comput Vis 60(60):91–110
2. Ke Y, Sukthankar R (2004) PCA-SIFT: a more distinctive representation for local image descriptors, p 506–513
3. Bay H, Tuytelaars T, Gool LV (2006) SURF: Speeded Up Robust Features. Comput Vis Image Underst 110(3):404–417
4. Calonder M, Lepetit V, Strecha C et al (2010) BRIEF: binary robust independent elementary features. In: European Conference on Computer Vision. Springer-Verlag, p 778–792
5. Rublee E, Rabaud V, Konolige K et al (2011) ORB: an efficient alternative to SIFT or SURF, p 2564–2571
6. Yiliu F, Yichun S, Hengzhu L (2013) The implement of calculating the corner orientation that based on moment in SIFT
7. Mikolajczyk K, Schmid C (2005) A performance evaluation of local descriptors. IEEE Trans Pattern Anal Mach Intell 27(10):1615–1630

Multi-sensor Fault Diagnosis of Aircraft Engine Based on Kalman Filter Group

Jixiang Hu and Lingfei Xiao

Abstract For the problem of Multi-sensor Fault Diagnosis in aircraft engine, according to the theory of Kalman filter, this paper proposed a novel fault diagnosis method based on Kalman filter group. Author used the engine model nonlinear system based on the least square fitting method, and the linear discrete system model of engine was obtained by discrete treatment. On this basis, further considering the effect of engine sensor fault and interferences, successively for single sensor and multi-sensor faults condition, we put forward the aircraft engine sensor fault diagnosis method based on Kalman filter group. The simulation results show that this method can quickly diagnose and have a good diagnostic accuracy for multiple sensor faults and gradual failure of the engine.

Keywords Aircraft engine · Multi-sensor fault diagnosis · Kalman filter group · Residual error

1 Introduction

With the constant improvement of the aircraft engine performance, more and more control signals need to collect and control. The acquisition of the information depends largely on the sensor, therefore, more and more sensors were used in aircraft engine. At the same time, with the variable of control system increase and complex, the number of sensors required and the types of sensors were gradually increase [1]. Aircraft engine working conditions are bad—not only it often works in the environment of high temperature and high pressure conditions, but also it will be flying missions in the fifty degrees below zero in the alpine region and work time is longer in this harsh environment, so the sensor faults occur frequently. Once the sensor fault, it may lead to failure of the entire control system. Therefore, it is

J. Hu · L. Xiao (✉)
College of Energy and Power Engineering, Nanjing University of Aeronautics and Astronautics, Nanjing 210016, China
e-mail: lfxiao@nuaa.edu.cn

Y. Jia et al. (eds.), *Proceedings of 2016 Chinese Intelligent Systems Conference*, Lecture Notes in Electrical Engineering 404, DOI 10.1007/978-981-10-2338-5_36

necessary to deeply study the sensor fault, improve the accuracy of fault location and the rapid response of emergency trouble shooting [2].

In recent years, many scholars have made a lot of research on the fault diagnosis of aircraft engine sensors, and they have made many achievements. A fault diagnosis system based on self associative neural network is designed by Mattern et al. [3], Moller et al. [4] Applied the control system sensor based on self association neural network to the vortex axis engine. Aretakis et al. [5] used pattern recognition technology for sensor fault diagnosis of turbofan engine. Li et al. [6] based on support vector machine regression proposed a sensor fault diagnosis method for a turbofan engine. Lu et al. [7] proposed a kind of self coordinated particle swarm optimization support vector regression algorithm of the fusion mechanism, and it achieved a single sensor and multi-sensor fault accurate judgment. Zhao et al. [8] improved the support vector machine, and they proposed a kind of online learning algorithm OPLS-SVR (parsimonious least squares support vector regression), the algorithm can online diagnose sensor fault and reconstruct signal.

This paper selected a turbofan engine in the form of a steady-state operating point incremental linear mathematical model, we chose engine high speed, low speed, combustion chamber inlet temperature, combustion chamber inlet pressure four sensors as the object of study and we verified the application Kalman filter group of sensor fault diagnosis which was feasible. On the basis of the predecessors, we particularly demonstrated multiple sensors. The results show that this method can effectively monitor both single sensor and multiple sensor faults.

2 Aircraft Engine Model

Aircraft engine system is a complicated and nonlinear system, and its nonlinear model can be expressed as:

$$\begin{cases} \dot{x}(t) = f(x,u) \\ y(t) = h(x,u) \end{cases} \tag{1}$$

Among them, $x(t) \in R^n$ is the state vector of the engine system, $u(t) \in R^p$ is the input vector of the engine system, and $y(t) \in R^m$ is the output vector of the engine system. Engine selects the high pressure rotor speed (N_h), low pressure rotor speed (N_l) as state variables, amount of oil for the control variables, high pressure rotor speed (N_h), low-pressure rotor speed (N_l), combustion chamber inlet temperature (T_3), combustion chamber inlet pressure (P_3) is the output variable. On the basis of the nonlinear component level model, the least square fitting method is used to establish the small deviation state variable model of the engine. As we build a small deviation model near the steady point, we need to linearize at a certain point (x_0, u_0, y_0). In order to simplify the calculation process, and according to the experience of the high order of the system effect is relatively small. So we have

carried out the Taylor series expansion of the nonlinear model in the case of ignoring the high order terms of two or more times:

$$\begin{cases} \dot{x}(t) = f(x,u) \approx f(x_0,u_0) + \frac{\partial f}{\partial x}\Big|_{(x_0,u_0)} \Delta x + \frac{\partial f}{\partial u}\Big|_{(x_0,u_0)} \Delta u \\ y(t) = h(x,u) \approx h(x_0,u_0) + \frac{\partial h}{\partial x}\Big|_{(x_0,u_0)} \Delta x + \frac{\partial h}{\partial u}\Big|_{(x_0,u_0)} \Delta u \end{cases} \tag{2}$$

Among them, $\Delta x(t) = x - x_0$, $\Delta x(t) = x - x_0$, A, B, C, D are the matrix of the state space model, and they are expressed as:

$$A = \frac{\partial f}{\partial x}\Big|_{(x_0,u_0)} \quad B = \frac{\partial f}{\partial u}\Big|_{(x_0,u_0)} \quad C = \frac{\partial h}{\partial x}\Big|_{(x_0,u_0)} \quad D = \frac{\partial h}{\partial x}\Big|_{(x_0,u_0)}$$

In this way, the state variable model can be written as:

$$\begin{cases} \Delta\dot{x}(t) = A\Delta x(t) + B\Delta u(t) \\ \Delta y(t) = C\Delta x(t) + D\Delta u(t) \end{cases} \tag{3}$$

Among them, $\Delta y(t) = h(x,u) - h(x_0,u)$, $x_0(t) \in R^n$, $u_0(t) \in R^p$ and $y_0(t) \in R^m$ are the state vector, the control vector and the output vector of the engine system in the steady state.

The discrete time system of the engine at a steady state operating point is:

$$\begin{cases} \Delta X(k+1) = A(k)\Delta X(k) + B(k)\Delta U(k) + W(k) \\ \Delta Y(k) = C(k)\Delta X(k) + D(k)\Delta U(k) + V(k) \end{cases} \tag{4}$$

Among them, A, B, C and D are the system state transition matrix, the control input coefficient matrix, observation matrix and observation of the control gain matrix; ΔX, ΔY, W and V are the system state vector, the observation vector, system dynamic noise and measurement noise vector. It is assumed that both W and V are zero mean and independent white noise [9]:

$$\begin{gathered} E[W(k)] = 0, \\ \operatorname{cov}[W(k), W(j)] = E\left[W(k)W(j)^T\right] = Q(k)\delta_{k-j}; \\ E[V(k)] = 0, \\ \operatorname{cov}[V(k), V(j)] = E\left[V(k)V(j)^T\right] = R(k)\delta_{k-j}; \\ \operatorname{cov}[W(k), V(j)] = E\left[W(k)V(j)^T\right] = 0. \end{gathered} \tag{5}$$

Among them, δ_{k-j} is the Kronecker-delta function, they is:

$$\delta_{k-j} = \begin{cases} 1 & k = j \\ 0 & k \neq j \end{cases} \tag{6}$$

$Q(k)$ is the symmetric nonnegative definite matrices, $W(k)$ is the covariance matrix, $R(k)$ is a symmetric positive definite matrix, and $V(k)$ is the variance matrix.

The initial state of the system $X(0)$ is Gauss random vector, whose mean and variance are:

$$\begin{aligned} X_0 &= E[X(0)] \\ P_0 &= Var[X(0)] \end{aligned} \tag{7}$$

The initial state of the system $X(0)$ is not related to the system noise $W(k)$ and the observation noise $V(k)$, and the expressions are:

$$\begin{aligned} \text{cov}[X(k), W(k)] &= 0 \\ \text{cov}[X(k), V(k)] &= 0 \end{aligned} \tag{8}$$

The observation noise is related to the observation equipment, and should not be related to the initial state of the system itself.

When the sensor fault occurs, the fault model of the aircraft engine is generally expressed as:

$$\begin{cases} \dot{x} = Ax + Bu + w \\ y = Cx + Du + v + Ef_a \end{cases} \tag{9}$$

Among them, $E \in R^{m \times q}$ refers to the sensor fault distribution matrix, $f_a \in R^q$ refers to the impact of failure on the system output function [10].

The fault of aircraft engine sensor is varied, and it can be expressed as the following two kinds:

(1) Sensor bias fault
Sensor bias fault model can be described as:

$$y_o = y_i + \Delta \tag{10}$$

Among them, Δ is a constant, y_o is the output of the sensor, and y_i is the sensor input. When $\Delta = 0$, the sensor works properly.

(2) Sensor drift fault
Sensor drift fault model can be described as:

$$y_o = p \cdot y_i \tag{11}$$

Among them, p is the ratio coefficient of the drift fault. When $p = 0$, the sensor does not work; when $p = 1$, the sensor is working properly.

3 Aircraft Engine Sensor Fault Diagnosis System Design

We design a sensor fault diagnosis system as shown in Fig. 1. From Fig. 1, we can see the engine will be the actual measure signal after a fault diagnosis system (as shown in Fig. 2) with the given signal to do bad, and then into the controller, to complete the engine control. From Fig. 2 we can see that the actual measurement signal from the sensor transmitted into the Kalman filters, all measurements are estimated, and then the estimated values are compared with the actual values, We can determine whether the sensor faults occur at this time and the type of fault.

3.1 Single Sensor Fault Diagnosis

Kalman filter in the process of the sensor signal filtering, when a sensor failure, the estimated value of this filter and observed value has a larger error. According to the characteristics of Kalman filter, we consider that the fault diagnosis of engine sensor use a set of Kalman filters, as shown in Fig. 3.

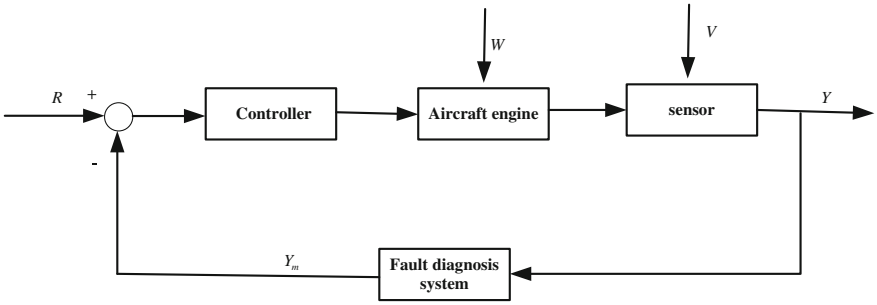

Fig. 1 Aircraft engine control system

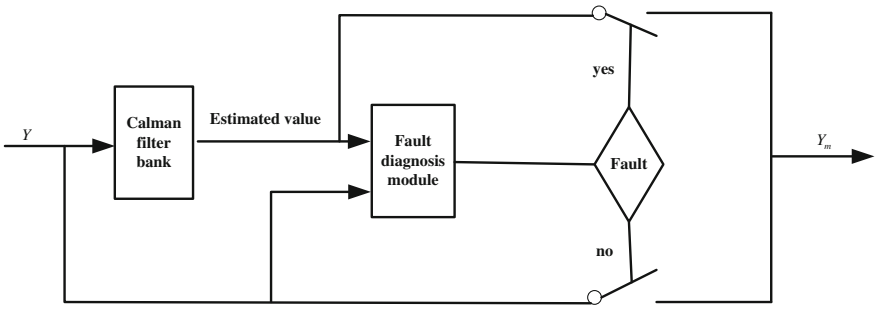

Fig. 2 Aircraft Engine sensor fault diagnosis system

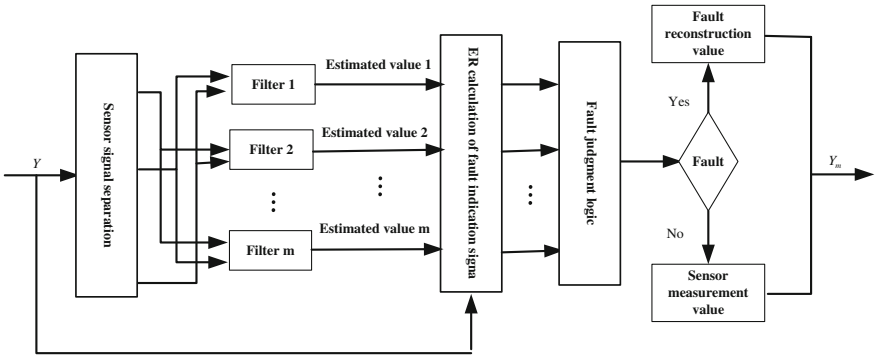

Fig. 3 Single sensor fault diagnosis system

The engine control system have m sensor signal, we should design m Kalman filters, each filter only input $m-1$ signals. The i-th Kalman filter as an example, it contains the remaining $m-1$ signals except the i-th sensor input. When the i-th sensor failure, except the i-th filter, other filter estimation value which access fault sensor signal and actual measurement values exist large deviation, so we can judge this sensor failures. Also, the estimated value of the i-th filter is not connected to the fault sensor, and the error of the estimated value is smaller than the actual measurement.

In order to improve the accuracy of sensor fault detection, the fault information is enlarged by the method of residual weighted sum of squares. The difference between the output of the Kalman filter and the output of the sensor is called residual, and the residual e of the first i-th Kalman filter is expressed as follows:

$$e^i = \widehat{Y}^i - Y \quad (i = 1, 2, \ldots, m) \tag{12}$$

In the Equation, $\widehat{Y}^i$ is the output of the filter and Y (high pressure rotor speed Nh, low-pressure rotor speed Nl, combustion chamber inlet temperature $T3$, combustion chamber inlet pressure $P3$) is the output of the linearized model. The calculation method of residual error is as follows:

$$ER_i = (e^i)^T \left[\mathrm{diag}(\sigma^j)^2\right]^{-1} e^i \quad (j = 1, 2, \ldots, i-1, i+1, \ldots, m) \tag{13}$$

Among them, σ^j is used to measure the sensor's measurement noise and its own characteristics of a standard deviation. When the sensor fault, because the residual e is the Gauss distribution with zero mean, and the variance is a positive definite symmetric matrix, then ER obey χ^2 distribution; when the sensor fails, the characteristics of white residual e was destroyed, the value of ER will be changed greatly, so we diagnose the sensor failures.

3.2 *Multiple Sensors Fault Diagnosis*

In the actual project, sometimes there will be multiple sensors fault, fault diagnosis system as shown in Fig. 3 will not be able to detect multiple sensors failures happen at the same time, therefore we need to improve the structure. Design the following fault diagnosis structure as shown in Fig. 4.

In the structure shown in Fig. 3, we add a Kalman filter, and the filter input signal contains all monitored sensors. According to the Eq. (13), we calculated the corresponding residual error of the zero-th Kalman filters: ER_0. We define variable LR_i, order:

$$LR_i = ER_0 - ER_i \tag{14}$$

For each monitored sensor, a threshold value is set to compare with the corresponding *LR*, which is used to judge whether the sensor is faulty. When a *LR* value is greater than the corresponding threshold, we can determine the corresponding sensor fault; when multiple *LR* values are greater than the corresponding threshold, we can determine multiple sensors faults exist at the same time. When multiple sensor faults, we can't use a Kalman filter of the estimated value for signal reconstruction, this time we directly use the simplify real-time model for signal reconstruction.

4 Simulation

According to the method in Sect. 1.2, the linear model of an aircraft engine at the steady state (H = 0, Ma = 0) can be given as Eq. (4), where *A*, *B*, *C* and *D* are shown as follows:

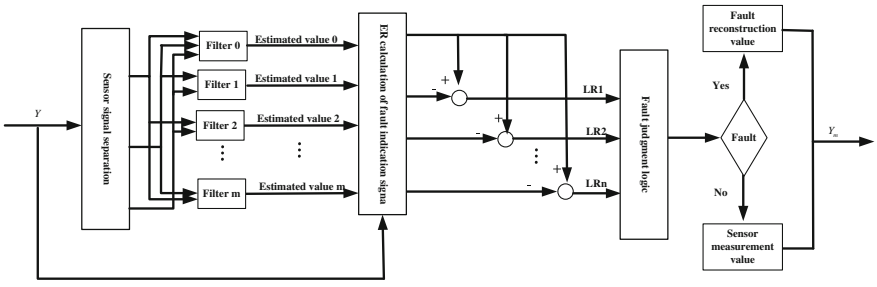

Fig. 4 Multiple sensors fault diagnosis system

$$A = \begin{bmatrix} 0.6330 & 0.2396 \\ -0.4136 & 1.2626 \end{bmatrix} \quad B = \begin{bmatrix} -0.0069 \\ -0.0044 \end{bmatrix}$$

$$C = \begin{bmatrix} 1 & 0 \\ 0 & 1 \\ -1.1473 & 1.2401 \\ -4.0467 & 4.2069 \end{bmatrix} \quad D = \begin{bmatrix} 0 \\ 0 \\ -0.0039 \\ -0.0179 \end{bmatrix}$$

Figure 5 shows the high pressure speed sensor has a hard fault ($f_a = 0.02$), the dotted line is the threshold. From Fig. 5, we can see that only ER_1 is less than the threshold value, it can be judged that the fault of the high pressure speed sensor.

In Fig. 6, the fault diagnosis effect of a single sensor with high pressure speed is given. The dotted line is the threshold. In fifth seconds, we added drift fault. We can know that ER_1 of high pressure speed sensor is not beyond the threshold value.

Figure 7 shows the system's diagnostic effect which the high pressure speed sensor and the turbine inlet gas temperature sensor have hard fault ($f_a = 0.02$). It can be found that in the period of the corresponding fault occurs, $LR1$ and $LR3$ exceed the threshold value, so we can determine the high pressure speed sensor and the turbine inlet gas temperature sensor fault.

Figure 8 shows a soft fault high speed sensor and turbine inlet gas temperature sensor soft fault diagnosis results, the dotted line is the threshold. From the figure, we can see the fault in the corresponding period, $LR1$ and $LR3$ exceeds the threshold, so we can determine the high rotational speed sensor and the turbine inlet gas temperature sensor fault.

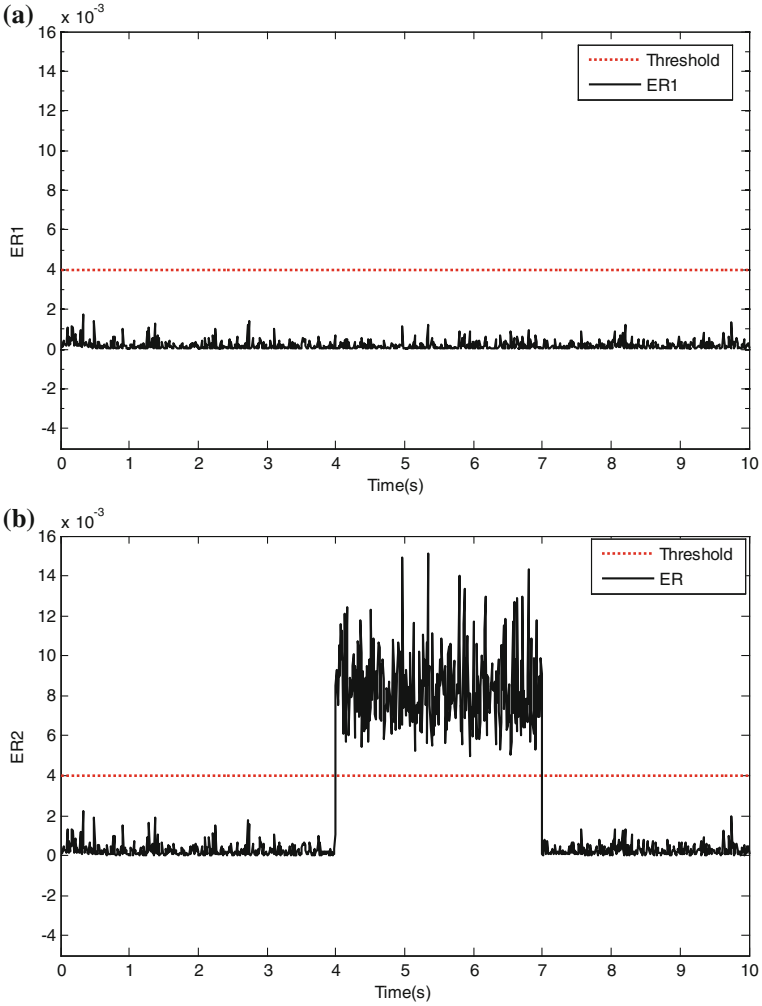

Fig. 5 High pressure speed sensor hard fault ($f_a = 0.02$) diagnosis effect chart. **a** High pressure rotor speed sensor (*Nh*) residual diagram. **b** Low pressure rotor speed sensor (*Nl*) residual diagram. **c** Turbine inlet gas temperature sensor ($T3$) residual diagram. **d** Turbine inlet gas pressure sensor ($P3$) residual diagram

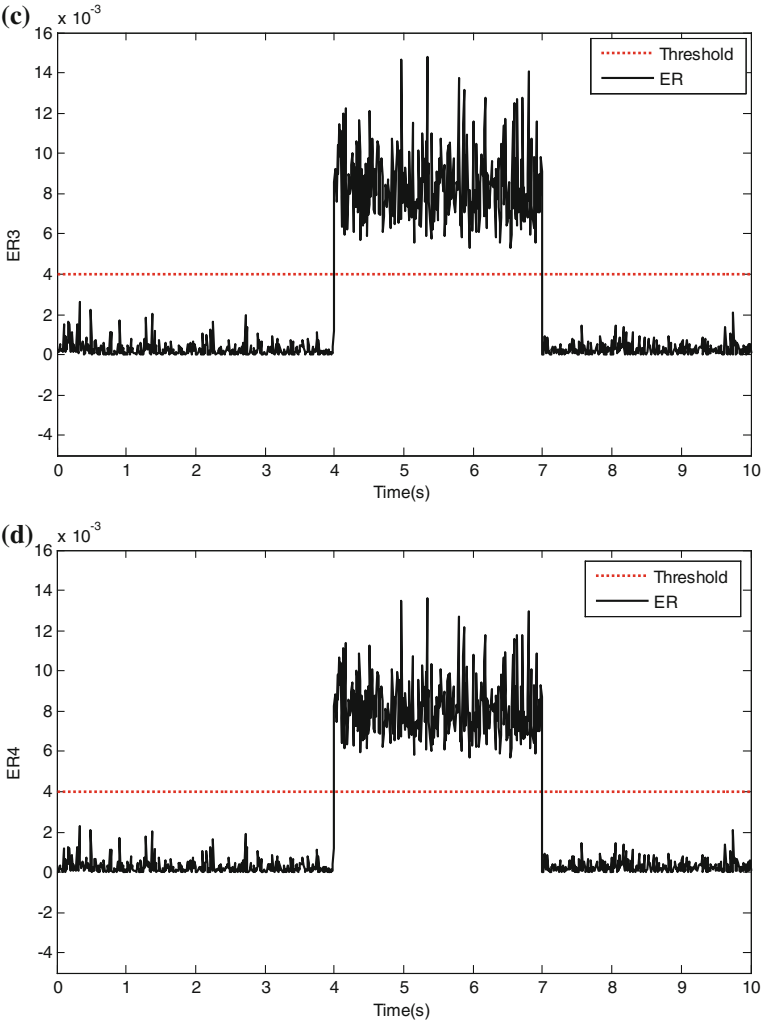

Fig. 5 (continued)

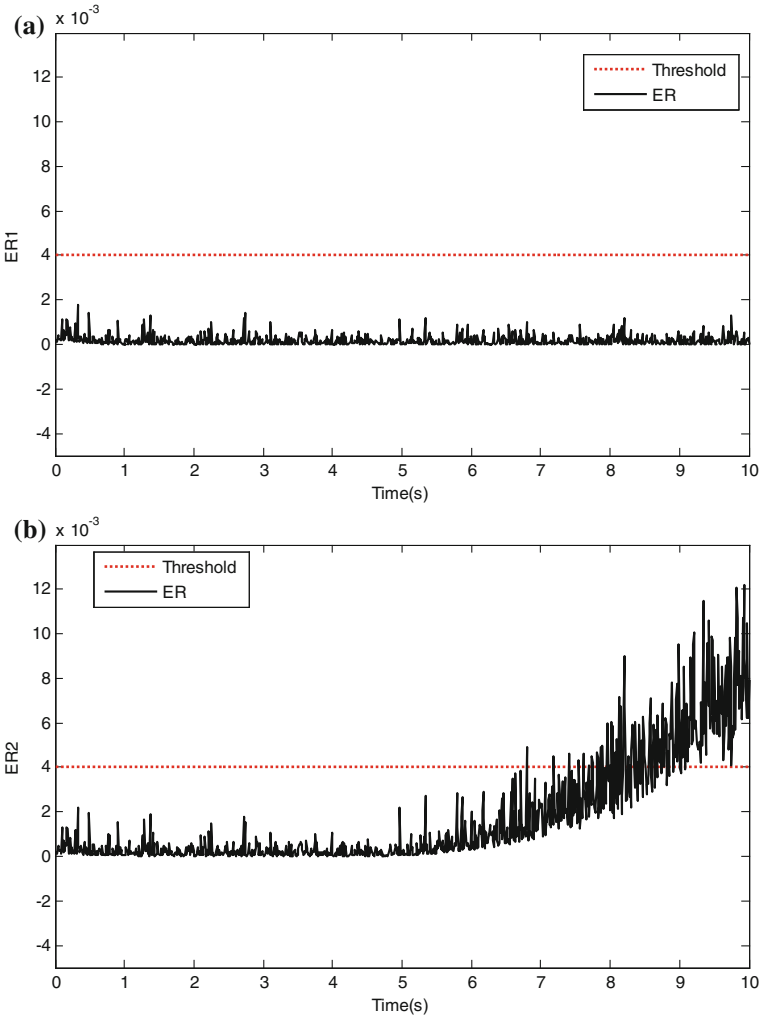

Fig. 6 High pressure speed sensor soft fault diagnosis effect chart. **a** High pressure rotor speed sensor (*Nh*) residual diagram. **b** Low pressure rotor speed sensor (*Nl*) residual diagram. **c** Turbine inlet gas temperature sensor (*T*3) residual diagram. **d** Turbine inlet gas pressure sensor (*P*3) residual diagram

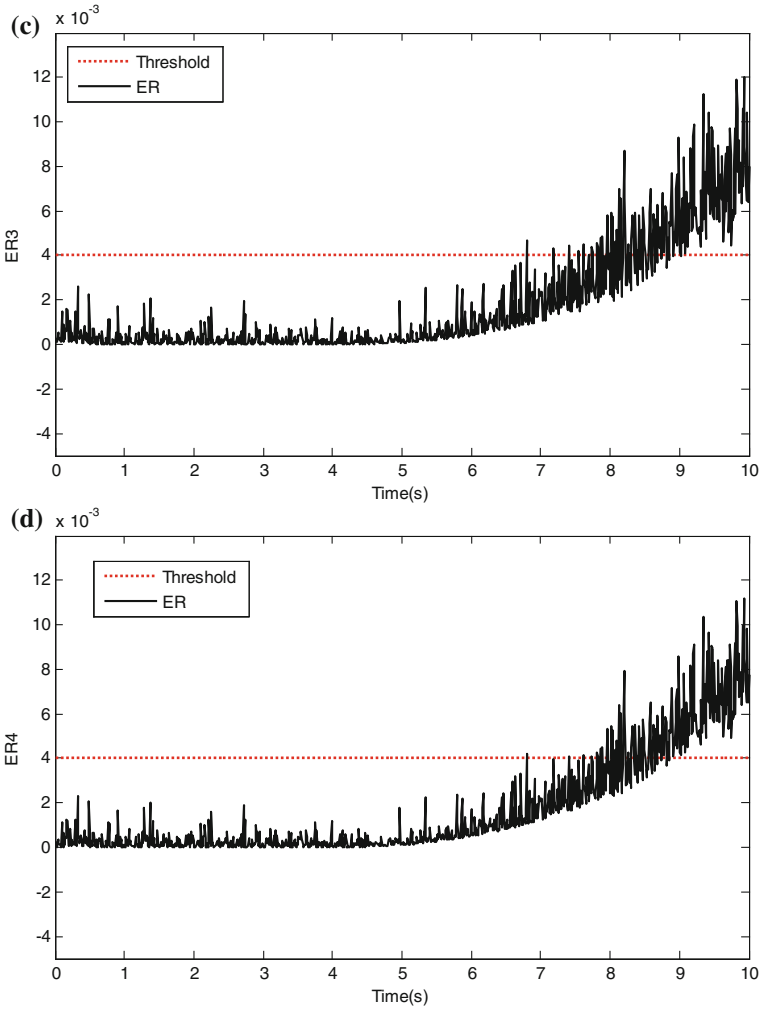

Fig. 6 (continued)

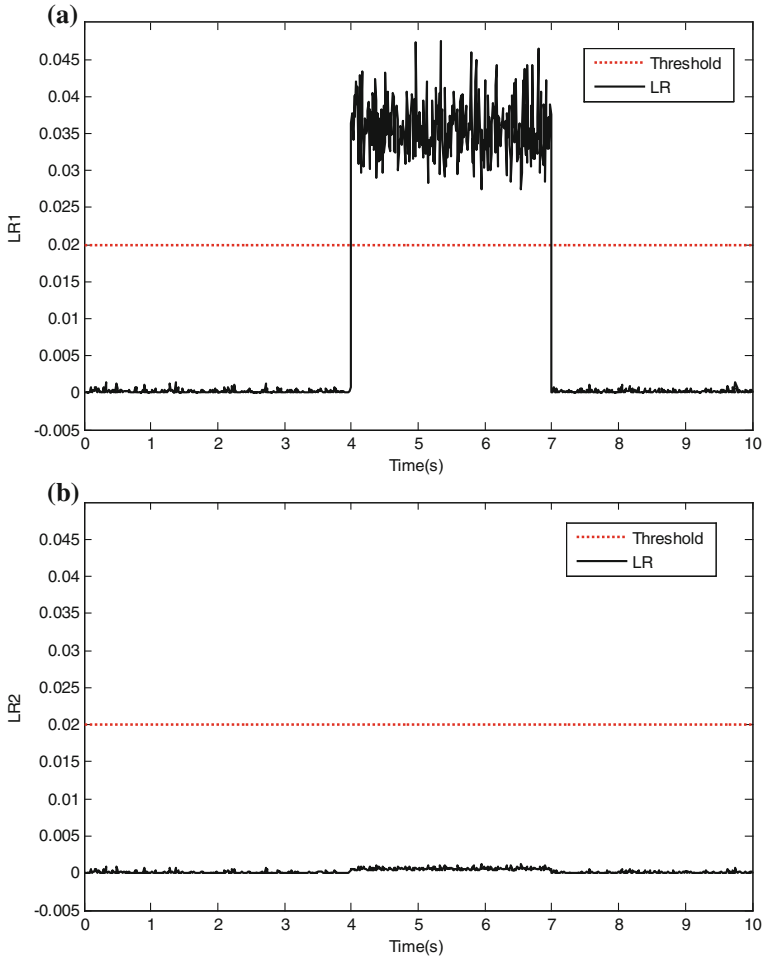

Fig. 7 High pressure speed sensor and turbine inlet gas temperature sensor hard fault diagnosis effect chart. **a** High pressure rotor speed sensor (*Nh*) residual diagram. **b** Low pressure rotor speed sensor (*Nl*) residual diagram. **c** Turbine inlet gas temperature sensor (*T*3) residual diagram. **d** Turbine inlet gas pressure sensor (*P*3) residual diagram

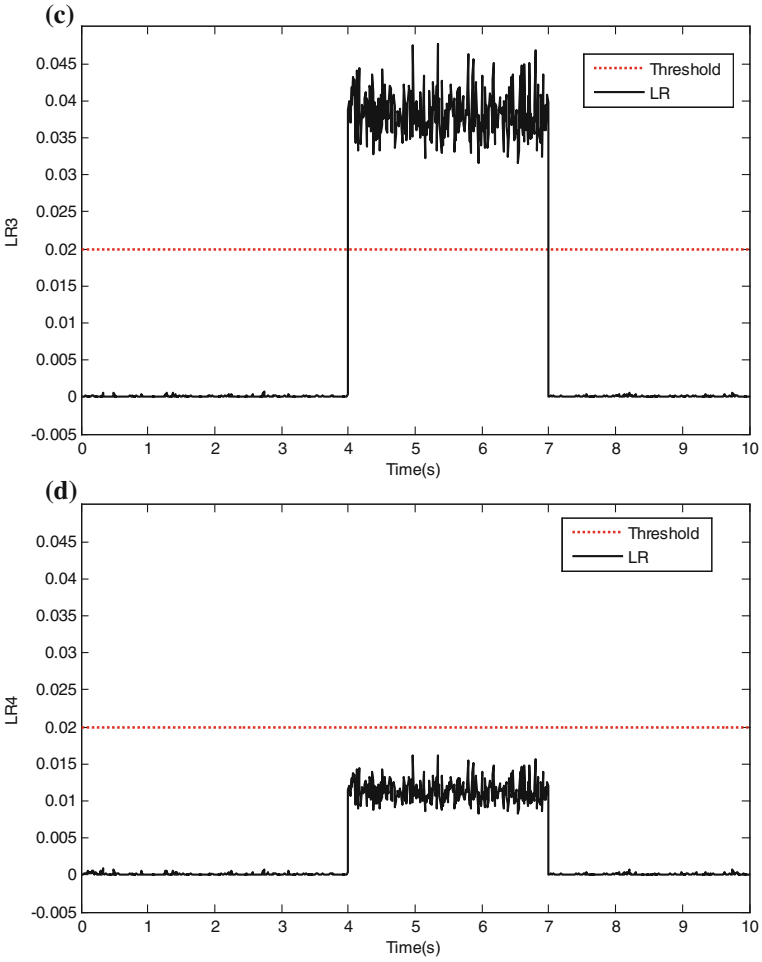

Fig. 7 (continued)

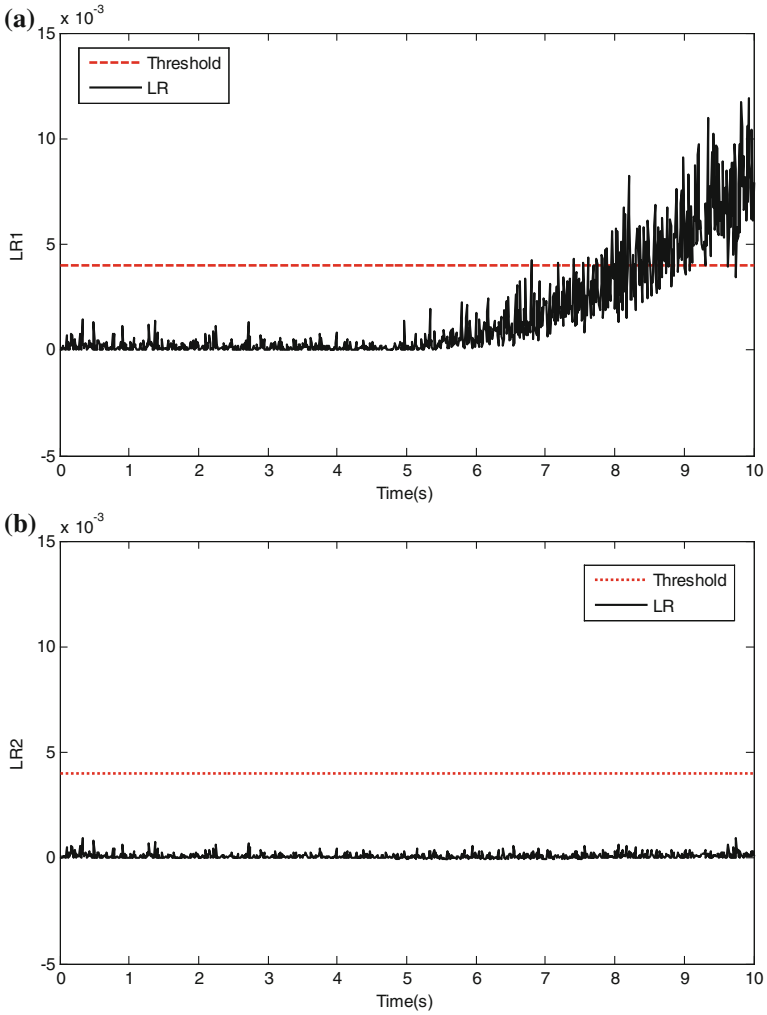

Fig. 8 High pressure speed sensor and T3 temperature sensor soft fault diagnosis effect chart. **a** High pressure rotor speed sensor (*Nh*) residual diagram. **b** Low pressure rotor speed sensor (*Nl*) residual diagram. **c** Turbine inlet gas temperature sensor (*T*3) residual diagram. **d** Turbine inlet gas pressure sensor (*P*3) residual diagram

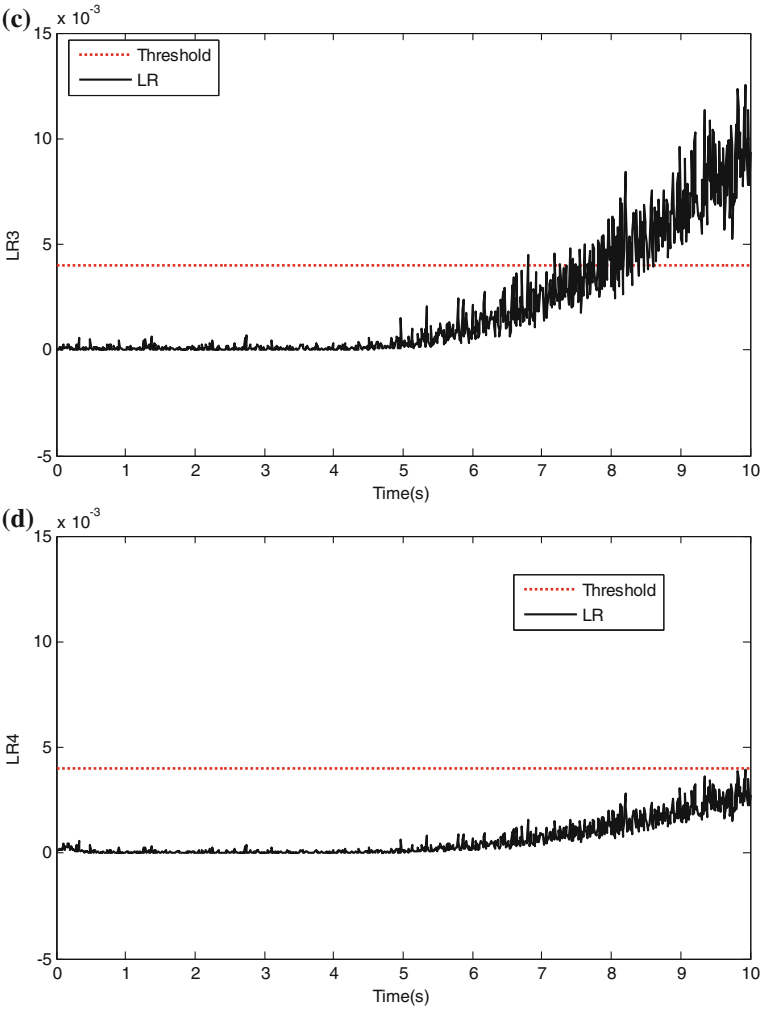

Fig. 8 (continued)

5 Conclusions

In this paper, the problem of frequent sensor failures was studied. The purpose of fault diagnosis was achieved by the design for a set of Kalman filters based on Kalman filter theory. Through the simulation, the design for sensor fault diagnosis system in the selection of threshold, whether it had a single sensor or multiple sensors can be completed, and the fault detection and isolation of fault was finished. The process mainly has two aspects: the realization of Kalman filter and the formation of fault modeling. From the simulation, Kalman filter has a good filtering

performance, and the estimated value can be really close to the measured value of the sensor. Once the sensor failure, the system can determine the fault sensor and complete the task of fault diagnosis quickly and accurately.

References

1. Xiang X (2004) Turbofan engine sensor fault diagnosis and fault tolerant control research [D]. Northwestern Polytechnical University, Xi'an
2. Gaoqian Z (2014) Fault diagnosis and fault tolerant control of aircraft engine sensor [D]. Nanjing University of Aeronautics and Astronautics, Nanjing
3. Mattern DL, Jaw LC, Guo T-H et al (1998) Using eural networks for sensor validation [M]. National Aeronautics and Space Administration, Lewis Research Center pp 73–114
4. Moller JC, Litt JS, Guo T-H (1998) Neural network-based sensor validation for turboshaft engines [R]. AIAA 98–3605
5. Aretakis N, Mathioudakis K (2004) A. stamatis. Identification of sensor faults on turbofan engines using pattern recognition techniques [J]. Control Eng Pract 12(7):827–836
6. Benwei L, Zhaoyuan F, Yonghua W et al (2007) Research on sensor fault diagnosis of X type engine based on SVR [J]. J Aerosp Power 22(10):1754–1759
7. Feng L, Jinquan H, Li C et al (2009) Fault diagnosis of fusion aero engine sensor based on SPSO-SVR [J]. J Aerosp Power 24(8):1856–1865
8. Yongping Z, Jianguo S, Jiankang W (2009) Online parsimonious least squares support vector regression and its application [J]. Trans Nanjing Univ Aeronaut Astronaut 26(4):280–287
9. Zhao C (2012) Theoretical and experimental research on fault diagnosis and signal reconstruction of aero engine sensor [D]. Nanjing University of Aeronautics & Astronautics, Nanjing
10. Shiquan Y (2014) Fault diagnosis and fault tolerant control of aero engine actuator [D]. Nanjing University of Aeronautics & Astronautics, Nanjing

Non-negative Matrix Semi-tensor Factorization for Image Feature Extraction and Clustering

Chi Ben, Zhiyuan Wang, Xuejun Yang and Xiaodong Yi

Abstract Non-negative Matrix Factorization (NMF) has been frequently applied to image feature extraction and clustering. Especially in image clustering tasks, it can achieve the similar or better performance than most of the matrix factorization algorithms due to its parts-based representations in the brain. However, the features extracted by NMF are not sparse and localized enough and the error of factorization is not small enough. Semi-tensor product of matrices (STP) is a novel operation of matrix multiplication, it is a generalization of the conventional matrix product for allowing the dimensions of factor matrices to be unequal. STP can manage the data hierarchically and the inverse process of STP can separate the data hierarchically. Based on this character of STP, we propose the Non-Negative Matrix Semi-Tensor Factorization (NMSTF). In this algorithm, we use the inverse process of Semi-Tensor Product of matrices for non-negative matrix factorization. This algorithm effectively optimizes the above two problems in NMF. While achieving similar even better performance on image clustering tasks, the size of features extracted by STNMF is at least 50 % smaller than the ones' extracted by NMF and the error of factorization reduces 30 % in average.

Keywords Non-negative Matrix Semi-tensor Factorization · Non-negative Matrix Factorization · Semi-tensor Product of matrices · Image feature extraction · Clustering

1 Introduction

With the development of computer science, robotics, and artificial intelligence in recent years, computer vision has higher requirements than before. Though the input data always have high dimension, this question makes learning from example

C. Ben · Z. Wang (✉) · X. Yang · X. Yi
State Key Laboratory of High Performance Computing (HPCL),
College of Computer, National University of Defense Technology,
137 Yanwachi Street, Changsha 410073, Hunan, People's Republic of China
e-mail: wang_zhiyuan17@163.com

Y. Jia et al. (eds.), *Proceedings of 2016 Chinese Intelligent Systems Conference*,
Lecture Notes in Electrical Engineering 404, DOI 10.1007/978-981-10-2338-5_37

infeasible [1]. The techniques for matrix factorization can effectively solve the problem of high dimension. The common matrix factorization techniques include Triangular Factorization, QR Factorization, Vector Quantization and Singular Value Decomposition (SVD). They aim to find two or more lower dimension matrices and their product is well approximated to the original one. Among these algorithms, SVD has been applied to various applications such as face recognition tasks [2].

However, because negative numbers are lack of practical meanings in image, the features extracted by these algorithms are difficult to understand. Previous studies have shown that there is psychological and physiological evidence for parts-based representations in the brain [3, 4], and certain computational theories of object clustering rely on such representations. The Non-negative Matrix Factorization (NMF) [5] learns the parts of objects like human faces. It aims to find two non-negative matrices whose product is well approximated to the original one. The non-negative constraints lead to a parts-based representation because they allow only additive, not subtractive, combinations [6]. NMF is superior to the common matrix factorization techniques for its 'eigenfaces' are localized features that correspond better with intuitive notion of the parts of faces. Nonetheless, NMF also has some weakness, such as feature images are not localized enough and error of the factorization is not small enough [7, 8].

Semi-tensor product (STP) of matrices is a novel operation of matrix multiplication [9]. It is a generalization of the conventional matrix product for the case when the dimensions of the factor matrices do not satisfy the requirement. Consider two matrices $A \in M_{m\times n}$ and $B \in M_{p\times q}$. For simple declaration, when $n = p$, A and B are said to satisfy matching dimension condition, as n is a factor of p or p is a factor of n, they are said to satisfy factor dimension condition, otherwise, they have general dimensions. STP of A and B is well defined for the above three cases and it is coincide with the conventional matrix one in matching dimension case [10]. STP for the factor dimension condition is widely used in many applications, such as dynamic system [11], abstract algebra [12], and mathematical logic [13]. In these applications, STP has shown the advantage of hierarchically seeking and matching the data. Specifically, data can seek and match their parameter according to their level. For this reason, STP can solve the problem with high dimension data effectively.

In this paper we propose a novel algorithm called Non-negative Matrix Semi-tensor Factorization (NMSTF), which uses the inverse process of semi-tensor product to for non-negative matrix factorization. As STP allows matrices with factor dimension condition to multiply, we can control the size of basis images by adjusting the multiple of factor dimension condition. We use a modified matrix factorization objective function and develop an optimization scheme to solve the objective function based on iterative updates of the two factor matrices.

Here are several highlights of our approach

(1) We first propose using the inverse process of semi-tensor product for non-negative factorization. We constitute the dimensions and parameter of the factor matrices to make sure that feature images are smaller and more localized.

(2) According to the above constitution, we rewrite the factorization formula and the objective function. Then we calculate the multiplicative updating rules for NMSTF based on Lagrange Multiplier method and the KKT conditions.
(3) Our clustering experiments on ORL, PIE, COIL20 datasets show that feature images obtained by our algorithm are at least 50 % smaller than by NMF, and they are more localized. the objective function is convergent by using our updating rules and the objective function value of NMSTF are 30 % smaller in average than the errors of NMF.

The rest of the paper is organized as follow: in Sect. 2, we introduce our related works. Section 3 introduces our algorithm and provides a inference of our update rules. Experimental results and analysis are shown in Sect. 4. In Sect. 5, we sum up our work and provide some points for our future work.

2 Related Works

This section is a brief review on non-negative matrix factorization and semi-tensor product of matrices. It plays an important role in the following paper. Meanwhile, we only use the left semi-tensor product for factor dimension case in this paper.

2.1 Non-negative Matrix Factorization

Non-negative matrix factorization [5] is a matrix factorization algorithm that all the datas in the matrices are non-negative. Given a data matrix $V \in M_{m\times n}$, that each column is a sample vector. NMF tries to find two matrices $W^N \in M_{m\times r}$ and $H^N \in R_{r\times n}$ ($r \ll m$ and $r \ll n$) which product is approximate to the original matrix.

$$V \approx W^N \cdot H^N \tag{1}$$

There are two common objective functions to evaluate the quality of approximation. One is called the euclidean distance function which is the square of the F-norms of two matrices' difference [14].

$$O_1 = \left\| V - W^N H^N \right\|^2 = \sum_{i,j} \left(v_{ij} - \left(W^N H^N \right)_{ij} \right)^2 \tag{2}$$

The other is called the divergence function which is reduces to the Kullback-Leibler divergence [15].

$$O_2 = D\left(V \parallel W^N H^N \right) = \sum_{i,j} \left(v_{ij} \log \frac{v_{ij}}{\left(W^N H^N \right)_{ij}} - v_{ij} + \left(W^N H^N \right)_{ij} \right) \tag{3}$$

Unfortunately, both of the objective functions cannot be convex in W^N and H^N together, they are convex only in W^N or only in H^N. So the global minimum is impossible to find. Lee and Seung provided two iterative update algorithms. For minimizing the euclidean distance function O_1, the update rules are as follow:

$$W_{ir}^N = W_{ir}^N \frac{\left(V(H^N)^T\right)_{ir}}{\left(W^N H^N (H^N)^T\right)_{ir}} \quad H_{rj}^N = H_{rj}^N \frac{\left((W^N)^T V\right)_{rj}}{\left((W^N)^T W^N H^N\right)_{rj}} \tag{4}$$

The update rules for minimizing the divergence function are:

$$W_{ir}^N = W_{ir}^N \frac{\sum_j H_{rj}^N V_{ij} \Big/ \left(W^N H^N\right)_{ij}}{\sum_j H_{rj}^N} \quad H_{rj}^N = H_{rj}^N \frac{\sum_i W_{ir}^N V_{ij} \Big/ \left(W^N H^N\right)_{ij}}{\sum_i W_{ir}^N} \tag{5}$$

It is proved that both of the above rules can find the local minimum [15]. Then we discuss the algorithm in each column of V.

$$V_i \approx \sum_{j=1}^{r} W_j^N h_{ji}^N \tag{6}$$

V_i is approximate to a linear combination of the columns of W^N, and the weights are the elements of H_i^N. So matrix W^N can be regarded as 'basis matrix' and matrix H^N can be regarded as 'coefficient matrix'. The non-negative constraints on W^N and H^N makes NMF can learn a parts-based representation because they allow only addictive among different basis vectors.

2.2 *Left Semi-tensor Product*

Left semi-tensor product for factor dimension is a generalization of the conventional matrix product [9, 10]. NMF uses the conventional matrix product to approximate V, NMSTF uses the left semi-tensor product and it is defined as follow:

(1) Let W be a row vector of dimension of np, and H be a column vector of dimension of p. Then we split W into p equal size blocks as $W^1, W^2, \ldots, W^p$, which are $1 \times n$ rows. Define the left STP, denote by $\ltimes$, as

$$\begin{cases} W \ltimes H = \sum_{i=1}^{p} W^i h_i \in R^n, \\ H^T \ltimes W^T = \sum_{i=1}^{p} h_i \left(W^i\right)^T \in R^n. \end{cases} \tag{7}$$

(2) Let $W \in M_{m\times n}$ and $H \in M_{p\times q}$. If either n is a factor of p, say $nt = p$ and denote it as $W \prec_t H$, or p is a factor of n, say $n = pt$ and denote it as $W \succ_t H$, then we define the left STP of W and H, denote by $V = W \ltimes H$, as the following: V consists of $m \times q$ blocks as $V = (V^{ij})$ and each block is

$$V^{ij} = W^i \ltimes H_j, \;\; i = 1, 2, \ldots, m, \; j = 1, 2, \ldots, q, \tag{8}$$

where W^i is i^{th} row of W and H_j is j^{th} column of H.

Left STP allows the factor matrices not to satisfy matching dimension condition, therefore matrix factorization using the rule of left STP can get factor matrix with lower dimension.

In this paper, we use the inverse process of left STP into non-negative matrix factorization, in order to extract a parts-based feature with lower dimension. This makes basis vectors become more localized and more independent.

3 Non-negative Matrix Semi-tensor Factorization

In this section, we describe the optimization problem of non-negative matrix semi-tensor factorization including objective function. Then give the updating rules minimizing the euclidean distance function.

3.1 NMSTF with Euclidean Distance

NMSTF is an optimization problem. In order to make the feature images smaller and sparser, we constitute the dimensions and parameter as follows:

Give a data matrix $V \in M_{m\times n}$, NMSTF aims to find two low-dimension matrices $W \in M_{\frac{m}{l}\times r}$ and $H \in M_{lr\times n}$ whose elements are non-negative. Objective function is euclidean distance, as follows:

$$O = \|V - W \ltimes H\|^2 \tag{9}$$

According to the description of this optimization problem, NMSTF is an extension of NMF. When $l = 1$, NMSTF is the same as NMF.

3.2 Updating Rules to Minimizing Objective Function

The euclidean distance function can not be convex in both W and H, it can only be convex in W or convex in H at the same time [5]. Therefore, it is not expected to find

the global minimum. We give a iterative algorithm that can achieve local minimum. In the following, we discuss how to minimize the objective function O. O can be written as follows:

$$\begin{aligned} O &= Tr((V - W \ltimes H)(V - W \ltimes H)^T) \\ &= Tr(VV^T) - 2Tr(V(H^T \ltimes W^T)) + Tr((W \ltimes H)(H^T \ltimes W^T)) \end{aligned} \tag{10}$$

This equality is correct because semi-tensor product satisfies the associative law and distribution law and $Tr(AB) = Tr(BA), Tr(A) = Tr(A^T)$, $Tr()$ is the function to calculate the trace.

To minimize O, we use the Lagrange Multiplier method and the KKT conditions. Let $A \in M_{\frac{m}{l} \times r}$ and $B \in M_{lr \times n}$ be the Lagrange Multiplier to make sure that all the elements in W and H is non-negative. So the Lagrange function L is

$$\begin{aligned} L = &Tr(VV^T) - 2Tr(V(H^T \ltimes W^T)) \\ &+ Tr((W \ltimes H)(H^T \ltimes W^T)) \\ &+ Tr(AW^T) + Tr(BH^T) \end{aligned} \tag{11}$$

The partial derivatives of L with respect to all the elements in W and H are

$$\frac{\partial L}{\partial W_{ir}} = -2Tr([V \ltimes H^T]_{ir}) + 2Tr([W \ltimes H \ltimes H^T]_{ir}) + A_{ir} \tag{12}$$

$$\frac{\partial L}{\partial H_{rj}} = -2(W^T \ltimes V)_{rj} + 2(W^T \ltimes W \ltimes H)_{rj} + B_{rj} \tag{13}$$

In above equations, $(X)_{rj}$ means the element in the *rth* row and the *jth* column of X, $[X]_{ir}$ is a submatrix. For example, $V \ltimes H^T$ is a matrix of $m \times lr$, we split this matrix into $\frac{m}{l} \times r \; l \times l$ submatrixs, $[V \ltimes H^T]_{ir}$ is the submatrix whose coordinate is (i, r).

According to the KKT conditions, $A_{ir} \times W_{ir} = 0$ and $B_{rj} \times H_{rj} = 0$, we can get the following equations:

$$-2Tr([V \ltimes H^T]_{ir}) \times W_{ir} + 2Tr([W \ltimes H \ltimes H^T]_{ir}) \times W_{ir} = 0 \tag{14}$$

$$-2(W^T \ltimes V)_{rj} \times H_{rj} + 2(W^T \ltimes W \ltimes H)_{rj} \times H_{rj} = 0 \tag{15}$$

These equations lead to the following updating rules:

$$W_{ir} = W_{ir} \frac{Tr([V \ltimes H^T]_{ir})}{Tr([W \ltimes H \ltimes H^T]_{ir})} \tag{16}$$

$$H_{rj} = H_{rj} \frac{(W^T \ltimes V)_{rj}}{(W^T \ltimes W \ltimes H)_{rj}} \tag{17}$$

When $l = 0$, it is clear that $[X]_{ir}$ is same as $(X)_{ir}$ and $X \ltimes Y$ is same as $X \times Y$. Therefore, the updating rules reduce to the updating rules of NMF.

For this objective function, there are many solutions using matrix multiplication. Such as W^N and H^N is a solution, then for any diagonal matrix D^N, $W^N D^N$ and $(D^N)^{-1} H^N$ is also a solution. To eliminate the uncertainty, people find a diagonal matrix D^N to make each column vector in $W'^N = W^N D$ equals to 1. At the same time, H^N is adjusted to $H'^N = D^{-1} H^N$ to make sure that $W'^N H'^N = W^N H^N$. Using semi-tensor product of matrix, it is also not unique and our STNMF also can adopt this strategy. We find a diagonal matrix $D \in M_{r \times r}$ to make each column vector in $W' = WD$ equals to 1, and H is adjusted to $H' = D'H$ to make sure that $W' \ltimes H' = W \ltimes H$. If $D = (D(i,i)), i = 1, 2, \ldots, r$, $D' = D'(j,j), j = 1, 2, \ldots, lr$.

$$D'(j,j) = \frac{1}{D(i,i)}, j = (i-1)l + 1, (i-1)l + 2, \ldots, il \tag{18}$$

3.3 Computational Complexity Analysis

In this subsection, we compare the computational complexity between our proposed algorithm STNMF and NMF. In order to clearly see the difference between STNMF and NMF, we express the complexity by counting arithmetic operations. According to the updating rules, we count the number of arithmetic operations and summarize the results in Table 1.

It is easy to count the operations of NMF. In the following, we calculate the operations of STNMF. To calculate all $Tr([V \ltimes H^T]_{ir})$ need mnr floating point additions and mnr floating point multiplications, while calculating all $Tr([W \ltimes H \ltimes H^T]_{ir})$ need $2mnr$ floating point additions and $2mnr$ floating point multiplications. To calculate $W^T \ltimes V$ needs mnr floating point additions and mnr floating point multiplications, while calculating $W^T \ltimes W \ltimes H$ needs $(\frac{m}{l} + ln)r^2$ floating point additions and $(\frac{m}{l} + ln)r^2$ floating point multiplications.

Table 1 Arithmetic operations of NMF and STNMF

	fladd	flmlt	fldiv	overall
NMF	$2mnr + 2(m+n)r^2$	$2mnr + (m+n)r + 2(m+n)r^2$	$(m+n)r$	O(mnr)
NMSTF	$4mnr + (\frac{m}{l} + ln)r^2$	$4mnr + (\frac{m}{l} + ln)(r^2 + r)$	$(\frac{m}{l} + ln)r$	O(mnr)

fladd: floating point addition
flmlt: floating point multiplication
fldiv: floating point division
l: the reduced multiple of basis image
n: the number of images
m: the number of image pixels
r: the number of basis images

In summary, $4mnr + (\frac{m}{l} + ln)r^2$ additions, $4mnr + (\frac{m}{l} + ln)(r^2 + r)$ multiplications and $(\frac{m}{l} + ln)r$ divisions are needed in one iteration. As $\frac{m}{l}r + lnr < mn$ results in $(\frac{m}{l} + ln)r^2 < mnr$. The overall complexity is $O(mnr)$.

4 Experiment

Previous works show that NMF works well on image feature extraction and clustering. An image can be seen as a combination of many parts. For example, a face image can be seen as a combination of nose, mouse, eyes, etc. NMF get basis images which are parts of human faces. It is the main reason for applying NMF on image clustering. In this section, we evaluate our NMSTF algorithm on image clustering problems comparing with NMF. Our experiment shows the details of our algorithm.

4.1 Data Sets

Our experiment has three data sets. All of them are image data sets. Their introductions are summarized blow

The first data set is the ORL image library, which contains 32×32 gray scale images of 40 people. Each person has 10 facial images under different expression and ornament conditions.

The second data set is the CMU-PIE image library, which contains 32×32 gray scale images of 68 people. Each person has 40 facial images under different light and illumination conditions.

The third data set is the COIL20 image library, which contains 32×32 gray scale images of 20 objects. Each object has 72 images from every 5 angles.

4.2 Feature Extraction

NMF can extract parts-based features as it allows only additive combinations between the basis images. Some studies show that the features extracted by NMF are not always independent. It implies that the vectors of basis images are not always sparse. In this subsection, we display the basis images learned by our NMSTF algorithm. Figures 1 and 2 show the basis images learned by NMF and NMSTF in the PIE and COIL20 data sets when $l = 2$. Images learned by NMF have 1024 pixels, we show them as 32×32 gray scale images. Images learned by NMSTF have 512 pixels, a half of 1024, we show them as 32×16 gray scale images. The shape of basis images are determined by the storage order of original image. If the original image saves to a vector by row, images learned by NMSTF can also be 16×32 gray scale images

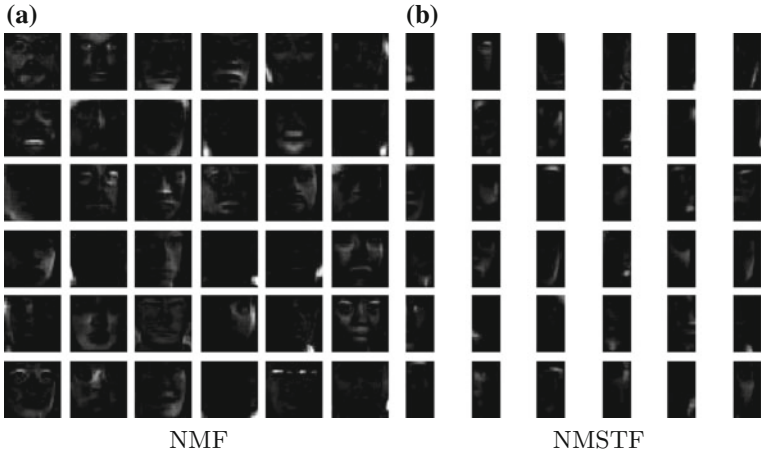

Fig. 1 Basis image learned by NMF and NMSTF with $l = 2$ on PIE database

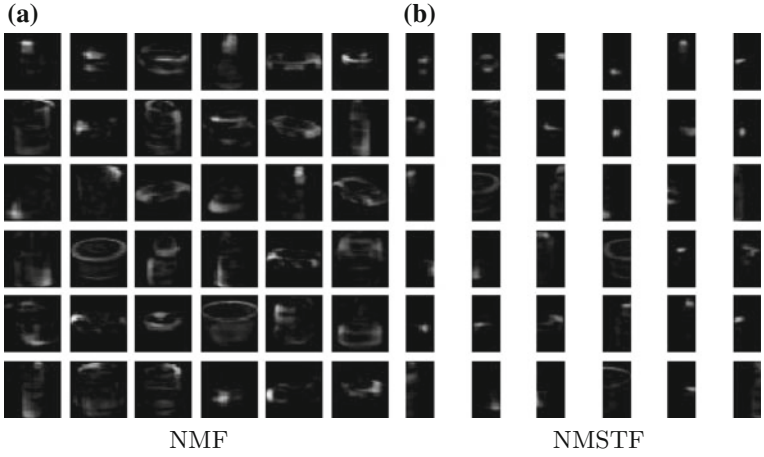

Fig. 2 Basis image learned by NMF and NMSTF with $l = 2$ on COIL20 database

when $l = 2$. In these figures, it is clear to see that basis vectors learned by NMSTF are sparser and much smaller than those learned by NMF.

4.3 Convergence Analysis

We test the convergence of our algorithm and investigate the number of iterations when the updating rules converge. Figure 3 shows the convergence curve of both NMF and NMSTF on each of the three data sets. For each figure, the y-axis is the

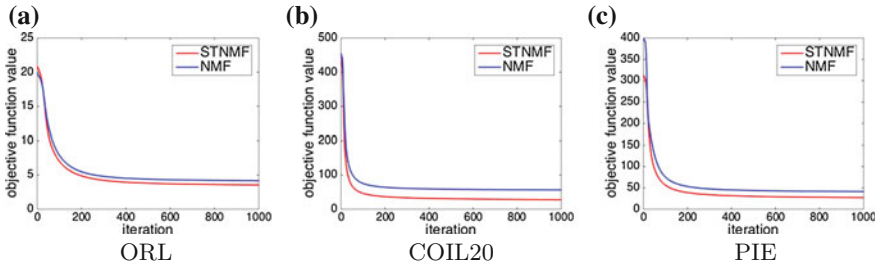

Fig. 3 The Convergence Curve of three data sets

value of objective function and the x-axis is the iteration number. We can see that both STNMF and NMF using multiplicative update rules converge very fast, usually within 100 iterations. The objective function value of STNMF is nearly 30 % smaller than the one of NMF.

4.4 Clustering Comparison

Tables 2, 3, and 4 show the clustering results on ORL, PIE and COIL20 image data sets. We choose part of the data set by the following way to make sure that our experiments are general. If k is the number of people or objects in each data set, we put all the cluster labels 1 to k as a circle out of order. For every r continuous cluster labels, we choose the corresponding data testing 20 times. We repeat the above test five times and calculate the average and mean square error of the accuracy rates of clustering.

Table 2 Clustering performance in ORL

r	NMF(%)	NMSTF($l = 2$)(%)	NMSTF($l = 4$)(%)	NMSTF($l = 8$)(%)
4	80.7 ± 12.9	80.5 ± 14.5	80.4 ± 13.6	87.4 ± 11.9
8	74.5 ± 7.8	73.0 ± 10.2	78.6 ± 8.5	80.0 ± 8.2
12	69.8 ± 7.2	72.4 ± 7.5	73.8 ± 7.3	74.8 ± 7.3
16	67.4 ± 5.6	69.1 ± 5.4	68.8 ± 6.0	70.6 ± 5.8
20	65.0 ± 5.0	66.8 ± 5.4	68.1 ± 5.0	69.0 ± 4.8
24	62.3 ± 4.6	63.9 ± 4.8	63.2 ± 4.4	63.9 ± 5.1
28	61.5 ± 4.0	62.3 ± 4.4	62.7 ± 5.0	63.0 ± 4.7
32	60.0 ± 3.5	60.7 ± 3.7	60.6 ± 4.0	61.1 ± 3.3
36	58.7 ± 3.3	59.1 ± 3.3	58.3 ± 3.3	59.7 ± 3.5
40	57.2	58.1	57.8	58.8

Table 3 Clustering performance in PIE

r	NMF(%)	NMSTF($l = 2$)(%)	NMSTF($l = 4$)(%)	NMSTF($l = 8$)(%)
10	49.7 ± 4.7	50.8 ± 4.8	49.2 ± 4.7	50.5 ± 6.5
20	45.7 ± 3.3	47.0 ± 4.1	48.3 ± 2.4	49.7 ± 3.7
30	42.4 ± 2.4	45.1 ± 2.3	46.4 ± 2.6	47.3 ± 2.8
40	41.5 ± 2.6	44.8 ± 2.5	44.2 ± 2.5	46.3 ± 2.7
50	39.8 ± 2.3	43.4 ± 2.5	44.0 ± 1.8	44.7 ± 1.6
60	38.6 ± 1.9	42.3 ± 2.2	43.3 ± 2.4	43.5 ± 2.3
68	38.0	45.0	45.4	46.4

Table 4 Clustering performance in COIL20

r	NMF(%)	NMSTF($l = 2$)(%)	NMSTF($l = 4$)(%)	NMSTF($l = 8$)(%)
4	80.8 ± 13.1	79.4 ± 14.8	80.0 ± 13.0	81.5 ± 13.4
6	75.5 ± 9.8	78.9 ± 7.6	78.4 ± 10.5	80.1 ± 11.2
8	73.0 ± 10.3	72.7 ± 8.5	73.6 ± 8.5	76.4 ± 12.2
10	71.3 ± 6.9	71.9 ± 7.0	72.5 ± 8.9	73.0 ± 6.2
12	68.0 ± 5.7	68.6 ± 4.8	69.9 ± 5.8	70.5 ± 6.4
14	65.5 ± 4.9	66.1 ± 4.9	66.2 ± 5.7	68.3 ± 5.1
16	63.8 ± 4.9	63.6 ± 4.7	64.0 ± 4.4	65.7 ± 5.6
18	63.1 ± 3.9	62.6 ± 5.0	64.3 ± 4.0	64.0 ± 4.0
20	62.6	62.9	63.3	64.1

These experiments show that regardless of the data sets, STNMF achieves similar performance than NMF in most of the conditions. For ORL, PIE, COIL20, the performance improve 3.1, 7.3, 3.0 %.

4.5 Parameter Analysis

There is only one parameter in our NMSTF algorithm, the multiple parameter l. Figure 4 shows how the average accuracy of NMSTF varies with the parameter l.

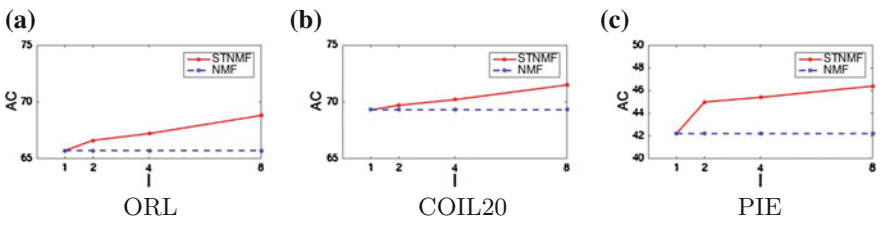

Fig. 4 The Clustering Accuracy of three data set with different l

As NMSTF reduce to NMF when $l = 1$, we regard NMF as NMSTF in the case of $l = 1$. From the figures, we can see the accuracy increases with the growth of l. But in reality, l has a limit: $\frac{m}{l}r + lnr < mn$ and running time increases fast with the growth of l.

5 Conclusions

In this paper, we have introduced a novel matrix factorization algorithm called Non-Negative Matrix Semi-Tensor Factorization. While achieving similar or better performance on image clustering tasks, the size of basis images are sparser and at least 50 % smaller. Features extracted are more independent. The error of the factorizaition is 30 % smaller in average.

Several questions remain to be investigated in our future work. This paper remains the question about l and the storage order of original image which influence the algorithm result. We do not theoretically prove that the updating rules are convergent.

Acknowledgments This work is supported by NSFC Fund No. 61303068, HPCL Project Fund No. 201502-02, NUDT Key Project Fund No ZDYYJCYJ20140601 and No. 434513322532.

References

1. Duda, RO, Hart PE, Stork DG (2000) Pattern classification (2nd edn). En broeck the statistical mechanics of learning rsity
2. Turk M, Pentland A (1991) Eigenfaces for recognition. J Cogn Neurosci 3.1:71–86
3. Palmer Stephen E (1977) Hierarchical structure in perceptual representation. Cogn Psychol 9(4):441–474
4. Wachsmuth E, Oram MW, Perrett DI (1994) Recognition of objects and their component parts: responses of single units in the temporal cortex of the macaque. Cereb Cortex 4(5):22–509
5. Lee DD, Seung HS (1999) Learning the parts of objects by non-negative matrix factorization. Nature 401(6755):788–91
6. Cai D et al (2011) Graph regularized nonnegative matrix factorization for data representation. IEEE Trans Pattern Anal Mach Intell 33.8:1548–1560
7. Guan N et al (2012) NeNMF: an optimal gradient method for nonnegative matrix factorization. IEEE Trans Signal Process 60.6:2882–2898
8. Guan N et al (2011) Non-negative patch alignment framework. IEEE Trans Neural Netw 22.8:1218–1230
9. Cheng D et al (2007) A survey on semi-tensor product of matrices. J Syst Sci Complex 20.2:304–322
10. Cheng D (2007) Semi-tensor product of matrices and its applications-A survey. In: Proceedings of ICCM'07, vol 3. pp 641–668
11. Jin MA et al (2006) Approximation of the boundary of power system stability region based on semi-tensor theory part one theoretical basis. Autom Electr Power Syst 30(10):1–5
12. Cheng D Some applications of semi-tensor product of matrix in algebra, Comput Math Appl Appear
13. Cheng D, Qi H (2007) Semi-tensor product of matrices-theory and applications. Science Press, Beijing

14. Paatero P, Tapper U (1994) Positive matrix factorization: a non-negative factor model with optimal utilization of error estimates of data values. Environmetrics 5.2:111–126
15. Lee DD (2001) Algorithms for non-negative matrix factorization. Adv Neural Inf Process Syst 13(6):556–562

Prediction of Air Target Intention Utilizing Incomplete Information

Pengcheng Xia, Mou Chen, Jie Zou and Xing Feng

Abstract This paper focuses on the application of UAVs (unmanned aerial vehicles) on the information battlefield, and an intention prediction method for air targets is studied. Four factors of the enemy UAVs including velocity, angle, offense, and detection are analyzed and predicted by Grey Markov chain. Then, by combining the predicted factors with the rules provided by rough set, the enemy UAVs' intention in the following short time can be deduced. The prediction method is studied utilizing incomplete information, and the feasibility of the developed prediction method is proved by the simulation results.

Keywords Incomplete information · Intention prediction · Grey markov chain · Rough set

1 Introduction

Since the UAVs have the advantages of mobility and autonomy, they have been widely used in the modern warfare. Especially, the joint operation mode of UAVs group has become one of the main attack modes. In order to render UAVs with capabilities of autonomous attack and defense, a method is needed to realize the prediction of the enemy targets' intention. At present, there are some classic methods used in this topic such as Bayesian Network method [1], D-S (Dempster–Shafer) evidence theory [2], and so on. An intention recognition method was developed based on MEBN (Multi-Entities Bayesian Network) theory in [1], and some prior knowledge is required to satisfy the reliability of the method. In [2], a situation forecast method on antimissile operation was studied with D-S evidence

P. Xia · M. Chen (✉)
College of Automation Engineering, Nanjing University of Aeronautics & Astronautics, Nanjing 211106, China
e-mail: chenmou@nuaa.edu.cn

J. Zou · X. Feng
Science and Technology on Electron-Optic Control Laboratory, Luoyang 471009, China

Y. Jia et al. (eds.), *Proceedings of 2016 Chinese Intelligent Systems Conference*, Lecture Notes in Electrical Engineering 404, DOI 10.1007/978-981-10-2338-5_38

theory. What's more, scientific literatures based on these methods are rarely involved in the incomplete information.

In the complex battlefield environment, considering the stealth of aircrafts, disturbance and limit of detection zones, incomplete data will probably be received by sensors. Thus, it is urgent to develop a method to handle the incomplete data. Soft set theory and rough set theory are two methods dealing with incomplete information. D-S fuzzy soft set theory is a new method in [3] to solve a decision making problem in the Internet environment, and rough set theory is a powerful tool in data mining [4] and it is also used in this paper to tackle the incomplete information.

The remainder of this paper is organized as follows. Section 2 mainly discusses the prediction of the threat factors by using Grey Markov chain. In Sect. 3, a rough set approach is introduced, which deals with the incomplete information decision table for rules. Section 4 shows the procedure of the prediction. And Sect. 5 gives a simulation example to show the feasibility of the method.

2 Threat Factors Prediction

2.1 Definition of the Threat Factors

The air fight status between two UAVs is shown in Fig. 1 [5], where A represents the enemy UAV and B represents one of our UAVs. The target line is the line between A and B, d is the distance between two UAVs along the target line, p is the entrance angle between the target line and the direction of velocity V_1 of A, q is the entrance angle between the target line and the direction of velocity V_2 of B.

Now, take B as the study object, and define four threat factors from the status of A against B, they are written as follows [5]:

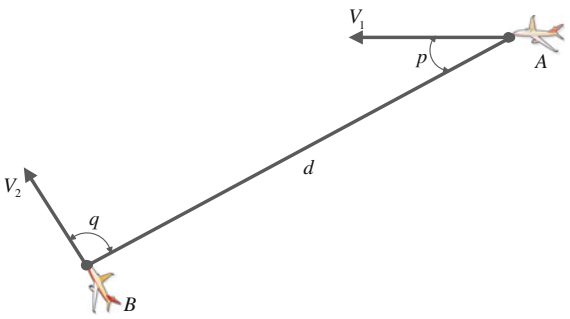

Fig. 1 Air fight status

(1) Angle threat factor [5]

$$T_a = 1/2 + (|q| - |p|)/2\pi \tag{1}$$

Typical condition: when $p = \pi/2, q = \pi/2, T_a = 1/2$, A and B are in balance.

(2) Velocity threat factor [5]

$$T_v = \begin{cases} 0.1 & V_1 \le 0.6V_2 \\ -0.5 + V_1/V_2 & 0.6V_2 < V_1 < 1.5V_2 \\ 1 & V_1 \ge 1.5V_2 \end{cases} \tag{2}$$

Typical condition: when $V_1 = V_2, T_v = 0.5$, A and B are at the same speeds.

(3) Offense threat factor [5]

① A is superior to B: $d_{mA} > d_{mB}$

$$T_o = \begin{cases} 0.5 & d < d_{mB} \vee d > d_{mA} \\ 0.5 + 0.5(d - d_{mB})/(d_{mA} - d_{mB}) & d_{mB} < d < d_{mA} \end{cases} \tag{3}$$

② B is superior to A: $d_{mB} > d_{mA}$

$$T_o = \begin{cases} 0.5 & d < d_{mA} \vee d > d_{mB} \\ 0.5 - 0.5(d - d_{mA})/(d_{mB} - d_{mA}) & d_{mA} < d < d_{mB} \end{cases} \tag{4}$$

Here, d_{mA} and d_{mB} represent the maximum ranges of the missiles of A and B, respectively.

(4) Detection threat factor [5]

① A is superior to B: $d_{rA} > d_{rB}$

$$T_d = \begin{cases} 0.5 & d < d_{rB} \vee d > d_{rA} \\ 0.5 + 0.5(d - d_{rB})/(d_{rA} - d_{rB}) & d_{rB} < d < d_{rA} \end{cases} \tag{5}$$

② B is superior to A: $d_{rB} > d_{rA}$

$$T_d = \begin{cases} 0.5 & d < d_{rA} \vee d > d_{rB} \\ 0.5 - 0.5(d - d_{rA})/(d_{rB} - d_{rA}) & d_{rA} < d < d_{rB} \end{cases} \tag{6}$$

Here, d_{rA} and d_{rB} represent the maximum detection ranges of the radars of A and B, respectively.

For each factor given in (1)–(6), a balance point of one factor means that the threat value A against B in this factor equals to the threat value B against A.

2.2 Prediction of Threat Factors Based on Grey Markov Chain

In an air combat, if the enemy UAV in our sight carries a tactical purpose against our UAV, each of the factors will fluctuate around constant value or approach constant value. Thus, Grey Markov chain will be a helpful method in the prediction of threat factors [6].

I. **GM (1, 1)**

Suppose that $X^{(0)} = \left(X^{(0)}(1), X^{(0)}(2), \ldots, X^{(0)}(n)\right)$ is the time series data of one factor. $X^{(1)}$ is called the accumulated sequence, and $X^{(1)}(i) = \sum_{k=1}^{i} X^{(0)}(k)$, $i = 1, 2, \ldots, n$. If $X^{(0)}$ and $X^{(1)}$ satisfy the condition of three tests which are given in [7]. Then, the GM (1, 1) model can be written as:

$$\hat{X}^{(0)}(i+1) = \hat{X}^{(1)}(i+1) - \hat{X}^{(1)}(i) = (1 - e^{a})(X^{(0)}(1) - u/a)e^{-ai} \tag{7}$$

where a and u can be calculated using least square method. $X^{(0)}$ can be fitted and predicted with model (7).

II. **Markov chain**

When m states are contained in a Markov chain $x(n)$ and one state can be written as $\otimes_a$, $a \in \{1, 2, \ldots, m\}$. The frequency of the state from $\otimes_a$ to $\otimes_b$ $(b \in \{1, 2, \ldots, m\})$ by one step transition is regarded as f_{ab}. p_{ab} is the element of the ath row and the bth column in the state transition matrix, $p_{ab} = f_{ab} / (\sum_{b=1}^{m} f_{ab})$. When $x(n)$ is the state $\otimes_k$, we have [6]:

(1) If $\max\limits_{1 \le b \le m} p_{kb} = p_{kl}$, $x(n+1)$ most probably is the state $\otimes_l$.
(2) If the kth row in the state transition matrix contains more than one element that equals to the maximum value in this row, then two steps or more steps state transition matrix should be taken into account to determine the state of $x(n+1)$.

3 Rules Acquisition from Incomplete Information Table

In this section, relating the predicted threat factors to the enemy's intention is the main task. The incomplete air combat decision information table is studied in this section to provide rules for the prediction, and the table is achieved from the database of the air combat records system.

Table 1 Decision factor

Attack	Feint	Defense	Escape	Decision factor(D)
1	0	0	0	6
1	1	0	0	5
0	1	0	0	4
0	0	1	0	3
0	0	1	1	2
0	0	0	1	1

3.1 Definition of the Decision Factors

Decision factor is the decision attribute in the rough set and denoted as D. The intentions of enemy UAVs can be concluded as four types: Attack, Feint, Defense, and Escape. The decision factor is listed as Table 1.

Each element in the decision factor corresponds to certain possible intentions. For instance, when $D=5$, the possible intentions of enemy UAV are attack and feint, when $D=1$, the possible intention is escape.

3.2 Dominance Relation Theory of Incomplete Fuzzy Rough Set

The following is definition about the dominance relation theory of incomplete fuzzy rough set:

Definition [8] Suppose that $S=(U, AT \cup d, V, f)$ is incomplete fuzzy decision information system, $A \subseteq AT$. $R^{TOD}(A)$ is called the dominance relation defined by A, which is denoted by

$$R^{TOD}(A)=\{(x,y)\in U\times U: \forall a\in A, (f(x,a)\geq f(y,a))\vee(f(x,a)\geq B(a)\wedge f(y,a)=^{*})$$
$$\vee(f(x,a)=^{*}\wedge f(y,a)\leq B(a))\vee(f(x,a)=^{*}\wedge f(y,a)=^{*})\}$$

Here, * represents the data failed to receive, and $B(a)$ represents the balance point of condition attribute a. Due to paper space limitation, readers can learn more about dominance relation theory in [8].

4 Procedure of the Intention Prediction

The specific process of the intention prediction for the target is given as Fig. 2:

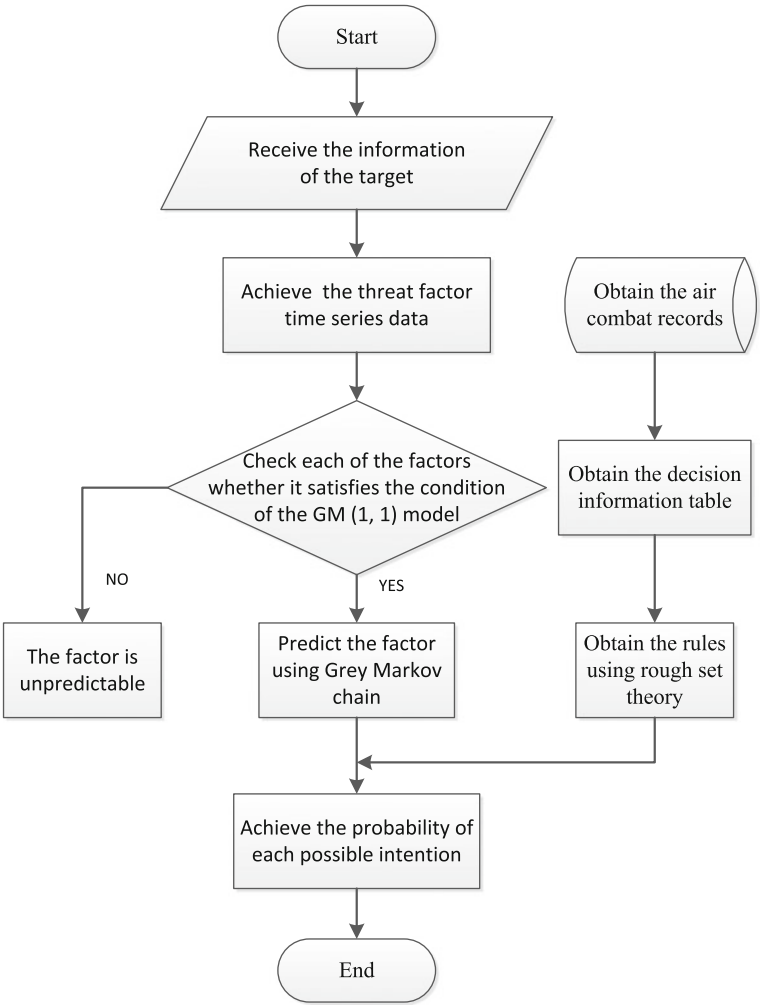

Fig. 2 Intention prediction procedure

Details of the intention prediction procedure are as follows:

(1) Receive the information about the enemy target.
(2) Compute the information and achieve the time series data of four threat factors.
(3) Check each factor whether it satisfies the condition of the GM (1, 1). If it is satisfied, then it can be predicted with GM (1, 1) and corrected with Markov chain. If it is not satisfied, it is marked as unpredictable.
(4) Get the air combat records from the database, and transform them into an air combat decision information table.

(5) Obtain the rules from the air combat decision information table using the dominance relation theory of incomplete fuzzy rough set.
(6) After looking up each predicted factor in its rule axis, achieve the probability of each possible intention.

5 Simulation and Analysis

Table 2 shows the time series data received by sensors in our UAV, it has been transformed into threat factors.

Now, take the factor T_v as an example. According to (7), the GM (1, 1) model is established as:

$$\hat{X}^{(0)}(1) = X^{(0)}(1), \hat{X}^{(0)}(i+1) = 0.51e^{0.0204i}$$

The relative error sequence: $\delta^{(0)}(i) = 100\,\% * \left(X^{(0)}(i) - \hat{X}^{(0)}(i)\right) / X^{(0)}(i)$. Five states are defined for $\delta^{(0)}$:

$(1) -30\,\% < \delta^{(0)}(i) \le -10\,\%$ $(2) -10\,\% < \delta^{(0)}(i) \le -2\,\%$
$(3) -2\,\% < \delta^{(0)}(i) < 2\,\%$ $(4)\ 2\,\% \le \delta^{(0)}(i) < 10\,\%$
$(5)\ 10\,\% \le \delta^{(0)}(i) < 30\,\%$

And the state transition matrix is $P = \begin{bmatrix} 0.67 & 0.33 & 0 \\ 0.33 & 0 & 0.67 \\ 0 & 0.5 & 0.5 \end{bmatrix}$.

According to the GM (1, 1) model, $\hat{X}^{(0)}(13) = 0.6513$, and $\delta^{(0)}(12)$ is state (2). After one step transition, it is most possible for $\delta^{(0)}(13)$ to be state (2). Take mid-value of [2 %, 10 %] as the value of $\delta^{(0)}(13)$ and the corrected value of $\hat{X}^{(0)}(13)$ is 0.6144.

The four factors are predicted as shown in Table 3.

Table 4 is an incomplete air combat decision information table.

According to process of attribute reduction and rules extraction of the dominance relation theory of incomplete fuzzy rough set, Table 4 can be processed as follows:

Table 4 $= (U, AT \cup d, V, f), \forall x \in U$.

(1) Obtain $\mu_{\underline{A^{TOD}}(d)}(x)$ and $\mu_{\overline{A^{TOD}}(d)}(x)$.

Table 2 Received threat factors

	1	2	3	4	5	6	7	8	9	10	11	12
T_a	0.65	0.67	0.69	0.71	0.70	0.68	0.69	0.67	0.66	0.67	*	*
T_v	0.53	0.51	0.50	0.53	0.56	0.59	0.60	0.61	0.60	0.63	0.62	0.60
T_o	0.68	0.68	*	*	0.72	0.75	0.76	0.79	0.80	0.79	0.79	0.80
T_d	0.52	0.51	0.53	*	0.55	0.57	0.59	0.62	0.61	*	0.60	0.59

Table 3 Predicting results

Factors	T_a	T_v	T_o	T_d
Predicting value	*	0.6144	0.8131	*

Table 4 Incomplete air combat decision information table

	T_a	T_v	T_o	T_d	D
x_1	0.91	0.55	0.95	*	6
x_2	0.89	0.60	0.78	0.46	4
x_3	0.93	0.47	0.99	0.65	6
x_4	0.90	*	0.81	0.53	5
x_5	0.53	0.50	*	0.55	3
x_6	0.41	0.75	0.45	0.47	1
x_7	0.35	0.79	0.36	0.31	1
x_8	*	0.61	0.51	0.51	2

(2) Get the minimal disjunctive forms $Red_L(x)$ and $Red_H(x)$.
(3) Use decision rules methods of "at least" and "at most":
If $A \subseteq Red_L(x)$, and if $\forall a \in A, f(y,a) \geq f(x,a)$, then $f(y,d) \geq \mu_{\underline{A^{TOD}}(d)}(x)$.
If $A \subseteq Red_H(x)$, and if $\forall a \in A, f(y,a) \leq f(x,a)$, then $f(y,d) \leq \mu_{\overline{A^{TOD}}(d)}(x)$.
(4) Obtain rules. The rules are expressed on four axes in Fig. 3, where $a \sim b$ means $a \leq D \leq b$

According to the prediction results in Table 3, after corresponding each factor in the axes in Fig. 3, we have the intersection: $5 \leq D \leq 6$. Then, look up the decision factor D in Table 1, and 1 1 0 0, 1 0 0 0 are obtained. Thus, the probabilities of possible intentions are: Attack—66.67 %, Feint—33.33 %. From the simulation results, we know that the developed prediction method is valid.

Fig. 3 Rule axes

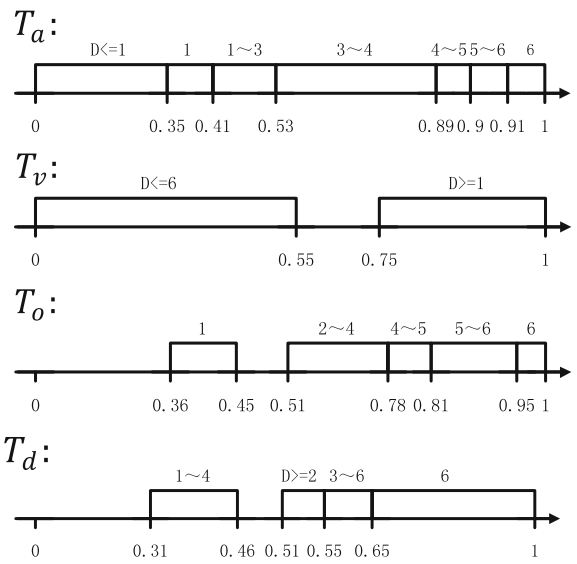

6 Conclusion

The prediction of UAVs' intentions has been developed with two methods: Grey Markov chain and the dominance relation theory of rough set, by utilizing incomplete information, and simulation has proved the reasonable. In general, this paper has provided a certain theoretical method for UAVs combat application.

Acknowledgments This work is partially supported by Aeronautical Science Foundation of China (No. 20145152029) and Science and Technology on Electron-Optic Control Laboratory.

References

1. Wang H (2011) Research on air target intention recognition based on multi-entities Bayesian network [D]. National University of Defense Technology
2. Zhiqiang Zhou, Jiangang Qian, Kangyin Yin et al (2014) Method of target prediction based on DS evidence theory [J]. J Air Force Early Warning Acad 28(2):116–118
3. Dong Y (2014) Study on approach of incomplete & inconsistent data analysis and decision making based on soft set theory [D]. Chongqing University
4. Liang M (2005) Rough set approach to data mining in incomplete information systems [D]. Guangxi University
5. Yanluo Geng, Changsheng Jiang (2004) Multi-fighter coordinated multi-target attack system [J]. Trans Nanjing Univ Aeronaut Astronaut 21(1):18–23
6. Xiangyong Li, Nan Zhang, Gefu Jiang (2003) Grey-Markov model for forecasting road accidents [J]. J Highw Trans Res Dev 20(4):98–104
7. Hualong Yang, Jinxia Liu, Bin Zheng (2011) Improvement and application of grey prediction GM (1, 1) model [J]. Math Pract Theory 41(23):39–46
8. Sun X (2012) Research on incomplete fuzzy rough set model extension based on dominance relation and its application [D]. Guangxi University

Robust Tracking Control of Wheeled Mobile Robots with Parameter Uncertainties and only Target's Position Measurement

Lixia Yan and Baoli Ma

Abstract Robust tracking control of wheeled mobile robots (WMRs) is studied in this work. Considering the dynamic model of WMRs with unknown parameters, a robust sliding-mode state feedback controller is proposed, guaranteeing the tracking errors converge to zero asymptotically. Later, combining robust exact differentiators with the proposed state feedback control law leads to a tracking controller, in which only the position of reference robot is included and the tracking errors are driven to the origin asymptotically too. Numerical simulation is carried out to verify the effectiveness of proposed controller.

Keywords Wheeled mobile robots · Robust tracking control · Sliding-mode control · Robust exact differentiator

1 Introduction

To date, the trajectory tracking and path following control of wheeled mobile robots have been widely studied. There are no continuous time-invariant controllers to achieve state stabilization of WMRs due to the limitation of Brockett necessary condition [1]. A trajectory tracking control law based on backstepping method is proposed in [2], within which the tracking errors converge to zero uniformly asymptotically. Using dynamic feedback linearization, a local asymptotical tracking control scheme is shown in [3]. Clearly, sliding-mode control method is also a good way to solve control problem and makes systems robust to uncertainties and

L. Yan · B. Ma (✉)
The Seventh Research Division, School of Automation Science and Electrical Engineering, Beihang University, Beijing 100191, China
e-mail: mabaoli@buaa.edu.cn

L. Yan
e-mail: robotyanlx@yahoo.com

Y. Jia et al. (eds.), *Proceedings of 2016 Chinese Intelligent Systems Conference*, Lecture Notes in Electrical Engineering 404, DOI 10.1007/978-981-10-2338-5_39

disturbances. By describing system from cartesian coordinate to polar coordinate, a sliding-mode tracking control law proposed in [4] guaranties the tracking errors ultimately bounded, while a large control may appear near the origin. Considering a universal sliding-mode control scheme for a class of nonlinear systems and transform the model equations of WMRs into a special form, controller proposed in [5] makes the system globally asymptotically stable. By designing a PI-type sliding-mode surface and an adaptive algorithm, the trajectory tracking errors are steered to zero asymptotically [6].

Almost under all situations, the trajectory tracking or path following controllers can be directly used for the tracking control of two WMRs if the position/orientation and linear/angular velocity information of reference robot are completely known by the tracker robot. However, under real circumstance, not all the information of the reference WMR can be known or easily detected, and less communication burden in hardware-layer of controller helps to build a reliable apparatus and decreases error-code rate [7]. Based on above practical considerations, it is desired to solve the tracking control problem of WMRs using only position information of the reference robot, which can be easily obtained even in indoor environment by camera [8] or UWB [9].

In this work, we first refer results in [10] to design estimators of reference robot using only its position information. Later, we introduce a full-state feedback sliding-mode controller which drives the system states converging to the stable sliding surface in finite time despite the model parameter uncertainties. The combination of state feedback control law with estimators contributes to a tracking controller with only position information of reference robot.

The paper is organized as follows. Section 2 contains problem formation, controller design is included in Sect. 3, simulation results and conclusion are presented in Sects. 4 and 5 respectively.

2 Problem Formation

Consider the dynamic model of WMRs described by

$$\begin{cases} \dot{x} = v\cos\theta, \dot{y} = v\sin\theta, \dot{\theta} = \omega \\ m\dot{v} = \dfrac{\tau_1+\tau_2}{R}, I\dot{\omega}=\dfrac{L}{R}\left(\tau_1 - \tau_2\right) \end{cases} \tag{1}$$

where (x, y) is the coordinate of mass center, θ denotes the posture angle, v and ω represent linear and angular velocity respectively. $(\dot{v}, \dot{\omega})$ are linear and angular accelerations. τ_1 and τ_2 denote driving torques of the right and left wheels. (m, I, R, L) are mass, inertia around the mass center, wheel diameter, distance between right and left wheel respectively, which are unknown parameters bounded by known bounds, i.e.,

$$\begin{array}{l} 0 < m_m \le m \le m_M, 0 < I_m \le I \le I_M \\ 0 < R_m \le R \le R_M, 0 < L_m \le L \le L_M \end{array} \tag{2}$$

where $m_m, m_M, I_m, I_M, R_m, R_M, L_m, L_M$ are known positive constants.

The kinematic equations of the reference robot are as follows:

$$\dot{x}_r = v_r \cos\theta_r, \dot{y}_r = v_r \sin\theta_r, \dot{\theta}_r = \omega_r \tag{3}$$

Assumption 1 *The reference speeds and their first- and second-order derivatives* $(v_r, \omega_r, \dot{v}_r, \dot{\omega}_r, \ddot{v}_r, \ddot{\omega}_r)$ *are bounded by*

$$\begin{cases} v_{rM} \ge v_r \ge v_{rm} > 0, \dot{v}_{rM} \ge \left|\dot{v}_r\right|, \ddot{v}_{rM} \ge \left|\ddot{v}_r\right| \\ \omega_{rM} \ge \left|\omega_r\right|, \dot{\omega}_{rM} \ge \left|\dot{\omega}_r\right|, \ddot{\omega}_{rM} \ge \left|\ddot{\omega}_r\right| \end{cases} \tag{4}$$

where $v_{rM}, v_{rm}, \omega_{rM}, \dot{v}_{rM}, \dot{\omega}_{rM}, \ddot{v}_{rM}, \ddot{\omega}_{rM}$ *are positive constants.*

Assumption 2 *The exact position* (x_r, y_r) *of the reference robot is known.*

Define the tracking errors as

$$e_x = x - x_r, e_y = y - y_r, e_\theta = \theta - \theta_r \tag{5}$$

With Assumptions 1 and 2, the control task in this paper is to design control law

$$\begin{bmatrix} \tau_1 \\ \tau_2 \end{bmatrix} = \begin{bmatrix} U_1\left(x, y, \theta, v, \omega, x_r, y_r, \Omega\right) \\ U_2\left(x, y, \theta, v, \omega, x_r, y_r, \Omega\right) \end{bmatrix} \tag{6}$$

such that

$$\lim_{t\to\infty} e_x = 0, \lim_{t\to\infty} e_y = 0, \lim_{t\to\infty} e_\theta = 0 \tag{7}$$

where Ω denotes the set of auxiliary variables.

3 Controller Design

In this section, we first give out some preliminary results that refer to [10] and estimate some values of reference robot that are not known exactly. Later, a robust state feedback controller will be introduced. Combining estimating algorithm and state feedback controller leads to the robust tracking controller with only position information of the target.

3.1 Target Observer Design

From Assumptions 1 and 2, we know that (x_r, y_r) is measurable and their derivatives are bounded, so that we can estimate their first, second, and third derivatives by the exact differentiators proposed in [10] as follows:

$$\begin{aligned}
&\dot{f}_{0x} = w_{0x}, w_{0x} = -\lambda_0 \left| f_{0x} - x_r \right|^{\frac{3}{4}} \operatorname{sign}\left(f_0 - x_r\right) + f_{1x} \\
&\dot{f}_{1x} = w_{1x}, w_{1x} = -\lambda_1 \left| f_{1x} - w_{0x} \right|^{\frac{2}{3}} \operatorname{sign}\left(f_{1x} - w_{0x}\right) + f_{2x} \\
&\dot{f}_{2x} = w_{2x}, w_{2x} = -\lambda_2 \left| f_{2x} - w_{1x} \right|^{\frac{1}{2}} \operatorname{sign}\left(f_{2x} - w_{1x}\right) + f_{3x} \\
&\dot{f}_{3x} = -\lambda_3 \operatorname{sign}\left(f_{3x} - w_{2x}\right)
\end{aligned} \tag{8}$$

$$\begin{aligned}
&\dot{f}_{0y} = w_{0y}, w_{0y} = -\lambda_0 \left| f_{0y} - y_r \right|^{\frac{3}{4}} \operatorname{sign}\left(f_{0y} - y_r\right) + f_{1y} \\
&\dot{f}_{1y} = w_{1y}, w_{1y} = -\lambda_1 \left| f_{1y} - w_{0y} \right|^{\frac{2}{3}} \operatorname{sign}\left(f_{1y} - w_{0y}\right) + f_{2y} \\
&\dot{f}_{2y} = w_{2y}, w_{2y} = -\lambda_2 \left| f_{2y} - w_{1y} \right|^{\frac{1}{2}} \operatorname{sign}\left(f_{2y} - w_{1y}\right) + f_{3y} \\
&\dot{f}_{3y} = -\lambda_3 \operatorname{sign}\left(f_{3y} - w_{2y}\right)
\end{aligned} \tag{9}$$

where $\lambda_i > L_r \, (i = 0, 1, 2, 3)$ with $L_r = \max\{|\dot{x}_r|, |\ddot{x}_r|, |\dddot{x}_r|, |\dot{y}_r|, |\ddot{y}_r|, |\dddot{y}_r|\}$. By using (8) and (9), the exact estimation of $(\dot{x}_r, \ddot{x}_r, \dddot{x}_r, \dot{y}_r, \ddot{y}_r, \dddot{y}_r)$ can be obtained by $(w_{0x}, w_{1x}, w_{2x}, w_{oy}, w_{1y}, w_{2y})$ in finite time.

Taking (3) into account and calculating the first- to third-order derivatives of (x_r, y_r), we get

$$\begin{cases}
\dot{x}_r = v_r \cos\theta_r, \ddot{x}_r = \dot{v}_r \cos\theta_r - v_r \omega_r \sin\theta_r \\
\dot{y}_r = v_r \sin\theta_r, \ddot{y}_r = \dot{v}_r \sin\theta_r + v_r \omega_r \cos\theta_r \\
\dddot{x}_r = \ddot{v}_r \cos\theta_r - 2\dot{v}_r \omega_r \sin\theta_r - v_r \dot{\omega}_r \sin\theta_r - v_r \omega_r^2 \cos\theta_r \\
\dddot{y}_r = \ddot{v}_r \sin\theta_r + 2\dot{v}_r \omega_r \cos\theta_r + v_r \dot{\omega}_r \cos\theta_r - v_r \omega_r^2 \sin\theta_r
\end{cases} \tag{10}$$

which suggests

$$\begin{cases}
\theta_r = \arctan 2\left(\dot{y}_r, \dot{x}_r\right), v_r = \sqrt{\dot{x}_r^2 + \dot{y}_r^2}, \dot{v}_r = \ddot{x}_r \cos\theta_r + \ddot{y}_r \sin\theta_r \\
\omega_r = \dfrac{\ddot{y}_r \cos\theta_r - \ddot{x}_r \sin\theta_r}{v_r}, \dot{\omega}_r = \dfrac{\dddot{y}_r \cos\theta_r - \dddot{x}_r \sin\theta_r - 2\dot{v}_r \omega_r}{v_r} \\
\forall \quad v_r > 0
\end{cases} \tag{11}$$

Thus, the estimated values of $(\theta_r, v_r, \omega_r, \dot{v}_r, \dot{\omega}_r)$ can be obtained as

$$\begin{cases}
\hat{\theta}_r = \arctan 2\left(w_{0y}, w_{0x}\right) \\
\hat{v}_r = \sqrt{\left(w_{0x}\right)^2 + \left(w_{0y}\right)^2}, \hat{\dot{v}}_r = w_{1x} \cos\hat{\theta}_r + w_{1y} \sin\hat{\theta}_r \\
\hat{\omega}_r = \dfrac{w_{1y} \cos\hat{\theta}_r - w_{1x} \sin\hat{\theta}_r}{\hat{v}_r}, \hat{\dot{\omega}}_r = \dfrac{w_{2y} \cos\hat{\theta}_r - w_{2x} \sin\hat{\theta}_r - 2\hat{\dot{v}}_r \hat{\omega}_r}{\hat{v}_r}
\end{cases} \tag{12}$$

Remark 1 As $\hat{v}_r$ appears in denominators of $\left(\hat{\omega}_r, \hat{\dot{\omega}}_r\right)$ and converges to real value in finite time, we adopt the following strategy in control to avoid possible singularity when $\hat{v}_r$ cross zero during transient process.

$$\hat{v}_r = \begin{cases} v_{rm}, \sqrt{\left(w_{0x}\right)^2 + \left(w_{0y}\right)^2} \leq v_{rm} \\ \sqrt{\left(w_{0x}\right)^2 + \left(w_{0y}\right)^2}, \sqrt{\left(w_{0x}\right)^2 + \left(w_{0y}\right)^2} > v_{rm} \end{cases} \tag{13}$$

3.2 Sliding-Mode Controller

Define the auxiliary position tracking errors

$$e_1 = e_x + l\left(\cos\theta - \cos\theta_r\right), e_2 = e_y + l\left(\sin\theta - \sin\theta_r\right) \tag{14}$$

where constant $l > 0$. Differentiating (14) along state trajectory of (5) results

$$\begin{bmatrix} \dot{e}_1 \\ \dot{e}_2 \end{bmatrix} = A(\theta) \begin{bmatrix} v \\ \omega \end{bmatrix} - A\left(\theta_r\right) \begin{bmatrix} v_r \\ \omega_r \end{bmatrix} \tag{15}$$

where

$$A(a) \stackrel{\Delta}{=} \begin{bmatrix} \cos a & -l\sin a \\ \sin a & l\cos a \end{bmatrix} \rightarrow A^{-1}(a) = \begin{bmatrix} \cos a & \sin a \\ -\dfrac{\sin a}{l} & \dfrac{\cos a}{l} \end{bmatrix} \tag{16}$$

Define the stable sliding-mode surfaces

$$s = \begin{bmatrix} s_1 \\ s_2 \end{bmatrix} = \begin{bmatrix} \dot{e}_1 + k_1 e_1 \\ \dot{e}_2 + k_1 e_2 \end{bmatrix} = A(\theta) \begin{bmatrix} v \\ \omega \end{bmatrix} - A\left(\theta_r\right) \begin{bmatrix} v_r \\ \omega_r \end{bmatrix} + k_1 \begin{bmatrix} e_1 \\ e_2 \end{bmatrix} \tag{17}$$

in which k_1 is a positive constant.

Let $\left(\bar{\tau}_1, \bar{\tau}_2\right) = \left(\tau_1 + \tau_2, \tau_1 - \tau_2\right)$ and $\left(p_1, p_2\right) = \left(\dfrac{1}{mR}, \dfrac{L}{IR}\right)$, the derivative of (17) becomes

$$\dot{s} = A(\theta) \begin{bmatrix} p_1\bar{\tau}_1 \\ p_2\bar{\tau}_2 \end{bmatrix} + A(\theta) B(\omega) \begin{bmatrix} v \\ \omega \end{bmatrix} - \begin{bmatrix} \Delta_1 \\ \Delta_2 \end{bmatrix} \tag{18}$$

where

$$B(a) = \begin{bmatrix} k_1 & -la \\ \dfrac{a}{l} & k_1 \end{bmatrix}, \begin{bmatrix} \Delta_1 \\ \Delta_2 \end{bmatrix} = A\left(\theta_r\right) \begin{bmatrix} \dot{v}_r \\ \dot{\omega}_r \end{bmatrix} + A\left(\theta_r\right) B\left(\omega_r\right) \begin{bmatrix} v_r \\ \omega_r \end{bmatrix} \tag{19}$$

To realize the input-output decoupling, define the new sliding-mode surfaces

$$\bar{s} = \begin{bmatrix} \bar{s}_1 \\ \bar{s}_2 \end{bmatrix} = A^{-1}(\theta)\, s \tag{20}$$

Differentiating $\bar{s}$ leads to

$$\dot{\bar{s}} = \begin{bmatrix} p_1 \bar{\tau}_1 \\ p_2 \bar{\tau}_2 \end{bmatrix} + \begin{bmatrix} \delta_{11} \\ \delta_{21} \end{bmatrix} + \begin{bmatrix} \delta_{12} \\ \delta_{22} \end{bmatrix} \tag{21}$$

where

$$\begin{aligned} \begin{bmatrix} \delta_{11} \\ \delta_{21} \end{bmatrix} &= B(\omega) \begin{bmatrix} v \\ \omega \end{bmatrix} + \dot{A}^{-1}(\theta) A(\theta) \begin{bmatrix} v \\ \omega \end{bmatrix} + \dot{A}^{-1}(\theta) k_1 \begin{bmatrix} e_x + l\cos\theta \\ e_y + l\sin\theta \end{bmatrix} \\ \begin{bmatrix} \delta_{12} \\ \delta_{22} \end{bmatrix} &= -A^{-1}(\theta) \begin{bmatrix} \Delta_1 \\ \Delta_2 \end{bmatrix} - \dot{A}^{-1}(\theta) A\left(\theta_r\right) \begin{bmatrix} v_r \\ \omega_r \end{bmatrix} - \dot{A}^{-1}(\theta) k_1 l \begin{bmatrix} \cos\theta_r \\ \sin\theta_r \end{bmatrix} \end{aligned} \tag{22}$$

Theorem 1 *Suppose that Assumption 1 establishes and the control parameters satisfy* $k_1 > 0, \varepsilon_1 > 0, \varepsilon_2 > 0$, *the sliding-mode control law*

$$\begin{cases} \bar{\tau}_1 = -\hat{\bar{p}}_1 \delta_{11} - \hat{\bar{p}}_1 \delta_{12} - \operatorname{sign}(\bar{s}) \left(\bar{p}_1' |\delta_{11}| + \bar{p}_1' |\delta_{12}| + \varepsilon_1\right) \\ \bar{\tau}_2 = -\hat{\bar{p}}_2 \delta_{21} - \hat{\bar{p}}_2 \delta_{22} - \operatorname{sign}(\bar{s}) \left(\bar{p}_2' |\delta_{21}| + \bar{p}_2' |\delta_{22}| + \varepsilon_2\right) \end{cases} \tag{23}$$

guarantees that $\left(\bar{s}_1, \bar{s}_2\right)$ *converge to the origin in finite time, where* $\bar{p}_1 = p_1^{-1}$, $\bar{p}_2 = p_2^{-1}$ *are unknown positive constants bounded by known constants* $\left(\bar{p}_{1M}, \bar{p}_{1m}, \bar{p}_{2M}, \bar{p}_{2m}\right)$, *i.e.*

$$\bar{p}_{1M} \geq \bar{p}_1 \geq \bar{p}_{1m} > 0, \bar{p}_{2M} \geq \bar{p}_2 \geq \bar{p}_{2m} > 0 \tag{24}$$

and

$$\begin{cases} \hat{\bar{p}}_1 = 0.5\left(\bar{p}_{1m} + \bar{p}_{1M}\right), \hat{\bar{p}}_2 = 0.5\left(\bar{p}_{2m} + \bar{p}_{2M}\right) \\ \bar{p}_1' = \max\left(|\bar{p}_1 - \hat{\bar{p}}_1|\right) = 0.5\left(\bar{p}_{1M} - \bar{p}_{1m}\right) \\ \bar{p}_2' = \max\left(|\bar{p}_2 - \hat{\bar{p}}_2|\right) = 0.5\left(\bar{p}_{2M} - \bar{p}_{2m}\right) \end{cases} \tag{25}$$

Proof Choose $V_1 = 0.5\bar{p}_1 \bar{s}_1^2$ and $V_2 = 0.5\bar{p}_2 s_2^2$ as Lyapunov candidates functions and compute their derivatives along with the trajectory of closed-loop system (21)–(23) as

$$\begin{aligned} \dot{V}_1 &= \bar{s}_1 \left[\delta_{11}\left(\bar{p}_1 - \hat{\bar{p}}_1\right) + \delta_{12}\left(\bar{p}_1 - \hat{\bar{p}}_1\right)\right] - |\bar{s}_1| \left(p_1' |\delta_{11}| + p_1' |\delta_{12}| + \varepsilon_1\right) \\ &\leq |\bar{s}_1| |\delta_{11}\left(\bar{p}_1 - \hat{\bar{p}}_1\right)| + |\delta_{12}\left(\bar{p}_1 - \hat{\bar{p}}_1\right)| - |\bar{s}_1| \left(p_1' |\delta_{11}| + p_1' |\delta_{12}| + \varepsilon_1\right) \\ &\leq -\varepsilon_1 |\bar{s}_1| - |\bar{s}_1| \left(p_1' - |\bar{p}_1 - \hat{\bar{p}}_1|\right) |\delta_{11}| - |\bar{s}_1| \left(p_1' - |\bar{p}_1 - \hat{\bar{p}}_1|\right) |\delta_{12}| \\ &\leq -\varepsilon_1 |\bar{s}_1| \\ \dot{V}_2 &= \bar{s}_2 \left[\delta_{21}\left(\bar{p}_2 - \hat{\bar{p}}_2\right) + \delta_{22}\left(\bar{p}_2 - \hat{\bar{p}}_2\right)\right] - |\bar{s}_2| \left(p_2' |\delta_{21}| + p_2' |\delta_{22}| + \varepsilon_2\right) \\ &\leq |\bar{s}_2| |\delta_{21}\left(\bar{p}_2 - \hat{\bar{p}}_2\right)| + |\delta_{22}\left(\bar{p}_2 - \hat{\bar{p}}_2\right)| - |\bar{s}_2| \left(p_2' |\delta_{21}| + p_2' |\delta_{22}| + \varepsilon_2\right) \\ &\leq -\varepsilon_2 |\bar{s}_2| - |\bar{s}_2| \left(p_2' - |\bar{p}_2 - \hat{\bar{p}}_2|\right) |\delta_{21}| - |\bar{s}_2| \left(p_2' - |\bar{p}_2 - \hat{\bar{p}}_2|\right) |\delta_{22}| \\ &\leq -\varepsilon_2 |\bar{s}_2| \end{aligned} \tag{26}$$

Let $W_1 = \sqrt{2\bar{p}_1^{-1} V_1} = |\bar{s}_1|, W_2 = \sqrt{2\bar{p}_2^{-1} V_2} = |\bar{s}_2|$, we then obtain

$$D^+ W_1 = \frac{2\bar{p}_1^{-1} \dot{V}_1}{2\sqrt{2\bar{p}_1^{-1} V_1}} \leq -\varepsilon_1 \bar{p}_1^{-1}, D^+ W_2 = \frac{2\bar{p}_2^{-1} \dot{V}_2}{2\sqrt{2\bar{p}_2^{-1} V_2}} \leq -\varepsilon_2 \bar{p}_2^{-1} \tag{27}$$

Comparison principle can then be used to obtain the conservative estimation of converging time of $\left(\bar{s}_1, \bar{s}_2\right)$ and we get

$$\bar{s}_1(t) = 0, \bar{s}_2(t) = 0, \forall t \geq T_1 = \max\left\{\bar{p}_{1M} \frac{\left|\bar{s}_1(0)\right|}{\varepsilon_1}, \bar{p}_{2M} \frac{\left|\bar{s}_2(0)\right|}{\varepsilon_2}\right\} \tag{28}$$

According to (21), we know that $\left(s_1(t), s_2(t)\right) = (0,0)$ for $t \geq T_1$. On the sliding surface $\left(s_1(t), s_2(t)\right) = (0,0)$, the auxiliary position tracking errors $\left(e_1, e_2\right)$ will converge to zero exponentially.

Next, we show that the overall tracking error system is asymptotically stable because the zero-dynamics subsystem of (15), associated with e_θ, is asymptotically stable. Nulling $\left(\dot{e}_1, \dot{e}_2\right)$ in (15) gives rise to

$$\begin{bmatrix} v \\ \omega \end{bmatrix} = A^{-1}(\theta) A\left(\theta_r\right) \begin{bmatrix} v_r \\ \omega_r \end{bmatrix} \tag{29}$$

Take out the angular velocity and write the dynamics of $\dot{e}_\theta$ as

$$\dot{e}_\theta = \dot{\theta} - \dot{\theta}_r = \omega - \omega_r = -\frac{v_r}{l} \sin e_\theta + \omega_r \left(\cos e_\theta - 1\right) \tag{30}$$

Linearize (30) at $e_\theta = 0$, we obtain

$$\dot{e}_\theta = -\frac{v_r}{l} e_\theta \tag{31}$$

which is exponentially stable under Assumption 1. So the overall closed-loop system is concluded locally asymptotically stable [11] and (7) establishes.

Replacing the unmeasurable variables $\left(\theta_r, v_r, \omega_r, \dot{v}_r, \dot{\omega}_r\right)$ with their estimates $\left(\hat{\theta}_r, \hat{v}_r, \hat{\omega}_r, \hat{\dot{v}}_r, \hat{\dot{\omega}}_r\right)$ in controller (23) leads to

$$\begin{cases} \bar{\tau}_1 = -\hat{\bar{p}}_1 \delta_{11} - \hat{\bar{p}}_1 \hat{\delta}_{12} - \text{sign}\left(\hat{\bar{s}}\right)\left(\bar{p}_1' |\delta_{11}| + \bar{p}_1' |\hat{\delta}_{12}| + \varepsilon_1\right) \\ \bar{\tau}_2 = -\hat{\bar{p}}_2 \delta_{21} - \hat{\bar{p}}_2 \hat{\delta}_{22} - \text{sign}\left(\hat{\bar{s}}\right)\left(\bar{p}_2' |\delta_{21}| + \bar{p}_2' |\hat{\delta}_{22}| + \varepsilon_2\right) \end{cases} \tag{32}$$

where

$$\begin{cases} \begin{bmatrix} \hat{\delta}_{12} \\ \hat{\delta}_{22} \end{bmatrix} = -A^{-1}(\theta) \begin{bmatrix} \hat{\Delta}_1 \\ \hat{\Delta}_2 \end{bmatrix} - \dot{A}^{-1}(\theta) A\left(\hat{\theta}_r\right) \begin{bmatrix} \hat{v}_r \\ \hat{\omega}_r \end{bmatrix} - \dot{A}^{-1}(\theta) k_1 l \begin{bmatrix} \cos\hat{\theta}_r \\ \sin\hat{\theta}_r \end{bmatrix} \\ \begin{bmatrix} \hat{\Delta}_1 \\ \hat{\Delta}_2 \end{bmatrix} = A\left(\hat{\theta}_r\right) \begin{bmatrix} \dot{\hat{v}}_r \\ \dot{\hat{\omega}}_r \end{bmatrix} + A\left(\hat{\theta}_r\right) B\left(\hat{\omega}_r\right) \begin{bmatrix} \hat{v}_r \\ \hat{\omega}_r \end{bmatrix} \\ \begin{bmatrix} \hat{s}_1 \\ \hat{s}_2 \end{bmatrix} = A^{-1}(\theta) \left[A(\theta) \begin{bmatrix} v \\ \omega \end{bmatrix} - A\left(\hat{\theta}_r\right) \begin{bmatrix} \hat{v}_r \\ \hat{\omega}_r \end{bmatrix} + k_1 \begin{bmatrix} \hat{e}_1 \\ \hat{e}_2 \end{bmatrix} \right] \\ \begin{bmatrix} \hat{e}_1 \\ \hat{e}_2 \end{bmatrix} = \begin{bmatrix} x - x_r + l\left(\cos\theta - \cos\hat{\theta}_r\right) \\ y - y_r + l\left(\sin\theta - \sin\hat{\theta}_r\right) \end{bmatrix} \end{cases} \tag{33}$$

Since the estimated variables $\left(\hat{\delta}_{12}, \hat{\delta}_{22}\right)$ converge to real ones in finite time, there exists $T_2 > 0$ such that the performance of controller (32) equals to that of (23) for $t \geq T_2$. Furthermore, we have

$$(\bar{\tau}_1, \bar{\tau}_2) \in L_\infty, 0 \leq t \leq T_2 \tag{34}$$

so that all states are bounded during transient process. Thus, the closed-loop system under control of (32) is also locally asymptotically stable.

4 Simulation Results

The model parameters of tracker robot are chosen from one real-wheeled mobile robot in the authors' laboratory that satisfy

$$\begin{cases} (2 - 0.2)\,\text{kg} \leq m \leq (2 + 0.2)\,\text{kg} \\ (0.2 - 0.02)\,\text{m} \leq L \leq (0.2 + 0.02)\,\text{m} \\ (0.08 - 0.008)\,\text{kg} \cdot \text{m}^2 \leq I \leq (0.08 + 0.008)\,\text{kg} \cdot \text{m}^2 \\ (0.05 - 0.005)\,\text{m} \leq R \leq (0.05 + 0.005)\,\text{m} \end{cases} \tag{35}$$

which contribute to the inequalities

$$\begin{cases} 0.121 = \bar{p}_{1M} \geq \bar{p}_1 \geq \bar{p}_{1m} = 0.081 \\ 0.027 = \bar{p}_{2M} \geq \bar{p}_2 \geq \bar{p}_{2m} = 0.015 \end{cases} \tag{36}$$

Let the position of reference robot be generated from an eight-shaped trajectory described by

$$\dot{x}_r = g_r \cos\left(2h_r\right), \dot{y}_r = g_r \sin\left(h_r\right), \dot{h}_r = \Omega_r \tag{37}$$

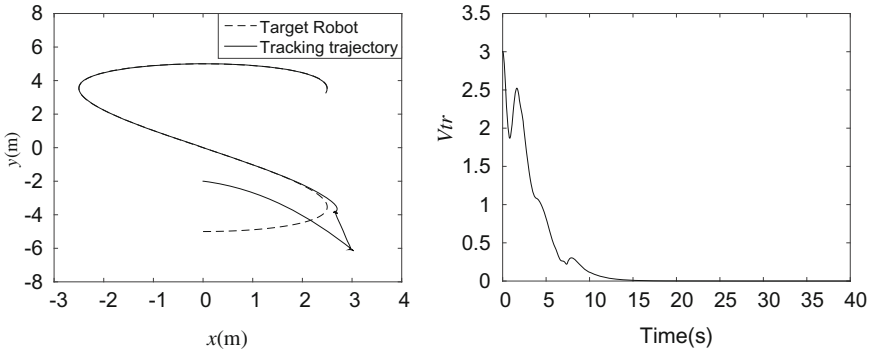

Fig. 1 The tracking trajectory and tracking error (39) under controller (32)

The initial states about robust differentiators are all set to zero, initial states and the rest parameters are

$$\begin{cases} \left[x(0), y(0), \theta(0)\right] = [0, -2, 0] \\ \left[x_r(0), y_r(0), \theta_r(0)\right] = [0, -5, 0] \\ l = 0.1, k_1 = 0.5, \varepsilon_1 = \varepsilon_2 = 0.2 \\ m = 1.8, L = 0.19, I = 0.081, R = 0.05 \\ \lambda_0 = 1.6, \lambda_1 = 1.2, \lambda_2 = 0.4, \lambda_3 = 0.2 \\ g_r = 0.5, \Omega_r = 0.1 \end{cases} \tag{38}$$

Define the tracking error function

$$V_{tr} = \sqrt{e_x^2 + e_y^2 + e_\theta^2} \tag{39}$$

The simulation results are all shown in Fig. 1.

Simulation results show that the robot has successfully catched up with the reference robot under proposed controller (33) and V_{tr} converges to zero asymptotically.

5 Conclusion

A robust sliding-mode controller with only position information of reference robot is obtained by combining sliding-mode control method with robust exact differentiators. Theoretical analysis shows that the overall closed-loop system is locally asymptotically stable. Numerical simulation results verify the efficiency of the propose controller. The proposed controller is robust to model parameters based on the sliding-model technique. The author would like to investigate the multiagent control

problem of WMRs with uncertain model parameters and with only position information of neighbors in future work.

References

1. Brockett RW (1983) Asymptotic stability and feedback stabilization. Differ Geom Control Theory
2. Fierro R, Lewis FL (1995) Control of a nonholonomic mobile robot: backstepping kinematics into dynamics. In: Proceedings of the 34th IEEE conference on decision and control, vol 4. pp 3805–3810
3. Oriolo G, De Luca A, Vendittelli M (2002) WMR control via dynamic feedback linearization: design, implementation, and experimental validation. IEEE Trans Control Syst Technol 10(6):835–852
4. Chwa D (2004) Sliding-mode tracking control of nonholonomic wheeled mobile robots in polar coordinates. IEEE Trans Control Syst Technol 12(4):637–644
5. Mu J, Yan X-G, Jiang B (2015) Sliding mode control for a class of nonlinear systems with application to a wheeled mobile robot. In: 54th IEEE conference on decision and control. pp 4746–4751
6. Koubaa Y, Boukattaya M, Dammak T (2015) Adaptive sliding-mode dynamic control for path tracking of nonholonomic wheeled mobile robot. J Autom Syst Eng 9(2):119–131
7. Ren W, Beard RW (2008) Distributed consensus in multi-vehicle cooperative control. Springer
8. Yang JM, Kim JH (1999) Sliding mode control for trajectory tracking of nonholonomic wheeled mobile robots. IEEE Trans Robot Autom 15(3):578–587
9. Yu K, Montillet JP, Rabbachin A et al (2006) UWB location and tracking for wireless embedded networks. Sig Process 86(9):2153–2171
10. Levant A (2003) Higher-order sliding modes, differentiation and output-feedback control. Int J Control 76(9–10):924–941
11. Khalil HK (2011) Nonlinear control system. Prentice Hall

Parabola-Based Flue Gas Temperature Modeling and Its Application in BTP Control of a Sintering Process

Shengfei Liu, Qinglin Sun and Cheng Ma

Abstract It is very important to predict the accurate position of the burning through point (BTP) in the sintering process. When BTP is controlled accurately, the energy consumption in the sintering process can be reduced greatly. Although BTP cannot be measured directly, we can measure the flue gas temperature to predict BTP. When the flue gas temperature of the twenty-third bellow is controlled at 600 °C, BTP will be controlled on the center of the twenty-third bellow. In this case, the sinter mix can be converted into the sinter ore with the maximum conversion rate. A method of modeling the flue gas temperature based on parabola is discussed in the paper. By means of the least square method (LSM), the relationship between the flue gas temperature and the negative pressure is modeled. The position of the burning through point (BTP) can be controlled by adjusting the negative pressure of the motor which can be controlled by adjusting the duty cycle. By comparing the measured flue gas temperature with the set temperature and comparing the measured negative pressure with the set negative pressure, the fuzzy controller with 81 rules can output the appropriate duty cycle which can control the motor properly. The flue gas temperature of the twenty-third bellow is checked so that the real position of the burning through point can be obtained. Simulations show that the position of the burning through point in the sintering process can be controlled exactly.

Keywords Parabola · Least square method · Negative pressure · Flue gas temperature · Burning through point · Sintering process

S. Liu · Q. Sun (✉) · C. Ma
College of Computer and Control Engineering, Nankai University,
Tianjin 300350, China
e-mail: sunql@nankai.edu.cn

Y. Jia et al. (eds.), *Proceedings of 2016 Chinese Intelligent Systems Conference*,
Lecture Notes in Electrical Engineering 404, DOI 10.1007/978-981-10-2338-5_40

1 Introduction

Steel is one of the most important raw materials in the economic construction, and therefore the development of the steel industry is very important for architecture, transportation, machine industry, etc. Hence, the steel industry is the basic industry and it will play a very important role in future. The sintering process, as an essential part of steel making, consumes 10–15 % of the total energy in the steel making. Energy consumption includes the consumption of the solid fuel, the electricity and the gas for ignition etc. The solid fuel accounts for 75–80 % of the total energy consumption in the sintering process; the electricity accounts for 13–20 %; the ignition consumption accounts for 5–10 %. Nowadays, energy cannot meet demands, and it restricts the development of the steel industry. Hence, it is very necessary to develop the new device which can reduce the consumption of the energy. In order to reduce the amount of energy consumed in the sintering process, the burning through point (BTP) is discussed by many authors [1–10]. The burning through point is a point where the flame front reaches the bottom of the sinter bed, as described in Fig. 1. If the position of the BTP can be controlled accurately, the energy consumption will be reduced greatly. Therefore, it is very meaningful to design the new model and the efficient algorithm for the better control of the BTP. In the paper, a new method, based on parabola, is discussed which can be used to model the relationship between the negative pressure and the flue gas. With the help of the model, a new controller, based on a group of rules, is designed according to fuzzy control method. Simulations show that the position of the BTP can be controlled accurately.

1.1 Sintering Process

Sintering is a process in which sinter mix, including particles of iron ore, limestone, coke and returned sinter, is transformed into sintered ore for a blast furnace. A sintering process is illustrated in Fig. 2.

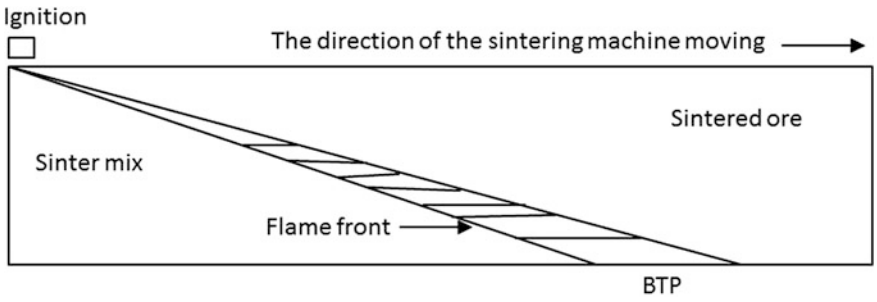

Fig. 1 Burning Through Point(BTP)

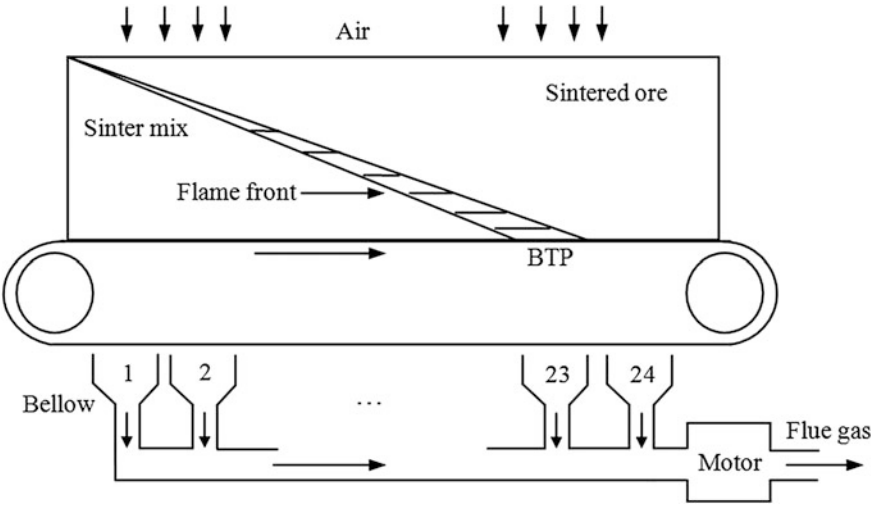

Fig. 2 Sintering process

There are 24 bellows in the sintering process. The burning through point is expected to be located on the twenty-third bellow where the flue gas temperature should reach 600 °C in order that agglomeration can occur.

Parameters of a sintering machine are described in Table 1. Because there are 24 bellows in the sintering process, the position of the burning through point should be controlled on the twenty-third bellow. Although we cannot measure the flame front temperature directly, we can predict T_{Flame} by measuring the flue gas temperature. When the flue gas temperature reaches 600 °C, the flame front will reach the bottom of the sinter bed, where the burning through point is located. Therefore, if the flue gas temperature of the twenty-third bellow reaches 600 °C, the burning through point will be located on the twenty-third bellow, which is our control objective.

Table 1 Parameters of a Dwight-Lloyd sintering machine

Parameter	Value	Denotation
L_{strand}	62 m	Length of the strand
v_{strand}	2.65 m/min	Velocity of the strand
H_{sinter_mix}	1 m	Height of the sinter mix
N_{bellow}	24	Number of bellows
W_{bellow}	2.583 m	Width of every bellow
$Position_{BTP}$	58.118 m	Distance between strand head and BTP
$Center_{23rd\_bellow}$	58.118 m	Distance between strand head and center of 23rd bellow
T_{BTP}	600 °C	Flue gas temperature of BTP
T_{Flame}	1381 °C	Flame front temperature
$Area_{sintering}$	230 m_2	Area of the sintering machine
$v_{\perp}$	45.60 mm/min	Average vertical sintering velocity

1.2 Burning Through Point (BTP) of a Dwight–Lloyd Sintering Machine

Burning through point of a Dwight–Lloyd sintering machine is defined as a point in which the flame front reaches the bottom of the sinter bed. In the paper, BTP should occur on the twenty-third bellow in order that sinter mix can be converted into sintered ore as much as possible. If BTP is located before the twenty-third bellow, the quantity of the sintered ore will decrease. If BTP is located behind the twenty-third bellow, the quality of the sintered ore will become worse. Therefore, it is very important to make BTP occur on the set position accurately.

1.3 Modeling of Relationship Between the Flue Gas Temperature and the Negative Pressure

We have obtained the data which can describe the relationship (R_1) between the flue gas temperature and the negative pressure. These data are: (p_i, T_i), $i = 1,\ldots,1000$. After observation, we discover that the relationship (R_1) can be described by means of the parabola. Therefore, we can get the relationship (R_1) through the data identification. Here, we adopt the least square method (LSM). Assume the relationship (R_1) is described by (1).

$$T = f(p) = ap^2 + bp + c \tag{1}$$

Here, T denotes the flue gas temperature and p denotes the negative pressure. According to LSM, parameters a, b, and c should meet conditions described by (2), (3), and (4).

$$a\sum_{i=1}^{1000} p_i^4 + b\sum_{i=1}^{1000} p_i^3 + c\sum_{i=1}^{1000} p_i^2 = \sum_{i=1}^{1000} T_i p_i^2 \tag{2}$$

$$a\sum_{i=1}^{1000} p_i^3 + b\sum_{i=1}^{1000} p_i^2 + c\sum_{i=1}^{1000} p_i = \sum_{i=1}^{1000} T_i p_i \tag{3}$$

$$a\sum_{i=1}^{1000} p_i^2 + b\sum_{i=1}^{1000} p_i + 1000c = \sum_{i=1}^{1000} T_i \tag{4}$$

The solutions are: $a = 18$, $b = 378$, and $c = -1380$. Hence, (1) becomes (5), which is illustrated in Fig. 3.

$$T = f(p) = -18p^2 + 378p - 1380 \tag{5}$$

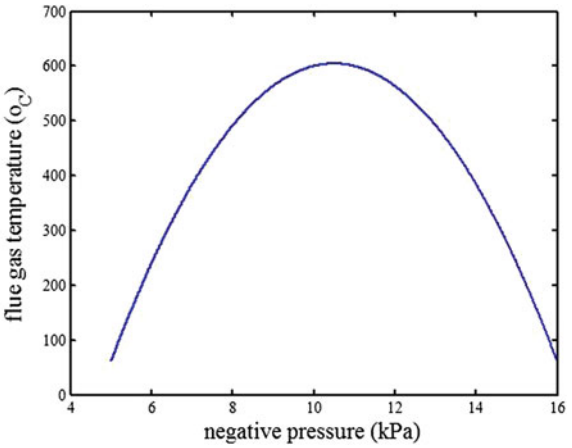

Fig. 3 $T = -18p^2 + 378p - 1380$

1.4 Modeling of Relationship Between the Negative Pressure and the Duty Cycle

We have obtained the data which can depict the relationship between the negative pressure and the duty cycle of the motor. Here, p_i (i = 1,…,1000) denotes the negative pressure and it belongs to the interval [5 kPa,16 kPa]; u_i (i = 1,…,1000) denotes the duty cycle of the motor. We define the relationship as R_2 which is illustrated in Fig. 4. We can utilize the least square method (LSM) to identify R_2. We assume that R_2 can be modeled as (6).

$$p = h(u) = ku + d \tag{6}$$

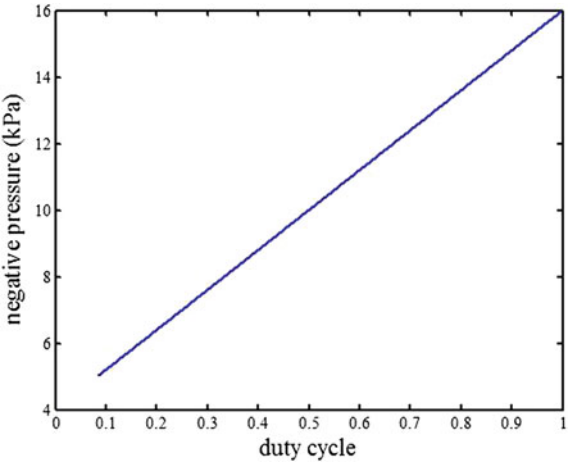

Fig. 4 p = 12u + 4

Here, p and u meet conditions depicted in (7) and (8).

$$k\sum_{i=1}^{1000}u_i^2+d\sum_{i=1}^{1000}u_i=\sum_{i=1}^{1000}u_ip_i \tag{7}$$

$$k\sum_{i=1}^{1000}u_i+1000d=\sum_{i=1}^{1000}p_i \tag{8}$$

We can solve (7) and (8), and the solutions are: $k = 12$, $d = 4$. Therefore, (6) becomes (9).

$$p=h(u)=12u+4 \tag{9}$$

1.5 Modeling of Relationship Between the Flue Gas Temperature and the Duty Cycle

From (5) and (9), we can obtain (10) which is illustrated in Fig. 5.

$$T=f(h(u))=-2592u^2+2808u-156 \tag{10}$$

From Fig. 5, we can see that the flue gas temperature can be set at a point by adjusting the duty cycle of the motor, which is the output of the controller.

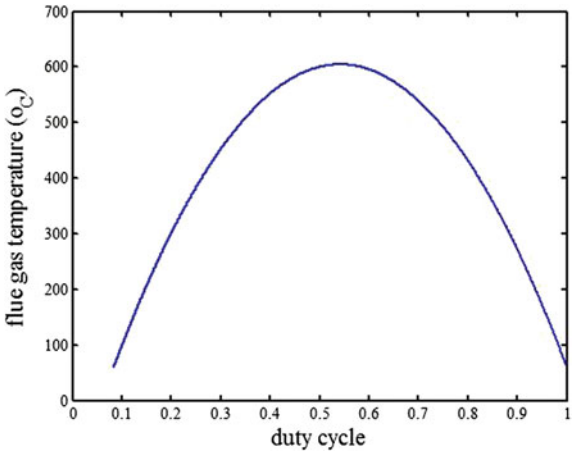

Fig. 5 T = −2592u^2 + 2808u − 156

1.6 The Fuzzy Control System for the Burning Through Point Control in a Sintering Process

The structure of the fuzzy control system for the burning through point control in a sintering process is illustrated in Fig. 6. Here, r_1 denotes the set flue gas temperature of the twenty-third bellow; r_2 denotes the set negative pressure of the wind box; y_1 denotes the measured flue gas temperature of the 23rd bellow; y_2 denotes the measured negative pressure of the wind box; e_1 denotes the error between r_1 and y_1; e_2 denotes the error between r_2 and y_2; u denotes the duty cycle calculated by the fuzzy controller which can control y_1 and y_2. For example, if we set r_1 as 600 °C and set r_2 as 10 kPa, the fuzzy controller will output u according to y_1, y_2 and the fuzzy rules. If $y_1 < 600$ °C and $y_2 < 10$ kPa, the fuzzy controller will increase u so that y_1 and y_2 will increase. As a result, e_1 will decrease and the flue gas temperature will approach 600 °C step by step. On the other hand, if $y_1 < 600$ °C and $y_2 > 10$ kPa, the fuzzy controller will reduce u so that y_2 will decrease. Consequently, e_1 will decrease and y_1 will be close to 600 °C gradually.

1.7 Design of Fuzzy Control Rules

There are 81 rules in the fuzzy control rule table as described in Table 2. Here, NB denotes Negative Big; NM denotes Negative Middle; NS denotes Negative Small; NZ denotes Negative Zero; ZE denotes ZERO; PZ denotes Positive Zero; PS denotes Positive Small; PM denotes Positive Middle; PB denotes Positive Big. x denotes fuzzy value of temperature error; y denotes fuzzy value of negative pressure error; z denotes fuzzy value of duty cycle. Rule_1 means: if x is NB and y is NB, then z is NM. Rule_2 means: if x is NB and y is NM, then z is NM. Rule_{81} means: if x is PB and y is PB, then z is PB. u denotes the duty cycle of the motor which controls the negative pressure in the sintering process. y_1 denotes the flue gas temperature of the 23rd bellow; y_2 denotes the negative pressure of the bellow; e_1 denotes temperature error; e_2 denotes negative pressure error. Relationships among these variables are described in (11), (12), (13), (14), and (15).

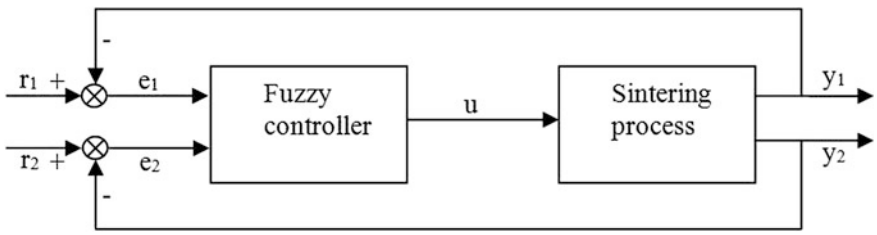

Fig. 6 Structure of fuzzy control system for burning through point control in a sintering process

Table 2 Fuzzy control rule table

y z x	NB	NM	NS	NZ	ZE	PZ	PS	PM	PB
NB	NM	NM	NS	NS	NM	NM	NM	ZE	PM
NM	NM	NM	NS	NS	ZE	ZE	ZE	PZ	PB
NS	NM	NS	NS	ZE	ZE	ZE	ZE	PS	PM
NZ	NM	NM	ZE	ZE	ZE	ZE	ZE	PZ	PM
ZE	NM	NM	NS	ZE	ZE	ZE	ZE	PM	PB
PZ	NB	NM	NS	ZE	ZE	ZE	ZE	PS	PB
PS	NB	NM	NS	ZE	ZE	ZE	ZE	PM	PB
PM	NB	NM	NS	ZE	ZE	ZE	ZE	PM	PB
PB	NB	NM	NS	ZE	ZE	ZE	ZE	PM	PB

$$e_1 = 600 - y_1 \tag{11}$$

$$e_2 = 10 - y_2 \tag{12}$$

$$x = \text{round}[\frac{e_1 - 190}{65}] \tag{13}$$

$$y = \text{round}[\frac{6e_2 + 3}{9.5}] \tag{14}$$

$$u = \frac{1}{12}z + \frac{1}{2} \tag{15}$$

Here, round[] denotes the operation which can get the nearest integer to the number in the brackets. x, y, and z belong to $\{-6, -5, -4, -3, -2, -1, 0, 1, 2, 3, 4, 5, 6\}$.

1.8 Simulations and Analysis

Simulations are illustrated in Figs. 7, 8, and 9.The set temperature is 600 °C and the initial temperature is 60 °C. In Fig. 7, the flue gas temperature error decreases from 540 to 0 quickly. In Fig. 8, the flue gas temperature of the twenty-third bellow reaches 600 °C in a very short time. The flue gas temperature error of the steady state is less than 1 %. In Fig. 9, the duty cycle of the motor increases from 0.083 to 0.75, and then decreases to 0.5. From Fig. 8, we can see that the flue gas temperature of the twenty-third bellow is kept at 600 °C accurately.

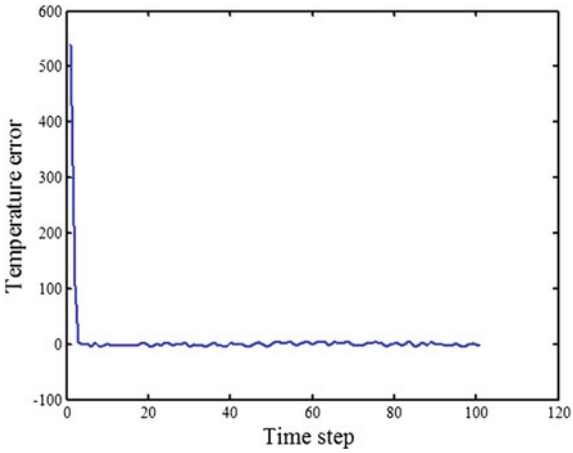

Fig. 7 Temperature error

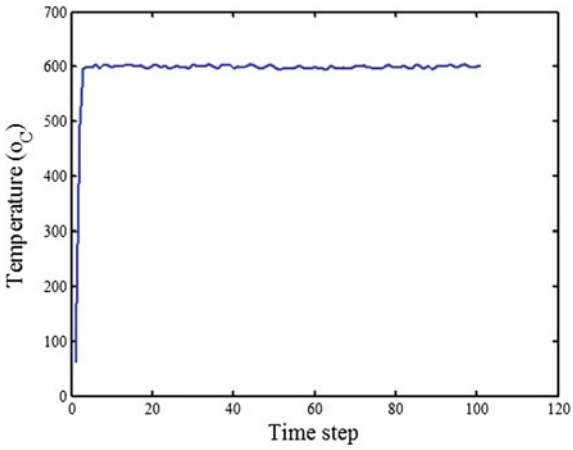

Fig. 8 Flue gas temperature

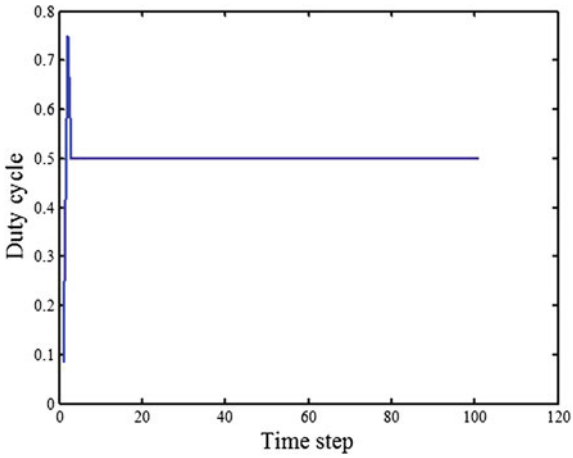

Fig. 9 Duty cycle

2 Conclusion

From simulations, we can make a conclusion that the parabola-based model for the relationship between the flue gas temperature and the negative pressure is correct. We also can see that the flue gas temperature of the twenty-third bellow can be controlled exactly. As a result, the burning through point of the sintering process is located on the twenty-third bellow accurately.

Acknowledgments This work is supported by the National Natural Science Foundation of China under Grant No. 61273138, 61573197, the National Key Technology R&D Program under Grant No. 2015BAK06B04, the key Fund of Tianjin under Grant No. 14JCZDJC39300 and the key Technologies R&D Program of Tianjin under Grant No. 14ZCZDSF00022.

References

1. Wang D, Liu DR, Wei QL, Zhao DB, Jing N (2012) Optimal control of unknown nonaffine nonlinear discrete-time systems based on adaptive dynamic programming. Automatica 48:1825–1832
2. Li SY, Hu CF (2007) Two-step interactive satisfactory method for fuzzy multiple objective optimization with preemptive priorities. IEEE Trans Fuzzy Syst 15(3):417–425
3. Umadevi T, Brahmacharyulu A, Karthik P, Mahapatra PC, Prabhu M, Ranjan M (2012) Ironmaking Steelmaking 39(3):222–227
4. de Castro JA, Sazaki Y, Yagi J-i (2012) Three dimensional model of the iron ore sintering process based on multiphase theory. Mater Res 15(6):848–858
5. Zhao Jia P, Loo Chin E, Dukino Rodney D (2015) Modelling fuel combustion in iron ore sintering. Combust Flame 162:1019–1034
6. Chen XL, Fan XH, Wang Y, Long HM, Jiang T, Shi J et al (2009) Control guidance system for sintering burn through point. Ironmaking Steelmaking 36(3):209–211
7. ChengWS (2006) Prediction system of burning through point(BTP) based on adaptive pattern clustering and feature map. In: Proceedings of 2006 international conference machine learning and cybernetics. pp 3089–3094
8. Kim YH, Kwon WH (1998) An application of min-max generalized predictive control to sintering processes. Control Eng Pract 6(8):999–1007
9. Soyguder S, Alli H (2010) Fuzzy adaptive control for the actuators position control and modeling of an expert system. Expert Syst Appl 37(3):2072–2080
10. Zhang JH, Xie AG, Shen FM (2007) Multi-objective optimization and analysis model of sintering process based on BP neural network. J Iron Steel Res 14(2):1–5

Passive Control of Lorenz Chaos System with Nonlinear Virtual Contraction Analysis

Yunzhong Song

Abstract In order to pave the way for the exploration of Lorenz chaos system control, one kind of observer which was based upon nonlinear virtual contraction analysis was suggested, and on account of that, states of the Lorenz chaos system can be made available via just the single variable output. And thereafter, passive control of Lorenz chaos system was made possible under auspices of the available observed states of the Lorenz chaos system. Results demonstrated that, the expected phase points as well as the origin targeting in helps of passive control can be made possible, and the expected phase point targeting was not like that reported in the already published literature. In comparison with the Lorenz chaos system control with full states, our assumption is much more near the reality, and when compared with the other state observer, the nonlinear virtual contraction analysis method suggested here is much more simple, and from the view point of the fusion of passive control, nonlinear virtual contraction analysis observer, the configuration of the control action is also different from the already existing results, so the specified phase points targeting can also be new, thus, the targeting phase zone can be flexible, which is promising for the potential usage of chaos systems.

Keywords Nonlinear virtual contraction analysis · Observer · Lorenz chaos system · Passive control

1 Introduction

Lorenz chaos system which was developed via the pioneer scientist Edward Lorenz plays an irreplaceable role in nonlinear control field [1], and since then, pours of articles are followed to explore this benchmark chaos system. Among them, impulse control was presented to change the state variables of the Lorenz system to some

Y. Song (✉)
School of Electrical Engineering and Automation, Henan Polytechnic University, 454003 Jiaozuo, China
e-mail: songhpu@126.com

Y. Jia et al. (eds.), *Proceedings of 2016 Chinese Intelligent Systems Conference*, Lecture Notes in Electrical Engineering 404, DOI 10.1007/978-981-10-2338-5_41

given values in a time interval that is very small compared with the characteristic time of the dynamics of the Lorenz system [2]. Adaptive backstepping control scheme was suggested to avoid the singularity for stabilization of the Lorenz chaos system [3], while delayed feedback control of Lorenz chaos system was put forward to investigate the fine structure of the Lorenz system, and some of them were not possible to be made stable by the other methods [4]. Exact linearization, which was based on the nonlinear geometric control, was also borrowed to deal with chaos control of the Lorenz chaos system [5], while an indirect way to stabilize the nonchaotic motion via first stabilizing certain stationary points to destroy the homoclinic connections was also proposed. In this way, stabilization of the Lorenz trajectories about nonchaotic motion is achieved [6]; invariant manifold, which was the extended notion of the linear subspace of linear system into the nonlinear system, was also borrowed to describe the interested targeting locus of the Lorenz system [7, 8], and minimum principle based on optimal control of Lorenz chaos system were reported in [9, 10]. It is well known that the input action which executed by the linear motor or the other mechanical valves is always limited by the energy or the space, so the input constrained control of Lorenz chaos system is also necessarily important and some results have been reported to deal with that [11, 12]. Intelligent information approximation based control of Lorenz chaos system was demonstrated in [13, 14], and composite control of Lorenz system, which takes several control laws into consideration at once time is reported in [15]. Passive equivalence of the Lorenz chaos system was investigated and some phase points targeting was also reported, where the control action was selected to be added in the second equation [16]. Besides these mentioned chaos control ways to the initial Lorenz chaos system itself, some breakthrough works have also been done to transform the Lorenz chaos system from one single bachelor into one kind of family. It has three different members, and they were named as Lorenz chaos system, Chen chaos system, and Lü chaos system, respectively. The first one is the initial member of Loren chaos family system, and the finally found unified chaos system was much more strikingly attractive than the other ones. The different members of the Loren chaos family system can be made to transition from one to another if we change the key parameter from one value to the another value of the unified chaos system, and the related works were reported in [17].

It is undoubtedly that all the just mentioned works have been done to drive the research of the Loren chaos system forward, and also have great positive influence for the upcoming work towards it. And our work here is not the exception, the main attention of our work is that the states of the Loren chaos system are not always available, so the control with full states of Loren chaos system can be failed at some time. On account of that, we try to reconstruct the states of the Loren chaos system with its single output, and we try to make that this kind of work as simple as possible, and in auspices of the nonlinear virtual contraction analysis of the nonlinear system, one special observer is made ready here to make the full states of the Loren chaos system possible. Besides that, the passive control law will be designed to drive the Loren chaos system into the expected target phase points. Unlike the already existing results, for we employ the fist variable as the output state, not only the passive equivalence strategy is different from that demonstrated in the literature,

but also the expected target points are different from references there in. In this point, we expand the target zones of the Loren chaos system, and it is vital importance for the Lorenz chaos system to be used in the coming future.

The rest of the paper is organized as follows: In Sect. 2, some preliminary results of nonlinear virtual contraction analysis together with the passive control theory are reviewed at first. And then, at the incipient part of the Sect. 2, the background of the Loren chaos system will be browsed as short as possible to provide only the minimum necessary background information for this work. In Sect. 3, the observer based on the nonlinear virtual contraction analysis as well as the passive control strategy will be covered in detail, the main results will be reported in this section. Some comments will also be given to highlight the pros of the suggested strategies. And Sect. 4 will be the conclusions.

2 Some Preliminary Results

2.1 Introduction of the Lorenz Chaos System

For Lorenz system

$$\begin{aligned} \dot{x}_1 &= f_1(x_1, x_2, x_3) = -\sigma(x_1 - x_2),\ \dot{x}_2 = f_2(x_1, x_2, x_3) = \rho x_1 - x_2 - x_1 x_3, \\ \dot{x}_3 &= f_3(x_1, x_2, x_3) = x_1 x_2 - \beta x_3. \end{aligned} \tag{1}$$

Parameters like $\sigma = 10$, $\rho = 28$, and $\beta = 8/3$ are taken, which results in chaotic motion. And the corresponding three system equilibria are

$$x_e^{(1)} = [0,\ 0,\ 0]^T,\ x_e^{(2,3)} = \left[\pm\sqrt{\beta(\rho-1)},\ \pm\sqrt{\beta(\rho-1)},\ \rho-1\right]^T = \left[\pm 6\sqrt{2},\ \pm 6\sqrt{2},\ 27\right]^T.$$

It is well known that the Lorenz system can be chaotic in the specified parameters.

2.2 Nonlinear Contraction Analysis

Since the observer design is based on nonlinear contraction analysis, so we will take some time to say something about it [18]. Consider the system

$$\dot{x} = f(x, t). \tag{2}$$

where f is an n times 1 nonlinear vector function and x is the n times 1 state vector. And now we care about the local flow at a given point x leads to a convergence analysis between two neighbouring trajectories. If all neighbouring trajectories

converge to each other, we say that the system is with the contraction behaviour, and then global exponential convergence to a single trajectory can then be concluded. Assume that f(x, t) is continuously differential, (2) yields the exact differential relation

$$\delta\dot{x} = \frac{\partial f}{\partial x}(x,\ t)\delta x. \tag{3}$$

where δx is a virtual displacement. And the square distance between two neighbouring trajectories can be defined as $\delta x^T \delta x$, and the rate of change of the squared distance can be described as

$$\frac{d}{dt}(\delta x^T \delta x) = 2\delta x^T \frac{\partial f}{\partial x}\delta x. \tag{4}$$

Denoting by $\lambda_{\max}(x,\ t)$ the largest eigenvalue of the symmetric part of the Jacobian matrix $\frac{\partial f}{\partial x}$, that is the largest eigenvalue of $\frac{1}{2}\left(\frac{\partial f}{\partial x} + \frac{\partial f^T}{\partial x}\right)$, we thus have

$$\frac{d}{dt}(\delta x^T \delta x) \leq 2\lambda_{\max}(x, t)\delta x^T \delta x. \tag{5}$$

Assume that $\lambda_{\max}(x,\ t)$ is uniformly strictly negative that is $\exists\beta > 0,\ \forall x,\ \forall t \geq 0,\ \lambda_{\max}(x,\ t) \leq -\beta < 0$. Then any two neighbouring trajectories of system (2) converge to each other exponentially.

2.3 A Glimpse of Passive Theory

Consider the nonlinear affine system

$$\dot{x} = f(x) + g(x)u,\ y = h(x). \tag{6}$$

where the state $x \in R^n$, the $u \in R^m$ and output $y \in R^m$, f and the m column of g are smooth vector fields, h is a smooth mapping. The system is said to be passive if there exists a real constant β such that for $\forall t \geq 0$ the following inequality holds

$$\int_0^t u^T(\tau)y(\tau)d\tau \geq \beta. \tag{7}$$

Or there exists a $\rho > 0$ and a real constant β such that

$$\int_0^t u^T(\tau)y(\tau)d\tau + \beta \geq \int_0^t \rho y^T(\tau)y(\tau)d\tau. \tag{8}$$

The physical meaning is that the energy of the nonlinear system can be increased only through the supply from the external source. The stability properties of the passive system are well known [19]. Once the system is rendered passive, the control law such as

$$u = -\varphi(y). \tag{9}$$

can asymptotically stabilize the equilibrium x = 0 of the nonlinear system (6) And in this paper, we will use the passive technique to control the Lorenz chaos system, where Loren chaos system states based only on its single output will be made possible through the observer, and just from this point of view, our results can be different from the already existing results.

3 The Main Results

3.1 *Observer Design for Lorenz Chaos System via Nonlinear Virtual Contraction Analysis*

For system (1), assume that the system output is the first variable, then it can be turned into the following form:

$$\begin{aligned} \dot{x}_1 &= f_1(x_1, x_2, x_3) = -\sigma(x_1 - x_2), \\ \dot{x}_2 &= f_2(x_1, x_2, x_3) = \rho x_1 - x_2 - x_1 x_3, \\ \dot{x}_3 &= f_3(x_1, x_2, x_3) = x_1 x_2 - \beta x_3, \\ y &= x_1. \end{aligned} \tag{10}$$

And we want to design observer for system (10) to get the asymptotical approximation of the second variable and the third variable of the system when the first variable is available. So, we give the following observer system for system (10)

$$\begin{aligned} \dot{y} &= \hat{f}_1(y, \hat{x}_2, \hat{x}_3) = -\sigma(y - \hat{x}_2), \\ \dot{\hat{x}}_2 &= \hat{f}_2(y, \hat{x}_2, \hat{x}_3) = \rho y - \hat{x}_2 - y\hat{x}_3, \ \dot{\hat{x}}_3 = \hat{f}_3(y, \hat{x}_2, \hat{x}_3) = y\hat{x}_2 - \beta\hat{x}_3. \end{aligned} \tag{11}$$

From system (11), we can say that the observer system of (11) for the original system is cost effective, for we use the decreased dimension observer. Now we check system (11) is indeed the ideal observer for system (10). The first order variation of system (11) is as follows

$$\begin{bmatrix} \delta\dot{\hat{x}}_2 \\ \delta\dot{\hat{x}}_3 \end{bmatrix} = \begin{bmatrix} \frac{\partial \hat{f}_2}{\partial \hat{x}_2} & \frac{\partial \hat{f}_2}{\partial \hat{x}_3} \\ \frac{\partial \hat{f}_3}{\partial \hat{x}_2} & \frac{\partial \hat{f}_3}{\partial \hat{x}_3} \end{bmatrix} \begin{bmatrix} \hat{x}_2 \\ \hat{x}_3 \end{bmatrix} = \begin{bmatrix} -1 & -\hat{x}_2 \\ \hat{x}_2 & -\beta \end{bmatrix} \begin{bmatrix} \hat{x}_2 \\ \hat{x}_3 \end{bmatrix} \tag{12}$$

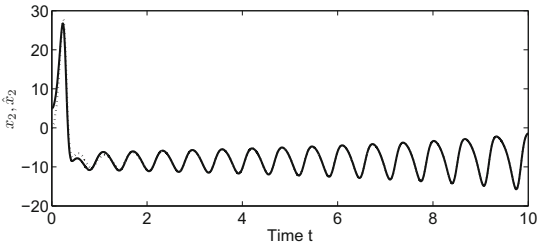

Fig. 1 Reconstruction of the second variable of Loren chaos system

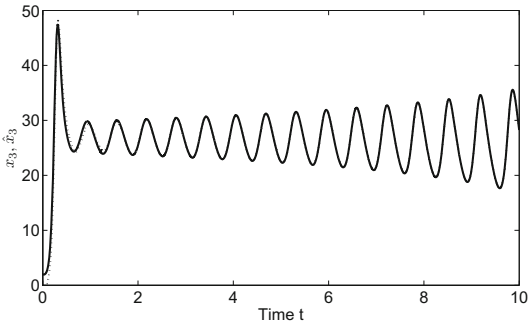

Fig. 2 Reconstruction of the third variable of Loren chaos system

And the corresponding Jacobian matrix is

$$J = \begin{bmatrix} -1 & -\hat{x}_2 \\ \hat{x}_2 & -\beta \end{bmatrix} \tag{13}$$

so

$$\frac{1}{2}(J + J^T) = \begin{bmatrix} -1 & 0 \\ 0 & -\beta \end{bmatrix}. \tag{14}$$

Obviously, the maximum value of the eigenvalue of matrix (14) is negative, that means the system (11) is the exact observer of the system (10). And results of the observer (11) to system (10) are listed as Figs. 1 and 2, respectively.

Remark 1 Loren chaos system has its essential structure peculiarity, and if this kind of peculiarity is taken into account, things will turn into easy. The observer of Loren chaos system design based on nonlinear virtual contraction analysis takes full advantage of this point.

Remark 2 It is easy to acquire that we just use the copy version of the observed system to construct the observer, where its input is from the observed single output, the resulted observer is decreased dimension observer, and on this points of view, our observer is convenient to be realized.

3.2 *Passive Control of Lorenz Chaos System with the Observed States*

3.2.1 Passive Control of Lorenz Chaos System When the Full States Are Available

We start with passive control of Lorenz chaos system with the situation where full states are available. If the system (6) has relative degree [1, 0.1] at x = 0 (Lgh(0) is nonsingular) and the distribution spanned by the vector field $g_1(x)$, $g_2(x)$, …, $g_m(x)$ is involutive, then it can be represented as the so-called normal form

$$\dot{z} = f_0(z) + p(z, y)y,\ \dot{y} = b(z, y) + a(z, y)u. \tag{15}$$

And Eq. (15) can be rendered passive by a state feedback as follows [20, 21]:

$$u = \alpha(x) + \beta(x)v. \tag{16}$$

Now we use this idea to control chaos in Lorenz chaos system. The controlled Loren chaos system is given by

$$\begin{aligned} &\dot{x}_1 = f_1(x_1, x_2, x_3) = -\sigma(x_1 - x_2) + u,\ \dot{x}_2 = f_2(x_1, x_2, x_3) = \rho x_1 - x_2 - x_1 x_3, \\ &\dot{x}_3 = f_3(x_1, x_2, x_3) = x_1 x_2 - \beta x_3,\ y = x_1. \end{aligned} \tag{17}$$

The Lorenz Eq. (10) is already in the normal form of (15), where

$$\begin{aligned} &y = x_1,\ z_1 = x_2,\ z_2 = x_3,\ z = [z_1, z_2]^{\mathrm{T}},\ f_0(z) = [-z_1 \quad -\beta z_2]^{\mathrm{T}}, \\ &p(z, y) = [\rho - z_2 \quad z_1]^{\mathrm{T}},\ a(z, y) = 1,\ b(z, y) = \sigma(z_1 - y). \end{aligned} \tag{18}$$

Our objective is to design a smooth control of (16) for the Lorenz equation to make the closed loop system passive. Choose a storage function candidate

$$V(z, y) = W(z) + \frac{1}{2}y^2. \tag{19}$$

where $W(z)$ is Lypunov function with $W(0) = 0$

$$W(z) = \frac{1}{2}(z_1^2 + z_2^2).$$

The zero dynamics of the system (15) describe internal dynamics which are consistent with external constraint $y = 0$, i.e.

$$\dot{z} = f_0(z). \tag{20}$$

Consider (19) and because constant β is positive,

$$\frac{d}{dt}W(z) = [z_1,\ z_2]\begin{bmatrix} -z_1 \\ -\beta z_2 \end{bmatrix} \leq 0. \tag{21}$$

The zero dynamics of the Loren chaos system is Lyapunov stable, i.e. the Lorenz chaos system is minimum phase. The derivative of $V(z, y)$ along the trajectory of the Lorenz chaos system of (17) is

$$\begin{aligned} \frac{d}{dt}V(z,\ y) &= \frac{\partial}{\partial z}W(z)\dot{z} + y\dot{y} \\ \frac{d}{dt}V(z,\ y) &= \frac{\partial}{\partial z}W(z)f_0(z) + \frac{\partial}{\partial z}W(z)p(z,\ y)y + [b(z,\ y) + a(z,\ y)u]y. \end{aligned} \tag{22}$$

As the Lorenz chaos system is minimum phase

$$\frac{\partial}{\partial z}W(z)f_0(z) \leq 0$$

(22) becomes

$$\frac{d}{dt}V(z,\ y) \leq \frac{\partial}{\partial z}W(z)p(z,\ y)y + [b(z,\ y) + a(z,\ y)u]y. \tag{23}$$

If we select the feedback control (16) as the following form and consider (18):

$$u = a^{-1}(z,\ y)[-b^{\mathrm{T}}(z,\ y) - \frac{\partial}{\partial z}W(z)p(z,\ y) - \lambda y + v] = -(\sigma+\rho)z_1 + (\sigma-\lambda)y + v. \tag{24}$$

where λ is a positive constant and $v = -\varphi(y)$ s.t. $y\varphi(y) > 0$. The above inequality can be rewritten as

$$\frac{d}{dt}V(z,\ y) \leq vy - \lambda y^2. \tag{25}$$

Then, taking integration for both sides of inequality (25), we have

$$V(z,\ y) - V(z_0,\ y_0) \leq \int_0^t v(\tau)y(\tau)d\tau - \lambda\int_0^t y^2(\tau)d\tau. \tag{26}$$

For $V(z, y) \geq 0$, let $\mu = V(z_0, y_0)$, then we obtain

$$\int_0^t v(\tau)y(\tau)d\tau + \mu \geq \lambda\int_0^t y^2(\tau)d\tau + V(z,y) \geq \lambda\int_0^t y^2(\tau)d\tau = \lambda\int_0^t y^{\mathrm{T}}(\tau)y(\tau)d\tau.$$

It satisfies the passive definition (8). Therefore, Eq. (17) has been rendered output strict passive (OSP) under Eq. (24).

If external signal $v = 0$ (zero-input state response), from (26)

$$V(z, y) \leq V(z_0, y_0). \tag{27}$$

Because $W(z)$ is radially unbounded, it follows from (19) that $V(z, y)$ is also radially unbounded, so the closed loop system is bounded state stable for $[z^T, y]^T$. This means that we can use the very simple passive control (24) to regulate the Loren chaos system to the origin.

If the external signal $v \neq 0$, then we want to steer the state of Loren chaos system to a set point $\left[x_1^*, x_2^*, x_3^*\right]$. In the view of (17), we have

$$\rho x_1^* - x_2^* = x_1^* x_3^*, \; x_1^* x_2^* = \beta x_3^*. \tag{28}$$

Substitute (24) to (17) and consider (28), we have

$$v = \rho x_2^* + \lambda x_1^* = \frac{(\rho x_1^*)^2}{1 + \frac{(x_1^*)^2}{\beta}} + \lambda x_1^*. \tag{29}$$

3.2.2 Passive Control of Lorenz Chaos System with Only the Single Available Output

When the full states of the Lorenz chaos system are not available, the direct use of control with (14) is impossible, so we come to take advantage of the observer based on nonlinear virtual contraction analysis, and that turns into the augmented system

$$\begin{aligned}
&\dot{x}_1 = f_1(x_1, x_2, x_3) = -\sigma(x_1 - x_2) + u, \dot{x}_2 = f_2(x_1, x_2, x_3) = \rho x_1 - x_2 - x_1 x_3, \\
&\dot{x}_3 = f_3(x_1, x_2, x_3) = x_1 x_2 - \beta x_3, \; y = x_1. \dot{y} = \hat{f}_1(y, \hat{x}_2, \hat{x}_3) = -\sigma(y - \hat{x}_2), \\
&\dot{\hat{x}}_2 = \hat{f}_2(y, \hat{x}_2, \hat{x}_3) = \rho y - \hat{x}_2 - y\hat{x}_3, \; \dot{\hat{x}}_3 = \hat{f}_3(y, \hat{x}_2, \hat{x}_3) = y\hat{x}_2 - \beta \hat{x}_3. \\
&u = -(\sigma + \rho)\hat{z}_1 + (\sigma - \lambda)y + v = -(\sigma + \rho)\hat{x}_2 + (\sigma - \lambda)y + v.
\end{aligned} \tag{30}$$

Remark 3 The closed loop control system of (30) is fifth order, and it integrates both passive control design method and nonlinear contraction analysis observer, which realized the passive control of Lorenz chaos system with only the single available output variable.

Remark 4 It should be noted that the control action in our work is executed on the first equation of the Lorenz chaos system, and it is different from its counterpart in [16], where the control action is executed on the second equation of the Lorenz

chaos system, so the set point in our case under control is different from that in [16]. And the advantage of our scheme lies in that we extend the reachable sets of Lorenz chaos system, and which is vital importance from the point of usage of Lorenz chaos system.

3.3 Simulation Results

First, let us check the zero-input state response, to drive the complete dynamics as to the origin. The Lorenz chaos system starts from $x_0 = [0, 5, 2]^{\mathrm{T}}$. We select $\lambda = 2$ and $\lambda = 20$, respectively. As in (24) with $v = 0$. According to (27), the closed loop system converge to the origin $[0, 0, 0]^{\mathrm{T}}$; the results are shown in Fig. 3. We note that the system is free of chaotic transients. Each of the states subjected to passive control reaches a constant value in a short time and stays there for a long period. The positive constant λ only influences the transient dynamics. The bigger the λ value is, the faster the transient dynamics is.

Now we will manage to force the Loren chaos system into a set point $[0.1903, 5.2559, 0.375]^{\mathrm{T}}$, which is fulfilled the condition (28), the external signal v is calculated as in (29). Here, we select $\lambda = 2$ and the corresponding $v = 147.5457$. Note that when the Lorenz chaos system is rendered to a passive system, a very simple control modification, i.e. change the value of v, can drive the chaotic system to a set point. And the simulation results are listed at Figs. 4 and 5, respectively.

It should be noted that, the control action is not zero with set point targeting, it is easy to understand if we follow the first equation of the augmented system (30), for in this kind of case, $x_1^* = x_2^*$ does not satisfy, so some cost must be paid via the control from the outside.

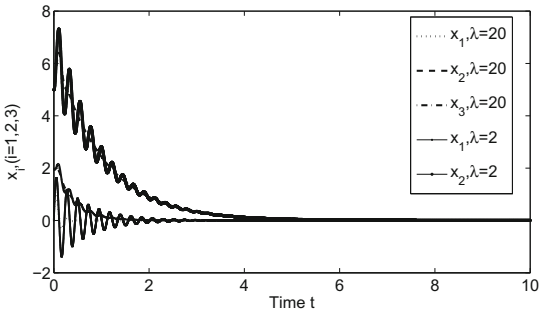

Fig. 3 Passive control of the origin targeting

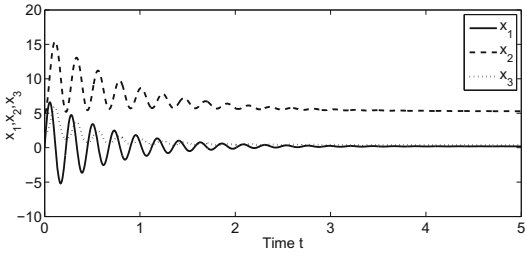

Fig. 4 Loren chaos system set point targeting

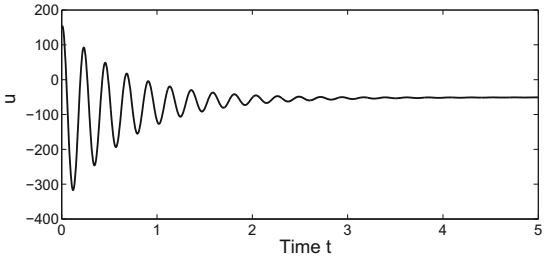

Fig. 5 Control action evolution curve of set point targeting

4 Conclusions

Lorenz chaos system passive control with only the single output variable available is discussed in this paper, and nonlinear virtual contraction analysis is borrowed for building the observer to reconstruct the other states, and on account of that, the closed loop system is the augmented system which is composed by the original Lorenz chaos system, the nonlinear virtual contraction observer and the control action which is finally used for control with feedback of the output and the observed states, and simulation results verify the powerfulness of the suggested scheme.

Acknowledgments This work was supported in part by National Science Foundation of China (61340041 and 61374079), and The Project-sponsored by SRF for ROCS, SEM to Yunzhong Song.

References

1. Lorenz EN (1963) Deterministic non-periodic flow. J Atmos Sci 20:130–141
2. Yang Tao, Yang Lin-Bao, Yang Chun-Mei (1997) Impulsive control of Lorenz system. Phys D 110:18–24
3. Pishkenari HN, Jalili N, Mahboobi SH, Alasty A, Meghdari A (2010) Robust adaptive backstepping control of uncertain Lorenz system. Chaos 20:023105
4. Pyragas V, Pyragas K (2006) Delayed feedback control of the Lorenz system: an analytical treatment at a subcritical Hopf bifurcation. Phys Rev E 73:036215
5. Li-Qun Chen, Yan-Zhu Liu (1998) Control of the Lorenz chaos system by the exact linearization. Appl Math Mech 19:67–73

6. Alvarez-Ramirez Jose, Solis-Daun Julio, Puebla Hector (2005) Control of the Lorenz system: destroying the homoclinic orbits. Phys Lett A 338:128–140
7. Tian Yu-Ping (1999) Controlling chaos using invariant manifolds. Int J Control 72:258–266
8. Tian Y-P, Xing-huo Yu. Adaptive Control of chaotic dynamical systems using invariant manifold approach. IEEE Trans. Circuits & Systems, Part I, Vol.47,pp. 1537–1542,2000
9. Tian Yu-Chu, Tadé Moses O, Levy David (2002) Constrained control of chaos. Phys Lett A 296:87–90
10. Song Yun-Zhong, Zhao Guang-Zhou, Qi Dong-Lian (2006) Some comments on constrained control of chaos. Phys Lett A 359:624–626
11. Gao Shi-Gen, Dong Hai-Rong, Sun Xu-Bin, Ning Bin (2015) Neural adaptive chaotic control with constrained input using state and output feedback. Chin Phys B 24:010501
12. Yaua Her-Terng, Chenb Chieh-Li (2007) Chaos control of Lorenz systems using adaptive controller with input saturation. Chaos, Solitons Fractals 34:1567–1574
13. Zheng-Guang Wu, Shi Peng, Hong-Ye Su, Chu Jian (2014) Sampled-data fuzzy control of chaotic systems based on a T-S fuzzy model. IEEE Trans Fuzzy Syst 22:153–163
14. Wang Cong, Chen Tian-Rui, Chen Guan-Rong, Hill David J (2009) Deterministic learning of nonlinear dynamical systems. International Journal of Bifurcation and Chaos 19:1307–1328
15. Lenz Henning, Obradovic Dragan (1997) Robust control of the chaotic Lorenz system. Int J Bifurc Chaos 7:2847–2854
16. Wen Yu (1999) Passive equivalence of chaos in Lorenz system. IEEE Trans Circuits Syst Part I 46:876–878
17. Qi Dong-Lian, Wang Qiao, Hu Gu (2008) Chaotic attractor transforming control of hybrid Lorenz-Chen system. Chin Phys B 17:847–851
18. Lohmiller W, Slotine JJ (1998) On contraction analysis for nonlinear systems. Automatica 34:683–696
19. Byrnes CI, Isidori A, Willem JC (1991) Passivity, feedback equivalence, and the global stabilization of minimum phase nonlinear systems. IEEE Trans Autom Control 36:1228–1240
20. DJ Hill, Moylan P (1976) The stability of nonlinear dissipative systems. IEEE Trans Autom Control 21:708–711
21. Song Yun-Zhong, Zhao Guang-Zhou, Qi Dong-Lian (2006) Passive control of chaotic system with multiple strange attractors. Chin Phys 15:2266–2270

A Method of Virtual Test Based on Model Checking and a Case Study

Qiqige Wuniri, Xiaoping Li, Fan Yang, Shilong Ma, Yifan Liu and Naihai Li

Abstract In this paper a virtual test method, which is a fusion approach on the combination of automata-based model checking theory and systems engineering theory, is proposed. An automaton of Window Tree Model (WTM) based on multi-tree to describe the system behavior as a system model is used on one hand, and a State Transition Graph (STG) based on Büchi automaton to describe design correctness as a specification is used on the other hand. An automaton-based model checking mechanism is designed to build the foundation of the virtual test method. Moreover, the two main aspects of the method, which are the design correctness verification and the interface test, are defined. A case study is followed to illustrate the modeling and verification process. Finally, a Virtual Test Platform (VTP), which implements the method, is introduced to unfold the virtual test configuration, virtual test execution as well as the virtual test evaluation features.

Keywords Virtual test method · State transition graph · Model checking · Window tree model · Test case generation · Virtual test platform

Q. Wuniri · X. Li (✉) · F. Yang · S. Ma
State Key Laboratory of Software Development Environment, Beihang University, Beijing 100191, China
e-mail: lee.rex@163.com

Q. Wuniri
e-mail: qiqige.wuniri@nlsde.buaa.edu.cn

F. Yang
e-mail: yangfan06@buaa.edu.cn

S. Ma
e-mail: slma@nlsde.buaa.edu.cn

Y. Liu · N. Li
Beijing Institute of Spacecraft System Engineering, Beijing 100094, China
e-mail: ayifan2004@163.com

N. Li
e-mail: linaihai2006@163.com

Y. Jia et al. (eds.), *Proceedings of 2016 Chinese Intelligent Systems Conference*, Lecture Notes in Electrical Engineering 404, DOI 10.1007/978-981-10-2338-5_42

1 Introduction

The assurance on the reliability of complex system, such as satellite, needs an effective and cost-safe system-level test to meet the ever increasing demands. A multitude of heterogeneous computer models, tools and techniques are employed during the test process of complex system [1]. Among them, a virtual test [2, 3] of system-level verification tends to be a new challenging area.

Virtual test does not mean there is a substitute for the real world physical test. But, for some of the system test such as design correctness, there is no need to wait until the post manufacture. Thus, virtual test is valuable to correct-by-construction development. Usually a virtual test of system-level verification relies on proper virtual prototyping [4]. There are kinds of virtual prototyping techniques, while in this paper, we focus on system-level models and pure software simulator of a target system. And the corresponding virtual test method is also narrowed down to software virtual prototype.

Our method is inspired from Model checking theory [5], which is one of the formal verification methods. In Model checking, a common approach is that the temporal logic specification is used to check system properties where the system is modeled as a finite state machine. While in this paper, we focused on another approach of using automaton as a specification.

The detail discussions on the related work of virtual test and formal methods are presented in the next section. The rest of this paper is organized as follows. Sections 3 and 4 discusses the computer models of Window Tree Model and State Transition Graph separately. In Sect. 5, we focused on discussing the virtual test method proposed in this paper. This section presents our research motivation, test relevant algorithms, definition and the basic concept of the virtual test. A case study and its virtual test result are shown in Sect. 5. And finally, the conclusions are drawn in Sect. 6.

2 Related Work

2.1 Virtual Test

Several virtual test approaches have been proposed in literatures. For embedded system a virtual test lab [3] is developed to reduce the cost of real hardware test. For distributed computational system a virtual test tube [2] based on biomolecules computing theory has been proposed. The test or verification based on Virtual Prototyping [4, 6] has been still prevailing over other virtual test in recent years in plenty of different areas [7–11]. Virtual Prototyping [4] is not only to prove design concepts, evaluate design alternatives, test product manufacturability, but also test product's form or performance and support for training or other studies.

The existing virtual test methods seemed to be focused too closely on the construction of a prototype of the physical system. While, for a system-level behavior test, virtual reality is not that necessary. Sometimes simply a pure software simulator of the system under test is sufficient to perform system-level verification. Meanwhile, a modeling method or tool of system-level behavior is much more important than its visualization model.

2.2 Formal Methods

Modern software and hardware complexity increases the requirements on its reliability. Formal methods are mathematically based on specifying and verifying these kinds of software or hardware systems [12]. Formal methods include formal specification and formal verification. Specification is the process of describing a system and its desired properties. This might include: functional behavior, timing behavior, performance characteristics, as well as system's internal structure. Formal specification uses a language with mathematically defined syntax and semantics. Formal verification includes two main approaches, one is theorem proving, another is model checking [13].

Several formal methods of model checking were used in critical system verification [12]. While, due to some disadvantages of existing formal methods, such as too obscure notations, inadequate tool support, inconvenience usage of tools, or not scalable techniques, the feasibility of model checking is still under query in practice. Previous formal verification documents are mainly focused on temporal logic to describe the desired properties [14–16]. While recent research on Window Tree Modeling method [17] is a new approach to this area. But it still needs corresponding tool support. Upon these realities, in this article, we propose a light weight modeling tool from which extended existing modeling platform. It aims at the following three points. First, describing a system's partial or all functional behaviors in formal specification of automaton; second, generating equivalence of xml description automatically; finally, generating a test case suite upon the Window tree.

3 Window Tree Modeling

Window Tree Model [18] is a newly introduced formal modeling method on describing system-level behavior. A system-level behavior of complex system can be recognized as a process which can be divided into a set of APIs invocation. The APIs indicate the interfaces provided by a specific unit of the system involved in the process. In this model, a Window is represented as the trigger of a process and an Event is represented as the actual invocations of APIs from the related window. A sample WTM is shown in Fig. 1.

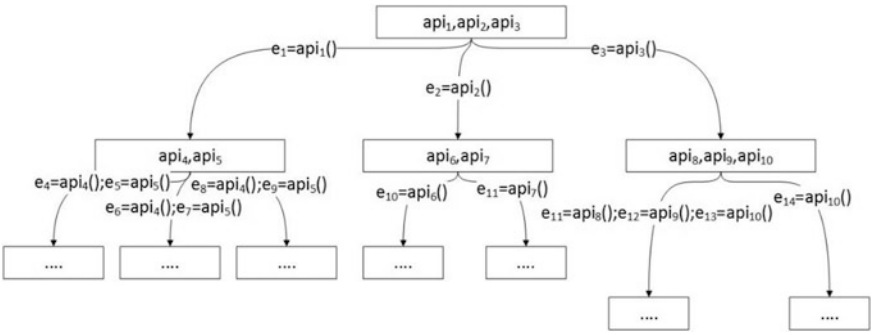

Fig. 1 General window tree model

A rectangle in the figure represents a Window, while a link in the figure represents an Event. At the top of the sample model, there is a root Window provides three APIs called api_1, api_2 and api_3 individually. Suppose a process begins from this Window, the Event e_1 (an invocation of api_1) will continue the process to the next Window which provide APIs called api_4, api_5, while the Event e_2 (an invocation of api_2) will continue the process to the next Window which provide APIs called api_6, api_7. Similarly, e_3 (an invocation of api_3) will make the process flow to a Window of APIs called api_8, api_9, api_{10}. As the Window Tree is actually a multi-tree, we called the root of the tree as a root Window and the leaf of the tree as a leaf Window. Each path from a root Window to a leaf Window constitutes a process. All processes in the Window Tree are expected to simulate the system-level behavior of a complex system.

As a new modeling method, its relevant definitions of WTM include Window, Event, and Window Tree. Each notion is listed below.

Definition 1 (*Window*) A Window is a 2-tuple (wName, APIs) where wName is the label of a window; APIs is the interfaces provided by the Window.

Suppose there is a transition from a window A to a window B, it means the invocation sequence of a subset of the APIs provided by the window A flow to the window B. Each invocation of an API called Event. Event is a basic behavior of a window transition.

Definition 2 An Event is a 3-tuple (eName, APIs, Parameters) where eName is the label of an Event, APIs is the interfaces invoked in the Event, and Parameters is the given list of parameters.

Definition 3 (*Parameter*) A parameter can be defined as 2-tuple (paraName, paraType) where paraName is parameter name, paraType is its type.

Definition 4 (*Window Tree*) A Window Tree is a 4-tuple (W, w_0, E, $R_{W,E}$) where W is a finite set of Windows with $w_0 \in W$ the initial window, $R_{W,E} \subseteq W \times E \times W$ is a finite set of transition relations, E is a finite set of Event representing all transition between Windows.

From the graphical model of a Window Tree, it is a special case of digraph (multi-tree). Any features of multi-tree can be applied to this model to support scientific research. Furthermore, a Window Tree is also an automaton. With all of its formal definitions, a Window Tree Model can also be analyzed and verified with formal method. The application of how WTM supports system-level verification will be discussed later in detail.

4 State Transition Graph

State Transition Graph (STG) is a Büchi automaton to model a target system's design correctness. The main concept of this model is to use states and transitions to describe a system designed behavior. A state indicates an observable status of a system after a process of a behavior. While a transition indicates an event which is triggered to change the system state. A STG can be modeled in a digraph, but as the state and the transition number grow, it's recommended to use a list to store all of the transition rules like in the following table (Table 1).

In this table, there are three columns of 'From State ID', 'Event ID' and 'To State ID'. Every row in the table indicates a state transition from the state of first column to the state of third column triggered by an event in the second column. While the event here is the same meaning with previously defined Event. The relevant notions are also listed as follows.

Definition 5 (*State*) A State is a status of a system at a given point in the process of a behavior.

A State is always accompanied with an Event.

Definition 6 (*State Transition Graph*) A State Transition Graph is a 5-tuple (S, s_0, E, $R_{S,E}$, F) where S is a finite set of states with $s_0 \in S$ the initial state, E is a finite set of Event, $R_{S,E} \subseteq S \times E \times S$ is a finite set of state transition rule, F is a subset of states representing all terminal states.

Definition 7 (*State Transition Sequence*) A State Transition Sequence is a sequence of State s_1; s_2;…; s_n ($n \geq 1$). Each State s_i ($n \geq i \geq 1$) is accompanied with an Event e_i($n \geq i \geq 1$) according to a transition rule.

Table 1 State transition rules

From State ID	Event ID	To State ID
S1	e1	S2
S2	e2	S3
S3	e3	S4
S4	e4	S5
S5	e5	S6
S6	e6	S7
S7	e7	S8

Like the WTM, a STG is a Büchi automaton which can be presented as digraph. Any features of digraph can be applied to this model to support scientific research. Moreover, STG is a formal modeling method on simulating target system's normal correct behaviors.

5 Virtual Test Method

5.1 Motivation and Mechanism

Our motivation of the virtual test method is inspired from the analysis of the relationship between WTM and STG. Similarities of the two models are (1) both of them are automaton; (2) both have interacted with event information; (3) both have formal definitions. While, obviously their difference is the modeling objectives are not the same.

With formal definitions, both the languages of the models are feasible to be automatically processed by computer. As an automaton, both of them can be analyzed and verified with formal method, especially model checking [19]. Model checking is the basis of system test [5]. Therefore, if we use WTG as a model of a system-level behavior and STG as a specification to describe design correctness, a solid foundation of automata-based model checking method were built.

Event, which connected the two models, plays an important role in actual usage indeed. On one hand, an event in WTG is the corresponding API invocation with its instances of parameters. And API invocation sequence can be seen as a test case. Hence, a sequence of events can be generated by a test case with actual test data. It is also a behavior of a system under the WTG specification. On the other hand, an event in STG conducts a state transition. Hence sequences of events are accompanied with a State Transition Sequence according to the state transition rules.

As a system-level test is mainly [20] to check whether a system behavior is correctly moved from one state to another state or not. Therefore, in this paper a system-level test can be translated into a checking process of whether the accompanied state transition sequences of the event sequences follow the state transition rules in STG or not. Specifically, the language recognized by the STG automaton includes all of the correct state transition sequences those follow the state transition rules in STG. The detail mechanism of checking process is shown in Fig. 2.

In the left side of the figure, there are the system model of WTM, and its corresponding automaton $A_{simulator}$. It simulates the system behavior, supports for automatic test case generation and test case execution. While in the right side, there are the specification of the STG and its corresponding automaton A_{check}. It checks the correctness of the system behavior and returns the checking results.

As an automaton, both of the automata have their input and output, which are shown in the figure in red line and green line separately.

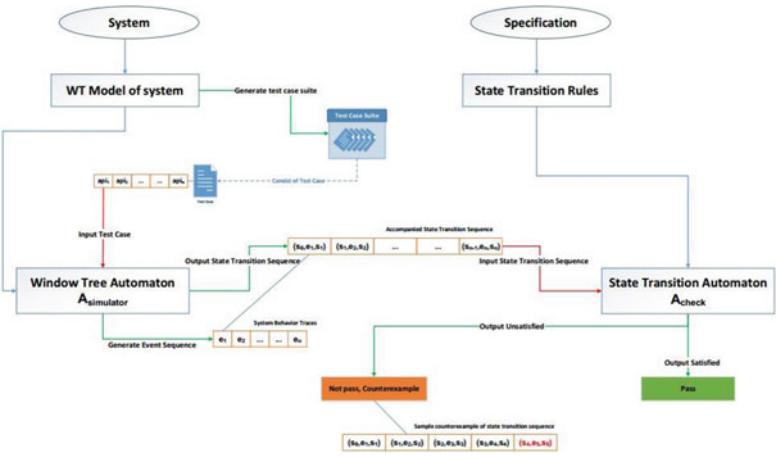

Fig. 2 Automata-based checking mechanism

For the $A_{simulator}$, the input is a test case in the test case suite which is automatically generated on the basis of WTM. And this automaton generates an event sequence after a test case execution, more importantly, it also outputs the accompanied state transition sequence of the event sequence.

For the A_{check}, the input is the state transition sequence output by $A_{simulator}$. The automaton checks all of the adjacent state transitions in the sequence based on its rules. Finally, outputs two possible results. One, if all of the state transitions from the input follows the rules, it outputs 'pass' indicating the behavior of the test case is correct. Another, if any state transition from the input violated the rules, it outputs 'Not pass' and the prefix of the input (from the first state to the violated point) as a counterexample. It indicates the behavior of the test case is not under the rule.

Hence, in Fig. 2, there are two main algorithms in the process of checking. One is the test case generation algorithm based on WTM, another is the model checking algorithm. Both will be discussed in detail in the following sections.

5.2 *Test Case Generation*

We will give an automatic test case generation algorithm and use the test case suite to simulate all system-level behavior modeled in WTM. The relevant formal definitions are given below

Definition 8 (*Test Case*) A Test Case is a 2-tuple (tcName, APIs) where tcName is the label of a test case, APIs is a sequence of API.

Definition 9 (*Test Case Suite*) A finite set of test cases.

There are two basic algorithms in the test case generation based on the Window Tree Model. One is a FindPath Algorithm based on traditional Depth-First Traversal(DFT) algorithm to get a longest path based on a given root window. Another is a Test Case Generation algorithm to automatically generate a test case suite regarding to a whole Window Tree.

```
Algorithm 1. FindPath
Input: root, adjM   /* the given root id and the adjacent matrix */
Output: path  /* the test case suite */
begin
    (1)  path = DFTraverse ();/* the longest path of rw in the adjM */
    (2)  return path ;          /* return the path in the adjM */
end.
```

```
Algorithm 2. Test Case Generation
Input: wt /* the Given Window Tree */
Output: tcSuite  /* the list of test case suite */
begin
    (1)  Initialize(wt, adjM);     /* Initialize the adjM from wt */
    (2)  For each root window in wt.roots
         a)  pathi=FindPath (rw, adjM);     /* find the longest path of rw */
         b)  apilist=Map2APIs(pathi);       /* map the path id to a list of APIs */
         c)  tcSuite.add(apilist);  /* add the APIs to the test case suite */
    (3)  return tcSuite;            /* return the test case suite */
end.
```

5.3 Model Checker Algorithms

Like traditional model checker, there are system model on the left and specification on the right. In this paper, we use (1) WTM which is focusing on system-level behavior as a system model; (2) STG which is aimed to describing design correctness as a specification. As we found the intersections of these two models is the sequence of events shown in Fig. 2, the main process the model checker algorithm is narrowed down to the Check. Its formal definition is given below:

Definition 10 (*Check*) A Check is a process of checking a given State Transition Sequence is a word of the language recognized by the STG automaton.

Therefore, a model checker we designed is a State Transition Sequence verification process regarding to the given state transition rules. If every adjacent state in the queue follows the transition rules in the STG, the queue is a word of the

language recognized by the STG, otherwise the checker will return a counterexample regarding to the STG. The detailed steps are shown in Algorithms 3 and 4.

Algorithm 3. BaseCheck

```
Input: currSt, nxtSt, rule/* the current and the next state, a transition rule */
Output: matchFlag/* include match, one side match or not match */
begin
    (1) If currSt==rule.fromState && nxtSt==rule.toState return Match;
    (2) Else if currSt==rule.fromState && nxtSt!=rule.toState return RightNMatch;
    (3) Else if currSt!=rule.fromState && nxtSt==rule.toState return LeftNMatch;
    (4) Else return NMatch;
end.
```

Algorithm 4. Checker

```
Input: StateQ, RuleSet          /* the State Transition Sequence, the STG Rules */
Output: counterexample /* the State Transition Sequence with counterexample */
begin
    (1) Enqueue(ProcessingStQ, currentSt); /* initialize a processing state transition sequence */
    (2) Enqueue(PossibleCounterExampleQ, currentSt); /* initialize a possible counterexample of state transition sequence. */
    (3) currentSt=Dequeue(StateQ); /* poll a state */
    (4) nextSt=Dequeue(StateQ);     /* poll a state */
    (5) allMatchFlag=false;
    (6) do
        a) oneMatchFlag =false;
        b) for each rule RuleSet
            i.   Enqueue(ProcessingStQ, nextSt);   /* push a state */
            ii.  if BaseCheck(currentSt, nextSt, rule) == Match then
                 1. oneMatchFlag=true;
                 2. break;
            iii. else then
                 1. get next rule in STG rules
                 2. Enqueue(PossibleCounterExampleQ, nextSt); /* push a state to the possible counterexample of state transition sequence.*/
        c) currentSt = nextSt;              /* step to the next state */
        d) nextSt = Dequeue(StateQ);        /* poll a new state in the StateQ */
    (7) Until the size of StateQ is zero
    (8) If oneMatchFlag ==true and the size of StateQ is zero
        a) allMatchFlag=true;
        b) Return ALLMatch;
    (9) Else if allMatchFlag ==false
        a) Enqueue(PossibleCounterExampleQ, nextSt); /* push the last state to the possible counterexample of state transition sequence.*/
        b) Return PossibleCounterExampleQ; /* return the counterexample of state transition sequence.*/
end.
```

5.4 Virtual Test

Virtual test method consists of two parts of verification. One is to verify design concept. The other is to test interface. They are regarded as pillars of system-level test. Both of them can be performed on the basis of the mechanism elaborated previously.

A. Design concept verification

Design concept verification is the first main content of the virtual test method. It means that for a given test requirement, there is at least one test case in the Test Case Suite can perform this requirement according to the state transition rules in the STG. The detail process of design concept verification can be elaborated as follows.

Let tr be a given test requirement with API invocation sequence mapped to vocabulary Λ and let TCSuite be the auto generated test case suite. Design is verified correct if $\exists tc \in$ TCSuite at least, where tc.APIs $= \Lambda$ and its corresponding State Transition Sequence has no counterexample after being processed with the Checker algorithm.

By design concept verification, system design correctness can be checked before actual manufacturing. This verification process can give an indication on the coverage of the test case suite and improves the value of virtual test.

B. Interface Test

Interface test is another main content of the virtual test method. Interface test indicates that for a given test requirement and a target fault injection, there is at least one test case in the Test Case Suite violated the rules in the STG. The detail process of interface test can be elaborated as follows:

Let TCSuite be the auto-generated test case suite. For a given fault injection and a given test requirement, interface fault is tested if $\exists tc \in$ TCSuite at least, where its corresponding State Transition Sequence has counterexample after processed with the Checker algorithm.

By interface test, it is possible to verify the adequacy of the test case suite. Hence, this verification process can give an indication on the quality of the test case suite.

6 Case Study

6.1 Target System—Sample Satellite

We use a sample satellite as a target system to model in our case study. Sample satellite is consisted of several subsystems, including TCC, PSS, GL, AOC, and CTU subsystems. Among them, the On Board Data Handling (OBDH) in CTU subsystem is made to support the satellite core mission. OBDH should continuously

be available to all the other sub systems, because it usually has functions to monitor, control, acquire, analyze, take a decision, and the most importantly execute the command. Hence, it is usually regarded as a heart of the Satellite [21]. For static model, we use UML to assure its data consistency as other literature [22]. The final model is shown in Fig. 3. UML model of Sample Satellite.

6.2 *Sample Satellite WT Model*

The WTM method has been used to model avionic system and successfully supported its system verification [17]. But the modeling languages are not formally defined in previous documents. In this article, we extended the Window Tree Modeling method in two ways. First, we provided a visual representation of the modeling language based on self-developed Microsoft Visio stencils and templates [23] to supplement its formal syntax; Second, we developed a script to automatically generate the XML-based metadata interchangeable file to support model transformation as well as to support automatic test case generation based on the XML file.

In this case study we choose Window Tree Model to describe a sample satellite's system-level behavior. The detail graphical model is shown in Fig. 4.

Graphical representation of WTM is a WYSIWYG model. It is easy to read, while for machine processing a more flexible way is needed. That is the reason why we developed the stencils and templates for the Window Tree modeling. The XML format of the same description will be exported by corresponding script of the stencils as shown in the following table (Table 2).

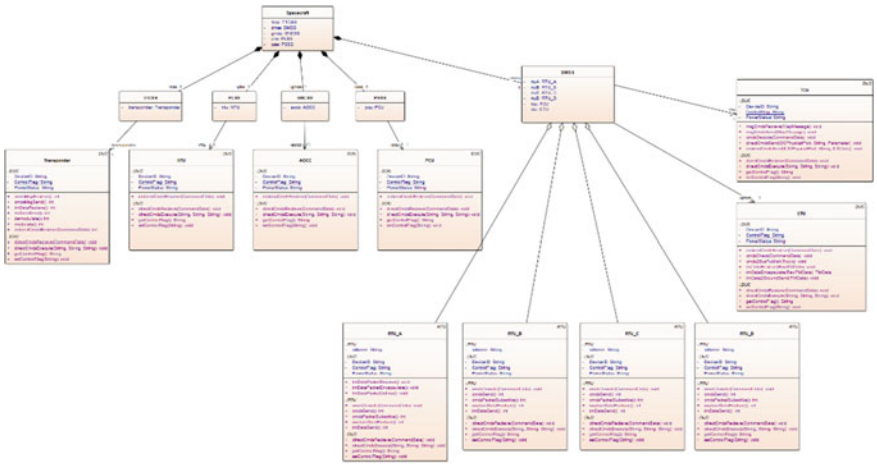

Fig. 3 UML model of sample satellite

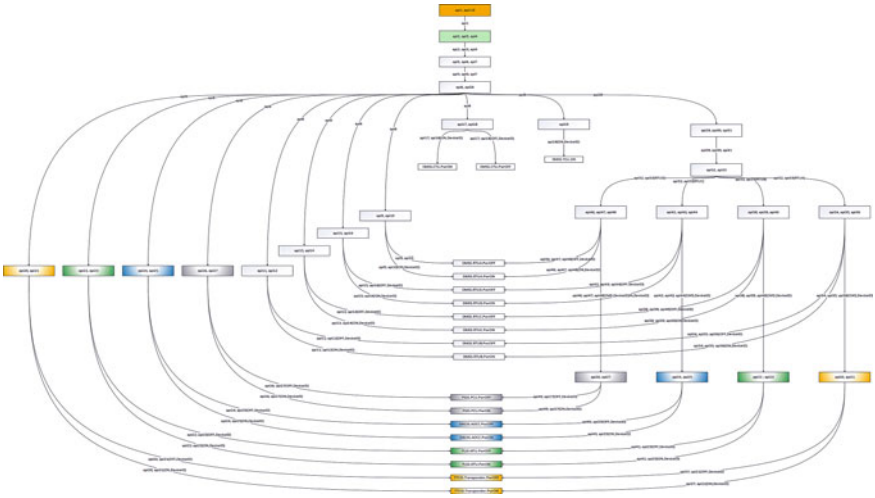

Fig. 4 Window tree model of sample satellite

Table 2 XML format of WT Model

```
<?xml version="1.0" encoding=" UTF-8" ?>
<document>
<Windows>
      <Window id=" 1 " APIs="api1, api119 " />
      <Window id=" 3 " APIs="api2, api3, api4 " />
      ….
      <Window id=" 89 " APIs="api24, api25 " />
      <Window id=" 90 " APIs="api26, api27 " />
</Windows>
<Edges>
      <Edge id=" 2 " Events="api1" />
      <Edge id=" 4 " Events="api2; api3; api4" />
      ....
      <Edge id=" 100 " Events="api37; api21(OFF,DeviceID)" />
      <Edge id=" 101 " Events="api37; api21(ON,DeviceID)" />
</Edges>
<Relations>
      <Relation fromWindow=" 1 " Edgeid=" 2 " toWindow=" 3 "  />
      <Relation fromWindow=" 3 " Edgeid=" 4 " toWindow=" 5 "  />
      ....
      <Relation fromWindow=" 87 " Edgeid=" 100 " toWindow=" 62 "  />
      <Relation fromWindow=" 87 " Edgeid=" 101 " toWindow=" 63 "  />
</Relations>
</document>
```

6.3 Sample Satellite STG Model

STG can be represented in graphical mode or table mode, while it is easier to process in computer when export the rules into XML format. An XML-based state transition rule is also a raw data of Checker algorithm. It can be simply preprocessed and constructed to a list of state transition rule which ready to be used in Checker. The construction of the list will be omitted in this paper due to space limitation. A detail XML format of the sample satellite's STG model is shown in the following table (Table 3).

6.4 Virtual Test Result

We developed the Virtual Test Platform as the engine to perform the virtual test of the sample satellite. The platform itself can be layered into three main features of virtual test configuration, virtual test execution and virtual test assessment. (1) The virtual test configuration provides a user interface to input the model of UML structure, WTM and STG as parameters of the virtual test. (2) Later in the virtual test execution, the Model checking algorithms invoked to perform a specific virtual test according to the different test requirements or the fault injection modes. (3) In virtual test assessment, the test result on design correctness and the adequacy of the test suite will be illustrated in detail.

Design correctness verification results show that for each test requirement, a proper test case can be found to meet this requirement and the corresponding states are transmitted according to the state transition rules. As in Fig. 5, to power on a CTU device of the satellite, a test case in the test case suite matches to meet the requirement and more importantly the accompanied state transition sequence of its event sequence has no counterexample after the check. If all of the test requirements are met, it indicates the design of the satellite is correct.

Interface test results show that for each test requirement and a given fault injection, there is always one test case at least can be found that its corresponding state transitions are violated the rules. As in Fig. 6, suppose a given fault injection of wiring in a RTU device of the satellite, there is at least one test case in the test case suite has a counterexample after the check. It indicates the faulty interface can be tested.

In the interface test, we used a mutation test approach to evaluate the adequacy of the test case suite. As in the result shown in Fig. 7, all the faults injected are tested, which indicates the test case suite is adequate to these faults.

Table 3 XML format of STG Model

```
<?xml version="1.0" encoding="UTF-8" ?>
<document>
<States>
    <State id=" 1 " stateId="S1" name="Ground, null" />
    <State id=" 2 " stateId="S2" name="TCC.trnaspondor,ready4Recieve" />
    ….
    <State id=" 88 " stateId="S121" name="TCC.trnaspondor,ready4Recieve" />
    <State id=" 89 " stateId="S122" name="Ground,finish" />
</States>
<Edges>
    <Edge id=" 90 " edgeId="e1" Events="Ground.send" />
    <Edge id=" 91 " edgeId="e2" Events=" TCC.trnaspondor.cmdRecive" />
    ….
    <Edge id=" 94 " edgeId="e5" Events="DHM.TCU.cmdsRecieve" />
    <Edge id=" 95 " edgeId="e6" Events="DHM.TCU.cmdsDecode" />
</Edges>
<Transitions>
    <Transition fromState=" 1 " tid=" 90 " toState=" 2 "  />
    <Transition fromState=" 2 " tid=" 91 " toState=" 3 "  />
    ….
    <Transition fromState=" 10 " tid=" 100 " toState=" 49 "  />
    <Transition fromState=" 8 " tid=" 97 " toState=" 11 "  />
</Transitions>
</document>
```

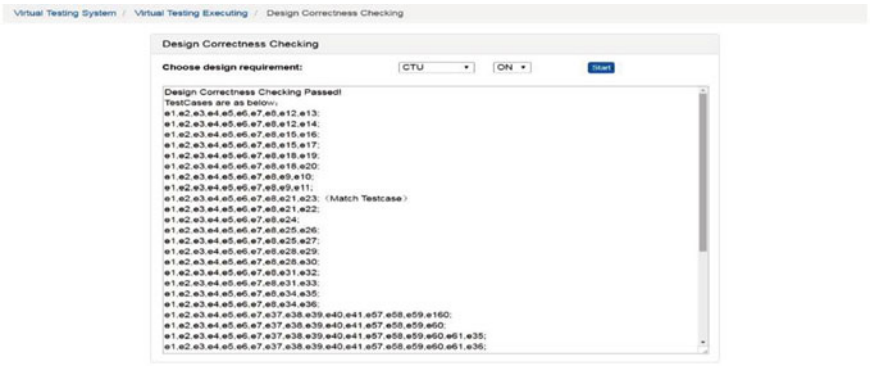

Fig. 5 Design correctness verification

Fig. 6 Interface test

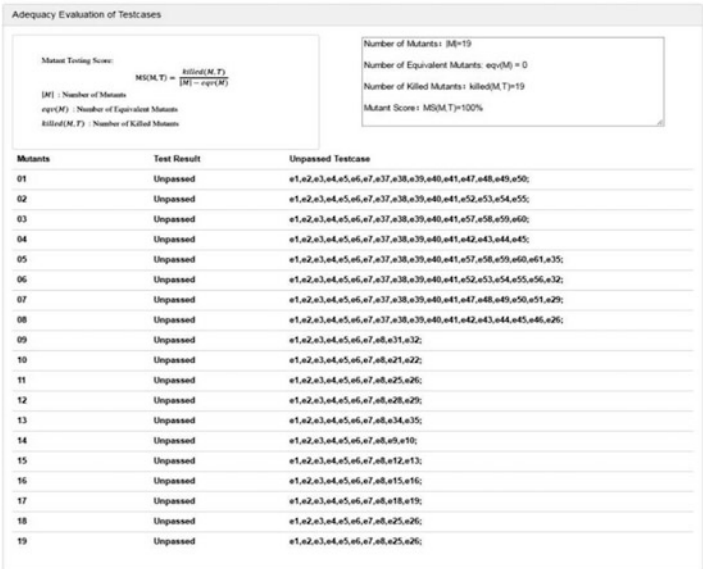

Fig. 7 Mutation test approach of test case suite evaluation

7 Conclusion

We proposed a new virtual test method based on model checking concept. The virtual test method mainly focused on two parts of system-level test, design correctness verification and interface test. By design correctness verification a design concept can be checked before the real system is built. By interface test, the quality of the test suite can be verified before physical test. Both parts utilize automata-based model checking approach. The virtual test method can improve the assurance on 'correct by construction' of complex system such as a satellite. Meanwhile, the interface test results can be used to further research on fault diagnosis, test adequacy evaluation and test oracle generation.

The virtual test in this paper is performed (but not limited) by a virtual software simulator. It simulates the target system under test, also simulates the virtual test process.

The performance of traversing a Window Tree is not discussed in this paper while it will be a challenging problem when the node and the depth of the tree increase. Another research interest of us is to build a generic automata-based checker which can process a specification modeled in other modeling languages.

Acknowledgments This work was supported by the National Natural Science Foundation of China under Grant Nos. 61300007 and 61305054, the Fundamental Research Funds for the Central Universities of China under Grant Nos. YWF-15-GJSYS-106 and YWF-14-JSJXY-007, and the Project of the State Key Laboratory of Software Development Environment of China under Grant Nos. SKLSDE-2015ZX-09 and SKLSDE-2014ZX-06.

References

1. Chen M et al (2012) System-level validation: high-level modeling and directed test generation techniques
2. Garzon MH, Blain DR, Neel AJ (2004) Virtual test tubes. Nat Comput 3(4):461–477
3. Magnusson PS (2005) The Virtual Test Lab. Computer 38(5):95–97
4. Wang GG (2002) Definition and review of virtual prototyping. J Comput Inf Sci Eng 2 (3):232–236
5. Baier C, Katoen JP (2008) Principles of model checking. Mit Press
6. Rowson JA (1997) Virtual prototyping. In: Proceedings of the IEEE 1997 Custom Integrated Circuits Conference
7. Huang T et al (2007) A virtual prototyping system for simulating construction processes. Automation in construction 16(5):576–585
8. Van der Auweraer H et al (2008) Breakthrough technologies for virtual prototyping of automotive and aerospace structures, pp 397–419
9. Wang Y, Wang L, Zheng Z (2012) Application of virtual prototype technology to simulation test for airborne software system. Springer, Berlin, pp 653–658
10. Gokdere LU et al (2002) A virtual prototype for a hybrid electric vehicle. Mechatronics 12 (4):575–593(19)
11. Bezin Y et al (2015) Virtual testing environment tools for railway vehicle certification. Proc Inst Mech Eng Part F J Rail Rapid Transit 22(4):221–249

12. Heitmeyer C et al (2007) Applying formal methods to a certifiably secure software system. IEEE Trans Softw Eng 34(1):82–98
13. Clarke EM, Wing JM (1996) Formal methods: state of the art and future directions. ACM Comput Surv 28(4):626–643
14. Carcenac F, Boniol F (2004) Verification of an avionic system using timed model checking. In: International symposium on leveraging applications of formal methods, ISoLA 2004, October 30–November 2, 2004, Paphos, Cyprus. Preliminary proceedings
15. Mota A, Sampaio A (2001) Model-checking CSP-Z: strategy, tool support and industrial application. Sci Comput Program 40(1):59–96
16. Bjørner N et al (1996) STeP: deductive-algorithmic verification of reactive and real-time systems. Springer, Berlin, pp 415–418
17. Li R et al (2015) Avionics system testing based on formal methods. J Softw 2:181–201
18. Lian H (2013) Research on key technology of test method for credibility validation of safety-critical system. In: Computer science. Beihang University, p 107
19. Vardi MY, Wolper P (1986) An automata-theoretic approach to automatic program verification (preliminary report). In: Symposium on logic in computer science, 16–18 June 1986, Cambridge, Massachusetts, USA
20. Duarte EP, Ziwich RP, Albini LCP (2011) A survey of comparison-based system-level diagnosis. ACM Comput Surv 43(3):194–218
21. Vladimirova T, Sweeting M (2004) System-on-a-chip development for small satellite onboard data handling. J Aerosp Comput Inf Commun 1(1):36–43
22. Gross J (2009) An executable unified product model based on UML to support satellite design. AIAA J
23. Biafore B (2007) Visio 2007 Bible. Wiley

Adaptive Synchronization of Networked Mechanical Systems with Communication Delays

Bin Zhang and Yingmin Jia

Abstract This paper addresses the adaptive synchronization problem of networked mechanical systems in task space with time-varying communication delays, where both kinematic and dynamic uncertainties are considered and the information flow in the networks is represented by a directed graph. Based on a novel coordination auxiliary system, we extend existing feedback architecture to achieve synchronization of networked mechanical systems in task space. The control scheme is established with time-domain approaches by using Lyapunov–Krasovskii functions. Simulation results are provided to demonstrate the effectiveness of the proposed control schemes.

Keywords Networked mechanical systems · Synchronization · Adaptive control · Communication delays

1 Introduction

Resent years have witnessed considerable advances in cooperative control of networked mechanical systems under various frameworks and objectives. Synchronization problem, focused by several research communities, has been recognized as a benchmark problem for cooperative control [1–4]. Synchronization control schemes for linear multi-agent systems is well established in recent literature involving state feedback control schemes [5–7], observer-based output feedback control schemes [8, 9], finite-time control schemes [10–13] and control schemes with switching topologies [14–16]. Despite the useful results cited above, synchronization control

B. Zhang (✉)
School of Automation, Beijing University of Posts and Telecommunication (BUPT), Beijing 100876, China
e-mail: zb362301@126.com

Y. Jia
The Seventh Research Division, Beihang University (BUAA), Beijing 100191, China
e-mail: ymjia@buaa.edu.cn

Y. Jia et al. (eds.), *Proceedings of 2016 Chinese Intelligent Systems Conference*, Lecture Notes in Electrical Engineering 404, DOI 10.1007/978-981-10-2338-5_43

for multiple mechanical robots, which is more practical in applications, is still a challenging problem due to the high nonlinearity. In particular, this problem becomes more difficult when external restrictions, generated by measurement and network uncertainties, are taken into consideration.

Considerable effort has been focused on adaptive control schemes for multiple mechanical robots with kinematics or dynamics uncertainties. In [17], an adaptive robust control problem was studied for multiple mobile manipulators grasping a common object in contact with a rigid surface. In [18], synchronization of a network of Euler-Lagrange systems was investigated with leader tracking. A unified synchronization framework with application to precision formation flying spacecraft was presented in [19]. Adaptive cooperative control laws were proposed for cooperative control of nonholonomic dynamic systems with uncertainty in [20].

Unfortunately, limited by current communication instruments, time delays are inevitable within communication networks, which may lead to degraded performance and unpredictable responses in cooperative behavior. A similar problem (i.e., consensus problem) has been widely investigated in networked systems with time delays. In [21], both time-domain and frequency-domain approaches are used to study consensus algorithms for first-order and second-order multi-agent systems with time delays. In [22], by using small-μ stability theorem, second-order consensus problem in a directed graph with non-uniform time delays was considered. In [23], the formation control problem of high-order linear multi-agent systems with time delays was addressed. In [24], a class of fast consensus algorithms was studied for a group of identical multi-agent systems using both the current and delayed state information. In [25], the authors studied the synchronization problem for an array of N identical delayed neutral-type neural networks, where both the mode-dependent discrete-time delays and the mode-dependent unbounded distributed time delays were involved. In [26], the authors extended the passivity-based architecture to guarantee state synchronization of bilateral teleoperators with constant time delays. In [27, 28], adaptive synchronization problem of networked mechanical systems with constant delays was addressed by frequency-domain approaches.

Up to now, much work need to be addressed for cooperative control problem of networked mechanical systems. First, many manufacturing and assembly works are conducted in task space. However, most existing results on this problem are obtained in joint space and few efforts have been made to deal with cooperative control problem in task space. Second, although many important results have been obtained for linear multi-agent systems with time delays, these results cannot be used directly to deal with cooperative control problem of multiple mechanical robots because of the high nonlinearity, especially when kinematics and dynamics uncertainties are considered. In this paper, we propose an adaptive synchronization scheme in task space for networked mechanical systems with both kinematics and dynamics uncertainties in the presence of time-varying delays. Compared with frequency-domain approaches proposed in [27, 28], we present time-domain approaches by using auxiliary systems. In addition, in contrast to [27, 28], where constant time delays are considered, we investigate time-varying delays. Therefore, our results can also be regarded as extensions of [27, 28] to time-varying delays.

Notations: Throughout this paper, $\mathbb{R}$ denotes the set of real numbers and $\mathbb{R}^n$ denotes the set of all n dimensional real column vectors. Matrix $I_n \in \mathbb{R}^{n\times n}$ denotes the n dimensional unit matrix. The space $\mathcal{L}_\infty$ is defined as the set of all Lebesgue measurable functions $f : \mathbb{R}_{\geq 0} \to \mathbb{R}^n$ such that $\|f\|_\infty := \sup_{t\geq 0} \|f(t)\| < \infty$. For $\epsilon = (\epsilon_1, \epsilon_2, ..., \epsilon_n)^T \in \mathbb{R}^n$, vector $\mathrm{Tanh}(\epsilon) \in \mathbb{R}^n$ and matrix $\mathrm{Cosh}(\epsilon) \in \mathbb{R}^{n\times n}$ are defined as $\mathrm{Tanh}(\epsilon) = (\tanh(\epsilon_1), \tanh(\epsilon_2), ..., \tanh(\epsilon_n))^T$ and $\mathrm{Cosh}(\epsilon) = \mathrm{diag}\{\cosh(\epsilon_1), \cosh(\epsilon_2), ..., \cosh(\epsilon_n)\}$. For $x = (x_1, x_2, ..., x_n)^T \in \mathbb{R}^n$ and $y = (y_1, y_2, ..., y_n)^T \in \mathbb{R}^n$, matrix $\mathrm{Tanh}(x, y) = \mathrm{diag}\{\tanh(x_1)\tanh(y_1), ..., \tanh(x_n)\tanh(y_n)\}$.

2 Preliminaries

2.1 Graph Theory

Let $\mathcal{G}(\nu, \varepsilon)$ be a directed graph of order N with the set of nodes $\nu = \{\nu_1, \nu_2, ..., \nu_N\}$ and edges $\varepsilon \subseteq \nu \times \nu$. The index set of neighbors of node ν_i is denoted by $\mathcal{N}_i = \{j : (\nu_i, \nu_j) \in \varepsilon\}$. If there is a path between any two nodes of the graph $\mathcal{G}(\nu, \varepsilon)$, then $\mathcal{G}(\nu, \varepsilon)$ is said to be strongly connected. Throughout, it is assumed that the interaction graph is strongly connected. The adjacency matrix $A = [a_{ij}] \in \mathbb{R}^{N\times N}$ is defined as $a_{ii} = 0$ and $a_{ij} \geqslant 0$, where $a_{ij} > 0$ if and only if $(\nu_j, \nu_i) \in \varepsilon$. The Laplacian matrix of graph $\mathcal{G}$ is denoted by $L = [l_{ij}] \in \mathbb{R}^{N\times N}$, where $l_{ii} = \sum_{j=1}^{N} a_{ij}$ and $l_{ij} = -a_{ij}$ if $i \neq j$.

Lemma 1 ([29]) *Suppose that $\mathcal{G}$ is a strongly connected digraph with Laplacian L. Let $\gamma = (\gamma_1, \gamma_2, ..., \gamma_N)^T = (\det(L_{11}), \det(L_{22}), ..., \det(L_{NN}))^T$, where $L_{ii} \in \mathbb{R}^{(N-1)\times(N-1)}$ is obtained by deleting the ith row and column of L and $\det(L_{ii})$ is the determinant of L_{ii}. Then, we have*

$$\gamma^T L = 0 \tag{1}$$

meanwhile, γ is positive.

2.2 Robot Model

Consider a group of N networked robot systems with dynamics given by

$$M_i(q_i)\ddot{q}_i + C_i(q_i, \dot{q}_i)\dot{q}_i + G_i(q_i) = \tau_i, \quad i \in \mathcal{I} = \{1, 2, ..., N\} \tag{2}$$

where $q_i \in \mathbb{R}^n$ is the joint configuration variable, $M_i(q_i) \in \mathbb{R}^{n\times n}$ represents the symmetric inertia matrix, $C_i(q_i, \dot{q}_i) \in \mathbb{R}^{n\times n}$ is the matrix of centripetal and coriolis torques, $G_i(q_i) \in \mathbb{R}^n$ is the gravitational torque, and $\tau_i \in \mathbb{R}^n$ denotes the torque input vector.

In the field of robotics, the task space is related to the joint space as the following equations

$$\begin{cases} x_i = F_i(q_i) \\ \dot{x}_i = J_i(q_i)\dot{q}_i \end{cases} \tag{3}$$

where $x_i \in \mathbb{R}^n$ and $\dot{x}_i \in \mathbb{R}^n$ are the position and velocity of the i-th end-effector in task space, $F_i(q_i) : \mathbb{R}^n \to \mathbb{R}^n$ is the mapping between the joint space and the task space, and $J_i(q_i) = \frac{\partial F_i(q_i)}{\partial q_i} \in \mathbb{R}^{n\times n}$ is the Jacobian matrix.

Several useful properties for the mechanical kinematics and dynamics are presented as follows.

Property 1 *The symmetric inertia matrix $M_i(q_i)$ is uniformly positive definite.*

Property 2 *The centripetal and coriolis matrix $C_i(q_i, \dot{q}_i)$ can be appropriately chosen such that $\dot{M}_i(q_i) - 2C_i(q_i, \dot{q}_i)$ is skew-symmetric, i.e., $\gamma^T \left(\dot{M}_i(q_i) - 2C_i(q_i, \dot{q}_i)\right) \gamma = 0$ for $\forall \gamma \in \mathbb{R}^n$.*

Property 3 *For any differentiable vector $\gamma \in \mathbb{R}^n$, the robot dynamics is linearly parameterizable, which gives rise to*

$$M_i(q_i)\dot{\gamma} + C_i(q_i, \dot{q}_i)\gamma + G_i(q_i) = Y_i(q_i, \dot{q}_i, \gamma, \dot{\gamma})\theta_i \tag{4}$$

where θ_i is a physical parameter vector and $Y_i(q_i, \dot{q}_i, \gamma, \dot{\gamma})$ is the regressor matrix.

Property 4 *The velocity mapping from joint space to task space is linearly parameterizable*

$$\dot{x}_i = J_i(q_i)\dot{q}_i = H_i(q_i, \dot{q}_i)\phi_i \tag{5}$$

where ϕ_i is a constant vector of parameters and $H_i(q_i, \dot{q}_i)$ is the regressor matrix.

3 Adaptive Synchronization with Time Delays

In this section, we consider the synchronization problem in task space for networked robot systems (2) with uncertain parameters and time delays. The control objective is to design distributed adaptive control protocol in task space such that $x_i \to x_j$ as $t \to \infty$ for $\forall i, j \in \mathcal{I}$. It is unavoidable that time delays turn up when robot systems communicating over unreliable wireless networks. Therefore, it is necessary to discuss synchronization control problem for networked robot systems with communication delays. In the following, we define $T_{ij}(t)$, $\forall i, j \in \mathcal{I}$, as the bounded time-varying time delay from the j-th robot to the i-th robot. More specifically, we suppose that $T_{ij}(t)$ satisfies

$$\dot{T}_{ij}(t) \le \psi_{ij} < 1 \tag{6}$$

for $\forall i, j \in \mathcal{I}$, where $\psi_{ij} > 0$ is a positive constant.

To establish our control protocol, we first introduce the following auxiliary vectors

$$
\begin{aligned}
s_{X,i} =& \dot{x}_i + \gamma_i \sum_{k\in\mathcal{N}_i} a_{ik}\Big((d^2 + w_i)\mathrm{Tanh}(x_i) \\
&- d^2\mathrm{Tanh}(x_k(t - T_{ik}(t)))\Big) + \mathrm{Tanh}(\eta_i) \\
\dot{q}_{r,i} =& -\hat{J}_i^{-1}(q_i)\Big(\gamma_i \sum_{k\in\mathcal{N}_i} a_{ik}(d^2 + w_i)\mathrm{Tanh}(x_i) \\
&- d^2\mathrm{Tanh}(x_k(t - T_{ik}(t))) + \mathrm{Tanh}(\eta_i)\Big) \\
s_i =& \dot{q}_i - \dot{q}_{r,i}
\end{aligned} \tag{7}
$$

where $\hat{J}_i(q_i) \in \mathbb{R}^{n\times n}$ is an estimate of $J_i(q_i)$, γ_i is a positive constant defined in (1), $w_i = \frac{\alpha}{\gamma_i \sum_{k\in\mathcal{N}_i} a_{ik}}$ with $\alpha > 0$ being a constant parameter, $d^2 \le \min\{1 - \psi_{ij} : \forall i, j \in \mathcal{I}\}$, and $\eta_i \in \mathbb{R}^n$ is an auxiliary filter variable which is assumed to have the following dynamics

$$
\dot{\eta}_i = -\gamma_i \sum_{k\in\mathcal{N}_i} a_{ik}\left(\mathrm{Tanh}(\eta_i) - \mathrm{Tanh}(\eta_k)\right) + \mathrm{Tanh}(x_i) - s_{X,i}. \tag{8}
$$

Let $\dot{\hat{x}}_i = \hat{J}_i(q_i)\dot{q}_i = H_i(q_i, \dot{q}_i)\hat{\phi}_i$ and $\tilde{\phi}_i = \hat{\phi}_i - \phi_i$. Then, we can obtain that

$$
\begin{aligned}
s_{X,i} &= \dot{x}_i - \hat{J}_i(q_i)\dot{q}_{r,i} = \dot{x}_i + \hat{J}_i(q_i)(s_i - \dot{q}_i) \\
&= \hat{J}_i(q_i)s_i + \dot{x}_i - \dot{\hat{x}}_i = \hat{J}_i(q_i)s_i - H_i(q_i, \dot{q}_i)\tilde{\phi}_i
\end{aligned} \tag{9}
$$

where the estimate $\hat{\phi}_i$ is generated by update law

$$
\dot{\hat{\phi}}_i = \Lambda_i H_i^T(q_i, \dot{q}_i)(\mathrm{Tanh}(x_i) - \mathrm{Tanh}(\eta_i)) \tag{10}
$$

with $\Lambda_i > 0$ being a positive definite matrix.

Based on the auxiliary vectors presented in (7) and (8), we propose adaptive control protocol

$$
\tau_i = Y_i(q_i, \dot{q}_i, \dot{q}_{r,i}, \ddot{q}_{r,i})\hat{\theta}_i + \hat{J}_i^T(q_i)(-\mathrm{Tanh}(x_i) + \mathrm{Tanh}(\eta_i)) \tag{11}
$$

where $\hat{\theta}_i$ is the estimate of θ_i and $\hat{\theta}_i$ evolves as

$$
\dot{\hat{\theta}}_i = -\Gamma_i Y_i^T(q_i, \dot{q}_i, \dot{q}_{r,i}, \ddot{q}_{r,i})s_i \tag{12}
$$

with $\Gamma_i > 0$ being a positive definite matrix.

Substituting (11) into (2), we can obtain the closed-loop dynamics for s_i as

$$\begin{aligned} & M_i(q_i)\dot{s}_i + C_i(q_i, \dot{q}_i)s_i \\ =& M_i(q_i)\ddot{q}_i + C_i(q_i, \dot{q}_i)\dot{q}_i - \left(M_i(q_i)\ddot{q}_{r,i} + C_i(q_i, \dot{q}_i)\dot{q}_{r,i}\right) \\ =& Y_i(q_i, \dot{q}_i, \dot{q}_{r,i}, \ddot{q}_{r,i})\tilde{\theta}_i + \hat{J}_i^T(q_i)(-\mathrm{Tanh}(x_i) + \mathrm{Tanh}(\eta_i)) \end{aligned} \tag{13}$$

where $\tilde{\theta}_i = \hat{\theta}_i - \theta_i$ is the parameter error.

To present the main result in this subsection, we need the following lemma.

Lemma 2 *Consider the following system*

$$\dot{\varphi}_i - \dot{\varphi}_j = -\rho(\tanh(\varphi_i) - \tanh(\varphi_j)) + f(t) \tag{14}$$

where φ_i, $\varphi_j \in \mathbb{R}$, $\rho > 0$ *is a positive constant, and* $f(t) : \mathbb{R} \to \mathbb{R}$ *is a continuous function. If* φ_i *and* φ_j *are all bounded and* $\lim_{t\to\infty} f(t) = 0$, *then* $\lim_{t\to\infty}(\varphi_i(t) - \varphi_j(t)) = 0$.

Proof It is easy to verify that $\tanh(\varphi_i) - \tanh(\varphi_j) = (1 - \tanh(\varphi_i)\tanh(\varphi_j))\tanh(\varphi_i - \varphi_j)$. Then, since φ_i and φ_j are all bounded, we can define $w = \sup\left\{|\tanh(\varphi_i)|, |\tanh(\varphi_j)|\right\} < 1$. Let $e = \varphi_i - \varphi_j$. Then (14) can be rewritten as

$$\dot{e} = -g(t)\tanh(e) + f(t) \tag{15}$$

where $g(t) = \rho(1 - \tanh(\varphi_i)\tanh(\varphi_j))$. It is obvious that

$$0 < \rho(1 - \omega^2) \le g(t) \le \rho(1 + \omega^2). \tag{16}$$

Consider the following Lyapunov function

$$V = \ln(\cosh(e)) \tag{17}$$

The time derivative of V along (15) is given by

$$\begin{aligned} \dot{V} =& -g(t)\tanh(e)\left(\tanh(e) - \frac{f(t)}{g(t)}\right) \\ \le& -g(t)|\tanh(e)|\left(|\tanh(e)| - \frac{|f(t)|}{g(t)}\right) \\ \le& -\rho(1-\omega^2)|\tanh(e)|\left(|\tanh(e)| - \frac{|f(t)|}{\rho(1-\omega^2)}\right). \end{aligned} \tag{18}$$

Since $\lim_{t\to\infty} f(t) = 0$, then for $\forall 0 < \epsilon < 1$, there exists $T > 0$ such that $|f(t)| \le \rho(1-\omega^2)\epsilon$, $\forall t > T$. From (18), we can see that $\dot{V} < 0$ outside $\{e : |\tanh(e)| \le \frac{|f(t)|}{\rho(1-\omega^2)} = \epsilon\}$. Therefore, e is ultimately bounded to set $\left\{e : |e| \le \tanh^{-1}(\epsilon)\right\}$. By

the arbitrariness of ϵ, together with the fact that $\lim_{\epsilon\to 0}\tanh^{-1}(\epsilon)=0$, we can obtain that $\lim_{t\to\infty} e(t)=0$.

With the help of the above descriptions, we can provide one of the main result as follows:

Theorem 1 *Consider networked robot systems (2), for which the interaction graph $\mathcal{G}$ is connected. The adaptive control protocol and update laws (10), (11), (12) solves the synchronization control problem with slow-varying communication delays (6) if $\alpha>1$ and $\frac{d^2}{2}+w_i\geq\frac{1}{2}$.*

Proof Rewrite vector x_i and η_i, $i\in\mathcal{I}$, in component forms as $x_i=(x_{i1},x_{i2},...,x_{in})^T$ and $\eta_i=(\eta_{i1},\eta_{i2},...,\eta_{in})^T$. Consider Lyapunov function

$$\begin{aligned}V=&\sum_{i=1}^{N}\sum_{l=1}^{n}\ln(\cosh(x_{il}))+\sum_{i=1}^{N}\sum_{l=1}^{n}\ln(\cosh(\eta_{il}))\\&+\frac{1}{2}\sum_{i=1}^{N}s_i^TM_i(q_i)s_i+\frac{1}{2}\sum_{i=1}^{N}\sum_{k\in\mathcal{N}_i}\gamma_ia_{ik}\times\\&\int_{t-T_{ik}(t)}^{t}\mathrm{Tanh}^T(x_k(\tau))\mathrm{Tanh}(x_k(\tau))d\tau\\&+\frac{1}{2}\sum_{i=1}^{N}\tilde{\phi}_i^T\Lambda_i^{-1}\tilde{\phi}_i+\frac{1}{2}\sum_{i=1}^{N}\tilde{\theta}_i^T\Gamma_i^{-1}\tilde{\theta}_i\end{aligned}\tag{19}$$

Taking the derivative of V, we can obtain

$$\begin{aligned}\dot{V}\leq&-\frac{d^2}{2}\sum_{i=1}^{N}\sum_{k\in\mathcal{N}_i}\gamma_ia_{ik}\|\mathrm{Tanh}(x_i)-\mathrm{Tanh}(x_k(t-T_{ik}(t)))\|^2\\&-\frac{1}{2}\sum_{i=1}^{N}\sum_{k\in\mathcal{N}_i}\gamma_ia_{ik}\|\mathrm{Tanh}(\eta_i)-\mathrm{Tanh}(\eta_k)\|^2\\&-\frac{1}{2}\gamma^TL\mathrm{Tanh}^2(X)-\frac{1}{2}\gamma^TL\mathrm{Tanh}^2(\Phi)\end{aligned}\tag{20}$$

where the N-dimension vectors $\mathrm{Tanh}^2(X)$ and $\mathrm{Tanh}^2(\Phi)$ in (20) are defined as $\mathrm{Tanh}^2(X)=\left(\mathrm{Tanh}^T(x_1)\mathrm{Tanh}(x_1),\mathrm{Tanh}^T(x_2)\mathrm{Tanh}(x_2),...,\mathrm{Tanh}^T(x_N)\mathrm{Tanh}(x_N)\right)^T$ and $\mathrm{Tanh}^2(\Phi)=\left(\mathrm{Tanh}^T(\eta_1)\,\mathrm{Tanh}(\eta_1),\ \mathrm{Tanh}^T(\eta_2)\,\mathrm{Tanh}(\eta_2),...,\mathrm{Tanh}(\eta_N)\,\mathrm{Tanh}(\eta_N)\right)^T$. Besides, for (20), $s_{X,i}^T-s_i^T\hat{J}_i^T(q_i)+\tilde{\phi}_i^TH_i^T=0$ and $\frac{d^2}{2}+w_i\geq\frac{1}{2}$ is used. From Lemma 1, we can obtain

$$\begin{aligned}\dot{V} \leq & -\frac{d^2}{2}\sum_{i=1}^{N}\sum_{k\in\mathcal{N}_i}\gamma_i a_{ik}\|\mathrm{Tanh}(x_i) \\ & -\mathrm{Tanh}(x_k(t-T_{ik}(t)))\|^2 \\ & -\frac{1}{2}\sum_{i=1}^{N}\sum_{k\in\mathcal{N}_i}\gamma_i a_{ik}\|\mathrm{Tanh}(\eta_i)-\mathrm{Tanh}(\eta_k)\|^2 \leq 0.\end{aligned} \tag{21}$$

Invoking Barbalat's lemma, we have $\lim_{t\to\infty}\dot{V}(t)=0$. It follows that $\lim_{t\to\infty}(x_i(t)-x_k(t-T_{ik}(t)))=0$ and $\lim_{t\to\infty}(\eta_i(t)-\eta_k(t))=0$ for $\forall a_{ik}\neq 0$. Since $\mathcal{G}$ is connected, then for $\forall i,j\in\mathcal{I}$, there exists a path $\nu_i=\nu_{k_1},\nu_{k_2},...,\nu_{k_s}=\nu_j$ connecting ν_j to ν_i. Hence, we can obtain $\lim_{t\to\infty}(\eta_i(t)-\eta_j(t))=\lim_{t\to\infty}\sum_{i=1}^{s-1}(\eta_{k_i}(t)-\eta_{k_{i+1}}(t))=\sum_{i=1}^{s-1}\lim_{t\to\infty}(\eta_{k_i}(t)-\eta_{k_{i+1}}(t))=0$ for $\forall i,j\in\mathcal{I}$. From (7), we can see that

$$\begin{aligned}&\dot{x}_i-\dot{x}_j \\ &=s_{X,i}-\mathrm{Tanh}(\eta_i)-w_i\gamma_i\sum_{k\in\mathcal{N}_i}a_{ik}\mathrm{Tanh}(x_i) \\ &\quad -d^2\gamma_i\sum_{k\in\mathcal{N}_i}a_{ik}(\mathrm{Tanh}(x_i)-\mathrm{Tanh}(x_k(t-T_{ik}(t)))) \\ &\quad -\Big(s_{X,j}-\mathrm{Tanh}(\eta_j)-w_j\gamma_j\sum_{k\in\mathcal{N}_j}a_{jk}\mathrm{Tanh}(x_j) \\ &\qquad -d^2\gamma_j\sum_{k\in\mathcal{N}_j}a_{jk}(\mathrm{Tanh}(x_j)-\mathrm{Tanh}(x_k)(t-T_{ik}(t)))\Big).\end{aligned} \tag{22}$$

Since $w_i=\frac{\alpha}{\gamma_i\Sigma_{k\in\mathcal{N}_i}a_{ik}}$ for $\forall i\in\mathcal{I}$. Then, we can see

$$\begin{aligned}&\dot{x}_i-\dot{x}_j \\ &=\big(s_{X,i}-s_{X,j}\big)-\big(\mathrm{Tanh}(\eta_i)-\mathrm{Tanh}(\eta_j)\big) \\ &\quad -\alpha(\mathrm{Tanh}(x_i)-\mathrm{Tanh}(x_j)) \\ &\quad -d^2\gamma_i\sum_{k\in\mathcal{N}_i}a_{ik}(\mathrm{Tanh}(x_i)-\mathrm{Tanh}(x_k(t-T_{ik}(t)))) \\ &\quad +d^2\gamma_j\sum_{k\in\mathcal{N}_j}a_{jk}(\mathrm{Tanh}(x_j)-\mathrm{Tanh}(x_k)(t-T_{ik}(t))).\end{aligned} \tag{23}$$

Substituting (7) into (23) gives

$$\begin{aligned}&\dot{\eta}_i-\dot{\eta}_j+\dot{x}_i-\dot{x}_j \\ &=-(\alpha-1)(I_n-\mathrm{Tanh}(x_i,x_j))(I_n+\mathrm{Tanh}(\eta_i-\eta_j, \\ &\quad x_i-x_j))\mathrm{Tanh}\left(\eta_i-\eta_j+x_i-x_j\right)+f_{ij}(t)\end{aligned} \tag{24}$$

where $f_{ij}(t)$ is defined as

$$\begin{aligned} & f_{ij}(t) \\ &= -\Bigg(\gamma_i \sum_{k\in\mathcal{N}_i} a_{ik}(\mathrm{Tanh}(\eta_i) - \mathrm{Tanh}(\eta_k)) \\ &\quad - \gamma_j \sum_{k\in\mathcal{N}_j} a_{jk}(\mathrm{Tanh}(\eta_j) - \mathrm{Tanh}(\eta_k))\Bigg) \\ &\quad + (\alpha-1)\,(I_n - \mathrm{Tanh}(x_i, x_j))\times \\ &\quad (I_n - \mathrm{Tanh}(\eta_i, \eta_j))^{-1}(\mathrm{Tanh}(\eta_i) - \mathrm{Tanh}(\eta_j)) \\ &\quad - \big(\mathrm{Tanh}(\eta_i) - \mathrm{Tanh}(\eta_j)\big) \\ &\quad - d^2\gamma_i \sum_{k\in\mathcal{N}_i} a_{ik}(\mathrm{Tanh}(x_i) - \mathrm{Tanh}(x_k)(t - T_{ik}(t))) \\ &\quad + d^2\gamma_j \sum_{k\in\mathcal{N}_j} a_{jk}(\mathrm{Tanh}(x_j) - \mathrm{Tanh}(x_k)(t - T_{jk}(t))). \end{aligned} \tag{25}$$

Note that $\lim_{t\to\infty}(x_i(t) - x_j(t - T(t))) = 0$ for $\forall a_{ij} \neq 0$ and $\lim_{t\to\infty}(\eta_i(t) - \eta_j(t)) = 0$, for $\forall i, j \in \mathcal{I}$. Then, we can see

$$\lim_{t\to\infty} f_{ij}(t) = 0, \quad i, j \in \mathcal{I}. \tag{26}$$

By Lemma 2, we get that $\lim_{t\to\infty}(\eta_i(t) - \eta_j(t) + x_i(t) - x_j(t)) = 0$. Note that $\lim_{t\to\infty}(\eta_i(t) - \eta_j(t)) = 0$. Then, it follows that $\lim_{t\to\infty}(x_i(t) - x_j(t)) = \lim_{t\to\infty}(\eta_i(t) - \eta_j(t) + x_i(t) - x_j(t)) - \lim_{t\to\infty}(\eta_i(t) - \eta_j(t)) = 0$, which completes the proof.

Remark 1 By the proof of Theorem 1, we cannot conclude that the estimated parameters $\hat{\phi}_i$ and $\hat{\theta}_i$ converge to their true values ϕ_i and θ_i under our adaptive synchronization schemes. It follows from the construction of Lyapunov function V that the parameter errors are uniformly bounded and satisfy $\sum_{i=1}^{N} \|\tilde{\phi}_i\|^2 \leq \frac{2V(0)}{\min_{i\in\mathcal{I}}\{\lambda_{\min}(\Lambda_i^{-1})\}}$ and $\sum_{i=1}^{N} \|\tilde{\theta}_i\|^2 \leq \frac{2V(0)}{\min_{i\in\mathcal{I}}\{\lambda_{\min}(\Gamma_i^{-1})\}}$. To guarantee a satisfactory convergence region, we need to choose matrixes Λ_i^{-1} and Γ_i^{-1} with sufficiently large eigenvalues.

Remark 2 An alternative auxiliary dynamics for η_i is

$$\begin{aligned} \dot{\eta}_i = -\mathrm{Cosh}^2(\eta_i)\Bigg(&\sum_{k\in\mathcal{N}_i} a_{ik}\left(\mathrm{Tanh}(\eta_i) - \mathrm{Tanh}(\eta_k)\right) \\ &- \mathrm{Tanh}(x_i) + s_{X,i}\Bigg) \end{aligned} \tag{27}$$

where $\text{Cosh}^2(\eta_i)$ serves as a dynamic feedback parameter which enlarges the convergence rate. By choosing the following Lyapunov function

$$\begin{aligned} V = & \sum_{i=1}^{N}\sum_{l=1}^{n}\ln(\cosh(x_{il})) + \frac{1}{2}\sum_{i=1}^{N} s_i^T M_i(q_i)s_i \\ & + \sum_{i=1}^{N}\sum_{l=1}^{n}\int_0^{\eta_{il}} \tanh(\upsilon)\text{sech}^2(\eta_{il})d\upsilon + \frac{\alpha}{2}\sum_{i=1}^{N}\sum_{k\in\mathcal{N}_i} a_{ik} \\ & \int_{t-T_{ik}(t)}^{t} \text{Tanh}^T(x_k(\tau))\text{Tanh}(x_k(\tau))d\tau \\ & + \frac{1}{2}\sum_{i=1}^{N}\tilde{\phi}_i^T\Lambda_i^{-1}\tilde{\phi}_i + \frac{1}{2}\sum_{i=1}^{N}\tilde{\theta}_i^T\Gamma_i^{-1}\tilde{\theta}_i \end{aligned} \tag{28}$$

we can obtain the same conclusion as that of Theorem 1.

4 Simulation Examples

In this section, six two-link robot manipulators are utilized to verify the effectiveness of the proposed control schemes and we assume the interaction graph $\mathcal{G}$ between the agents are strongly connected as shown in Fig. 1. The i-th Jacobian matrix $J_i(q_i)$ is given by

$$\begin{aligned} & J_i(q_i) \\ & = \begin{pmatrix} -l_{i,1}s(q_{i,1}) - l_{i,2}s(q_{i,1}+q_{i,2}) & -l_{i,2}s(q_{i,1}+q_{i,2}) \\ l_{i,1}c(q_{i,1}) + l_{i,2}c(q_{i,1}+q_{i,2}) & l_{i,2}c(q_{i,1}+q_{i,2}) \end{pmatrix} \end{aligned} \tag{29}$$

where $s(\cdot) = \sin(\cdot)$, $c(\cdot) = \cos(\cdot)$, $q_i = (q_{i,1}, q_{i,2})^T$, and $l_{i,1}$ and $l_{i,2}$ are the lengths of the links for the i-th manipulators. The regressor matrix $H_i(q_i, \dot{q}_i)$ and ϕ_i are

$$H_i(q_i, \dot{q}_i) = \begin{pmatrix} -s(q_{i,1})\dot{q}_{i,1} & -s(q_{i,1}+q_{i,2})(\dot{q}_{i,1}+\dot{q}_{i,2}) \\ c(q_{i,1})\dot{q}_{i,1} & c(q_{i,1}+q_{i,2})(\dot{q}_{i,1}+\dot{q}_{i,2}) \end{pmatrix} \tag{30}$$

$$\phi_i = (l_{i,1}, l_{i,2})^T. \tag{31}$$

The inertia matrix $M_i(q_i)$ and centripetal matrix $C_i\left(q_i, \dot{q}_i\right)$ are defined as $M_{i11} = a_{i,1} + 2a_{i,2}\cos(q_{i,2})$, $M_{i12} = M_{i21} = a_{i,3} + a_{i,2}\cos(q_{i,2})$, $M_{i22} = a_{i,3}$, $C_{i11} = -a_{i,2}\sin(q_{i,2})\dot{q}_{i,2}$, $C_{i12} = -a_{i,2}\sin(q_{i,2})(\dot{q}_{i,1}+\dot{q}_{i,2})$, $C_{i21} = a_{i,2}\sin(q_{i,2})\dot{q}_{i,1}$, $C_{i22} = 0$, where $a_{i,1} = I_{i,1} + m_{i,1}l_{i,c1}^2 + m_{i,2}l_{i,1}^2 + I_{i,2} + m_{i,2}l_{i,c2}^2$, $a_{i,2} = m_{i,2}l_{i,1}l_{i,c2}$, $a_{i,3} = I_{i,2} + m_{i,2}l_{i,c2}^2$ with $m_{i,1}$ and $m_{i,2}$ being the masses of the links, $I_{i,1}$ and $I_{i,2}$ being the moments of inertia, and $l_{i,c1}$ and $l_{i,c2}$ being the mass centers of the links. The gravitational torque $G_i(q_i)$ are assumed to be zero for simplicity. Let $\gamma = (\gamma_1, \gamma_2)^T \in \mathbb{R}^2$. For

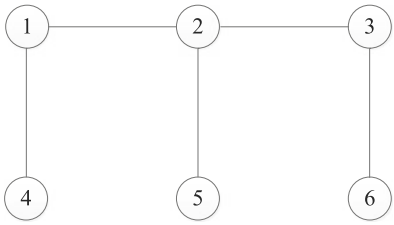

Fig. 1 The strongly connected topology

Property 3, we define the parameter vector $\theta_i = (a_{i,1}, a_{i,2}, a_{i,3})^T$ and define the regressor matrix $Y_i(q_i, \dot{q}_i, \gamma, \dot{\gamma}) = [y_{ij}] \in \mathbb{R}^{2\times 3}$ as $y_{11} = \dot{\gamma}_1$, $y_{12} = 2\cos(q_{i,2})\dot{\gamma}_1 + \cos(q_{i,2})\dot{\gamma}_2 - \sin(q_{i,2})\dot{q}_{i,2}\gamma_1 - \sin(q_{i,2})(\dot{q}_{i,1} + \dot{q}_{i,2})\gamma_2$, $y_{13} = \dot{\gamma}_2$, $y_{21} = 0$, $y_{22} = \cos(q_{i,2})\dot{\gamma}_i + \sin(q_{i,2})\dot{q}_{i,1}\gamma_1$ and $y_{23} = \dot{\gamma}_1 + \dot{\gamma}_2$. The parameters of the manipulators are shown in Table 1.

We give an example for adaptive synchronization control problem in task space with slow-varying time delays. The time delays are chosen as $T_{12} = 0.1 + 0.2\sin(t)$, $T_{14} = 0.2 + 0.2\sin(t)$, $T_{21} = 0.1 + 0.1\sin(t)$, $T_{23} = 0.1\sin(t)$, $T_{25} = 0.1 + 0.2\sin(t)$, $T_{32} = 0.1 + 0.2\sin(t)$, $T_{36} = 0.2\sin(t)$, $T_{41} = 0.1 + 0.1\sin(t)$, $T_{52} = 0.1 + 0.2\sin(t)$, $T_{63} = 0.1\sin(t)$. The initial configurations and the initial estimated parameters of the manipulators are shown in Table 2. By using control protocol (11) and update laws

Table 1 The physical parameters of the manipulators

Manipulator i	$m_{i,1}, m_{i,2}$	$I_{i,1}, I_{i,2}$	$l_{i,1}, l_{i,2}$	$l_{i,c1}, l_{i,c2}$
1	1.6, 1.7	0.52, 0.41	2.0, 1.8	1.1, 1.2
2	1.4, 1.5	0.37, 0.46	1.9, 1.8	0.9, 1.3
3	1.3, 1.2	0.32, 0.51	2.0, 1.7	1.3, 1.2
4	1.6, 1.4	0.50, 0.51	1.7, 1.6	1.1, 1.4
5	1.5, 1.7	0.51, 0.40	1.8, 1.8	1.5, 1.2
6	1.7, 1.5	0.46, 0.49	1.6, 2.0	1.7, 1.6

Table 2 The initial values

Manipulator i	$q_{i,1}, q_{i,2}$(rad)	$\hat{\phi}_{i,1}, \hat{\phi}_{i,2}$	$\hat{\theta}_{i,1}, \hat{\theta}_{i,2}, \hat{\theta}_{i,3}$
1	0.43π, -0.52π	1.0, 1.2	1.6, 1.2, 2.0
2	0.36π, -0.71π	1.8, 1.9	1.3, 1.5, 1.1
3	0.37π, -0.30π	1.7, 1.4	1.1, 1.0, 1.6
4	0.40π, -0.60π	1.5, 1.6	1.4, 1.5, 1.0
5	0.38π, -0.70π	1.7, 1.8	1.3, 1.2, 1.0
6	0.35π, -0.65π	2.0, 1.6	1.5, 1.6, 1.9

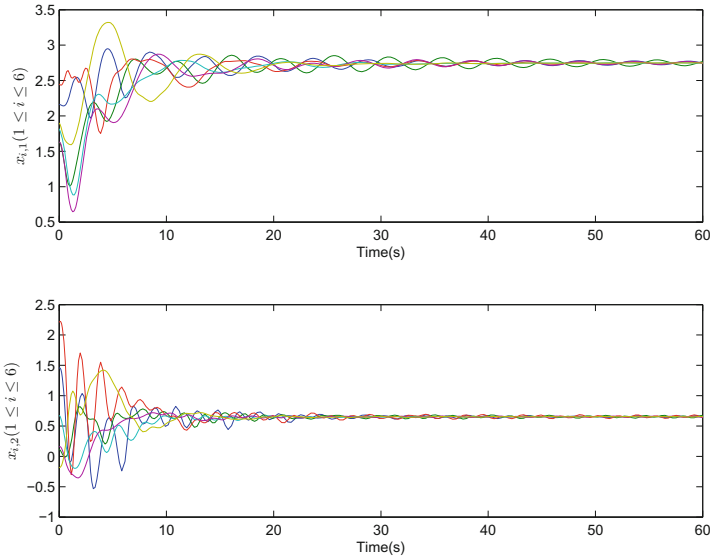

Fig. 2 Trajectories of the robotic agents with protocol (11)

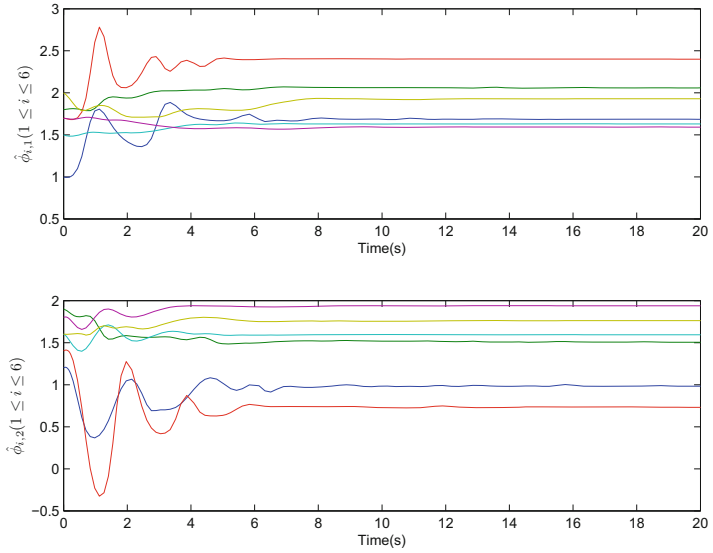

Fig. 3 Parameter estimates $\hat{\phi}_i$ with update law (10)

(10) and (12), we obtain simulation results in Figs. 2, 3 and 4. In Fig. 2, we can see that all the trajectories converge to the same. In Figs. 3 and 4, we can see that all the estimated parameters are bounded.

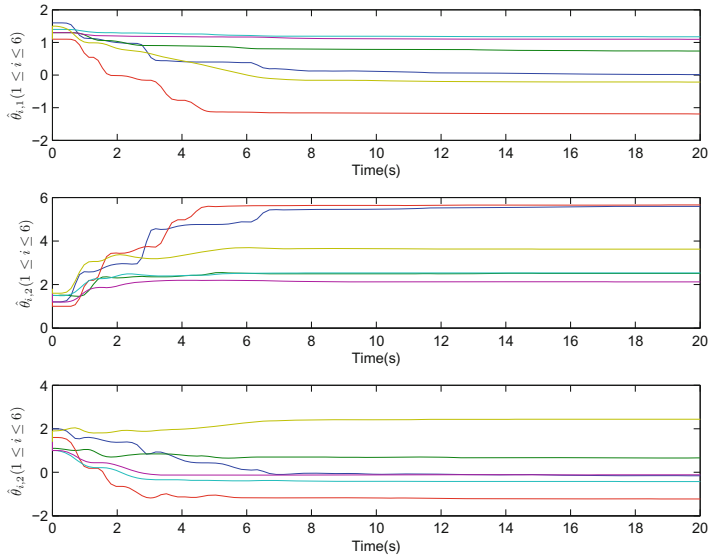

Fig. 4 Parameter estimates $\hat{\theta}_i$ with update law (12)

5 Conclusion

The task space adaptive synchronization problem of networked mechanical systems in the presence of time-varying communication delays has been addressed. Based on a kind of novel coordination auxiliary systems, an adaptive control scheme has been established by using Lyapunov–Krasovskii functions. Simulation results have been provided to demonstrate the effectiveness of the proposed control schemes.

Acknowledgments This work was supported by the National Basic Research Program of China (973 Program: 2012CB821200, 2012CB821201) and the NSFC (61134005, 61327807, 61521091, 61520106010).

References

1. Xiao Y, Zhu KY (2006) Optimal synchronization control of high-precision motion systems. IEEE Trans Ind Electron 53(4):1160–1169 August
2. Ren L, Mills JK, Sun D (2004) Adaptive synchronization control of a planar parallel manipulator. In: Proceedings of the American Control Conference, Boston, Massachusetts, USA, pp 3980–3985, 30 June–2 July 2004
3. Wang W, Jiang Y (2014) Community-aware task allocation for social networked multiagent systems. IEEE Trans Cybern 44(9):1529–1543 September
4. Zou A (2014) Distributed attitude synchronization and tracking control for multiple rigid bodies. IEEE Trans Control Syst Technol 22(2):478–490 March

5. Olfati-Saber R, Fax JA, Murray M (2007) Consensus and cooperation in networked multi-agent systems. Proc IEEE 95(1):215–233 January
6. Zuo Z, Zhang J, Wang Y (2015) Adaptive fault tolerant tracking control for linear and Lipschitz nonlinear multi-agent systems. IEEE Trans Ind Electron 62(6):3923–3931 June
7. Chen Z, Zhang H (2003) Analysis of joint connectivity condition for multiagents with boundary constraints. IEEE Trans Cybern 43(2):437–444 April 2013
8. Zhou B, Xu C, Duan G (2014) Distributed and truncated reduced-order observer based output feedback consensus of multi-agent systems. IEEE Trans Autom Control 59(8):2264–2270 August
9. Zhang H, Feng G, Yan H, Chen Q (2014) Observer-based output feedback event-triggered control for consensus of multi-agent systems. IEEE Trans Ind Electron 61(9):4885–4893 September
10. Wang X, Hong Y (2008) Finite-time consensus for multi-agent networks with second-order agent dynamics. In: Proceedings of IFAC World Congress, Seoul, Korea, pp 15185–15190, 6–11 July 2008
11. Wang X, Li S, Shi P (2014) Distributed finite-time containment control for double-integrator multiagent systems. IEEE Trans Cybern 44(9):1518–1528 September
12. Li S, Du H, Lin X (2011) Finite-time consensus algorithm for multi-agent systems with double-integrator dynamics. Automatica 47(8):1706–1712 August
13. Zhang B, Jia Y, Matsuno F (2014) Finite-time observers for multi-agent systems without velocity measurements and with input saturations. Syst Control Lett 68:86–94 June
14. Zhang B, Jia Y (2014) On weak-invariance principles for nonlinear switched systems. IEEE Trans Autom Control 59(6):1600–1605 June
15. Cheng D, Wang J, Hu X (2008) An extension of LaSalles invariance principle and its application to multi-agent systems. IEEE Trans Autom Control 53(7):1765–1770 August
16. Qin J, Yu C, Gao H (2014) Coordination for linear multiagent systems with dynamic interaction topology in the leader-following framework. IEEE Trans Ind Electron 61(5):2412–2422 May
17. Li Z, Li J, Kang Y (2010) Adaptive robust coordinated control of multiple mobile manipulators interacting with rigid environments. Automatica 46(12):2028–2034 December
18. Miyasato Y (2011) Adaptive H_∞ formation control for Euler-Lagrange systems by utilizing neural network approximators. In: Proceedings of the American Control Conference, San Francisco, CA, USA, pp 1753–1758, 29 June–1 July 2011
19. Chung S, Ahsun U, Slotine JE (2009) Application of synchronization to formation flying spacecraft: lagrangian approach. J Guid Control Dyn, 32(2): 512–526, March–April 2009
20. Dong W, Farrell JA (2009) Decentralized cooperative control of multiple nonholonomic dynamic systems with uncertainty. Automatica 45(3):706–710 March
21. Meng Z, Ren W, Cao Y, You Z (2011) Leaderless and leader-following consensus with communication and input delays under a directed network topology. IEEE Trans Syst Man Cybern 41(1):75–88 February
22. Yang W, Bertozzi AL, Wang X (2008) Stability of a second order consensus algorithm with time delay. In: Proceedings of the IEEE Conference on Decision and Control, Cancun, Mexico, pp 2926–2931, 9–11 December 2008
23. Abdessameud A, Tayebi A (2011) Formation control of VTOL unmanned aerial vehicles with communication delays. Automatica 47(11):2383–2394 November
24. Meng Z, Li Z, Vasilakos A, Chen S (2013) Delay-induced synchronization of identical linear multiagent systems. IEEE Trans Cybern 43(2):476–489 April
25. Liu Y, Wang Z, Liang J, Liu X (2013) Synchronization of coupled neutral-type neural networks with jumping-mode-dependent discrete and unbounded distributed delays. IEEE Trans Cybern 43(1):102–114 February
26. Chopra N, Spong MW, Lozano R (2008) Synchronization of bilateral teleoperators with time delay. Automatica 44(8):2142–2148 August
27. Nuno E, Ortega R, Basanez L, Hill D (2011) Synchronization of networks of nonidentical Euler-Lagrange systems with uncertain parameters and communication delays. IEEE Trans Autom Control 56(4):935–941 April

28. Wang H (2014) Consensus of networked mechanical systems with communication delays: a unified framework. IEEE Trans Autom Control 59(6):1571–1576 June
29. Li Z, Jia Y (2009) Algebraic criteria for consensus problems of continuous-time networked systems. Int J Control 41(4):643–658 April

Robust H_∞ Consensus of the Second-Order Multi-agent Systems with Random Time-Delays

Xin Zong and Yan Cui

Abstract This paper investigates the consensus problem for directed networks of agents with external disturbances and random time-delays. Both networks under the fixed and switching topologies are taken into consideration. Based on Lyapunov stability theory, sufficient conditions for all agents achieving stability with the directed H_∞ performance are given in the forms of liner matrix inequality (LMI). Finally, the simulation results show the correctness and effectiveness of the designed protocols.

Keywords Multi-agent systems · Consensus · Random time-delays · Robust control

1 Introduction

Recently, multi-agent systems have attracted a lot of concern in many fields such as robotics, physics, biology, and control engineering. The fundamental problem of the application is consensus, which means that all agents reach an agreement on certain quantities of interest by developing distributed control polices based on local information.

In recent years, consensus problem of multi-agents systems has attracted many researchers and has a lot of research results both in theory and application. In Vicsek et al., the authors proposed a simple model for the phase transition of a group of self-driven particles [1]. Jadbabaie et al. provided a theoretical explanation for the Vicsek's model using graph theory [2]. Olfati-Saber and Murray studied the average consensus problem of multi-agents [3]. In reality, time-delays always arise from the information communication among the agents, and they are often present in form of random. The consensus problem of multi-agent systems with time-delays is often

X. Zong (✉) · Y. Cui
School of Physics and Information Technology, Shanxi Normal University, Linfen 041000, China
e-mail: zongxin729@163.com

Y. Jia et al. (eds.), *Proceedings of 2016 Chinese Intelligent Systems Conference*, Lecture Notes in Electrical Engineering 404, DOI 10.1007/978-981-10-2338-5_44

discussed [4–7]. The author analyzed the multi-agent systems with several kinds of time-delays, and provided the sufficient condition of all agents achieving stability [8]. Q.W. Gao et al. considered multi-agent systems with random time-delays [9].

However, in practical, the parameter and characteristics of the system are affected by the factor of environment, which will affect the stability of system. So people became concerned about a problem is that if a system is stable when it is influenced by other factors. The robust consensus of multi-agent systems under the situation that both time-delay and noise existence is considered. And the authors used the time-varying control gains of the consensus protocol to attenuate measurement noises [10]. The authors studied the consensus of high-order multi-agent systems with different time-delays and external disturbances by the tree-type transformation approach, and analyzed the robust consensus problem [11]. Methods of adaptive H_∞ consensus control of multi-agent systems composed of the first-order and the second-order regression models with unknown time-delays were presented [12].

In this paper, we extend the results of [9] to second-order systems with external disturbances. Sufficient conditions in terms of LMI are obtained to ensure asymptotical consensus with the desired disturbances attenuation performance, and further obtained the allowable time-delay. The effectiveness of the proposed algorithms is illustrated by a simulation example.

2 Graph Theory

Assume that a multi-agent system with n agents, the interaction among them can be modeled by a directed graph $\boldsymbol{G = (V, E, A)}$, where $\boldsymbol{V} = \{v_1, v_2, ..., v_n\}$ is the set of node. $e_{ij} = (v_i, v_j) \in \boldsymbol{E}$ is a set of edges, where the first element v_i is said to be the tail of edge and the other element v_j to be the head. And $\boldsymbol{A} = (a_{ij})_{n\times n}(a_{ij} \geq 0)$ is a weighted adjacency matrix. The elements of an adjacency matrix are positive. Correspondingly, the Laplacian of the directed graph is defined as $\boldsymbol{L} = \Delta - \boldsymbol{A}$, where $\Delta = [\Delta_{ij}]$ is a diagonal matrix with $\Delta = \sum_{j=1}^{n} a_{ij}$. For a directed graph, $\boldsymbol{L}$ is not symmetric. A directed graph is said to be strongly connected, if there exists a node such that there is a directed path from every other node to this node.

3 Problem Statement and Control Protocol

3.1 Problem Statement

Suppose that the multi-agent system consists of n agents, each agent is regarded as a node in a directed graph $\boldsymbol{G}$.

Let x_i be the position state of the ith agent, v_i be the speed state of the ith agent. Suppose the ith agent has the dynamics as follows:

$$\begin{aligned}\dot{x}_i(t) &= v_i(t)\\ \dot{v}_i(t) &= u_i(t) + w_i(t)\end{aligned} \tag{1}$$

where $u_i(t) \in \boldsymbol{R}$ is the control input(or protocol), and $w(t) \in L_2[0, \infty]$ is the external disturbance.

In general case, accurate consensus may be hard to achieve since the controlled protocol are usually subjected to external disturbances. First, *z(t)* is defined as controlled output. Suppose $z(t) = \boldsymbol{C}\xi(t)$, where $\boldsymbol{C} = \begin{bmatrix} \boldsymbol{L}_c & \boldsymbol{0} \\ \boldsymbol{0} & \boldsymbol{L}_c \end{bmatrix}$,

$$\boldsymbol{L}_c = \begin{bmatrix} \frac{n-1}{n} & \frac{-1}{n} & \cdots & \frac{-1}{n} \\ \frac{-1}{n} & \frac{n-1}{n} & \cdots & \frac{-1}{n} \\ \frac{-1}{n} & \vdots & \ddots & \frac{-1}{n} \\ \frac{-1}{n} & \frac{-1}{n} & \cdots & \frac{n-1}{n} \end{bmatrix}$$

It is obvious that consensus of the second-order multi-agent system (1) can asymptotically solve the consensus problem, if and only if the state of agents satisfy $\lim_{t\to\infty}(x_i - x_j) = 0$, $\lim_{t\to\infty}(v_i - v_j) = 0$.

And the attenuating ability of the multi-agent system against external disturbance can be quantitatively measured by the H_∞ performance index of the closed-loop transfer function matrix from the external disturbance input to the controlled output shown as

$$\|\boldsymbol{T}_{wz}\|_\infty = \sup_{0 \neq w(t) \in \boldsymbol{L}_2[0,\infty)} \frac{\|z(t)\|_2}{\|w(t)\|_2} \tag{2}$$

where $\|z(t)\|_2 = \sqrt{\int_0^\infty \|z(t)\|^2 \mathrm{d}t}$, $\|w(t)\|_2 = \sqrt{\int_0^\infty \|w(t)\|^2 \mathrm{d}t}$.

Therefore we should design the protocol to satisfy, and any scalar. Then the consensus problem of multi-agent system can be transformed into the robust control problem.

3.2 Control Protocol

To solve robust H_∞ consensus of the second-order multi-agent systems with random time-delays, we use the following protocol:

$$\begin{aligned} u_i(t) = &\sum_{j\in N_i} a_{ij}[(x_j(t) - x_i(t)) + \delta(\mathrm{t})(x_j(t-\tau) - x_i(t-\tau))] \\ &+ \sum_{j\in N_i} a_{ij}[(v_j(t) - v_i(t)) + \delta(\mathrm{t})(v_j(t-\tau) - v_i(t-\tau))] \end{aligned} \tag{3}$$

where $\delta(t)$ is random, which represents the probability of the event of time-delay. It satisfies the following condition:

$$\begin{cases} \delta(t)=1, & \text{If event A occurs} \\ \delta(t)=0, & \text{If event A doesn}'\text{t occurs} \end{cases} \tag{4}$$

$$\begin{cases} prob\{\delta(t)=1\}=E\{\delta(t)\}=d \\ prob\{\delta(t)=0\}=1-E\{\delta(t)\}=1-d \end{cases} \tag{5}$$

Suppose $x_i(0)=0, \quad v_i(0)=0.$

Then, under the protocol (2), the network dynamic can be summarized as

$$\xi(t)=-\boldsymbol{E}\xi(t)-\boldsymbol{H}\delta(t)\xi(t-\tau)+\boldsymbol{F}\omega(t) \tag{6}$$

where $\xi(t)=[x_1(t),x_2(t),\ldots x_n(t),v_1(t),v_2(t),\ldots v_n(t)]^T$, $\boldsymbol{E}=\begin{bmatrix}\boldsymbol{0} & -\boldsymbol{I_n}\\ \boldsymbol{L} & \mathbf{L}\end{bmatrix}$, $\boldsymbol{H}=\begin{bmatrix}\boldsymbol{0} & \boldsymbol{0}\\ \boldsymbol{L} & \boldsymbol{L}\end{bmatrix}$, $\boldsymbol{F}=\begin{bmatrix}\boldsymbol{0}\\ \boldsymbol{I_n}\end{bmatrix}$.

4 Main Result

In this section, we will present consensus conditions in directed networks with random time-delay on fixed and switching topologies.

Before presenting the main result, the following lemmas are introduced.

Lemma 1 ([13]) *For any vector* $\boldsymbol{x}, \boldsymbol{y} \in \boldsymbol{R}^{n\times n}$ *and any symmetric positive matrix* $\boldsymbol{M} \in \boldsymbol{R}^{n\times n}$, *we have* $\boldsymbol{x^Ty}\le\boldsymbol{x^TM^{-1}x}+\boldsymbol{y^TMy}$.

Lemma 2 ((Schur Complement Formula) [14]) *For given symmetric matrix* $\boldsymbol{S}=[\boldsymbol{S}_{ij}]$,

$i,j\in\{1,2\}$

$\boldsymbol{S}_{11}\in\boldsymbol{R}^{n\times n},\boldsymbol{S}_{12}\in\boldsymbol{R}^{r\times(n-r)},\boldsymbol{S}_{22}\in\boldsymbol{R}^{(n-r)\times(n-r)}$,

then, $\boldsymbol{S}<0\Leftrightarrow\boldsymbol{S}_{22}<0,\boldsymbol{S}_{11}-\boldsymbol{S}_{12}\boldsymbol{S}_{22}^{-1}\boldsymbol{S}_{12}^{\mathrm{T}}<0$ or $\boldsymbol{S}_{11}<0,\boldsymbol{S}_{22}-\boldsymbol{S}_{12}^{\mathrm{T}}\boldsymbol{S}_{11}^{-1}\boldsymbol{S}_{12}<0.$

4.1 Network with Random Time-Delay on Fixed Topology

Theorem 1 *Consider a directed network with random time-delay* τ *and fixed topology. For the multi-agent system* (6), *consensus can be achieved with*

$\|T_{wz}(s)\|_\infty < \gamma$ if there exists a common symmetric positive definite matrix ***P, Q, R*** *and satisfying*

$$\begin{bmatrix} -\boldsymbol{E}^{\boldsymbol{T}}\boldsymbol{P}-\boldsymbol{P}\boldsymbol{E}+\tau\boldsymbol{E}^{\boldsymbol{T}}\boldsymbol{R}\boldsymbol{E}+ & & & \\ \boldsymbol{Q}-d\boldsymbol{H}^{\boldsymbol{T}}\boldsymbol{P}-d\boldsymbol{P}\boldsymbol{H}+\boldsymbol{C}^{\boldsymbol{T}}\boldsymbol{C} & d\boldsymbol{P}\boldsymbol{H} & \tau d\boldsymbol{E}^{\boldsymbol{T}}\boldsymbol{R}\boldsymbol{H} & \boldsymbol{P}-\tau\boldsymbol{E}^{\boldsymbol{T}}\boldsymbol{R}\boldsymbol{F} \\ d\boldsymbol{H}^{\boldsymbol{T}}\boldsymbol{P}^{\boldsymbol{T}} & -\frac{d}{\tau}\boldsymbol{R} & \boldsymbol{0} & \boldsymbol{0} \\ d\tau\boldsymbol{H}^{\boldsymbol{T}}\boldsymbol{R}\boldsymbol{E} & \boldsymbol{0} & -\boldsymbol{Q}+\tau d\boldsymbol{H}^{\boldsymbol{T}}\boldsymbol{P}\boldsymbol{H} & -\tau d\boldsymbol{H}^{\boldsymbol{T}}\boldsymbol{R}\boldsymbol{F} \\ \boldsymbol{P}-\tau\boldsymbol{F}^{\boldsymbol{T}}\boldsymbol{R}\boldsymbol{E} & \boldsymbol{0} & -\tau d\boldsymbol{F}^{\mathrm{T}}\boldsymbol{R}\boldsymbol{H} & \tau\boldsymbol{F}^{\boldsymbol{T}}\boldsymbol{R}\boldsymbol{F}-\gamma^2\boldsymbol{I} \end{bmatrix} \tag{7}$$

Proof Define a Lyapunov function

$$\boldsymbol{V}(t)=\xi^{\mathrm{T}}(t)\boldsymbol{P}\xi(t)+\int_{t-\tau}^{t}\xi^{\mathrm{T}}(s)\boldsymbol{Q}\xi(s)ds+\int_{-\tau}^{0}\int_{t+\theta}^{t}\xi^{\mathrm{T}}(s)\boldsymbol{R}\xi(s)dsd\theta$$

where ***P, Q, R*** are symmetric positive definite matrices. The time derivative of ***V***(t) along the solution of the system (6) is, From the Newton–Leibniz formula $\int_{\mathrm{t}-\tau}^{\mathrm{t}}\xi(s)ds=\xi(t)-\xi(t-\tau)$ and Lemma 1, we have

$$\begin{aligned}\dot{V}(t)\le&-2\xi^{\mathrm{T}}(t)PE\xi(t)+2\xi^{\mathrm{T}}(t)PFw(t)\xi^{\mathrm{T}}(t)Q\xi(t)-\xi^{\mathrm{T}}(t-\tau)Q\xi(t-\tau)\\&+\tau\xi^{\mathrm{T}}(t)E^{\mathrm{T}}RE\xi(t)+\tau\delta(t)\xi^{\mathrm{T}}(t)E^{\mathrm{T}}RH\xi(t-\tau)\\&-\tau\xi^{\mathrm{T}}(t)E^{\mathrm{T}}RFw(t)+\tau\delta(t)\xi^{\mathrm{T}}(t-\tau)H^{\mathrm{T}}RE\xi(t)\\&+\tau\delta^2(t)\xi^{\mathrm{T}}(t-\tau)H^{\mathrm{T}}RH\xi(t-\tau)-\tau\delta(t)\xi^{\mathrm{T}}(t-\tau)H^{\mathrm{T}}RFw(t)\\&-\int_{t-\tau}^{t}\xi^{\mathrm{T}}(s)R\xi(s)ds-\tau w^{\mathrm{T}}(t)F^{\mathrm{T}}RE\xi(t)-\tau\delta(t)w^{\mathrm{T}}(t)F^{\mathrm{T}}RH\xi(t-\tau)\\&+\tau w^{\mathrm{T}}(t)F^{\mathrm{T}}RFw(t)-\int_{t-\tau}^{t}\xi^{\mathrm{T}}(s)R\xi(s)\mathrm{d}s\end{aligned}$$

Then

$$\boldsymbol{V}(t)\le\begin{bmatrix}\xi^{\mathrm{T}}(t) & \xi^{\mathrm{T}}(t-\tau) & \omega^{\mathrm{T}}(t)\end{bmatrix}*\begin{bmatrix}-2\boldsymbol{P}\boldsymbol{E}-2\delta(t)\boldsymbol{P}\boldsymbol{H}+\boldsymbol{Q}+\tau\boldsymbol{E}^{\mathrm{T}}\boldsymbol{R}\boldsymbol{E} & & \\ +\tau\delta^2(t)\boldsymbol{P}\boldsymbol{H}\boldsymbol{R}^{-1}\boldsymbol{H}^{\mathrm{T}}\boldsymbol{P}^{\mathrm{T}} & \tau\delta(t)\boldsymbol{E}^{\mathrm{T}}\boldsymbol{R}\boldsymbol{H} & \boldsymbol{P}-\tau\boldsymbol{E}^{\mathrm{T}}\boldsymbol{R}\boldsymbol{F} \\ \tau\delta(t)\boldsymbol{H}^{\mathrm{T}}\boldsymbol{R}\boldsymbol{E} & \tau\delta^2(t)\boldsymbol{H}^{\mathrm{T}}\boldsymbol{R}\boldsymbol{H}-\boldsymbol{Q} & -\tau\delta(t)\boldsymbol{H}^{\mathrm{T}}\boldsymbol{R}\boldsymbol{F} \\ \boldsymbol{P}-\tau\boldsymbol{F}^{\mathrm{T}}\boldsymbol{R}\boldsymbol{E} & -\tau\delta(t)\boldsymbol{F}^{\mathrm{T}}\boldsymbol{R}\boldsymbol{H} & \tau\boldsymbol{F}^{\mathrm{T}}\boldsymbol{R}\boldsymbol{F}\end{bmatrix}$$
$$*\begin{bmatrix}\xi(t) & \xi(t-\tau) & \omega(t)\end{bmatrix}^{\mathrm{T}}$$

The mathematical expectation of above formula is

$$E\{\boldsymbol{V}(t)\}\le\begin{bmatrix}\xi^{\mathrm{T}}(t) & \xi^{\mathrm{T}}(t-\tau) & w^{\mathrm{T}}(t)\end{bmatrix}*\begin{bmatrix}E\{-2\boldsymbol{P}\boldsymbol{E}-2\delta(t)\boldsymbol{P}\boldsymbol{H}+\tau\boldsymbol{E}^{\mathrm{T}}\boldsymbol{R}\boldsymbol{E} & & \\ +\boldsymbol{Q}+\tau\delta^2(t)\boldsymbol{P}\boldsymbol{H}\boldsymbol{R}^{-1}\boldsymbol{H}^{\mathrm{T}}\boldsymbol{P}^{\mathrm{T}}\} & E\{\tau\delta(t)\boldsymbol{E}^{\mathrm{T}}\boldsymbol{R}\boldsymbol{H}\} & \boldsymbol{P}-\tau\boldsymbol{E}^{\mathrm{T}}\boldsymbol{R}\boldsymbol{F} \\ E\{\tau\delta(t)\boldsymbol{H}^{\mathrm{T}}\boldsymbol{R}\boldsymbol{E}\} & E\{\tau\delta^2(t)\boldsymbol{H}^{\mathrm{T}}\boldsymbol{R}\boldsymbol{H}-\boldsymbol{Q}\} & E\{-\tau\delta(t)\boldsymbol{H}^{\mathrm{T}}\boldsymbol{R}\boldsymbol{F}\} \\ \boldsymbol{P}-\tau\boldsymbol{F}^{\mathrm{T}}\boldsymbol{R}\boldsymbol{E} & E\{-\tau\delta(t)\boldsymbol{F}^{\mathrm{T}}\boldsymbol{R}\boldsymbol{H}\} & \tau\boldsymbol{F}^{\mathrm{T}}\boldsymbol{R}\boldsymbol{F}\end{bmatrix}$$
$$*\begin{bmatrix}\xi(t) & \xi(t-\tau) & w(t)\end{bmatrix}^{\mathrm{T}}$$

$E\{\delta(t)\}=E\{\delta^2(t)\}=d$. Therefore, the sufficient condition of $\dot{V}(t)<0$ is

$$\begin{bmatrix} -2\boldsymbol{PE}-2d\boldsymbol{PH}+\boldsymbol{Q}+\tau\boldsymbol{E}^{T}\boldsymbol{RE} \\ +\tau d\boldsymbol{PHR}^{-1}\boldsymbol{H}^{T}\boldsymbol{P}^{T} & \tau d\boldsymbol{E}^{T}\boldsymbol{RH} & \boldsymbol{P}-\tau\boldsymbol{E}^{T}\boldsymbol{RF} \\ \tau d\boldsymbol{H}^{T}\boldsymbol{RE} & \tau d\boldsymbol{H}^{T}\boldsymbol{RH}-\boldsymbol{Q} & -\tau d\boldsymbol{H}^{T}\boldsymbol{RF} \\ \boldsymbol{P}-\tau\boldsymbol{F}^{T}\boldsymbol{RE} & -\tau d\boldsymbol{F}^{T}\boldsymbol{RH} & \tau\boldsymbol{F}^{T}\boldsymbol{RF} \end{bmatrix} < 0$$

Consider H_∞ as performance index: $J_t = \int_0^t [z^{\mathrm{T}}(t)z(t) - \gamma^2\omega^{\mathrm{T}}(t)\omega(t)]$.

Under the zero-valued initial state condition $V(0) = 0$, we define the cost performance for any $t \geq 0$

$$J_t = \int_0^t \left[z^{\mathrm{T}}(t)z(t) - \gamma^2 w^{\mathrm{T}}(t)w(t)\right]\mathrm{d}t = \int_0^t \left[z^{\mathrm{T}}(t)z(t) - \gamma^2 w^{\mathrm{T}}(t)w(t) + \boldsymbol{V}(t)\right]\mathrm{d}t$$
$$-\boldsymbol{V}(t) + \boldsymbol{V}(0) \leq \int_0^t \zeta^{\mathrm{T}}(t)\Xi\zeta(t)\mathrm{d}t - \boldsymbol{V}(t)$$

where $\zeta^{\mathrm{T}}(t) = [\xi^{\mathrm{T}}(t), \xi^{\mathrm{T}}(t-\tau), w^{\mathrm{T}}(t)]$

$$\Xi = \begin{bmatrix} -2\boldsymbol{PE}-2d\boldsymbol{PH}+\boldsymbol{Q}+\tau\boldsymbol{E}^{\mathrm{T}}\boldsymbol{RE} \\ +\tau d\boldsymbol{PHR}^{-1}\boldsymbol{H}^{\mathrm{T}}\boldsymbol{P}^{\mathrm{T}}+\boldsymbol{C}^{\mathrm{T}}\boldsymbol{C} & \tau d\boldsymbol{E}^{\mathrm{T}}\boldsymbol{RH} & \boldsymbol{P}-\tau\boldsymbol{E}^{\mathrm{T}}\boldsymbol{RF} \\ \tau d\boldsymbol{H}^{\mathrm{T}}\boldsymbol{RE} & \tau d\boldsymbol{H}^{\mathrm{T}}\boldsymbol{RH}-\boldsymbol{Q} & -\tau d\boldsymbol{H}^{\mathrm{T}}\boldsymbol{RF} \\ \boldsymbol{P}-\tau\boldsymbol{F}^{\mathrm{T}}\boldsymbol{RE} & -\tau d\boldsymbol{F}^{\mathrm{T}}\boldsymbol{RH} & \tau\boldsymbol{F}^{\mathrm{T}}\boldsymbol{RF}-\gamma^2\boldsymbol{I} \end{bmatrix} \tag{8}$$

Thus $\Xi < 0$ if $J_t < 0$. Then based on Lemma a we transform (8) into (7). Therefore, all agents of the multi-agent systems (6) can reach consensus with under the condition (7).

4.2 Network with Random Time-Delay on Switching Topology

Consider a directed graph $\boldsymbol{G}_{\sigma(t)}: \sigma(t) \in \boldsymbol{Z}^+$, where $\sigma(t)$ is the switching signal, the value of which determines the topology of the network.

We use the following protocol:

$$\begin{aligned} u_i(t) = & \sum_{j \in N_i(\sigma(t))} a_{ij}(\sigma(t))[(x_j(t) - x_{\mathrm{i}}(t)) + \delta(\mathrm{t})(x_{\mathrm{j}}(t-\tau) - x_{\mathrm{i}}(t-\tau))] \\ & + \sum_{j \in N_i(\sigma(t))} a_{ij}(\sigma(t))[(v_j(t) - v_{\mathrm{i}}(t)) + \delta(\mathrm{t})(v_{\mathrm{j}}(t-\tau) - v_{\mathrm{i}}(t-\tau))] + \omega(t) \end{aligned} \tag{9}$$

where $\mathbf{N}_i(\sigma(t))$ is the set of adjacency matrix. $a_{ij}(\sigma(t))$ is the element of the adjacency matrix.

The dynamic of the multi-agent system is

$$\dot{\xi}(t) = -\boldsymbol{E}_{\sigma(t)}\xi(t) - \boldsymbol{H}_{\sigma(t)}\delta(t)\xi(t-\tau) + \boldsymbol{F}\omega(t) \tag{10}$$

$$\xi(t) = [x_1(t), x_2(t), \ldots x_n(t), v_1(t), v_2(t), \ldots v_n(t)]^{\mathrm{T}}$$

where $\boldsymbol{E}_{(\sigma(t))} = \begin{bmatrix} \boldsymbol{0} & -\boldsymbol{I_n} \\ \boldsymbol{L}_{(\sigma(t))} & \boldsymbol{L}_{(\sigma(t))} \end{bmatrix}, \boldsymbol{H}_{(\sigma(t))} = \begin{bmatrix} \boldsymbol{0} & \boldsymbol{0} \\ \boldsymbol{L}_{\sigma(t)} & \boldsymbol{L}_{(\sigma(t))} \end{bmatrix}, \boldsymbol{F} = \begin{bmatrix} \boldsymbol{0} \\ \boldsymbol{I_n} \end{bmatrix}$

Theorem 2 *Consider a directed network with random time-delay* τ *and switching topology. For the multi-agent system* (10)*, consensus can be achieved with* $\|\boldsymbol{T}_{wz}(s)\|_\infty < \gamma$ *if there exist common symmetric positive definite matrices* ***P, Q, R,*** *and satisfying*

$$\begin{bmatrix} -\boldsymbol{E}_{\sigma(t)}^{\mathrm{T}}\boldsymbol{P} - \boldsymbol{P}\boldsymbol{E}_{\sigma(t)} + \boldsymbol{Q} + \tau\boldsymbol{E}_{\sigma(t)}^{\mathrm{T}}\boldsymbol{R}\boldsymbol{E}_{\sigma(t)} - & d\boldsymbol{P}\boldsymbol{H}_{\sigma(t)} & \tau d\boldsymbol{E}_{\sigma(t)}^{\mathrm{T}}\boldsymbol{R}\boldsymbol{H}_{\sigma(t)} & \boldsymbol{P} - \tau\boldsymbol{E}_{\sigma(t)}^{\mathrm{T}}\boldsymbol{R}\boldsymbol{F} \\ d\boldsymbol{H}_{\sigma(t)}^{\mathrm{T}}\boldsymbol{P} - d\boldsymbol{P}\boldsymbol{H}_{\sigma(t)} + \boldsymbol{C}^{\mathrm{T}}\boldsymbol{C} & & & \\ d\boldsymbol{H}_{\sigma(t)}^{\mathrm{T}}\boldsymbol{P}^{\mathrm{T}} & -\frac{d}{\tau}\boldsymbol{R} & \boldsymbol{0} & \boldsymbol{0} \\ d\tau\boldsymbol{H}_{\sigma(t)}^{\mathrm{T}}\boldsymbol{R}\boldsymbol{E}_{\sigma(t)} & \boldsymbol{0} & -\boldsymbol{Q} + \tau d\boldsymbol{H}_{\sigma(t)}^{\mathrm{T}}\boldsymbol{P}\boldsymbol{H}_{\sigma(t)} & -\tau d\boldsymbol{H}_{\sigma(t)}^{\mathrm{T}}\boldsymbol{R}\boldsymbol{F} \\ \boldsymbol{P} - \tau\boldsymbol{F}^{\mathrm{T}}\boldsymbol{R}\boldsymbol{E}_{\sigma(t)} & \boldsymbol{0} & -\tau d\boldsymbol{F}^{\mathrm{T}}\boldsymbol{R}\boldsymbol{H}_{\sigma(t)} & \tau\boldsymbol{F}^{\mathrm{T}}\boldsymbol{R}\boldsymbol{F} - \gamma^2\boldsymbol{I} \end{bmatrix} < 0 \tag{11}$$

Proof The proof of Theorem 2 can be straightly derived from Theorem 1.

5 Simulation

In this section, numerical simulations will be given to illustrate the theoretical results obtained in the previous section. These simulations are performed with four agents, whose initial conditions are all zeros. Figure 1 shows four different directed networks$\{\boldsymbol{G}_1, \boldsymbol{G}_2, \boldsymbol{G}_3, \mathbf{G}_4\}$, and the weights a_{ij} are all 1. Suppose initial state is zero and the performance index.

We present the simulation results for the network with random time-delay and fixed topology Fig. 1 $\mathbf{G}_1$. Based on Theorem 1, we can get time-delay $\tau \leq 0.4339$. Figure 2 shows the position trajectories and velocity trajectories. Then the simulation results of network with random time-delay and switching topology are considered. Based on Theorem 2, we can obtain $\tau = 0.3925$. Suppose $\tau \leq 0.38$.

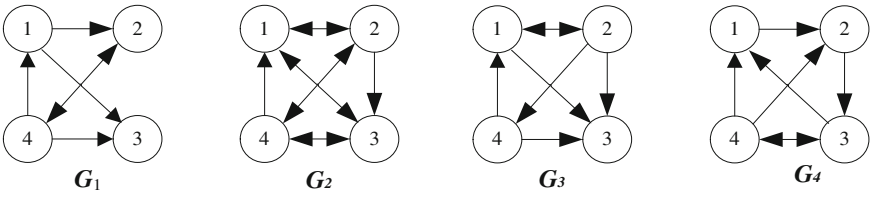

Fig. 1 Four directed graphs

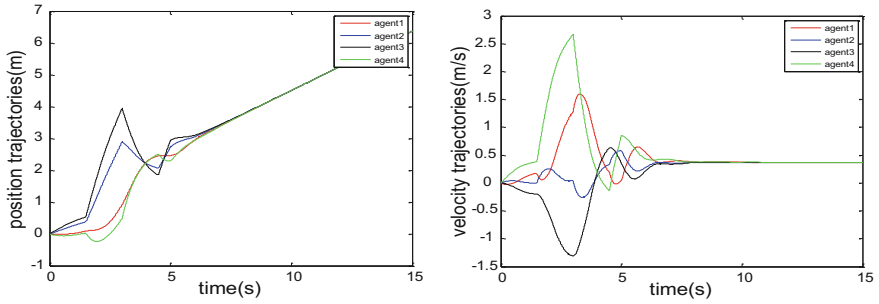

Fig. 2 The position trajectories and velocity trajectories of network with fixed topology

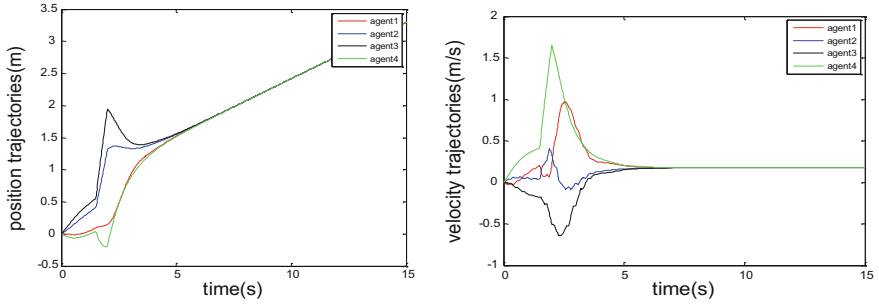

Fig. 3 The position trajectories and velocity trajectories of network with switching topology

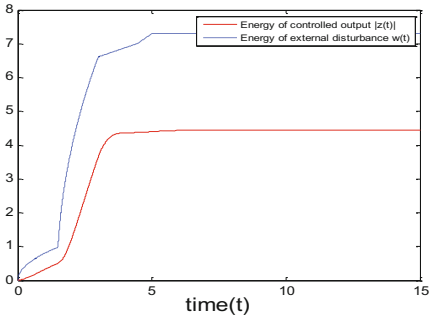

Fig. 4 Shows the corresponding energy trajectory of the controlled output z(t) and the disturbance signal $w(t)$ of network with fixed topology

Figure 3 shows the position trajectories and velocity trajectories. Figures 4 and 5, respectively, show the corresponding energy trajectory of the controlled output z(t) and disturbance signal $w(t)$.

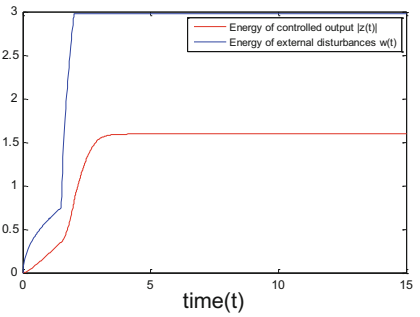

Fig. 5 Shows the corresponding energy trajectory of the controlled output z(t) and the disturbance signal w(t) of network with switching topology

6 Conclusion

In this paper, we have employed a robust control method to solve the consensus problem of the second-order multi-agent systems with random time-delays and external disturbances. Several conditions are presented to ensure all agents to reach consensus satisfying H_∞ performance index. Finally, numerical simulations are provided to show the effectiveness of our theoretical results. In addition, the finite-time consensus of multi-agent systems with random time-delays can be investigated in the future.

Acknowledgments This work was supported by the NSFC(61503231).

References

1. Vicsek T, Czirok A, Ben-Jacob E et al (1995) Novel type of phase transition in a system of self-driven particles. Phys Rev Lett 75(6):1226–1229
2. Jadbabaie A, Lin J, Morse AS (2003) Coordination of groups of mobile autonomous agents using nearest neighbor rules. IEEE Trans Autom Control 48(6):998–1001
3. Ren W, Beard RW (2005) Consensus seeking in multi-agent systems under dynamically changing interaction topologies. IEEE Trans Autom Control 50(5):611–655
4. Blinman P-A, Ferrari-Trecate G (2008) Average consensus problems in networks of agents with delayed communications. Automatica 44(8):1985–1995
5. Liu XL, Xu BG (2012) Distributed H_∞ consensus control for multiple-agent systems with communication delays. Control and Decision 27(4):0494–0500 刘学良,胥布工.具有多个通信时延的多智能体系统分布式H_∞一致性控制[J].控制与决策, 2012, 27(4): 0494–0500
6. Song L, Wu QH (2013) Average consensus of second-order multi-agent systems with time-delays and uncertain topologies. Control Theory Appl 30(8): 1047–1052
7. Liu XQ, Kang HQ, Zeng C (2014) Application research in multi-agent system about consensus on initial state. Comput Eng Appl 50(13):53–56 刘孝琪,康怀祺,曾超.多智能体系统初始状态一致性应用研究[J].计算机工程与应用, 2014, 50(13): 53–56

8. Kang YT, Lin L (2016) Average-consensus of a class of multi-gent systems with time-varying delay[J]. Inf Technol 37(1):143–145 康玉婷,李琳. 时滞多智能体系统的平均一致性[J]. 信息技术, 2016, 37(1): 143–145
9. Gao QW, Fan CX, Wei QY (2013) Research on consensus of multi-agent system with random time-delay. Comput Technol Dev 23(10):52–55 高庆文,樊春霞,韦庆阳.具有随机时延的多智能体系统的一致性研究[J].计算机技术及发展, 2013, 23(10): 52–55
10. Huang X, Li D (2014) Robust consensus for multi-agent systems with noises and delays. J Anhui Univ Sci Technol (Natl Sci), 2(34): 17–22. 黄新余,李德权. 具有噪声与时延的多个体系统的鲁棒一致性[J].安徽理工大学学报(自然科学版), 2014, 2(34): 17–22
11. Cui Y, Jia YM (2013) Robust consensus approach to high-order multi-agent systems based-on tree-type transformation. J Beijing Univ Aeronaut Astronaut 39(3):386–390 崔艳,贾英民.树形变换下高阶多智能体系统鲁棒一致性办法[J].北京航天航空大学学报, 2013, 39(3): 386–390
12. Miyasato Y (2015) Adaptive H_∞ consensus control of multi-agent systems with time delays. In: Proceedings of the 54th Society of Instrument and Control Engineers of Japan(SICE), Annual Conference, pp 572–577
13. Horn R, Johnson C (1985) Matrix analysis. Cambridge Univ. Press, Cambridge, UK
14. Boyd S, Ghaoui LE, Feron E et al (1994) Linear matrix inequalities in system and control theory. Society for Industrial and Applied Mathematics, Philadelphia, PA, pp 19–20

Multi-exposure Dynamic Image Fusion Based on PatchMatch and Illumination Estimation

Dan Fan, Junping Du and JangMyung Lee

Abstract In this study, we present a novel image fusion algorithm for multi-exposure dynamic images based on PatchMatch and illumination estimation. To eliminate the ghosting artifacts which often occur in the fusion results of existing exposure fusion methods when there are moving objects in the scenes, the fusion process of our proposed algorithm is as follows. First, we take advantage of the PatchMatch method to align the selected reference image with the other input images and then we fuse these images together based on illumination estimation to obtain the final fusion image. Experimental results demonstrate that our proposed method performs better than the existing fusion methods both in visual effect and objective indicators.

Keywords Image fusion · Dynamic scenes · Patchmatch · Illumination estimation · Multi-exposure

1 Introduction

Because of the complicated environmental conditions, light intensity may change suddenly and unpredictably, which results in that the images captured by cameras may include over-exposed or under-exposed image parts. This means that the poor

D. Fan · J. Du (✉)
Beijing Key Lab of Intelligent Telecommunication Software and Multimedia,
School of Computer Science, Beijing University of Posts and Telecommunications,
100876 Beijing, China
e-mail: junpingdu@126.com

D. Fan
e-mail: komaconss@163.com

J. Lee
Department of Electronics Engineering, Pusan National University, Busan, Korea
e-mail: jmlee1@pusan.ac.kr

Y. Jia et al. (eds.), *Proceedings of 2016 Chinese Intelligent Systems Conference*,
Lecture Notes in Electrical Engineering 404, DOI 10.1007/978-981-10-2338-5_45

quality of collected images and can severely affect the accurate identification and acquisition of dynamic targets.

To solve these problems, image sequences can be captured at different exposure levels and then synthesized into high dynamic range (HDR) images. HDR images have a visual quality that is more vivid than images produced by standard methods. Moreover, an HDR image can include all details of a real scene. Currently, two main types of synthetic techniques exist: HDR imaging and multi-exposure fusion technologies. This study proposes a multi-exposure fusion algorithm based on image alignment, which is a type of multi-exposure fusion technology. We review the current research on multi-exposure fusion technology.

Multi-exposure fusion technology is more efficient than HDR imaging technology. It combines captured images from a multi-exposure sequence into a well-exposed fusion image. Other studies have considered various environmental conditions when images are captured in proposing several multi-exposure fusion methods.

Mertens et al. proposed a fusion method based on reconstructing Laplacian pyramid and Gaussian pyramid and takes three features, which are contrast, saturation and well-exposure, as the fusion weights [1]. Shen et al. proposed a probability fusion method in the framework of random walks, by using local contrast and consistency measurements of neighborhood colors [2]. Based on brightness contrast and gradient measurements, Song et al. adopted a framework of maximum a posteriori probability to construct a probability model that can determine pixels that can be used in the fusion process [3]. Although these technologies produce fusion results of high quality, they can be applied only to image sequences of certain scenes. In addition, in the fusion of some exposure sequences, some aberrant phenomena remain, such as exposure deviation, color distortion, and so on. Moreover, similar to typical HDR technologies, most fusion methods assume that a captured low dynamic range (LDR) image sequence is aimed at static scene without considering the influence of moving targets. Unfortunately, when we capture an exposure sequence, displacement usually exists in the adjacent image frames because of the movement of targets and cameras [4].

To solve the problem caused by target or camera movement, a variety of solutions have been proposed. Some methods have adopted filter and virtual shadow elimination to solve the ghosting problem [5–7]. However, these methods do not completely eliminate the influence of motion messages and also discard certain valuable information, which leads to suboptimal results. Other methods use motion estimation and alignment to eliminate the negative effect of movement during image fusion [8]. These methods have achieved worthy results. However, when these methods are used to implement image alignment in an image sequence that has different types of exposure, errors occurred, yielding inaccurate fusion results. Moreover, if we directly use the fusion method to synthesize fusion image without preprocessing the LDR image sequence, motion blur and ghosting artifacts occur in the image results.

To solve this problem, this study proposes a multi-exposure dynamic image fusion method based on PatchMatch and illumination estimation. The novelty and contributions of this study are as follows:

(1) By taking advantage of the PatchMatch method before image fusion occurs, we can find the corresponding patches among the reference image and the other input images, then we can align the other images with the reference image to obtain the effect that they seem being captured in the static scene. The final fusion image shows high quality and the method obviates the ghosting phenomenon.
(2) By using illumination estimation during the image fusion process, the proposed method can obtain good fusion quality.

The remainder of the paper is organized as follows. Section 2 describes the process of the proposed method. Section 3 presents details of the experimental result and analysis. A conclusion is given in Sect. 4.

2 Proposed Image Fusion Algorithm Based on PatchMatch and Illumination Estimation

To overcome the limitation of traditional exposure fusion methods, which are not adapted to dynamic scenes, our algorithm adopts an image alignment method based on PatchMatch to align the reference image and other input images. We then fuse images within the multi-exposure dynamic image sequence based on illumination estimation to obtain the fusion image. Our proposed method produces a quality fusion result from a multi-exposure dynamic image sequence. Specifically, the resulting fusion image retained the areas from both low and high exposure images that are well displayed. Moreover, compared with the original multi-exposure dynamic image sequence, our fusion image yielded a more vivid visual effect and abundant scene details.

Our proposed algorithm can be divided into two steps. In the first step, we select an image which has most well-exposed pixels as the reference image. Corresponding images having different types of exposure must be aligned with the reference image. The second step involves fusing images within the image sequence that has been aligned. We ultimately acquire a fusion image that yields quality fusion effects. The specific process of our proposed algorithm is shown in Fig. 1.

2.1 Dynamic Image Alignment Based on PatchMatch

Our proposed method first must align the original multi-exposure dynamic image sequence so that background and dynamic targets are aligned with corresponding

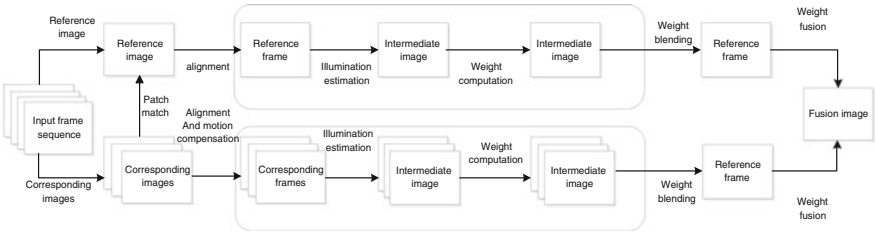

Fig. 1 Running process of the proposed algorithm

images having different types of exposure. We can then fuse the images within the multi-exposure dynamic image sequence that has been aligned. Our proposed method can adapt different dynamic scenes and produce a vivid visual effect and abundant scene details.

In this section, we describe the first step of our proposed method: dynamic image alignment based on PatchMatch. In this step, in order to align the dynamic targets in the multi-exposure image sequence, the running process of our proposed method is described as follows:

First, we must select the reference image from the original multi-exposure dynamic image sequence. We choose a reference image among those with different types of exposure, and usually we select the image with middle exposure. We then align corresponding images with the selected reference frame. This allows us to obtain aligned images with that of the reference image except with different types of exposure. Although dynamic targets exist in the image sequence, these dynamic targets are aligned in the corresponding images having different types of exposure after the alignment process is completed [9]. The image alignment process based on PatchMatch mainly includes the following three steps.

Step 1: Considering the quality exposure areas of the reference image, the corresponding images can locate similar areas in the reference image by using the PatchMatch method [10]. Then we can find the corresponding patches between the reference image and the other input images. These images can then reconstruct the corresponding area based on the quality exposure areas of the reference image and assign it to the aligned images obtained after the alignment process. This process can be described by the following equation:

$$C_r(L, R, \tau) = \sum_{i \in \Omega} \left(d(L, \tau(R)) + \alpha d(\nabla L, \nabla \tau(R)) + \beta d(\nabla L, \nabla \lambda(R)) \right) \quad (1)$$

where Ω represents the image domain, and $d(x, y) = \|x - y\|^2$. The variable α can be used to balance the consistency of color and gradients among corresponding frames and β can be used to balance the feature consistency among corresponding frames. In addition, the color matching function τ can be used to describe the change in RGB values between the reference and corresponding frames. Similarly,

the feature matching function λ can be used to describe the change of image feature values between the reference and corresponding frames.

Step 2: For areas in the reference frames that are either over- or under-exposed, the corresponding frames should reserve their original corresponding areas and add some consistency constraints, then assign these areas to the aligned frames to maintain consistency of color, gradients, and features with those areas obtained from the first step. We use the following equation to describe the process:

$$C_t(S, L, u) = \frac{1}{p^2} \sum_{i \in \Omega} \left(d(P_i^L, P_{i+u(i)}^S)\right) \tag{2}$$

where P_i^S is a block of image S, its size is $p \times p$, and its central point is pixel i(P_i^L and L have a similar relationship). The variable $u(i)$ refers to the block of the aligned frame L that corresponds to the original input frame S.

Step 3: After the previous two steps, we must combine step1 with step2 to obtain the ultimate aligned frame L^*.

$$L* = \arg\min_{L,\tau,u} (C_r(L, R, \tau) + C_t(S, L, u)) \tag{3}$$

where L^* is the aligned frame that we hope to obtain. We obtain alignment results having a quality effect. Specifically, the background and dynamic targets are aligned between the reference and corresponding image frames. Moreover, the foundation for the next fusion process has been prepared.

2.2 *Multi-exposure Dynamic Image Fusion Based on Illumination Estimation*

Through the image alignment process previously mentioned, we obtain a multi-exposure dynamic image sequence whose background and dynamic targets have been aligned. We must then perform the second step of our proposed method, namely to conduct the fusion process for the aligned image sequence to acquire the fusion image [11].

The multi-exposure dynamic image fusion process based on illumination estimation includes the following three steps:

Step 1: Based on the 'spatial smoothness' of the pass years, the final illumination estimation is an image smoothed in the regions where there are soft edges or uniform areas, and sharp in the strong intensity transitions. The proposed method takes advantage of the recursive method described in [12] to obtain the illumination estimation images.

Step 2: After estimating the illumination from each image of the sequence, we now need to determine the weights of all the pixels from every image in the sequence. The process can be described by the following equation:

$$\begin{aligned} &W_U = F_U(S_U) \quad W_R = F_R(S_R) \quad W_O = F_O(S_O) \\ &\forall R \in (2, N-1) \end{aligned} \tag{4}$$

where W_U, W_R and W_O are the weights of under-exposed, reference and over-exposed images, respectively, S_U, S_R and S_O are the illumination estimation images of under-exposed, reference and over-exposed images, respectively, and F_U, F_R and F_O are the mapping function, respectively.

For the reference image, the weight of the pixel is one if the value of the pixel is 128, then the weights of the pixels are linear function and down to zero if the value of the pixel is 0 or 255. Different from the method [11], when address the high-exposed image, we set the weight of the pixel as 1 if its value is less than or equal to 128, and as 0 if its value is higher than 128. Because of which, we can obtain more useful message from the over-exposed image. Reversely, we set the weight of the pixel as 0 if its value is less than or equal to 128, and as 1 if its value is higher than 128 when we address the under-exposed image.

Step 3: At last, we need to blend the weights and output the fusion weights. The process is shown as follows:

$$P_{out} = \frac{\sum_{k=1}^{N} P_k * W_k}{\sum_{k=1}^{N} W_k}, P \in \{R, G, B\} \tag{5}$$

where P_{out} means the final fusion result of every pixel, N denotes the total number of pixels in the scene, and P are the three channels of the RGB color space.

After these three steps of processing, we obtain the fusion image with a quality fusion effect. The fusion image retained the areas of both under- and over-exposed images that were well displayed. Simultaneously, our proposed method also conducted processing for keeping a good exposure, and we acquired the fusion image with normal exposure.

3 Analysis of Experimental Results

To evaluate the performance of our proposed method objectively, we adopted the following three objective indicators: the degree of visual fidelity (VIF), gradient retention ($Q_{AB/F}$), and feature similarity index (FSIMc). VIF quantifies the distortion and extent of visual quality improvement, $Q_{AB/F}$ reflects the degree to which

edge information in the fusion image is retained, and FSIMc evaluates image quality based on low-level features in the image. For these three measurements, the higher the evaluation index is, the better fusion quality of the image is.

Simultaneously, in order to validate the performance of our proposed method, we compare it to several existing methods. We objectively evaluate our method based on the visual effect it produces and quantitative indicators. We selected the exposure fusion algorithms [1, 3, 5], and Photomatix [13], a commercial software, as tools for use in the comparison.

We next perform three comparative experiments. These are based on the standard multi-exposure dynamic image sequence and that of a robot captured by our cameras. The experimental results from our proposed method and that of the four contrasting methods based on a "park" image sequence are shown in Fig. 2.

First, as the visual effects shown in Fig. 2d, reveal the experimental results of the Mertens et al. method had distinct ghosting artifacts both in the region of the sky and the region of the cars. Similarly, as shown in Fig. 2e, the Vassilios et al. method had ghosting artifacts both in the region of the sky and the region of the cars, and also had lower illumination. As shown in Fig. 2f, the Li et al. method also had ghosting artifacts both in the region of the sky and the region of the cars. Figure 2g shows that the experimental results for Photomatix are fuzzy with respect to both the building and sky, though it eliminated the ghosting artifacts. The experimental results from our proposed method, as shown in Fig. 2h, indicate quality exposure without ghosting artifacts. In addition, the method retained the region of the original multi-exposure image sequence that was well displayed. Moreover, compared to the original multi-exposure dynamic image sequence, our fusion image showed better visual effects, more abundant scene details, and more obvious contrast.

Second, the quantitative indicators allow us to obtain objective evaluation indices of different methods, as shown in Table 1.

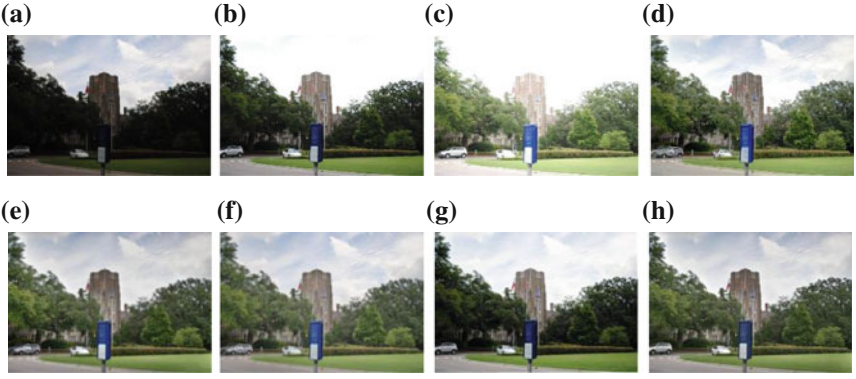

Fig. 2 "Park" image sequence. **a**, **b**, **c** input images **d** Mertens et al. method **e** Vassilios et al. method **f** Li et al. method **g** Photomatix and **h** the proposed method

Table 1 Quantitative indicators used to contrast different methods on the "park" image sequence

Measurement indicators	Different reconstruction methods				
	Mertens et al. method	Vassilios et al. method	Li et al. method	Photomatix	The proposed method
VIF	0.4275	0.3328	0.3885	0.3520	**1.2641**
$Q_{AB/F}$	0.2828	0.1989	0.2087	0.1550	**0.6971**
FSIMc	0.7729	0.8161	0.7940	0.7635	**0.8852**

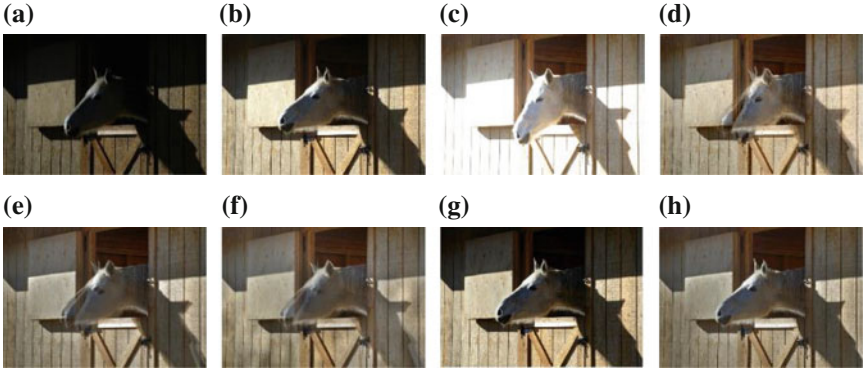

Fig. 3 "Horse" image sequence. **a**, **b**, **c** input images **d** Mertens et al. method **e** Vassilios et al. method **f** Li et al. method **g** Photomatix and **h** the proposed method

Table 1 shows that our proposed method performed much better than the other four methods according to the evaluation indices of VIF, $Q_{AB/F}$ and FSIMc. Especially in VIF and $Q_{AB/F}$, our proposed method achieved much better results.

The experimental results from our proposed method and that of the four contrasting methods based on a "horse" image sequence are shown in Fig. 3.

First, as shown in Fig. 3d, reveal the experimental results of the Mertens et al. method had ghosting artifacts both in the region of horse's head and the shadow. Similarly, in Fig. 3e, the Vassilios et al. method performed ghosting artifacts both in the region of horse's head and the shadow, and also had lower illumination. As shown in Fig. 3f, the Li et al. method also achieved ghosting both in the region of horse's head and the shadow. Figure 3g shows that the experimental results for Photomatix eliminated the ghosting artifacts, while performed lower illumination

Table 2 Quantitative indicators used to contrast different methods on the "horse" image sequence

Measurement indicators	Different reconstruction methods				
	Mertens et al. method	Vassilios et al. method	Li et al. method	Photomatix	The proposed method
VIF	0.2826	0.2410	0.2432	0.1461	**0.6707**
$Q_{AB/F}$	0.2726	0.2248	0.1770	0.1135	**0.6233**
FSIMc	0.7659	0.7741	0.7678	0.6848	**0.9055**

and bad color effect. The experimental result from our proposed method, as shown in Fig. 3h, indicated quality exposure without ghosting artifacts. In addition, the method retained the region of the original multi-exposure image sequence that was well displayed. Moreover, our fusion image achieved better visual effects, more abundant scene details, and better illumination and coloration.

The quantitative indicators allow us to obtain objective evaluation indices for different methods, as shown in Table 2.

Table 2 shows that our proposed method performed much better than the other four methods according to the evaluation indices of VIF, $Q_{AB/F}$ and FSIMc. Especially in VIF and $Q_{AB/F}$, our proposed method achieved much better results. And the FISMc result of our proposed method showed improvements of 17 % for the best result of the other four methods.

The experimental results from our proposed method and that of the four contrasting methods based on a "robot" image sequence are shown in Fig. 4.

First, as shown in Fig. 4d, e, f, reveal the experimental results of the Mertens et al. method, the Vassilios et al. method, the Li et al. method all achieved ghosting in the region of the robot. Figure 4g shows that the experimental results for Photomatix eliminated the ghosting artifacts, while performed lower illumination. Experimental results for our proposed method, as shown in Fig. 4h, yielded quality

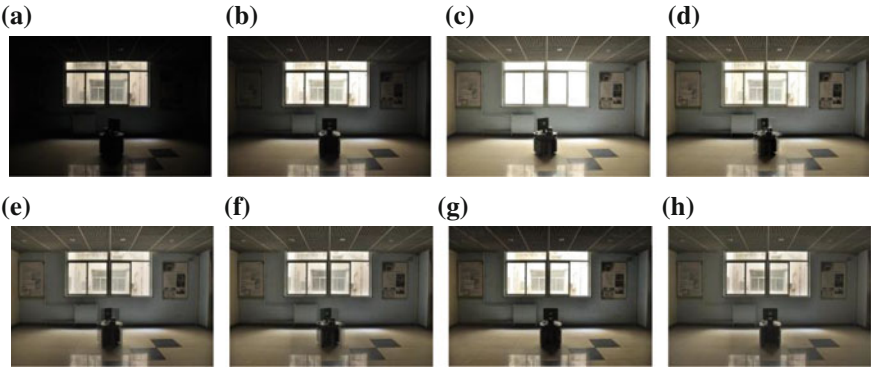

Fig. 4 "Robot" image sequence. **a**, **b**, **c** input images **d** Mertens et al. method **e** Vassilios et al. method **f** Li et al. method **g** Photomatix and **h** the proposed method

Table 3 Quantitative indicators used to contrast different methods on the "robot" image sequence

Measurement indicators	Different reconstruction methods				
	Mertens et al.method	Vassilios et al. method	Li et al. method	Photomatix	The proposed method
VIF	1.1253	1.1183	1.1005	1.0061	**1.1761**
$Q_{AB/F}$	0.5623	0.6151	0.5660	0.6668	**0.7551**
FSIMc	0.9158	0.9290	0.9117	0.9387	**0.9430**

exposure for both the room interior and outer window and without ghosting artifacts. Moreover, our fusion image had a clearer robot and more scene details.

The quantitative indicators allow us to obtain objective evaluation indices for different methods, as shown in Table 3.

Table 3 shows that our proposed method performed the best result in $Q_{AB/F}$, VIF and FSIMc, compared to the other four methods. When the experimental results of Tables 1, 2 and 3 are combined, our proposed method achieved best and satisfactory fusion results.

4 Conclusions

This paper reviewed the background and significance of related scientific research on multi-exposure image fusion. In addition, we proposed image fusion algorithm for multi-exposure dynamic images based on PatchMatch and illumination estimation. To correct the ghosting phenomenon caused by current image fusion methods when they address multi-exposure image sequences with dynamic targets, we first conduct an image alignment process based on the PatchMatch method prior to image fusion. Our proposed method allows us to conduct image fusion effectively on a multi-exposure dynamic image sequence. The fusion image obtained retains the regions of both under- and over-exposed images that are well displayed. Moreover, compared with the original multi-exposure dynamic image sequence, our fusion image has a more vivid visual effect and more abundant scene details. Finally, our experimental results validate the effectiveness of our proposed method regarding both visual effect and objective evaluation indicators.

Acknowledgments This work was supported by National Basic Research Program of China (973 Program) 2012CB821200 (2012CB821206) and the National Natural Science Foundation of China (No. 61320106006, No. 61532006, No. 61502042).

References

1. Mertens T, Kautz J, Van Reeth F (2009) Exposure fusion: a simple and practical alternative to high dynamic range photography. In: Computer graphics forum, vol 28, no 1. Blackwell Publishing Ltd, pp 161–171
2. Shen R, Cheng I, Shi J et al (2011) Generalized random walks for fusion of multi-exposure images. IEEE Trans on Image Process 20(12):3634–3646
3. Song M, Tao D, Chen C et al (2012) Probabilistic exposure fusion. IEEE Trans Image Process 21(1):341–357
4. Zhang W, Cham WK (2012) Reference-guided exposure fusion in dynamic scenes. J Vis Commun Image Represent 23(3):467–475
5. Li S, Kang X (2012) Fast multi-exposure image fusion with median filter and recursive filter. IEEE Trans Consum Electron 58(2):626–632
6. Chapiro A, Cicconet M, Velho L (2011) Filter based deghosting for exposure fusion video. ACM SIGGRAPH 2011 Posters

7. Li Z, Zheng J, Zhu Z et al (2014) Selectively detail-enhanced fusion of differently exposed images with moving objects. IEEE Trans Image Process 23(10):4372–4382
8. Wu S, Xie S, Rahardja S et al (2010) A robust and fast anti-ghosting algorithm for high dynamic range imaging. In: Proceedings of 17th IEEE international conference on image processing (ICIP), pp 397–400
9. Hu J, Gallo O, Pulli K et al (2013) Hdr Deghosting: How to deal with saturation. In: IEEE Conference on Computer Vision and Pattern Recognition (CVPR)
10. Barnes C, Shechtman E, Goldman DB, Finkelstein A (2010) The generalized PatchMatch correspondence algorithm. In: ECCV
11. Vonikakis V, Bouzos O et al (2007) Multi-exposure image fusion based on illumination estimation. In: Proceedings of pacific graphics
12. Shaked D, Keshet R (2002) Robust recursive envelope operators for fast Retinex. Hewlett-Packard Research Laboratories Technical report
13. http://www.hdrsoft.com

Fast Moving Crowd Counting for Unconstrained Videos

Xinlei Wei, Junping Du, Dan Fan and JangMyung Lee

Abstract It is important to estimate the number of people in fast moving crowd scenarios for the surveillance systems. Regression-based techniques achieved promising results for counting the number of people in crowded scenes. However, appearance features used in the most existing techniques are not able to mirror the motion state of crowds. The motion state of crowds is important to solve the counting problem of fast moving crowds, since it is decided by the amount of people. In this study, we propose a novel method to address this problem from three perspectives: (1) train a crowd counting estimation model suited to all of the crowded scenes; (2) combine motion states with multiappearance features for crowd counting; and (3) count fast moving crowds in unconstrained videos. These ideas are implemented in a fast object segment framework, which can segment fast moving crowds in the unconstrained videos. Extensive experiments validate the effectiveness of our proposed method.

Keywords Motion feature · Crowd counting · Fast moving crowd · Superpixel · Spatiotemporal structure

X. Wei (✉) · J. Du · D. Fan
Beijing Key Lab of Intelligent Telecommunication Software and Multimedia, Beijing University of Posts and Telecommunications, 100876 Beijing, China
e-mail: XinleiWei@bupt.edu.cn

J. Du
e-mail: junpingdu@126.com

D. Fan
e-mail: komaconss@163.com

X. Wei · J. Du · D. Fan
School of Computer Science, Beijing University of Posts and Telecommunications, 100876 Beijing, China

J. Lee
Department of Electronics Engineering, Pusan National University, Busan, South Korea
e-mail: jmlee1@pusan.ac.kr

Y. Jia et al. (eds.), *Proceedings of 2016 Chinese Intelligent Systems Conference*, Lecture Notes in Electrical Engineering 404, DOI 10.1007/978-981-10-2338-5_46

1 Introduction

Video-imagery-based crowd counting is important to profile the people movement over time across spaces for establishing global situational awareness. For example, once abnormal event happens, it often appears that crowded people run away fast and disorderedly, which will lead to disaster in most cases. Aiming at detecting abnormal events and rescuing people in time, it is quite important to count the people number in the chaotic situation. Counting people in crowded public places is nontrivial due to the severe interobject occlusion, scene perspective distortion, and visual ambiguity introduced by challenging illumination condition and fast moving crowds. The state-of-the-art methods typically adopt regression-based techniques to learn a mapping function between low-level features and crowd counting [1], so as to circumvent explicit object segmentation and detection in crowded scenes. And some researchers learn two kinds of mappings to estimate the number of crowds. The first mapping relationship is between the density and the sift feature of each point in crowded scene, and the other one is between crowd density and the number of people [2]. Though these methods have high performance for stationary and slowly moving crowds, when emergency happens, people will move fast and the video will be unconstrained. In such conditions, it is difficult to capture high-quality crowd images for the video surveillance systems. Hence, most methods cannot estimate the number of fast moving crowd accurately in the unconstrained videos. These methods based on low-level appearance feature will loss efficacy with the low quality videos. In order to solve these problems, we adopt fast object segmentation method in unconstrained videos [3] to segment foreground regions containing the fast moving objects. Meanwhile, we propose to use the motion channels as complements of the appearance channels to learn a mapping between feature groups and the number of crowds. Moreover, the feature group contains both motion features and appearance features.

In this paper, we propose a novel method for feature combination, considering the static features and dynamic features extracted from superpixel blocks (e.g., micro-behavioral [4] characteristic, the optical flow feature, and the direction information entropy). These features have both invariant and local properties, so they are suitable for various kinds of scenes. The underlying assumption is that if the crowds move in natural conditions, the quantity and velocity of flow are only decided by the crowd density, according to the crowd dynamic model. Therefore, the velocity and motion status can reflect the quantity of flow and then reflect the number of crowds. Rather than appearance features, it is a more effective way to detect fast moving people based on motion features. When the crowds move fast, the action is spatial–temporal continuous. Hence, we assume that the intrinsic spatial–temporal distribution structure of those data can be computed to facilitate the learning of a regression counting model.

The contributions of this paper include: (1) propose a framework of counting fast moving crowd; (2) fuse appearance features with motion features based on superpixel blocks to generate an invariant feature for the estimation of crowd counting in various scenes; and (3) construct a crowd counting model for fast moving crowds based on motion features and appearance features.

2 Related Work of Fast Moving Crowd Counting

Various approaches for crowd counting have been proposed in recent years [1]. Using multiple low-level features rather than a single feature can achieve a higher accuracy for crowd counting [5]. But in large-scale scenes, the accuracy may be lower because of the interference of noises. Hence, some researchers divided the images of large-scale scene into several blocks and extracted the features of each block to reduce the noises [6]. But it is more effective to estimate the number of people by crowd density [2] of crowded people. However, people always move fast when an abnormal event happens, making it very difficult to count the number of people. Meanwhile, in the panic cases, the video quality is usually poor due to the interferences such as blur and distortion. It is a challenge to count people under these circumstances. Some researchers used superpixel and optical flow to segment fast moving objects from unconstraint videos [3]. Because the performance of the classical supervised learning algorithms is mainly decided by the size of training dataset, regression-based methods need a lot of training data. However, it is difficult to manually label the amount of crowds in the crowded videos. And semisupervised algorithms use the relationship between instances to find the labeled result of instances [7].

3 The Framework of Fast Moving Crowd Counting Algorithm

3.1 The Implementing Procedures of the Proposed Algorithm

In this paper, we fuse the appearance features with motion features, and combine the semisupervised regression algorithm with support vector regression algorithm to construct the crowd counting model. The workflow is shown in Figs. 1 and 2. Figure 1 shows the training process of crowd counting model, and Fig. 3 shows the prediction process of crowd counting.

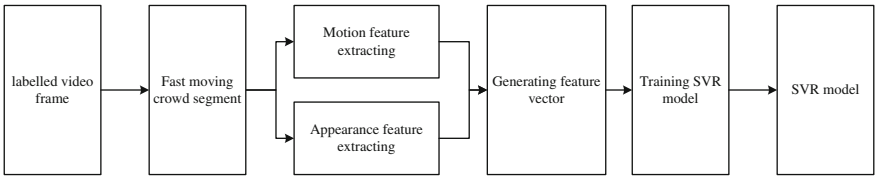

Fig. 1 The training process of crowd counting model

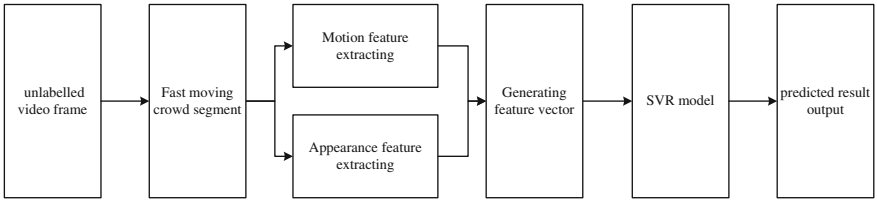

Fig. 2 The prediction process of crowd counting

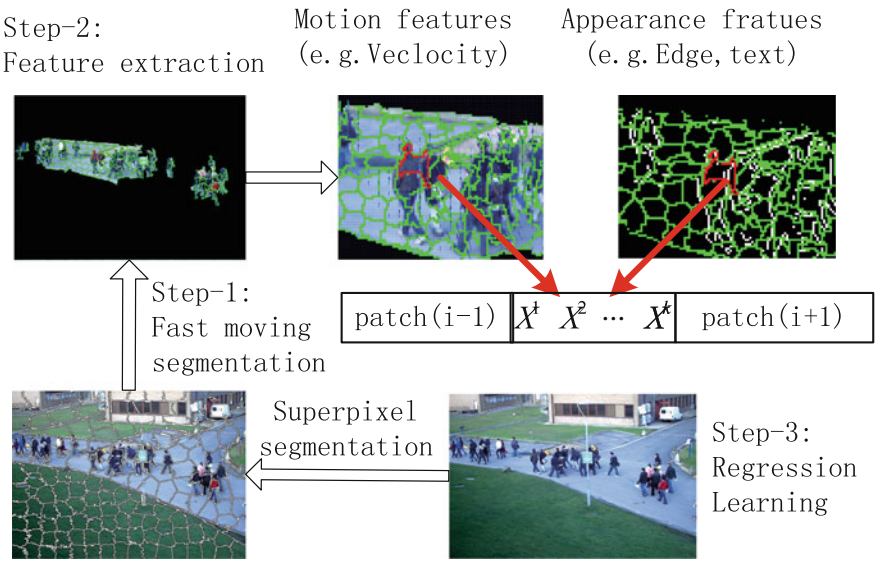

Fig. 3 The framework of fast moving crowds counting algorithm

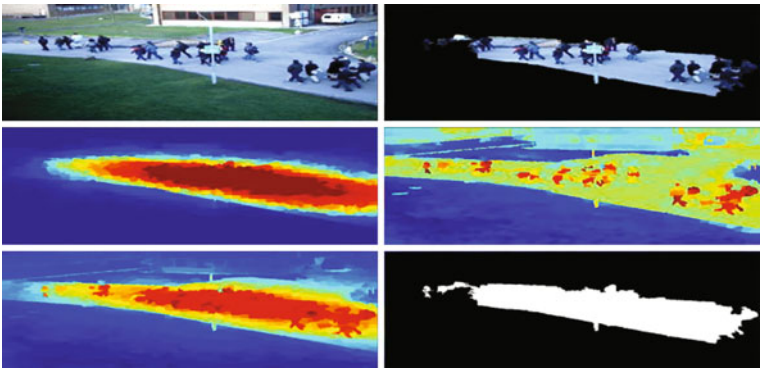

Fig. 4 The result of fast movement pedestrian segment

3.2 *Fast Moving Pedestrian Segmentation for Unconstrained Videos*

State-of-the-art methods for pedestrian foreground segmentation drop mixture dynamic texture. However, it is difficult to identify the fast moving crowd. We adopt the fast moving object segmentation algorithm in paper [2] to obtain the fast moving crowd region. Based on the superpixels and optical flow the proposed approach generated, we can extract local features and motion features. Then we can save a lot of computing time and the fast moving crowd segment result is shown in Fig. 4.

3.3 *The Extraction and Combination Process of Motion Features and Appearance Features*

State-of-the-art methods mostly combine many kinds of features which include the segment feature, internal edge feature, and texture feature [5]. And some methods add the local features to obtain local information such as local texture feature, gray level co-occurrence matrix (GLCM), structural-based feature, and histogram of the edge orientation [6]. According to dynamic continuum model of pedestrian flow [8], the flow of large-scale pedestrians relates to the flow velocity and density. Though appearance features are able to reflect the current pixel information, they cannot reflect the information of motion state. However, the information of motion state will not change with the scenes, which is important for the fast moving crowd counting. As a result, in this work we extract not only the local appearance features but also the motion features. The motion features exploited here include Jacobi matrix eigenvalues [4], movement velocity of crowds, velocity orientation, and information entropy.

(1) Appearance Features
Appearance features include several kinds of features, shown as follows.
Segmentation features: based on the fast object segmentation algorithm, we can easily extract the segment features. And these features are utilized to capture the segment properties such as shape and size in fast moving crowds. Moreover, the segment perimeter, computed by morphological erosion, is also helpful in extracting features such as area, perimeter, perimeter edge orientation, perimeter-area ratio and segment shape [5].
Internal edge features: edge length, edge orientation [5].
Texture features: we adopt the homogeneity, energy, entropy, gray level co-occurrence matrix (GLCM), and the local bitmap patterns (LBP) as texture features.

(2) Motion features
Jacobi matrix eigenvalues: the Jacobi matrix eigenvalues are used to identify the behaviors in crowded scenes [4]. They are based on the crowd flow dynamic system and are able to reflect the movement information of the crowd flow. In this work, we adopt a set of similar measurements for estimating the number of pedestrians in each segment. The moving crowd is regarded as a dynamic system, so we can obtain the Jacobi matrix of each pixel's velocity using optical flow by Taylor's theorem. We identify five kinds of crowd behaviors (Bottlenecks, Fountainheads, Lane Formation, Ring/Arch Formation, and Blocking) by the Jacobi matrix eigenvalues [4]. Through the statistics histogram and the weights of these behaviors, we can estimate the number of pedestrians.

Movement velocity histogram of crowd: the movement velocity is repressed by the optical flow, and the average velocity of each superpixel block is used to measure the region velocity. We compute the histogram of the average velocity with 10 bins.

Orientation information entropy: according to the method described in [8], we compute the average orientation information entropy of superpixel blocks in the crowd segmentation regions as a motion feature [9].

We follow [6] to combine these features to obtain an intermediate feature vector $x_i \in \mathbb{R}^d$. And all images are transformed to grayscale before feature extraction. In addition, features are perspective normalized using the method described in [10] and scaled into the range of $[0, 1]$.

3.4 The Proposed Crowd Counting Regression Algorithm

The support vector regression algorithm (SVR) and semisupervised regression algorithm (SSR) are used to count the number of crowd, respectively [11]. It is easy to prove that using SVR, we can achieve a higher accuracy [12]. But by exploiting the underlying geometric structure of abundant unlabeled data and the temporal

continuity of crowd patterns, the SSR can produce accurate counting with only sparse labeled data.

$$f^*(x^*) = \sum_i^{l+u} a_i K(x^*, x_i) + b \tag{1}$$

We learn the expansion coefficient vector $\alpha = [\alpha_1, \ldots, \alpha_{l+u}]^T$ and the optimal bias b from the training set, based on SVR. As SSR only needs sparse labeled data, we add a joint regularization [1] as Eq. (2) through learning the crowd pattern intrinsic distribution (geometric) structure and imposing temporal smoothness of activity patterns.

$$f^* = \arg\min_{f \in H_K} \frac{1}{l} \sum_{i=1}^{l} [y_i - f(x_i)]^2 + \lambda_A \|f\|_K^2 + \lambda_I f^T B f + \lambda_T f^T L f \tag{2}$$

4 Experiment Results and Discussion

We use three public datasets to verify the proposed approach, respectively. Each dataset includes different video sequences. The three datasets are shown in Table 1. And these images are randomly selected as training data and testing data according to a fixed ratio.

We employ three metrics for performance evaluation. They are mean absolute error [MAE], mean squared error [MSE], and mean deviation error [MDE] 3. The experiment results are shown in 0.

As is shown in Table 2, the proposed approach remarkably improves the performance of crowd counting in UCSD dataset. We use the appearance features and motion features combined with appearance features to test our approach, respectively. We find from Table 2 that the method using motion features combined with appearance features achieves a better performance than only using appearance features on various indexes.

But in difference datasets, the predicted results are different. For example, the predicted result is not good enough for the image sequences in PESt2009 datasets. The reason is that the image sequences in PEST2009 dataset are denser and people move much faster. However, the performance of our method is still quite good. Not only the MSE value and the MAE value in Fig. 2, but also the trends in Figs. 5, 6, 7 and 8 can demonstrate the superiority of our proposed algorithm.

Table 1 The information of different datasets

Image sequence	Property
UCSD	Sparse, walk slow
PEST2009.S1.L1	Dense, walk fast
PEST2009.S1.L2	Very dense, walk fast
PEST2009.S1.L3	Very dense, run fast

Table 2 The comparison results of different methods

Image sequence	Training	Approaches	MSE	MAE	MDE
UCSD	50	LBP + SSR4	7.06		
	50	GPR [9]	11.10		
	98	proposed	2.51	1.35	0.10
	98	Appearance feature + SVR	3.52	1.74	0.11
PEST2009.S1. L1_Time13-57_view001	109	proposed	5.68	2.025	0.11
	98	Appearance feature + SVR	7.41	2.37	0.13
PEST2009.S1. L2_Time13-57_view001	99	proposed	21.86	4.29	0.30
	98	Appearance feature + SVR	28.28	4.96	0.77
PEST2009.S1.L3. Time_14-17_view001	44	Proposed	28.62	4.58	0.29
	44	Appearance feature + SVR	30.17	4.78	0.32

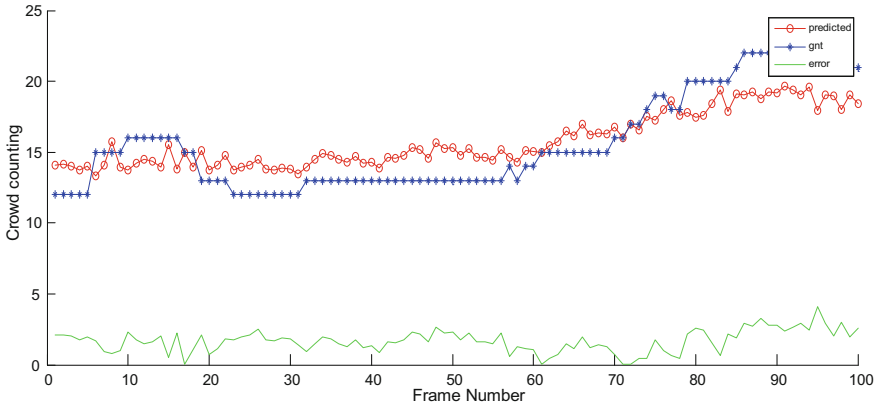

Fig. 5 The predicted result of UCSD.vidf1_33_000.y image sequences

However, from the comparison result in Table 2, we can find that the MSR value and the MAE value of the proposed approach are better than the approach only using appearance features. It demonstrates that it is more effective to estimate the number of moving dense crowd.

Especially, the sequence PEST2009.S1.L3.Time_14-17_view001 contains fast running crowds and the MAE value and MSE value that are calculated by the proposed approach are better as well. It demonstrates that the proposed approach is effective in fast moving crowd counting.

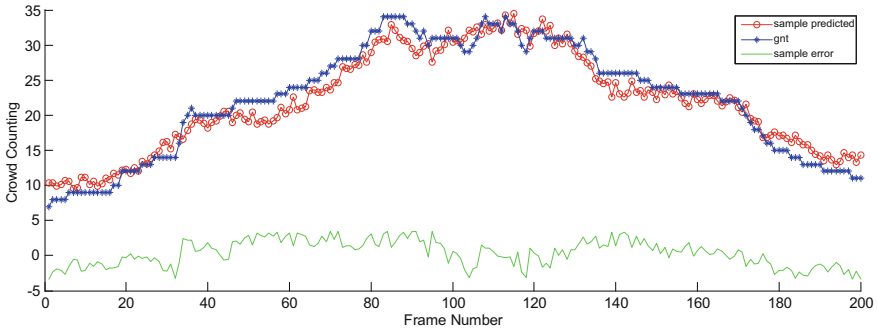

Fig. 6 The crowd counting predicted result of sample data in the dataset PEST2009.S1.L1

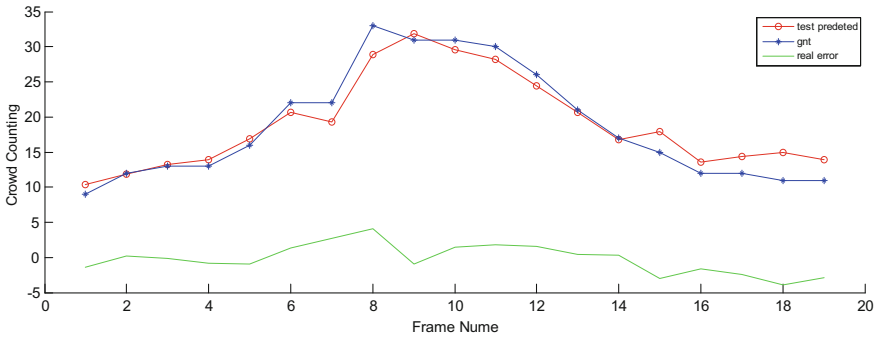

Fig. 7 The crowd counting predicted result of test data in the dataset PEST2009.S1.L2

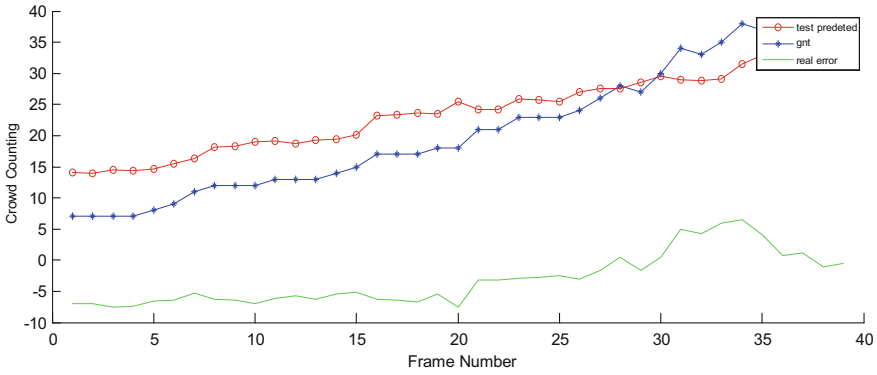

Fig. 8 PEST2009.S1.L3.Time_14-17 dataset predicted result of test dataset

5 Conclusion

In contrast to most current crowd counting studies that rely on appearance features and motion features for model training, a unified activation and regression approach is formulated to enable the crowd counting exploiting the underlying distribution structure of crowd patterns. We demonstrate that the motion features used in crowd counting can improve performance, which can bring in significant practical value. We take advantage of an assumption that if the source and target data sharing a similar manifold representation, then the motion feature is the manifold representation of the crowds. Future work will explore ways to relax this assumption through constructing unify regression model for different scenes.

Acknowledgments This work was supported by National Basic Research Program of China (973 Program) 2012CB821200 (2012CB821206) and the National Natural Science Foundation of China (No. 61320106006, No. 61532006, No. 61502042).

References

1. Loy CC, Chen K, Gong S, Xiang T (2013) Crowd counting and profiling: methodology and evaluation. In: Modeling, Simulation and Visual Analysis of Crowds, vol 11. Springer, pp 347–382
2. Ma Z, Yu L, Chan AB (2015)Small instance detection by integer programming on object density maps. In: CVPR
3. Papazoglou A, Ferrari V (2013) Fast object segmentation in unconstrained video. In: Proceedings of the IEEE International Conference on Computer Vision (ICCV), p 1777–1784
4. Solmaz B, Moore BE, Shah M (2012) Identifying behaviors in crowd scenes using stability analysis for dynamical systems. IEEE Trans Pattern Anal Mach Intell 34(10):2064–2070
5. Chan Antoni B, Vasconcelos Nuno (2012) Counting people with low-level features and Bayesian regression. IEEE Trans Image Process Publ IEEE Signal Process Soc 21 (4):2160–2177
6. Chen K, Change Loy C, Gong S, Xiang T (2012). Feature mining for localised crowd counting. In: BMVC
7. Change Loy C, Gong S, Xiang T (2013) From semi-supervised to transfer counting of crowds. In: IEEE International Conference on Computer Vision, pp 2256–2263
8. Hughes RL (2000) The flow of large crowds of pedestrians. Math Comput Simul 53:367–370
9. Wang Lu, Lin Gao, Lei Yan et al (2012) Key-frame retrieval method based on optical flow and entropy statistic for blooming video. Trans Chin Soc Agric Eng (Trans CSAE) 28 (17):125–130
10. Chan AB, Liang Z-SJ, Vasconcelos N (2008) Privacy preserving crowd monitoring: counting people without people models or tracking. In: IEEE Conference on Computer Vision and Pattern Recognition, pp 1–7
11. Keerthi S, DeCoste D (2005) A modified finite Newton method for fast solution of large scale linear SVM. JMLR 6(1):341–361
12. Melacci S, Belkin M (2011) Laplacian support vector machines trained in the primal. JMLR 2 (4):1149–1184

An Augmented Multiple-Model Adaptive Estimation for Time-Varying Uncertain Systems

Kai Xiong, Chunling Wei and Liangdong Liu

Abstract An augmented multiple-model adaptive estimation (MMAE) algorithm is presented for a time-varying system, where the model uncertainty may occur occasionally. Generally, it is difficult for a single filter to achieve superior performance for both the certain system and the uncertain system. An algorithm that is designed for an uncertain system may yield suboptimal performance in the situation, where the model uncertainty does not occur. To cope with this problem, we propose to use two filters in parallel in a multiple-model framework. One of the filters, an augmented Kalman filter (AKF), provides estimates of uncertain parameters when the model uncertainties occur, whereas the second filter, a Kalman filter (KF), yields high precision in the absence of the uncertainties. A practical example is given in simulation to show the potential application of the presented algorithm. It indicates that the augmented MMAE is efficient to deal with the occasional model uncertainty.

Keywords Multiple-model adaptive estimation · Uncertain system · Augmented Kalman filter · Space surveillance

1 Introduction

Many practical systems with unknown dynamic or measurement properties can be described by system model with uncertain parameters. When the model uncertainty occurs, the traditional Kalman filter (KF) suffers from a performance loss due to the uncertain effect in the model. Special techniques are required to mitigate the effect of the model uncertainty on the estimation accuracy. An augmented Kalman filter (AKF) is capable of estimating the uncertain parameters jointly with the state vector, such that the estimator is less sensitive to the uncertainty. The estimation

K. Xiong (✉) · C. Wei · L. Liu
Science and Technology on Space Intelligent Control Laboratory,
Beijing Institute of Control Engineering, Beijing 100190, China
e-mail: tobelove2001@vip.tom.com

Y. Jia et al. (eds.), *Proceedings of 2016 Chinese Intelligent Systems Conference*,
Lecture Notes in Electrical Engineering 404, DOI 10.1007/978-981-10-2338-5_47

accuracy can be improved using the AKF instead of the KF in the presence of the uncertainty. However, if the model uncertainties do not occur, the performance of the AKF may be worse than this of the KF due to the inaccurate estimated parameters. The AKF trades off robustness in the uncertain case and efficiency in the certain case, and it is difficult to achieve both with the same filter.

A solution to this difficulty is to design a multiple-model adaptive estimation (MMAE) algorithm, where multiple parallel Kalman filters are designed based on different models, such that the whole algorithm can adapt to different cases. During the past four decades, multiple-model techniques have been applied to deal with model uncertainties [1–4]. For the implementation of a traditional multiple model adaptive estimator, an elaborate model set should be constructed to cover all possible uncertain parameters. The MMAE algorithm uses a bank of parallel Kalman filters, termed "elemental filters," to provide multiple estimates, where each elemental filter is based on a hypothesized uncertain model in the model set. The overall state estimate is provided through a weighted sum of each elemental filter's estimate. The weight, which is calculated based on the measurement innovation, gives an indicator whether the model associated with the elemental filter is the correct one. The MMAE has been studied extensively and gains success in application [5–7].

In this paper, we present an augmented MMAE algorithm by combining a KF and an AKF in parallel. The KF is designed based on the nominal system model and the AKF is designed based on the augmented system model. The KF suits for the certain system and the AKF suits for the uncertain system. Simulation result involving a space surveillance problem is shown. It is illustrated that the augmented MMAE algorithm can achieve satisfactory performance for the systems with and without uncertainty. High performance is achievable using only two elemental filters, which correspond to a saving of computational burden.

2 System Model and Filter Equation

The considered time-varying system with model uncertainty is described as

$$\mathbf{x}_k = \mathbf{F}_k \mathbf{x}_{k-1} + \mathbf{D}_k \boldsymbol{\Delta}_k + \mathbf{w}_k \tag{1}$$

$$\mathbf{y}_k = \mathbf{H}_k \mathbf{x}_k + \mathbf{G}_k \boldsymbol{\theta}_k + \mathbf{v}_k \tag{2}$$

where k is the time index, $\mathbf{x}_k$ the state vector, $\mathbf{y}_k$ the measurement vector, $\mathbf{w}_k$ the process noise, $\mathbf{v}_k$ the measurement noise, $\mathbf{F}_k$ the transition matrix of the state $\mathbf{x}_k$, $\mathbf{D}_k$ the gain of unknown input $\boldsymbol{\Delta}_k$, $\mathbf{H}_k$ the measurement matrix, and $\mathbf{G}_k$ the gain of unknown bias $\boldsymbol{\theta}_k$. $\mathbf{w}_k$ and $\mathbf{v}_k$ are assumed as uncorrelated zero-mean white noise sequences with covariance matrices $\mathbf{Q}_k$ and $\mathbf{R}_k$. The unknown vectors $\boldsymbol{\Delta}_k$ and $\boldsymbol{\theta}_k$ can be seen as model uncertainty. Suppose that the vectors and matrices have compatible dimensions.

A common approach for state estimation is the KF. Given the exact model, the state vector $\mathbf{x}_k$ can be estimated easily based on the measurement sequence $\{\mathbf{y}_1, \mathbf{y}_2, \ldots, \mathbf{y}_k\}$. For each iterative cycle, two steps are computed. In the prediction step, the state vector is predicated based on the dynamic model shown in (1). Then, in the update step, the innovation, i.e., the difference between the predicted measurement and the observed measurement is computed. The final state estimate is the sum of the predicted state vector and the innovation multiplied by the Kalman gain. The KF achieves high accuracy in the absence of the model uncertainty. However, in the presence of the model uncertainty, the KF deteriorates since the uncertain parameter vectors $\mathbf{\Delta}_k$ and $\boldsymbol{\theta}_k$ occur in the predication and the innovation, and consequently in the estimate of the filter.

The MMAE approach can be adopted to handle the model uncertainty. For the design of the traditional MMAE algorithm, a model set with the size of M is constructed to approximate the uncertain parameter vectors. If we roughly know that the uncertain parameter vectors are in a bounded region, a discrete model set can be constructed by sampling M potential parameter vectors in the predetermined region. Then, M elemental filters, which depend on the associated parameter vectors in the model set, are implemented in parallel to mitigate the effect of the model uncertainty, and obtain accurate overall state estimate. However, this approach, in particular for large M, suffers from a high computational burden and is therefore not attractive.

In order to decrease the computational burden, here we propose to use only two models. In the first model, the uncertain parameter vectors $\mathbf{\Delta}_k$ and $\boldsymbol{\theta}_k$ are assigned to be zero vectors. In the second model, $\mathbf{\Delta}_k$ and $\boldsymbol{\theta}_k$ are augmented as the state vector. The first model suits for the scenario where the model uncertainty does not occur, while the second model suits for the scenario where the uncertainty comes into play. Accordingly, a KF and an AKF are used in parallel to provide the individual state estimate. Then the elemental filters' outputs are combined in a weighted fashion to produce the overall state estimate. A description of the augmented MMAE algorithm is provided as follows.

Step 1 Initialization

The initial state estimates of the two elemental filters are set as $\hat{\mathbf{x}}_0^{(1)} = \hat{\mathbf{x}}_0^{(2)}$. The corresponding initial weights are chosen as $\omega_0^{(1)} = \omega_0^{(2)} = 0.5$.

Step 2 Parallel Kalman filtering

Two elemental filters are run in parallel to predict and update the state estimates. The first elemental filter is a KF with the equations

$$\hat{\mathbf{x}}_{k|k-1}^{(1)} = \mathbf{F}_k \hat{\mathbf{x}}_{k-1}^{(1)} \tag{3}$$

$$\hat{\mathbf{x}}_k^{(1)} = \hat{\mathbf{x}}_{k|k-1}^{(1)} + \mathbf{K}_k \left(\mathbf{y}_k - \mathbf{H}_k \hat{\mathbf{x}}_{k|k-1}^{(1)} \right) \tag{4}$$

and the second elemental filter is an AKF with the equations

$$\begin{bmatrix} \hat{\mathbf{x}}_{k|k-1}^{(2)} \\ \hat{\boldsymbol{\Delta}}_{k|k-1} \\ \hat{\boldsymbol{\theta}}_{k|k-1} \end{bmatrix} = \begin{bmatrix} \mathbf{F}_k & \mathbf{D}_k & 0 \\ 0 & \mathbf{I} & 0 \\ 0 & 0 & \mathbf{I} \end{bmatrix} \begin{bmatrix} \hat{\mathbf{x}}_{k-1}^{(2)} \\ \hat{\boldsymbol{\Delta}}_{k-1} \\ \hat{\boldsymbol{\theta}}_{k-1} \end{bmatrix} \tag{5}$$

$$\begin{bmatrix} \hat{\mathbf{x}}_{k}^{(2)} \\ \hat{\boldsymbol{\Delta}}_{k} \\ \hat{\boldsymbol{\theta}}_{k} \end{bmatrix} = \begin{bmatrix} \hat{\mathbf{x}}_{k|k-1}^{(2)} \\ \hat{\boldsymbol{\Delta}}_{k|k-1} \\ \hat{\boldsymbol{\theta}}_{k|k-1} \end{bmatrix} + \begin{bmatrix} \mathbf{K}_k \\ \mathbf{K}_{\Delta,k} \\ \mathbf{K}_{\theta,k} \end{bmatrix} \left(\mathbf{y}_k - \begin{bmatrix} \mathbf{H}_k & 0 & \mathbf{G}_k \end{bmatrix} \begin{bmatrix} \hat{\mathbf{x}}_{k|k-1}^{(2)} \\ \hat{\boldsymbol{\Delta}}_{k|k-1} \\ \hat{\boldsymbol{\theta}}_{k|k-1} \end{bmatrix} \right) \tag{6}$$

where $\hat{\mathbf{x}}_{k|k-1}^{(\tau)}$ and $\hat{\mathbf{x}}_{k}^{(\tau)}$ $(\tau = 1, 2)$ are the predicated and updated state estimates respectively, $\mathbf{K}_k$ is the gain matrix, which can be tuned to achieve optimized filtering performance, $\hat{\boldsymbol{\Delta}}_{k|k-1}$, $\hat{\boldsymbol{\theta}}_{k|k-1}$, $\hat{\boldsymbol{\Delta}}_k$ and $\hat{\boldsymbol{\theta}}_k$ are the predictions and estimates of the uncertain parameter vectors, $\mathbf{K}_{\Delta,k}$ and $\mathbf{K}_{\theta,k}$ are the gain matrices for the parameter estimator.

Step 3 Weight update

The weights $\omega_k^{(\tau)}$ for the elemental filters are calculated using the innovations $\tilde{\mathbf{y}}_k^{(\tau)}$ and normalized such that they sum up to one. This process is formulated as

$$\omega_k^{(1)} = \frac{\omega_{k-1}^{(1)} \Lambda_k^{((1))}}{\omega_{k-1}^{(1)} \Lambda_k^{(1)} + \omega_{k-1}^{(2)} \Lambda_k^{(2)}}, \omega_k^{(2)} = \frac{\omega_{k-1}^{(2)} \Lambda_k^{(2)}}{\omega_{k-1}^{(1)} \Lambda_k^{(1)} + \omega_{k-1}^{(2)} \Lambda_k^{(2)}} \tag{7}$$

where the function $\Lambda_k^{(\tau)}$ is calculated as

$$\Lambda_k^{(\tau)} = \frac{1}{\sqrt{|2\pi \mathbf{C}_k|}} \exp\left[-\frac{1}{2} \left(\tilde{\mathbf{y}}_k^{(\tau)} \right)^T \mathbf{C}_k^{-1} \tilde{\mathbf{y}}_k^{(\tau)} \right] \tag{8}$$

with $\tilde{\mathbf{y}}_k^{(1)} = \mathbf{y}_k - \mathbf{H}_k \hat{\mathbf{x}}_{k|k-1}^{(1)}$ and $\tilde{\mathbf{y}}_k^{(2)} = \mathbf{y}_k - \mathbf{H}_k \hat{\mathbf{x}}_{k|k-1}^{(2)} - \mathbf{G}_k \boldsymbol{\theta}_k$, $\mathbf{C}_k$ is a positive definite matrix. The adaptive law shown in (7) is widely used in the multiple-model approaches to update the weights. It is set up such that the model that is similar to the real system receives large weight. The convergence analysis in the next section shows that, for the considered system, the weight that corresponds to the appropriate model converges to 1, while the other converges to 0.

Step 4 State Combination

The overall estimate of the MMAE is calculated as a weighted sum of the elemental filters' estimates, i.e.,

$$\hat{\mathbf{x}}_k = \omega_k^{(1)} \hat{\mathbf{x}}_k^{(1)} + \omega_k^{(2)} \hat{\mathbf{x}}_k^{(2)}. \tag{9}$$

Step 2–Step 4 are run recursively to update the state estimate and the weight for each filter. The main difference between the presented algorithm and the traditional MMAE approach lies on the fact that the estimates of the uncertain parameter vectors $\hat{\boldsymbol{\Delta}}_k$ and $\hat{\boldsymbol{\theta}}_k$ are used to approximate different level of model uncertainty. The AKF is used to provide the estimate of the uncertain parameters. In fact, other relevant estimators (such as the least square approach) can also be adopted for parameter identification. The main conclusion of the paper is expected to be valid with different parameter estimators.

The augmented MMAE algorithm trades off performance versus complexity in a graceful manner. It adapts to different operation situations, and yields close to optimal performance, while keeping the number of elemental filters on a reasonable level. Although the algorithm is formulated for linear system, it can be used for nonlinear system using the EKF instead of the KF. The EKF is derived with the assumption that the linearized system provides close approximation to the true system. The linearization approach is valid for the nonlinear case where the first-order Taylor series approximates the system model effectively.

3 Convergence Analysis

To demonstrate the feasibility of the algorithm, the weight convergence property of the augmented MMAE is studied for the considered time-varying uncertain system. We expected that for the MMAE algorithm to converge, one of the weight is nearly equal to 1 and the other is close to 0. Define the state estimation error of the elemental filter as $\tilde{\mathbf{x}}_k^{(\tau)} = \mathbf{x}_k - \hat{\mathbf{x}}_k^{(\tau)}$, $\tilde{\mathbf{x}}_{k|k-1}^{(\tau)} = \mathbf{x}_k - \hat{\mathbf{x}}_{k|k-1}^{(\tau)}$ $(\tau = 1, 2)$. Define the covariance matrices of the state estimation error and the innovation as $\boldsymbol{\Sigma}_k^{(\tau)} = E\left[\hat{\mathbf{x}}_k^{(\tau)}\left(\hat{\mathbf{x}}_k^{(\tau)}\right)^T\right]$, $\boldsymbol{\Omega}_k^{(\tau)} = E\left[\tilde{\mathbf{y}}_k^{(\tau)}\left(\tilde{\mathbf{y}}_k^{(\tau)}\right)^T\right]$.

First, we evaluate the weights of the elemental filters in the absence of the model uncertainty, i.e., $\boldsymbol{\Delta}_k = 0$ and $\boldsymbol{\theta}_k = 0$. Let

$$L_n^{(2)} = \frac{\omega_n^{(2)}}{\omega_n^{(1)}} (n = 1, 2, \ldots). \tag{10}$$

According to the adaptive law for the MMAE algorithm, we have

$$L_n^{(2)} = \frac{\Lambda_n^{(2)}}{\Lambda_n^{(1)}} L_{n-1}^{(2)} \tag{11}$$

or

$$L_n^{(2)} = \frac{\exp\left[-\frac{1}{2}\left(\tilde{\mathbf{y}}_n^{(2)}\right)^T \mathbf{C}_n^{-1}\tilde{\mathbf{y}}_n^{(2)}\right]}{\exp\left[-\frac{1}{2}\left(\tilde{\mathbf{y}}_n^{(1)}\right)^T \mathbf{C}_n^{-1}\tilde{\mathbf{y}}_n^{(1)}\right]} L_{n-1}^{(2)}. \tag{12}$$

Extending this equation by going backwards in time though the recursive law in (12) yields

$$\frac{L_n^{(2)}}{L_0^{(2)}} = \exp\left[-\frac{1}{2}\sum_{k=1}^{n}\left(\tilde{\mathbf{y}}_k^{(2)}\right)^T \mathbf{C}_k^{-1}\tilde{\mathbf{y}}_k^{(2)} + \frac{1}{2}\sum_{k=1}^{n}\left(\tilde{\mathbf{y}}_k^{(1)}\right)^T \mathbf{C}_k^{-1}\tilde{\mathbf{y}}_k^{(1)}\right]. \tag{13}$$

Taking the natural logarithm of both sides gives

$$\ln\left(\frac{L_n^{(2)}}{L_0^{(2)}}\right) = \frac{1}{2}\sum_{k=1}^{n}\left\{tr\left[-\left(\tilde{\mathbf{y}}_k^{(2)}\right)^T \mathbf{C}_k^{-1}\tilde{\mathbf{y}}_k^{(2)} + \left(\tilde{\mathbf{y}}_k^{(1)}\right)^T \mathbf{C}_k^{-1}\tilde{\mathbf{y}}_k^{(1)}\right]\right\}. \tag{14}$$

where tr() denotes the matrix trace. Let $\alpha_n^{(2)} = -2\ln\left(\frac{L_n^{(2)}}{L_0^{(2)}}\right)$. We obtain the following recursive relationship

$$L_n^{(2)} = L_0^{(2)}\exp\left(-\frac{1}{2}\alpha_n^{(2)}\right). \tag{15}$$

It can be seen from (15) that the convergence property of the weight depend on the value of $\alpha_n^{(2)}$. For the convenience of our notation, we define the following functions

$$\begin{aligned}\varphi(\mathbf{x},\boldsymbol{\Delta},\boldsymbol{\theta},\varepsilon) = {} & \mathbf{H}_k\mathbf{F}_k\mathbf{x}\boldsymbol{\Delta}^T\mathbf{D}_k^T\mathbf{H}_k^T + \mathbf{H}_k\mathbf{F}_k\mathbf{x}\boldsymbol{\theta}^T\mathbf{G}_k^T + \mathbf{H}_k\mathbf{D}_k\boldsymbol{\Delta}\mathbf{x}^T\mathbf{F}_k^T\mathbf{H}_k^T \\ & + \varepsilon\mathbf{H}_k\mathbf{D}_k\boldsymbol{\Delta}\boldsymbol{\Delta}^T\mathbf{D}_k^T\mathbf{H}_k^T + \mathbf{H}_k\mathbf{D}_k\boldsymbol{\Delta}\boldsymbol{\theta}^T\mathbf{G}_k^T + \mathbf{G}_k\boldsymbol{\theta}\mathbf{x}^T\mathbf{F}_k^T\mathbf{H}_k^T + \mathbf{G}_k\boldsymbol{\theta}\boldsymbol{\Delta}^T\mathbf{D}_k^T\mathbf{H}_k^T + \varepsilon\mathbf{G}_k\boldsymbol{\theta}\boldsymbol{\theta}^T\mathbf{G}_k^T\end{aligned} \tag{16}$$

$$\begin{aligned}\boldsymbol{\chi}(\mathbf{x},\boldsymbol{\Delta},\boldsymbol{\theta},\varepsilon) = {} & (\mathbf{I}-\mathbf{K}_k\mathbf{H}_k)\mathbf{F}_k\mathbf{x}\boldsymbol{\Delta}^T\mathbf{D}_k^T(\mathbf{I}-\mathbf{K}_k\mathbf{H}_k)^T + (\mathbf{I}-\mathbf{K}_k\mathbf{H}_k)\mathbf{F}_k\mathbf{x}\boldsymbol{\theta}^T\mathbf{G}_k^T\mathbf{K}_k^T \\ & + (\mathbf{I}-\mathbf{K}_k\mathbf{H}_k)\mathbf{D}_k\boldsymbol{\Delta}\mathbf{x}^T\mathbf{F}_k^T(\mathbf{I}-\mathbf{K}_k\mathbf{H}_k)^T + \varepsilon(\mathbf{I}-\mathbf{K}_k\mathbf{H}_k)\mathbf{D}_k\boldsymbol{\Delta}\boldsymbol{\Delta}^T\mathbf{D}_k^T(\mathbf{I}-\mathbf{K}_k\mathbf{H}_k)^T \\ & + (\mathbf{I}-\mathbf{K}_k\mathbf{H}_k)\mathbf{D}_k\boldsymbol{\Delta}\boldsymbol{\theta}^T\mathbf{G}_k^T\mathbf{K}_k^T + \mathbf{K}_k\mathbf{G}_k\boldsymbol{\theta}\mathbf{x}^T\mathbf{F}_k^T(\mathbf{I}-\mathbf{K}_k\mathbf{H}_k)^T + \mathbf{K}_k\mathbf{G}_k\boldsymbol{\theta}\boldsymbol{\Delta}^T\mathbf{D}_k^T(\mathbf{I}-\mathbf{K}_k\mathbf{H}_k)^T + \varepsilon\mathbf{K}_k\mathbf{G}_k\boldsymbol{\theta}\boldsymbol{\theta}^T\mathbf{G}_k^T\mathbf{K}_k^T\end{aligned} \tag{17}$$

where $\mathbf{I}$ is the identity matrix of appropriate dimension, ε. a positive scale that satisfies $0 < \varepsilon \leq 1$. With these prerequisites, the mean of the term $\alpha_n^{(2)}$ in the absence of the model uncertainty (i.e., $\boldsymbol{\Delta}_k = 0$ and $\boldsymbol{\theta}_k = 0$) is evaluated in the following theorem.

Theorem 1 *For the system model without* $\boldsymbol{\Delta}_k$ *and* $\boldsymbol{\theta}_k$*, assume that for the scale* $\varepsilon = 1$*, the following inequalities hold*

$$E\left[\varphi\left(-\hat{\mathbf{x}}_{k-1}^{(2)}, \hat{\Delta}_{k-1}, \hat{\theta}_{k-1}, \varepsilon\right)\right] \geq 0 \tag{18}$$

$$E\left[\boldsymbol{\chi}\left(-\hat{\mathbf{x}}_{k-1}^{(2)}, \hat{\boldsymbol{\Delta}}_{k-1}, \hat{\boldsymbol{\theta}}_{k-1}, \varepsilon\right)\right] \geq 0. \tag{19}$$

If the tuning matrix is set as $\mathbf{C}_k = \sigma^2\mathbf{I}$, where σ. a design parameter, and $tr\left(\boldsymbol{\Omega}_k^{(1)}\right) \neq tr\left(\boldsymbol{\Omega}_k^{(2)}\right)$, then there exists a positive constant $\delta_{\min}^{(2)}$, such that

$$E\left(\alpha_n^{(2)}\right) \geq \frac{1}{\sigma^2}\delta_{\min}^{(2)} n. \tag{20}$$

The proof of the theorem is omitted here for simplicity. Similar deduction can be found in literature (see e.g., [1, 7]). The relation between Theorem 1 and the convergence of the weight $\omega_n^{(\tau)}$ $(\tau = 1, 2)$ is shown as follows. Substituting (10) into (15) yields

$$\frac{\omega_n^{(2)}}{\omega_n^{(1)}} = L_0^{(2)} \exp\left(-\frac{1}{2}\alpha_n^{(2)}\right). \tag{21}$$

As the initial weights in the algorithm are chosen as $\omega_0^{(1)} = \omega_0^{(2)} = 0.5$, we obtain

$$\frac{\omega_n^{(2)}}{\omega_n^{(1)}} = \exp\left(-\frac{1}{2}\alpha_n^{(2)}\right). \tag{22}$$

Notice that $\delta_{\min}^{(2)}$ in (20) is a positive constant. From the result in Theorem 1, we expect that $\alpha_n^{(2)}$ will increase as time goes on. It indicates that as $n \to \infty$, $\omega_n^{(2)} \to 0$. Considering the relationship shown in (7), we have $\omega_n^{(1)} + \omega_n^{(2)} = 1$. Thus, we infer that as $n \to \infty$, $\omega_n^{(1)} \to 1$.

The presented MMAE algorithm is a combination of a KF and an AKF. The first elemental filter is the KF and the second one is the AKF. In the absence of the model uncertainty, the MMAE algorithm will converge to the KF adaptively. The KF yields precise state estimates for the system without the uncertain parameter vectors $\boldsymbol{\Delta}_k$ and $\boldsymbol{\theta}_k$. The conditions shown in (18) and (19) are reasonable as the expectations of the cross-correlation terms are negligible. It can be verified via the numerical simulation that the non-negativeness property of the terms $E\left[\varphi\left(-\tilde{\mathbf{x}}_{k-1}^{(2)}, \tilde{\Delta}_{k-1}, \tilde{\theta}_{k-1}, \varepsilon\right)\right]$ and $E\left[\boldsymbol{\chi}\left(-\tilde{\mathbf{x}}_{k-1}^{(2)}, \tilde{\Delta}_{k-1}, \tilde{\theta}_{k-1}, \varepsilon\right)\right]$ is true.

Similarly, the weights of the elemental filters in the presence of the model uncertainty are evaluated. In this case, we assume that the estimation errors of the uncertain parameter vectors $\tilde{\Delta}_{k|k-1}$ and $\tilde{\theta}_{k|k-1}$ are sufficiently small, i.e.,

$$E\left(\hat{\boldsymbol{\Delta}}_{k|k-1}\hat{\boldsymbol{\Delta}}_{k|k-1}^{T}\right) \le \frac{1-\varepsilon}{1+\varepsilon}E\left(\boldsymbol{\Delta}_k\boldsymbol{\Delta}_k^{T}\right) \tag{23}$$

$$E\left(\hat{\boldsymbol{\theta}}_{k|k-1}\hat{\boldsymbol{\theta}}_{k|k-1}^{T}\right) \le \frac{1-\varepsilon}{1+\varepsilon}E\left(\boldsymbol{\theta}_k\boldsymbol{\theta}_k^{T}\right). \tag{24}$$

Let

$$L_n^{(1)} = \frac{\omega_n^{(1)}}{\omega_n^{(2)}}(n=1,2,\ldots). \tag{25}$$

It is easy to derive that

$$\ln\left(\frac{L_n^{(1)}}{L_0^{(1)}}\right) = \frac{1}{2}\sum_{k=1}^{n}\left\{tr\left[-\left(\tilde{\mathbf{y}}_k^{(1)}\right)^{T}\mathbf{C}_k^{-1}\tilde{\mathbf{y}}_k^{(1)} + \left(\tilde{\mathbf{y}}_k^{(2)}\right)^{T}\mathbf{C}_k^{-1}\tilde{\mathbf{y}}_k^{(2)}\right]\right\}. \tag{26}$$

Let $\alpha_n^{(1)} = -2\ln\left(\frac{L_n^{(1)}}{L_0^{(1)}}\right)$. This leads to

$$L_n^{(1)} = L_0^{(1)}\exp\left(-\frac{1}{2}\alpha_n^{(1)}\right). \tag{27}$$

The mean of the term $\alpha_n^{(1)}$ in the presence of the model uncertainty is evaluated in the following theorem.

Theorem 2 *For the system model with $\boldsymbol{\Delta}_k$ and $\boldsymbol{\theta}_k$, suppose that the assumptions shown in (23) and (24) hold, and the following inequalities are fulfilled*

$$E\left[\varphi\left(\tilde{\mathbf{x}}_{k-1}^{(1)}, \boldsymbol{\Delta}_k, \boldsymbol{\theta}_k, \varepsilon\right)\right] \ge 0 \tag{28}$$

$$E\left[\varphi\left(\tilde{\mathbf{x}}_{k-1}^{(2)}, \tilde{\boldsymbol{\Delta}}_{k|k-1}, \tilde{\boldsymbol{\theta}}_{k|k-1}, -\varepsilon\right)\right] \le 0 \tag{29}$$

$$E\left[\boldsymbol{\chi}\left(\tilde{\mathbf{x}}_{k-1}^{(1)}, \boldsymbol{\Delta}_k, -\boldsymbol{\theta}_k, \varepsilon\right)\right] \ge 0 \tag{30}$$

$$E\left[\boldsymbol{\chi}\left(\tilde{\mathbf{x}}_{k-1}^{(1)}, \tilde{\boldsymbol{\Delta}}_{k|k-1}, -\tilde{\boldsymbol{\theta}}_{k|k-1}, -\varepsilon\right)\right] \le 0. \tag{31}$$

If the tuning matrix is set as $\mathbf{C}_k = \sigma^2\mathbf{I}$, and $tr\left(\boldsymbol{\Omega}_k^{(1)}\right) \ne tr\left(\boldsymbol{\Omega}_k^{(2)}\right)$, then there exists a positive constant $\delta_{\min}^{(1)}$, such that

$$E\left(\alpha_n^{(1)}\right) \ge \frac{1}{\sigma^2}\delta_{\min}^{(1)}n. \tag{32}$$

The proof of Theorem 2 is similar to that of Theorem 1. From Theorem 2, the expectation of $\alpha_n^{(1)}$ will increase with n. From (7), (25) and (27), we infer that as $k \to \infty$, $\omega_k^{(1)} \to 0$ and $\omega_k^{(2)} \to 1$. It indicates that the MMAE algorithm will converge to the AKF adaptively. Using the state augmentation approach, the uncertain parameter vector is estimated jointly with the state vector. The estimate of the uncertain parameter vector is used to compensate for the model uncertainty, such that the filtering performance is improved. From Theorem 1 and Theorem 2, we find that appropriate elemental filter can be chosen adaptively to suit for different situations.

4 Numerical Simulations

Space surveillance encompasses reconnaissance of space targets, and the prediction of space events, possible collisions, and threats. Fundamental to space surveillance is the problem of knowing precisely where a space target is. In the orbit determination system, a star camera can provide the line-of-sight (LOS) measurement for uncooperative targets, and a dynamical model is adopted for orbit propagation [8]. Suppose that a chief observing spacecraft cooperates with an auxiliary observing spacecraft to measure the LOS vector of a space target, which has the capability to orbital maneuver. The maneuvers may be executed occasionally. Generally, the magnitude and interval of the space target maneuver are unknown for the observing spacecrafts.

The state vector is chosen as the position and velocity of the space target in the earth-scentered inertial (ECI) reference frame, given by $\mathbf{x} = \begin{bmatrix} \mathbf{r}_t^T & \mathbf{v}_t^T \end{bmatrix}^T$. The time evolution of the state is described using its dynamic model

$$\dot{\mathbf{r}}_t = \mathbf{v}_t \tag{33}$$

$$\dot{\mathbf{v}}_t = -\frac{\mu \mathbf{r}_t}{|\mathbf{r}_t|^3} + \mathbf{p}(\mathbf{r}_t) + \mathbf{u}_t \tag{34}$$

where μ is the Earth's gravitational constant, $\mathbf{p}(\mathbf{r}_t)$ encapsulates the perturbation accelerations of the space target other than those due to the two-body gravitational acceleration, which includes the gravitational acceleration of the non-spherical mass distribution of Earth, the atmospheric drag, the solar radiation pressure, and the lunisolar gravity perturbation. $\mathbf{u}_t$ is the unknown acceleration caused by the thrusters, which is modeled as the uncertain parameter vector. The measurement model is given by [9]

$$\mathbf{y}_k = \begin{bmatrix} \frac{(\mathbf{r}_t(t_k - \Delta t_{1k}) - \mathbf{r}_{o1}(t_k))^T}{\mathbf{r}_t(t_k - \Delta t_{1k}) - \mathbf{r}_{o1}(t_k)} & \frac{(\mathbf{r}_t(t_k - \Delta t_{2k}) - \mathbf{r}_{o2}(t_k))^T}{\mathbf{r}_t(t_k - \Delta t_{2k}) - \mathbf{r}_{o2}(t_k)} \end{bmatrix}^T + \mathbf{v}_k \tag{35}$$

where $\mathbf{r}_{o1}$ and $\mathbf{r}_{o2}$ are the position vectors of the chief observing spacecraft and the auxiliary observing spacecraft. Suppose that the positions of the observing spacecrafts are known, t_k is the measurement time according to the clock on the chief observing spacecraft, $\Delta t_{jk}(j=1,2)$ is the light propagation time from the space target to the observing spacecrafts. Since the dynamic model and the measurement model are nonlinear, the linearization approach is used to design the elemental filters in the MMAE.

The true orbit data of the space target and the observing spacecrafts are produced using a high accurate numerical orbit propagator. The initial orbit elements are given in Table 1. With the initial values, numerical integrations are performed to generate the time history of the states and measurements. The filtering algorithms operate on simulated measurements and produce state estimates. The estimation error curves are obtained by comparing the estimates with the true states.

The space target's initial per-axis position and velocity errors are sampled from zero-mean distribution with respective standard deviations of 1000 m and 0.1 m/s. The position errors of the observing spacecrafts are modeled as random errors with standard deviation of 10 m. The star cameras are assumed to sample 1 time per second. The standard deviation of the LOS measurement noise is $5''$. The mass of the space target is 1000 kg. The thruster force has a nominal value of 100 mN, and the burn duration is on the order of 20 min. Two orbital maneuvers are executed by the space target during the simulation.

The augmented MMAE is compared with a KF, an AKF and a predictive filter (PF) via numerical simulations. The PF is a good method in coping with the model uncertainty. It can determine the uncertain parameter vector during the minimum model error estimation (MME) process. The PF algorithm is proposed by Lu and developed by Crassidis and Markley [10, 11]. In addition, a predictive iterated Kalman filter (PIKF) is presented for nonlinear systems [12]. The algorithms are run individually to process the same measurement data in the presence of the model uncertainty. For the augmented MMAE algorithm, the first elemental filter is designed based on the KF, and the second elemental filter is designed based on the AKF. In the KF and the first elemental filter in the MMAE, the acceleration $\mathbf{u}_t$ is not taken into consideration. In the AKF and the second elemental filter in the MMAE, $\mathbf{u}_t$ is augmented as state and estimated together with the position and the velocity. The KF suits for the target without maneuver and the AKF suits for the target with maneuver. The estimation error curves of the KF and the MMAE algorithm are given in Figs. 1 and 2.

Table 1 Initial orbit elements of the spacecrafts

Spacecraft	Semi-major axis (km)	Eccentricity	Inclination (°)	Right ascending node (°)	Argument of perigee (°)	Mean anomaly (°)
Space target	7471.004	0	63.41	0	1.077	0
Observer 1	7471.004	0	63.41	0	0	−0.074
Observer 2	7471.004	0	63.41	0	0	1.038

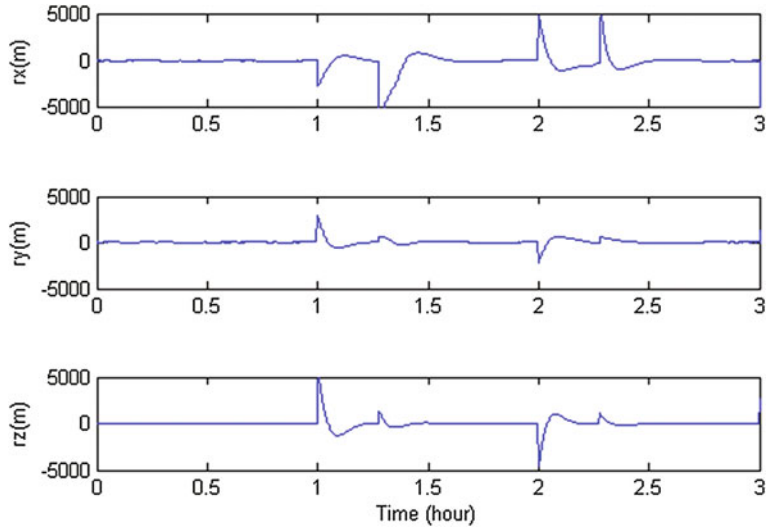

Fig. 1 Estimation error of KF in the presence of maneuver

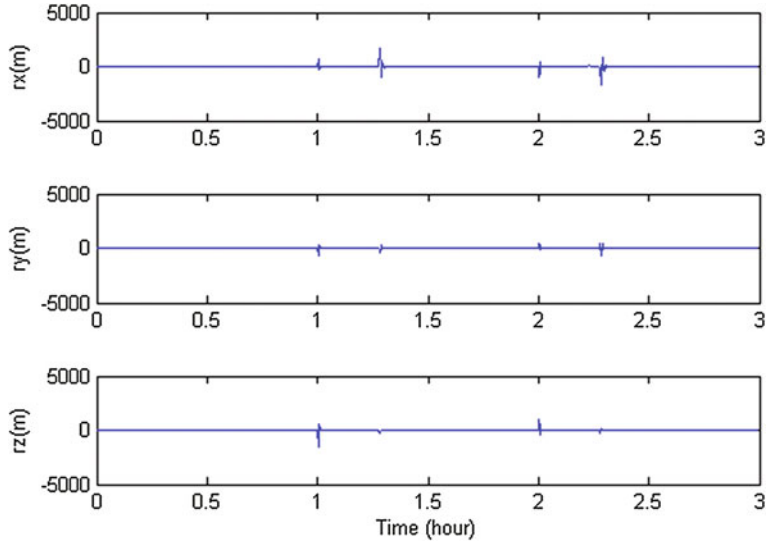

Fig. 2 Estimation error of MMAE in the presence of maneuver

We observe that the performance of KF is sensitive to the model uncertainty. The unknown acceleration $\mathbf{u}_t$ affects the KF estimates as it is not well represented in the filtering model. The estimation error curve jumps evidently at the beginning and the end of the maneuver. In contrast, the MMAE is able to reduce the position error

because the weights $\omega_k^{(1)}$ and $\omega_k^{(2)}$ adapt to the underlying situation. For the first elemental filter, large innovations and consequently a small weight $\omega_k^{(1)}$ is calculated, whereas a large weight $\omega_k^{(2)}$ is obtained for the second elemental filter. As the AKF in the MMAE algorithm is dominant during the maneuvering interval, the unknown acceleration $\mathbf{u}_t$ is well compensated using its estimate, such that the positioning accuracy is improved. The error curve of the single AKF is similar to that of the MMAE and it is not presented here.

The position RMSE (root mean square error) of the filtering algorithms on the whole duration is shown in Table 2. To facilitate the comparison, the last column of the table gives the norm of the position RMSE. In the presence of model uncertainty, the MMAE algorithm yields positioning accuracy similar to the AKF and significantly outperforms the KF.

Next, we compare the performance of the filtering algorithms in the absence of the model uncertainty, i.e., the acceleration $\mathbf{u}_t = 0$. The estimation result of the MMAE algorithm is shown in Fig. 3.

As small innovations yield a larger weight $\omega_k^{(1)}$ for the first elemental filter and a smaller one for the second elemental filter, the KF in the MMAE dominates the state estimate. From Table 2, one can notice that the KF and the MMAE generate similar small position error, whereas the AKF slightly loses compared to the other two estimators. It is not appropriate to adopt an AKF due to its compromised performance in the case that the target maneuver does not occur. The MMAE algorithm performs better overall as it can adapt to different operation scenarios.

It is shown in Table 2 that the PF is also an effective method to handle the model uncertainty. However, its estimation error is larger than the MMAE in the absence of the uncertainty. It is understood that the PF lacks the adaptive capability. It is possible to improve the estimation accuracy in this scenario by fine tuning the weighting matrix $\mathbf{W}$ in the PF algorithm. However, the choice of $\mathbf{W}$ is a compromise between the efficiency in the absence of the uncertainty and robustness in the presence of the uncertainty. Generally, it is difficult to achieve superior performance in both cases using the same weighting matrix.

Table 2 Comparison of filtering performance for space surveillance

Target maneuver	Algorithm	RMS position error (m)			
		x	y	z	Norm
Presence	KF	1046.0	307.9	521.1	1208.5
	AKF	110.7	46.5	65.5	136.8
	PF	272.2	100.9	131.0	318.5
	MMAE	110.4	46.8	65.2	136.5
Absence	KF	1.4	1.0	0.9	1.9
	AKF	16.6	5.4	4.4	18.0
	PF	4.1	2.8	2.7	5.7
	MMAE	1.3	0.9	0.9	1.8

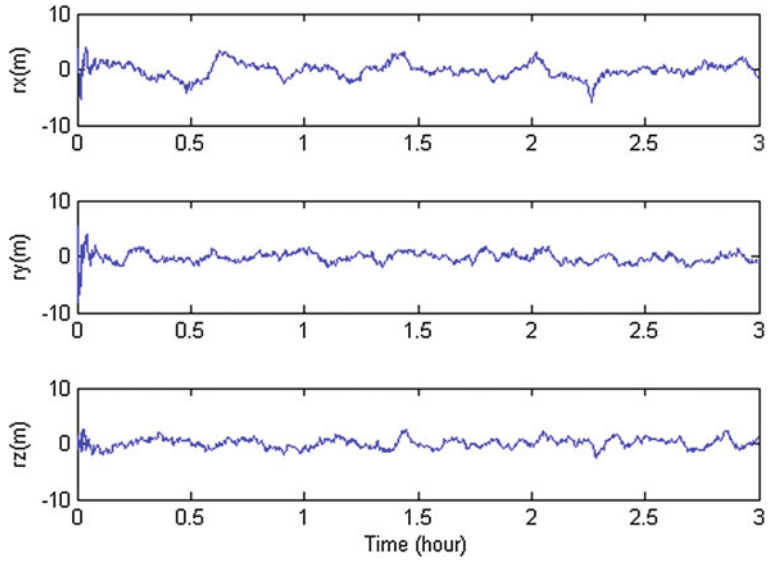

Fig. 3 Estimation error of MMAE in the absence of maneuver

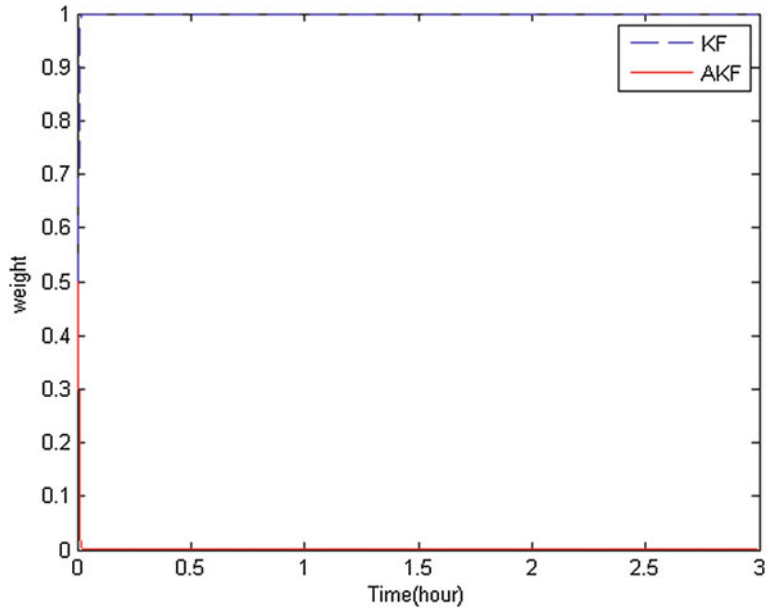

Fig. 4 Weight convergence for MMAE in the absence of maneuver

Finally, the convergence of the weights is illustrated. When the parameter σ chosen as $\sigma_S = 5''$, the weights of the two elemental filters in the MMAE algorithm are plotted versus time in Fig. 4. As expected, the weight for the first elemental filter converges toward 1, while the weight for the second elemental filter converges to 0.

5 Conclusion

An augmented MMAE algorithm based on parallel KF and AKF is proposed to cope with the uncertainty in dynamic model or measurement model. Suppose that the model uncertainty may occur occasionally, it is difficult to achieve high performance for the systems with and without model uncertainty using the same filter. To overcome this difficulty, the augmented MMAE algorithm is presented using two filters in parallel, where a KF suits for the certain system, whereas an AKF is adapted to the uncertain system. This algorithm outperforms the KF in the presence of the model uncertainty and achieves better precision than the AKF in the absence of the uncertainty. It is proven that the convergence of the algorithm can be ensured under mild conditions. The efficiency of the presented algorithm is demonstrated through a numerical example. Simulation result shows that the presented algorithm can provide ideal convergence to the appropriate estimator, and obtain satisfactory performance in different operation scenarios.

Acknowledgments This work was supported in part by China Natural Science Foundation (61573059) and Beijing Natural Science Foundation (4162070).

References

1. Alsuwaidan BN, Crassidis JL, Cheng Y (2011) Generalized multiple-model adaptive estimation using an autocorrelation approach [J]. IEEE Trans Aerosp Electron Syst 47 (3):2138–2152
2. Hammes U, Zoubir AM (2011) Robust MT tracking based on M-estimation and interacting multiple model algorithm [J]. IEEE Trans Signal Process 59(7):3398–3409
3. Li W, Jia Y, Du J, Zhang J (2013) Distributed multiple-model estimation for simultaneous localization and tracking with NLOS mitigation [J]. IEEE Trans Veh Technol 62 (6):2824–2830
4. Lan J, Li XR (2013) Equivalent-model augmentation for variable-structure multiple-model estimation [J]. IEEE Trans Aerosp Electron Syst 49(4):2615–2630
5. Gao C, Duan G (2014) Fault diagnosis and fault tolerant control for nonlinear satellite attitude control systems [J]. Aerosp Sci Technol 33:9–15
6. Yun J, Ryoo CK (2014) Missile guidance law estimation using modified interactive multiple model filter [J]. J Guid Control Dyn 37(2):484–496

7. Xiong K, Wei CL, Liu LD (2015) Robust multiple model adaptive estimation for spacecraft autonomous navigation [J]. Aerosp Sci Technol 42:249–258
8. Chen T, Xu S (2010) Double line-of-sight measuring relative navigation for spacecraft autonomous rendezvous [J]. Acta Astronaut 67:122–134
9. Psiaki ML (2011) Absolute orbit and gravity determination using relative position measurements between two satellites [J]. J Guid Control Dyn 34(5):1285–1297
10. Lu P (1994) Nonlinear predictive controllers for continuous systems [J]. J Guid Control Dyn 17(3):553–560
11. Crassidis JL, Markley FL (1997) Predictive filtering for nonlinear systems [J]. J Guid Control Dyn 20(3):566–572
12. Fang J, Gao X (2010) Predictive iterated Kalman filter for INS/GPS integration and its application to SAR motion compensation [J]. IEEE Trans Instrum Meas 59(4):909–915

Robust $H\infty$-optimal Output Feedback Actuator Placement with a Class of Actuator Constraints

Xuhui Lu, Lei Zhang, Yingmin Jia, Dayi Wang and Chengrui Liu

Abstract This paper investigates the actuator placement of uncertain linear systems. The designed actuator locations are subject to a class of nonlinear equality constraints, and a dynamic output feedback controller should also be derived based on measured outputs. To minimize $H\infty$ norm of the closed-loop systems, the actuator placement problem is formulated as an uncertain non-convex optimization problem. A series of transformations are developed to convert this problem into a deterministic successive convex problem. Correspondingly, an optimization algorithm is derived based on prediction-correction procedure.

Keywords Robust actuator placement · Output feedback · Non-convex constraints · Successive convex optimization

1 Introduction

Actuator and sensor locations are essential parameters in the design of control systems, since they would determine several properties of the systems, e.g., controllability, observability, etc. However in applications, these parameters are designed just based on trial and error. As pointed out in [1], if the actuator and sensor locations are carefully derived based on some optimization methods, the performance of the whole closed-loop systems can be enhanced.

X. Lu (✉) · L. Zhang · Y. Jia
The Seventh Research Division and the Department of Systems and Control,
School of Automation Science and Electrical Engineering,
Beihang University (BUAA), Beijing 100191, China
e-mail: by12091asp@163.com

D. Wang · C. Liu
Beijing Institute of Control Engineering, Beijing 100190, China

D. Wang · C. Liu
Science and Technology on Space Intelligent Control Laboratory,
Beijing 100190, China

Y. Jia et al. (eds.), *Proceedings of 2016 Chinese Intelligent Systems Conference*,
Lecture Notes in Electrical Engineering 404, DOI 10.1007/978-981-10-2338-5_48

Among the literatures on actuator/sensor placement, there are two basic methods: open-loop actuator placement and closed-loop actuator placement [2]. For the closed-loop methods, they will choose the desired actuator/sensor locations and the corresponding controllers simultaneously and, compared with the open-loop counterparts, possess better control/estimation performances [2]. Geromel [3] attemptes to design the actuator placement joint with the corresponding state feedback controller, and if there are only finite actuator locations to be choosed, an algorithm is proposed to attain the globally optimal solution. Then an output feedback closed-loop actuator/sensor placement approach is also derived in [2]. As for satellites, Wang et al. [4] attempt to design the thruster locations with geometric symmetry, and the corresponding nonlinear optimization problem is approached by genetic algorithm. An iterative method is developed in [5] to obtain the desired solution of two coupled Riccati equations, and is applied into the actuator and sensor placement of fluid flow system. Recently in [6], the authors focuses on actuator placement of linear-time-invariant (LTI) system, where these actuators are subject to a class of nonlinear constraints, and a successive optimization method is introduced to obtain the locally optimal solution of the actuator locations.

However, it should be noted that uncertainties are inevitable during the operation of the control systems. For example, the exact values of inertia parameters of the satellites may be unavailable due to the fuel consumption. If the uncertainties are overlook in the actuator/sensor location design, the control performance of the closed-loop system would be deteriorated. Besides, the information of some state variables may be absent owing to the loss or failure of some sensors. In face of these problems, the authors go further to investigate the output feedback closed-loop actuator placement, considering a class of actuator location constraints and model uncertainties simultaneously. First the actuator placement problem with uncertainties is formulated as a robust optimization problem with nonlinear constraints, and is then converted into the corresponding high-order deterministic optimization problem. To deal with the non-convex constraints, this optimization problem is transformed into a successive optimization problem, and an algorithm is eventually designed to attain the locally optimal solution according to the prediction-correction procedure.

The remainder of the paper is organized as follows. Section 2 introduces the preliminaries, including the notations, system description, and problem formulation. The main result of this paper, i.e., the proposed output feedback closed-loop actuator placement algorithm, is shown in Sect. 3. The conclusions are given in Sect. 4.

2 Preliminaries

2.1 Notation

First the matrices $0_{m,n} \in \mathbb{R}^{m\times n}$ and $I_n \in \mathbb{R}^{n\times n}$ are zero matrix and identity matrix with appropriate dimension, respectively. Besides, the elements of matrix $E_{ij}^n \in \mathbb{R}^{n\times n}$ are

set as 0 at almost all entries except the (i,j) entry, i.e., $E_{ij}^n(i,j) = 1$. Based upon E_{ij}^n, the matrix $\Theta^n(\lambda) \in \mathbb{R}^{n\times n}$ is set as $\Theta^n(\lambda) = \lambda I_n + (I - E_{ii})$ with $\lambda > 0$. In the following, the superscripts of E_{ij}^n and $\Theta^n(\lambda)$ are sometimes dropped when there is no confusion of dimension in the context.

2.2 System Description and Problem Formulation

This paper focuses on the following system [2]

$$\dot{x} = Ax + B_1 w + B_2 u, \quad z = C_1 x + D_1 u, \quad y = C_2 x + D_2 w, \tag{1}$$

where $x \in \mathbb{R}^n$, $w \in \mathbb{R}^{p_1}$, $u \in \mathbb{R}^{p_2}$, $z \in \mathbb{R}^{q_1}$, $y \in \mathbb{R}^{q_2}$ are the states, the disturbances, the control inputs, the controlled outputs, and the measured outputs of the above linear system, respectively. Correspondingly $A \in \mathbb{R}^{n\times n}$, $B_1 \in \mathbb{R}^{n\times q_1}$, $B_2 \in \mathbb{R}^{n\times q_2}$, $C_1 \in \mathbb{R}^{q_1\times n}$, $D_1 \in \mathbb{R}^{q_1\times p_2}$, $C_2 \in \mathbb{R}^{q_2\times n}$, $D_2 \in \mathbb{R}^{q_2\times p_1}$. In the system (1), the actuator matrix B_2 can be designed in the process.

Unlike the problem and results in [6], the system (1) suffers from uncertainties, and in this paper, the matrix A is assumed uncertain. Thus, we can obtain

$$A = A_0 + E_A \Sigma F_A, \tag{2}$$

where uncertain matrix Σ obeys $\|\Sigma\| < \rho$. Therefore, similar to [6], the following assumptions are introduced.

Assumption 1 For B_2, two matrices $J \in \mathbb{R}^{n\times n}$ and $\bar{B}_2 \in \mathbb{R}^{n\times p_2}$ exist such that $B_2 = J\bar{B}_2$. Besides, $\bar{B}_2 = [\bar{B}_{21}, \ldots, \bar{B}_{2k}]$ obeys the constraints $\|\bar{B}_{2i}^T\| = 1$, $i = 1, \ldots, p_1$. For simplicity of notations, it is denoted that $\bar{\Upsilon} = \{\bar{B}_2 \mid \|\bar{B}_{2i}\| = 1, i = 1, \ldots, p_2\}$, $\Upsilon = \{B_2 = J\bar{B}_2 \mid \bar{B}_2 \in \bar{\Upsilon}\}$.

Assumption 2 For matrices C_1 and D_1, $C_1^T D_1 = 0_{n\times k}$. Besides, for any $\|\Sigma\| < \rho$, the pair $(A(\Sigma), B_2)$ is stabilizable for some $B_2 \in \Upsilon$, and $(A(\Sigma), C_2)$ is also detectable.

Assumption 3 For the matrix D_1, $D_1^T D_1$ is diagonal and positive definite, and, for simplicity, is denoted as $D_1^T D_1 = \mathrm{diag}\{d_1, \ldots, d_k\} > 0$.

Based on Assumptions 1–3, the problem to be attacked is shown as follows.

Probelm 1 Consider the system (1) with uncertainties (2), and derive the actuator location $B_2 \in \Upsilon$ and the corresponding output feedback law

$$\dot{x}_c = A_c x_c + B_c y \quad u = C_c x_c \quad x_c \in \mathbb{R}^n, \tag{3}$$

such that for the transfer function matrix $H_{wz}(s)$ of the closed-loop system, the index $r \triangleq \{\min \tilde{r} \mid \|H_{wz}(\Sigma)\|_\infty < \tilde{r}, \|\Sigma\| < \rho\}$ would attain its local minimum value.

3 Output Feedback Actuator Location Algorithm

To address this problem, the controller (3) is substituted into the system (1), and the closed-loop system is in the following form

$$\dot{\bar{x}} = \bar{A}\bar{x} + \bar{B}_1 w, \quad y = \bar{C}\bar{x}, \tag{4}$$

where $\bar{x} = \mathrm{col}(x, x_c)$, and

$$\bar{A} = \begin{bmatrix} A & B_2 C_c \\ B_c C_2 & A_c \end{bmatrix} \in \mathbb{R}^{2n\times 2n}, \bar{B}_1 = \begin{bmatrix} B_1 \\ B_c D_2 \end{bmatrix} \in \mathbb{R}^{2n\times p_1}, \bar{C}_1^T = \begin{bmatrix} C_1^T \\ C_c^T D_1^T \end{bmatrix} \in R^{2n\times q_1}. \tag{5}$$

According to bounded real lemma from [6, 7], the minimal $H\infty$ norm can be obtained from the following optimal problem

$$\begin{aligned} &Problem\ Q^1\ : \\ &\min\ \bar{r} \\ &\begin{bmatrix} X\bar{A}^T + \bar{A}X & \bar{B}_1 & X\bar{C}_1^T \\ \bar{B}_1^T & -\bar{r}I_j & 0_{j\times k} \\ \bar{C}_1 X & 0_{k\times j} & -I_k \end{bmatrix} < 0, \\ &X > 0, \quad B_2 \in Y, \end{aligned} \tag{6}$$

where $r_{min} = \sqrt{\bar{r}_{min}}$.

To simplify the above optimal problem, the matrix $X \in \mathbb{R}^{2n\times 2n}$ and $Y = X^{-1} \in \mathbb{R}^{2n\times 2n}$ are partitioned into the following forms

$$X = \begin{bmatrix} X_1 & X_2 \\ X_2^T & X_3 \end{bmatrix}, \quad Y = \begin{bmatrix} Y_1 & Y_2 \\ Y_2^T & Y_3 \end{bmatrix}, \tag{7}$$

where $X_i, Y_i \in \mathbb{R}^{n\times n}$, $i = 1, 2, 3$. In accordance with the similar procedures in [2, 8], and the uncertainty structure of $A(\Sigma)$ in (2), the above optimal problem can then be equivalently converted into the following form

$$\begin{aligned} &Problem\ Q^2 \\ &\min\ \bar{r} \\ &\begin{bmatrix} X_1 & I \\ I & Y_1 \end{bmatrix} > 0, \\ &\Psi_1^0 + L_1 \bar{\Sigma} R_1 + R_1^T \bar{\Sigma}^T L_1^T < 0, \\ &B_2 \in Y, \end{aligned} \tag{8}$$

where

$$\Psi_1^0 = \begin{bmatrix} \Xi_{10} & 0 & B_1 & 0 & Y_1 C_1^T \\ 0 & \Xi_{20} & X_1 B_1 + F D_2 & C_1^T & 0 \\ B_1^T & B_1^T X_1 + D_2^T F^T & -\bar{r} I & 0 & 0 \\ 0 & C_1 & 0 & -I & 0 \\ C_1 Y_1 & 0 & 0 & 0 & -I \end{bmatrix} \tag{9}$$

with $\Xi_{10} = A_0 Y_1 + Y_1 A_0^T - B_2 (D_1^T D_1)^{-1} B_2^T$ and $\Xi_{20} = X_1 A_0 + A_0^T X_1 + F C_2 + C_2^T F^T$, and

$$L_1^T = \begin{bmatrix} E_A^T & 0 & 0\,0\,0 \\ 0 & E_A^T X_1 & 0\,0\,0 \end{bmatrix}, \quad R_1^T = \begin{bmatrix} F_A Y & 0 & 0\,0\,0 \\ 0 & F_A & 0\,0\,0 \end{bmatrix}, \quad \bar{\Sigma} = \begin{bmatrix} \Sigma & 0 \\ 0 & \Sigma \end{bmatrix}. \tag{10}$$

From the above optimization problem, the desired output feedback controller can be derived as

$$\begin{aligned} &L = -(D_1^T D_1)^{-1} B_2^T, \quad Z = A + Y_1 A^T X_1 + L^T B_2^T X_1 + Y_1 C_2^T F^T, \\ &M = -Z - (Y_1 C_1^T + L^T D_1^T) C_1, \quad U = X_1 - Y_1^{-1} \quad V = -Y_1, \\ &A_c = U^{-1} M^T V^{-T}, \quad B_c = U^{-1} F \quad C_c = L V^{-T}. \end{aligned} \tag{11}$$

In face of the robust optimization problem Q^2, Lemma 3.1 in [9] is utilized to convert it to the following optimization problem

$$\begin{aligned} &\textit{Problem } Q^3 : \\ &\min\ \bar{r} \\ &\begin{bmatrix} X_1 & I \\ I & Y_1 \end{bmatrix} > 0, \\ &\begin{bmatrix} \Xi_{30} & * & \cdots & * \\ & \Xi_{20} & & \\ B_1^T & B_1^T X_1 + D_2^T F & -\bar{r} I & \\ & C_1 & & -I \\ C_1 Y_1 & & & -I \\ F_A Y_1 & & & & -\frac{\eta_1}{\rho^2} I \\ & \eta_2 F_A & & & & -\frac{\eta_2}{\rho^2} I & * \\ & E_A^T X_1 & & & & & -\eta_2 I \end{bmatrix} < 0, \\ &B_2 \in \Upsilon, \end{aligned} \tag{12}$$

where $\Xi_{30} = \Xi_{10} + \eta_1 E_A E_A^T$, η_1 and η_2 are positive variables.

It should be noted that the second constraint in (12) is concave toward B_2. Therefore in accordance with the Assumption 1, the optimization problem (12) can be equivalently converted into

$$
\begin{aligned}
&\textit{Problem } Q^4\\
&\min\ \bar{r}\\
&\begin{bmatrix} X_1 & I \\ I & Y_1 \end{bmatrix} > 0,\\
&\begin{bmatrix}
\Xi_4 & * & \cdots & * \\
 & \Xi_{20} & & \\
B_1^T & B_1^T X_1 + D_2^T F\ -\bar{r}I & & \\
 & C_1 & -I & \vdots \\
C_1 Y_1 & & -I & \\
F_A Y_1 & & & -\frac{\eta_1}{\rho^2} I \\
 & \eta_2 F_A & & & -\frac{\eta_2}{\rho^2} I & \\
 & E_A^T X_1 & & & & -\eta_2 I\ * \\
\Phi^T(B_2) & & & & & -P_B
\end{bmatrix} \triangleq \Psi_2 < 0, \qquad (13)\\
&B_2 \in Y,
\end{aligned}
$$

where $\Xi_4 = Y_1 A_0^T + A_0 Y_1 + \eta_1 E_A E_A^T - (1+\lambda)\sum_{i=1}^{k} d_i^{-1} J J^T$ with $\lambda > 0$, $\Phi(B_2) = [J\Lambda^T(\bar{B}_{21}), \ldots, J\Lambda^T(\bar{B}_{2k})]$ with $\Lambda(\bar{B}_{2i}) = I_n \otimes \bar{B}_{2i}$, $i = 1, \ldots, k$, and $P_B = \mathrm{diag}(d_1 R_B^{-1}, \ldots, d_{p_2} R_B^{-1})$ with

$$
R_B = \begin{pmatrix}
\Theta_1(\lambda) & * & \cdots & * \\
-E_{12} & \Theta_2(\lambda) & * & * \\
\vdots & \vdots & \ddots & \vdots \\
-E_{p_2 n} & -E_{p_2 n} & \cdots & \Theta_{p_2}(\lambda)
\end{pmatrix}. \qquad (14)
$$

Here $R_B > 0$, $P_B > 0$ for any $\lambda > 0$.

Moreover, note that the constraints $B_2 \in Y$ are still concave equality constraints and should be transformed into the nonlinear inequality constraints, which would lead to the following problem Q^5.

$$
\begin{aligned}
&\textit{Problem } Q^5\\
&\min\ \bar{r}\\
&\begin{bmatrix} X_1 & I \\ I & Y_1 \end{bmatrix} > 0, \quad \Psi_2 < 0 \qquad (15)\\
&\bar{B}_{2i}^T \bar{B}_{2i} \geq 1, i = 1, \ldots, p_2.
\end{aligned}
$$

To verify the properties of the problem Q^5, denote $\mathfrak{R}_4, \mathfrak{R}_5$ are the feasible sets of problems Q^4 and Q^5 respectively, and correspondingly $\zeta = (X_1, Y_1, \bar{B}_2, F, \eta_1, \eta_2, \bar{r})$ is the variable of the above problems. It can be seen from the structure of Q^4 and Q^5 that the $\mathfrak{R}_4 \subset \mathfrak{R}_5$ and besides the Theorem below would also be verified.

Theorem 1 *The following properties hold for (13):*

(A): For any locally optimal solution $\zeta^* = (X_1^*, Y_1^*, \bar{B}_2^*, F^*, \eta_1^*, \eta_2^*, \bar{r}^*)$ *of problem* Q^5*, it obeys* $\bar{B}_2^* \in \bar{Y}$.

(B): Any locally optimal solution $\zeta^* = (X_1^*, Y_1^*, \bar{B}_2^*, F^*, \eta_1^*, \eta_2^*, \bar{r}^*)$ *of problem* Q^5 *is also the locally optimal solution of problem* Q^4*, and vise versa.*

Proof In order to prove property (a), the second constraint $\Psi(\zeta) < 0$ in (15) should be equivalently converted as

$$\begin{bmatrix} \Xi_4 & \Xi_5 \\ \Xi_5^T & \Xi_6 \end{bmatrix} < 0, \tag{16}$$

$$\Xi_4(\zeta) = Y_1 A_0^T + A_0 Y_1 - (1+\lambda)\sum_{i=1}^{k} d_i^{-1} J J^T + Y_1 C_1^T C_1 Y_1 + \frac{\rho^2}{\eta_1} Y_1 F_A^T F_A Y_1 + \frac{1}{\bar{r}} B_1 B_1^T + \Phi(B_2) P_B^{-1} \Phi^T(B_2), \tag{17}$$

$$\Xi_5(\zeta) = \frac{1}{\bar{r}} B_1 (B_1^T X_1 + D_2^T F), \tag{18}$$

$$\Xi_6(\zeta) = X_1 A_0 + A_0^T X_1 + F C_2 + C_2^T F^T + C_1^T C_1 + \eta_2 \rho^2 F_A^T F_A + \frac{1}{\eta_2} X_1 E_A E_A^T X_1 + \frac{1}{\bar{r}} (X_1 B_1 + F^T D_2)(B_1^T X_1 + D_2^T F). \tag{19}$$

Suppose that there exists a locally optimal solution $\zeta^* = (X_1^*, Y_1^*, B_2^*, F^*, \eta_1^*, \eta_2^*, \bar{r}^*)$ such that $\bar{B}_{2w}^{*T} \bar{B}_{2w}^* > 1$ for some positive integer $1 \le w \le p_2$. Therefore, we obtain

$$\begin{bmatrix} X_1^* & I \\ I & Y_1^* \end{bmatrix} > 0, \quad \begin{bmatrix} \Xi_4^*(\zeta^*) & \Xi_5^*(\zeta^*) \\ \Xi_5^{*T}(\zeta^*) & \Xi_6^*(\zeta^*) \end{bmatrix} < 0. \tag{20}$$

Correspondingly, set $\tilde{\zeta}^*(\alpha, \beta) = (\tilde{X}_1^*, \tilde{Y}_1^*, \tilde{B}_2^*, \tilde{F}^*, \tilde{\eta}_1^*, \tilde{\eta}_2^*, \tilde{\bar{r}}^*)$ as $\tilde{X}_1^* = \alpha X_1^*$, $\tilde{F}^* = \alpha F^*$, $\tilde{\bar{r}}^* = \alpha \bar{r}^*$, $\tilde{Y}_1^* = \frac{1}{\alpha} Y_1^*$, $\tilde{\eta}_2^* = \alpha \eta_2^*$, $\tilde{\eta}_1^* = \frac{1}{\alpha} \eta_1^*$, $\tilde{\bar{B}}_{2i}^* = \bar{B}_{2i}^*, i = 1, \ldots, k, i \ne w$ and $\tilde{\bar{B}}_{2w}^* = \beta \bar{B}_{2w}^*$, where $\alpha \in (0, 1], \beta \in (0, 1]$.

First it can be seen from the structure of $\tilde{\zeta}^*(\alpha, \beta)$ that $\tilde{\zeta}^*(1, \beta) \in \mathfrak{R}_5$ if $\beta \in (\frac{1}{\|\bar{B}_{2w}^*\|}, 1]$. Then for any $\beta \in (\frac{1}{\|\bar{B}_{2w}^*\|}, 1)$, we can obtain that

$$\|\tilde{\bar{B}}_{2i}^*(\tilde{\zeta}^*)\| = \begin{cases} \beta \|\tilde{\bar{B}}_{2i}^*(\zeta^*)\|, \ i = w; \\ \|\tilde{\bar{B}}_{2i}^*(\zeta^*)\|, \quad \text{else.} \end{cases} \tag{21}$$

The Eq. (21) implies that $\|\tilde{\bar{B}}_{2i}(\tilde{\zeta}^*)\| \ge 1$.

Besides, substituting $\tilde{\zeta}^*$ into (16)–(19) yields

$$\Xi_4(\tilde{\zeta}^*) = \frac{1}{\alpha}(\Xi_4(\zeta^*) - \Delta_1(\tilde{\zeta}^*)) \tag{22}$$

$$\Xi_5(\tilde{\zeta}^*) = \Xi_5(\zeta^*) \tag{23}$$

$$\Xi_6(\tilde{\zeta}^*) = \alpha(\Xi_6(\zeta^*) + \frac{1-\alpha}{\alpha} C_1^T C_1) \tag{24}$$

where

$$\begin{aligned}\Delta_1(\tilde{\zeta}^*) = &-(1-\alpha)((1+\lambda)\sum_{i=1}^{k} d_i^{-1} JJ^T + \frac{1}{\alpha} Y_1^* C_1^T C_1 Y_1^*) \\ &+ \Phi(B_2^*) P_B^{-1} \Phi^T(B_2^*) - \alpha \Phi(\tilde{B}_2^*) P_B^{-1} \Phi^T(\tilde{B}_2^*).\end{aligned} \tag{25}$$

Moreover, note that $\lim_{\alpha\to 1} \Xi_6(\tilde{\zeta}^*) = \Xi_6(\zeta^*)$, $\lim_{\alpha\to 1} \Delta_1(\tilde{\zeta}^*) = \Phi(B_2^*) P_B^{-1} \Phi^T(B_2^*) - \Phi(\tilde{B}_2^*) P_B^{-1} \Phi^T(\tilde{B}_2^*) = \Delta_2(\beta)$, where $\Delta_2(\beta) = d_w(1-\beta^2) \Lambda^T(\bar{B}_{2w}^*) R_B \Lambda(\bar{B}_{2w}^*) > 0$. Due to the positive definiteness of matrix $\Delta_2(\beta)$, there exists $\epsilon > 0$ such that $\frac{\Delta_2}{2} \geq -\frac{\epsilon}{1-\epsilon} \Xi_4(\zeta^*)$. Accordingly, there also exists $\bar{\alpha} \in (0,1)$ such that, for any $\alpha \in [\bar{\alpha}, 1]$,

$$\Delta_1(\tilde{\zeta}^*, \alpha) \geq \frac{\Delta_2}{2}, \quad \frac{1-\alpha}{\alpha} C_1^T C_1 < -\epsilon \Xi_6(\zeta^*). \tag{26}$$

Thus for any $\alpha \in [\bar{\alpha}, 1]$,

$$\begin{aligned}\begin{bmatrix} \Xi_4(\tilde{\zeta}^*) & \Xi_5(\tilde{\zeta}^*) \\ \Xi_5^T(\tilde{\zeta}^*) & \Xi_6(\tilde{\zeta}^*) \end{bmatrix} &\leq \begin{bmatrix} \frac{1}{\alpha}(\Xi_4(\zeta^*) - \frac{\Delta_2}{2}) & \Xi_5(\zeta^*) \\ \Xi_5^T(\zeta^*) & \alpha(\Xi_6(\zeta^*) + \frac{1-\alpha}{\alpha} C_1^T C_1) \end{bmatrix} \\ &\leq U^T(\alpha, \epsilon) \begin{bmatrix} \Xi_4(\zeta^*) & \Xi_5(\zeta^*) \\ \Xi_5^T(\zeta^*) & \Xi_6(\zeta^*) \end{bmatrix} U(\alpha, \epsilon) \\ &< 0,\end{aligned} \tag{27}$$

$$\begin{bmatrix} \tilde{X}_1^* & I \\ I & \tilde{Y}_1^* \end{bmatrix} = \begin{bmatrix} \sqrt{\alpha} I & \\ & \frac{1}{\sqrt{\alpha}} I \end{bmatrix} \begin{bmatrix} X_1^* & I \\ I & Y_1^* \end{bmatrix} \begin{bmatrix} \sqrt{\alpha} I & \\ & \frac{1}{\sqrt{\alpha}} I \end{bmatrix} > 0. \tag{28}$$

where $U = \mathrm{diag}(\frac{1}{\sqrt{\alpha(1-\epsilon)}}, \sqrt{\alpha(1-\epsilon)})$.

From (21), (27), and (28), it can be obtained that $\tilde{\zeta}^*(\alpha, \beta) \in \mathfrak{R}_5$ with $\tilde{\bar{r}}^* = \alpha \bar{r}^* < \bar{r}^*$. Since $\lim_{\beta\to 1} \lim_{\alpha\to 1} \tilde{\zeta}^*(\alpha, \beta) = \zeta$, the value $\bar{\alpha} \in (0,1)$ and $\beta \in (0,1)$ can be found in any neighbor of ζ, denoted as $U(\zeta)$, such that for any $\alpha \in [\bar{\alpha}, 1)$, $\tilde{\zeta}(\alpha, \beta) \in U(\zeta) \cap \mathfrak{R}_5$ with $\tilde{\bar{r}} = \alpha \bar{r}^* < \bar{r}^*$. Therefore, the above solution ζ^* is not the locally optimal solution of the optimization problem Q^5, and according to the generality of the

solution ζ^*, we can obtain that any optimal solution of the optimization problem Q^5, denoted as $\zeta^* = (X_1^*, Y_1^*, \bar{B}_2^*, F^*, \eta_1^*, \eta_2^*, \bar{r}^*)$, would satisfies $\bar{B}_2^* \in \bar{Y}$.

Moreover, the property (b) can be easily verified based on the similar procedure of the proof of Theorem 1 in [6]. Therefore the proof of this theorem is complete.

Theorem 1 implies that we can just search the locally optimal solution of the problem Q^5, and this solution would also be the locally optimal solution of the problem Q^4. Besides, in order to deal with the concave constraints in Q^5, the local linearization procedure [10] and the corresponding prediction-correction method [6] are utilized. First the problem Q^5 is converted into the sequential convex optimization problem

$$\begin{aligned}
&\textit{Problem } Q_{[i]}^6\\
&\min\ \bar{r}\\
&\begin{bmatrix} X_1 & I \\ I & Y_1 \end{bmatrix} > 0,\\
&\Psi_2 < 0,\\
&(\bar{B}_{2i}^{[k]})^T(\bar{B}_{2i} - \bar{B}_{2i}^{[k]}) \geq 0, i = 1, \ldots, k,\\
&\|\zeta - \zeta^{[k]}\| < M,
\end{aligned} \tag{29}$$

where each linearized optimization problem $Q_{[i]}^6$ is linearized at the solution $\zeta^{[k]} = (X_1^{[k]}, Y_1^{[k]}, \bar{B}_2^{[k]}, F^{[k]}, \eta_1^{[k]}, \eta_2^{[k]}, \bar{r}^{[k]})$. Then for the optimal solution $\hat{\zeta}^{[k]} = (X_1^{[k+1]}, Y_1^{[k+1]}, \hat{\bar{B}}_2^{[k]}, F^{[k+1]}, \eta_1^{[k+1]}, \eta_2^{[k+1]}, \bar{r}^{[k+1]})$ of the problem $Q_{[i]}^6$, we use the correction method [6] to obtain $\bar{B}_2^{[k+1]}$ as follows

$$\bar{B}_{2i}^{[k+1]} = \frac{\hat{\bar{B}}_{2i}^{[k]}}{\|\hat{\bar{B}}_{2i}^{[k]}\|}, i = 1, \ldots, p_2, \tag{30}$$

meaning that $\bar{B}_2^{[k+1]} \in \bar{Y}$, and correspondingly denote $\zeta^{[k+1]} = (X_1^{[k+1]}, Y_1^{[k+1]}, \bar{B}_2^{[k+1]}, F^{[k+1]}, \eta_1^{[k+1]}, \eta_2^{[k+1]}, \bar{r}^{[k+1]})$. According to the theorems and corollaries in [10], it can be obtained that we can find a subsequence in $\{\zeta^{[i]}\}$, named as $\{\zeta^{[i_k]}\}$, such that $\lim_{k\to\infty}\{\zeta^{[i_k]}\} = \zeta^*$. Moreover, ζ^* is a locally optimal solution of the problems Q^4 and Q^5.

4 Conclusions

In this paper, the output feedback closed-loop actuator placement is studied. The designed actuator locations are constrained into a class of nonlinear non-convex sets, and the linear system is subject to model uncertainties. A set of transformations are

derived to convert the uncertain non-convex optimization problem into a successive convex problem, and accordingly a prediction–correction procedure is developed to search the locally optimal solution.

Acknowledgments This work was supported by the National Basic Research Program of China (973 Program: 2012CB821200, 2012CB821201) and the NSFC (61134005, 61327807, 61521091, 61520106010).

References

1. Morris K, Yang S (2015) Comparison of actuator placement criteria for control of structures. J Sound Vib 353(29):1–18
2. de Oliveira MC, Geromel JC (2000) Linear output feedback controller design with joint selection of sensors and actuators. IEEE Trans Autom Control 45(12):2412–2419
3. Geromel JC (1989) Convex analysis and global optimization of joint actuator location and control problems. IEEE Trans Autom Control 34(7):711–720
4. Wang SX, Deng Y, Wang DY, Liu CR (2015) Reconfigurability design for thrusters of satellite attitude control system based on optimal energy consumption. Aerosp Control, 33(5): 46–53 (in Chinese)
5. Chen KK, Rowley CW (2014) Fluid flow control applications of H_2 optimal actuator and sensor placement. In: Proceedings of the American Control Conference. Portland, Oregon, pp 4044–4049
6. Lu XH, Jia YM, Wang DY, Liu CR (2016) $H\infty$-optimal actuator placement with a class of nonlinear constrains. In: The 35th Chinese Control Conference (accepted)
7. Jia YM (2007) Robust $H\infty$ Control. Science Press, Beijing (in Chinese)
8. Geromel JC, Bernussou J, de Oliveira MC (1999) H_2-norm optimization with constrained dynamic output feedback controllers: decentralized and reliable control. IEEE Trans Autom Control 44(7):1449–1454
9. Ghaoui LE, Oustry F, Lebret H (1998) Robust solutions to uncertain semidefinite programs. SIAM J Optim 9(1):33–52
10. Liu XF, Lu P (2014) Solving nonconvex optimal control problems by convex optimization. J Guid Control Dyn 37(3):750–765

Tourism Activity Recognition and Discovery Based on Improved LDA Model

Yifan Yuan, Junping Du and JangMyung Lee

Abstract More and more tourist travels can be found on the Internet, these travels include travel activity, time, and space information. Using machine learning methods to identify and discover tourism activities has become a hot spot in the present study. In this paper, considering the particularity of tourism travel journey, we improve the original latent Dirichlet distribution model, and put forward a model of tourism activity recognition and discovery based on activity-topic latent Dirichlet allocation. This model extends the latent Dirichlet allocation model with tourist activities, aiming to obtain the probability of tourism activities that belongs to a certain topic. From the relationship between travel text–topic–vocabulary–-tourism, we can efficiently identify and discover the purpose of tourism activities.

Keywords Latent Dirichlet allocation · Text mining · Gibbs sampling

1 Introduction

With the rapid development of the mobile Internet industry, personal intelligent terminals have been used in large scale.

Y. Yuan · J. Du (✉)
Beijing Key Lab of Intelligent Telecommunication Software and Multimedia, Beijing University of Posts and Telecommunications, 100876 Beijing, China
e-mail: junpingdu@126.com

Y. Yuan
e-mail: komaconss@163.com

Y. Yuan · J. Du
School of Computer Science, Beijing University of Posts and Telecommunications, 100876 Beijing, China

J. Lee
Department of Electronics Engineering, Pusan National University, Busan, South Korea
e-mail: jmlee1@pusan.ac.kr

Y. Jia et al. (eds.), *Proceedings of 2016 Chinese Intelligent Systems Conference*, Lecture Notes in Electrical Engineering 404, DOI 10.1007/978-981-10-2338-5_49

This makes all kinds of information in the network grow exponentially. At the same time, the data mining technology, which is used to obtain valuable information, is constantly developing. With the continuous improvement of the consumption level and life quality, more and more people choose to travel as a kind of entertainment. Meanwhile, more and more tourists tend to publish their travels on the intelligent terminal. The content of travel journey includes all aspects of the travel information, such as tourism activities, travel time, and location information.

After collecting and analyzing the information of travel journey issued by tourists, we can get the tourists' travel time, travel route, travel strategy, travel experience, and travel content. Through these we can design the tourism activity recognition and discovery system based on the improved LDA model. It is very meaningful to mine the behavior of tourists. On the one hand, the results of mining visitors' behavior can directly participate in the development, planning, and marketing of tourism destination. On the other hand, tourist behavior is an important factor for ecological environmental protection, capacity management and control, and the sustainable development of tourism destination. Tourist behavior research is the basis and premise to guide and regulate the behavior of tourists and maintain the sustainable use of tourism resources.

2 Related Work on LDA Improvement

Semantic-based feature expansion generally implements via synonym dictionary or Internet knowledge. Sahami et al. proposed using Google and other search engines to achieve more context information for short text. However, it is difficult to apply this method to practical use. This approach is excessively dependent on the quality of the search engine, which may lead the results very unstable. [1] Hu et al. proposed a three-tier architecture to enrich the short text feature expression with Wikipedia and WordNet. [2] Phan improved the characterization of short text by appending additional knowledge to the subject information. In addition, he also made a study of using the semantic relation of the text set to realize the feature expansion. [3] Quan et al. used the subject information of the text set directly, and established a correlation mapping between different words in the text. [4] However, this method cannot model the short text and only can be applied to the classification and clustering algorithm based on distance, such as KNN or K-means clustering. Moreover, this approach also fails to be used in SVM for text classification which is more efficiency.

LDA (Latent Dirichlet Allocation) is a complete probabilistic generative model, which is widely used in the subject model. Its basic idea is that each text is composed of multiple hidden topics, each of which is composed of a number of words. Most of the researchers utilize the LDA to classify text directly. Rubin et al. established a topic model of multi-label classification for documents classification, and compare the statistical topic model and the discriminative model in terms of the advantages and disadvantages systematically. [5] On the other hand, the researchers

also begin to use the topic model to expand the text features. Among them, Phan et al. expand the text feature based on the external corpus. [6] Chen et al. implemented the text feature expansion and selection based on the optimal topic of different labels via multi-grain topic model (Multi-granularity Topics) in the short text classification. This method also applied new features to the expansion algorithm in the summary search (Search-snip-pet), achieved better classification results (improve the 4.14 % compared to using LDA directly). [7] The probabilistic topic models expand the features and establish the potential semantic relation between words and documents. It can not only expand the external corpus, but also establish an association of the internal semantic. As a result, it provides more means for short text classification.

3 Improved LDA Model Based on Activity-Topic

3.1 Definition of LDA Model Based on Activity-Topic

This paper puts forward a tourism activity recognition model based on activity-topic. The model makes a new combination of the content and category of tourism activities. The model is responsible for the generation of the document and the formation of tourism activities, the first generation all words from all document, then for the document belongs to the type of tourism activities, randomly selected from a word in a document, with the word implied topic to generate the corresponding tourism activities. This model can be divided into three parts: the data collection module, construction module, and application module. The architecture of this tourism activity recognition and discovery model based on activity-topic is shown in Fig. 1:

Parameters in the model are shown in Table 1.

When modeling the text topic, the subject structure that needs to be analyzed and mining is the information in each section of the travels, which is formed as a document. Each paragraph of the travel text can be expressed as a mixture distribution of series topics, denoted as P (z). Meanwhile, each subject is subject to the probability distribution of the vocabulary. Because the analyzing method adopted in

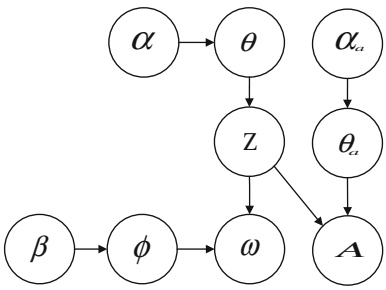

Fig. 1 Bayesian network graph based on activity-topic

Table 1 Variables and implications of LDA model based on activity-topic

Variable	Definition of variables
α, β, αa	Topic, vocabulary, tourism activities subject to the prior distribution of Dirichlet parameters
θ	The probability of document generation
ϕ	The probability of generating words in a document
θa	The probability of a document to generate tourism activity
z	The topic of vocabulary and tourism activities
w, a	Vocabulary, tourism activities

the LDA model is the bag of words, it is necessary to take the word frequency into account. As a result, we should segment the word in the journey text, and the lexical information obtained is the vocabulary mentioned in the LDA model, denoted P (w|z). The probability of generating a word in the travel journey is shown in the formula (1).

$$P(\omega_i) = \sum_{j=1}^{T} P(\omega_i | z_i = j) P(z_i = j) \tag{1}$$

Tourism activity recognition and discovery based on improved LDA model is an improvement LDA. It combines the tourism information, travel information, and travel information together and form a model that is suitable for tourism activities identification and discovery. Therefore, the generation of topic tourism activities probability can be represented by the formula (2):

$$P(a_i) = \sum_{j=1}^{T} P(a_i | z_i = j) P(z_i = j) \tag{2}$$

3.2 Solution Probability Distribution Based on Gibbs Sampling

For LDA model based on activity-topic, a topic can be selected based on the topic of the document, a word is generated based on the distribution of the vocabulary, and a tourism activity is generated according to the distribution of the topic based on the tourism activity. But for the known text information, vocabulary and tourism activity are the information which can be observed, and the topics are the hidden variable which is unknown. So we need to build the topic model of that document through posterior probability, and generate the probability of the topic vocabulary and the topic tourism activities. For the document vocabulary and tourism activities, the probability distribution formula of the subject information can be mined through the posterior probability. The posteriori probability distribution of the vocabulary

and topic is shown in Eq. 3, and the posterior probability distribution of the tourism activity categories and topics is shown in Eq. 4:

$$P(\theta, z|\omega, \alpha, \beta) = \frac{P(\theta, z, \omega|\alpha, \beta)}{P(\omega|\alpha, \beta)} \tag{3}$$

$$P(\theta, z|a, \alpha, \alpha_{\mathrm{a}}) = \frac{P(\theta, z, a|\alpha, \alpha_{\mathrm{a}})}{P(\omega|\alpha, \alpha_{\mathrm{a}})} \tag{4}$$

After computing the marginal distribution of Eqs. 3 and 4, we can achieve Eqs. 5 and 6:

$$P(D|\alpha, \beta) = \prod_{d=1}^{M} \int P(\theta_d|\alpha)(\prod_{n=1}^{N_d} \sum_{z_{dn}} P(z_{dn}|\theta_d)P(w_{dn}|z_{dn}, \beta))d\theta_d \tag{5}$$

$$P(D|\alpha, \alpha_a) = \prod_{d=1}^{M} \int P(\theta_d|\alpha)(\prod_{n=1}^{N_d} \sum_{z_{dn}} P(z_{dn}|\theta_d)P(w_{dn}|z_{dn}, \alpha_a))d\theta_d \tag{6}$$

However, it is very complex and difficult to calculate the posterior probability, and always need to solve with an approximation method. This paper uses Gibbs sampling to infer this probability. Gibbs sampling is a MCMC (Markov chain Monte Carlo) sampling method. It is often used to solve Bayesian graph model and can obtain the probability distribution of the document topic and the vocabulary distribution model effectively. For example, we want to obtain the value of sample X in high-dimensional distribution, where X is an N-dimensional variable and the sample values is x, x i. We can obtain the sample values by conditional probability distribution P(x i|x 1, x 2, ……, x i − 1, x i + 1, ……, x n). After applying the model proposed in this paper, the calculating formula is as follows:

$$P(z_i = j|z_{-i}, w_i, d_i) \propto \frac{C_{w_i j}^{WT} + \beta}{\sum_{w=1}^{W} C_{w_i j}^{WT} + W\beta} * \frac{C_{d_i j}^{DT} + \alpha}{\sum_{t=1}^{T} C_{d_i j}^{DT} + T\alpha} \tag{7}$$

$$P(z_i = j|z_{-i}, w_i, d_i) \propto \frac{C_{w_i j}^{WT} + \alpha_{\mathrm{a}}}{\sum_{w=1}^{W} C_{w_i j}^{WT} + W\alpha_{\mathrm{a}}} * \frac{C_{d_i j}^{DT} + \alpha}{\sum_{t=1}^{T} C_{d_i j}^{DT} + T\alpha} \tag{8}$$

In the process of sampling Gibbs, the sampling results will be converged after iteration.

3.3 Evaluation Model Based on Perplexity

The indicator of content perplexity is widely used in the evaluation of the topic model. Lower the perplexity is, the better performance the topic model will have. The calculation method is shown as a formula 9:

$$perplexity(x) = \exp(-\sum_{j}^{J}\sum_{i}^{N_j}\log p(x_{ji})/\sum_{j}^{J}N_j) \quad (9)$$

where $\sum\log(p(x_{ji}))$ means to calculate the logarithm of all the words, which will help to deal with multiplication. N is the number of words in the test set. This indicator can be regarded as the uncertainty of an article belonging to a subject. The content perplexity will be smaller with more topics, but with more topics, the model will be easy of over fitting.

3.4 Algorithm of LDA Model Based on Activity-Topic

LDA model based on activity-topic is improved on the basis of LDA. It is also a complete topic model, and the process of generating a text can be represented in the Fig. 2. First of all, the LDA generation model based on activity-topic extracts the relationship between the topic and the vocabulary from the Dirichlet distribution of β, which is achieved from the travel. At the same time, this model achieves the relationship between topic and the travel journey from the Dirichlet distribution

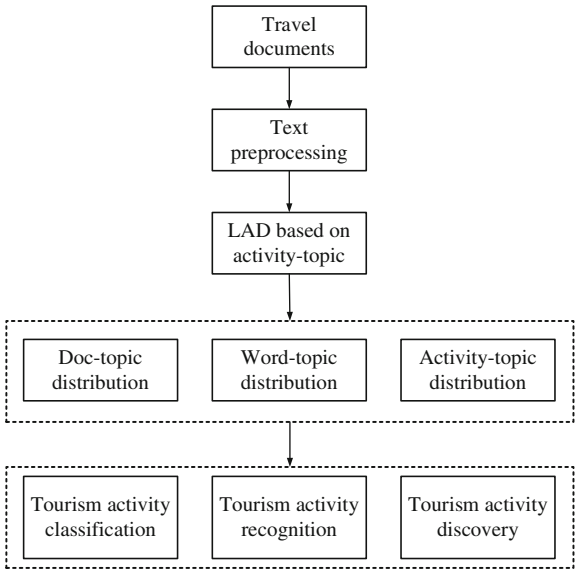

Fig. 2 Tourism activity discovery based on activity-topic

Table 2 Steps of LDA model algorithm based on activity-topic

Step	Operation
Step 1	Extraction the relationship between topics and vocabularies from the Dirichlet distribution with β in the document
Step 2	Extraction the relationship between topics and tourism activities from the Dirichlet distribution with α a in the tag of the tourism activities
Step 3	Generating the relationship θ between that text and each topics from the Dirichlet distribution with α. The text is produced by the LDA model
Step 4	Sampling the subject z which current vocabulary and tourism activities belongs to from the polynomial distribution with θ
Step 5	Extract the specific vocabulary w and tourism activities from the polynomial distribution of the relationship between the parameter topics and the vocabularies

based on αa. Based on these relationships, the LDA generation model based on activity-topic is used to generate a text. The parameter θ between that travel and each topics will be sampled from the Dirichlet distribution ofα. The subject z, which the current vocabulary and tourism activity belongs to, is extracted from the multinomial distribution with θ. Finally, the specific vocabulary w and tourism activities a can be inferred from the multinomial distribution of the relationship between topics and vocabulary. In the LDA generation model based on activity-topic, the process of generating tourism activity information is shown in Table 2.

For the generative model based on activity-topic, it can select a topic through the distribution based on a topic in a document, generate a word according to the distribution based on vocabulary, and generate tourism activities with the distribution of tourism activities.

4 Discovery of Tourism Activities Based on Activity-Topic

The tourism activity recognition and discovery model is implemented based on text information, and will pay more attention to the preprocessing of text, the combination of text mining technology, and tourism activity recognition and discovery. On the one hand, the text data collected is very irregular that is not suitable for all kinds of text classification and mining algorithms. It is necessary to preprocessing the original text data. On the other hand, a text classification model will be used to deal with the processed text, in order to identify and discover the tourism information in the text. The flowchart is shown in the Fig. 2.

First, the collected data is stored as the training data set, which is used to train the tourism activity recognition and discovery model based on activity-topic. However, the collected data is the original text, which cannot be directly used for modeling and computing. Here, we utilize a text preprocessing module to deal with the data, which involves the removal of function words, word segmentation, and word filtering. On the basis of data processing, the travel content and tourism

activities can be modeled based on the tourism activity recognition and discovery model based on activity-topic. Due to the addition of the category of tourism activities, we can generate the distribution between travel–topic, vocabulary–topic and tourism activities–topic. Based on these three distributions, we can classify, recognize, and discover the tourism activities.

5 Experimental Results and Analysis

5.1 Experimental Data and System Environment

The experimental travel journey texts are selected from ChanYouJi website. It is an unbalanced corpus and contains about 1000 documents, which can be divided into nine classes. And the tourism activities will be divided into eight categories: health care category, living experience category, outdoor sports category, tourism and sightseeing, shopping and food, entertainment facilities, festivals, and research categories. As the travel is a place while the tourists express their feeling, it is necessary to add a category which is tourism activities unrelated. As a result, the total tourism activities will be divided into nine categories..

The hardware platform is an individual PC, Intel Core/core i72.4 GHz, 8G memory. The software environment is the Windows7 operating system, combined with Chinese segmentation which is under python2.7 development environment.

5.2 Experimental Results Analysis

In order to verify the validity of the LDA model based on activity-topic on tourism activities identification and discovery, three groups of experiments are carried out. Experiment one: comparing the performance of the original LDA and the LDA model based on activity-topic. Experimental results show that the LDA model based on activity-topic achieved a lower content perplexity, achieving a better effect than the original LDA. Experiment two: Through modeling the subjects of travel journeys from ChanYouJi, we will achieve the corresponding topic = word–-tourism activity model. Then the text related to the tourism activities will be classified according to the generated model, and the classification result is the destination of tourism activity resignification and discovery. Experiment three: compared the proposed LDA model based on activity-topic with the text classifier based on Bayesian and classifier based on SVM. The evaluation indicator chose here is the recall rate, accuracy rate, F1-score. Experimental results show that the classifier based on LDA activity-topic model has the best classification performance.

The performance of the original LDA and the proposed LDA is tested according to the degree of confusion. The experimental results are shown in Fig. 3:

From the graph, we can find that the content perplexity of the original LDA and the LDA based on activity-topic will converge after 200 iterations. But the proposed LDA model obtains a lower content perplexity in summary, which proves that the LDA model based on activity-topic is more effective in topic classification.

After modeling the travels on ChanYouJi by the proposed LDA model, we will classify tourism activity based on the topic–vocabulary–tourism model. After calculating the recall, recall, F-measure, we evaluate the experimental results. The evaluation parameters are shown in Table 3.

From Table 3, it can be concluded that the average accuracy of the activity-topic-based LDA model is 85 %, the average recall rate is 72 %, and the average F1-score is 0.78. After analyzing the classification results of each type of tourism activity, the proposed LDA model received a better classification result for the outdoor sports category, holiday category, and shopping food category. The F1-score of corresponding categories reaches: the activity 0.90, Festival 0.85, and shop_food 0.86. But for entertainment and medicine this model obtains a suboptimal result, with the F1-score of entertainment is 0.64 and medicine is 0.48. However, these two types achieve a better classification accuracy, the accuracy rate of entertainment has reached 74 % and for medicine is 92 %. The reason of the bad performance of F-value is that the recall rate is too low, which demonstrates that the coverage of the classification results is not ideal.

We also test the data with other mature text classifier in F1-score. The result is shown in Table 4.

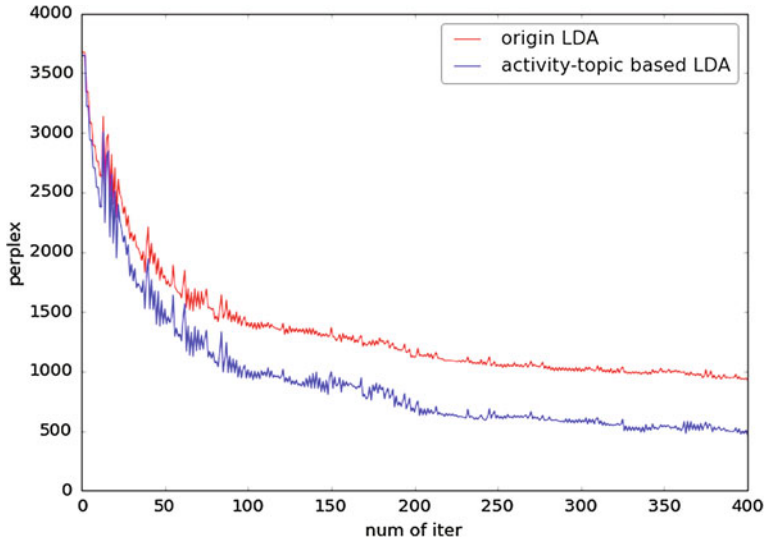

Fig. 3 Index of the content of the improved algorithm

Table 3 Accuracy rate, recall rate, F1-score of activity-topic model based on LDA

	Precision	Recall	F1-score
Activity	0.92	0.88	0.90
Entertainment	0.74	0.57	0.64
Exp	0.86	0.67	0.75
Festival	0.89	0.82	0.85
Medicine	0.92	0.33	0.48
Noteleate	0.91	0.58	0.70
Research	0.85	0.71	0.77
Shop_food	0.82	0.91	0.86
Visit	0.78	0.85	0.81
Avg/total	0.85	0.72	0.78

Table 4 Comparison of F1-score of each classification algorithm

F1-score	Activity-topic LDA	SVM	Ba Yes
Activity	0.8	0.76	0.78
entertainment	0.64	0.74	0.54
Exp	0.75	0.55	0.65
Festival	0.85	0.82	0.71
Medicine	0.48	0.6	0.51
Noteleate	0.7	0.57	0.4
Research	0.77	0.67	0.62
Shop_food	0.86	0.76	0.85
Visit	0.81	0.61	0.71

We also draw a contrast curve in F1-score for the tourism activities classification results by proposed LDA model based on activity-topic, SVM classification, and the Bayesian classification, as shown in Fig. 4.

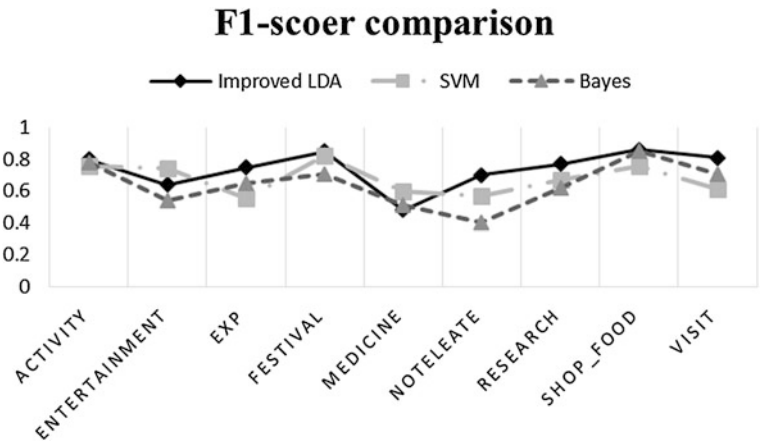

Fig. 4 Performance comparison of different text classifiers

After comparing the tourism activity results of different classifiers, we can find that the performance of three classifiers is similar on the categories of activity, medicine and shop_food. But for the categories of exp, entertainment, and visit, there is a large performance difference between these three classifiers. LDA model based on activity-topic achieves the best classification performance, the SVM based classifier follows, and the Bayesian-based classifier achieves the most unsatisfactory performance. The SVM-based classifier reaches a better performance than the proposed classifier in classifying the categories of entertainment and medicine. But the LDA model based on activity-topic performs better as a whole. Therefore, this paper chooses the LDA model based on activity-topic to identify and discover the tourism activities.

6 Conclusion

The problems text classification faced is the high dimension of features, too large number of categories and samples, noise interference, and unbalanced corpus. The text feature representation and the choice of the classification algorithm have a greater impact on the entire text classification system. Aiming at solving these problems existed in the traditional text classification system, we proposed a LDA model based on activity-topic. This model appends the categories information into the existing feature selection algorithm based on LDA, and explores the potential differences between different types of documents.

The experimental results show that this method can effectively improve the classification accuracy. The LDA model based on activity-topic achieves a lower content perplexity than the original LDA model and a better performance. Compared with other classification algorithms, the LDA model based on activity-topic has a good classification performance in many types of text data sets.

Acknowledgments This work was supported by National Basic Research Program of China (973 Program) 2012CB821200 (2012CB821206) and the National Natural Science Foundation of China (No. 61320106006, No. 61532006, No. 61502042).

References

1. Sahami M, Heilman TDA (2013) Web-based kernel function for measuring the similarity of short text snippets. In: Proceedings of the 15th international conference on World Wide Web, WWW 2013, Edinburgh, Scotland, UK, 23–26 May 2013, pp 377–386
2. Hu X, Sun N, Zhang C et al (2012) Exploiting internal and external semantics for the clustering of short texts using world knowledge. In: ACM Conference on Information and Knowledge Management, CIKM 2012, Hong Kong, China, November. 2012, pp 919–928
3. Phan XH, Nguyen L-M, Horiguchi S (2012) Learning to classify short and sparse text & web with hidden topics from large-scale data collections. In: The International Conference of World Wide Web, pp 91–100

4. Quan X, Liu G, Lu Z et al (2013) Short text similarity based on probabilistic topics. Knowl Inf Syst 25(3):473–491
5. Rubin TN, Chambers A, Smyth P et al (2011) Statistical topic models for multi-label document classification. Mach Learn 88(1–2):157–208
6. Le DT, Nguyen CT, Ha QT et al (2012) Matching and ranking with hidden topics towards online contextual advertising. In: IEEE/WIC/ACM International Conference on Web Intelligence and Intelligent Agent Technology, IEEE, pp 888–891
7. Chen M, Jin X, Shen D (2011) Short text classification improved by learning multi-granularity topics. IJCAI 2011, Proceedings of the International Joint Conference on Artificial Intelligence, Barcelona, Catalonia, Spain, July 2011, pp 1776–1781

Community Detection Based on Local Similarity Index in Chinese Aviation Network

Lingling Yan, Zengqiang Chen and Qing Zhang

Abstract This paper proposes a fast and efficient method based on local similarity index for detecting community structure in Chinese aviation network, and compares the partition accuracies of seven similarity measures. Simulation results on Chinese aviation network show that the algorithm proposed by us can perform better than the other six pre-existing methods. It can achieve better accuracy in community detection with low algorithm complexity for the reason of requiring only the local information of the network.

Keywords Community detection · Chinese aviation network · Node similarity · Complex networks

1 Introduction

Air transportation infrastructure has enormous impact on the development of a country [1] and is critical indicators of its travel industry and economic growth. With the improvement of living standards, the civil aviation transport demand will be greater and greater, the requirements of aviation universal service are also getting higher and higher. Therefore, through the construction of airport group to optimize the configuration of the airport and realize the efficient use of resources of regional airport, we can achieve the social and economic sustainable development strategy.

L. Yan · Z. Chen (✉)
College of Computer and Control Engineering, Nankai University,
Tianjin 300350, China
e-mail: chenzq@mail.nankai.edu.cn

L. Yan · Z. Chen
Key Laboratory of Intelligent Robotics of Tianjin, Nankai University,
Tianjin 300350, China

Z. Chen · Q. Zhang
College of Science, Civil Aviation University of China, Tianjin 300350, China

Y. Jia et al. (eds.), *Proceedings of 2016 Chinese Intelligent Systems Conference*,
Lecture Notes in Electrical Engineering 404, DOI 10.1007/978-981-10-2338-5_50

It has become a real problem that we need to face that how to optimize the allocation of the airport by constructing the airport group. Then we can realize the effective utilization of regional airport resources and achieve the sustainable development of society and economy.

As a common but vital property of complex networks, community structure has obtained more and more attention in recent years. It is the tendency for nodes to divide into groups according to similar properties or function, with dense connections within groups and only sparse connections between them [2]—see Fig. 1. The ability to discover and analyze these groups can provide invaluable help for understanding and visualizing the structure of networks. In addition, many research results show that ignoring community structure may miss a number of interesting properties, because the properties at the community level and the properties at the level of the entire networks are quite different [2].

In the past few years, there are many methods that have been proposed to discover the community structure of the network. Partitioning algorithm and hierarchical clustering method are two main clustering algorithm. The Kernighan–Lin algorithm [3] and the spectral bisection algorithm [4] are two traditional algorithms based on the ideas of graph partitioning. The GN [5] and MFC [6] methods are two types of hierarchical clustering algorithms to find community structure in networks.

Aviation network can be expressed by graphs where nodes represent airports and edges represent routes between two airports. This paper proposes a new method for detecting community structure by redefining a local similarity index and applies it to the Chinese airline network.

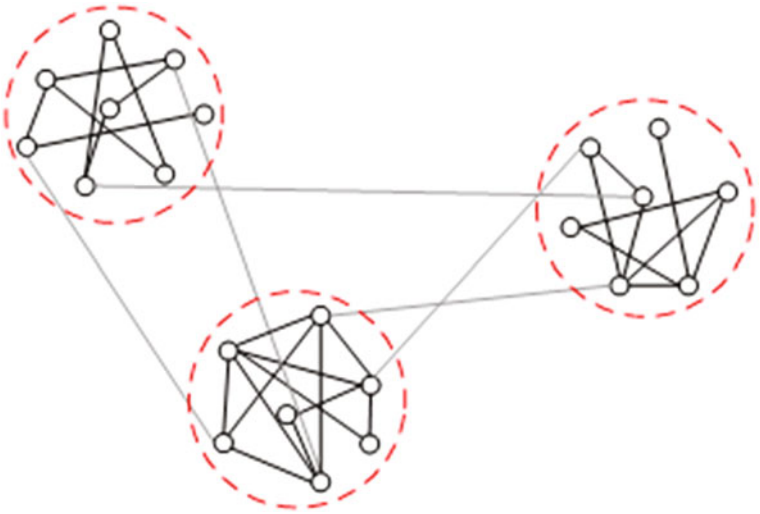

Fig. 1 A schematic representation of a network with community structure. In this network there are three communities of densely connected vertices (*circles* with *solid lines*), with sparse connections (*gray lines*) between them

2 Modularity Measure

The modularity Q is put forward for the quantitative research of a given partition of community structure. As a simple evaluation index has be widely accepted for assessing the quality of a particular network division, it is proposed by Newman and Girvan [7] in 2004, and it can be written as follows:

$$Q = \sum_{i=1}^{k} (e_{ii} - a_i^2) \tag{1}$$

where k is the number of communities, e is a symmetric matrix of size $k \times k$, each element e_{ij} represents the fraction of total links that connect nodes from partition i to nodes in partition j (i.e., therefore, e_{ii} is the proportion of links that connect vertices inside partition i) and $a_i = \sum_j e_{ij}$ (i.e., the proportion of links with at least one node in the partition i) [7].

Given a division, the greater the value of Q implies that the more reasonable the results of community division, the more obvious the community structure of the network. If the number of within community edges is no better than random, Q = 0 [8]. While the value of Q is close to 1, which is the maximum, indicates strong community structure. In real network, the value of Q is usually between, 0.3 to 0.7.

3 Construct Chinese Aviation Network

Construct Chinese aviation network model base on summer and fall season passenger routes data published by the civil aviation administration of China's official website. Chinese aviation network can be expressed by graphs where nodes represent airports and edges represent routes between two airports. We use the reciprocal of the distance between two city nodes as the weights of the edges in the network. In order to facilitate the calculation, we multiply it by a fixed parameter 1000, then the results are the weights, expressed as w_{ij}. So we got a weighted network with 148 nodes and 1153 undirected edges. It can be expressed by a 148×148 adjacency matrix A, $a_{ij} = w_{ij}$ if there can be up to the flight between node i and node j, otherwise $a_{ij} = 0$.

It needs to be explained here:

(1) The route selected in the network is a return route, so in the late operation process, it is not required to consider the direction of the course.
(2) For cities with two or more of the airports, the data will be combined, such as Pudong airport and Hongqiao airport in Shanghai can be unified into the city node 'Shanghai' Fig. 2.

The basic topological features of Chinese aviation network are summarized in Table 1. N and M represent the sum of nodes and edges in the network, respectively. ⟨k⟩ denotes the average degree. That is to say, each city airport has a direct

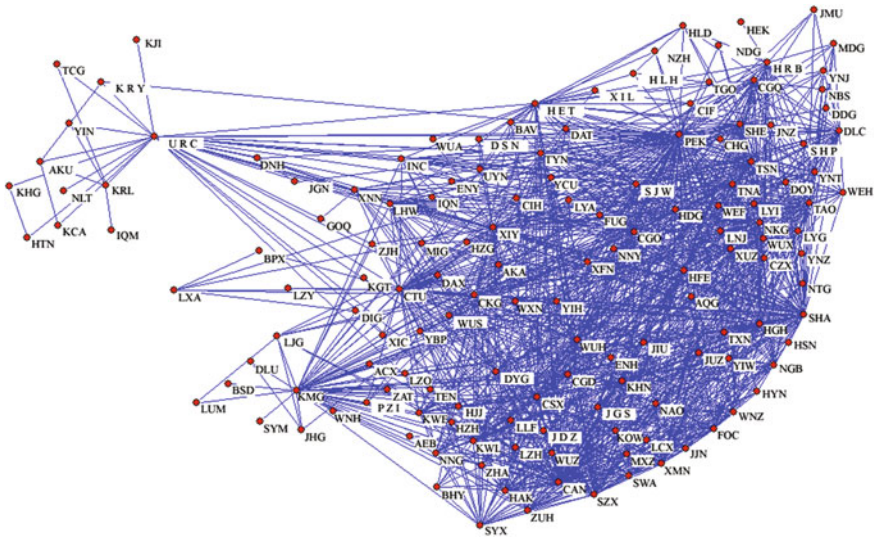

Fig. 2 The structure of Chinese aviation network

Table 1 The basic topological features of six example networks

Net	N	M	⟨k⟩	L	E	C	r
CNAir	148	1153	15.58	2.2165	0.5012	0.6877	-0.3843

air link with the other 16 cities on average. L represents the average path length, which means that any two city airport transfer by less than two times can be connected to each other by transferring less than two times. E is the efficiency of the network [9], defined as $E = \frac{2}{N(N-1)} \sum_{x,y \in V, x \neq y} d_{xy}^{-1}$, where d_{xy} is the shortest distance between x and y, and $d_{xy} = +\infty$ if x and y are belong to two different components. C and r represent the clustering coefficient [10] and assortative coefficient [11], respectively.

4 The Proposed Method

The principle and implementation of the proposed method are detailed in this section.

4.1 Node Similarity

The similarity is used to describe the probabilities that nodes belong to the same community, which is on the basis of the assumption that the more similar two nodes

are, the more likely they are in the same community [12]. A new similarity index is proposed in this paper. Given a particular network, the topological information can be described by an adjacent matrix A, then the similarity index can be written:

$$\text{similarity} = A + \alpha A^2 \tag{2}$$

α is the adjustable parameters. The number of paths with length of n between nodes x and y is given by $(A^n)_{xy}$.

4.2 Weight Improvement

In order to fully reflect the impact of geographical factors, we introduce a new influencing parameter c. It represents the number of provinces that the routes across. For example, the route Baotou–Guangzhou crosses five provinces. Then the weight can be improved as follows:

$$w = \frac{1}{d} \times 1000 \times (1 + \frac{1}{c}) \tag{3}$$

d represents the distance between two city nodes.

4.3 Community Detection

Given a network with n nodes, firstly, we compute the value of similarity of node pairs according to Eq. (2), then we can get a $n \times n$ similarity matrix $S = \{s_{ij}\}$, where the element s_{ij} represents the similarity between node i and node j. The detailed process is as follows:

(1) Divide all the nodes in the given network into p communities randomly, then we can get initial communities $C_1, C_2 \ldots C_p$.p is a parameter to adjust the number of communities. (We predivide the Chinese aviation network into 10 initial communities. The urban nodes that rank top 10 measured by betweenness are located in 10 different communities).
(2) Select an random node as the initial node. Repeat the Step 3 until all nodes in the networks have been visited.
(3) For node i, calculate similarity(i, C_j) between node i and each community C_j, $(j = 1, 2 \cdots n)$ according to Eq. (3).

$$\text{similarity}(i, C_j) = \frac{1}{N_j} \sum_{p \in C_j} \text{similarity}(i, p) \tag{3}$$

N_j represents the number of nodes in community C_j.

Assign node i to the community C^i with the maximum value of similarity(i, C_j).

$$C^i = \arg \max_{C_j, (j=1,2\cdots k)} \text{similarity}(i, C_j) \tag{4}$$

(4) Go to step (2) until it reaches the given number of iterations or assignments of each node do not change any more.

4.4 Complexity Analysis

In order to calculate the similarity between nodes, the algorithm considers only the information of the neighbors, which can be arrived by less than two steps. The average degree of nodes in the network is defined as $\langle k \rangle$, and assume that each node has $\langle k \rangle$ neighbors to simplify the discussion. The number of first-order neighbor nodes is $\langle k \rangle$, and the number of second-order neighbor nodes is $\langle k \rangle^2$. So the time complexity of computing the similarity matrix of the network with N nodes is $O(N\langle k \rangle^2)$. Since the processes of computing the similarity between each node is independent, we can consider using parallel operations to reduce the time consumption of the algorithm. Take a similar operation for each node in the network to find its community attribution, that is, traversing the nonzero elements in similarity matrix to find the maximum value of each line. Then the complexity of the whole partition process is $O(tN\langle k \rangle^2)$, in which t is the number of iterations required for the stability of the community.

5 Comparison of Similarity Index

5.1 Similarity Index

In this section, we compare the partition accuracies of six pre-existing similarity measures with the index we proposed. First, we introduce each kind of similarity measures briefly.

Common Neighbors—The most simple index used in previous work is to compute the number of two nodes' common neighbors. In this sense, the similarity of nodes depends on the extent that their neighborhoods overlap. It is defined as follows:

$$\text{similarity}(x, y) = |\Gamma(x) \cap \Gamma(y)| \tag{5}$$

where $\Gamma(x)$ represents the set of neighbors of x. This index is common and easy to calculate, but has a flaw that the high-degree nodes are more likely to have higher

similarity than the low-degree nodes, because the vertices with high degree would have a large value even if only a small fraction of their neighbors are shared. Therefore, this approach cannot get very accurate results.

Jaccard Index—For the sake of overcoming the above problem, Jaccard [13] normalizes the number of shared nodes based on the size of its two neighborhoods' union.

$$\text{similarity}(x, y) = \frac{|\Gamma(x) \cap \Gamma(y)|}{|\Gamma(x) \cup \Gamma(y)|} \tag{6}$$

Resource Allocation Index—Consider a pair of nodes x and y, and the node x can send some resource to y, with their common neighbors playing the role of transmitters. Making the assumption that each transmitter has a unit of resource, and will equally distribute it between all its neighbors, the amount of resource y received, namely the similarity between nodes x and y is [14]:

$$\text{similarity}(x, y) = \sum_{z \in \Gamma(x) \cap \Gamma(y)} \frac{1}{w(z)} \tag{7}$$

where $\Gamma(x)$ is the set of neighbors of x, and $\Gamma(x) \cap \Gamma(y)$ are the common neighbors of nodes x and y, and $w(z)$ is the strength of node z.

However, this index cannot distinguish whether a tightly related pairs of nodes are connected or not. It may result in inaccurate partition for community structure on the networks. Thus Pan et al. [15] redefine the similarity between x and y as follows:

$$\text{similarity}(x, y) = \begin{cases} \sum_{z \in \Gamma(x) \cap \Gamma(y)} \frac{1}{w(z)} & \text{if } x, y \text{ are connected,} \\ 0 & \text{otherwise.} \end{cases} \tag{8}$$

Adamic-Adar Index—This index gives a weight value to each node according to the degree of common neighbor nodes. The weight is equal to the reciprocal of the logarithm of the degree of the node [16].

$$\text{similarity}(x, y) = \sum_{z \in \Gamma(x) \cap \Gamma(y)} \frac{1}{\log\ w(z)} \tag{9}$$

Katz Index—Katz index is proposed as the number of paths between vertices, and defined as

$$\text{similarity} = \beta A + \beta^2 A^2 + \beta^3 A^3 + \cdots = (I - \beta A)^{-1} - I \tag{10}$$

with parameter β controlling different influence of paths. This measure is based on the global information of the network. However, it is difficult to obtain global topology and hard to count.

Local Path Index—It considers the information of the three order neighbors based on the CN index, then it can be written as follows:

$$\text{similarity} = A^2 + \beta A^3 \tag{11}$$

This index requires a little more information of network with low computational cost relatively. However, it is developed to predict links between the node pairs without connection, which ignores direct edges as similarity between linked nodes.

5.2 Simulation Results

The classification of Chinese aviation network by the above seven similarity indexes is carried out. We present the modularity of community detection in Table 2.

The results shown in the table are the best results after adjusting the parameters. We can see from Table 2 that the corresponding modularity value of community detection using the above seven kinds of similarity indexes are generally very low. Among the seven measures, the similarity index proposed by us performs the best with $\alpha = 0.002$. The Katz index performs the next best with $\alpha = 0.003$, and its modularity are close to the best one. The LP index ranks the third with $\alpha = 0.009$, while others, such as the CN index, Jaccard index, and AA index, perform far worse.

Specific community detection result using LS index is presented in Table 3. The Chinese airport cities are expressed by international airport codes (refer to Appendix 1). We can see from Table 3 that several important node cities, such as Beijing(13), Guangzhou(11), and Shanghai(9), are basically divided into different groups. As everyone knows, they are the political and economic center of China. And refer to the result we get in previous works,the most influential city airport and the areas they affected (North China-Beijing, East China-Shanghai, Central China-Changsha, Southern China-Guangzhou, Northwest China-Wulumuqi, Southwest China-Kunming, and Northeast China-Ha'erbin) are consistent with the community division basically. But there are still some suspicious city nodes, for example, Qinhuangdao should not belong to the community which take Xi'an as the center. So further analysis still needs to be explored.

Table 2 The modularity of community detection

Measures	CN	Jaccard	RA	AA	Katz	LP	LS
Modularity	0.0210	0.0147	0.0587	0.0289	0.4428	0.3634	0.4518
Number of community	6	10	4	5	9	9	8

Table 3 Community detection result using LS index

Community	Nodes in community				
1	CAN (11) XMN (41) KWL (46) KHN (77) JJN (124) ACX (130)	ZUH (18) KOW (42) HAK (49) NNG (80) TEN (125)	BHY (19) SWA (43) SYX(50) JUZ(87) MXZ (126)	ZHA (23) SZX (44) JIU (65) WUS (119) WUZ (128)	FOC (40) KWE (45) LZH (71) AEB (121) HZH(129)
2	AQG (8) TXN(56) NKG (79) XUZ (102)	SHA (9) HYN(57) NTG(81) YIW (104)	CZX (26) JGS (63) NGB (82) FUG(120)	HGH (52) JDZ (64) YNZ (88) HSN (127)	HFE (53) LYG (69) WNZ (90) LCX (143)
3	PEK (13) DLC (32) HRB (47) JMU (60) TAO (84) HLH (97)	TSN (15) WEH (33) HEK (48) JNZ (62) YNT (85) XIL (100)	CGQ (21) DAT (34) HLD (51) LYI (70) YNJ (86) NBS (111)	CIH (24) DDG (35) SHE (54) MDG (76) TGO (94) CHG (112)	CIF (30) DOY (36) TNA (58) NDG (83) WEF (96)
4	CSX (20) LYA (73) CGO (107)	HJJ (22) YIH (91) NNY (108)	CGD (25) WUX (98) CKG (109)	WUH (59) ENH (99) LLF (122)	LZO (72) DYG (106)
5	CTU (27) WXN (95) KGT (135)	JZH (28) BPX (110) LZY (148)	LXA (29) PZI (113)	DAX (31) XIC (114)	NAO (78) YBP (115)
6	AKA (6) DSN (38) SJW (89) INC (105) GOQ (147)	XIY (7) UYN (39) YCU (92) HDG (117)	BAU (10) WUA (55) XNN (93) HZG (131)	HET (12) LHW (68) XFN (101) IQN (134)	TYN (14) NZH (74) ENY (103) SHP (142)
7	BSD (16) DLU (116) WNH (139)	KMG (17) LUM (118) ZAT (140)	LJG (66) DIG (123)	JHG (67) LNJ (137)	MIG (75) SYM (138)
8	AKU (1) DNH (37) IQM (141)	KRY (2) JGN (61) YIN (144)	URC (3) HTN (132) KJI (145)	KRL (4) KHG (133) NLT (146)	TCG (5) KCA (136)

6 Concluding Remarks

In this paper, a community partition algorithm based on similarity index is proposed to discover communities in Chinese aviation network. Simulation results on Chinese aviation network demonstrate that our algorithm can obtain the better performance than the other six pre-existing methods. It can achieve better accuracy in community detection with low algorithm complexity for the reason of requiring only the local information of the network. But the community division results are not ideal enough according to the value of modularity. There are still some

suspicious city nodes, for example, Qinhuangdao should not belong to the community which take Xi'an as the center. So the next step we need to continue to explore more effective methods for Chinese aviation network.

Acknowledgments This work was supported in part by the Natural Science Foundation of China Under Grants of 61573199 and 61573200, the Tianjin Natural Science Foundation Grant No. 14JCYBJC18700.

Appendix 1

See Table 4.

Table 4 Three code of Chinese airport city

	City	Acronym		City	Acronym		City	Acronym
1	Akesu	AKU	51	Hailaer	HLD	101	Xiangfan	XFN
2	Kelamayi	KRY	52	Hangzhou	HGH	102	Xuzhou	XUZ
3	Wulumuqi	URC	53	Hefei	HFE	103	Yan'an	ENY
4	Kuerle	KRL	54	Shenyang	SHE	104	Yiwu	YIW
5	Tacheng	TCG	55	Wuhai	WUA	105	Yinchuan	INC
6	Ankang	AKA	56	Huangshan	TXN	106	Zhangjiajie	DYG
7	Xi'an	XIY	57	Huangyan	HYN	107	Zhengzhou	CGO
8	Anqing	AQG	58	Jinan	TNA	108	Nanyang	NNY
9	Shanghai	SHA	59	Wuhan	WUH	109	Chongqing	CKG
10	Baotou	BAV	60	Jiamusi	JMU	110	Changdu	BPX
11	Guangzhou	CAN	61	Jiayuguan	JGN	111	Baishan	NBS
12	Huhehaote	HET	62	Jinzhou	JNZ	112	Zhaoyang	CHG
13	Beijing	PEK	63	Jinggangshan	JGS	113	Panzhihua	PZI
14	Taiyuan	TYN	64	Jingdezhen	JDZ	114	Xichang	XIC
15	Tianjin	TSN	65	Jiujiang	JIU	115	Yibin	YBP
16	Baoshan	BSD	66	Lijiang	LJG	116	Dali	DLU
17	Kunming	KMG	67	Xishuangbanna	JHG	117	Handan	HDG
18	Zhuhai	ZUH	68	Lanzhou	LHW	118	Dehong	LUM
19	Beihai	BHY	69	Lianyungang	LYG	119	Wuyishan	WUS
20	Changsha	CSX	70	Linyi	LYI	120	Fuyang	FUG
21	Changchun	CGQ	71	Liuzhou	LZH	121	Baise	AEB
22	Huaihua	HJJ	72	Luzhou	LZO	122	Yongzhou	LLF
23	Zhanjiang	ZHA	73	Luoyang	LYA	123	Diqing	DIG
24	Changzhi	CIH	74	Manzhouli	NZH	124	Quanzhou	JJN
25	Changde	CGD	75	Mianyang	MIG	125	Tongren	TEN
26	Changzhou	CZX	76	Mudanjiang	MDG	126	Meizhou	MXZ
27	Chengdu	CTU	77	Nanchang	KHN	127	Zhoushan	HSN
28	Jiuzhai	JZH	78	Nanchong	NAO	128	Wuzhou	WUZ

(continued)

Table 4 (continued)

	City	Acronym		City	Acronym		City	Acronym
29	Lasa	LXA	79	Nanjing	NKG	129	Liping	HZH
30	Chifeng	CIF	80	Nanning	NNG	130	Xingyi	ACX
31	Dazhou	DAX	81	Nantong	NTG	131	Hanzhong	HZG
32	Dalian	DLC	82	Ningbo	NGB	132	Hetian	HTN
33	Weihai	WEH	83	Qiqihaer	NDG	133	Kashi	KHG
34	Datong	DAT	84	Qingdao	TAO	134	Qingyang	IQN
35	Dandong	DDG	85	Yantai	YNT	135	Kangding	KGT
36	Dongying	DOY	86	Yanji	YNJ	136	Kuche	KCA
37	Dunhuang	DNH	87	Quzhou	JUZ	137	Lincang	LNJ
38	Eerduosi	DSN	88	Yancheng	YNZ	138	Simao	SYM
39	Yulin	UYN	89	Shijiazhuang	SJW	139	Wenshan	WNH
40	Fuzhou	FOC	90	Wenzhou	WNZ	140	Zhaotong	ZAT
41	Xiamen	XMN	91	Yichang	YIH	141	Qiemo	IQM
42	Ganzhou	KOW	92	Yuncheng	YCU	142	Qinhuangdao	SHP
43	Shantou	SWA	93	Xining	XNN	143	Liancheng	LCX
44	Shenzhen	SZX	94	Tongliao	TGO	144	Yining	YIN
45	Guiyang	KWE	95	Wanzhou	WXN	145	Buerjin	KJI
46	Guilin	KWL	96	Weifang	WEF	146	Nalati	NLT
47	Haerbin	HRB	97	Wulanhaote	HLH	147	Geermu	GOQ
48	Heihe	HEK	98	Wuxi	WUX	148	Linzhi	LZY
49	Haikou	HAK	99	Enshi	ENH			
50	Sanya	SYX	100	Xilinhaote	XIL			

References

1. Raguraman K (1998) Troubled passage to India. Tour Manag 19(6):533–543
2. Newman MEJ (2006) Finding community structure in networks using the eigenvectors of matrices. Phys Rev E 74(3): 036104
3. Kernighan BW, Lin S (1970) An efficient heuristic procedure for partitioning graphs. Bell Syst Tech J 49(2):291–307
4. Fiedler M (1973) Algebraic connectivity of graphs. Czechoslov Math J 23(2):298–305
5. Michelle G, Newman MEJ (2002) Community structure in social and biological networks. Proc Natl Acad Sci 99(12):7821–7826
6. Flake GW, Lawrence S, Giles CL, Coetzee FM (2002) Self-organization and identification of web communities. Computer 35(3):66–70
7. Newman MEJ, Girvan M (2004) Finding and evaluating community structure in networks. Phys Rev E 69(2):026113
8. Newman MEJ (2003) Mixing patterns in networks[J]. Phys Rev E 67:026126
9. Latora V, Marchiori M (2001) Efficient behavior of small-world networks. Phys Rev Lett 87:198701
10. Watts DJ, Strogatz SH (1998) Collective dynamics of small-world networks. Nature 393:440–442
11. Newman MEJ (2002) Assortative mixing in networks. Phys Rev Lett 89:208701–208704

12. Chen Z, Zheng X, Zhang Q (2014) Community detection based on local topological information in power grid. In: International joint conference on neural networks, 170 (C):384–392
13. Jaccard P (1901) Étude comparative de la distribution florale dans une portion des Alpes et des Jura. Bulletin de la Société Vaudoise des Sciences Naturelles 37:547–579
14. Zhou T, Lü L, Zhang YC (2009) Predicting missing links via local information. Eur Phys J B 71(4):623–630
15. Ying P, Li D-H, Liu J-G, Liang J-Z (2010) Detecting community structure in complex networks via node similarity. Phys A 389:2849–2857
16. Adamic LA, Adar E (2003) Friends and neighbors on the web. Social Netw 25(3):211–230

The Transformer Fault Diagnosis Based on AdaBoost Least Square Support Vector Machine

Wenxia Du, Xiuping Zhao, Feng Lv and Hailian Du

Abstract Least square support vector machine integrated with adaptive boost algorithm was applied to the transformer fault diagnosis. In order to obtain the training sample, characteristic gases dissolved in the faulty transformer oil were collected and normalized, then a number of different classifiers are to be constructed though adaptive boost algorithm on the same training set. Subsequently, least squares support vector machine is used as the base classifier, which was fast in calculation and was improved by iteration in classification ability. The fault diagnosis results show that the method was simple and flexible, it has high accuracy rate of fault diagnosis. To a certain extent,this method makes up for the deficiencies of three-ratio method, such as code missing and boundary absolute.

Keywords AdaBoost algorithm · Support vector machine · Fault diagnosis

1 Introduction

Power transformer is the most important electric equipment in power system. The reliable operation of power system is decided by the running state of power transformer. Therefore, it is important to research fault diagnosis technology of the power transformer. There is no function mapping relationship between the gas content and the transformer fault types though analysis of fault mechanism which dissolve gas in transformer oil. The distribution characteristics of gas content are also difficult to predicte. So it is difficult and complicated to diagnose the transformer fault. Artificial intelligence neural network provides a new solution for transformer fault diagnosis. Backpropagation (BP) neural network based on Levenberg–Marquardt algorithm is used in transformer fault diagnosis successfully [1]. RBF neural network is applied to transformer fault diagnosis to solve the problem about dissolved gas analysis [2]. The mapping between fault characteristic

W. Du · X. Zhao (✉) · F. Lv · H. Du
College of Vocational and Technical, Hebei Normal University, Shijiazhuang, China
e-mail: zhaoxiuping07111@sina.com

Y. Jia et al. (eds.), *Proceedings of 2016 Chinese Intelligent Systems Conference*,
Lecture Notes in Electrical Engineering 404, DOI 10.1007/978-981-10-2338-5_51

and fault mode is realized by neural network, because it has a highly nonlinear mapping ability [3–5].

The application of artificial neural network is restricted, because of overfitting and local minimum. At the same time, in order to fault diagnosis and intelligent recognition, a lot of fault data samples and priori knowledge are required.

Support Vector Machine (SVM) based on statistical learning theory overcomes the deficiency of neural network, such as over fitting, local minimum, etc. It has distinct advantages if it is applied to power transformer fault diagnosis [6–10, 11]. SVM is applied to broken rotor bar fault diagnosis of squirrel-cage induction motor. It is trained by fault current samples to obtain the function of classification [6]. Fuzzy support vector machine is applied to transformer fault diagnosis [7]. Gu obtained the fault samples by measuring a variety of motor vibration and stator current signals and used independent component analysis (ICA) method to recover or extract the independent testing, and then got SVM classifier [8].

The algorithm of Least Square Support Vector Machine (LS-SVM) is an extension of SVM algorithm. The inequality constraints in SVM algorithm is transformed into equality constraints due to the loss function of least squares linear system, then corresponding solving process is transformed into solving a set of equality equations, calculating speed is increased. According to characteristics of the transformer, in this paper RBF is regarded as kernel function, the least squares support vector machines based on AdaBoost algorithm is applied to fault diagnosis of power transformers.

2 LS-SVM Algorithm Based on AdaBoost

AdaBoost algorithm is an iterative algorithm. The sample weight adjusts constantly based on the misclassification rate of samples, thereby the data distribution is updated, and multiple different base classifiers from the same original training set could be obtained. Finally, base classifiers are fused as a final classifier to improve the classification accuracy of the algorithm.

2.1 Least Squares Support Vector Machine

The algorithm of least squares support vector machine which is proposed by Suyken is one of the important achievements in statistical learning theory in recent years. It is an extension of the SVM algorithm. For a given training data set (x_i, y_i), where $i = 1, 2, \ldots, l$ $x_i \in R, y_i \in R$, using the nonlinear mapping $\varphi(\cdot)$, original sample space R^n could be mapped into feature space $\varphi(x_i)$, and the optimal decision function in the high-dimensional feature space is constructed,

$$y(x) = \omega \cdot \varphi(x) + b \tag{1}$$

According to the principle of structural risk minimization, the decision function parameters ω and b are determined, it equals to solving the following optimization problem:

$$\min J(\omega, \xi) = \frac{1}{2}\omega \cdot \omega + \frac{1}{2} C \sum_{i=1}^{l} \xi_i^2 \tag{2}$$

Constraints: $y_i = w^T \varphi(x_i) + b + \xi_i, i = 1, 2, \ldots, l.$

Where C is a constant, b is the deviation. The optimization problem needs Lagrangian method to solve

$$L(w, b, \xi, a,) = J(w, \xi) - \sum_{i=1}^{l} a_i (w^T \varphi(x_i) + b + \xi_i - y_i) \tag{3}$$

where a_i (i = 1, 2, …, l) is Lagrange multipliers. By optimizing conditions:

$$\begin{aligned} &\frac{\partial L}{\partial w} = 0 \Rightarrow w = \sum_{i=1}^{l} a_i \varphi(x_i); \\ &\frac{\partial L}{\partial b} = 0 \Rightarrow \sum_{i=1}^{l} a_i = 0; \\ &\frac{\partial L}{\partial \xi_i} = 0 \Rightarrow a_i = C\xi_i; \\ &\frac{\partial L}{\partial a_i} = 0 \Rightarrow w^T \varphi(x_i) + b + \xi_i - y_i = 0 \end{aligned} \tag{4}$$

Define kernel $K(x, x_i) = \varphi(x_i)$, and then optimization problem is transformed into solving the following linear equations:

$$\begin{bmatrix} 0 & 1 & \cdots & 1 \\ 1 & K(x_1, x_1) + \frac{1}{C} & \cdots & K(x_1, x_l) \\ \cdots & \cdots & \cdots & \cdots \\ 1 & K(x_l, x_1) & \cdots & K(x_l, x_l) + \frac{1}{C} \end{bmatrix} \cdot \begin{bmatrix} b \\ a_1 \\ \cdots \\ a_l \end{bmatrix} = \begin{bmatrix} 0 \\ y_1 \\ \cdots \\ y_l \end{bmatrix} \tag{5}$$

Making use of the least square method, regression coefficients a_i and deviation b are calculated. A nonlinear prediction model is got

$$f(x) = \sum_{i=1}^{l} a_i K(x, x_i) + b \tag{6}$$

2.2 AdaBoost Algorithms

AdaBoost is an abbreviation for Adaptive boost. It is an iterative algorithm. First, a weak classifier (class 2 classifications) is got by training with initial weight data. Then according to the classification results increase the weight of misclassified sample, reduce the weight of the sample that is classified accurately. The data distribution is changed by adjusting the weight of the sample data, the new weak classifier is got under the new data distribution, run in circle, and multiple weak classifiers are obtained. Finally, each training classifier overlaps together according to certain right, as the final decision classifier.

Using AdaBoost classifier can exclude some unnecessary training data features; key data is used to train the key classifiers. The algorithm is a process of weak classifier boosting and the classification ability is improved, the theory proves that when a simple classification number tends to infinity, the strong classifier's error rate will tend to zero.

AdaBoost algorithm is specifically described as following:

Let X denotes the sample space, Y shows a sample set of categories to identify. Make $S = \{(X_i Y_i) | i = 1, 2, L, m\}$ as training set, among them $X_i \in X, Y \in_i Y$.

(1) Initialize the weights of samples
Assuming the sample distribution as a uniform distribution: $D_t(i) = 1/m$. $D_t(i)$ represents weights at the t round of iteration sample (X_i, Y_i)

(2) Set the upper limit
The iterations indicated by the variable t, $t = 1, 2, L \ldots, T$ (T represents the upper limit of the number of iterations)

a. Get training sets

According to the sample distribution D_t, Get training set S_t;

b. Trained classifier h_t on the training set S_t;
c. Calculate the Classification error rate

Classifier h_t is used to classify all samples in original training set S. If the result is correct, it will not be included in the error, or record errors, and multiply the t-th classifier X_i corresponding weights, the weighted error on the training set ε_t,

$$\varepsilon_t = \sum_{i=1}^{m} D_t \| y_i \neq h_t(x_i) \| \tag{7}$$

d. Update sample weights

According to the weighted error rate $D_{t+1}(i)$

$$D_{t+1}(i) = \frac{D_t(i)}{Z_i} e^{l} \quad l = \begin{cases} e^{-\alpha_t} & (h_t(x_i) = y_i) \\ e^{\alpha_t} & (h_t(x_i) \neq y_i) \end{cases} \tag{8}$$

where $\alpha_t = \frac{1}{2}\ln\frac{1-\varepsilon_t}{\varepsilon_t}$.

$Z_t = \sum_{i=1}^{m} D_t(i)e^{(-\alpha_t y_i h_t(x_i))}$ is a formal factor, to ensure $\sum_{i=1}^{m} D_t(i) = 1$.

(3) Obtain the final output of strong classifier

By T cycles, there are T weak classifiers, According to refreshed weight overlay, resulting strong classifier's to predict the final output is

$$H(x) = \sum_{t=1}^{T} \alpha_t h_t(x) \tag{9}$$

3 Fault Diagnosis of Power Transformers

3.1 Power Transformer Fault Type

In the process of power transformer operation, carried out by gas chromatography oil dissolved gas analysis (Dissolved Gases Analysis, DGA), by variation of the gas composition and concentration analysis to determine the state in which the transformer is, this technology has become a transformer supervision of the most important and most effective means, and has been widely used. Fault diagnosis for classification of oil-filled power transformers, dissolved gases H_2, CH_4, C_2H_2, $C_2H_42H_6$ as feature parameters, to reduce the influence due to the large difference of the magnitude between them due to the need for the DGA raw data were normalized processing, namely, making the various dissolved gas content converted to the relative content in the range of [0, 1], in order to reduce the mutually exclusion between gas. Internal failure of the main oil-immersed transformer mainly includes overheating fault and fault discharge, under the IEC60599, a common type of fault can be divided into four kinds: low overheating (T1) (t < 300 °C), referred to as low fever; low energy discharge, referred low energy; energy discharge, referred to as high energy; high temperature overheating (T3) (t > 700 °C), referred to as high fever.

3.2 Fault Diagnosis of Power Transformers

The Specific steps of LS-SVM transformer fault diagnosis based on AdaBoost algorithm is as follows:

(1) Selected standard feature samples

From 139 transformer sample data which had clear conclusion and were published publicly in journals, selected 12 standard characteristic sequence of samples, corresponding to four fault types, as shown in Table 1.

Table 1 Standard features of the sequence data

Serial number	H_2	CH_4	C_2H_6	C_2H_4	C_2H_2	Actual failure
1	160	130	33	96	0	Low fever
2	120	120	33	84	0.55	Low fever
3	93	58	37	43	0	Low fever
4	80	53	42	276	18	High fever
5	86	110	18	92	7.4	High fever
6	42	97	157	600	0	High fever
7	980	73	58	12	0	Low energy
8	650	53	34	20	0	Low energy
9	1565	93	34	47	0	Low energy
10	187	240	12	99	47	High energy
11	9.9	2.8	1.0	3.2	3.4	High energy
12	9.2	2.7	1.1	4.0	11.5	High energy

(2) Sample normalization process

DGA data law generally believed change by many factors, such as load, temperature, pressure and the like, and the data itself, the quality of data collected depends on factors such as process equipment or a human, it is usually DGA data need to be normalized, as follows:

$$x_{ij}^{'} = \frac{x_{ij} - x_{i\min}}{x_{i\max} - x_{i\min}} \tag{10}$$

Among them $x_{ij}(i = 1, 2, \ldots, 12; j = 1, 2, L, 5)$ is the original volume fraction data, $x_{i\min}, x_{i\max}$ are the maximum and minimum values of the same sample volume fraction five kinds of gases; $X_{ij}^{'}$ is normalized data after normalized. After conversion, the data values are between 0 and 1.

(3) Construct the input matrix **X**

$$\mathbf{X} = [x_1, x_2 \ldots, x_i, \cdots, x_{12}]^T, x_i = [x_{i1}, x_{i2}, \cdots, x_{ij}, \cdots, x_{i12}]^T$$

(4) Initialization 12 right values of sample

In the sample set, the same number of samples overheat fault and fault discharge, so the initial weight of each sample is

$$D_t(i) = 1/12 = 0.083, \quad i = 1, 2, \ldots, 12$$

(5) Use AdaBoost algorithm to train multiple LS-SVM classifiers
The upper limit of the number of iterations of T = 18

a. Calculate the input matrix of least squares support vector machine X_D

$$X_D = \begin{bmatrix} 0 & 1 & \cdots & 1 \\ 1 & K(D_t(1)x_1, D_t(1)x_1) + \frac{1}{C} & \cdots & K(D_t(1)x_1, D_t(l)x_l) \\ \cdots & \cdots & \cdots & \cdots \\ 1 & K(D_t(l)x_l, D_t(1)x_1) & \cdots & K(D_t(l)x_l, D_t(l)x_l) + \frac{1}{C} \end{bmatrix}$$

$$l = 1, 2, \ldots, 12$$

b. Construction output vector Y

$$Y = [0 \quad 0.5658 \quad 0.5658 \quad 0.5658 \quad 0.8058 \quad 0.8058 \quad 0.8058 \quad 1.2692 \quad 1.2692 \quad 1.2692 \quad 0.9546 \quad 0.9546 \quad 0.9546]$$

Vector elements Y correspond to the type of fault in Table 1.

c. Calculate the parameter vector θ

$$\theta = [b \quad a_1 \quad \cdots \quad a_t]^T$$

According to the formula $\theta = \left(\mathbf{X}_D^{\mathrm{T}}\mathbf{X}_D\right)^{-1}\mathbf{X}_D^T\mathbf{Y}$, obtaining regression coefficients a_i and bias b

d. Get classifier

$$h_t = \sum_{\mathbf{i}=\mathbf{1}}^{\mathbf{l}} \mathbf{a_i}\mathbf{K}(\mathbf{x}, \mathbf{x_i}) + \mathbf{b}$$

e. Calculate the Classification error rate

According to formula (7) calculate the weighted error rate samples ε_t

f. Determine whether to end the loop

If iterations are less than the upper limit value T, then return to a), otherwise exit the loop and continue to (6).

(6) Obtain the LS-SVM classifier

According to formula (10) eventually least square support vector machine classifier.

(7) Test samples to be diagnosed

The sample to be tested according to formula (9) is normalized, substituting into Eq. (10) to obtain an output, and find the closest value to the output y_i, the fault type of the sample belongs to i.

4 Fault Diagnosis Examples

A standard assumption in the classical control theory is that the data transmission required by the control or state estimation algorithm can be performed with infinite precision. However, due to the growth in communication technology, it is becoming more common to employ digital limited capacity communication networks for exchange of information between system components.

In the example, c and σ using cross-validation get the optimal parameters $c = 50, \sigma = 3$.

Diagnosis Example 1
A main transformer by gas chromatography analysis of dissolved gases in oil. The various gas contents (10^{-6}),

$$H_2 = 57, CH_4 = 77, C_2\mathrm{H}_6 = 19, C_2H_4 = 21, C_2H_2 = 0$$

The code of three ratios is 021, diagnosed as medium temperature overheat. The sample to be tested according to the above steps for processing, got the $f = 0.5832$, from the results we can see $f = 0.5832$ the closest $y_2 = 0.5658$, to determine the initial failure of the transformer: low heat. After having core examination it was found to be insulated wire overheating.

Diagnosis Example 2
Two main transformers by gas chromatography analysis of dissolved gases in oil, measured various gas contents (10^{-6})

$$H_2 = 36, CH_4 = 30, C_2H_6 = 10, C_2H_4 = 93, C_2H_2 = 7.1;$$

this set of data encoding is not found in the three-ratio encoding, application of LS-SVM algorithm diagnosis was: the corresponding output value of 1.0345, approximately equal to $y_6 = 0.9546$, a transformer fault diagnosis is high temperature; the practical investigation, all with the actual match.

5 Conclusion

Based on the measurement of dissolved gases in transformer oil, the sample pairs of input and output data are constructed. In order to obtain stronger classifier, the multiple different base-classifiers are obtained using AdaBoost algorithm on same

training set, the function of classification is completed by the least square support vector machines. The whole diagnostic process is time-saving and reliable. The diagnostic results of transformer examples show that the effectiveness and reliability of diagnostic method has greatly improved than that of three-ratio method, it plays a better role in guiding on-site analysis.

Acknowledgments This work has been partly supported by Natural Science Foundation of Hebei Province (NO. F2014205115), Hebei Education Department Program (ZD2016053, Z2011141), Major Foundation of Hebei Normal University (L2013Z06), Hebei Province Science and Technology Department Program (13201711D, 11215650).

References

1. Qiang W, Zhang, Heng W et al (2011) LM algorithm based on BP network in fault diagnosis of transformer. Electr Prot Control Syst 39(8): 100–103
2. Hongqi W, Nina Z, Chun-ying W (2010) Fault diagnosis based on RBF neural network and MATLAB simulation transformer. Sci Technol Eng, 10(5):1249–1251
3. Sheng L, Peilin Z (2014) Bing and other quantum BP neural network in the engine fault diagnosis. Chin Mech Eng (16) doi:10.3969 ISSN.1004–132X. 2014.16. 005
4. Zheng Z, Lina G, Shanshan Z (2014) Application of neural network technology for transformer fault diagnosis fuzzy. Consumer Electron (20). doi:10.3969, ISSN1674-7712. 2014.20.064
5. Yang, Jin L, Jing Z BP neural network in fault diagnosis of transformer. Transformers 46 (1):71–74
6. Squirrel—cage motor fault diagnosis support vector machine. J Sci Instrum 25 (6):738–741
7. Choi XY, Ching C (2010) Transformer fault diagnosis based on fuzzy support vector machine. Beijing Jiaotong University 36 (1):117–121
8. Yu G, Jinhui Z (2005) Intrusion detection method based on independent component analysis and support vector machine. Xi'an Jiaotong University 08:876–879
9. Xiaoyan C, Bing SL, Yang W (2014) Fault diagnosis based on neural network. Electron Softw Eng 1:211–211
10. Chao Zhang (2012) Tuha oilfield SVM-based diesel engine fault diagnosis. Value Eng 9:31–32

Evolution and Spread of Public Opinion in Structured Multi-agent Systems

Qiaoyu Li, Chunyan Zhang and Zengqiang Chen

Abstract This paper investigates the evolution and spread of public opinion by the aid of evolutionary game theory. Moreover, we employ the complex networks to model the interactions between the members of the multi-agent systems. For one specific opinion, we assume that three roles exist in the population: supporter, objector, and neutral. And, the supports and objectors will try to persuade the neural to adopt their strategies, in the form of game theory. The supports and objectors will make strategy updating according to the payoff-based updating rules. The findings on complex networks (BA scale-free networks) reveal that the initial distribution of the opinions and the adoption probability of the neutral players would be two important factors for the spread and evolution of opinions.

Keywords Multi-agent system · Evolutionary game theory · Opinion dynamics · Complex networks

1 Introduction

The swarm behaviors of multi-agent systems have attracted an increasing attention of researchers from multiple disciplines these years. Inspired by the phenomenon in nature, the swarm intelligence resulted by the self-organization of the individuals in the multi-agent systems, is indeed a puzzle and remains a hot topic for the researchers [1–4]. Along this line, past research has identified that the relationships among the individuals can be effectively described by the complex networks. The

Q. Li · C. Zhang (✉) · Z. Chen
Department of Automation, College of Computer and Control Engineering,
Nankai University, Tianjin 300071, China
e-mail: zhcy@nankai.edu.cn

Q. Li · C. Zhang · Z. Chen
Tianjin Key Laboratory of Intelligent Robotics, Nankai University,
Tianjin 300071, China

Y. Jia et al. (eds.), *Proceedings of 2016 Chinese Intelligent Systems Conference*,
Lecture Notes in Electrical Engineering 404, DOI 10.1007/978-981-10-2338-5_52

integration of the microscopic patterns of interactions among the agents composing a large population provides us with a way to model the reality more relevantly.

Moreover, the rapid expansion of online social networks, such as friendships networks, increase the importance of the question: how do opinions form in a social network [5, 6]? The opinion of each person is influenced by many factors such as her friends, family members, profession, etc. Understanding such interactions and predicting how specific opinions spread throughout social networks has triggered vast research in multiple areas or disciplines [7, 8].

The past decade has witnessed the contributions of researchers who focus on the opinion dynamics and spread among the multi-agent systems. There is a rich and still growing literature on this topic. One of the frequently used models is the two-state voter model [9], in which a randomly selected agent imitates the state of one of her neighbors. Through evolution process, this update is repeated until the consensus state occurs in the studied finite system. Then, further studies of the voter model on heterogeneous networks, found that the system could approach consensus by a two-stage process of quick evolution to an opinion-homogeneous state followed by a diffusive evolution to final consensus. Besides, another classical description for consensus formation is the Ising model with zero-temperature Glauber kinetics [10]. In this setting, a randomly selected agent imitates the state of the majority in her neighborhood. Notably this updating is beneficial for agreement, however consensus does not necessarily arise [11]. Another often-used model for the opinion dynamics is the majority rule [12–14]. In this setting, each member of the system faces the choice of two distinct opinions. The opinions evolve by the following two steps: first, randomly pick a group of agents with fixed odd size; this group is an arbitrary set of agents in the mean-field limit, or a contiguous group for finite spatial dimension. Second, all agents in this group adopt the local majority state. These two steps are repeated until achieving the unanimity of opinions [15].

Further, in the bounded confidence model of continuous opinion dynamics proposed by Deffuant et al. [16], agents can affect each other's opinion if the opinions in question are already sufficiently close enough. Under this setting, a parameter of tolerance threshold is introduced, thus to limit the influence between the agents with difference in opinion larger than the threshold. Then along this line, several variants of the model have been inspired and proposed in [15, 17].

Notably, to understand and predict how specific opinions spread throughout social networks, cross-over study of game theory and opinion dynamics have also been established [18, 19]. Among these studies, the process by which opinions spread through a network can be thought of as a networked interaction game: each individual obtains information from certain number of agents in her local neighborhood, and adapts her opinion to increase her benefit [20, 21]. In spite of ample progress that has been accumulated recently, there are situations of practical relevance that remain less explored, including the model settings in the framework of game theory which is used in analyzing opinion dynamics [22–24]. In our proposed game model of opinions, we have made new assumptions about the referred payoffs in the pairs of persuader-adopter, (non)persuader- adopter, persuader-(non)adopter, and (non)persuader-(non)adopter. Moreover, the payoff matrix between the support-

ers and neutral players is different with that which describes the game playing of objectors and neutral agents. Along this line, there are two types of games employed in the system, and opinion spread occurs between any pair of game players.

In this paper we focus on the opinion dynamics in the framework of game theory which describes the process of strategy spread. Section 2 of this paper develops the framework of the models. Sections 3–4 then presents the major analytical results. Section 5 summarizes and provides conclusions.

2 Model Description

Basically, the aim of most opinion models is to establish some potential local dynamical rules from individual level, and provide hints for opinion spread among the multi-agent system, especially the special steady state of global evolution and synchronization. Inspired by the effective roles of game theory in describing strategy evolution, our focus is also put on using evolutionary games to model the local dynamical rule, i.e., how agents update their opinions through the strategy evolution.

Following the traditional assumption, we employ a group of agents who join in the opinion interaction, with edges representing interacting relations among them. In the simulation, the social networks on which the opinion evolution takes place could be described by different type of complex networks. For simplicity, we focus on the static networks during the opinion interaction. Consider a group of agents among whom some process of opinion formation takes place, and the schematic diagram is shown below for a clear description about the game playing and opinion spread under consideration.

To establish this game model, in the following we will specify players of the game, their available strategies (opinions), payoff of each option, as well as evolving rules for evolutionary games. For one specific opinion, we assume that there are three roles exist in the population: the supporters, objectors and the neutral players. We assume that the game occurs between the determined players (i.e., the supporters and objectors) and the neutral agents. In the framework of networks, the determined agents (i.e., supporters and objectors) exchange their opinions with their directed linked neighbors in the interaction networks. Thus through the game interaction, the supports and objectors have chances to persuade the neural neighbors to adopt their strategies (opinions).

Considering the fact that supporters and objectors have determined perceptions, while the uncertainty of the neutral will influence the spread of this specific opinion in the population. In this case, we assume that the supports and objectors will try to persuade the neural agents to adopt their strategies, in the form of game theory. From the above payoff matrix (Fig. 1), we can see that the persuader will receive a benefit $\omega - c_{A1}$ if the neutral neighbor adopts her strategy and gains the payoff of $r - c_{B1}$ accordingly. Otherwise, if the neutral neighbor does not adopt her strategy,

B	A (Supporter or objector)	
	Persuade	Not Persuade
Adopt	$(W\text{-}C_{A1}/P_A, r\text{-}C_{B1})$	$(VP_A, r\text{-}C_{B1}\text{-}C_{B2})$
Not Adopt	$(-C_{A1}/P_A, -C)$	(0,0)

Fig. 1 The schematic diagram of the interactions between the group members holding the three opinions respectively. Thus three roles exist in the population: the supporters, objectors, and the neutral agents. Games are played by the determined players (i.e., supporters and objectors) and the neutral agents. Strategy updating takes place among the interacted determined players (i.e., denoted by *green* and *blue nodes*)

the persuader will gain the payoff $\frac{-c_{A1}}{p_A}$, and the neutral agent will get the payoff of $-c$. The other case is that the determined players (i.e. the supporters and objectors) do not take the action of persuading. In this case, the two situations of the neighboring neutral players need to be considered. One is that the determined player will receive the payoff vp_A, if the neutral player adopts the determined player's strategy and her payoff is thus $r - c_{B1} - c_{B2}$. Another one is that the neutral player does not adopt this determined player's strategy, and in this case, their payoffs are both 0 as listed in the Fig. 1.

Notably, we assume that the supporters and objectors representatively play different type of games with the neutral players. It is understandable that the supporters may be keener on persuading the neutral agents to adopt their opinions, may be the rumor, to gain higher benefits. In this sense, the payoff matrix given by Table 1 is a general one, and the values of the parameters will be endowed in the following analysis to distinguish these two types of roles: supporters and objectors (Fig. 2).

Besides, it is a reasonable assumption that the supports and objectors will gather and calculate their payoffs after the game playing with the neutral agents. It should be noted that the determined players on some topic of interest also need to make strategy updating within the evolution process according the given rules. Such kind of modeling can closely describe the spread of opinion within the population. The wide variety of existing models assumes that the opinions are updated over repeated interactions among neighboring agents. Different models assume different rules of opinion adaptation, such as imitation, averaging over people with similar opinions, following the majority, or more sophisticated equations.

Initially each player is designated either as a supporter or objector with equal probability unless stated otherwise, and players obtain their payoffs by means of pairwise interactions with their partners. But the strategy of each player could change

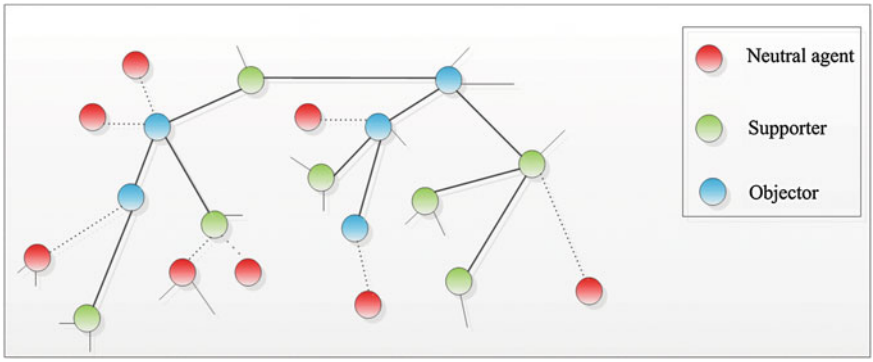

Fig. 2 The schematic diagram of the interactions between the group members holding the three opinions respectively. Thus three roles exist in the population: the supporters, objectors, and the neutral agents

during a simulation due to payoff-based learning. Herein we assume that at each time step, an individual is chosen at random to update either its opinion or neighborhood according to the following rule:

$$W(s_x \to s_y) = \frac{P_{total}(y) - P_{total}(x)}{Dk_{max}} \tag{1}$$

where $D = \max\{P_{total}(y) - P_{total}(x)\}$, $k_{max} = \max\{k_x, k_y\}$, and k_x and k_y are the connectivity numbers of player x and y. Player x will randomly select one player y from her adjacent k_x neighbors. Given the total payoffs ($P_{total}(x)$ and $P_{total}(y)$) from the previous round, x will adopt y's strategy s_y with a probability depending on the payoff difference.

3 Replicate Dynamics Analysis

Let us first concentrate on a well-mixed population of sufficiently large size, and combine game theory and population dynamics in a replicator equation. In the continuous-time model, the evolution of the frequency x_i of the strategy i is given by the following replicator equation:

$$\dot{x}_i = x_i(p_i - \bar{p}) \tag{2}$$

where $\bar{p} = x_a p_a + (1 - x_a)p_b$ is the average payoff in the population, and correspondingly p_i is the payoff of strategy i. This payoff is determined by the inter-actions in

randomly formed groups of cooperators and defectors. This way, in our model, we have assumed that the determined players (i.e. the supporters and objectors) persuade the neutral neighbor with a probability of p. Meanwhile, the neutral player will adopt the persuader's opinion with a probability of q, and otherwise keep her own neutral strategy with a probability of $1 - q$. The analysis by the aid of replication dynamics is given as follows.

Role I: As for the determined players who face the strategy choices of persuading and not persuading.

Here, we adopt the parameter U_A to be the payoff of persuaders who take the action of persuading:

$$U_A = q(\omega - \frac{c_{A1}}{p_A}) + (1-q)(-\frac{c_{A1}}{p_A}) = q\omega - \frac{c_{A1}}{p_A} \tag{3}$$

and then U'_A denotes the payoff of persuaders who do not take the action of persuading,

$$U'_A = qvp_A \tag{4}$$

Thus the expected payoff of a determined player is given by the following equation,

$$\bar{U}_A = pU'_A + (1-p)U'_A = pq\omega - p\frac{c_{A1}}{p_A} - (1-p)qvp_A \tag{5}$$

Since the strategy updating driven by payoffs will occur through the evolution, we take the $p(t)$ as the fraction of persuaders in the determined players. According to the replicate dynamics of the evolutionary system, we can get

$$F(p) = \frac{dp}{dt} = p(U_A - \bar{U}_A) = p(1-p)[q(\omega - p_A v) + \frac{c_{A1}}{p_A}] \tag{6}$$

Then the results depend on the parameters values, which are discussed as follows:

(1) If $q = \frac{-c_{A1}}{p_A(\omega - p_A v)}$, $F(p) \equiv 0$. In this case, all the composition of the two opinions (persuading and not-persuading) are the steady states for the system.

(2) If $q \neq \frac{-c_{A1}}{p_A(\omega - p_A v)}$, $F(p) = 0$ will lead to two steady states of the system: $p = 0$ and $p = 1$.

After the calculation of $\frac{dp}{dt} = (1-2p)[q(\omega - p_A v) + \frac{c_{A1}}{p_A}]$, we can get the following results under different cases:

(1) If $0 < q < \frac{-c_{A1}}{p_A(\omega - p_A v)}$, it will result $\frac{dF(p)}{dp}\,|_{p=0} > 0$ and $\frac{dF(p)}{dp}\,|_{p=1} > 0$. Under this situation, $p = 0$ is the evolutionary stable state which means that all the determined players take the action of not persuading.

(2) If $\frac{-c_{A1}}{p_A(\omega - p_A v)} < q < 1$, we will get $\frac{dF(p)}{dp} |_{p=0} > 0$ and $\frac{dF(p)}{dp} |_{p=1} < 0$. Under this situation, $p = 1$ is the evolutionary stable state which means that all the determined players take the action of persuading.

Role II: As for the neutral players who face the strategy choices of adopting and not adopting.

Similarly, we adopt the parameter U_B to represent the payoff of persuaders who take the action of adopting:

$$\bar{U}_B = p(r - c_{B1}) + (1 - p)(r - c_{B1} - c_{B2}) = r - c_{B1} - (1 - p)c_{B2} \tag{7}$$

and U'_B denotes the payoff of neutral agents who do not take the action of adopting,

$$U'_B = -pc \tag{8}$$

Thus the expected payoff of a determined player is given by the following equation,

$$\bar{U}_B = qU_B + (1 - q)U'_B = qr - qc_{B1} - q(1 - p)c_{B2} - (1 - p)pc \tag{9}$$

According to the replicate dynamics mentioned above, we can analysis the steady state of the system involving adopters and non-adopters in the following way.

$$F(q) = \frac{dq}{dt} = q(U_B - \bar{U}_B) = q(1 - q)[p(c_{B2} + c) - (c_{B1} + c_{B2} - r)] \tag{10}$$

Then the results depends on the parameters values, which are discussed as follows:

(1) If $p = \frac{c_{B1} - c_{B2} - r}{c_{B2} + c}$, $F(q) \equiv 0$. In this case, all the states of the two strategies are all the stead states for the system.

(2) If $p \neq \frac{c_{B1} - c_{B2} - r}{c_{B2} + c}$, $F(p) = 0$ will lead two steady states of the system: $q = 0$ and $q = 1$.

After the calculation of $\frac{dq}{dt} = (1 - 2q)[q(c_{B2} + c) - (c_{B1} + c_{B2} - r)]$, we can get the following results under different cases:

(1) If $r > c_{B1} + c_{B2}$, we can get that $\frac{dF(q)}{dq} |_{q=0} > 0$ and $\frac{dF(q)}{dq} |_{q=1} < 0$. Under this situation, $q = 1$ is the evolutionary stable state which means that all the determined players take the action of adoption.

(2) If $r < c_{B1} + c_{B2}$ and $0 < p < \frac{c_{B1} + c_{B2} - r}{c_{B2} + c}$, it leads to $\frac{dF(q)}{dq} |_{q=0} < 0$ and $\frac{dF(q)}{dq} |_{q=1} > 0$. Thus $q = 0$ is the evolutionary stable state which means that all the determined players take the action of not adopting.

(3) If $r < c_{B1} + c_{B2}$ and $\frac{c_{B1}+c_{B2}-r}{c_{B2}+c} < p < 1$, it leads to $\frac{dF(q)}{dq} |_{q=0} > 0$ and $\frac{dF(q)}{dq} |_{q=1} < 0$. Thus $q = 1$ is the evolutionary stable state which means that all the determined players take the action of not adopting.

4 Simulation Results

We consider the opinion dynamics where each player is connected to her nearest neighbors. In addition, isolated vertices and duplicate links are not allowed. Initially, individuals located on a BA scale-free network are uniformly assigned to the vertices randomly. Specially, we distinguish the population by four types of players: supporting-persuading (NP) players, supporting-notpersuading (SNP) players, objecting-persuading (OP) players, objecting-notpersuading (ONP) players. As for the payoffs, we adopt the following values: persuader i will receive a benefit $4 - \frac{1}{1+p_i}$ if the neutral neighbor adopts her strategy. Otherwise, if the neutral neighbor does not adopt her strategy, the persuader will gain the payoff $\frac{-1}{1+p_i}$. If the determined players do not persuade the neutral players, she will get the payoff of $2p_i$ if the neutral players adopt her strategy. Otherwise, she will get the payoff of 0. The process will be repeated until a stationary state is reached, where the distribution of strategies does not change any more. Typically we run each simulation for 10^6 steps. For each parameter combination we ran 100 replicate simulations. The results reported are averages over these replicates.

The results in Fig. 3 suggest that the initial fraction of supporters in the population will significantly influence the evolution dynamics. For a fixed and small

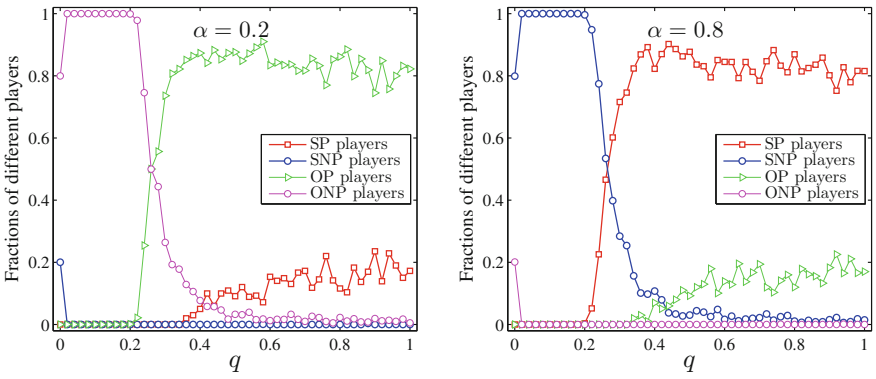

(a) $\alpha = 0.2$ (b) $\alpha = 0.8$

Fig. 3 The final distribution of the four types of players in the system, in dependence on the adoption probability q and the initial fraction α of supporters in the population. NP: supporting-persuading players, SNP: supporting-notpersuading players, OP: objecting-persuading players, ONP: objecting-notpersuading players. Parameters: population size $N = 1000$, $D = \max\{P_{total}(y) - P_{total}(x)\} = 4$

(e.g., $q < 0.2$) adoption probability q of the neutral agents, $\alpha = 0.2$ will result in a steady state dominated by ONP players, while $\alpha = 0.8$ will lead to a state dominated by SNP players. For a fixed and large (e.g. $q < 0.4$) adoption probability q of the neutral agents, $\alpha = 0.2$ will result in a coexistence state of OP (in the majority) and SP (in the minority) players. However under the condition of $\alpha = 0.8$, OP players get the dominance over the SP players who coexist with them in the final system. Notably, the roles of other key parameters, such as the population size N and the frequency of the strategy updating, are worthy of further investigation.

5 Conclusions

We have studied the evolution of opinions in the spatial opinion game where the determined players (i.e., the supporters and objectors) and the neutral agents join in. Successful persuading will help improve the benefits of persuaders and thus be beneficial for the spread of her opinion. In this case, the payoffs of the two types of opinion holders (i.e., the supporters and objectors) will change through the game playing. In order to achieve this, we have assumed that four types of players: supporting-persuading (NP) players, supporting-notpersuading (SNP) players, objecting-persuading (OP) players, objecting-notpersuading (ONP) players. We have found that the initial distribution of these players will significantly influence the evolution an spread of opinions. Besides, the adoption probability of the neutral agents also affects the spread of the opinions. In summary, we conclude the payoff matrix which describes the opinion spread between the determined players and the neutral players may have more influences on the evolution of cooperation. The interaction between the determined players and the learning network should also be given more attention.

References

1. Maes P (1994) Modeling adaptive autonomous agent. Artif Life 1(3):135–162
2. Reynolds G (1987) Flocks, birds and schools: a distributed behavioral model. Comput Graph 21(1):25–34
3. Wooldrige M, Jennings NR (1995) Intelligent agents: theory and practice. Knowl Eng Rev 10(2):112–152
4. DeGroot MH (1974) Reaching a consensus. J Am Stat Assoc 69(345):118–121
5. Kenett DY, Perc M, Boccaletti S (2015) Networks of networks-an introduction. Chaos, Solitons Fractals 80:1–6
6. Gao JX, Barzel B, Barabsi A (2016) Universal resilience patterns in complex networks. Nature 530(7291):307–312
7. Acemoglu D, Ozdaglar A (2011) Opinion dynamics and learning in social networks. Dyn Game Appl 1(1):3–49
8. Liang HL, Linag H, Yang Y, Wang X (2013) Opinion dynamics in networks with heterogeneous confidence and influence. Physica A 392(9):2248–2256

9. Liggett TM (1985) Introduction. In: Interacting Particle Systems. Springer, New York, pp 1–5
10. Glauber RJ (1963) Time-dependent statistics of the Ising model. J Math Phys 4(2):294–307
11. Spirin V, Krapivsky PL, Redner S (2001) Fate of zero-temperature Ising ferromagnets. Phys Rev E 63(3):036118
12. Galam S (1999) Application of statistical physics to politics. Physica A 274(1):132–139
13. Chen P, Redner S (2005) Consensus formation in multi-state majority and plurality models. J Phys A Math Gen 38(33):7239
14. Chen P, Redner S (2005) Majority rule dynamics in finite dimensions. Phys Rev E 71(3):036101
15. Krapivsky PL, Redner S (2003) Dynamics of majority rule in two-state interacting spin systems. Phys Rev Lett 90(23):238701
16. Deffuant G, Neau D, Amblard F (2000) Mixing beliefs among interacting agents. Adv Complex Syst 3:87–98
17. Ben-Naim E, Krapivsky PL, Redner S (2003) Bifurcations and patterns in compromise processes. Physica D 183(3):190–204
18. Ghaderi J, Srikant R (2013) Opinion dynamics in social networks: a local interaction game with stubborn agents. In: American Control Conference (ACC), pp 1982–1987
19. Ding F, Liu Y, Li Y (2009) Co-evolution of opinion and strategy in persuasion dynamics: an evolutionary game theoretical approach. Int J Mod Phys C 20(3):479–490
20. Di Mare A, Latora V (2007) Opinion formation models based on game theory. Int J Mod Phys C 18(9):1377–1395
21. Ding F, Liu Y, Shen B (2010) An evolutionary game theory model of binary opinion formation. Physica A 18(9):1745–1752
22. Nowak MA, Bonhoeffer S, May R (1996) Robustness of cooperation. Nature 379(9):125–126
23. Smith JM, Price GR (1973) The logic of animal conflict. Nature 246:15–18
24. Nowak MA, May RM (1992) Evolutionary games and spatial chaos. Nature 359:826–829

Proposal Generating Method Using Geometrical Features for Vehicle Detection

Wanzeng Cai, Zhengfa Liang, Xiaolong Liu and Hengzhu Liu

Abstract Region proposal methods have been widespreadly applied in object detection, which aim to use less bounding boxes to cover the potential objects. In this paper, we propose to use geometrical features of the proposals to improve the performance of vehicle detection. Two kinds of method are exploited to the geometrical features: (1) regression analysis technique is used to estimate each proposal's score, where the higher score indicates higher possibility of the proposal containing an object; (2) geometrical constraints are applied on these features to improve the recall with less proposals. Experiments are conducted on the KITTI dataset for vehicle detection. The results show that our method achieves a recall of 98 % at IoU of 0.5 with only 1000 proposals, which outperforms the state-of-the-art algorithms.

Keywords Region proposal · Vehicle detection · Regression analysis · Geometrical constraints

1 Introduction

The goal of vehicle detection is to recognize whether the object is a vehicle or not and determines its location in an image. Most traditional detection methods use the sliding windows paradigm [1–3] in which the object classification is performed at every location and scale in an image. Sliding window detector probably generates 10^4-10^5 windows per image, and the number of windows grows exponentially with the scale of image. Modern detection datasets [4–6] still require the prediction of object aspect ratio, the search space increases up to 10^6-10^7 windows per image, which heavily restricts the computation speed.

W. Cai (✉) · Z. Liang · X. Liu · H. Liu
School of Computer Science, National University of Defense Technology, Changsha 410073, China
e-mail: zengzeng2016@sina.com

Y. Jia et al. (eds.), *Proceedings of 2016 Chinese Intelligent Systems Conference*, Lecture Notes in Electrical Engineering 404, DOI 10.1007/978-981-10-2338-5_53

In order to boost the performance of object detection, effective framework for object detection has been proposed. Instead of evaluating over a large number of candidate subwindows, a set of region proposals is first generated with the goal to reduce the set of positions that need to be further analyzed. The benefits of region proposals are discussed in [7–12]. Intuitively, the regions of interests have some same features which can be used to distinguish them from the background. Therefore, one can design or train a method to generate a number of proposals which can contain objects we are interested in. The result of the method is that, given an image, outputs a fewer number of region proposals than sliding window method and reaches better recall rate. It is helpful to speed up the detection velocity for the classifier.

In this paper, we concentrate on region proposals for vehicle detection. Edge Box [13] is a very fast and efficient region proposal method, which can generate millions of candidate boxes in a fraction of one second, and achieve over 96 % recall at overlap threshold of 0.5 by using just 1000 proposals on the PASCAL VOC dataset [6] for all classes. The concept of Edge Box is to use the edge information of object for scoring. It is obvious that many boxes with high score may not really contain vehicles. The result is that the recall is not very satisfactory for vehicles tested on the KITTI dataset, only reach 90 % at overlap threshold of 0.5 by using 1000 proposals. To solve this problem, we apply some geometrical features of proposals to regression analysis and train a model to rescore each box. Besides, the geometrical constraint is also used to improve the performance of vehicle detection. The results of our method can reach over 98 % recall at overlap threshold of 0.5 given just 1000 proposals and reduce about half number of proposals on KITTI moderate dataset [14]. As far as we know, the KITTI dataset is harder than the PASCAL VOC dataset.

2 Related Work

Region proposal method is aimed at searching for regions of interest, just like interest point detectors [15, 16]. Currently, the region proposal methods are divided into two categories [17]: grouping proposal methods and window scoring proposal methods.

2.1 Grouping Proposal Methods

Grouping proposal methods first split an integrated image into many fragments, and then use the similarity of some features (color, size, texture, gradient and so on) to merge these fragments. The significant grouping proposal methods are shown as follows:

SelectiveSearch [18] first gets the original regions through graph-based image segmentation [19], and then merges the original regions using hierarchical grouping algorithm, finally uses selective search to estimate the possible position of the object. SelectiveSearch has been widely used as the proposal method by many state-of-the-art object detectors, including the R-CNN and Fast R-CNN detectors [7, 8].

CPMC [20] generates and ranks objects hypotheses in an image using bottom-up processes and mid-level cues. The object hypotheses are extracted automatically by solving multiple constrained parametric min-cuts (CPMC) with different seeds and unary terms, and ranked by training a model to predict how plausible the hypotheses are.

MCG [21] proposes a fast normalized cuts algorithm and high performance hierarchical segmenter. Segment are merged by grouping strategy based on edge magnitude, and the resulting hypotheses are ranked using features such as location, shape and size.

2.2 Window Scoring Proposal Methods

Window scoring proposal methods generate a large number of bounding boxes and score each box using some features of the object. A box is more likely to cover an object with higher score. This approach is always fast but the localization accuracy is lower than the grouping methods. The common three methods are shown as follows:

Objectness [22] is one of the earliest window scoring proposal method. The method trains a model to distinguish objects from background. An initial set of proposals is generated from salient locations in an image, and then is scored according to characteristics of objects, such as color, edge density, saliency and so on.

Bing [23] also trains a measure to produce a small set of proposals, which can speed up the traditional sliding window object detection paradigm. The author find that objects with closed boundary can be well distinguished, and the normed gradients feature that is binarized can be used to estimate the reliability of proposals.

RandomizedSeeds [24] enables an efficient selection of proposals that contain object, which uses multiple randomized SEED superpixel maps [25] to score each proposals. The scoring is done using a simple metric similar to "superpixel straddling" from Objectness [22], no additional cues are used. The authors show that using multiple superpixel maps significantly improves recall and leads to higher speed.

3 Approach

In this section, we propose a novel approach to reduce the object proposals. As the number of invalid boxes in an image is huge, we must be able to select candidates efficiently. The geometrical features extracted from candidate regions can be used to

discriminate two types of boxes. We build a model to rescore each box using regression analysis. Moreover, the geometrical constraint is used to eliminate the useless bounding boxes.

3.1 Regression Analysis Prediction

Regression analysis method uses mathematical statistics to build a prediction model based on the observations. After the observation of many proposals generated by Edge Box [13], we find some geometrical features of proposals can be used to distinguish some boxes that contain vehicles from the other boxes that may not contain vehicles. There is no doubt that the regression analysis can be used for discriminating two kinds of boxes. We use geometrical features of proposals as independent variable and use the label of proposals as dependent variable for regression analysis, and build a model to predict weather a box should be reserved or removed. We first search for the independent variable, and then determine the dependent variable.

a. **Aspect ratio**

Vehicles are rigid objects with relatively regular shape like a rectangle. The size of all vehicles is almost same, which means their aspect ratio has a certain range. Hence, we can use the aspect ratio of boxes as an independent variable.

The bounding box is defined by its upper left coordinate (x_l, y_t), width w_b and height h_b. The aspect ratio of boxes is calculated as follows:

$$box_{AspectRatio} = \frac{w_b}{h_b} \tag{1}$$

b. **The relationship between distance and area**

Depth information has been utilized for object detection in recent years, which can be computed from disparity map or directly measured by depth sensors, such as Kinect. Actually, the depth data represents the distance information in real word. According to the optical imaging principles, we know that the actual area A_T and the imaging area A_I of the object have a certain relationship.

As shown in Fig. 1, by using the homothetic triangle theory, the relationship between A_T and A_I is described as follows:

$$A_T = \frac{d^2}{v^2} A_I \tag{2}$$

where d is the object distance, v is the camera focal length. To simplify the calculation, we assume that the A_T and v are fixed or in a certain range. Hence, the Eq. (2) is converted as follows:

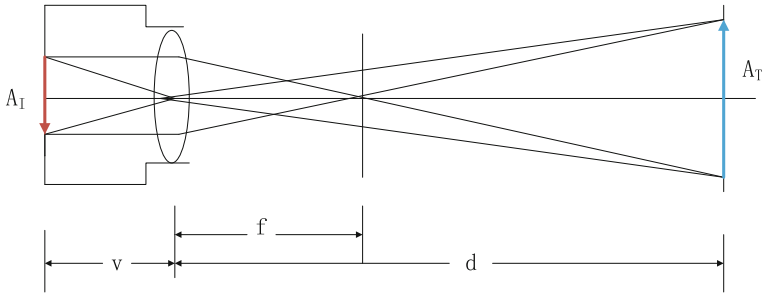

Fig. 1 The imaging principle of the camera

$$A_I = \frac{A_T v^2}{d^2} = \frac{C}{d^2} \pm \varepsilon \tag{3}$$

where $A_I = \text{box}_{\text{area}} = w_b * h_b$ is the number of pixels in a bounding box, ε is the bias of the area range. The object distance d can be computed from disparity map. The KITTI dataset provides the left image and the right image. We first use stereo matching algorithm MeshStereo [26] to get the disparity map from left image and right image, and then calculate the depth according to binocular vision theory. The binocular vision theory is:

$$\text{depth} = \frac{f \times b}{\text{disparity}} \tag{4}$$

where f is the focal length of the two lenses, b is the distance between the two optical centers, and disparity is the horizontal disparity of two stereo-corresponding points. After calculating all pixel points' depth for each image, we compute the average depth in a 3×3 pixel region of the bounding box center to represent the object distance, that is:

$$d = \text{box}_{\text{depth}} = \frac{1}{9} \sum_{x_i = x_c - 1}^{x_c + 1} \sum_{y_i = y_c - 1}^{y_c + 1} \text{depth}(x_i, y_i) \tag{5}$$

where $\text{depth}(x_i, y_i)$ is the depth of point (x_i, y_i) $x_c = x_l + w_b/2$ and $y_c = y_t + h_b/2$ is the coordinate of box central point.

From Eq. (3), we know that $A_I \times d^2$ is constant, which means the relationship between A_I and d can be used to distinguish vehicles from the other object. Therefore, we use $A_I \times d^2$ as another independent variable.

c. **Bounding box score**

Edge Box [13] first sliding image with different scale of windows to generate a large number of boxes, and then score all of the boxes using edge features of the

object. As the object is likely to fall into a box with high score, we can also use the score of boxes as independent variable. The score is calculated as follows:

$$S_b^{in} = S_b - \frac{\sum_{p \in b^{in}} m_p}{2(w_b^{'} + h_b^{'})^k} \tag{6}$$

where S_b is the whole box's score, $p \in b^{in}$ is the pixel in bounding box, m_p is edge magnitude, the values of the $w_b^{'}$ and $h_b^{'}$ is $w_b/2$ and $h_b/2$ respectively, k is used to offset the bias of larger boxes having more edges on average, and S_b^{in} is the score of a whole box minus a quarter of box center.

After the independent variables of regression analysis are determined, we then search for the dependent variable of regression analysis. We divide the boxes generated by Edge Box into two categories: one is the Intersection over Union (IoU) with ground truth over 0.5 and labeled 1, and the other is the IoU with ground truth less than 0.5 and labeled 0. The label (1 or 0) is used as the dependent variable.

3.2 Geometrical Constraints

From the previous section, we know that the distance and the area of an object have a certain relationship, but it is only used as a feature and combined with another features. After the statistic on a large number of labeled bounding boxes contained vehicles, the distribution of the relationship between the distance and area is shown in Fig. 2 and the typical fitted curve is presented. In this section, the relationship between the distance and area is separated as a constraint to remove some boxes which may not cover vehicles.

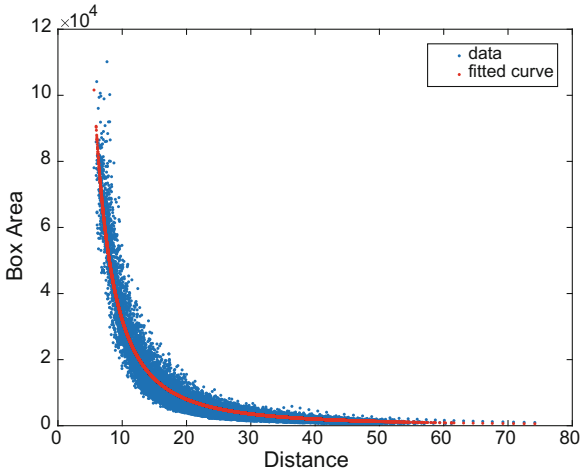

Fig. 2 Fitting result. *Blue point* is the data of box area and distance, *red curve* is the fitted result

In Eq. (3), the image area A_I and the distance d are calculated by $w_b * h_b$ and Eq. (5) respectively. The value of C and ε can be determined by fitted curve. If the value of the area and distance of a bounding box satisfy Eq. (3) with an acceptable error, the box will be considered to be more possible to contain a vehicle and then preserved. Otherwise, the box will be removed. This method can significantly reduce the number of bounding boxes and improve the recall rate.

4 Experiments and Analysis

In this section, we verify the effectiveness and the accuracy of our method in comparison to the Edge Box for vehicle detection. We evaluate our method on the KITTI moderate dataset [14], which contains 7481 right and 7481 left images, all results on variants and different method are reported on the left training labeled image set.

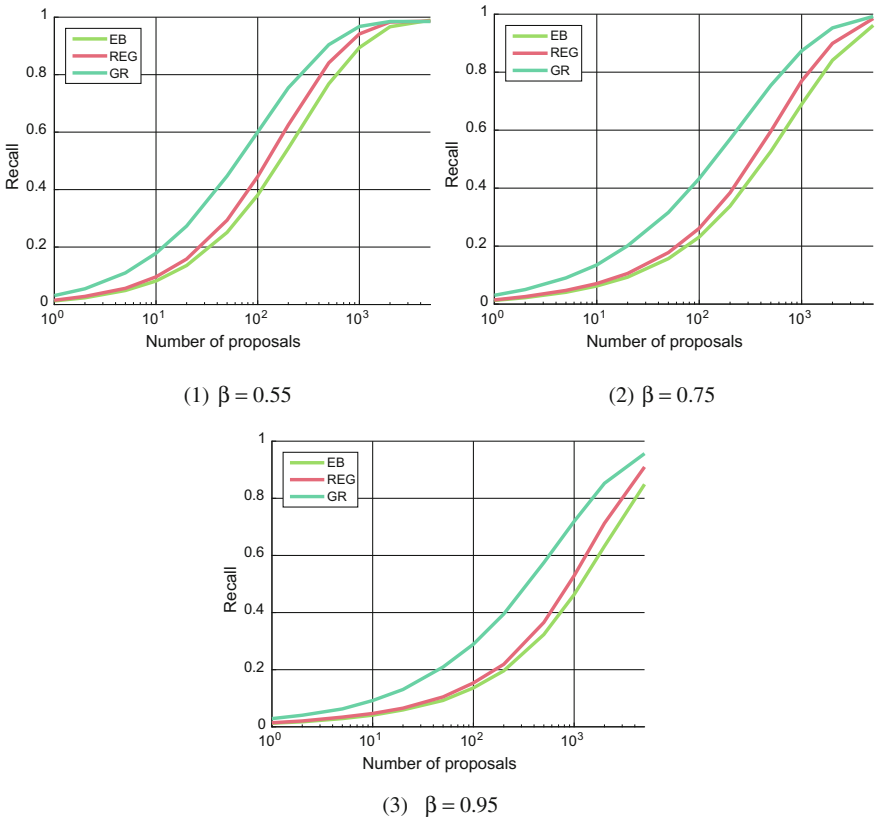

Fig. 3 The result of different methods and NMS threshold used compared to Edge Box

We set up the same parameters as the Edge Box [13]. The parameters $\alpha = 0.65$ and $\beta = 0.55, 0.75, 0.95$ that control the step size of the sliding window search and the NMS threshold. The accuracy of a bounding box is typically measured by using the IoU, which computes the intersection of a bounding box and the ground truth box divided by the area of their union. When evaluating the performance of an object detection algorithm, an IoU threshold of 0.5 is generally used to estimate whether a detection is correct or not [6].

We calculate the area and distance of every ground truth box labeled with 'Car'. And then plotting these points in the two-dimensional coordinate system, x-axis is distance, y-axis is area. Finally, we fit a curve using Matlab according to the Eq. (3). The fitted curve is shown in the Fig. 2. The result of the parameters is $C = 3.1975 \times 10^6$, $\varepsilon = 1.12 \times 10^4$.

And then, we use the random forest regression to build a prediction model. Moreover, the model is applied to rescore every box. The score of box is either

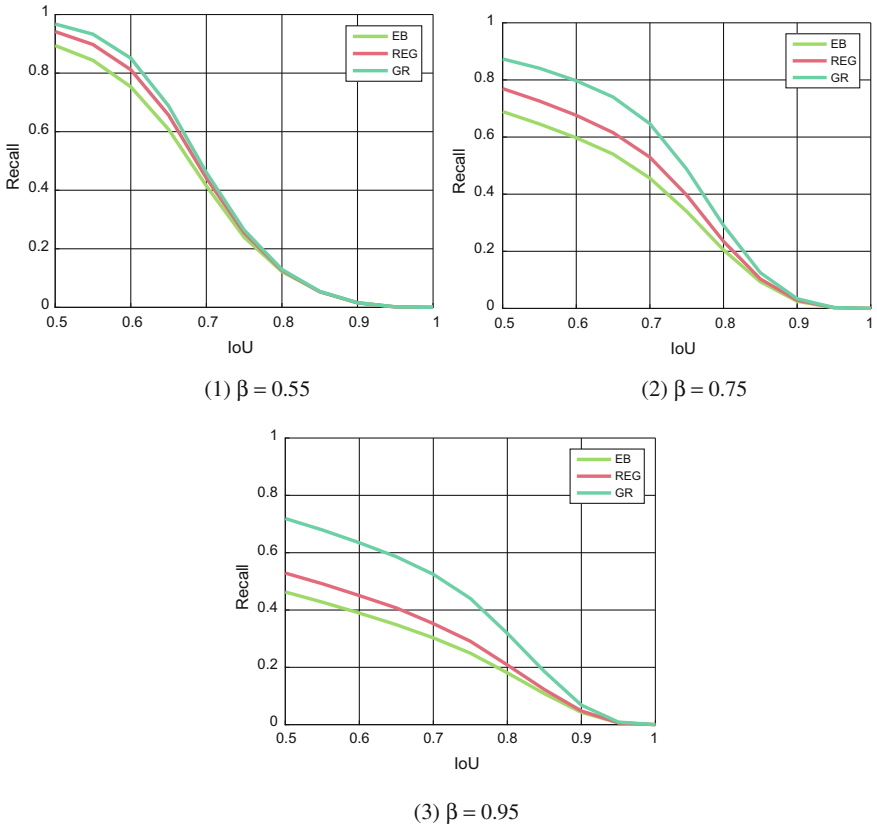

(1) $\beta = 0.55$ (2) $\beta = 0.75$

(3) $\beta = 0.95$

Fig. 4 The recall versus intersection over union for various methods, the number of proposals is 1000

positive or negative after prediction, we select the boxes with positive score. The reason is that the boxes with positive score is more likely to contain vehicles.

Figure 3 shows the recall when varying the NMS threshold β for different numbers of proposals and different method, the IoU threshold is set to 0.5. EB is Edge Box [13], REG is the regression analysis, and GR is the geometrical relationship between distance and area used. As shown in Fig. 3, when we used the regression analysis to remove some bounding boxes, the recall is improved a little, but when the relationship between distance and area of vehicles is used at the same time, the recall is significantly improved. Especially when the number of proposals is 10^3, NMS threshold is 0.95, the recall approximately achieves 30 % higher than the Edge Box.

Although the IoU threshold of 0.5 is typically used to estimate the performance of an object detector [6], but the IoU threshold of 0.5 is quite loose. Even if an object proposal is produced with an IoU threshold of 0.5 to the ground truth, the detection score maybe worse. As a result, the value of the IoU threshold greater than 0.5 is generally desired. To verify the performance of our method for various IoU thresholds on KITTI moderate dataset, we plot the IoU-Recall using 1000 bounding boxes, the result is shown in Fig. 4.

Figure 4 shows the change of recall with the different IoU threshold and different method. The recall of our method is still better than the Edge Box [13] at any IoU threshold, but we can see that when IoU threshold exceeds 0.65, the recall is less than 80 %, which means our method is still not so well when a vehicle detector requires the IoU threshold over 0.5.

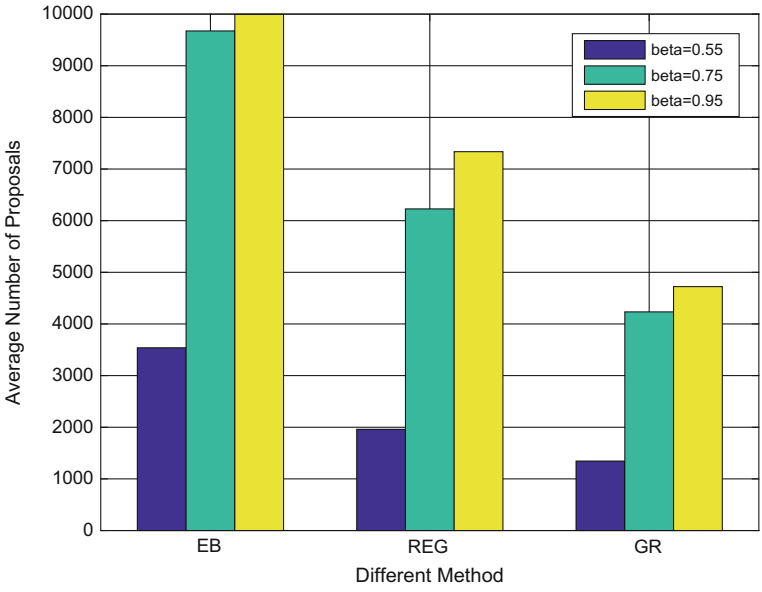

Fig. 5 The average number of proposals versus different NMS threshold and method

Due to that the goal of our method is not only to improve the vehicle detection recall, but also to reduce the number of candidate proposals. We calculate the average number of proposals generated from an image at different NMS thresholds for different methods, the result is shown in Fig. 5.

As shown in Fig. 5, we can see that the higher values of NMS threshold, the more bounding boxes are generated. Although the recall is only improved a little when using regression analysis method, but the number of boxes is largely reduced. More specifically, the number of proposals is decreased into half at any NMS threshold when both of our methods are used. Hence, our method can remarkably reduce the number of proposals, which is very helpful to reduce the computational cost.

5 Conclusion

In this paper, we proposed an effective method to improve recall and reduce the number of proposals for vehicle detection. Regression analysis technique is used to rescore each box, and boxes with lower score are removed. Meanwhile, geometrical constrains are applied to improve the recall with less proposals. We eliminate the boxes with higher score calculated by Edge Box [13] but not really contain vehicles. The results demonstrate that the accuracy of our method for vehicle detection is significantly improved compared to Edge Box, and the number of proposals is also reduced. However, the recall is still worse when the IoU threshold exceeds 0.65, which may affect the performance of vehicle detection. In future, we plan to further improve the recall for vehicle detection and apply our methods to actual vehicle detectors.

References

1. Dalal N, Triggs B (2005) Histograms of oriented gradients for human detection. In: CVPR, vol 1, pp 886–893
2. Forsyth D (2010) Object detection with discriminatively trained part-based models. IEEE Trans Software Eng 32(9):1627–1645
3. Viola P, Jones MJ (2004) Robust real-time face detection. Int J Comput Vision 57(2):137–154
4. Deng J, Dong W, Socher R et al (2009) Imagenet: a large-scale hierarchical image database. pp 248–255
5. Lin TY, Maire M, Belongie S et al (2014) Microsoft COCO: common objects in context. In: Computer Vision—ECCV 2014. Springer International Publishing, pp 740-755
6. Everingham M, Eslami SMA, Gool LV et al (2014) The pascal, visual object classes challenge: a retrospective. Int J Comput Vision 111(1):98–136
7. Girshick R (2015) Fast R-CNN. Comput Sci 2015
8. Xiaoyu W, Ming Y, Shenghuo Z et al (2015) Regionlets for generic object detection. IEEE Trans Pattern Anal Mach Intell 37(10):17–24
9. Girshick R, Donahue J, Darrell T et al Rich feature hierarchies for accurate object detection and semantic segmentation. Comp Sci 580–587

10. Szegedy C, Reed S, Erhan D et al (2014) Scalable, high-quality object detection. Comput Sci
11. Cinbis RG, Verbeek J, Schmid C (2013) Segmentation driven object detection with Fisher vectors. In: IEEE international conference on computer vision, pp 2968–2975
12. He K, Zhang X, Ren S et al (2014) Spatial pyramid pooling in deep convolutional networks for visual recognition. IEEE Trans Pattern Anal Mach Intell 37(9):1904–1916
13. Zitnick CL, Dollár P (2014) Edge boxes: locating object proposals from edges. In: Computer Vision—ECCV 2014, pp 391–405
14. Geiger A (2012) Are we ready for autonomous driving? The KITTI vision benchmark suite. In: IEEE conference on computer vision and pattern recognition, pp 3354–3361
15. Mikolajczyk K, Tuytelaars T, Schmid C et al (2005) A comparison of affine region detectors. Int J Comput Vision 65(1–2):43–72
16. Tuytelaars T, Mikolajczyk K. (2007) Local invariant feature detectors: a survey. Found Trends Comput Graph Vis 3(3):177–280
17. Hosang J, Benenson R, Dollar P et al (2016) What makes for effective detection proposals? IEEE Trans Pattern Anal Mach Intell 38(4):6644–6665
18. Uijlings JRR, Sande KEAVD, Gevers T et al (2013) Selective search for object recognition. Int J Comput Vision 104(2):154–171
19. Felzenszwalb PF, Huttenlocher DP (2010) Efficient graph-based image segmentation. Int J Comput Vision 59(2):167–181
20. Carreira J, Sminchisescu C (2010) Constrained parametric min-cuts for automatic object segmentation. In: Conference on Computer Vision and Pattern Recognition. pp 3241–3248
21. Arbelaez P, Pont-Tuset J, Barron J et al (2014) Multiscale combinatorial grouping. In: IEEE Conference on computer vision and pattern recognition. pp 328–335
22. Alexe B, Deselaers T, Ferrari V (2010) What is an object?. In: 2010 IEEE Conference on Computer Vision and Pattern Recognition (CVPR). IEEE, pp 73–80
23. Cheng MM, Zhang Z, Lin WY et al (2014) BING: binarized normed gradients for objectness estimation at 300fps. In: IEEE conference on computer vision and pattern recognition. IEEE Computer Society. pp 3286–3293
24. Bergh MVD, Boix X, Roig G et al (2015) SEEDS: superpixels extracted via energy-driven sampling. Int J Comput Vision 111(3):298–314
25. ScienceOpen (2013) SEEDS: Superpixels Extracted via Energy-Driven Sampling
26. Zhang C, Li Z, Cheng Y et al (2015) MeshStereo: a global stereo model with mesh alignment regularization for view interpolation. In: IEEE international conference on computer vision. IEEE, pp 2057–2065

Abnormal Event Detection Based on Crowd Density Distribution and Social Force Model

Yaomin Wen, Junping Du and JangMyung Lee

Abstract In this study, we proposed a new method for the detection of abnormal event based on the social force model (SFM), combined with the local density information of the crowd. The method extracts the local density of the people based on the feature point clustering algorithm. The Latent Dirichlet Allocation (LDA) model is established based on the bag of words method combined with the temporal and spatial features of visual words, then identify the abnormal event using the maximum likelihood function.

Keywords Social force model · Feature point clustering · LDA model · Maximum likelihood

1 Introduction

With the improvement of people's living standard and consumption level, travel as a kind of leisure consumption people generally choose, especially during the holidays, many tourist attraction are overcrowded and congestion has become a common problem faced by the various scenic spots. Such as: a serious stampede event on January 1, 2014 in Shanghai caused by the large flow and crowded has brought a serious loss. In order to accelerate the development of the wisdom of

Y. Wen · J. Du (✉)
Beijing Key Lab of Intelligent Telecommunication Software and Multimedia,
School of Computer Science, Beijing University of Posts and Telecommunications,
Beijing 100876, China
e-mail: junpingdu@126.com

Y. Wen
e-mail: 18782950298@163.com

J. Lee
Department of Electronics Engineering, Pusan National University, Busan, Korea
e-mail: jmlee1@pusan.ac.kr

Y. Jia et al. (eds.), *Proceedings of 2016 Chinese Intelligent Systems Conference*,
Lecture Notes in Electrical Engineering 404, DOI 10.1007/978-981-10-2338-5_54

tourism industry, the identification and prediction of the abnormal event is very necessary.

The traditional detection method of crowd abnormal event is divided into two categories, one is based on the characteristic of pedestrian abnormal behavior [1] and the other is based on the global characteristic [2]. In the area of high traffic scenarios, because of the complexity of the scene and the mutual shielding effect of the crowd, local abnormal behavior monitoring is difficult. In the global characteristic detection method, the social force is often used to measure the congestion level of the crowd [3]. In the traditional SFM based abnormal event detection algorithm [4], it takes into account the movement of people in the crowd, but it does not consider the distribution information of the crowd and the influence of crowd density on social force calculation which simply assume all the particle mass and aggregate parameters as a constant [5].

In this paper, we proposed a weighted SFM based on the combination of local density features [6] and SFM, then established the visual LDA model to detection the abnormal event [7]. Finally, the performance of the proposed method is evaluated on the publicly available datasets from UMN and PETS.

2 Proposed Abnormal Event Detection Method

For the scenic environment is complex, the particle mass and aggregation parameter setting of the traditional SFM is not reasonable, we proposed a weighted SFM based on the combination of local crowd density and SFM. The higher the local density, the impact of pedestrians will be higher and the quality of the particles will be bigger. We use multi frame overlay method to associate the spatial and temporal feature of the frames and the pressure of the crowd. The process of the proposed abnormal event detection methods are shown in Fig. 1.

The steps of abnormal event detection method are as follows:

(1) Preprocess video frames to reduce the interference of background noise, using Gaussian Mixture Model (GMM) to get the crowd foreground, extracting the feature points in the crowd foreground. Use the feature clustering algorithm based on feature point density by SVR regression to obtain each cluster crowd density.
(2) According to the frame size, each frame is divided into n * n grids, each grid is regarded as a moving particle, and the motion vector of each particle is calculated by the block matching method.
(3) The panic factor and particle quality of SFM is affected by the crowd density, and obtained the crowd pressure based on the weighted SFM.
(4) To use LDA, we partition the force flow into blocks of T frames which we refer as clips, next, from each clip we extracted the visual words. We pick visual words of size $n \times n \times T$ from locations, then detection the abnormal event based on maximum likelihood.

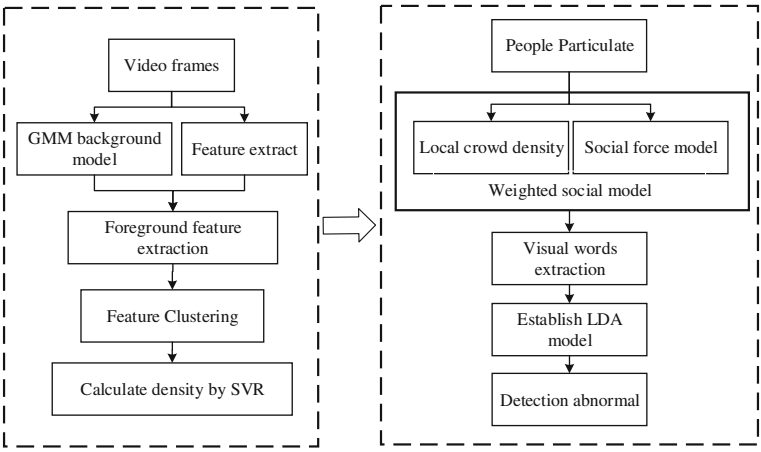

Fig. 1 Process of the proposed abnormal event detection method

2.1 Local People Density Extraction Using Feature Point Clustering

Considering the complex environment of scenic spot, we use GMM model to extract the foreground. GMM is an adaptive hybrid Gauss model for background extraction, in the process of Gauss background maintenance, each pixel in an image of a scenic spot can be represented by a mixture of K Gauss components. The probability of J in the image at the moment t is x_t.

$$p(x_t) = \sum_{i=1}^{k} w_{i,t} \times \eta(x_t, \mu_{i,t}, \tau_{i,t}) \tag{1}$$

where $w_{i,t}$ represents the weight of the Gauss component of I in the model of the pixel J, *and* $\eta(x_t, \mu_{i,t}, \tau_{i,t})$ denotes the t moments of the first i Gauss distribution, $\mu_{i,t}$ denotes its mean value, $\delta_{i,t}^2$ denotes the variance, and I is the 3D unit matrix.

Then we use the SURF algorithm to extract the feature points in the foreground. After extracting the foreground feature points, we use the density based clustering algorithm to cluster the feature points and obtain the density through the number of clusters and the cluster area (Fig. 2).

We regard the distance between cluster centers and the camera as camera distance d, building sample with PETS dataset S1.L1.13 and S1.L2.13. We made regression prediction based on SVR, and produced 400 training samples. Through the training samples, we calculate the population density of each cluster by Eq. (2).

$$\rho_{\text{people}} = f(n_{\text{surf}}, d, s) \tag{2}$$

Fig. 2 Crowd foreground feature point extraction and clustering

where n_{surf} denotes the number of feature points, d denotes the distance between cluster center and the camera, and s denotes the area of cluster. We set up the mapping between cluster areas, feature points, camera distance feature number, and the crowd density.

2.2 Abnormal Event Detection Based on Weighted Social Force Model

2.2.1 The Extraction Process of the Particle Feature

Optical flow method is widely used in crowd motion feature extraction. However, the traditional optical flow method estimates the motion for each pixel, which is inefficiency. In order to reduce the computing time, we use the block matching method to extract motion vector which divides the frames into 16 * 16 size block.

Just as Fig. 3b shows, we divide the UMN dataset frames of 480 * 480 into 30 * 30 blocks with the size of 16 * 16. We obtain the motion vectors of crowd after block matching. Based on the motion vectors, we can compute the crowd weighted social force of each frame.

2.2.2 The Process of Traditional Social Force Model

The traditional SFM is a pedestrian dynamics model which has been widely accepted. This model is proposed by Helbing first. In this model, the pedestrians are attracted by the targets and have a driving power, meanwhile, they are also been repulsed by the other pedestrians and obstacles, always keeping a safe distance with the surroundings. The algorithm of this model is shown in Eq. (3).

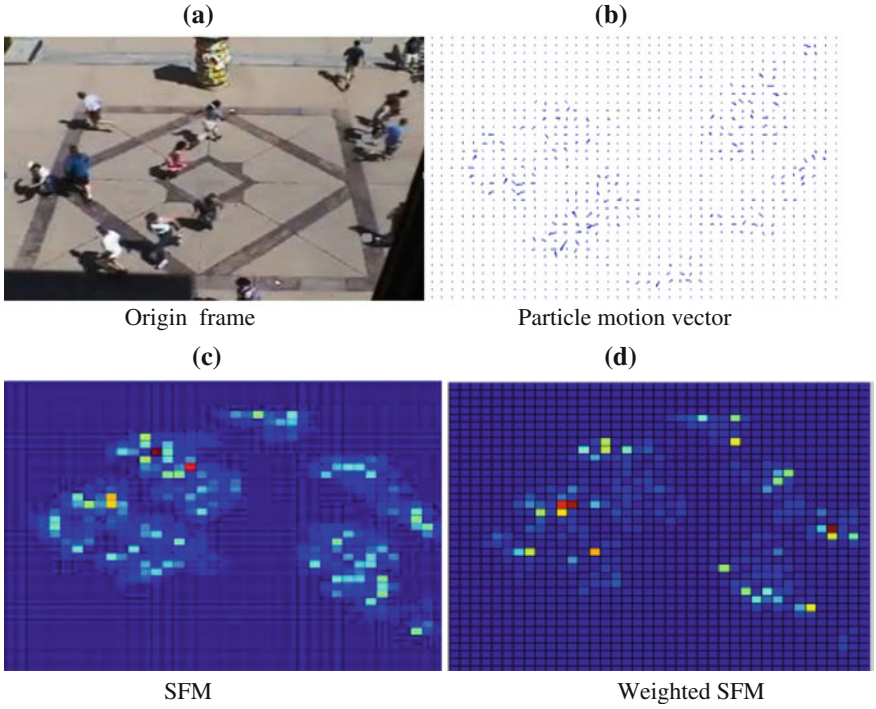

Fig. 3 Particle motion vector and the pressure graph of SFM and weighted SFM

$$m_i \frac{dv_i(t)}{dt} = F_p + F_{\text{int}} \tag{3}$$

where F_P is the personal expectation reaction and computed in Eq. (4).

$$F_P = m_i \frac{v_i^0(t) - v_t(t)}{\tau_i} \tag{4}$$

where m_i is the quality of pedestrians, v_i^0 denotes the movement velocity pedestrians expected, v_t denotes the actual speed limited by environment and τ_i is the time parameter which modifies the velocity feedback, F_{int} is the interaction force between pedestrians. The resultant social force of pedestrians is shown as follows.

$$F_{\text{social}} = m_i \frac{v_i^0(t) - v_t(t)}{\tau_i} + \sum_{i \neq j} f_{ij}, \tag{5}$$

where $f_{i,j}$ is the interaction force between pedestrian i and j.

2.2.3 The Proposed Weighted Social Force Model

For different people have different expected speed, the crowd in a high degree of aggregation, the movement of pedestrian crowd tends to the desired speed field. In place of the low degree of aggregation, people tend to be more independent movement. We use $\overline{V_i^c}$ to denote the average velocity field. The real-time speed v_i denote pedestrians. The desired velocity of crowd is shown in Eq. (6).

$$v_i^0 = (1 - p_i)v_i + p_i\overline{V_i^c} \tag{6}$$

The p_i denotes the aggregation degree for pedestrian i, considering the computational efficiency we use block matching method to estimate motion vector, where $O(x_i, y_i)$ denotes the motion vector of particle i. $O_{\text{ave}}(x_i, y_i)$ is the average emotion vector in particle field, the social interaction force F_{int} is shown in Eq. (7).

$$F_{\text{int}} = \frac{dv_i}{dt} + \frac{1}{\tau}p_i(O(x_i, y_i) - O_{\text{ave}}(x_i, y_i)) \tag{7}$$

The relationship between flow state, crowd density and velocity is denoted as $Q(p) = \rho V(\rho)$, the ρ denotes the crowd density, $V(\rho)$ is the crowd motion under density ρ, $Q(\rho)$ is the crowd flow state. For the traditional SFM, the value of m_i and p_i is assumed as constant, however, the higher the local density, the higher the degree of aggregation, and the particle quality is larger. Therefore, we relate the local crowd density and the quality parameters to the aggregation parameters, and calculate the weighted social forces.

$$F_{\text{int}} = \frac{dv_i}{dt} + \frac{k\rho_i}{\tau}(O(x_i, y_i) - O_{\text{ave}}(x_i, y_i)) \tag{8}$$

As shown in the Eq. 8. We introduce the local density ρ_i into the calculation of the interaction force of the crowd.

For the abnormal event, it is generally accompanied by a sudden change in crowd density; therefore, we can use the local density change to represent the stability of the crowd. The density change information can be integrated into the SFM. For the representation of local density, when the change rate is 0, the weighted SFM is equal to the traditional SFM, when the rate of change of the linear growth, the growth of pressure is slightly higher than density changes, so we use the exponential function to present the weighted SFM.

$$P = e^{\left|\frac{d\rho}{dt}\right|^{\alpha}} \cdot (F_{\text{int}} + F_p) \tag{9}$$

We test the UMN dataset to compare the pressure calculation graph between SFM and weighted SFM as shown in Fig. 3.

From the Fig. 3, we can see the weighted SFM based on crowd local density gets a good performance in inhibiting the effect of environmental noise because of the adopting of local crowd density, the pressure detection has better performance compare to traditional SMF. When the abnormal event occurs, the sudden change of the crowd density can be monitored, and the crowd abnormal event detection is more effective based on the weighted SMF.

2.2.4 Abnormal Event Detection Based on LDA Model

In the proposed model, we consider the effect of local crowd density on social forces, however, the threshold of social force is different in different scenarios. In the two-way pedestrian fellow, the social force threshold is higher than that in the one-way channel. Therefore, we take the successive frames of visual words into account, introducing the spatial and temporal characteristics in order to make the weighted SMF adapt to different environments. We use the UMN normal dataset as a training set, the pressure map as a block of ten, for each of the 10 frames, we extract their visual words on the pressure map, the visual word size is n * n * T.

After extracting the visual words, we use the K-means algorithm to cluster the visual words and get the visual dictionary. We use UMN normal dataset to set up visual corpus $D = \{D_1, D_2, D_3 \ldots D_n\}$ and the theme model of the normal frames with LDA. Using the modified Expectation Maximization (EM) algorithm, we approximate the bag of words model to maximize the likelihood of corpus as Eq. (10).

$$\varphi(\alpha, \beta) = \sum_{j=1}^{M} \log_p(D_j \mid \alpha, \beta) \tag{10}$$

α, β is the parameter of LDA model which is calculated by the EM algorithm, through this model, we estimate the maximum likelihood $\varphi(\alpha, \beta)$ of each frame. We set a threshold for the maximum likelihood value, when the frame block exceeds this threshold, we mark the ten frames as the abnormal frame.

3 Experiment and Analysis

3.1 Experimental Results of the UNM and PETS Abnormal Datasets

We use two sequence datasets in experiment, one from University of Minnesota and another from PETS. The resolution ratio of videos in UMN dataset is 320 * 214. It

Fig. 4 Abnormal scenes in the meadow, indoor, and square of UMN dataset

Fig. 5 Two abnormal scene sequences of PETS dataset

contains 3 indoor and outdoor scenes, 11 sequences, and a total of 7736 frames, as shown in Fig. 4. The resolution ratio of videos in PETS dataset is 768 * 576. And it contains 2 different scenes, 756 frames in total, as shown in Fig. 5. In both datasets, crowds suddenly scattered in all directions after a period of normal movement.

We use three-dimensional data of 5 * 5 and 10 to create a visual dictionary, visual words are extracted from the 10th frame of the video frame sequence. The final dictionary includes 10 topics trained from LDA model. We test the proposed method on the UMN and PETS datasets.

As the result shown in Table 1, the weighted SFM obtain a better events detection result in the PETS and UMN datasets. We use the precision, recall and total rate of correctness to judge the detection result which is shown in Table 2.

As shown in Table 2, compared with the baseline and the SFM, the proposed weighted SFM model is more accurate and reliable because the weighted SFM not only using local density to represent the parameters, which makes the model more accuracy, but also considering the change of local density, which archives better exclusion of useless information.

Table 1 The statistics of abnormal event detection using the PETS and UMN

Scenes		UMN 1		UMN 2		UMN 3		PETS	
Baseline		Normal	Abnormal	Normal	Abnormal	Normal	Abnormal	Normal	Abnormal
SFM	Normal	719	67	706	3	756	23	334	14
	Abnormal	0	39	85	99	21	55	0	27
Weighted SFM	Normal	719	53	718	1	761	18	333	9
	Abnormal	0	53	73	101	16	60	1	32

Table 2 Comparion of precision and recall rate of abnormal event detection

Datasets	Algorithms	Precision	Recall	Total rate of correctness
UMN 1	SFM	1	0.3679	0.9188
	Weighted SFM	1	0.5000	0.9358
UMN 2	SFM	0.5380	0.9706	0.9015
	Weighted SFM	0.9519	0.9902	0.9171
UMN 3	SFM	0.7237	0.7051	0.9348
	Weighted SFM	0.7895	0.7692	0.9602
PETS	SFM	1	0.6585	0.9627
	Weighted SFM	0.9722	0.7805	0.9733

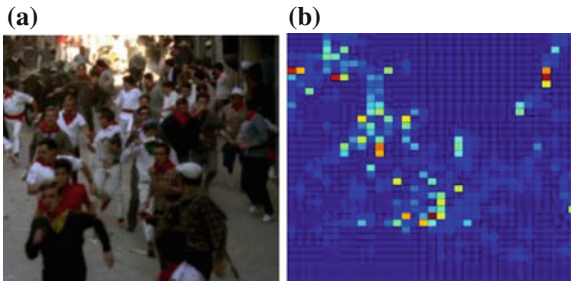

Fig. 6 Test of scenic spot video using the proposed abnormal event detection method

3.2 Experimental Results of a Scenic Spot Video on Website

We use a web scenic spot video to test the weighted SFM, as shown in Fig. 6, in the upper left and right, the pressure color is deeper because of higher density. And in the middle of the pressure figure, because the crowd movement rapidly, the pressure color is deeper than both sides of the crowd.

The relationship between true positive rate (TPR) and false positive rate (FRR) is widely used in the judgment of abnormal event detection methods. Generally through calculating the area under the ROC curve (Area Under the Curve, AUC) to judge the algorithm, the value of AUC closer to 1, the better the performance of the abnormal event detection algorithm.

As shown in the Fig. 7, the calculated values of AUC are: optical flow: 0.8713, SFM: 0.9242, and weighted SFM: 0.9665. Compared with the optical flow method and the SFM, the proposed weighted SFM for abnormal event detection is more accurate and reliable, because the weighted SFM model not only using the local density to represent SFM parameters, but also taking the change of crowd local density into the model, which archives better exclusion of useless information and enhance the scene change information.

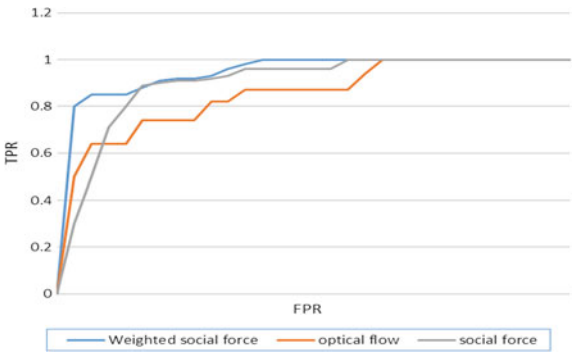

Fig. 7 The ROC of abnormal event detection

4 Conclusions

We proposed the weighted SFM which combines the local density information and social interaction force model based on the concept of fluid dynamics. Established the LDA model with the visual dictionary and integrating the temporal and spatial characteristics of the frames, then identify the abnormal event based on maximum likelihood function. We effectively improve the accuracy of abnormal event detection. Experiment results show that the proposed method obtain a better result than the traditional SFM.

Acknowledgments This work was supported by National Basic Research Program of China (973 Program) 2012CB821200 (2012CB821206) and the National Natural Science Foundation of China (No. 61320106006, No. 61532006, No. 61502042).

References

1. Li Y et al (2014) Counting pedestrian with mixed features and extreme learning machine. Cogn Comput 6(3):462–476
2. Conte D et al (2010) A method for counting moving people in video surveillance videos. J Adv Signal Process 1:10
3. Zhang Y et al (2014) Abnormal crowd behavior detection using interest points. In: IEEE international symposium on broadband multimedia systems and broadcasting, pp 1–4
4. Greenewald K, Hero A (2014) Detection of anomalous crowd behavior using spatio-temporal multiresolution. Model and Kronecker Sum Decompositions. Eprint Arxiv
5. Mingliang X et al (2015) miSFM: on combination of mutual information and social force model towards simulating crowd evacuation. Neurocomputing 168:529–537
6. Qin L, Zhang L (2014) Crowed abnormal detection based on GLCM and optical flow. Comput Modern 3:114–118
7. Shao J, et al (2015) Deeply learned attributes for crowded scene understanding. Comput Vision Pattern Recogn 4657–4666

Study on the Leakage Current and Neutral-Point Potential Balance in TL-Boost Photovoltaic System

Gang Cheng, Yong Xie, Yu Fang, Jinyan Zheng and Chuanchao Yang

Abstract In this paper, TL-Boost is adopted as a front-end converter in the non-isolated photovoltaic grid-connected system, the common-mode leakage current equivalent circuit of TL-Boost circuit is established, and the calculation formula of leakage current of the system is derived. On this basis, a conclusion that the common-mode leakage current of the system can be reduced using the synchronous modulation strategy is obtained. Aiming at the problem of unbalanced neutral-point potential in the process of starting up when DC bus voltage is building up, a fuzzy control strategy based on pre-TL-Boost circuit is proposed, thus realizing the balance of two capacitors' voltage on the DC side. And the experimental results verify the theoretical analysis.

Keywords Non-isolated · TL-Boost · Common-mode leakage current · Neutral-point potential balance

G. Cheng · Y. Xie (✉) · Y. Fang · J. Zheng · C. Yang
College of Information Engineering, Yangzhou University, Yangzhou 225127, China
e-mail: yzxieyong@126.com

G. Cheng
e-mail: chenggang__@126.com

Y. Fang
e-mail: yzfangyu@126.com

J. Zheng
e-mail: zhengjinyannt@163.com

C. Yang
e-mail: chuanchaoyang@163.com

Y. Jia et al. (eds.), *Proceedings of 2016 Chinese Intelligent Systems Conference*,
Lecture Notes in Electrical Engineering 404, DOI 10.1007/978-981-10-2338-5_55

1 Introduction

With the improvement of the power level and bus voltage of the photovoltaic system, it is difficult to meet the actual requirements by using two-level converter whether in the front-end circuit or back-end circuit. When the bus voltage is in a high level, the two-level converter will have a large dv/dt, thus resulting in a serious EMI problem. The voltage and current level of the power device should be correspondingly improved. The three-level converter device has an advantage on these two points, and the output current harmonics is very small. Therefore, in this case, it is a better choice to adopt the three-level converter in both the front-end and back-end of the photovoltaic system [1, 2]. The main circuit of the 17 KW PV system is shown in Fig. 1. In order to improve reliability of the system, the dual three-level Boost (TL-Boost), which is parallely connected is adopted in the front-end circuit of the DC-DC converter, and diode-clamped three-phase three-level inverter topology is adopted in the back-end circuit since the power is very large.

In the photovoltaic system of three-level structure, the unbalanced bus neutral-point potential [3] and common-mode leakage current [4] are generally analyzed around the grid-connected inverter. In order to examine the influences of the front-end circuit, this paper first analyzes the influences on common-mode leakage current when two power switches in the front-end TL-Boost DC/DC converter are controlled by different phase shift angles, then it analyzes the reasons for the unbalanced bus neutral-point potential in the three-level photovoltaic system, and finally a method to solve the problem by using fuzzy control in the TL-Boost DC/DC converter is introduced.

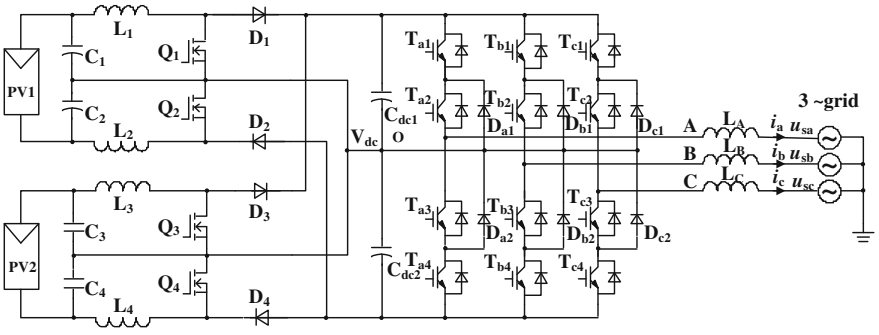

Fig. 1 Main circuit topology of the system

2 Influences on the Common-Mode Leakage Current in TL-Boost Converter

In order to facilitate the research on what influences the front-end TL-Boost circuit has on the common-mode leakage current, a TL-Boost circuit in parallel is chosen as an example for analysis, as shown in Fig. 2. A common-mode leakage current equivalent model of the system is established based on Ref. [5], as shown in Fig. 3. In Fig. 3, voltage sources u_{AN}, u_{BN}, u_{CN}, u_{pN}, and u_{nN} are, respectively ,used to replace the voltage between the inverter output terminals A, B, C boost converter terminals p, n, and the reference node N. Parasitic capacitance $C_{pv} = C_{pv1} + C_{pv2}$, Meanwhile, the influences of low-frequency voltage source grid on common-mode leakage current are ignored. Make $L_1 = L_2 = L_D$, $L_A = L_B = L_C = L$.

$u_{N'}$ can be deduced by the node voltage method, thereby the common-mode leakage current is given by:

$$i_{N'} = K_1(u_{AN} + u_{BN} + u_{CN}) + K_2(u_{pN} + u_{nN}) \tag{1}$$

Coefficients K_1 and K_2 in the formula (1), respectively, are as follows:

$$K_1 = \frac{2sC_{PV}}{s^2C_{PV}(2L + 3L_D) + 6} \tag{2}$$

$$K_2 = \frac{3sC_{PV}}{s^2C_{PV}(2L + 3L_D) + 6} \tag{3}$$

Formula (1) shows that the common-mode leakage current is affected not only by the modulation strategy in back-end inverter, but is also affected by the switching states in the front-end of TL-Boost converter. Here, only the impact of

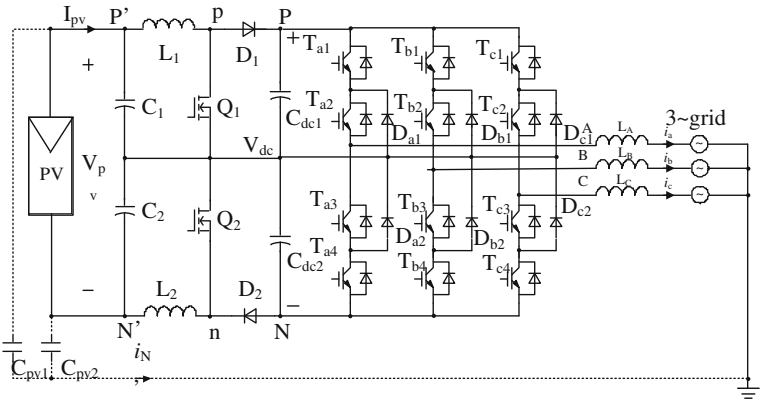

Fig. 2 Simplified main circuit topology

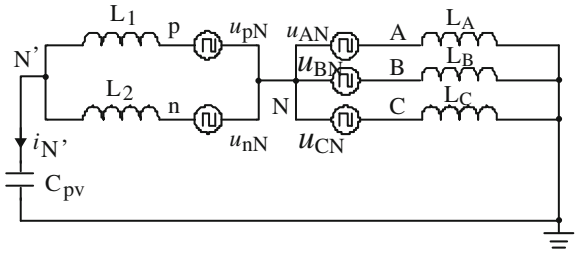

Fig. 3 Common-mode leakage current equivalent model

the front-end circuit on common-mode leakage current is discussed. As u_{pN} and u_{nN} are square wave signals, whose period is the same with the switching cycle. After Fourier transform, the expressions are as follows:

$$u_{nN} = \frac{V_{dc}}{2} \cdot \left(1 - \frac{V_{PV}}{V_{dc}}\right) + \sum_{m=1}^{\infty} V_m \cdot \cos\left(m \cdot \omega_c \cdot t\right) \tag{4}$$

$$u_{pN} = \frac{V_{dc}}{2} \cdot \left(1 + \frac{V_{PV}}{V_{dc}}\right) - \sum_{m=1}^{\infty} V_m \cdot \cos\left(m \cdot \omega_c \cdot t - m \cdot \varphi\right) \tag{5}$$

In formula (5), φ is the phase shift of control signals for two switches in front-end TL-Boost circuit. ω_c is the frequency of carrier angular. V_m is the amplitude of m switching harmonics. As the common-mode leakage current is the maximal current in switching harmonic, in order to analyze the influences of phase shift φ of the common-mode leakage current on the two switches, analysis of switching harmonics ($m = 1$) on $u_{pN} + u_{nN}$ is needed.

$$u_{pN} + u_{nN} = V_{dc} + V_1 \cdot \cos\left(\omega_c \cdot t\right) - V_1 \cdot \cos\left(\omega_c \cdot t - \varphi\right) \tag{6}$$

$$\text{make } V(t, \varphi) = V_1 \cos\left(\omega_c \cdot t\right) - V_1 \cos\left(\omega_c \cdot t - \varphi\right) \tag{7}$$

Since the DC value V_{dc} does not produce common-mode leakage current, only the analysis of the relationship between the value of V (t, φ) and φ is needed. According to formula (7), when φ is 0, namely in the synchronous control, V (t, φ) = 0; and when φ is another angle, namely in the phase shift control, V (t, φ) is not zero. Although the current ripple is small when employing phase shift modulation in the TL-Boost circuit, considering the strict requirements on the common-mode leakage current in non-isolated grid-connected PV inverter, synchronous control is adopted, that is, taking $\varphi = 0$ to suppress common-mode leakage current to the maximum.

In order to further verify the theoretical analysis, a simulation model of the circuit in Fig. 2 is built in the PSIM9.0 software. The front-end is TL-Boost DC converter, and the back-end inverter uses space vector modulation. Under the same conditions, the simulation results of the common-mode leakage current are shown in Fig. 4. When φ is 0, the common-mode leakage current is significantly smaller

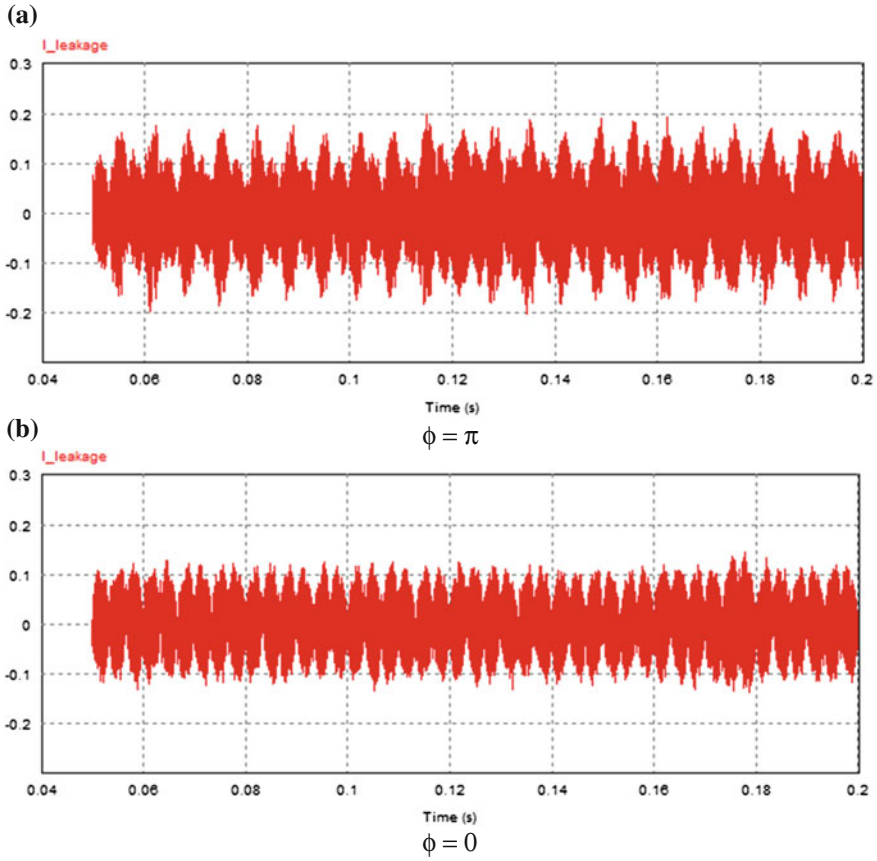

Fig. 4 Common-mode leakage current simulation waveforms

when φ is π. The common-mode leakage current is mainly caused by the back-end when φ is 0.

3 Fuzzy Control Strategy for Voltage Balance of TL-Boost Circuit

In the system shown in Fig. 2, there are two main reasons for the unbalanced neutral-point potential. On the one hand, due to the differences in front-end drive circuit, control circuit, and device parameters, the conduction time of main switches Q_1 and Q_2 is not completely equal, which leads to the unbalanced voltage on the C_{dc1} and C_{dc2}. On the other hand, it is influenced by the modulation strategy in the back-end of the inverter. In general, the traditional three-level modulation strategy and the space vector modulation strategy will produce three times AC fluctuations

compared to the fundamental frequency. When the DC capacitance value is fixed, the amplitude of the neutral-point potential will become larger with the increase of the output voltage, the increase of the load current, and the reduction of the power factor. At present, the domestic and foreign scholars have done a lot of research work on the neutral-point voltage balance of three-level inverter [6–8]. The traditional method is to achieve a balanced neutral-point potential by the modulation strategy and corresponding control method in the inverter. However, the back-end inverter circuit does not work when the grid-connected inverter starts. Therefore, the traditional control method cannot be used to solve the problem of the unbalanced DC bus capacitor voltage. In view of this situation, it is necessary to study the control strategy of the neutral-point balance in the process of starting and building up the voltage. In this paper, a fuzzy control strategy based on the front-end TL-Boost circuit to realize the neutral-point balancing is proposed. Compared with PI control, it enhances the robustness of the system and has a better dynamic response speed.

3.1 Methods of Achieving Neutral-Point Potential Balance

By working on the analysis of working principle on the TL-Boost DC−DC converter, it can be obtained that when Q_1 turns on and Q_2 turns off, C_{dc2} stores energy while C_{dc1} releases energy, and the amount of change on the voltage difference between the two capacitors is related to the duty cycle ratio d_1 of Q_1. When Q_1 turns off and Q_2 turns on, C_{dc1} stores energy while C_{dc2} releases energy, and the amount of change on the voltage difference between the two capacitors is related to the duty cycle ratio d_2 of Q_2. Thus, at the end of a switching cycle, how to adjust d_1 and d_2 in the next switching cycle can be determined by detecting the amount of V_{dc1} and V_{dc2}. If $V_{dc1} < V_{dc2}$, increase d_2, reduce d_1, increase the charging time of C_{dc1}, and reduce the charging time C_{dc2}. On the contrary, if $V_{dc1} > V_{dc2}$, increase d_1, reduce d_2, increase the charging time of C_{dc2}, and reduce the charging time C_{dc1}. Therefore, the difference between V_{dc1} and V_{dc2} can be directly viewed as the deviation e, and then deviation increment Δe can be obtained after calculation. Use e and Δe as the input variables of fuzzy controller and a duty cycle ratio adjustment signal for neutral-point potential balancing control d_S can be obtained after fuzzy, fuzzy reasoning and decision-making, and defuzzification through the method of center of gravity. The duty cycle ratio control signal d_M obtained from the maximum power point tracking control is added or subtracted with d_S to get the modulation signals v_{reg1} and v_{reg2} , which control the two main switches. Finally, driving signals, v_{g1} and v_{g2}, can be obtained by comparing with carrier signals, v_{carry1} and v_{carry2}, which are of the same phase. Thus, in the realization of tracking the maximum power point of the PV modules, neutral-point voltage balance control on the bus voltage can also be achieved. Block diagram of pressure control is shown in Fig. 5.

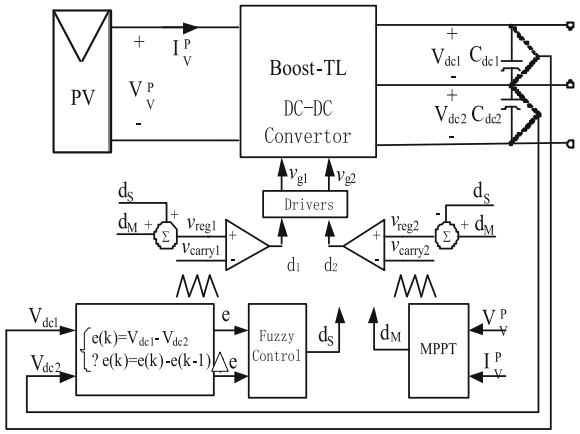

Fig. 5 Control strategy of neutral-point voltage balance

3.2 Determination of Fuzzy Control Rule

The range of e, Δe,and d_S is defined as the domain of fuzzy sets and fuzzy membership function are all triangular. Normalizations of the three variables are: e, $d_S = \{-1, -2/3, -1/3, 0, 1/3, 2/3, 1\}$, $\Delta e = \{-1, -1/2, 0, 1/2, 1\}$. In the specific design process, suitable scale factor should be selected according to the actual situation, so as to achieve the best dynamic and static performance of the system.

The control rules designed in this paper is mainly considered from the following aspects:

(1) When $e > 0$ and $\Delta e > 0$, the amount of deviation is positive and has a tendency to increase. In order to decrease the deviation of V_{dc1} and V_{dc2}, output d_S should be positive. When the deviation is large and the speed of change is fast, strong control can be implemented. When the deviation is small and the change rate is slow, general control can be implemented.

(2) When $e > 0$ and $\Delta e < 0$, the amount of deviation is positive and has a tendency to decrease. When the deviation is large, output d_S can be positive, so as to rapidly reduce the deviation. When the deviation is small, general control can be implemented.

(3) When $e < 0$ and $\Delta e > 0$, the amount of deviation is negative and has a tendency to decrease. The analysis is similar to (2).

(4) When $e < 0$ and $\Delta e < 0$, the amount of deviation is negative and has a tendency to increase. The analysis is similar to (1).

(5) When $e \bullet \Delta e = 0$, appropriate control action is implemented according to the deviation or deviation increment.

Based on the analysis above, the proper fuzzy rule table is designed, and 35 control rules are obtained from the table as follows: IF e is NB and Δe is PB then d_S

is NM; IF e is NM and Δe is PB then d_S is ZE; IF e is NS and Δe is PB then d_S is PS…, where NB, NM, NS, ZE, PS, PM, PB, respectively, represents negative big, negative, negative small, zero, positive small, positive, and positive big.

4 Experimental Results

In order to verify the correctness of theoretical analysis, the experimental prototype of a 17 KW non-isolated three-phase three-level PV grid-connected inverter is developed. The main parameters are as follows: the range of V_{PV} is 430−800 V_{dc}, the rated bus voltage V_{dc} = 650 V, bus voltage ripple ΔV_{dc} = 6.5 V, maximum output power P_{Omax} of single TL-Boost is 8.5 KW, L1 = L2 = 0.9 mH, C_{dc1} = C_{dc2} = 300 uF, and the switching frequency fs = 40 kHz.

In the experiment, the FZ06NBA045FH module from Vincotech Company is selected as the power switch device of the TL-Boost circuit. The voltage stress of the switch switches Q_1 and Q_2 is 600 V, the current stress is 44 A, and the turn-on resistance is only 0.045 Ω. The voltage stress of diodes D_1 and D_2 is 600 V, the current stress is 29 A, the maximum reverse current can reach 70A, and the reverse recovery time is only 8 ns.

In addition to the basic switching tube and diode, the module also has two bypass diodes whose voltage stress is 1600 V, current stress is 50 A and turn-on resistance is only 0.009 Ω. When the output voltage of the PV module is higher than the bus reference voltage, bypass diodes can bypass the TL-Boost circuit, thus improving the efficiency of the inverter. Amorphous iron core as the magnetic core of inductor and VISHAY Company's 50 uF, 85 °C film capacitor, whose rated voltage is 800 V, as the bus capacitor are selected. Total number of the capacitor is 14, with two cascades, and then the seven groups in parallel. The final value of the capacitor C_f = 175 uF, voltage is 1600 V, which meets the design requirements.

As the double TL-Boost circuit is adopted in the front-end DC converter, the working states of paralleled in the DC bus and two parallel TL-Boost circuit are exactly the same. So, only one working waveform of the TL-Boost circuit is analyzed here.

In order to facilitate the observation of changes in the positive and negative bus voltage V_{dc1} and V_{dc2}, reference points testing positive and negative bus voltage channel in the oscilloscope are not in the same position. Figure 6 is the startup waveform of positive and negative bus voltage when pressure control is not added, namely the soft-start process of TL-Boost circuit. As it can be seen from Fig. 6 that V_{dc1} will decline at the startup and then it will rise very slowly. While V_{dc2} rises quickly after TL-Boost circuit starts, and the maximum deviation of positive and negative bus voltage is nearly 100 V during the startup. Figure 7 is the startup waveform, adding voltage balance control based fuzzy control. V_{dc1} and V_{dc2} increases consistently. Figure 8 is the steady state waveform of inverter after the startup. The voltage of V_{dc1} and V_{dc2} remains equal, thus verifying the correctness of the theory analysis and the feasibility of fuzzy control strategy.

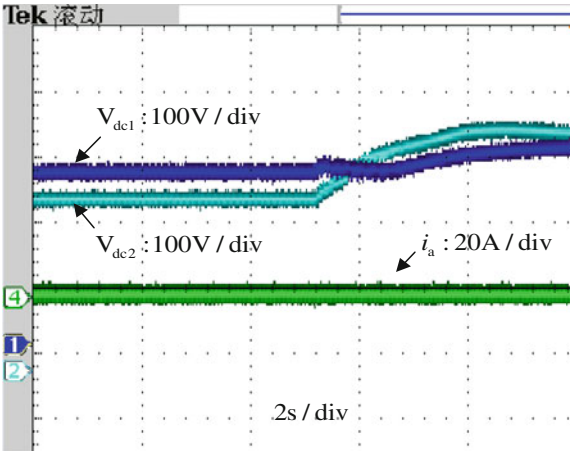

Fig. 6 The startup waveform when fuzzy control is not added

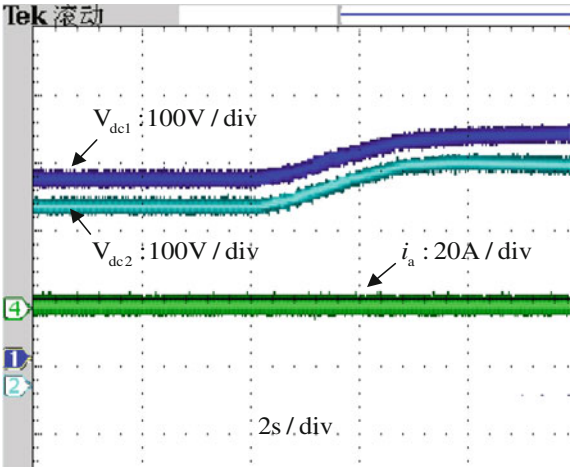

Fig. 7 The startup waveform when fuzzy control is added

Figure 9 shows the experimental waveforms of V_{dc1} and V_{dc2} when PV module power suddenly changes from 4000 to 8000 W, and V_{dc1} and V_{dc2} mutation experiment waveforms. Figure 10 shows the experimental waveforms of V_{dc1} and V_{dc2} when PV module power suddenly changes from 8000 to 4000 W. It can be seen from the experimental results that when power suddenly changes, positive and negative bus voltage will both have a small fluctuation, but they can still achieve a neutral-point potential balance, thus achieving the good dynamic characteristics via fuzzy controller.

In order to verify the advantages on efficiency of the selected power module, the efficiency of the TL-Boost circuit is tested under different power levels, and the efficiency curve of prototype is drawn according to the measured experimental data.

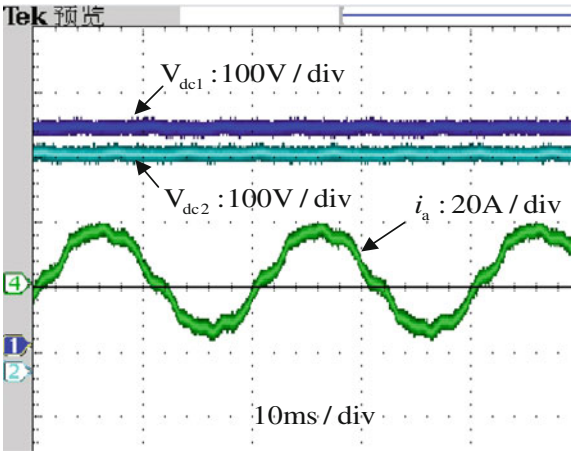

Fig. 8 The final steady state waveform when fuzzy control is added

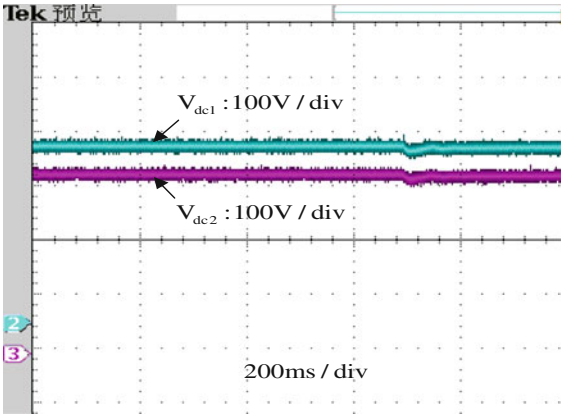

Fig. 9 Waveforms of positive and negative bus voltage when power suddenly bursts

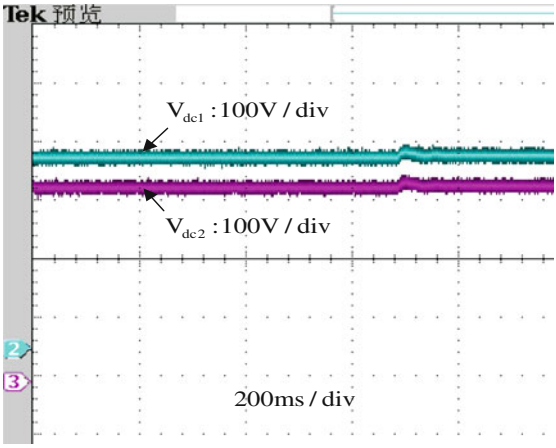

Fig. 10 Waveforms of positive and negative bus voltage when power suddenly reduces

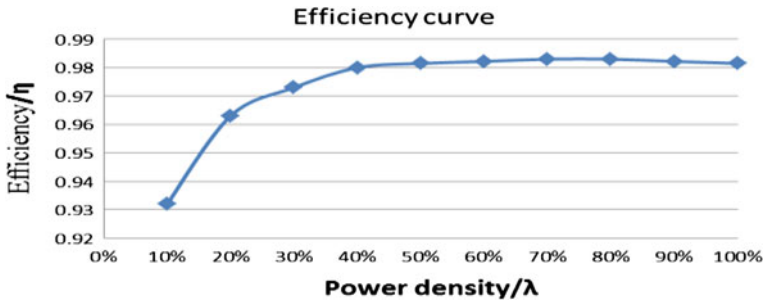

Fig. 11 Efficiency curve of TL-boost circuit

As shown in Fig. 11, efficiency can reach the maximum at about 80 % load and the maximum efficiency is about 98.3 %.

5 Conclusion

In this paper, the common-mode leakage current on two power switches in the TL-boost converter under synchronous and phase control is analyzed. It points out that the synchronous control can reduce the common-mode leakage current of system impacted by the front-end of TL-Boost circuit. As DC bus voltage may have the problem of neutral-point potential imbalance at system startup and load mutation, a fuzzy control strategy based on the front-end of TL-Boost circuit is put forward, thus achieving the balance of the bus voltage between the two capacitors on the bus side. Finally, an experimental platform is set up and the experimental results verify the theoretic analysis.

References

1. Kwon J-M, Kwon B-H, Nam K-H (2008) Three-phase photovoltaic system with three-level boosting MPPT control. IEEE Trans Power Electron 23(05):2319–2325
2. Xiao H, Xie S (2012) Transformerless split-inductor neutral point clamped three-level PV grid-connected inverter. IEEE Trans Power Electron 27(4):1799–1808
3. Lee, H-H, Choi U.M, Lee K-B (2012) Neutral-point voltage control for grid-connected three-level inverters using a discontinuous pulse width modulation. In: Vehicle Power and Propulsion Conference (VPPC), pp 638−642
4. Yang B, Li W, Gu Y, Cui W, He X (2012) Improved transformerless inverter with common-mode leakage current elimination for a photovoltaic grid-connected power system. IEEE Trans. Power Electron 27(2):752−762
5. Su N (2012) Current analysis and suppression of photovoltaic inverter. Doctoral dissertation, Zhejiang University

6. Xia C (2010) Neutral-Point potential balancing of three-level inverters in direct-driven wind energy conversion system. IEEE Trans Energy Convers 26(01):18–27
7. Du E, Gao H, Li X, Ma Y (2011) Parameter self-tuning fuzzy control for neutral point balancing of three-level inverter. Power Electron Technol 45(01):12–14
8. Lee DH, Lee SR, Lee FC (1998) An analysis of neutral-point balance for the neutral-point-clamped three-level VSI. In: IEEE Power Electronics Specialists Conference, pp 193−199

Path Following Control for Nonholonomic Mobile Robots with a Distance Between the Mass Center and the Geometrical Center

Jiaxin Zuo and Chaoli Wang

Abstract Currently, some path following control problems have been proposed for nonholonomic wheeled mobile robot (WMR) with driven wheels under the condition that there is a distance between the mass center and the geometrical center. However, there is lack of the relevant experiment verification except for several simulations. In this paper, the mathematical model of WMR kinematics is analyzed. In polar coordinates a new kinematics tracking error model is put forward based on the WMR, whose mass center does not coincide with its geometrical center. In view of the grid map model composed of discrete path point path, on the principle of point stabilization, a new dynamic feedback tracking controller is designed. The stability of the closed-loop system is rigorously proved. Simulation and experiment results are provided to illustrate the performance of the control law.

Keywords Nonholonomic system · WMR · Path following · Point stabilization

1 Introduction

WMR is a typical highly nonlinear nonholonomic system, by the theorem of Brockett [1], a nonholonomic system cannot be stabilized at a single equilibrium point by a smooth feedback controller. Mobile robot tracking control mainly includes the trajectory tracking control [2–4] and path following control [5–7]. Path following control is for a desired position without time tracking requirements.

The above literature, for the study of the control law is the standard of mobile robot with two wheel drive, the center of mass and geometric are overlapping. In

J. Zuo (✉) · C. Wang
Control Science and Engineering, University of Shanghai for Science and Technology, Shanghai 200093, China
e-mail: 297529759@qq.com

C. Wang
e-mail: clclwang@126.com

Y. Jia et al. (eds.), *Proceedings of 2016 Chinese Intelligent Systems Conference*, Lecture Notes in Electrical Engineering 404, DOI 10.1007/978-981-10-2338-5_56

most instances, the mass center of WMR does not coincide with its geometrical center. Literature [8] for center of mass and geometric center of the model is not coincidence, using the time-varying continuous control law the problem of controlling the mobile robot's stabilization can be solved, and using the adaptive technology to solve the stabilization problem when the distance between the mass center and the geometrical center is unknown, but did not realize the path following control. But it lacks the experimental verification.

In this paper, we consider the path following of WMR with driven wheels under the condition that there is a distance between the mass center and the geometrical center. In polar coordinates, a new kinematics tracking error model is put forward, and a new dynamic feedback tracking controller is designed. Based on the kinematics of WMR, whose mass center does not coincide with its geometrical center tracking error model, implementation of a given reference path of the global asymptotic tracking, the stability of the closed-loop system is rigorously proved.

This paper is organized as follows: Section 2 describes the mathematical model of WMR. In Sect. 3, In polar coordinates, a new kinematics tracking error model is put forward and a new dynamic feedback tracking controller is designed. In Sect. 4, the dynamic stability of the proposed controller is explained. In Sect. 5, the controllers performance is illustrated through simulation and experiment results. Finally, Sect. 6 draws conclusions.

2 Problem Formulation

The WMR, whose mass center does not coincide with its geometrical center, a typical example of a WMR is shown in Fig. 1. The two rear wheels of the robot are controlled independently by motors, and a front castor wheel prevents the robot from tipping over as it moves on a plane. Point G is geometric center of the WMR, (x_G, y_G) is the robot center of mass G coordinates in X_Y coordinate system. Point M is mass center of the WMR, (x_M, y_M) is the robot center of mass M coordinates in X_Y coordinate system. The distance between the geometric center point and the mass center point of the robot is d as shown in Fig. 1.

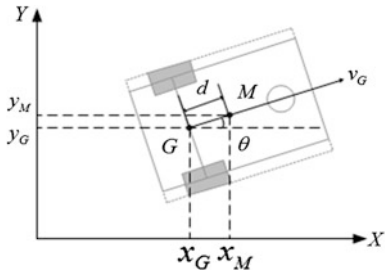

Fig. 1 The model of WMR

v_M is the speed of the mobile robot center of mass M, according to the robot model of the kinematic, we can get as follows:

$$\begin{cases} \dot{x}_M = v_M \cos\theta \\ \dot{y}_M = v_M \sin\theta \end{cases} \tag{1}$$

The geometric center of the mobile robot G and the position relationship between the center of mass of mobile robot M are shown in Fig. 1.

$$\begin{cases} x_G = x_M - d\cos\theta \\ y_G = y_M - d\sin\theta \end{cases} \tag{2}$$

Derivation of Eq. (2), get (3):

$$\begin{cases} \dot{x}_G = \dot{x}_M + d\theta\sin\theta \\ \dot{y}_G = \dot{y}_M - d\theta\cos\theta \end{cases} \tag{3}$$

Substituting Eq. (1) into Eq. (3), according to the WMR whose mass center does not coincide with its geometrical center, analysis, we can get the robot nonholonomic constraints.

$$\dot{x}_G\sin\theta - \dot{y}_G\cos\theta - d\theta = 0 \tag{4}$$

The robot model of the kinematic based on WMR, whose mass center does not coincide with its geometrical center, can be obtained by the constraint equations.

$$\begin{cases} \dot{x}_G = v_G\cos\theta + d\omega\sin\theta \\ \dot{y}_G = v_G\sin\theta - d\omega\cos\theta \\ \theta = \omega \end{cases} \tag{5}$$

Eq. (5) into a more general kinematics model [6]:

$$\begin{cases} \dot{x} = v\cos\theta + d\omega\sin\theta \\ \dot{y} = v\sin\theta - d\omega\cos\theta \\ \theta = \omega \end{cases} \tag{6}$$

where (x, y, θ) is WMR pose. The robot has linear velocity v and angular velocity ω.

3 Controller Design

First of all to build the global coordinate system X_Y, the position of the robot's current position and target position relations there are four kinds of circumstances, as shown in Fig. 2.

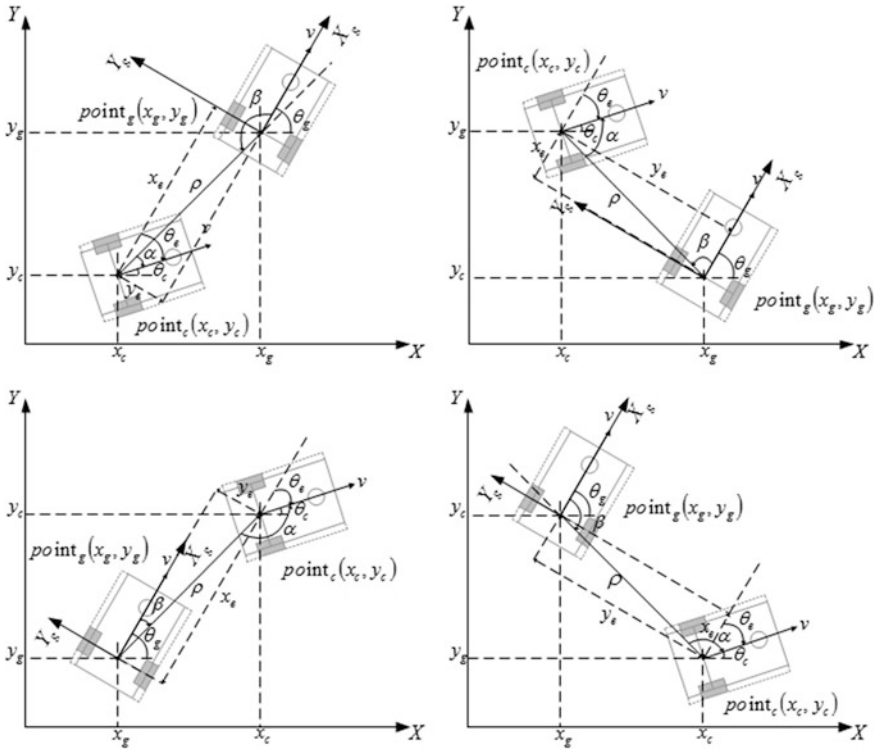

Fig. 2 WMR pose relations in polar coordinates and global coordinates

The robot's current position in the global coordinate system for $\text{point}_c(x_c, y_c)$, the robot's current posture in the global coordinate system for θ_c, define the counterclockwise rotation θ_c is positive, $\theta_c \in (-\pi, \pi]$, counterclockwise rotation θ_c is positive, $\theta_c \in (-\pi, \pi]$. The robot's target posture in the global coordinate system for θ_g defines the counterclockwise rotation θ_g is positive, $\theta_g \in (-\pi, \pi]$.

For the convenience of describing the car position, polar coordinates are established $X_g\_Y_g$ as shown in Fig. 2.

In the new coordinate system $X_g\_Y_g$, the robot's current position coordinates of (x_e, y_e), the current attitude to θ_e, $\theta_e \in (-\pi, \pi]$.

According to the coordinate transformation formula (7) available (8):

$$\begin{pmatrix} x_e \\ y_e \\ \theta_e \end{pmatrix} = \begin{pmatrix} \cos\theta_g & \sin\theta_g & 0 \\ -\sin\theta_g & \cos\theta_g & 0 \\ 0 & 0 & 1 \end{pmatrix} \begin{pmatrix} x_c - x_g \\ y_c - y_g \\ \theta_c - \theta_g \end{pmatrix} \tag{7}$$

$$\begin{cases} x_e = (x_c - x_g)\cos\theta_g + (y_c - y_g)\sin\theta_g \\ y_e = -(x_c - x_g)\sin\theta_g + (y_c - y_g)\cos\theta_g \\ \theta_e = \theta_c - \theta_g \end{cases} \tag{8}$$

Derivation of Eq. (8) available (9):

$$\begin{cases} \dot{x}_e = v\cos\theta_e + d\hat{\omega}\sin\theta_e \\ \dot{y}_e = v\sin\theta_e - d\hat{\omega}\cos\theta_e \\ \theta_e = \hat{\omega} \end{cases} \tag{9}$$

After coordinate transformation, in the new coordinate system $X_g\_Y_g$, the Robot's current posture $\theta_e \in (-2\pi, 2\pi]$. If $\theta_e > \pi$ then $\theta_e - = 2\pi$, if $\theta_e < -\pi$ then $\theta_e + = 2\pi$, available $\theta_e \in (-\pi, \pi]$. θ_e is the angle between the robot's current posture and target posture, with posture toward the target as polar axis direction. Define the counterclockwise rotation θ_e is positive, $\theta_e \in (-\pi, \pi]$.

Let ρ be the Euclidean distance between the current robot position and the target position, $\rho \geq 0$; αis the angle between the robot's current posture and ρ, with direction of the current point to the target point as polar axis direction. Define the counterclockwise rotation α is positive, $\alpha \in (-\pi, \pi]$; β the angle between the robot's target posture and ρ, with direction of the target point to the target point as polar axis direction. Define the counterclockwise rotation β is positive, $\beta \in (-\pi, \pi]$; $\arctan 2(y_e, x_e)$ expression β.

Applying a change of variables, we obtain (10):

$$\begin{pmatrix} \rho \\ \beta \\ \alpha \end{pmatrix} = \begin{pmatrix} \sqrt{x_e^2 + y_e^2} \\ \arctan 2(y_e, x_e) \\ \theta_e - \beta + \pi \end{pmatrix} \tag{10}$$

Derivation of Eq. (10) available (11):

$$\begin{cases} \dot{\rho} = \frac{x_e\dot{x}_e + y_e\dot{y}_e}{\sqrt{x_e^2 + y_e^2}} = -v\cos\alpha - d\hat{\omega}\sin\alpha \\ \beta = \frac{\dot{y}_e x_e - \dot{x}_e y_e}{x_e^2 + y_e^2} = -\frac{v}{\rho}\sin\alpha + \frac{d\hat{\omega}}{\rho}\cos\alpha \\ \dot{\alpha} = \hat{\omega} - \beta = \frac{v}{\rho}\sin\alpha + \frac{d\hat{\omega}}{\rho}\cos\alpha + \hat{\omega} \end{cases} \tag{11}$$

If $d = 1$, Eq. (11) is equivalent to Eq. (12).

$$\begin{pmatrix} \dot{\rho} \\ \beta \\ \dot{\alpha} \end{pmatrix} = \begin{pmatrix} -v\cos\alpha - \hat{\omega}\sin\alpha \\ -\frac{v}{\rho}\sin\alpha + \frac{\hat{\omega}}{\rho}\cos\alpha \\ \frac{v}{\rho}\sin\alpha + \frac{\hat{\omega}}{\rho}\cos\alpha + \hat{\omega} \end{pmatrix} \tag{12}$$

c, s is equivalent to $\cos\alpha$, $\sin\alpha$.

Set

$$\begin{pmatrix} -c & -s \\ -\frac{s}{\rho} & \frac{c}{\rho} \end{pmatrix}\begin{pmatrix} v \\ \hat{\omega} \end{pmatrix} = \begin{pmatrix} u_1 \\ u_2 \end{pmatrix}, \begin{pmatrix} v \\ \hat{\omega} \end{pmatrix} = \begin{pmatrix} cu_1 - \rho s u_2 \\ su_1 + c\rho u_2 \end{pmatrix}$$

then (13) yields

$$\begin{pmatrix} \dot{\rho} \\ \beta \end{pmatrix} = \begin{pmatrix} -c & -s \\ -\frac{s}{\rho} & \frac{c}{\rho} \end{pmatrix}\begin{pmatrix} v \\ \hat{\omega} \end{pmatrix} = \begin{pmatrix} u_1 \\ u_2 \end{pmatrix} \tag{13}$$

In the same way too:

$$\begin{aligned} \dot{\alpha} &= \frac{v}{\rho}\sin\alpha + \frac{\hat{\omega}}{\rho}\cos\alpha + \hat{\omega} = \begin{pmatrix} \frac{s}{\rho} & \frac{c}{\rho} \end{pmatrix}\begin{pmatrix} v \\ \hat{\omega} \end{pmatrix} + \hat{\omega} \\ &= \begin{pmatrix} \frac{s}{\rho} & \frac{c}{\rho} \end{pmatrix}\begin{pmatrix} cu_1 - s\rho u_2 \\ su_1 + c\rho u_2 \end{pmatrix} + (su_1 + c\rho u_2) \\ &= \frac{1}{\rho}(csu_1 - \rho ssu_2 + csu_1 + cc\rho u_2) + (su_1 + c\rho u_2) \\ &= c^2 u_2 + su_1 + c\rho u_2 = su_1 + (c\rho + c^2)u_2 \end{aligned}$$

Through the above calculation, we can get

$$\begin{cases} \dot{\rho} = u_1 \\ \beta = u_2 \\ \dot{\alpha} = su_1 + (c^2 + c\rho)u_2 \end{cases} \tag{14}$$

Design method of u_1 and u_2 are as follows:

$$\begin{cases} u_1 = -k_1 \operatorname{sgn}(\rho - \rho_d) \\ u_2 = -k_2\beta \end{cases} \tag{15}$$

Set $\rho_d > 0$, k_1 and k_2 are the parameters of the greater than zero.

4 Stability Analysis

By (15) available: $\dot{\rho} = -k_1 \operatorname{sgn}(\rho - \rho_d)$, So ρ the finite time convergence to zero. $\beta = -k_2\beta$, So β Exponentially converge to zero. Will u_1 and u_2 into (14), available (16).

$$\dot{\alpha} = -k_1 s \operatorname{sgn}(\rho - \rho_d) + (c^2 + c\rho)(-k_2)\beta \tag{16}$$

Presume $\rho > \rho_d$, available (17).

$$\dot{\alpha} = -k_1 s + (c^2 + c\rho)(-k_2)\beta \tag{17}$$

Because of the $(c^2 + c\rho)$ bounded, so β exponentially $\to 0$.
Make for $\dot{\alpha} = -k_1 s$ the asymptotic stability.
Therefore, $\dot{\alpha} = -k_1 s + (c^2 + c\rho)(-k_2)\beta$ is the asymptotic stability.
Thus, $\rho \to \rho_d$, $\beta \to 0$, $\alpha \to 0$ meet the requirements.

5 Simulation and Experimental Results

The simulation with the robot operating system (ROS) [9]. In view of the above chapters, the path following control law is designed for simulation is used to verify the effectiveness of the control algorithm. The path is many track points of an ordered set, constructs a path composed with path points and a complete path following simulation used to characterize the design of the path following controller.

The sampling period is set to $T = 5$ ms of the controller. The control parameter is set to $k_1 = 2$ and $k_2 = 1$ of the controller, according to formula (15) shown in complete control law for the path following simulation.

Simulation 1
The path following in any curve. Figure 3(1) shows drawing through software, rendering any curve. Figure 3(2) shows reference curve on ROS. Figure 3(3) shows a robot path with the control law.

Simulation 2
Drive movement of robot in arbitrary path and real-time data gathering, as shown in Fig. 4(1). In ROS, the data is read as shown in Fig. 4(2) from the reference path. Path following by robot is shown in Fig. 4(3)–(6).

Through the simulation results, it can be seen above that the control law (15) can make the robot tracking control for any path. So in this section, the designed path following controller is effective in accord with the actual ability to execute nonholonomic mobile robot.

Experiment on Turtlebot which is wheeled mobile robot, the experiment platform, is shown in Fig. 5 to design the path following experiment.

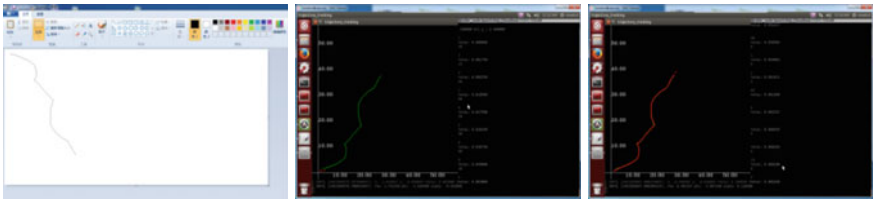

(1) (2) (3)

Fig. 3

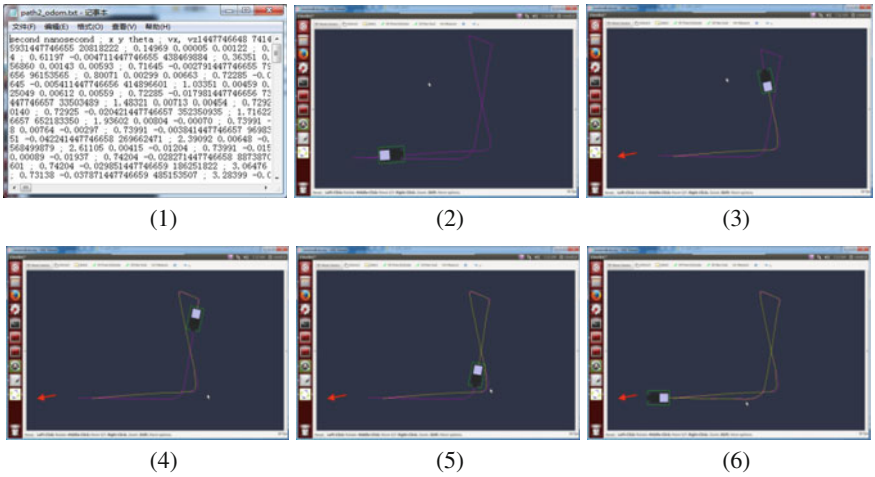

(1) (2) (3)

(4) (5) (6)

Fig. 4

Fig. 5

Set the maximum linear velocity of $v_{\max} = 2\,\mathrm{m/s}$ and the maximum angular velocity of $\omega_{\max} = 1\,\mathrm{rad/s}$. Set the maximum linear acceleration of $\dot{v}_{\max} = 0.4\,\mathrm{m/s^2}$ and the maximum angular acceleration of $\dot{\omega}_{\max} = 0.7\,\mathrm{rad/s^2}$.

Figure 6(1) shows the robot experiment in real environment. Figure 6(2) shows the robot with a laser radar built map in the real environment. Figure 6(3) shows the reference path of the robot from the starting position to the target position. Figure 6 (4) shows the robot path with the control law.

Combined with Fig. 6, we can see that with the adoption of a reasonable speed and acceleration limit strategy, robot's actual motion path is very smooth and very

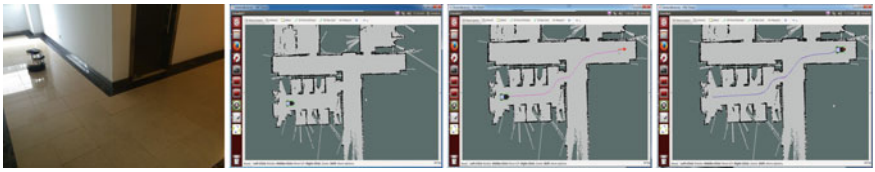

(1) (2) (3) (4)

Fig. 6

close to the planned path. Through the analysis of the above results, the stability of the path following controller under the action of the control of the controller, WMR path following was completed well.

6 Conclusions

In this article, the center of mass and geometric center misalignment of WMR path following problems were studied. In this paper, a new dynamic feedback tracking controller is designed. The controller ensures that the actual path asymptotically converges to a given reference path, and the controller is smooth and global. The method has strong robustness and is suitable for the control of center of mass and geometric center misalignment of WMR. Simulation and experimental results show the effectiveness of the proposed control law. In the future, further improvement is needed for the wheeled mobile robot movement speed, and control strategies need further ascension.

References

1. Brockett R (1983) Asymptotic stability and feedback stabilization, Differential geometric control theory, pp 181–208
2. Antonelli G, Chiaverini S (2007) A fuzzy-logic-based approach for mobile robot path tracking [J]. IEEE Trans Fuzzy Syst 15(2):211–221
3. Chwa D (2004) Sliding-mode tracking control of nonholonomic wheeled mobile robots in polar coordinates [J]. IEEE Trans Control Syst Technol 12(4):637–644
4. Yue M, Hu P, Sun W (2010) Path following of a class of non-holonomic mobile robot with underactuated vehicle body [J]. IET Control Theory Appl 4(10):1898–1904
5. Baoli MA, Wei HUO (1995) Path tracking control and stabilization of mobile cart [J]. Robot 17(6):358–362
6. Duoqing SUN, Wei HUO, Xiao YANG (2004) Path following control of mobile robots with model uncertainty based on hierarchical fuzzy systems [J]. Control Theory Appl 21(4): 489–494
7. Dongyao WANG, Xudong MA, Xianzhong DAI (2004) Non-time based path tracking control for mobile robots [J]. Robot 26(3):198–203

8. Li C, Wang C (2006) Robust stabilization of kinematic systems of uncertain nonholonomic mobile robots. In: 2006 6th world congress on intelligent control and automation
9. Quigley M et al (2009) ROS: an open-source robot operating system. In: ICRA workshop on open source software
10. Murray R, Sastry S (1993) Nonholonomic motion planning: steering using sinusoids. IEEE Trans Autom Control 38(5):700–716

Looking After the House Using the Mobile Phone to Control the Robot Remotely on the Internet

Hongwu Sun and Chaoli Wang

Abstract In this chapter, we can use our mobile phone to remotely control our mobile robot on the Internet basing on the TCP/IP protocol. We make an app installed in our mobile phone based on Android. We can see the real-time video translated from the camera fixed on the robot. The robot can translate the real-time video of the environment the robot stays to our mobile phone. The mobile phone can display the real-time video directly. When we control the robot, we can see how the mobile robot moves at the same time. When the robot meets the obstacles using the ultrasonic sensors, the robot can stop and translate this warning to the mobile phone. When we finish the control work, we can control our robot to move to the destination to get the electric charge. We can use our robot to see the rooms of our house, when we have left our house for a long time. It is very convenient for us to look after our house.

Keywords Mobile robot · Remotely control · Android · Real-time video

1 Introduction

In recent years, the intelligence of the mobile robot is improved very quickly. The mobile robot can do many things that human beings cannot do. Using the robot to look after the house is necessary in our life. There are many mass casualties and disaster events occur everyday, such as fire disaster, earthquake, flood, mine disaster, and nuclear radiation. In such dangerous situations, the mobile robot is very important for us to help us to rescue in disasters [1]. We can also use our mobile robot to explore the strange places[2, 3].

H. Sun (✉) · C. Wang
Department of Control Science and Engineering, University of Shanghai for Science and Technology, Shanghai 200093, China
e-mail: hongwulucky@163.com

C. Wang
e-mail: clclwang@126.com

Y. Jia et al. (eds.), *Proceedings of 2016 Chinese Intelligent Systems Conference*, Lecture Notes in Electrical Engineering 404, DOI 10.1007/978-981-10-2338-5_57

When we want to control the mobile robot to do some things, the communication is very important for us. The Bluetooth technology is often used to communicate in our life [4, 5]. But, the transmission distance of the Bluetooth is short about 10 meters. So, the Bluetooth is fit only for the short distance transmission. The ZigBee technology and CAN communication technology are used in the industry widely. In this chapter, we use the WiFi technology to communicate. We can use our mobile phone to control the mobile robot remotely on the Internet. The CDMA networking is used to make sure that the robot can move safely [6]. This method by using the mobile phone based on Android is convenient and clear to control the robot. Now the Android is widely used in our life [7, 8]. The mobile phone can be used for the mobile robot to navigate [9]. The mobile phone is used to monitor the temperature and the humidity of the house remotely [10].

The real-time video is very important for us to control the robot. The remote video surveillance is necessary for us to rescue. Based on the vision, the mobile robot can navigate well. Based on visual feedback, [11] remotely controls the manipulator to accomplish a task. The video can be used to recognize the object. Now the video surveillance is used widely in our life.

This chapter discusses on how we can use our mobile phone to control the mobile robot to move using WiFi technology on the Internet. We will also discuss how the real-time video is translated from the robot, when we control the mobile robot at the same time. By doing that, the mobile robot can move to the destination safely. We can use our mobile phone to choose the parameters and modes of robot.

2 System Analysis and Design

Our system contains the mobile phone and the mobile robot. We call the mobile phone as the client and the mobile robot as the server. We connect the client and the server using the WiFi on the Internet. The robot can make videos using the camera fixed on it. Once the client gets communicated with the server successfully, the client gets the real-time video from the server. We can control the mobile robot based on the video.

Ultrasonic sensors are fixed on the mobile robot. The server prevents the mobile robot crashing the obstacles. When the obstacles are in the range, the mobile robot can identify, stop, and translate the warning to the client, thereby overcome the obstacles and move safely without any crash. We can adjust the direction based on the message translated from the robot and the real-time video. We have made an app that can control the mobile robot based on Android. The communication between the client and the server based on TCP/IP protocol can provide high quality correspondence. In this experiment, the MT-R robot with a computer is the server, and the mobile phone with an app installed is the client. The procedure of the system is shown as Fig. 1.

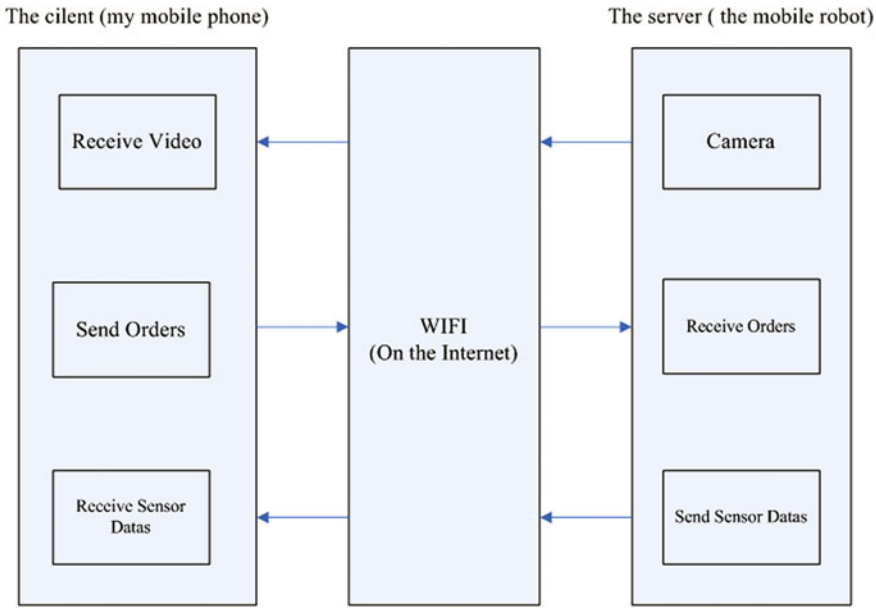

Fig. 1 The procedure of the system

As shown in Fig. 1, we know that the system has two parts: the client and the server. The client, an app made based on Android, should be installed in the mobile phone. Once the client gets communicated with the server, the client can send the orders to the server. The client will receive the real-time video from the server at the same time. Certainly, when the robot meets the obstacles using the sensors, the client will get the warning from the robot. The robot will stop to wait for next order.

The server, the MT-R robot is installed with the computer and the camera and some sensors as the server. After the client gets communicated with the server, the server will open the camera fixed on the robot and send the real-time video to the client. After the server receives the orders from the client, the robot can go ahead, go back, turn left, turn right, and stop.

3 The Function of the System

3.1 The Introduction of the Client

As shown in Fig. 2, we can know the procedure that the client works. The figure tells us how they get communicated with each other and how the mobile phone controls the mobile robot.

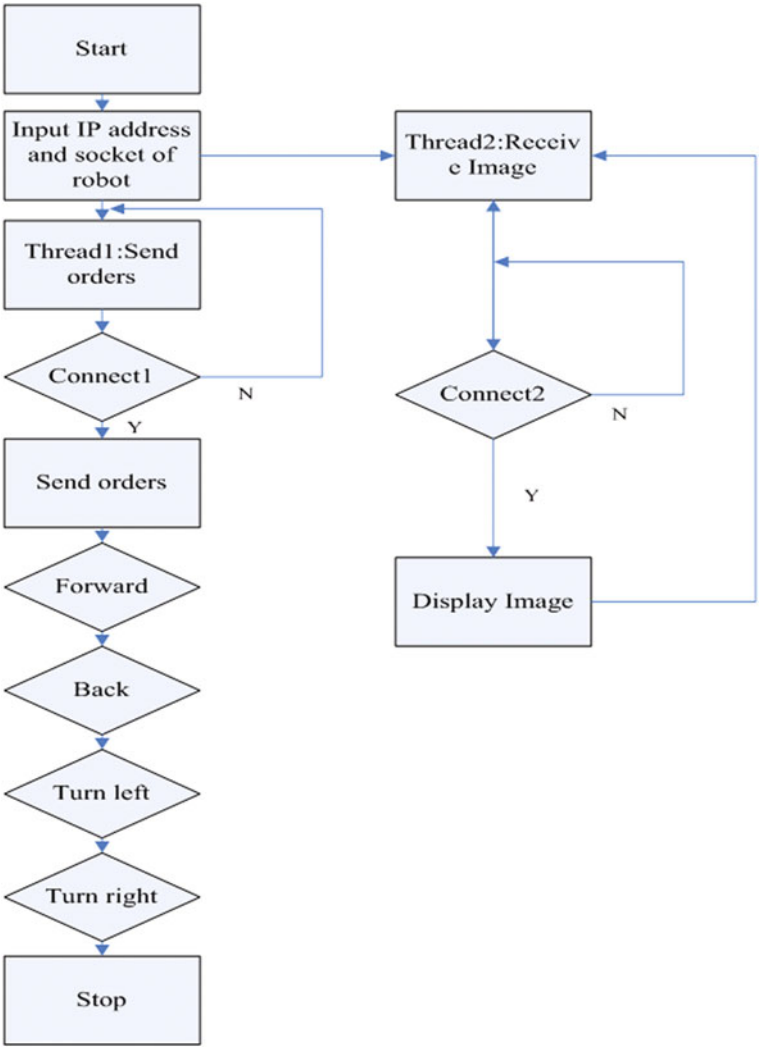

Fig. 2 The flow diagram of the client

We make an app based on Android and we install the app in our mobile phone. The control surface is shown in Fig. 3.

(1) As shown in Fig. 3a, when the app is opened in our mobile phone, we can choose to input some parameters. We can choose whether open the camera and some sensors or not. We also can choose the modes. As shown in the control surface of the client, we should input the server's IP address and socket. Then we click the save button, the client will save the parameters we setting.

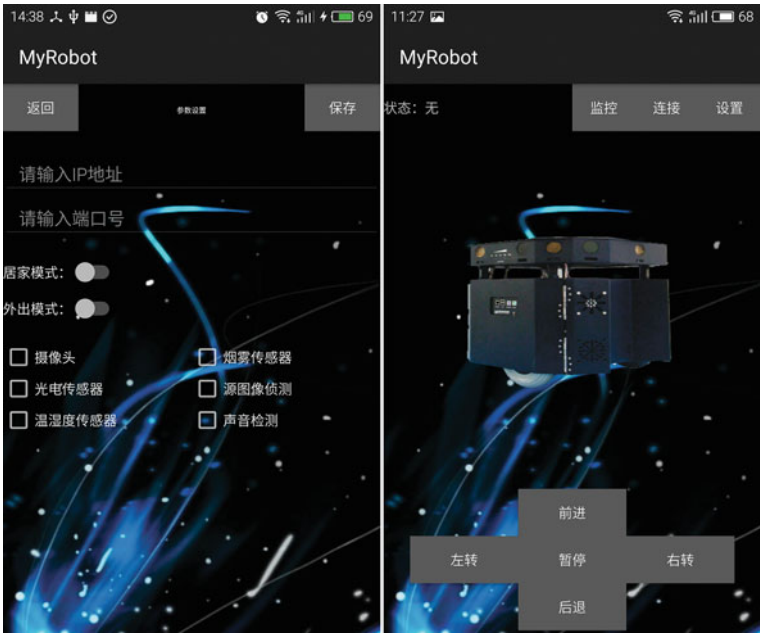

(a) The client control panel-1 (b) The client control panel-2

Fig. 3 The client control panel

(2) After we click the back button, we go back to the Fig. 3b. We should click the connection and the monitor button. The client will get communicated with the server. After they get connected with each other, we can click the forward button, back button, turn left button, turn right button, and stop button to send the orders to the server. The client will receive the real-time video from the server as the same time and display on the screen of the mobile phone.

3.2 The Introduction of the Server

As shown in Fig. 4, we know how the server works. There are two flow diagrams in the server. The first flow diagram shows how the server receives different motion orders. The second flow diagram shows how the real-time video is translated.

The server control panel is shown as Figs. 5 and 7. The client receive the real-time video is shown in Fig. 6.

(1) The server has two programs. The first program of the server can translate the real-time video to the client after the server gets connected with the client. The

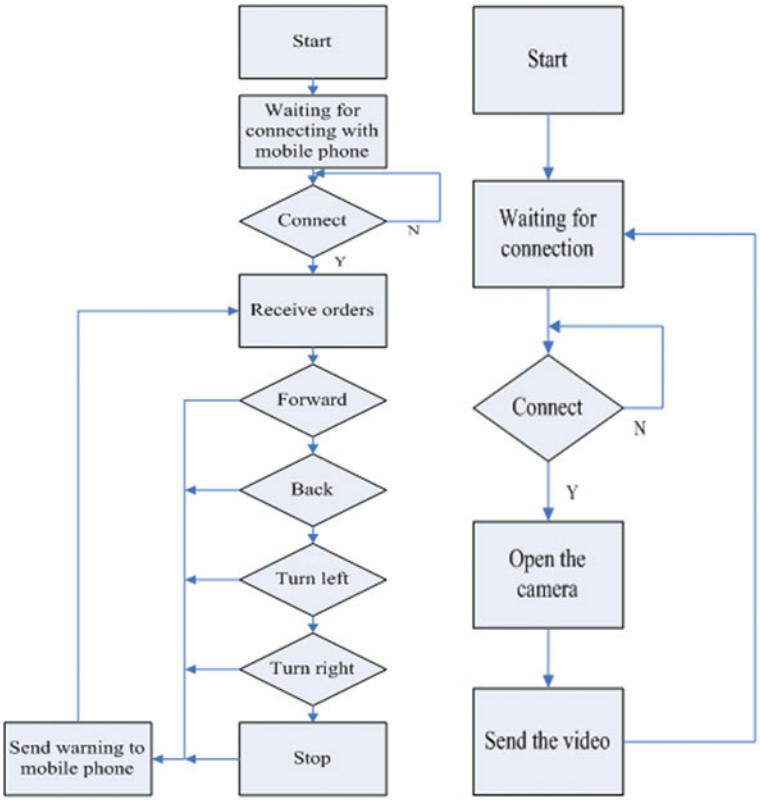

(a) The procedure of server panel-1 (b) The procedure of server panel-2

Fig. 4 The procedure of the server

second program of the server is used to control the mobile robot to move after receiving the orders from the client. The robot can translate the warning to the client after meeting the obstacles.

(2) As shown in Fig. 5, the program can translate the real-time video to the client and play the real-time video on the screen of the computer at the same time.

(3) As shown in Fig. 7, we make a MFC program to control the robot. After the mobile robot receives the orders from the mobile phone, the program uses the motors to realize that the robot can go forward, go back, turn left, turn right, and stop. We can set the speed and acceleration in the MFC program.

(4) As shown in Fig. 6, once the mobile phone gets connected with the robot, the robot begins to use the camera to get the real-time video and translates the video to the mobile phone. The mobile phone will play the real-time video. After the mobile phone receives the video, we can control the mobile robot to navigate better.

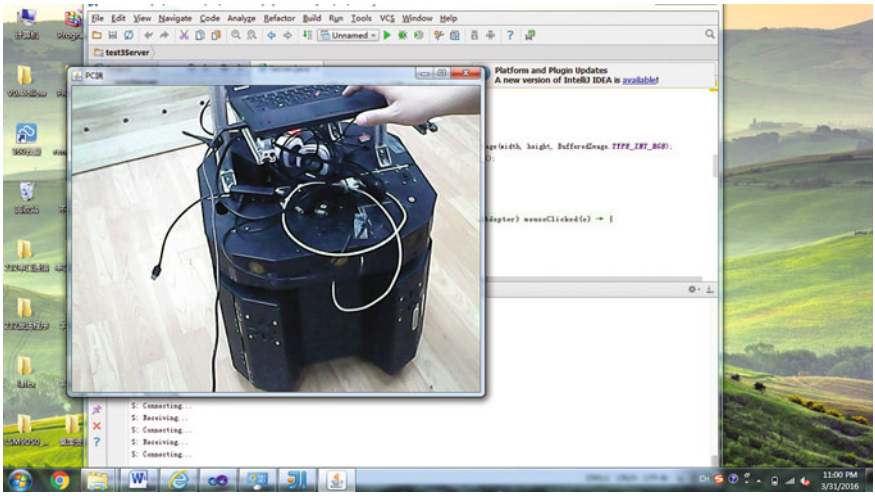

Fig. 5 The server video panel

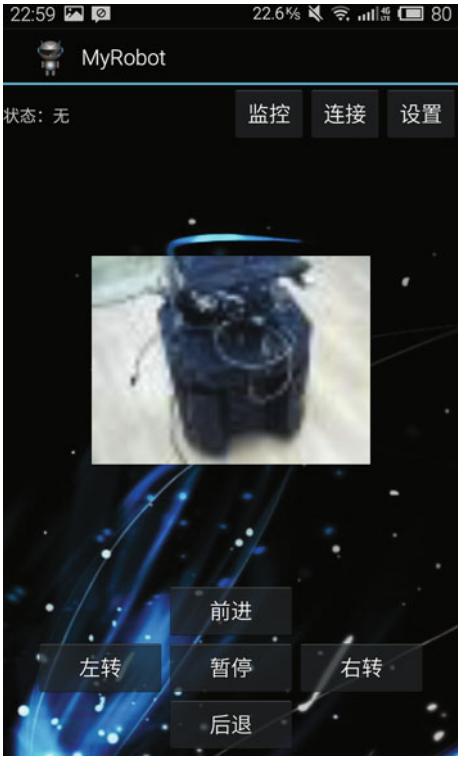

Fig. 6 The mobile phone panel

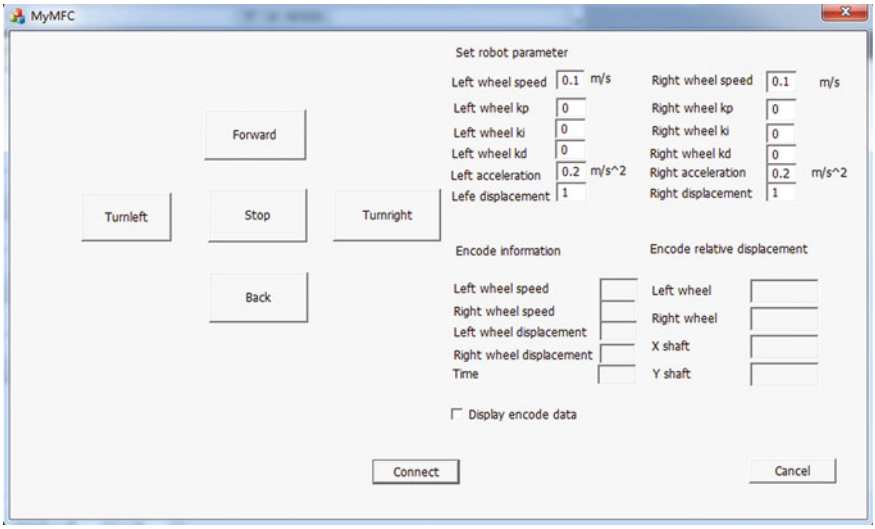

Fig. 7 The MFC panel

4 The Underlying Control of the Robot

Once the server receives the orders from the client, the robot moves based on different orders. The robot has three wheels. The two wheels should be driven by two servo motors. The last one is a tail wheel. We can control the speed of the two wheels based on different orders. The two wheels have the same positive speed; the robot can go ahead. The two wheels have the same negative speed; the robot can go back. The left wheel has a positive speed, and the speed of the right wheel is zero, the robot can turn left. The right wheel has a positive speed, and the speed of the left wheel is zero, the robot can turn right. When the speed of the two wheels is zero, the robot can stop.

The robot has six ultrasonic sensors. These ultrasonic sensors are fixed around the robot. It is important for us to insure that the robot does not crash the obstacles. When the obstacles are in the range, the sensors detect for the robot can stop and send the warning to the robot.

5 The Video Transmission

As shown in Fig. 6, we can see that the mobile phone plays the real-time video directly. We can control the mobile robot remotely by seeing the real-time video. The quality of the real-time video transmission is so important for us to control the

mobile robot remotely. In this experiment, the transmission of the video is based on the RTP/RTCP protocol. We use the H.264 compression algorithm to deal with the video. When the mobile phone receives the video data, it should be decompressed as the compression sequence. The mobile phone can display the video on the mobile phone after the video is decompressed.

We use the camera fixed on the robot to get the video. The robot can display the video on the computer screen. The robot can translate the video to the mobile phone at the same time.

We use the H.264 compression algorithm to deal with the video data. In this paper, we use the RTP protocol to translate the real-time video to the mobile phone. My mobile phone can display the video on the screen.

6 Conclusions

In this chapter, we learnt that how we can use our mobile phone to control the mobile phone remotely. We have also seen that the real-time video can be translated from the robot on the mobile phone. Even though we have faced many problems in the early stages, they are resolved in the end.

References

1. Fang X, Xi ZW (2009) Our country family service robot industry development present situation investigate report. Robot Tech Appl 2
2. Fong T, Nourbakhsh I (2005) Interaction challenges in human-robot space exploration. Interactions 12:42–45
3. Podnar G, Dolan J, Elfes A, Bergerman M, Brown HB, Guisewite AD (2005) Human telesupervision of a fleet of autonomous robots for safe and efficient space exploration. In: Proceedings of the 1st ACM SIGCHI/SIGART conference on human-robot interaction, Salt Lake City, Utah, USA
4. Nadvornik J, Smutny P (2014) Remote control robot using android mobile device. In: 2014 15th International Carpathian control conference (ICCC), 2014
5. Li H, Dai Z (2010) A semiautonomous sprawl robot based on remote wireless control. Robot Biomimetics—ROBIO
6. Ryu JG, Shin HM, Kil SK et al (2006) Design and implementation of real-time security guard robot using CDMA network[C]. In: Advanced communication technology, 2006. ICACT2006. The 8th international conference. IEEE, 2006, vol 3:6, pp 1906
7. Slany W (2012) A mobile visual programming system for android smartphones and tablets [C]. In: Symposium on visual languages and human-centric computing: poster and demos. IEEE, pp 265–266
8. Bodenstein C, Tremer M, Overhoff J et al (2015) A smartphone-controlled autonomous robot [C]. In: The 12th international conference on fuzzy systems and knowledge discovery (FSKD), 2015, pp 2314–2321

9. Wang Q, Pan W, Li M (2014) Robot's remote real-time navigation controlled by smart phone. In: 2012 IEEE international conference on robotics and biomimetics (ROBIO), China, 2014
10. Zhi-Hui D, Yun-hang Z (2014) The design and implement of household robot based on android platform. In: IEEE workshop on advanced research and technology in industry applications, pp 449–52
11. Kofman J, Xianghai W, Luu TJ, Verma S (2005) Teleoperation of a robot manipulator using a vision-based human-robot interface. IEEE Trans Ind Electron 52(5):1206–1219

Adaptive Neural Output Feedback Control for Flexible-Joint Robotic Manipulators

Lingjie Gao, Qiang Chen and Linlin Shi

Abstract In this chapter, an adaptive neural output feedback control scheme is proposed for flexible-joint robotic manipulators. First, the mathematical model of a robotic manipulator is built with considering flexible joints. Then, a Luenberger state observer is employed to estimate the unknown states such that the constriction that all the states should be available for measurements can be relaxed. In order to achieve a satisfactory tracking performance, an adaptive controller is designed by combining neural network control and dynamic surface control techniques to avoid the so-called "explosion of complexity" problem. With the proposed scheme, the tracking error can be guaranteed to converge to a small neighborhood around zero, and simulation results show the effectiveness of the developed method.

Keywords Flexible-joint system · Adaptive neural control · State observer

1 Introduction

Over the past decades, electromechanical servo system has been widely studied, such as robotic manipulators, motor servo system, and so on [1–3]. As a popular automatic equipment, robotic manipulators have attracted considerable attention and been widely applied to the field of industrial automation [4, 5]. Since the existence of the inferior flexibility may affect the practical control precision, the joint flexibility should be taken into account in both modeling and control of manipulators, in which torsional elasticity is introduced [6].

L. Gao · Q. Chen (✉)
College of Information Engineering, Zhejiang University of Technology, Hangzhou 310023, China
e-mail: sdnjchq@zjut.edu.cn

L. Shi
College of Electrical Engineering, Zhejiang University, Hangzhou 310007, China

Y. Jia et al. (eds.), *Proceedings of 2016 Chinese Intelligent Systems Conference*, Lecture Notes in Electrical Engineering 404, DOI 10.1007/978-981-10-2338-5_58

So far, many significant researches have been presented to handle the issue of joint flexibility to achieve a better tracking performance. In [6], an adaptive state feedback controller for flexible-joint manipulators is presented using the back-stepping technique. However, when some states are immeasurable, the above-mentioned researches may not be applied directly. In [7], an extended state observer-based control scheme is developed for trajectory tracking of flexible-joint robotic manipulators with partially known model. Therefore, the control task of the flexible-joint robotic manipulators with immeasurable states and model uncertainties is still a challenging work.

In this paper, an adaptive neural output feedback control scheme is presented for the tracking control of flexible-joint manipulators with immeasurable states and model uncertainties. The unknown states are estimated using a Luenberger state observer, and the output feedback controller is designed based on the estimated states and dynamic surface control technique. Moreover, the model uncertainties of the system are approximated by employing radial basis function (RBF) neural networks. The position tracking error is proven to converge to a small neighborhood around zero via the Lyapunov synthesis.

2 System Description

As shown in Fig. 1, the considered single-link robotic manipulator system taken from [6] is expressed as

$$\begin{cases} I\ddot{q}_1 + K(q_1 - q_2) + MgL\sin(q_1) = 0 \\ J\ddot{q}_2 - K(q_1 - q_2) = u \end{cases} \tag{1}$$

where q_1 and q_2 are the angles of the link and motor, respectively, g is the acceleration of gravity, I is the link inertia, J is the inertia of the motor, K is the spring stiffness, M and L are the mass and length of link, respectively, and u is the input torque.

For the purpose of simplifying the controller design, define $x_1 = q_1$, $x_2 = \dot{q}_1 = \dot{x}_1$, $x_3 = q_2$, and $x_4 = \dot{q}_2 = \dot{x}_3$ and the system (1) can be transformed into

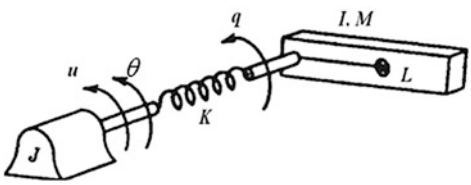

Fig. 1 Schematic of flexible-joint manipulator

$$\begin{cases} \dot{x}_1 = x_2 + f_1(X) \\ \dot{x}_2 = x_3 + f_2(X) \\ \dot{x}_3 = x_4 + f_3(X) \\ \dot{x}_4 = \frac{1}{J}u + f_4(X) \\ y = x_1 \end{cases} \tag{2}$$

where $X = [x_1, x_2, x_3, x_4]^T \in R^4, f_1(X) = 0, f_2(X) = -\frac{MgL}{I}\sin x_1 - \frac{K}{I}\left(x_1 - x_3 + \frac{I}{K}x_3\right)$, $f_3(X) = 0$, and $f_4(X) = \frac{K}{J}(x_1 - x_3)$, the output y is measurable directly and states $x_t (t = 2, 3, 4)$ are immeasurable.

Rewrite (2) in the following form:

$$\dot{X} = AX + F(X) + Bu + Ly \tag{3}$$

where $\mathrm{A} = \begin{bmatrix} L_3 & I_3 \\ l_4 & 0_{1\times 3} \end{bmatrix}$, $L_3 = [l_1, l_2, l_3]^T$, $\mathrm{B} = \left[0, 0, 0, \frac{1}{J}\right]^T$, and $\mathrm{F}(X) = [f_1(X), f_2(X), f_3(X), f_4(X)]^T$.

The parameters $l_i (i = 1, 2, 3, 4)$ are chosen such that the characteristic polynomial of matrix A is strictly Hurwitz, and the control objective is to design the controller u such that the output y follows the desired position trajectory y_r.

3 Observer Design

Consider the following observer that estimates the immeasurable state variables X in (3)

$$\dot{\hat{X}} = A\hat{X} + F(\hat{X}) + Bu + Ly \tag{4}$$

where $\hat{X} = [\hat{x}_1, \hat{x}_2, \hat{x}_3, \hat{x}_4]^T$ and $\hat{x}_i$ are the estimation of x_i,

$$\begin{aligned} &F(\hat{X}) = \left[f_1(\hat{X}), f_2(\hat{X}), f_3(\hat{X}), f_4(\hat{X})\right]^T, && f_1(\hat{X}) = 0, \\ &f_2(\hat{X}) = -\frac{MgL}{I}\sin\hat{x}_1 - \frac{K}{I}\left(\hat{x}_1 - \hat{x}_3 + \frac{I}{K}\hat{x}_3\right), && f_3(\hat{X}) = 0, \\ &f_4(\hat{X}) = l_4(x_1 - \hat{x}_1) + \frac{K}{J}(\hat{x}_1 - \hat{x}_3). \end{aligned}$$

Let $e_i = x_i - \hat{x}_i (i = 1, 2, 3, 4)$ be the observer error. From (3) and (4), the observer-error equation can be expressed as follows:

$$\dot{E} = AE + F(\mathrm{X}) - \mathrm{F}(\hat{X}), \tag{5}$$

where $\mathrm{E} = [e_1, e_2, e_3, e_4]^T$.

Construct the following Lyapunov function candidate

$$V_e = E^T P E \tag{6}$$

where $P = P^T > 0$.

In view of (5), the time derivative of V_e is

$$\dot{V}_e = E^T (A^T P + PA) E + 2E^T P\left[F(\mathrm{X}) - \mathrm{F}\left(\hat{X}\right)\right]. \tag{7}$$

According to the mean-value theorem, the term $2E^T P\left[F(\mathrm{X}) - \mathrm{F}(\hat{X})\right]$ can be transformed into

$$2E^T P\left[\mathrm{F}(X) - \mathrm{F}(\hat{X})\right] = E^T \left[P\frac{\partial F}{\partial x} + \left(\frac{\partial F}{\partial x}\right)^T P\right] E \tag{8}$$

where $\frac{\partial F}{\partial x}$ is a Jacobin matrix with its element at the of ith row and the jth column being $\frac{\partial f_i}{\partial x_j}$.

Substitute (8) into (7) and choose a proper matrix A such that and we have

$$\dot{V}_e \leq E^T \left[PA + A^T P + P\frac{\partial F}{\partial x} + \left(\frac{\partial F}{\partial x}\right)^T P + I\right] E < 0. \tag{9}$$

4 Controller Design and Stability Analysis

In this section, an adaptive neural control scheme is developed for flexible-joint robotic manipulators (2) based on the observer (4) and dynamic surface control technique. The whole control process includes the following steps.

Step 1:

Define the tracking error $s_1 = y - y_r$ and differentiating s_1 yields

$$\dot{s}_1 = \dot{y} - \dot{y}_r = \hat{x}_2 + e_2 - \dot{y}_r. \tag{10}$$

Consider the Lyapunov function candidate $V_1 = \frac{1}{2}s_1^2$, whose time derivative is

$$\dot{V}_1 = \dot{s}_1 s_1 = s_1(\hat{x}_2 - \dot{y}_r) + s_1 e_2. \tag{11}$$

Applying Young's inequality $2\mathrm{ab} \leq a^2 + b^2$, we can obtain the following inequality

$$s_1 e_2 \le \frac{1}{2}s_1^2 + \frac{1}{2}e_2^2 \le \frac{1}{2}s_1^2 + \frac{1}{2}E^T E. \tag{12}$$

By regarding $\hat{x}_2$ is a virtual control input, we choose $\alpha_1 \triangleq \hat{x}_2$ as intermediate control input as follows:

$$\alpha_1 = -(c_1 + 0.5)s_1 + \dot{y}_r \tag{13}$$

where $c_1 > 0$ is a positive parameter.

To avoid the problem of "explosion of complexity" in [6], we introduce a state variable z_2 and let α_1 pass through a first-order filter with a time constant $\tau_2 > 0$ as follows:

$$\tau_2 \dot{z}_2 + z_2 = \alpha_1,\ z_2(0) = \alpha_1(0). \tag{14}$$

Define the output error of the first-order filter as

$$\chi_2 = z_2 - \alpha_1 \tag{15}$$

From (11) to (15), we can obtain

$$\dot{V}_1 \le s_1 s_2 + s_1 \chi_2 - c_1 s_1^2 + \frac{1}{2}E^T E \tag{16}$$

where $s_2 = \hat{x}_2 - z_2$.

Step 2:

The time derivative of s_2 is

$$\dot{s}_2 = \dot{\hat{x}}_2 - \dot{z}_2 = \hat{x}_3 + l_2(x_1 - \hat{x}_1) - \dot{z}_2 + \hat{f}_2 \tag{17}$$

where the uncertainty $\hat{f}_2$ is approximated by the following neural network

$$\hat{f}_2 = W^* \varphi(Z) + \varepsilon_2 \tag{18}$$

where $Z = \left[\hat{x}_1^T, \hat{x}_3^T\right]^T \in R^2$ is the input vector, $W^* = [w_1, \ldots, w_L]^T \in R^L$ is the ideal weight matrix, and ε_2 is the bounded approximation error satisfying $|\varepsilon_2| \le \varepsilon_{N2}^*$ with ε_{N2}^* being a positive constant, the NN node number $L > 1 \varphi(Z) = [\varphi_1(Z), \ldots, \varphi_5(Z)]$ with $\varphi_i(Z)$ commonly being used as the Gaussian function, which is in the following form

$$\varphi_i(Z) = exp\left[\frac{-\|Z - c_j^2\|}{b_j^2}\right] (i = 1, 2, \ldots, n; j = 1, 2, \ldots, \mathrm{L}) \tag{19}$$

where the input of NN $n>1$, $c_j=[c_{11},c_{12},\ldots,c_{1L}]^T$ and b_j are the center of the receptive field and the width of the Gaussian function, respectively.

Construct the following Lyapunov function:

$$V_2=\frac{1}{2}s_2^2+\frac{1}{2}\chi_2^2+\frac{1}{2\gamma_2}\tilde{W}^T\tilde{W}+\frac{1}{2\eta_2}\tilde{\varepsilon}_{N2}^2 \tag{20}$$

where γ_2 and η_2 are positive parameters, $\tilde{W}=W^*-\hat{W}$ and $\tilde{\varepsilon}_{N2}=\varepsilon_{N2}^*-\hat{\varepsilon}_{N2}$, $\hat{W}$ and $\hat{\varepsilon}_{N2}$ are the estimations of W^* and ε_{N2}^*, respectively.

In view of (14) and (15), we can obtain

$$\dot{\chi}_2=\dot{z}_2-\dot{\alpha}_1=-\frac{\chi_2}{\tau_2}+B_2(s_1,s_2,\chi_2,y_r,\dot{y}_r,y_r) \tag{21}$$

where the function of B_2 satisfies $|B_2|\le M_2$ and M_2 is a positive parameter.

Set the virtual input α_2 as

$$\alpha_2=-l_2e_1-\hat{W}\varphi(Z)+\dot{z}_2-c_2s_2-\hat{\varepsilon}_{N2}\tanh\left(\frac{s_2}{\delta_2}\right) \tag{22}$$

where c_2 and δ_2 are positive parameters.

Similarly, introduce a new state variable z_3 and let α_2 pass through a first-order filter with a time constant $\tau_3>0$ as follows:

$$\tau_3\dot{z}_3+z_3=\alpha_2,\quad z_3(0)=\alpha_2(0). \tag{23}$$

Define the output error of the first-order filter as

$$\chi_3=z_3-\alpha_2. \tag{24}$$

From (14) and (15), we can obtain the derivative of V_2

$$\begin{aligned}\dot{V}_2\le{}&s_2(s_3+\chi_3)-c_2s_2^2-\frac{\chi_2^2}{\tau_2}+\frac{\sigma_2}{\gamma_2}\tilde{W}^T\hat{W}+\chi_2B_2+\varepsilon_{N2}^*\left[|s_2|-s_2\tanh\left(\frac{s_2}{\delta_2}\right)\right]\\&+\varepsilon_{N2}^*s_2\tanh\left(\frac{s_2}{\delta_2}\right)-\hat{\varepsilon}_{N2}s_2\tanh\frac{s_2}{\delta_2}-\frac{1}{\eta_2}\tilde{\varepsilon}_{N2}\dot{\hat{\varepsilon}}_{N2}\end{aligned} \tag{25}$$

where $s_3=\hat{x}_3-z_3$.

The adaptive laws of $\hat{W}$ and $\hat{\varepsilon}_{N2}$ are given as

$$\begin{cases}\dot{\hat{W}}=r_2s_2\varphi_2(Z)-\sigma_2\hat{W}\\ \dot{\hat{\varepsilon}}_{N2}=\eta_2s_2\tanh\left(\frac{s_2}{\delta_2}\right)\end{cases} \tag{26}$$

where r_2, σ_2, and δ_2 are positive parameters.

Then, use the facts

$$0 \le |x| - x \tanh\left(\frac{x}{\delta}\right) \le 0.2785\delta \tag{27}$$

and

$$\frac{\sigma_2}{\gamma_2}\tilde{W}^T\hat{W} = \frac{\sigma_2}{\gamma_2}\tilde{W}^T\left(W^* - \tilde{W}\right) \le -\frac{\sigma_2\|\tilde{W}^2\|}{2\gamma_2} + \frac{\sigma_2\|W^{*2}\|}{2\gamma_2} \tag{28}$$

Substitute (26)–(28) into (25), and we have

$$\dot{V}_2 \le s_2(s_3 + \chi_3) - c_2 s_2^2 - \frac{\chi_2^2}{\tau_2} + \chi_2 B_2 + 0.2785\delta_2\varepsilon_{N2}^* + \frac{\sigma_2\|W^{*2}\|}{2\gamma_2}. \tag{29}$$

Step 3:

Following the similar procedures of the Step 2, consider the following Lyapunov function candidate

$$V_3 = \frac{1}{2}s_3^2 + \frac{1}{2}\chi_3^2 \tag{30}$$

and set the virtual input α_3 as

$$\alpha_3 = -l_2 e_1 + \dot{z}_3 - c_3 s_3 \tag{31}$$

where c_3 is a positive parameter.

Then, we can obtain

$$\dot{V}_3 \le s_3(s_4 + \chi_4) - c_3 s_3^2 - \frac{\chi_3^2}{\tau_3} + \chi_3 B_3 \tag{32}$$

where $s_4 = \hat{x}_4 - z_4$, $\chi_3 = z_3 - \alpha_1$, and the function of B_3 satisfies $|B_3| \le M_3$ with M_3 being a positive parameter.

Step 4:

Similarly, the following neural network is utilized to approximate the nonlinear uncertainty $\hat{f}_4$

$$\hat{f}_4 = \theta^* \varphi(Z) + \varepsilon_4 \tag{33}$$

where $\theta^* = [\theta_1, \ldots, \theta_5]^T \in R^5$ is the ideal weight matrix and ε_4 is the bounded approximation error satisfying $|\varepsilon_4| \le \varepsilon_{N4}^*$ with ε_{N4}^* being a positive constant.

Construct the following Lyapunov function candidate

$$V_4 = \frac{1}{2}s_4^2 + \frac{1}{2}\chi_4^2 + \frac{1}{2\gamma_4}\theta^T\theta + \frac{1}{2\eta_4}\tilde{\varepsilon}_{N4}^2 \tag{34}$$

where γ_4 and η_4 are positive parameters, $\tilde{\theta} = \theta^* - \hat{\theta}$ and $\tilde{\varepsilon}_{N4} = \varepsilon_{N4}^* - \hat{\varepsilon}_{N4}$, $\hat{\theta}$ and $\hat{\varepsilon}_{N4}$ are the estimations of θ^* and ε_{N4}^*, respectively.

The control law u is designed as

$$u = -\mathrm{J}\left[l_4 e_1 + \hat{\theta}\varphi(Z) - \dot{z}_4 - c_4 s_4 - \hat{\varepsilon}_{N4}\tanh\left(\frac{s_4}{\delta_4}\right)\right] \tag{35}$$

where c_4 and δ_4 are positive constants, and the adaptive laws of $\hat{\theta}$ and $\hat{\varepsilon}_{N4}$ are

$$\begin{cases} \dot{\hat{\theta}} = r_4 s_4 \varphi(Z) - \sigma_4 \hat{\theta} \\ \dot{\hat{\varepsilon}}_{N4} = \eta_4 s_4 \tanh\left(\frac{s_4}{\delta_4}\right) \end{cases} \tag{36}$$

where r_4 are σ_4 are positive constants.

Differentiating (34) yields

$$\dot{V}_4 \le -c_4 s_4^2 - \frac{\chi_4^2}{\tau_4} + \chi_4 B_4 + 0.2785\delta_4\varepsilon_{N4}^* + \frac{\sigma_4\|\theta^{*2}\|}{2\gamma_4} \tag{37}$$

where the time constant $\tau_4 > 0$ and the function of B_3 satisfies $|B_3| \le M_3$ with M_3 being a positive parameter.

Finally, construct the following Lyapunov function candidate

$$\mathrm{V} = V_e + V_1 + V_2 + V_3 + V_4 \tag{38}$$

According to (9), (16), (29), (32), and (37), differentiate (39) with respect to time and we can obtain

$$\dot{V} \le -\sum_{k=1}^{4}\alpha_0 s_k^2 + 6\eta + 0.2785\left(\delta_2\varepsilon_{N2}^* + \delta_4\varepsilon_{N4}^*\right) + \frac{\sigma_2\|W^{*2}\|}{2\gamma_2} + \frac{\sigma_4\|\theta^{*2}\|}{2\gamma_4} \tag{39}$$

where α_0 and η are positive constants.

Consequently, all the signals of the closed-loop system are semiglobally uniformly bounded, and the output tracking error s_1 converges to a small neighborhood around zero on the condition that the parameters are chosen properly.

5 Simulation Results

In this section, simulation examples are carried out to show the feasibility and superiority of the proposed scheme. The sinusoidal wave $y_r = \sin t$ is adopted as the desired reference signal.

The initial conditions of the system are $[x_1, x_2, x_3, x_4]^T = [0, 0, 0, 0]^T$, $[\hat{x}_1, \hat{x}_2, \hat{x}_3, \hat{x}_4]^T = [0, 0.5, 0.5, 0.5]^T$, $\hat{\theta}_2 = \hat{\theta}_4 = [1, 1, 1, 1, 1, 1, 1]^T$, and $\hat{\varepsilon}_{N2} = \hat{\varepsilon}_{N4} = 0.01$. The parameters of state observer are $\mathrm{L} = [12, 40, -6, -32]^T$. The control parameters are chosen as $c_1 = 4.5$, $c_2 = 3.5$, $c_3 = 2.5$, and $c_4 = 9$. The constants of adaptive laws are $r_2 = 0.2$, $r_4 = 0.2$, $\delta_2 = 0.3$, and $\sigma_2 = \sigma_4 = 0.01$. The time constants are $\tau_1 = 0.01$, $\tau_2 = 3$, and $\tau_3 = 2$. The RBF NN parameters are $c_{ij} = [-3 -2 -1 0 1 2 3]$ and $b_j = 0.5$. The system parameters are $\mathrm{MgL} = 5$, $\mathrm{I} = 1$, $\mathrm{J} = 1$, and $\mathrm{K} = 40$. The simulation results are shown by Figs. 2, 3, 4, 5, 6, and 7.

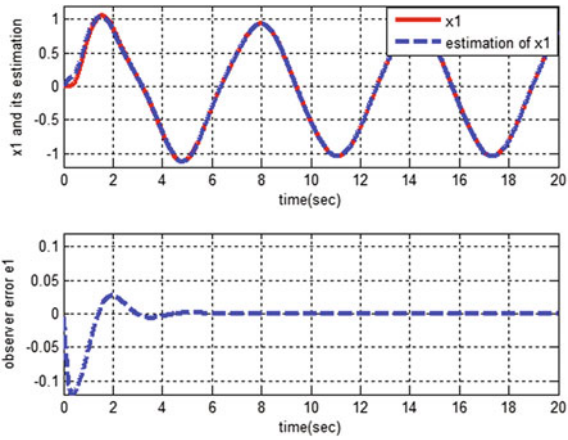

Fig. 2 State x_1 and its estimation $\hat{x}_1$

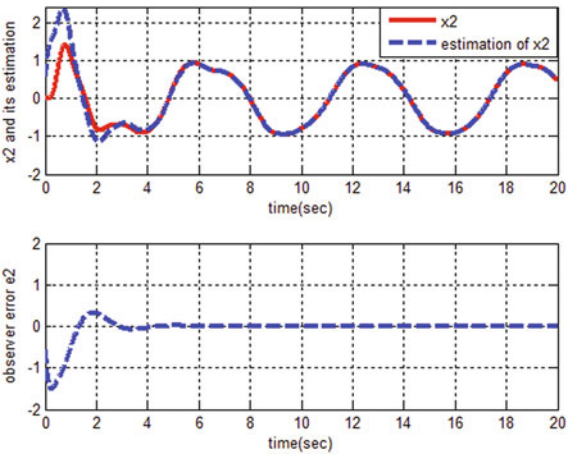

Fig. 3 State x_2 and its estimation $\hat{x}_2$

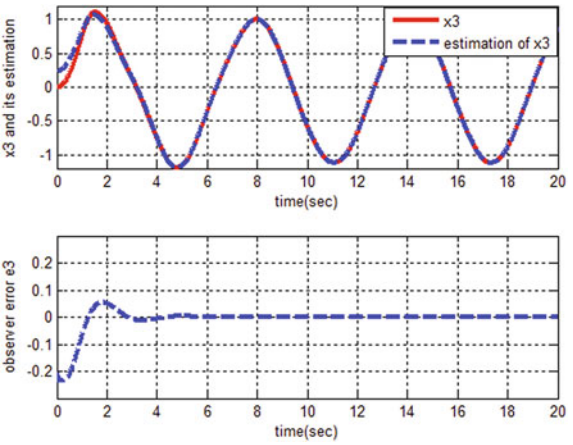

Fig. 4 State x_3 and its estimation $\hat{x}_3$

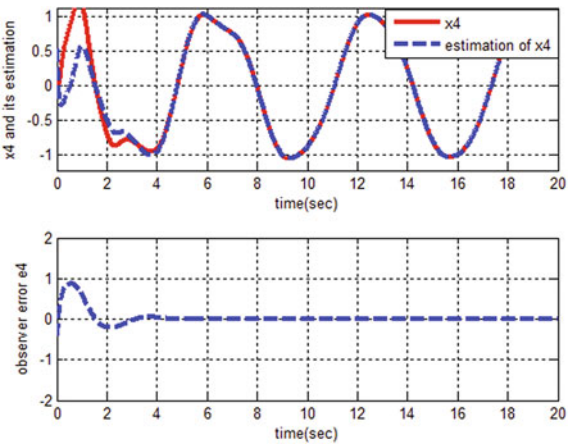

Fig. 5 State x_4 and its estimation $\hat{x}_4$

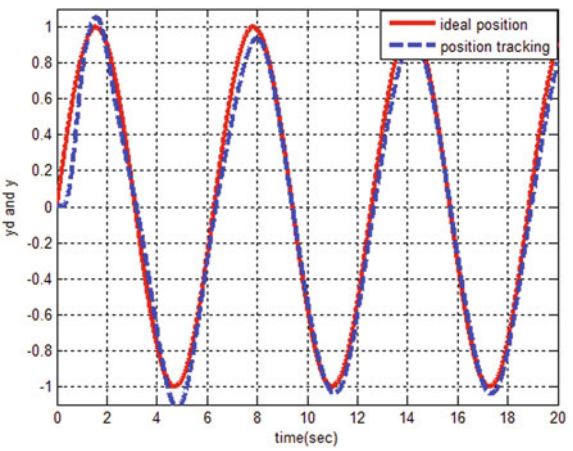

Fig. 6 Position tracking performance

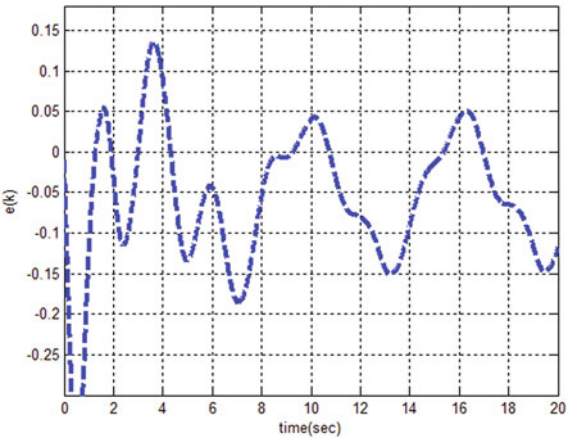

Fig. 7 Position tracking error

Figures 2, 3, 4, and 5 show the estimation performance of states $x_i(i = 1, 2, 3, 4)$ and corresponding errors e_i, respectively. We can clearly see that all the estimation states tracks actual states with a small observed errors. The tracking trajectory and tracking error are shown in Figs. 6 and 7, respectively. Obviously, the tracking error can converge to a small neighborhood around zero. From the aforementioned figures, it is clear that the proposed adaptive neural output feedback control scheme can achieve a good tracking performance for the system (2) with immeasurable states.

6 Conclusion

In this paper, an adaptive neural output feedback control scheme is investigated for single-link flexible-joint robotic manipulator systems with immeasurable states. The immeasurable states are estimated by constructing a Luenberger state observer, and model uncertainties are approximated by using RBF neural networks. Based on the dynamic surface control scheme, the adaptive controller is designed to avoid the problem of "explosion of complexity." Simulation results illustrate that the proposed method is effective to achieve a good tracking performance.

Acknowledgments This work is supported by National Natural Science Foundation (NNSF) of China under Grant No. 61403343, China Postdoctoral Science Foundation Funded Project Under Grant No. 2015M580521 and 12th Five-Year Plan Construction Project of Emerging University Characteristic Specialty (No. 080601).

References

1. Oh JH, Lee JS (1997) Control of flexible joint robot system by backstepping design approach. Intell Autom Soft Comput 4(4):267–278
2. Na J, Mahyuddin MN, Herrmann G, Ren XM, Barber P (2015) Robust adaptive finite-time parameter estimation and control for robotic systems. Int J Robust Nonlinear Control 25 (16):3045–3071
3. Na J, Chen Q, Ren XM, Guo Y (2014) Adaptive prescribed performance motion control of servo mechanisms with friction compensation. IEEE Trans Industr Electron 61(1):486–494
4. Liu C, Cheah CC, Slotine JJ (2006) Adaptive Jacobian tracking control of rigid-link electrically driven robots based on visual task-space information. Automatica 42(9):1491–1501
5. Huang AC, Chen YC (2004) Adaptive sliding control for single-link flexible-joint robot with mismatched uncertainties. IEEE Trans Control Syst Technol 12(5):770–775
6. Tang XQ, Chen Q, Nan YR et al (2015) Backstepping funnel control for prescribed performance of robotic manipulators with unknown dead zone. In: 27th Chinese control and decision conference, Qingdao, 23–25 May 2015
7. Talole SE, Kolhe JP, Phadke SB (2010) Extended-state-observer-based control of flexible-joint system with experimental validation. IEEE Trans Industr Electron 57(4):1411–1419